frontiers | Research Topics

Nanoscience editor's pick

2024

Edited by
Zoe Pikramenou

Published in
Frontiers in Chemistry

ISSN 1664-8714
ISBN 978-2-8325-5803-4
DOI 10.3389/978-2-8325-5803-4

About Frontiers

Frontiers is more than just an open access publisher of scholarly articles: it is a pioneering approach to the world of academia, radically improving the way scholarly research is managed. The grand vision of Frontiers is a world where all people have an equal opportunity to seek, share and generate knowledge. Frontiers provides immediate and permanent online open access to all its publications, but this alone is not enough to realize our grand goals.

Frontiers journal series

The Frontiers journal series is a multi-tier and interdisciplinary set of open-access, online journals, promising a paradigm shift from the current review, selection and dissemination processes in academic publishing. All Frontiers journals are driven by researchers for researchers; therefore, they constitute a service to the scholarly community. At the same time, the *Frontiers journal series* operates on a revolutionary invention, the tiered publishing system, initially addressing specific communities of scholars, and gradually climbing up to broader public understanding, thus serving the interests of the lay society, too.

Dedication to quality

Each Frontiers article is a landmark of the highest quality, thanks to genuinely collaborative interactions between authors and review editors, who include some of the world's best academicians. Research must be certified by peers before entering a stream of knowledge that may eventually reach the public - and shape society; therefore, Frontiers only applies the most rigorous and unbiased reviews. Frontiers revolutionizes research publishing by freely delivering the most outstanding research, evaluated with no bias from both the academic and social point of view. By applying the most advanced information technologies, Frontiers is catapulting scholarly publishing into a new generation.

What are Frontiers Research Topics?

Frontiers Research Topics are very popular trademarks of the *Frontiers journals series*: they are collections of at least ten articles, all centered on a particular subject. With their unique mix of varied contributions from Original Research to Review Articles, Frontiers Research Topics unify the most influential researchers, the latest key findings and historical advances in a hot research area.

Find out more on how to host your own Frontiers Research Topic or contribute to one as an author by contacting the Frontiers editorial office: frontiersin.org/about/contact

Nanoscience editor's pick 2024

Topic editor
Zoe Pikramenou — University of Birmingham, United Kingdom

Citation
Pikramenou, Z., ed. (2024). *Nanoscience editor's pick 2024*.
Lausanne: Frontiers Media SA. doi: 10.3389/978-2-8325-5803-4

Table of contents

frontiers | Frontiers in Chemistry

TYPE Original Research
PUBLISHED 04 January 2023
DOI 10.3389/fchem.2022.1102920

OPEN ACCESS

EDITED BY
Chiara Cappelli,
Scuola Normale Superiore, Italy

REVIEWED BY
Jiani Qin,
Shaanxi University of Science and Technology, China
Feng-Ming Zhang,
Harbin University of Science and Technology, China

*CORRESPONDENCE
Ayman H. Zaki,
✉ ayman.zaki@psas.bsu.edu.eg

SPECIALTY SECTION
This article was submitted to Nanoscience,
a section of the journal
Frontiers in Chemistry

RECEIVED 19 November 2022
ACCEPTED 12 December 2022
PUBLISHED 04 January 2023

CITATION
Abdel Aziz YS, Sanad MMS, Abdelhameed RM and Zaki AH (2023), *In-situ* construction of Zr-based metal-organic framework core-shell heterostructure for photocatalytic degradation of organic pollutants.
Front. Chem. 10:1102920.
doi: 10.3389/fchem.2022.1102920

In-situ construction of Zr-based metal-organic framework core-shell heterostructure for photocatalytic degradation of organic pollutants

Yasmeen S. Abdel Aziz[1], Moustafa M. S. Sanad[2], Reda M. Abdelhameed[3] and Ayman H. Zaki[4,5]*

[1]National Institute of Oceanography and Fisheries (NIOF), Cairo, Egypt, [2]Central Metallurgical Research and Development Institute, (CMRDI), Cairo, Egypt, [3]Applied Organic Chemistry Department, Chemical Industries Research Institute, National Research Centre, Giza, Egypt, [4]Materials Science and Nanotechnology Department, Faculty of Postgraduate Studies for Advanced Sciences, Beni-Suef University, Beni Suef, Egypt, [5]International Center for Materials Nanoarchitechtonics (WPI-MANA), National Institute for Materials Science, Tsukuba, Japan

Photocatalysis is an eco-friendly promising approach to the degradation of textile dyes. The majority of reported studies involved remediation of dyes with an initial concentration ≤50 mg/L, which was away from the existing values in textile wastewater. Herein, a simple solvothermal route was utilized to synthesize $CoFe_2O_4$@UiO-66 core-shell heterojunction photocatalyst for the first time. The photocatalytic performance of the as-synthesized catalysts was assessed through the photodegradation of methylene blue (MB) and methyl orange (MO) dyes at an initial concentration (100 mg/L). Under simulated solar irradiation, improved photocatalytic performance was accomplished by as-obtained $CoFe_2O_4$@UiO-66 heterojunction compared to bare UiO-66 and $CoFe_2O_4$. The overall removal efficiency of dyes (100 mg/L) over $CoFe_2O_4$@UiO-66 (50 mg/L) reached >60% within 180 min. The optical and photoelectrochemical measurements showed an enhanced visible light absorption capacity as well as effective interfacial charge separation and transfer over $CoFe_2O_4$@UiO-66, emphasizing the successful construction of heterojunction. The degradation mechanism was further explored, which revealed the contribution of holes (h^+), superoxide ($\bullet O_2^-$), and hydroxyl ($\bullet$OH) radicals in the degradation process, however, h^+ were the predominant reactive species. This work might open up new insights for designing MOF-based core-shell heterostructured photocatalysts for the remediation of industrial organic pollutants.

KEYWORDS

photocatalysis, MOFs, ferrite, core-shell, visible light, dyes

1 Introduction

Among various industrial sectors, the textile industry takes prominence due to the high utilization of water, raw materials, and chemicals including acids, chelating and bleaching agents, dyes, surfactants, *etc.* As a consequence, tremendous volumes of wastewater are released from this industry. It is estimated that 20% of global industrial wastewater emerges merely from textile industries (Holkar et al., 2016). In general, the textile effluent is characterized by high pH, intense color, high chemical and biochemical oxygen demands (COD and BOD5, respectively), and high concentrations of total suspended and dissolved solids (Yaseen and Scholz, 2019). Nevertheless, the composition of such effluents varies considerably in concentration and toxicity depending on the utilized chemicals, operating conditions, and the employed manufacturing steps (Ramos et al., 2021). Approximately 700,000 tons of synthetic dyes are produced annually and around 30% of this dyestuff ends up as industrial effluent (Al-Mamun et al., 2019). Owing to their complex aromatic structure and non-biodegradable nature, most of these dyes may present carcinogenic and/or mutagenic potentials to human health and aquatic ecosystem (Nidheesh et al., 2013; Dihom et al., 2022). Hence, efficient treatment of textile wastewater before discharge into water bodies has become of crucial importance.

Inspired by the natural photosynthesis process, photocatalysis has currently emerged as a promising green approach for the conversion of solar energy into chemical energy (Gao et al., 2017). Due to its high efficiency, feasibility, low energy consumption, and eco-friendly feature, semiconductor-induced photocatalysis has been successfully harnessed in diverse applications including energy storage and conversion (Wei et al., 2021; Han et al., 2022; Qin et al., 2022), CO_2 reduction (Li et al., 2020; Xiong et al., 2020), organic synthesis (Zhang et al., 2019b; Xiong and Tang, 2021), Cr(VI) reduction (Yi et al., 2019; Zhang et al., 2020) and water treatment (Zeng et al., 2018; Feng et al., 2022; Shi et al., 2022). Up to present, several semiconductor photocatalysts have been intensively studied such as metal oxides [TiO_2, ZnO, Fe_2O_3 (Ba-Abbad et al., 2013; Franking et al., 2013; Kreft et al., 2020)], metal sulphides [MoS_2, CdS, In_2S_4 (Ning et al., 2019; Liang et al., 2021; Pan et al., 2021)], and organic semiconductors [(g-C_3N_4, perylene diimide, covalent organic framework (Zhou et al., 2018; Sivula, 2020; Zhou et al., 2021)]. Nevertheless, the photocatalytic performance of these catalysts is far unsatisfactory owing to various limitations like photocorrosion, low photon absorption efficiency, inefficient charge separation, most importantly; deficiency of effective and stable catalytic sites to maintain dynamic photocatalytic reactions (Gao et al., 2017).

As a distinct group of organic-inorganic hybrid crystalline porous materials, metal-organic frameworks (MOFs) have shown considerable potential in a variety of applications involving adsorption, drug delivery, gas storage and separation, and catalysis (Lei et al., 2018; Wang et al., 2020a; Wang et al., 2020b; Connolly et al., 2020; Younes et al., 2022). Due to their distinguished features such as tunable pore structure, high specific surface area with abundant catalytic active sites, and adjustable electronic and optical properties, MOFs have recently perceived unparalleled progress in the field of photocatalysis (Qin et al., 2020; Xia et al., 2021). Unlike conventional photocatalysts, MOFs are characterized by a special charge transition mechanism, where, the electronic states are localized, reducing the transmission distance of photoinduced carriers (Liang et al., 2019; Zhang et al., 2021c). Upon light illumination, the organic linkers, as light-absorbing antennas, and metal clusters, as semiconductor quantum dots, are excited to generate electron-hole pairs (Dey and Gogate, 2021). Consequently, several photo-excitation pathways are proposed to explore the photon harvesting process in MOF-based photocatalysts such as metal-to-ligand charge transfer (MLCT), metal-to-metal-to-ligand charge transfer (MMLCT), ligand-to-metal charge transfer (LMCT), and ligand-to-ligand charge transfer (LLCT) (Wen et al., 2019).

Beyond other reported MOF's, zirconium Zr(IV)-based MOFs (e.g. UiO-66), have drawn tremendous interest because of their superb thermal and chemical stability even in acidic and some basic mediums, which is mostly attributed to the robust interaction between Zr-O clusters and carboxylate ligands (Yuan et al., 2018; Yuan et al., 2021). Hence, Zr-MOFs have emerged as an exciting class for photocatalytic potential applications in an aqueous environment (Zhang et al., 2021d; Zhang et al., 2021c). However, the photocatalytic performance of UiO-66(Zr) still does not reach the utmost level due to its relatively wide bandgap energy (~3.8 eV). Thus, UiO-66 can only absorb light in the ultraviolet region (3–4%), leaving more than 90% of the solar spectrum unutilized. This in turn, results in a low photoconversion efficiency and limits the practical application of UiO-66 photocatalyst for solar light harvesting (Cheng et al., 2016; Gao et al., 2017). To fulfill the sustainable development concepts, several approaches have been embraced for promoting the photocatalytic efficiency of UiO-66(Zr) including bandgap engineering (Taddei et al., 2019), element doping (Qiu et al., 2019), ligand functionalization (Wang et al., 2021c), active site regulation (Shen et al., 2015b), *etc.* Interestingly, the construction of heterojunction structures has been reported as one of the most prospective strategies to boost the photocatalytic performance of Zr-MOFs through the formation of an interface between the two semiconductors (Subudhi et al., 2020; Zhang et al., 2021b). This intimate interfacial contact, in turn, favors accelerated charge transfer and boosts solar energy exploitation by modulating the band gap energy to attain the utmost photocatalytic efficiency (Jabbar and Graimed, 2022).

For example, Zhang et al. adopted facile adsorption and thermal conversion technique to encapsulate the α-Fe_2O_3 nanoclusters inside UiO-66 cavities for the construction of a visible light-driven α-Fe_2O_3@UiO-66 photocatalyst heterostructure for catalytic degradation of MB (Zhang et al., 2019a). Under visible light excitation, Fe_2O_3@UiO-66 displayed considerably boosted degradation performance. This prominent improvement of photoactivity of Fe_2O_3@UiO-66 could be explained by the synergetic interaction between UiO-66 and α-Fe_2O_3, which is beneficial to enhancing charge migration and lowering the recombination rate. Similarly, Yassin et al. prepared Ag_3PO_4/Zr-BDC/g-C_3N_4 ternary heterostructure for discoloration of MB under visible and solar irradiations (Yassin et al., 2022). Noteworthy, the UiO-66 bandgap energy is modulated from 3.72 eV to 2.91 eV in the Ag_3PO_4/Zr-BDC/g-C_3N_4 heterojunction, interpreting the effective absorption toward the visible spectrum. In comparison with pristine materials, Ag_3PO_4/Zr-BDC/g-C_3N_4 showed remarkably high degradation efficiency (95.0%) within 240 min under visible illumination, which might be credited to the spatial charge separation and prolonged carrier lifetime, confirmed by the significantly suppressed intensity of photoluminescence (PL) emission spectra. In addition, although numerous reports have revealed the splendid catalytic activity of Zr-MOF/metal oxide heterostructures for wastewater treatment, the high cost of some metal nanoparticles (e.g. noble metals), metal-ion leaching, and instability often restrict their practical applications (Zhang et al., 2021d; Mukherjee et al., 2022).

At present, cobalt ferrite ($CoFe_2O_4$), a spinel-type ferrite, has displayed marked potential as a versatile photocatalyst due to its facile synthesis, low cost, excellent magnetic anisotropy, high chemical stability, and narrow bandgap energy (~2.0 eV) with visible light absorption capacity (Mathew and Juang, 2007; Mmelesi et al., 2021). In a recent study, it has been reported complete degradation of ciprofloxacin within 45 min of visible-light irradiation by $CoFe_2O_4$/ZnO nanoheterojunction (Shawky and Alshaikh, 2022). The excellent photocatalytic activity of the composite is explicated by the notable decline in the bandgap after the incorporation of $CoFe_2O_4$ as well as the inhibition of charge-transport resistance through the formed p-n nanoheterojunction. In another study, Khosroshahi et al. designed a novel magnetic $CoFe_2O_4$/Ce-UiO-66 nanocomposite through a self-assembly approach for photocatalytic oxidation of aliphatic alcohols. Upon visible irradiation, the embedded composite demonstrated superior performance for selective oxidation of alcohols with a conversion ratio of 75%–90% compared to 21% and 10% conversion for $CoFe_2O_4$ and Ce-UiO-66, respectively (Khosroshahi et al., 2021). Despite the fact that the magnetic behavior of $CoFe_2O_4$ has been extensively investigated, studies on its optical and photoelectrochemical properties are still in infancy, particularly, with concerns for poor efficiency owing to the swift recombination of carriers under light irradiation and its relatively low specific surface area (Kefeni and Mamba, 2020; Görmez et al., 2022). Based on that, the construction of core-shell Zr-MOF-based composites has been recognized as an attractive approach to effectively promote photostability and enlarge the specific surface area, which is conducive to exposing more active sites in the photocatalytic reaction (Liu et al., 2021).

In this report, we successfully prepared a novel $CoFe_2O_4$@UiO-66 core-shell heterostructure photocatalyst *via* a simple solvothermal route for photodegradation of textile MB and MO dyes under simulated solar irradiation. Even though the initial concentration of dyes in actual textile wastewater samples has been recorded as higher than 100 mg/L, the majority of reported studies involved dye removal with an initial concentration of less than 50 mg/L (Mukherjee et al., 2022). Thus, dyes of 100 mg/L as an initial concentration were used in this study to provide realistic conditions similar to that in real textile wastewater. The crystallinity, surface composition, morphology, porosity, thermal stability, and optical and photo electrochemical properties of the prepared catalysts were investigated in detail. In addition, radical quenching experiments were applied to explore the possible photocatalytic mechanism.

2 Experimental

2.1 Materials

Zirconyl chloride ($ZrOCl_2.8H_2O$, 99%), 1,4-benzenedicarboxylic acid (H_2BDC) ($C_8H_6O_4$, 98%), and benzoquinone (*p*-BQ) ($C_6H_4O_2$, ≥98%) were purchased from Sigma-Aldrich cooperation. Ethylenediaminetetraacetic acid disodium salt (EDTA-2Na, $C_{10}H_{14}N_2Na_2O_8$. H_2O) and ammonium hydroxide (NH_4OH) were supplied by BioChem Chemopharma Co. *N,N*-dimethylformamide (DMF, 99.5%), acetic acid (CH_3COOH, ≥99%), and ethanol (C_2H_6O, ≥99.8%) were acquired from Carlo Erba Reagent Co, Ltd. 2-propanol (C_3H_8O, 99.7%) was provided by Merck. Methylene blue (MB, $C_{16}H_{18}ClN_3S$) and methyl orange (MO, $C_{14}H_{14}N_3NaO_3S$) were supplied by LOBA Chemie Pvt. Ltd. Ferric chloride ($FeCl_3$), cobalt (II) chloride hexahydrate ($CoCl_2.6H_2O$) were purchased from Oxford Lab Reagents Co. All reagents were of analytical grade and utilized without further purification. Deionized water was applied in the following experiments.

2.2 Preparation of photocatalysts

2.2.1 Synthesis of $CoFe_2O_4$

$CoFe_2O_4$ nanoparticles were prepared by the co-precipitation method (Esmat et al., 2017). Briefly, 2.0 mol of $FeCl_3$ and 1.0 mol of $CoCl_2.6H_2O$ were dispersed into 30 ml of deionized water. Following that, NH_4OH (1.0 M) was added dropwise until the pH reaches 10 and then left for complete precipitation. Afterward, the precipitate was collected *via* filtration, followed by washing it with deionized water. Subsequently, the precipitate

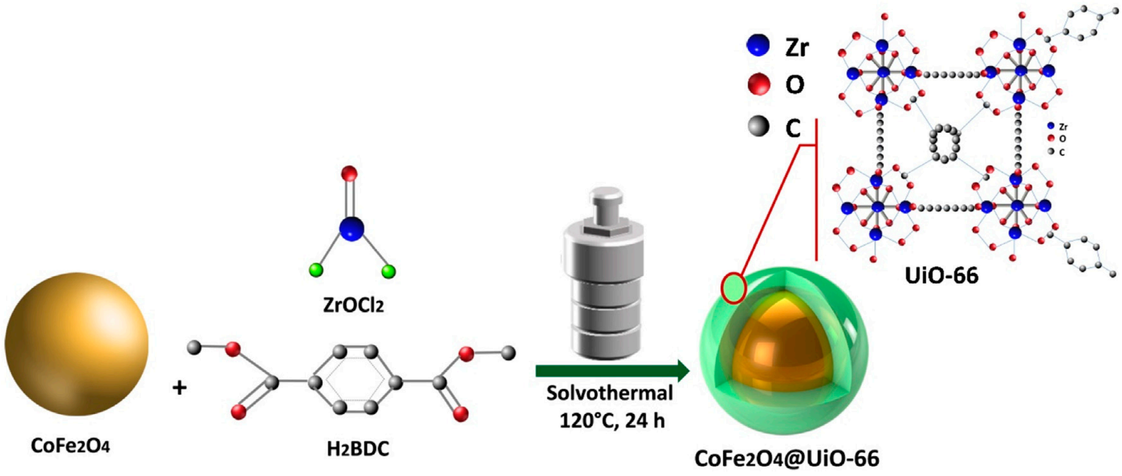

SCHEME 1
Schematic representation of $CoFe_2O_4$@UiO-66 composite preparation.

was air-dried at 100°C in a drying chamber. Lastly, the dried powder was calcined in a muffle furnace for 2 h at 500°C to get $CoFe_2O_4$ nanoparticles.

2.2.2 Synthesis of UiO-66

UiO-66 octahedrons were prepared through a modified scale-up procedure. Initially, 3.75 g of $ZrOCl_2$ and 3.7 g of H_2BDC were dispersed in 450 ml of DMF using ultrasonication for 60 min. Then, 20 ml of acetic acid was subsequently added to the mixture as a modulator to regulate the morphology of UiO-66. Next, the solution was poured into a 1,000 ml Teflon-lined stainless-steel reactor and heated for 24 h at 120°C. After cooling down, the white precipitate was obtained *via* filtration and washed meticulously several times with DMF and ethanol, respectively, to ensure the removal of any residual reactant. Finally, the UiO-66 nanoparticles were vacuum-dried for 12 h at 85°C.

2.2.3 Synthesis of $CoFe_2O_4$@UiO-66 composite

As illustrated in Scheme 1, a facile solvothermal method was adapted to prepare $CoFe_2O_4$@UiO-66 core-shell composite. Typically, 1.0 g of $CoFe_2O_4$ was dissolved in 450 ml DMF solution. Simultaneously, 3.75 g of $ZrOCl_2$ and 3.7 g of H_2BDC were dispersed in 20 ml of acetic acid. The prepared solutions were then mixed by ultrasonication for 60 min. Afterward, the homogenous solution was poured into a 1,000 ml Teflon-lined stainless-steel reactor and heated for 24 h at 120°C. After cooling down, the brown composite was separated and washed following the aforementioned washing process of UiO-66. In the end, the as-prepared product was vacuum-dried for 12 h at 85°C.

2.3 Characterization

The X-ray diffraction (XRD) patterns were recorded using an XRD diffractometer (PANalytical Empyrean, Switzerland) with Cu-Kα (ʎ = 1.5405 Å) radiation source, operating at a voltage and current of 30 mA and 40 kV, respectively. The morphology and microstructure characteristics of the as-fabricated materials were studied using a field emission scanning electron microscope equipped with an energy-dispersive spectrometer (EDS) system (FE-SEM, Zeiss Sigma 500 VP, Germany) and transmission electron microscope (TEM, JEOL JEM-2100F, Japan). Fourier transform infrared (FTIR) spectra were measured using a VERTEX 70 spectrophotometer (Bruker Optics, Germany). X-ray photoelectron spectroscopy (XPS) with Al-Kα radiation (Thermo ESCALAB 250XI, United State) was applied to examine the oxidation state of the prepared composite. N_2 adsorption-desorption analysis was performed on BELSORP-MAX II surface area analyzer (MICROTRAC, Germany) at 77 K. Brunauer-Emmett-Teller (BET) and Barrett- Joyner-Halenda (BJH) methods were utilized to calculate the specific surface area and pore size distribution. Prior to measurement, the samples were vacuum-activated for 12 h at 150°C and then degassed for 3 h at 120°C. Thermogravimetric analysis (TGA) was conducted employing a LabSys EVO thermogravimetric analyzer (SETARAM, France) from room temperature to 800 °C under N_2 atmosphere with a 10°C/min heating rate. The surface charge was measured on a Zeta potential analyzer (Zetasizer Nano ZS, Malvern, United Kingdom). The UV–visible diffuse reflectance spectra (UV–vis DRS) were determined using a UV–Vis spectrophotometer (Jasco V-770, Japan) with $BaSO_4$ as a

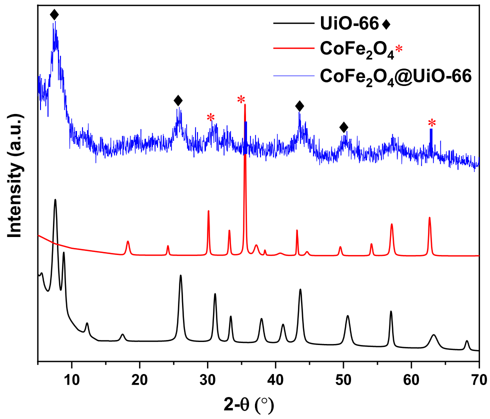

FIGURE 1
XRD patterns of UiO-66, $CoFe_2O_4$, and $CoFe_2O_4$@UiO-66 composite.

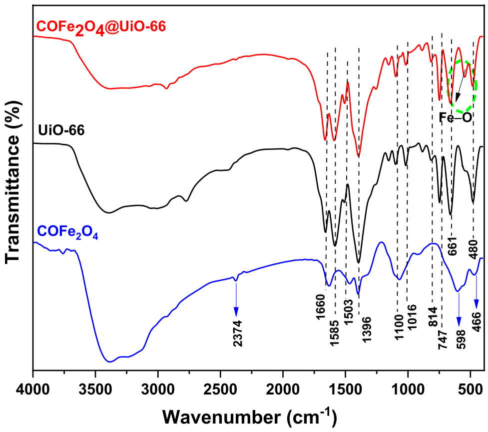

FIGURE 2
FTIR spectra of UiO-66, $CoFe_2O_4$, and $CoFe_2O_4$@UiO-66 composite.

reference in the spectral range of 200–800 nm. The photoluminescence (PL) spectra were obtained by a fluorescence spectrometer (Jasco FP-6500, Japan) with an excitation wavelength of 320 nm for $CoFe_2O_4$ and 297 nm for UiO-66 and $CoFe_2O_4$@UiO-66.

2.4 Photoelectrochemical measurements

The photoelectrochemical characterization of the as-prepared catalysts was analyzed using a standard three-electrode electrochemical workstation system (Parastat 4,000 Princeton, United State) equipped with a Xenon lamp (150 W) as an irradiation source. Indium-tin-oxide (ITO) glass coated by the catalysts ($\rho \sim 30\ \Omega/cm^2$) served as the working electrode against the Pt sheet and saturated Ag/AgCl as the counter and reference electrodes, respectively. 0.1 M Na_2SO_4 was adopted as the electrolyte solution. The Mott-Schottky plots were estimated with the same electrochemical instrument at 500 Hz frequency under dark conditions. The electrochemical impedance spectroscopy (EIS) was recorded over a frequency range of 1 MHz–10 mHz with an amplitude of 50 mV at an open-circuit potential. Linear sweep voltammetry (LSV) tests were performed by sweeping the potential from 0 to 1.0 V.

2.5 Photocatalytic reaction

The photocatalytic performance of UiO-66, $CoFe_2O_4$, and $CoFe_2O_4$@UiO-66 composite was assessed through the photodegradation of MB and MO dyes. The physicochemical properties of the former dyes are presented in Supplementary Table S1. In a typical procedure, 50 mg of catalysts were added to 25 mL of each dye solution (100 mg/L). After agitation for 60 min in dark to establish adsorption-desorption equilibrium, the solutions were irradiated by Solar Simulator (Oriel®Sol1A, Newport Co.) equipped with a 150 W xenon lamp (100 mW/cm^2 light intensity). At regular time intervals, 100 µL of the sample solution was extracted, diluted to 700 µL with deionized water, and then centrifuged to separate the residual photocatalyst. The concentration of MB and MO was calibrated using a UV–vis spectrophotometer (UV-2600, Shimadzu, Japan) at maximum absorption wavelength (λ_{max}) of 664 nm and 464 nm, respectively. The removal efficiency (%) was calculated following Eq. 1

$$\text{Removal efficiency (\%)} = \frac{C0 - Ct}{C0} \times 100 \tag{1}$$

where C_0 and C_t (mg/L) are the dye concentration at initial and each interval time, respectively.

To investigate the photocatalytic mechanism, disodium ethylenediaminetetraacetic acid (EDTA-2Na), *p*-benzoquinone (BQ), and isopropanol (IPA) were used as trapping agents for photogenerated holes (h^+), superoxide radicals ($\bullet O_2^-$) and hydroxyl radicals (•OH), respectively. The concentration of the scavengers was set as 2 m and the photocatalytic assays were carried out following the same procedure described above under the same pH.

3 Results and discussions

3.1 Photocatalysts characterization

3.1.1 Structure analysis

The crystallinity of the as-prepared samples was examined using XRD analysis. The simulated patterns of

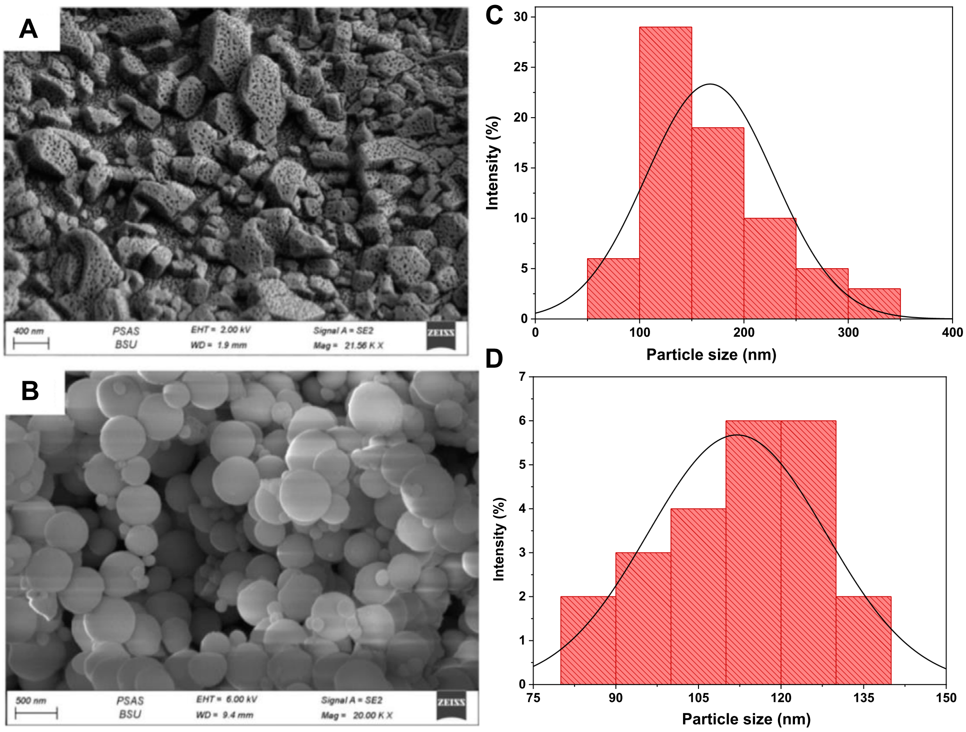

FIGURE 3
FESEM images of UiO-66 **(A)** and $CoFe_2O_4$@UiO-66 composite **(B)**; UiO-66 particle size distribution of UiO-66 **(C)** and $CoFe_2O_4$@UiO-66 composite **(D)**.

UiO-66 and $CoFe_2O_4$ are presented in Supplementary Figure S1. From Figure 1, it can be seen that the as-synthesized UiO-66 exhibited typical characteristic peaks cited at 7.5°, 8.6° indexed to the (111) and (200) crystal planes, respectively. Moreover, distinct peaks appeared at values of 12.21°, 17.4°, 25.9°, 31.0°, 33.4°, 37.7, 40.9°, 43.7°, 50.5°, and 57.1° agreed with (220), (400), (600), (711), (731), (751), (664), (933), (955), and (1242) crystal planes of UiO-66, respectively. This observation is in agreement with the former studies (Zhang et al., 2019c; Mirhosseini-Eshkevari et al., 2019; Gao et al., 2021), implying the successful preparation of the obtained material. Meanwhile, $CoFe_2O_4$ showed diffraction peaks at 18.27° (111), 30.21° (220), 35.51° (311), 43.32° (400), 53.9° (422), 57.14° (411), and 62.79° (440), which are consistent with the standard peak positions of spinel $CoFe_2O_4$ structure (Jia et al., 2019). For the $CoFe_2O_4$@UiO-66 heterojunction, the diffraction peaks correlating to UiO-66 appeared with a relative broadening and fluctuations of peak intensities, is indicative of a little alternation in the framework structural regularity (Bi et al., 2020). Even though the $CoFe_2O_4$ characteristic peaks noticeably weakened in the heterojunction owing to the *in-situ* growth of the UiO-66 shell, they still could be distinguished. Given this, the aforementioned findings suggest the successful fabrication of the MOF-hybrid material.

FTIR spectroscopy was implemented to investigate the surface functionalization of the as-prepared samples. Figure 2 displays the FTIR spectra of UiO-66, $CoFe_2O_4$, and $CoFe_2O_4$@UiO-66 composite. All samples showed a broad band at 3,200–3,500 cm^{-1} related to the O–H stretching vibration of absorbed water molecules (Ding et al., 2017; Basak et al., 2021). For UiO-66, typical bands can be identified at 1,585 and 1,396 cm^{-1}, corresponding to O–C–O asymmetric and symmetric vibrations of the -COOH group of the BDC ligand, respectively (Liu et al., 2018). The weak vibrational bands at 1,503 and 1,660 cm^{-1} occurred by the C=C vibration of benzene ring (Shangkum et al., 2018) and the C=O carbonyl stretching in the BDC linker (Ebrahim and Bandosz, 2013), respectively. Meanwhile, the bands sited around 1,016 and 1,100 cm^{-1} are ascribed to the Zr–O stretching vibration of the framework (Chen et al., 2017; Bariki et al., 2020). At lower frequency, the peaks appeared at 814, 747, and 661 cm^{-1} are associated with the O–H and C–H vibrations in the ligand (Ivanchikova et al., 2014). In addition, a distinct peak occurred at 480 cm^{-1} is assigned to asymmetric stretching of Zr-(OC) (Wang et al., 2021a). Concerning $CoFe_2O_4$, two characteristic peaks are

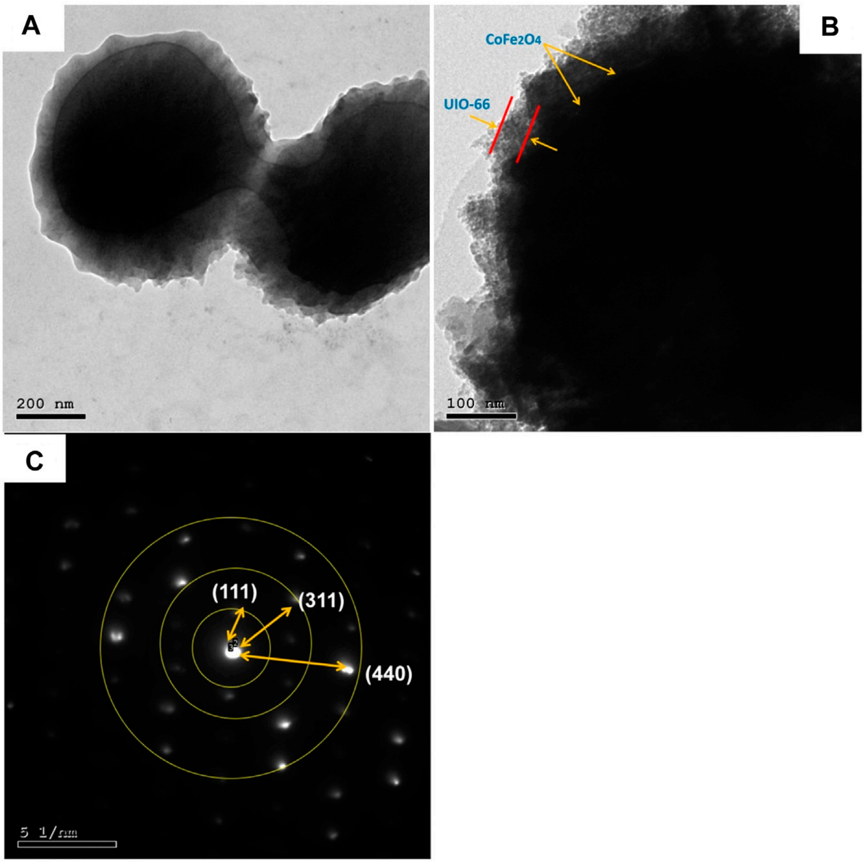

FIGURE 4
TEM images **(A,B)** and SAED pattern **(C)** of $CoFe_2O_4$@UiO-66 composite.

observed at 466 and 598 cm^{-1}, which are related to the metal-oxygen stretching vibrations at the octahedral and tetrahedral sites in the spinel structure, respectively (Shahjuee et al., 2017). The other peaks at 1,065, 1,392, and 1,629 cm^{-1} are appeared by O–H, C–O, and C–H bending vibration, respectively (Yavari et al., 2016). Meanwhile, a weak band noted at 2,374 cm^{-1} might be resulted from C–H stretching vibration (Johnson et al., 2020). As for $CoFe_2O_4$@UiO-66, the characteristic spectral bands of UiO-66 can be observed, nevertheless, with less intensity and slight blue-shift, indicating the changing of the chemical environment around UiO-66 following the incorporation of $CoFe_2O_4$. Unlike UiO-66, a new peak can be identified around 500–600 cm^{-1} in the composite material that is associated with the stretching vibration of Fe–O band (Deng et al., 2013). This observation confirms the effective integration of UiO-66 and $CoFe_2O_4$ to form the composite material, which corresponds with the above XRD findings.

3.1.2 Morphology analysis

FESEM analysis was adopted to explore the morphological characteristics of bare UiO-66 and CoFe2O4@UiO-66 composite. As displayed in Figure 3A, UiO-66 exhibited irregular cubic morphology with an average diameter approaching between 150–200 nm (Figure 3C). In fact, with increasing the concentration of monocarboxylic acid modulators, more comparatively uniform pores are created in the MOF network (Wang et al., 2021b). This explains the porous surface of the as-synthesized UiO-66, which could be resulting from the high concentration of acetic acid modulator utilized during the preparation process. Figure 3B shows the FESEM image of the $CoFe_2O_4$@UiO-66 composite. It is interestingly noted that after coating with UiO-66, $CoFe_2O_4$ maintained the original spherical-like structure previously reported (Mu et al., 2021), with a relatively uniform size and rough surface. On the other hand, the crystal size of UiO-66 has reduced to ~120 nm in the composite (Figure 3D), along with a morphological change from cubic to sphere-like crystals owing to the fast reaction between Zr and ligand (Han et al., 2017; Winarta et al., 2019).

TEM study was further carried out to explore the microstructure of the as-synthesized composite. As presented in Figures 4A, B, $CoFe_2O_4$@UiO-66 displayed a distinct core-shell structure comprised of $CoFe_2O_4$ core with an average diameter of approximately 550 nm,

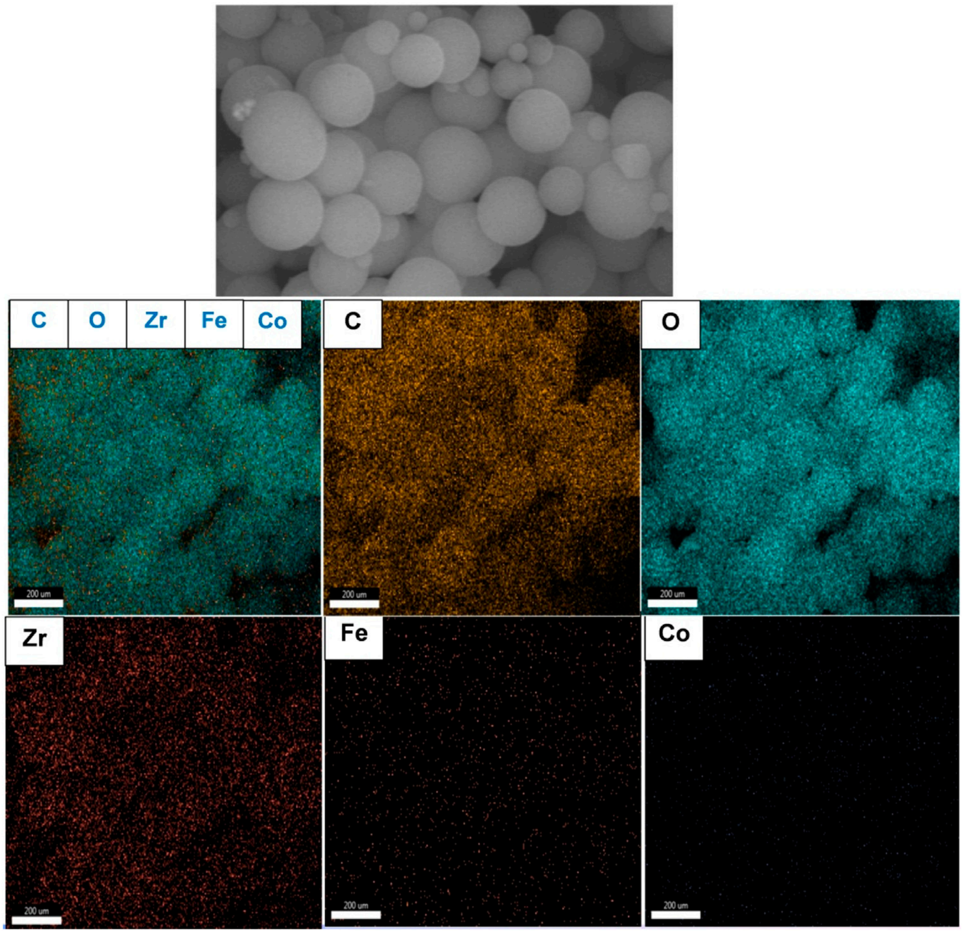

FIGURE 5
SEM-EDS elemental mapping of $CoFe_2O_4$@UiO-66 composite.

coated by an outer UiO-66 shell with a thickness of 42.4 ± 11.9 nm. Importantly, an obvious contact interface between UiO-66 and $CoFe_2O_4$ can be seen that accelerates the migration of charge carriers, thereby enhancing the photocatalytic performance. The selected area electron diffraction (SAED) pattern of the $CoFe_2O_4$@UiO-66 composite (Figure 4C) demonstrated the polycrystalline nature with d-spacing of 0.49, 0.26, and 0.15 nm correlated to (111), (311), and (440) planes of the magnetic $CoFe_2O_4$. The EDS elemental mapping of the $CoFe_2O_4$@UiO-66 composite is illustrated in Figure 5. Homogeneous distribution of Zr, O, C, Fe, and Co elements can be observed. This low content for Fe and Co elements might be ascribed to the entire coating of UiO-66 on $CoFe_2O_4$ microspheres. In addition, the photograph of different samples further proved that pristine and composite materials were successfully fabricated (Supplementry Figure S2).

3.1.3 XPS analysis

To explore the surface chemical state of the $CoFe_2O_4$@UiO-66 composite, the XPS spectra were recorded (Pan et al., 2022). The survey spectrum (Figure 6A) showed characteristic peaks for Zr 3d, Fe 2p, Co 2p, C 1s, and O 1s, accompanying intense peaks for the C and O elements corresponding to their relative abundance. For the C 1s spectrum (Figure 6B), three peaks at 284.5, 286.1, and 288.4 eV are respectively ascribed to C=C of the benzene ring and carboxylate groups of the BDC linker in the UiO-66 framework (Cao et al., 2018). As shown in Figure 6C, the O 1s spectrum demonstrated three deconvolution peaks cited at 530.1, 531.5, and 532.6 eV associated with the metal-oxygen bond (Zr–O) bond, C=O of the BDC linker, and surface adsorbed hydroxyl group, respectively (Yang et al., 2019). In Zr 3d XPS (Figure 6D), the characteristic binding energies of Zr $3d_{5/2}$ (at 182.5 eV) and Zr $3d_{3/2}$ (at 184.6 and 185.6 eV) can be seen, belonging to Zr–O core level interactions (Subhan et al., 2021). The energy spectrum of Co 2p depicted in Figure 6E demonstrated a pair of fitting peaks at 780.8 and 785.8 eV associated with Co $2p_{3/2}$ and another peak cited at 795.2 eV (with a relatively strong shake-up satellite peak at 800.4 eV) related to Co $2p_{1/2,}$ confirming the existence of Co^{2+} oxidation

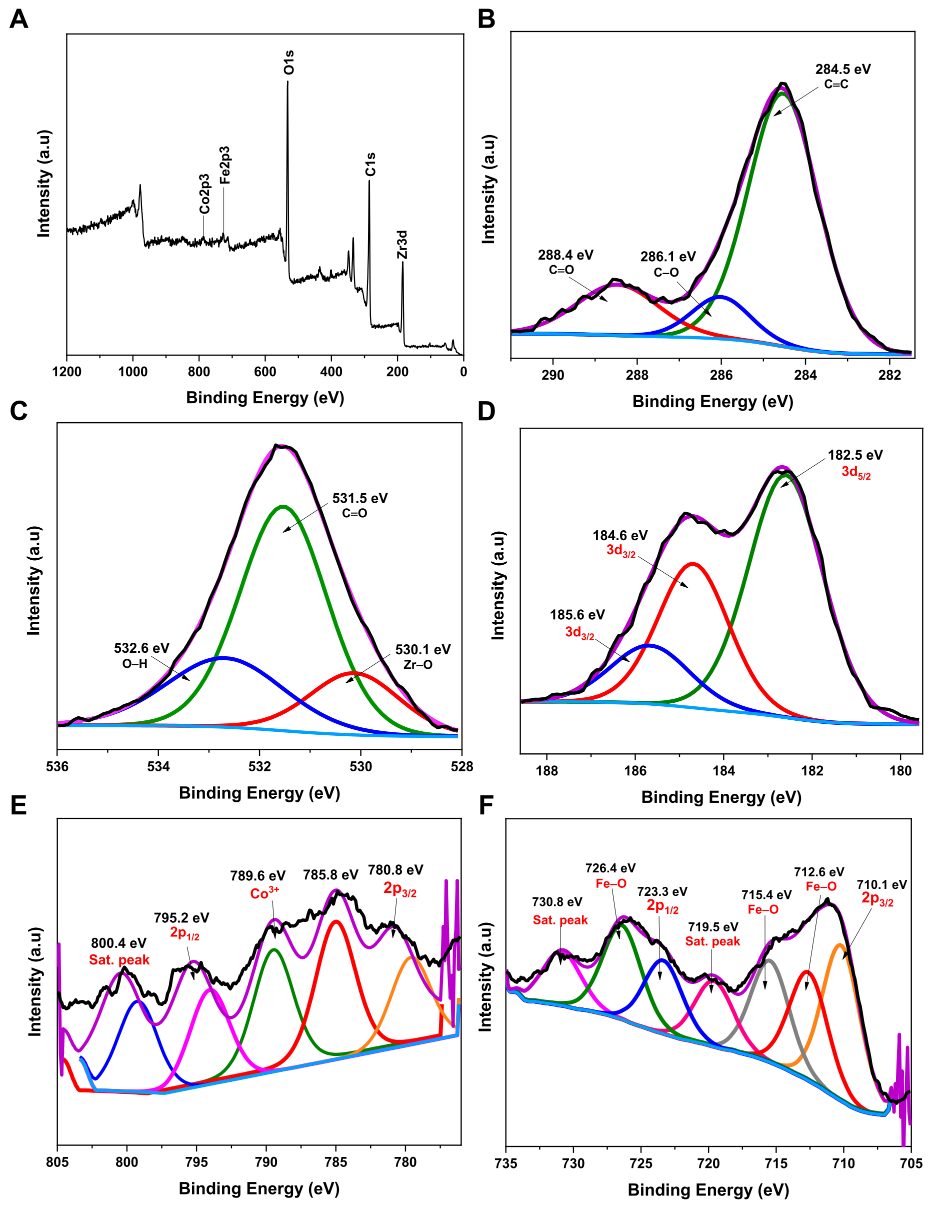

FIGURE 6
XPS spectra of CoFe$_2$O$_4$@UiO-66 composite: survey scan **(A)**, C 1s **(B)**, O 1s **(C)**, Zr 3 days **(D)**, Co 2p **(E)**, and Fe 2p **(F)**.

state in the spinal structure (Zhou et al., 2014; Chen et al., 2016). Typically, the satellite energy separation in oxides for Co^{3+} is approximately 8.5–9.5 eV (Xu et al., 2019). Given this, an extra peak centered at 789.6 eV corresponding to the binding energy of Co^{3+} 2p$_{3/2}$ is presumably due to the surface oxidation of Co species after coating by UiO-66 particles. In the Fe 2p spectrum (Figure 6F), two distinct peaks located at 710.1 and 723.3 eV associated with the binding energies of Fe 2p$_{3/2}$ and Fe 2p$_{1/2}$, respectively, suggesting the existence of Fe^{2+} (Zhou et al., 2022), whereas, the Fe 2p shakeup satellites observed at 719.5 and 730.8 eV are assigned to Fe^{3+} spin state (Ma et al., 2015; Salunkhe et al., 2015). Moreover, the peaks noticed at 712.6, 715.4, and 726.4 eV could be due to Fe–O bonds, which further assert the strong interaction between CoFe$_2$O$_4$ and UiO-66 *via* Fe-O-Zr linkages (Xu et al., 2017).

3.1.4 Surface area and thermal investigation

N$_2$ adsorption-desorption isotherm studies were employed to investigate the textural properties of UiO-66 and CoFe$_2$O$_4$@UiO-66 composite and relevant data are given in Figure 7; Table 1. UiO-66 (Figure 7A) displayed type IV isotherm with a well-defined H2 hysteresis loop, indicating the existence of mesopores,

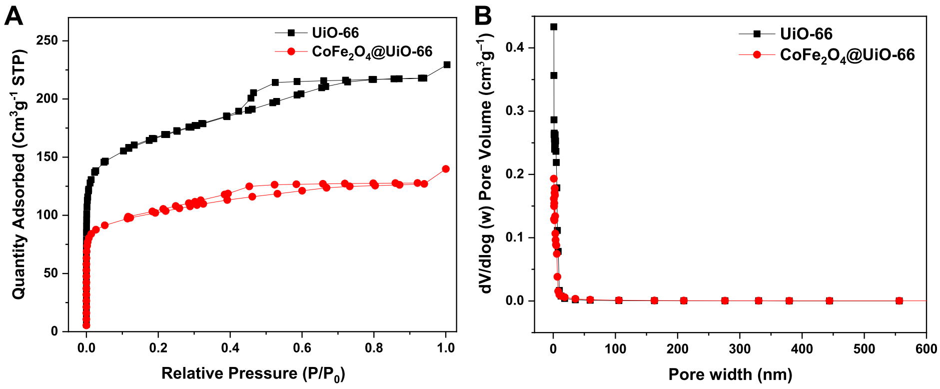

FIGURE 7
N_2 adsorption-desorption isotherms **(A)**, and pore size distribution curves **(B)** of UiO-66 and $CoFe_2O_4$@UiO-66 composite.

TABLE 1 Porous texture of the as-synthesized samples.

Sample	S_{BET} (m^2 g^{-1})[a]	$S_{Langmuir}$ (m^2 g^{-1})[b]	V_t (cm^3 g^{-1})[c]	Pore diameter (nm)[d]
UiO-66	593.94	742.31	0.35	2.36
$CoFe_2O_4$@UiO-66	375.7	480.03	0.21	2.27

[a] BET specific surface area.

[b] Langmuir specific surface area.

[c] Total pore volume measured at P/P_0 = .99.

[d] Pore size in diameter calculated by the desorption data using Barrett–Joyner–Halenda (BJH) method.

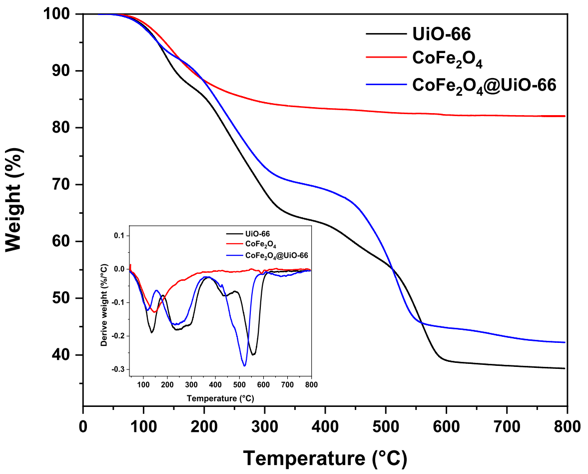

FIGURE 8
Thermal analysis of UiO-66, $CoFe_2O_4$, and $CoFe_2O_4$@UiO-66 composite, inset: the corresponding derivative thermogravimetric (DTG) plots.

thereby authenticating the results of FE-SEM. The S_{BET} of UiO-66 is 593.94 m^2 g^{-1}. Obviously, the $CoFe_2O_4$@UiO-66 composite attained the same isotherm pattern; however, with an H4 type hysteresis loop and S_{BET} of 375.7 m^2 g^{-1}. The pore size distribution of as-synthesized catalysts also showed a similar trend (Figure 7B), whereas, the total pore volumes for UiO-66 and $CoFe_2O_4$@UiO-66 are calculated to be 0.35 and 0.21 cm^3 g^{-1}, respectively. Distinctly, this reduction in the S_{BET} (~36%) and pore volume (~40%) of the composite material is possibly connected with the formation of larger mesopores owing to the encapsulation of $CoFe_2O_4$ particles into the MOF network (Lee et al., 2015; Qi et al., 2019).

To evaluate the thermal behavior of the as-prepared catalysts, TGA analysis was conducted and the findings are displayed in Figure 8. For $CoFe_2O_4$, two stages of weight loss with a total weight loss of ~16% can be observed. The major one occurred up to 100°C owing to the evaporation of moisture, whilst, the minor mass loss happened at 330°C could be assigned to the elimination of ammonium hydroxide and chloride from the surface (Chakhtouna et al., 2021). In contrast, no considerable weight loss can be detected above 330°C, revealing the high thermal stability of $CoFe_2O_4$. On the other side, both pristine and modified UiO-66 demonstrated similar TGA curves with three stages of weight loss. In the case of pristine UiO-66, an initial weight loss (13%) occurs from 33°C–161°C owing to the evaporation of physically adsorbed water molecules from the UiO-66 surface (Xu et al., 2022). In the second stage, nearly 19% weight loss observed in the range of 161°C–300°C is associated

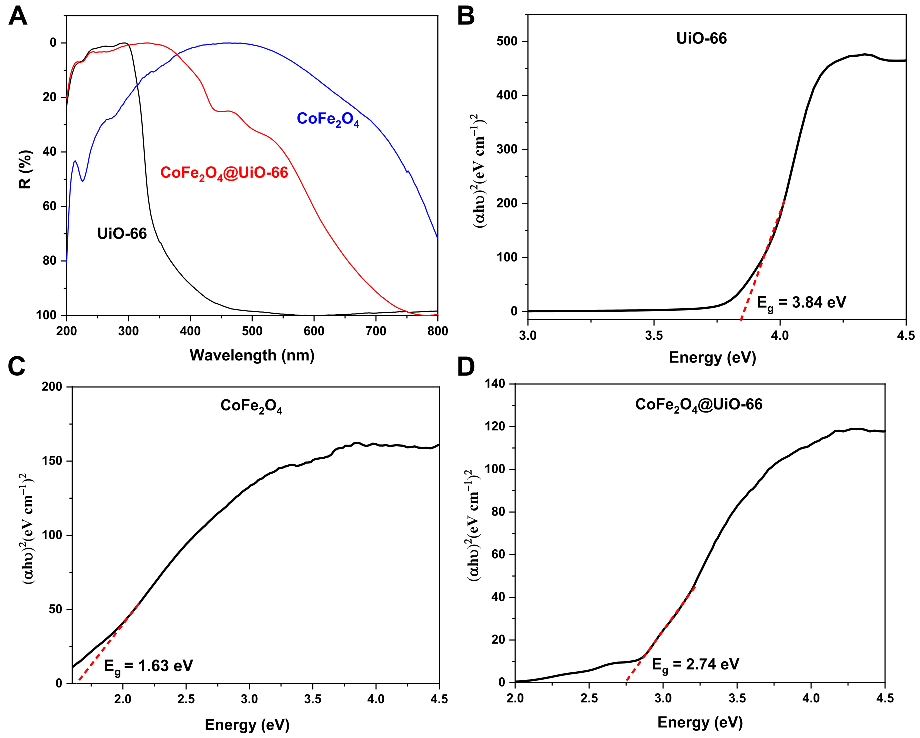

FIGURE 9
UV-vis DRS spectra **(A)**, bandgap (E_g) plots **(B–D)** of the as-synthesized samples.

with the removal of DMF molecules trapped inside the framework pores and thermal dehydration of zirconium clusters (Zhang et al., 2021a). The last weight loss (>30%) appeared at 430°C–600°C is ascribed to the thermal decomposition of the organic ligand to CO, CO_2, and ZrO_2 (Molavi et al., 2018). Compared to bare UiO-66, the TGA curve of $CoFe_2O_4$@UiO-66 showed a relative reduction in weight loss by about 6.22%, indicating an improvement of thermal stability after the introduction of $CoFe_2O_4$ nanoparticles.

3.2 Optical properties

The UV-Vis DRS was performed to study the photoabsorption characteristics of the as-synthesized photocatalysts and findings are shown in Figure 9A. It can be noticed that bare UiO-66 displayed no absorption in the visible region, however, strong absorption is obvious in the UV spectral region with an absorption peak at 296 nm that can be ascribed to Zr–Oxo-clusters (Wang et al., 2016). Otherwise, owing to the black color of pristine $CoFe_2O_4$, absorption peaks can be seen in both UV and visible regions (Jing et al., 2016). By comparison, the light absorption edge of $CoFe_2O_4$@UiO-66 composite is red-shifted to around 467 nm, evidencing the enhancement of light absorption intensity and visible light utilization efficiency after combining $CoFe_2O_4$. For certifying, the Kubelka-Munk equation was applied to estimate the bandgap energy (E_g) of semiconductors (Qiu et al., 2019):

$$(\alpha h\upsilon)^2 = A\left(h\upsilon - E_g\right)^{n/2} \tag{2}$$

where α, h, υ, and A are the diffuse absorption coefficient, Planck's constant, light frequency, and constant, respectively. As depicted in Figures 9B–D, direct bandgap energies were calculated from the tangent line obtained by plotting $(\alpha h\upsilon)^2$ vs energy (hυ). For UiO-66, $CoFe_2O_4$, and $CoFe_2O_4$@UiO-66 composite, the estimated E_g values are approximately 3.84, 1.63, and 2.74 eV, respectively. In the case of the composite, the relatively reduced bandgap observed might be assigned to the interface formed between UiO-66 and the narrow bandgap $CoFe_2O_4$ particles, resulting in more effective absorption of the solar spectrum and eventually better photocatalytic response.

3.3 Photoelectrochemical properties

Photoluminescence (PL) spectra were obtained to evaluate charge separation and transmission efficiency over different catalysts. In theory, the lower the PL intensity, the lower the reintegration of the charge carriers, which is advantageous to the

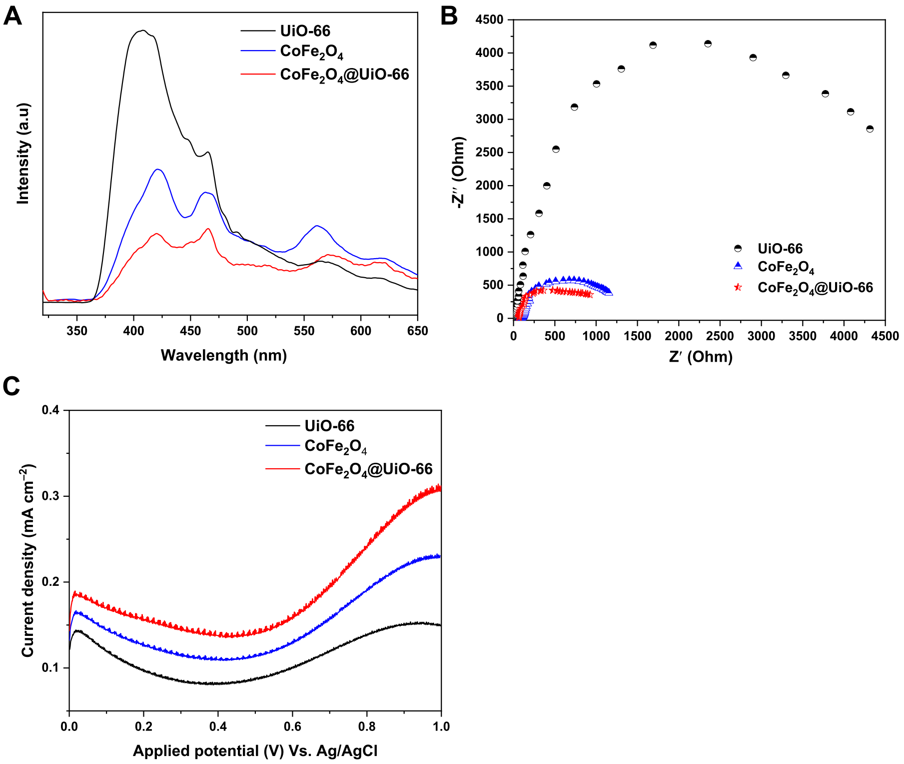

FIGURE 10
PL emission spectra **(A)**, EIS Nyquist **(B)**, and LSV curves **(C)** of UiO-66, $CoFe_2O_4$ and $CoFe_2O_4$@UiO-66 composite.

photocatalytic reaction (He et al., 2021). As revealed in Figure 10A, the PL spectral intensity decreased in the order of UiO-66 > $CoFe_2O_4$ > $CoFe_2O_4$@UiO-66, where, pristine UiO-66 exhibited the highest peak intensity at around 407 nm. Conversely, upon coupling with $CoFe_2O_4$ particles, the PL intensity is markedly suppressed and the signal is displaced to a higher wavelength (466 nm). Thus, it can be deduced that the formation of core-shell heterostructure significantly quenched the recombination of photoinduced charge carriers, accelerating the migration rate.

The photoelectrochemical characterizations were further investigated by electrochemical impedance spectroscopy (EIS) and linear sweep voltammetry (LSV) to verify the charge transfer and current density, thereby determining the photocatalytic performance of catalysts. Consistent with the findings of the PL analysis, EIS Nyquist plots displayed the same tendency (Figure 10B). Basically, the smaller the semicircle diameter in EIS plots, the lower the charge transfer resistance (Zhang et al., 2022). In this study, it is interestingly noted that $CoFe_2O_4$@UiO-66 displayed a smaller Nyquist arc radius than those of parent UiO-66 and $CoFe_2O_4$, reaffirming the depletion in charge transfer resistance and enhancement of charge carriers separation by constructing heterojunction. In addition, LSV profiles of as-synthesized catalysts are represented in Figure 10C. As can be seen, UiO-66 displayed the lowest current density (0.15 mA cm^{-2}), owing to inefficient utilization of visible light. In contrast, the current density is significantly improved to 0.31 mA cm^{-2} over $CoFe_2O_4$@UiO-66. On the other side, the anodic currents in LSV curves demonstrated the n-type semiconductor nature of the as-synthesized catalysts (Quach et al., 2022). To summarize, these findings assert that the successful interfacial contact between UiO-66 and $CoFe_2O_4$ can sufficiently hinder the charge recombination dilemma and induce effective separation of photoinduced carriers, leading to swift surface reaction dynamics and better photocatalytic activity.

3.4 Photocatalytic performance

The photocatalytic activities of bare and composite catalysts were studied through the degradation of MB and MO dyes as representative pollutants under simulated solar irradiation. Obviously, under dark conditions, the dye adsorption capacity follows the order UiO-66 > $CoFe_2O_4$@UiO-66 > $CoFe_2O_4$ (Figures 11A, B). In comparison with pure $CoFe_2O_4$, the adsorption capacity of $CoFe_2O_4$@UiO-66 composite is significantly boosted owing to the abundant exposed

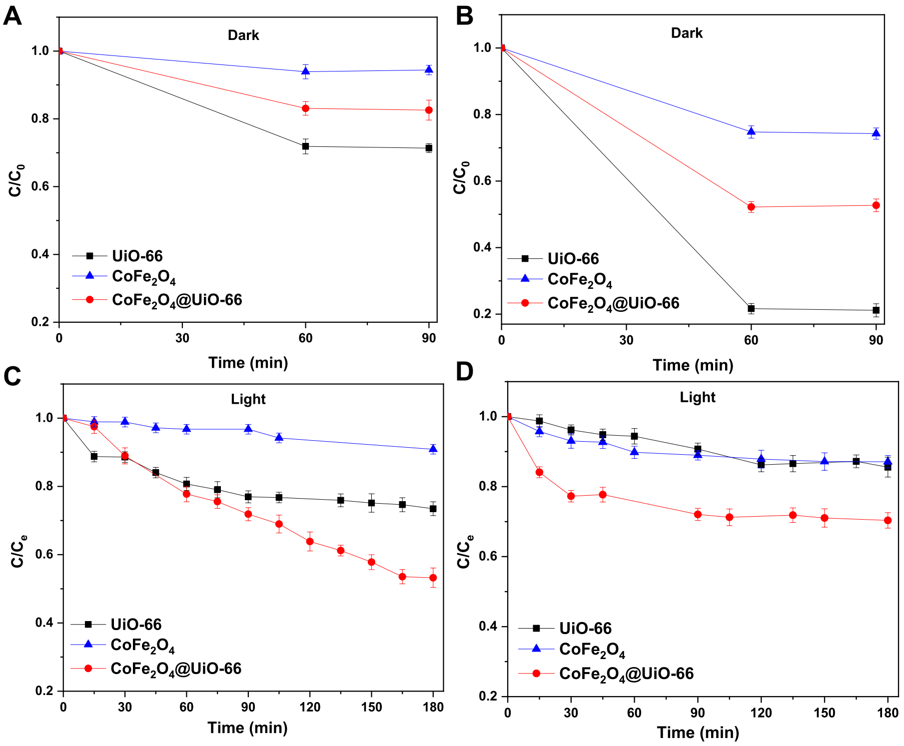

FIGURE 11
Adsorption and photodegradation performance of as-synthesized photocatalysts for removal of MB **(A,C)** and MO **(B,D)** dyes.

adsorption sites and internal porous structure of the outer UiO-66 shell. Noteworthy, the removal efficiencies of the different photocatalysts for MO dye are about 3.0–4.4-folds higher than that for MB dye. In general, the surface charge of the particles can prominently influence their interaction with target pollutants, affecting the adsorption capacity (Sohrabnezhad and Moghadamy, 2022). In this regard, the Zeta potentials of the as-synthesized catalysts were measured and the findings are depicted in (Supplementary Figure S3). As observed, all samples possess positive charges with a potential of +17.2, +19.5, and +23.8 mV for UiO-66, $CoFe_2O_4$, and $CoFe_2O_4$@UiO-66, respectively. Hence, anionic dye molecules are effectively adsorbed to the surface by electrostatic interaction, which is proposed as the predominated removal mechanism during the adsorption process. Following the accomplishment of adsorption-desorption equilibrium, the equilibrium dye concentration (C_e) was applied as the initial concentration. As presented in Figures 11C, D, upon simulated solar illumination, pristine UiO-66 and $CoFe_2O_4$ exhibited low degradation efficiency due to the weak visible light harvesting and ineffective segregation of photogenerated carriers, respectively. By comparison, considerable photocatalytic degradation was attained in presence of $CoFe_2O_4$@UiO-66 composite, with a 20%–40% increase in degradation efficiency (Figure 12A). The UV-Vis spectral changes of MB and MO dyes over $CoFe_2O_4$@UiO-66 photocatalyst at different illumination times are revealed in Figures 12B, C.

To further elucidate the photodegradation process, kinetic curves were plotted and rate constants k) were calculated. (Supplementary Figure S4) illustrates the pseudo-first-order kinetic equation to define the reaction rate constant of different samples following Eq. 3 (Yi et al., 2019):

$$(\ln (C_e/C) = kt \quad (3)$$

where k is the first-order rate coefficient (min^{-1}), C_e is the dye concentration at equilibrium and C is the concentration at time t. It is noteworthy that among the three catalysts, the $CoFe_2O_4$@UiO-66 composite possessed a greater rate constant, which is consistent with the photocatalytic results. As evident, the heterojunction constructed between UiO-66 and $CoFe_2O_4$ simultaneously reduced the charge carrier recombination and increased the photon absorption capacity, resulting in a faster photocatalytic reaction. The photocatalytic activity of $CoFe_2O_4$@UiO-66 composite for dye degradation was further compared with the previously reported photocatalysts (Table 2). Overall, the $CoFe_2O_4$@UiO-66 composite displayed outstanding efficiency for the degradation of dyes at high initial concentrations.

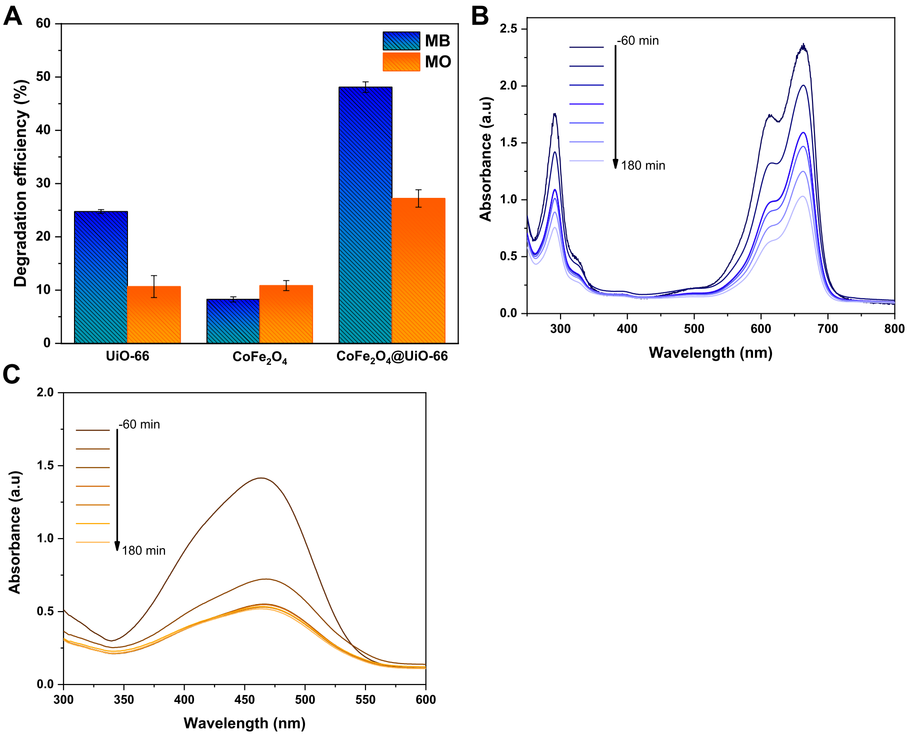

FIGURE 12
The photodegradation efficiency of as-synthesized photocatalysts **(A)**, UV-Vis absorption spectra for degradation of MB **(B)** and MO **(C)** dyes over $CoFe_2O_4$@UiO-66.

3.5 Proposed photocatalytic mechanism

To explore the possible mechanism for the photocatalytic degradation of MB and MO dyes, radical trapping experiments were performed over $CoFe_2O_4$@UiO-66 composite under simulated solar irradiation. EDTA-2Na, BQ, and IPA were utilized separately in the degradation system as h^+, $•O_2^-$, and •OH scavengers, respectively. As observed in Figure 13, all the reactive substances are contributed to the catalytic process. Nevertheless, EDTA-2Na has the most significant impact on the degradation reaction. When EDTA-2Na is added, the degradation rate decreased drastically to 12% and 15% for MB and MO, respectively. In the meanwhile, upon the introduction of BQ and IPA, a moderate influence on the degradation efficiency can be seen. This implies that photogenerated holes are the dominant active species, while $•O_2^-$ and •OH possess a certain contribution to the photocatalytic reaction.

For more insights into the mechanism of photogenerated charge separation, Mott-Schottky (M–S) measurement was further implemented to investigate the electronic band structure and the semiconductivity nature of UiO-66 and $CoFe_2O_4$. The positive slope of the tangent lines depicted in Figures 14A, B suggests that both materials are typical n-type semiconductors (Shen et al., 2015a), which is in agreement with the LSV results. The results showed that the flat band potential (E_{FB}) of UiO-66 and $CoFe_2O_4$ are set as −0.23 and −0.31 V vs. Ag/AgCl, respectively. Subsequently, the E_{FB} (vs. NHE) could be determined as follows (Man et al., 2022):

$$E_{(NHE,\, pH=7)} = E_{Ag/AgCl} - 0.059\,(7 - \text{pH of the electrolyte}) + 0.198 \tag{4}$$

Thence, the E_{FB} of UiO-66 and $CoFe_2O_4$ is −0.24 and −0.36 V (vs NHE), respectively. In general, the conduction band (E_{CB}) potential for n-type semiconductors is approximately 0.1–0.2 V more negative than the flat band potential (Ishikawa et al., 2002). Accordingly, the corresponding (E_{CB}) potential of UiO-66 and $CoFe_2O_4$ can be calculated as −0.44 and −0.56 V (vs. NHE), respectively. From the bandgap values obtained above, the valence band (E_{VB}) potential can be calculated using Eq. 4:

$$E_{VB} = E_g + E_{CB} \tag{5}$$

Subsequently, the E_{VB} potential of UiO-66 and $CoFe_2O_4$ is determined as 3.40 and 1.07 V (vs. NHE), respectively.

In the light of the aforementioned findings and discussion, the plausible reaction mechanism for photocatalytic degradation of MB and MO over $CoFe_2O_4$@UiO-66 photocatalyst is proposed (Figure 15). Upon simulated sunlight irradiation, both UiO-66

TABLE 2 Comparison of photocatalytic performance of $CoFe_2O_4$@UiO-66 with other reported photocatalysts for degradation of MB and MO.

Photocatalyst	Dye concentration (mg/L)	Catalyst amount (mg/L)	Light source	Irradiation time (min)	Removal rate (%)	Ref
MB dye						
Fe-UiO-66	20	10	60 W white LED lamp	160	84	Hosseini et al. (2022)
g-C_3N_4–xClx/0.5 M HCl	3	25	1000 W Xe lamp (λ ≥ 420 nm)	180	97	Bai et al. (2020)
$Co_{0.1}Mg_{0.9}Fe_2O_4$	10	10	A halogen lamp (intensity: 70 mWcm²)	240	80	Dojcinovic et al. (2021)
α-Fe_2O_3@UiO-66	13	100	300 W Xe lamp (λ ≥ 420 nm)	50	100	Zhang et al. (2019a)
UiO-66/g-C_3N_4 UC10:10	10	50	350 W Xe lamp (λ > 420 nm)	240	99	Zhang et al. (2018)
30% $CuNb_2O_6$/g-C_3N_4	10	20	500 W Xe lamp	150	98.5	Ahmad et al. (2022)
S–N-co-doped-$CoFe_2O_4$@rGO@TiO_2	5	8	300 W Xe lamp (λ > 420 nm)	360	94	Wei et al. (2019)
$CoFe_2O_4$@UiO-66	100	50	150 W Xe lamp	180	56.7	This work
MO dye						
UiO-66-NH_2@CNT (3 wt%)	15	30	100 W LED lamp	30	93	Abdi et al. (2021)
OV-BOC	10	100	300 W Xe lamp (λ > 400 nm)	120	82	Zhao et al. (2019)
40 wt%-AgBr/CeO_2	30	50	300 W Xe lamp (λ ≥ 400 nm)	180	93	Chen et al. (2021)
UiO-66/$BiFeO_3$	10	50	250 W high-pressure Hg lamp (λ > 400 nm)	180	88.7	Bargozideh et al. (2020)
Au-$CoFe_2O_4$/MoS_2	50	70	300 W iodine tungsten lamp	120	99	Jia et al. (2019)
rGO@In_2S_3@UiO-66	15	30	500 W Xe lamp (λ = 420 nm)	60	98.1	Gan et al. (2019)
3% TiO_2/g-C_3N_4	10	1,000	500 W Xe lamp (simulated sunlight)	80	62.6	Huang et al. (2016)
$CoFe_2O_4$@UiO-66	100	50	150 W Xe lamp	180	63.3	This work

and $CoFe_2O_4$ are excited, generating electrons (e^-) and holes (h^+) in their CB and VB, respectively. Since, the CB potential of $CoFe_2O_4$ (−0.56 V) is more negative than the LUMO of UiO-66 (−0.44 V), the excited electrons can directly transfer through the interface channels formed by the heterojunction to the LUMO of UiO-66, suppressing the recombination of photogenerated carriers (Wang et al., 2021d; Gao et al., 2021). Subsequently, the photoinduced electrons at LUMO of UiO-66 can reduce the dissolved oxygen to yield •O_2^- radicals. Meanwhile, the photogenerated holes would transfer from the VB of UiO-66 (+3.40 V) to the VB of $CoFe_2O_4$ (+1.07 V). However, as the VB potential of $CoFe_2O_4$ (+1.07 V) is lower than the redox potential of $^{-}$OH/•OH (1.99 V vs NHE), the photogenerated holes cannot oxidize H_2O to produce •OH radicals (Wang et al., 2022). Instead, the accumulated holes promptly degrade the dye molecules because of their strong oxidation properties. Otherwise, •OH reactive radicals could be indirectly generated through •O_2^- radicals at the CB of the photocatalyst (Zou et al., 2021). This is consistent with the results of quenching

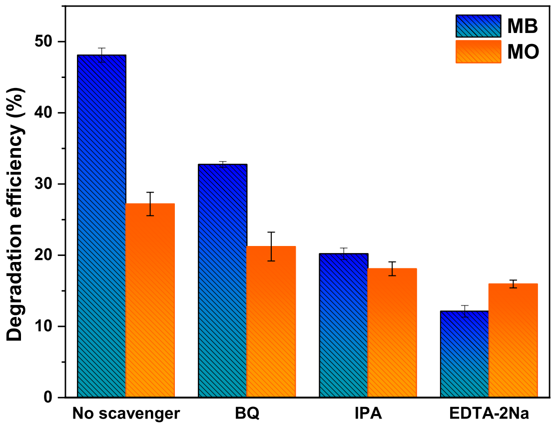

FIGURE 13
The effect of different quenchers on the photocatalytic activity of $CoFe_2O_4$@UiO-66 for degradation of MB and MO dyes.

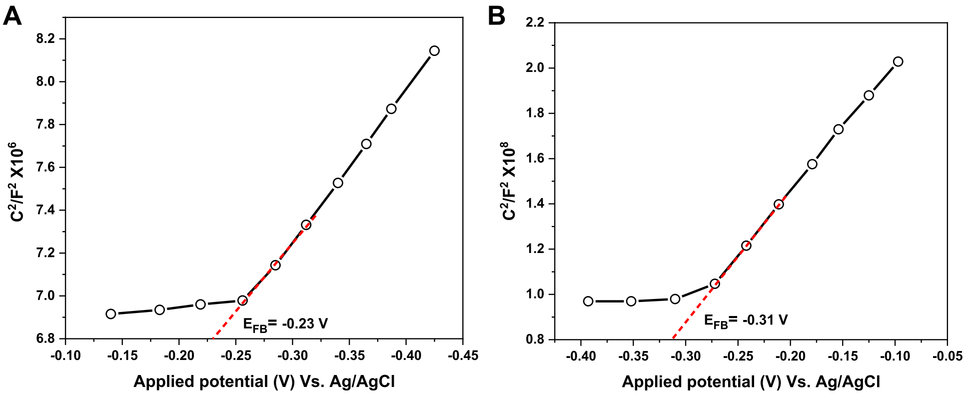

FIGURE 14
Mott-Schottky plots of UiO-66 **(A)** and $CoFe_2O_4$ **(B)**.

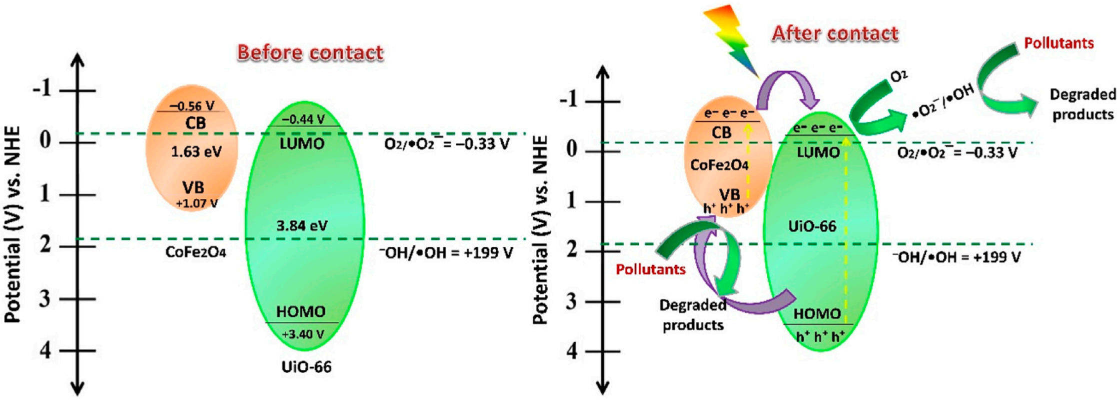

FIGURE 15
A proposed photocatalytic mechanism for dye degradation over $CoFe_2O_4$@UiO-66 heterojunction under simulative solar irradiation.

experiments, indicating the construction of a staggered type II heterojunction energy band alignment near the interface of UiO-66 and $CoFe_2O_4$. The following equations may summarize the degradation process:

$$CoFe_2O_4@UiO-66 + h\upsilon \rightarrow e^- + h^+ \tag{6}$$

$$e^- + O_2 \rightarrow \bullet O_2^- \tag{7}$$

$$\bullet O_2^- + 2h^+ + 2e^- \rightarrow H_2O_2 \tag{8}$$

$$H_2O_2 + 2e^- \rightarrow {}^-OH + \bullet OH \tag{9}$$

$$\text{Organic dye} + h^+ + \bullet OH + \bullet O_2^- \rightarrow \text{degradation products} \tag{10}$$

4 Conclusion

In summary, a novel $CoFe_2O_4$@UiO-66 core-shell heterojunction photocatalyst was successfully synthesized through a simple solvothermal route. In comparison with the UV-driven UiO-66 catalyst, the $CoFe_2O_4$@UiO-66 heterojunction displayed an enhanced photo-responsive capacity in the visible region with an absorption band of ~467 nm. This can be certified by the reduction of bandgap energy from 3.84 eV for UiO-66 to 2.74 eV for the composite material. The $CoFe_2O_4$@UiO-66 composite exhibited better performance than either UiO-66 or $CoFe_2O_4$ towards photodegradation of organic dyes at a high initial concentration under simulated solar light irradiation. The overall removal efficiency of dyes (100 mg/L) over $CoFe_2O_4$@UiO-66 (50 mg/L) reached >60% within 180 min irradiation. Moreover, the photoluminescence, impedance, and current density studies showed an effective charge separation and transfer over the $CoFe_2O_4$@UiO-66 composite. This was mainly ascribed to the tight interfacial contact formed through the heterojunction, which suppressed the charge recombination rate, thereby improving the photocatalytic activity. From radical scavenging experiments and Mott-Schottky analysis, it can be inferred that h^+ had the primarily significant contribution during the photocatalytic process. This study paved the way to design MOF-based core-shell heterostructured photocatalysts with more active sites, good optical properties, and enhanced photocatalytic activity for various environmental applications.

Data availability statement

The original contributions presented in the study are included in the article/Supplementary Material, further inquiries can be directed to the corresponding author.

Author contributions

YA: Writing -original draft, Conceptualization, Investigation, Methodology and Analysis. MS: Investigation. RA: Investigation. AZ: Supervision, Conceptualization, Investigation, review and editing.

Acknowledgments

The authors gratefully acknowledge the National Institute of Oceanography and Fisheries (NIOF) for complementary financial support and Aaisha M. Naim, MSc student at the Faculty of Postgraduate Studies for Advanced Sciences for her assistance.

Conflict of interest

The authors declare that the research was conducted in the absence of any commercial or financial relationships that could be construed as a potential conflict of interest.

Publisher's note

Supplementary material

The Supplementary Material for this article can be found online at: https://www.frontiersin.org/articles/10.3389/fchem.2022.1102920/full#supplementary-material

References

Abdi, J., Banisharif, F., and Khataee, A. (2021). Amine-functionalized Zr-MOF/CNTs nanocomposite as an efficient and reusable photocatalyst for removing organic contaminants. *J. Mol. Liq.* 334, 116129. doi:10.1016/j.molliq.2021.116129

Ahmad, N., Kuo, C. F. J., and Mustaqeem, M. (2022). Synthesis of novel CuNb2O6/g-C3N4 binary photocatalyst towards efficient visible light reduction of Cr (VI) and dyes degradation for environmental remediation. *Chemosphere* 298, 134153. doi:10.1016/j.chemosphere.2022.134153

Al-Mamun, M., Kader, S., Islam, M., and Khan, M. (2019). Photocatalytic activity improvement and application of UV-TiO2 photocatalysis in textile wastewater treatment: A review. *J. Environ. Chem. Eng.* 7, 103248. doi:10.1016/j.jece.2019.103248

Ba-Abbad, M. M., Kadhum, A. A. H., Mohamad, A. B., Takriff, M. S., and Sopian, K. (2013). Visible light photocatalytic activity of Fe3+-doped ZnO nanoparticle prepared via sol–gel technique. *Chemosphere* 91, 1604–1611. doi:10.1016/j.chemosphere.2012.12.055

Bai, X., Wang, X., Lu, X., Liang, Y., Li, J., Wu, L., et al. (2020). Surface defective g-C3N4–Cl with unique spongy structure by polarization effect for enhanced photocatalytic removal of organic pollutants. *J. Hazard. Mater.* 398, 122897. doi:10.1016/j.jhazmat.2020.122897

Bargozideh, S., Tasviri, M., Shekarabi, S., and Daneshgar, H. (2020). Magnetic BiFeO 3 decorated UiO-66 as ap–n heterojunction photocatalyst for simultaneous degradation of a binary mixture of anionic and cationic dyes. *New J. Chem.* 44, 13083–13092. doi:10.1039/d0nj02594a

Bariki, R., Majhi, D., Das, K., Behera, A., and Mishra, B. (2020). Facile synthesis and photocatalytic efficacy of UiO-66/CdIn2S4 nanocomposites with flowerlike 3D-microspheres towards aqueous phase decontamination of triclosan and H2 evolution. *Appl. Catal. B Environ.* 270, 118882. doi:10.1016/j.apcatb.2020.118882

Basak, M., Rahman, M. L., Ahmed, M. F., Biswas, B., and Sharmin, N. (2021). Calcination effect on structural, morphological and magnetic properties of nano-sized CoFe2O4 developed by a simple co-precipitation technique. *Mater. Chem. Phys.* 264, 124442. doi:10.1016/j.matchemphys.2021.124442

Bi, F., Zhang, X., Chen, J., Yang, Y., and Wang, Y. (2020). Excellent catalytic activity and water resistance of UiO-66-supported highly dispersed Pd nanoparticles for toluene catalytic oxidation. *Appl. Catal. B Environ.* 269, 118767. doi:10.1016/j.apcatb.2020.118767

Cao, J., Yang, Z.-h., Xiong, W.-p., Zhou, Y.-y., Peng, Y.-r., Li, X., et al. (2018). One-step synthesis of Co-doped UiO-66 nanoparticle with enhanced removal efficiency of tetracycline: Simultaneous adsorption and photocatalysis. *Chem. Eng. J.* 353, 126–137. doi:10.1016/j.cej.2018.07.060

Chakhtouna, H., Benzeid, H., Zari, N., and Bouhfid, R. (2021). Functional CoFe2O4-modified biochar derived from banana pseudostem as an efficient adsorbent for the removal of amoxicillin from water. *Sep. Purif. Technol.* 266, 118592. doi:10.1016/j.seppur.2021.118592

Chen, C., Chen, D., Xie, S., Quan, H., Luo, X., and Guo, L. (2017). Adsorption behaviors of organic micropollutants on zirconium metal–organic framework UiO-66: Analysis of surface interactions. *ACS Appl. Mater. interfaces* 9, 41043–41054. doi:10.1021/acsami.7b13443

Chen, C., Wang, D., Li, Y., Huang, H., and Ke, Y. (2021). Flower-like AgBr/CeO2 Z-scheme heterojunction photocatalyst with enhanced visible light photocatalytic and antibacterial activities. *Appl. Surf. Sci.* 565, 150534. doi:10.1016/j.apsusc.2021.150534

Chen, T., Du, P., Jiang, W., Liu, J., Hao, G., Gao, H., et al. (2016). A facile one-pot solvothermal synthesis of CoFe 2 O 4/RGO and its excellent catalytic activity on thermal decomposition of ammonium perchlorate. *RSC Adv.* 6, 83838–83847. doi:10.1039/c6ra16448j

Cheng, C., Fang, J., Lu, S., Cen, C., Chen, Y., Ren, L., et al. (2016). Zirconium metal-organic framework supported highly-dispersed nanosized BiVO4 for enhanced visible-light photocatalytic applications. *J. Chem. Technol. Biotechnol.* 91, 2785–2792. doi:10.1002/jctb.4885

Connolly, B. M., Madden, D. G., Wheatley, A. E., and Fairen-Jimenez, D. (2020). Shaping the future of fuel: Monolithic metal–organic frameworks for high-density gas storage. *J. Am. Chem. Soc.* 142, 8541–8549. doi:10.1021/jacs.0c00270

Deng, J., Shao, Y., Gao, N., Tan, C., Zhou, S., and Hu, X. (2013). CoFe2O4 magnetic nanoparticles as a highly active heterogeneous catalyst of oxone for the degradation of diclofenac in water. *J. Hazard. Mater.* 262, 836–844. doi:10.1016/j.jhazmat.2013.09.049

Dey, A., and Gogate, P. R. (2021). Nanocomposite photocatalysts-based wastewater treatment. *Handb. Nanomater. Wastewater Treat.* 2021, 779–809. doi:10.1016/B978-0-12-821496-1.00022-2

Dihom, H. R., Al-Shaibani, M. M., Mohamed, R. M. S. R., Al-Gheethi, A. A., Sharma, A., and Khamidun, M. H. B. (2022). Photocatalytic degradation of disperse azo dyes in textile wastewater using green zinc oxide nanoparticles synthesized in plant extract: A critical review. *J. Water Process Eng.* 47, 102705. doi:10.1016/j.jwpe.2022.102705

Ding, J., Yang, Z., He, C., Tong, X., Li, Y., Niu, X., et al. (2017). UiO-66 (Zr) coupled with Bi2MoO6 as photocatalyst for visible-light promoted dye degradation. *J. colloid interface Sci.* 497, 126–133. doi:10.1016/j.jcis.2017.02.060

Dojcinovic, M. P., Vasiljevic, Z. Z., Pavlovic, V. P., Barisic, D., Pajic, D., Tadic, N. B., et al. (2021). Mixed Mg–Co spinel ferrites: Structure, morphology, magnetic and photocatalytic properties. *J. Alloys Compd.* 855, 157429. doi:10.1016/j.jallcom.2020.157429

Ebrahim, A. M., and Bandosz, T. J. (2013). Ce (III) doped Zr-based MOFs as excellent NO2 adsorbents at ambient conditions. *ACS Appl. Mater. Interfaces* 5, 10565–10573. doi:10.1021/am402305u

Esmat, M., Farghali, A. A., Khedr, M. H., and El-Sherbiny, I. M. (2017). Alginate-based nanocomposites for efficient removal of heavy metal ions. *Int. J. Biol. Macromol.* 102, 272–283. doi:10.1016/j.ijbiomac.2017.04.021

Feng, C., Lu, Z., Zhang, Y., Liang, Q., Zhou, M., Li, X., et al. (2022). A magnetically recyclable dual Z-scheme GCNQDs-CoTiO3/CoFe2O4 composite photocatalyst for efficient photocatalytic degradation of Oxytetracycline. *Chem. Eng. J.* 435, 134833. doi:10.1016/j.cej.2022.134833

Franking, R., Li, L., Lukowski, M. A., Meng, F., Tan, Y., Hamers, R. J., et al. (2013). Facile post-growth doping of nanostructured hematite photoanodes for enhanced photoelectrochemical water oxidation. *Energy & Environ. Sci.* 6, 500–512. doi:10.1039/c2ee23837c

Gan, C., Xu, C., Wang, H., Zhang, N., Zhang, J., and Fang, Y. (2019). Facile synthesis of rGO@ In2S3@ UiO-66 ternary composite with enhanced visible-light photodegradation activity for methyl orange. *J. Photochem. Photobiol. A Chem.* 384, 112025. doi:10.1016/j.jphotochem.2019.112025

Gao, C., Wang, J., Xu, H., and Xiong, Y. (2017). Coordination chemistry in the design of heterogeneous photocatalysts. *Chem. Soc. Rev.* 46, 2799–2823. doi:10.1039/c6cs00727a

Gao, D., Zhang, Y., Yan, H., Li, B., He, Y., Song, P., et al. (2021). Construction of UiO-66@ MoS2 flower-like hybrids through electrostatically induced self-assembly with enhanced photodegradation activity towards lomefloxacin. *Sep. Purif. Technol.* 265, 118486. doi:10.1016/j.seppur.2021.118486

Görmez, Ö., Yakar, E., Gözmen, B., Kayan, B., and Khataee, A. (2022). CoFe2O4 nanoparticles decorated onto graphene oxide and graphitic carbon nitride layers as a separable catalyst for ultrasound-assisted photocatalytic degradation of Bisphenol-A. *Chemosphere* 288, 132663. doi:10.1016/j.chemosphere.2021.132663

Han, W., Shao, L.-H., Sun, X.-J., Liu, Y.-H., Zhang, F.-M., Wang, Y., et al. (2022). Constructing Cu ion sites in MOF/COF heterostructure for noble-metal-free photoredox catalysis. *Appl. Catal. B Environ.* 317, 121710. doi:10.1016/j.apcatb.2022.121710

Han, Y., Liu, M., Li, K., Sun, Q., Zhang, W., Song, C., et al. (2017). *In situ* synthesis of titanium doped hybrid metal–organic framework UiO-66 with enhanced adsorption capacity for organic dyes. *Inorg. Chem. Front.* 4, 1870–1880. doi:10.1039/c7qi00437k

He, Y., Wang, D., Li, X., Fu, Q., Yin, L., Yang, Q., et al. (2021). Photocatalytic degradation of tetracycline by metal-organic frameworks modified with Bi2WO6 nanosheet under direct sunlight. *Chemosphere* 284, 131386. doi:10.1016/j.chemosphere.2021.131386

Holkar, C. R., Jadhav, A. J., Pinjari, D. V., Mahamuni, N. M., and Pandit, A. B. (2016). A critical review on textile wastewater treatments: Possible approaches. *J. Environ. Manag.* 182, 351–366. doi:10.1016/j.jenvman.2016.07.090

Hosseini, M.-S., Abbasi, A., and Masteri-Farahani, M. (2022). Improving the photocatalytic activity of NH2-UiO-66 by facile modification with Fe (acac) 3 complex for photocatalytic water remediation under visible light illumination. *J. Hazard. Mater.* 425, 127975. doi:10.1016/j.jhazmat.2021.127975

Huang, S., Zhong, J., Li, J., Chen, J., Xiang, Z., Hu, W., et al. (2016). Z-scheme TiO2/g-C3N4 composites with improved solar-driven photocatalytic performance deriving from remarkably efficient separation of photo-generated charge pairs. *Mater. Res. Bull.* 84, 65–70. doi:10.1016/j.materresbull.2016.07.036

Ishikawa, A., Takata, T., Kondo, J. N., Hara, M., Kobayashi, H., and Domen, K. (2002). Oxysulfide Sm2Ti2S2O5 as a stable photocatalyst for water oxidation and reduction under visible light irradiation (λ≤ 650 nm). *J. Am. Chem. Soc.* 124, 13547–13553. doi:10.1021/ja0269643

Ivanchikova, I. D., Lee, J. S., Maksimchuk, N. V., Shmakov, A. N., Chesalov, Y. A., Ayupov, A. B., et al. (2014). Highly selective H2O2-based oxidation of alkylphenols to p-benzoquinones over MIL-125 metal–organic frameworks. *Eur. J. Inorg. Chem.* 2014, 132–139. doi:10.1002/ejic.201301098

Jabbar, Z. H., and Graimed, B. H. (2022). Recent developments in industrial organic degradation via semiconductor heterojunctions and the parameters affecting the photocatalytic process: A review study. *J. Water Process Eng.* 47, 102671. doi:10.1016/j.jwpe.2022.102671

Jia, Y., Ma, H., and Liu, C. (2019). Au nanoparticles enhanced Z-scheme Au-CoFe2O4/MoS2 visible light photocatalyst with magnetic retrievability. *Appl. Surf. Sci.* 463, 854–862. doi:10.1016/j.apsusc.2018.09.008

Jing, L., Xu, Y., Huang, S., Xie, M., He, M., Xu, H., et al. (2016). Novel magnetic CoFe2O4/Ag/Ag3VO4 composites: Highly efficient visible light photocatalytic and antibacterial activity. *Appl. Catal. B Environ.* 199, 11–22. doi:10.1016/j.apcatb.2016.05.049

Johnson, M., Gaffney, C., White, V., Bechelli, J., Balaraman, R., and Trad, T. (2020). Non-hydrolytic synthesis of caprylate capped cobalt ferrite nanoparticles and their application against Erwinia carotovora and Stenotrophomonas maltophilia. *J. Mater. Chem. B* 8, 10845–10853. doi:10.1039/d0tb02283g

Kefeni, K. K., and Mamba, B. B. (2020). Photocatalytic application of spinel ferrite nanoparticles and nanocomposites in wastewater treatment: Review. *Sustain. Mater. Technol.* 23, e00140. doi:10.1016/j.susmat.2019.e00140

Khosroshahi, N., Karimi, M., Taghvaei, T., and Safarifard, V. (2021). Ultrasound-assisted synthesis of CoFe2O4/Ce-UiO-66 nanocomposite for photocatalytic aerobic oxidation of aliphatic alcohols. *Mater. Today Chem.* 22, 100582. doi:10.1016/j.mtchem.2021.100582

Kreft, S., Wei, D., Junge, H., and Beller, M. (2020). Recent advances on TiO2-based photocatalytic CO2 reduction. *EnergyChem* 2, 100044. doi:10.1016/j.enchem.2020.100044

Lee, I., Choi, S., Lee, H. J., and Oh, M. (2015). Hollow metal–organic framework microparticles assembled via a self-templated formation mechanism. *Cryst. Growth & Des.* 15, 5169–5173. doi:10.1021/acs.cgd.5b00919

Lei, Z., Xue, Y., Chen, W., Qiu, W., Zhang, Y., Horike, S., et al. (2018). MOFs-based heterogeneous catalysts: New opportunities for energy-related CO2 conversion. *Adv. Energy Mater.* 8, 1801587. doi:10.1002/aenm.201801587

Li, D., Kassymova, M., Cai, X., Zang, S.-Q., and Jiang, H.-L. (2020). Photocatalytic CO2 reduction over metal-organic framework-based materials. *Coord. Chem. Rev.* 412, 213262. doi:10.1016/j.ccr.2020.213262

Liang, H., Guo, J., Yu, M., Zhou, Y., Zhan, R., Liu, C., et al. (2021). Porous loofah-sponge-like ternary heterojunction g-C3N4/Bi2WO6/MoS2 for highly efficient photocatalytic degradation of sulfamethoxazole under visible-light irradiation. *Chemosphere* 279, 130552. doi:10.1016/j.chemosphere.2021.130552

Liang, Z., Zhao, R., Qiu, T., Zou, R., and Xu, Q. (2019). Metal-organic framework-derived materials for electrochemical energy applications. *EnergyChem* 1, 100001. doi:10.1016/j.enchem.2019.100001

Liu, B., Liu, X., Liu, J., Feng, C., Li, Z., Li, C., et al. (2018). Efficient charge separation between UiO-66 and ZnIn2S4 flowerlike 3D microspheres for photoelectronchemical properties. *Appl. Catal. B Environ.* 226, 234–241. doi:10.1016/j.apcatb.2017.12.052

Liu, M., Xing, Z., Li, Z., and Zhou, W. (2021). Recent advances in core–shell metal organic frame-based photocatalysts for solar energy conversion. *Coord. Chem. Rev.* 446, 214123. doi:10.1016/j.ccr.2021.214123

Ma, S., Zhan, S., Jia, Y., and Zhou, Q. (2015). Highly efficient antibacterial and Pb (II) removal effects of Ag-CoFe2O4-GO nanocomposite. *ACS Appl. Mater. interfaces* 7, 10576–10586. doi:10.1021/acsami.5b02209

Man, Z., Meng, Y., Lin, X., Dai, X., Wang, L., and Liu, D. (2022). Assembling UiO-66@ TiO2 nanocomposites for efficient photocatalytic degradation of dimethyl sulfide. *Chem. Eng. J.* 431, 133952. doi:10.1016/j.cej.2021.133952

Mathew, D. S., and Juang, R.-S. (2007). An overview of the structure and magnetism of spinel ferrite nanoparticles and their synthesis in microemulsions. *Chem. Eng. J.* 129, 51–65. doi:10.1016/j.cej.2006.11.001

Mirhosseini-Eshkevari, B., Esnaashari, M., and Ghasemzadeh, M. A. (2019). Novel Brönsted acidic ionic liquids confined in UiO-66 nanocages for the synthesis of dihydropyrido [2, 3-d] pyrimidine derivatives under solvent-free conditions. *ACS omega* 4, 10548–10557. doi:10.1021/acsomega.9b00178

Mmelesi, O. K., Masunga, N., Kuvarega, A., Nkambule, T. T., Mamba, B. B., and Kefeni, K. K. (2021). Cobalt ferrite nanoparticles and nanocomposites: Photocatalytic, antimicrobial activity and toxicity in water treatment. *Mater. Sci. Semicond. Process.* 123, 105523. doi:10.1016/j.mssp.2020.105523

Molavi, H., Hakimian, A., Shojaei, A., and Raeiszadeh, M. (2018). Selective dye adsorption by highly water stable metal-organic framework: Long term stability analysis in aqueous media. *Appl. Surf. Sci.* 445, 424–436. doi:10.1016/j.apsusc.2018.03.189

Mu, X., Zhang, H., Zhang, C., Yang, S., Xu, J., Huang, Y., et al. (2021). Poly (vinylidene fluoride-trifluoroethylene)/cobalt ferrite composite films with a self-biased magnetoelectric effect for flexible AC magnetic sensors. *J. Mater. Sci.* 56, 9728–9740. doi:10.1007/s10853-021-05937-8

Mukherjee, D., Van der Bruggestn, B., and Mandal, B. (2022). Advancements in visible light responsive MOF composites for photocatalytic decontamination of textile wastewater: A review. *Chemosphere* 295, 133835. doi:10.1016/j.chemosphere.2022.133835

Nidheesh, P. V., Gandhimathi, R., and Ramesh, S. T. (2013). Degradation of dyes from aqueous solution by fenton processes: A review. *Environ. Sci. Pollut. Res.* 20, 2099–2132. doi:10.1007/s11356-012-1385-z

Ning, X., Wu, Y., Ma, X., Zhang, Z., Gao, R., Chen, J., et al. (2019). A novel charge transfer channel to simultaneously enhance photocatalytic water splitting activity and stability of CdS. *Adv. Funct. Mater.* 29, 1902992. doi:10.1002/adfm.201902992

Pan, B., Wu, Y., Rhimi, B., Qin, J., Huang, Y., Yuan, M., et al. (2021). Oxygen-doping of ZnIn2S4 nanosheets towards boosted photocatalytic CO2 reduction. *J. Energy Chem.* 57, 1–9. doi:10.1016/j.jechem.2020.08.024

Pan, B., Zhou, L., Qin, J., Liao, M., and Wang, C. (2022). Modulating CoFeOX nanosheets towards enhanced CO2 photoreduction to syngas: Effect of calcination temperature and mixed-valence multi-metals. *Chemistry–A Eur. J.* 2022, e202201992. doi:10.1002/chem.202201992

Qi, P., Luo, R., Pichler, T., Zeng, J., Wang, Y., Fan, Y., et al. (2019). Development of a magnetic core-shell Fe3O4@ TA@ UiO-66 microsphere for removal of arsenic (III) and antimony (III) from aqueous solution. *J. Hazard. Mater.* 378, 120721. doi:10.1016/j.jhazmat.2019.05.114

Qin, L., Wang, R., Xin, X., Zhang, M., Liu, T., Lv, H., et al. (2022). A dual-functional supramolecular assembly for enhanced photocatalytic hydrogen evolution. *Appl. Catal. B Environ.* 312, 121386. doi:10.1016/j.apcatb.2022.121386

Qin, Y., Hao, M., and Li, Z. (2020). Metal–organic frameworks for photocatalysis. *Interface Sci. Technol.* 31, 541–579. doi:10.1016/B978-0-08-102890-2.00017-8

Qiu, J., Zhang, X., Xie, K., Zhang, X.-F., Feng, Y., Jia, M., et al. (2019). Noble metal nanoparticle-functionalized Zr-metal organic frameworks with excellent photocatalytic performance. *J. colloid interface Sci.* 538, 569–577. doi:10.1016/j.jcis.2018.12.024

Quach, T.-A., Becerra, J., Nguyen, D.-T., Sakar, M., Vu, M.-H., Dion, F., et al. (2022). Direct Z-scheme mediated SmVO4/UiO-66-NH2 heterojunction nanocomposite for the degradation of antibiotic tetracycline hydrochloride molecules under sunlight. *Chemosphere* 303, 134861. doi:10.1016/j.chemosphere.2022.134861

Ramos, M., Santana, C., Velloso, C., Da Silva, A., Magalhães, F., and Aguiar, A. (2021). A review on the treatment of textile industry effluents through Fenton processes. *Process Saf. Environ. Prot.* 155, 366–386. doi:10.1016/j.psep.2021.09.029

Salunkhe, R. R., Tang, J., Kamachi, Y., Nakato, T., Kim, J. H., and Yamauchi, Y. (2015). Asymmetric supercapacitors using 3D nanoporous carbon and cobalt oxide electrodes synthesized from a single metal–organic framework. *ACS Nano* 9, 6288–6296. doi:10.1021/acsnano.5b01790

Shahjuee, T., Masoudpanah, S. M., and Mirkazemi, S. M. (2017). Coprecipitation synthesis of CoFe2O4 nanoparticles for hyperthermia. *J. Ultrafine Grained Nanostructured Mater.* 50, 105–110.

Shangkum, G. Y., Chammingkwan, P., Trinh, D. X., and Taniike, T. (2018). Design of a semi-continuous selective layer based on deposition of UiO-66 nanoparticles for nanofiltration. *Membranes* 8, 129. doi:10.3390/membranes8040129

Shawky, A., and Alshaikh, H. (2022). Cobalt ferrite-modified sol-gel synthesized ZnO nanoplatelets for fast and bearable visible light remediation of ciprofloxacin in water. *Environ. Res.* 205, 112462. doi:10.1016/j.envres.2021.112462

Shen, L., Liang, R., Luo, M., Jing, F., and Wu, L. (2015a). Electronic effects of ligand substitution on metal–organic framework photocatalysts: The case study of UiO-66. *Phys. Chem. Chem. Phys.* 17, 117–121. doi:10.1039/c4cp04162c

Shen, L., Luo, M., Liu, Y., Liang, R., Jing, F., and Wu, L. (2015b). Noble-metal-free MoS2 co-catalyst decorated UiO-66/CdS hybrids for efficient photocatalytic H2 production. *Appl. Catal. B Environ.* 166, 445–453. doi:10.1016/j.apcatb.2014.11.056

Shi, L., Zou, X., Wang, T., Wang, D., Fan, M., and Gong, Z. (2022). Sunlight photocatalytic degradation of ofloxacin using UiO-66/wood composite photocatalysts. *Chin. Chem. Lett.* 33, 442–446. doi:10.1016/j.cclet.2021.06.048

Sivula, K. (2020). Are organic semiconductors viable for robust, high-efficiency artificial photosynthesis? *ACS Energy Lett.* 5, 1970–1973. doi:10.1021/acsenergylett.0c01084

Sohrabnezhad, S., and Moghadamy, S. (2022). Zinc oxide nanorods incorporated magnetic isoreticular metal–organic framework for photodegradation of dyes. *J. Mol. Struct.* 1247, 131353. doi:10.1016/j.molstruc.2021.131353

Subhan, S., Yaseen, M., Ahmad, B., Tong, Z., Subhan, F., Ahmad, W., et al. (2021). Fabrication of MnO2 NPs incorporated UiO-66 for the green and efficient oxidative desulfurization and denitrogenation of fuel oils. *J. Environ. Chem. Eng.* 9, 105179. doi:10.1016/j.jece.2021.105179

Subudhi, S., Paramanik, L., Sultana, S., Mansingh, S., Mohapatra, P., and Parida, K. (2020). A type-II interband alignment heterojunction architecture of cobalt titanate integrated UiO-66-NH2: A visible light mediated photocatalytic approach directed towards norfloxacin degradation and green energy (hydrogen) evolution. *J. Colloid Interface Sci.* 568, 89–105. doi:10.1016/j.jcis.2020.02.043

Taddei, M., Schukraft, G. M., Warwick, M. E., Tiana, D., McPherson, M. J., Jones, D. R., et al. (2019). Band gap modulation in zirconium-based metal–organic frameworks by defect engineering. *J. Mater. Chem. A* 7, 23781–23786. doi:10.1039/c9ta05216j

Wang, A., Zhou, Y., Wang, Z., Chen, M., Sun, L., and Liu, X. (2016). Titanium incorporated with UiO-66 (Zr)-type metal–organic framework (MOF) for photocatalytic application. *RSC Adv.* 6, 3671–3679. doi:10.1039/c5ra24135a

Wang, C., Li, A.-R., and Ma, Y.-L. (2021a). Phosphomolybdic acid niched in the metal-organic framework UiO-66 with defects: An efficient and stable catalyst for oxidative desulfurization. *Fuel Process. Technol.* 212, 106629. doi:10.1016/j.fuproc.2020.106629

Wang, J., Yuan, M., Li, C., Zhang, B., Zhu, J., Hao, X., et al. (2022). One-Step construction of polyimide/NH2-UiO-66 heterojunction for enhanced photocatalytic degradation of sulfonamides. *J. Colloid Interface Sci.* 612, 536–549. doi:10.1016/j.jcis.2021.12.190

Wang, P., Sun, L., Ye, J., Liu, Q., Fei, Z., Chen, X., et al. (2021b). Construction of crystal defect sites in UiO-66 for adsorption of dimethyl phthalate and phthalic acid. *Microporous Mesoporous Mater.* 312, 110778. doi:10.1016/j.micromeso.2020.110778

Wang, Y., Jin, H., Ma, Q., Mo, K., Mao, H., Feldhoff, A., et al. (2020a). A MOF glass membrane for gas separation. *Angew. Chem.* 132, 4395–4399. doi:10.1002/ange.201915807

Wang, Y., Yan, J., Wen, N., Xiong, H., Cai, S., He, Q., et al. (2020b). Metal-organic frameworks for stimuli-responsive drug delivery. *Biomaterials* 230, 119619. doi:10.1016/j.biomaterials.2019.119619

Wang, Y., Zhang, S., Zhao, Y., Bedia, J., Rodriguez, J., and Belver, C. (2021c). UiO-66-based metal organic frameworks for the photodegradation of acetaminophen under simulated solar irradiation. *J. Environ. Chem. Eng.* 9, 106087. doi:10.1016/j.jece.2021.106087

Wang, Z., Jiang, L., Wang, K., Li, Y., and Zhang, G. (2021d). Novel AgI/BiSbO4 heterojunction for efficient photocatalytic degradation of organic pollutants under visible light: Interfacial electron transfer pathway, DFT calculation and degradation mechanism study. *J. Hazard. Mater.* 410, 124948. doi:10.1016/j.jhazmat.2020.124948

Wei, F., Wang, H., Ran, W., Liu, T., and Liu, X. (2019). Preparation of S–N co-doped CoFe 2 O 4@ rGO@ TiO 2 nanoparticles and their superior UV-Vis light photocatalytic activities. *RSC Adv.* 9, 6152–6162. doi:10.1039/c8ra10238d

Wei, Q., Xiong, S., Li, W., Jin, C., Chen, Y., Hou, L., et al. (2021). Double Z-scheme system of α-SnWO4/UiO-66 (NH2)/g-C3N4 ternary heterojunction with enhanced photocatalytic performance for ibuprofen degradation and H2 evolution. *J. Alloys Compd.* 885, 160984. doi:10.1016/j.jallcom.2021.160984

Wen, M., Li, G., Liu, H., Chen, J., An, T., and Yamashita, H. (2019). Metal–organic framework-based nanomaterials for adsorption and photocatalytic degradation of gaseous pollutants: Recent progress and challenges. *Environ. Sci. Nano* 6, 1006–1025. doi:10.1039/c8en01167b

Winarta, J., Shan, B., Mcintyre, S. M., Ye, L., Wang, C., Liu, J., et al. (2019). A decade of UiO-66 research: A historic review of dynamic structure, synthesis mechanisms, and characterization techniques of an archetypal metal–organic framework. *Cryst. Growth & Des.* 20, 1347–1362. doi:10.1021/acs.cgd.9b00955

Xia, T., Lin, Y., Li, W., and Ju, M. (2021). Photocatalytic degradation of organic pollutants by MOFs based materials: A review. *Chin. Chem. Lett.* 32, 2975–2984. doi:10.1016/j.cclet.2021.02.058

Xiong, L., and Tang, J. (2021). Strategies and challenges on selectivity of photocatalytic oxidation of organic substances. *Adv. Energy Mater.* 11, 2003216. doi:10.1002/aenm.202003216

Xiong, X., Zhao, Y., Shi, R., Yin, W., Zhao, Y., Waterhouse, G. I., et al. (2020). Selective photocatalytic CO2 reduction over Zn-based layered double hydroxides containing tri or tetravalent metals. *Sci. Bull.* 65, 987–994. doi:10.1016/j.scib.2020.03.032

Xu, F., Zhang, Q., An, R., Li, L., and Zhou, L. (2022). Facile fabrication of flower-like NH2-UIO-66/BiOCl Z-scheme heterojunctions with largely improved photocatalytic performance for removal of tetracycline under solar irradiation. *J. Alloys Compd.* 899, 163324. doi:10.1016/j.jallcom.2021.163324

Xu, J., Varghese, J., Portale, G., Longo, A., Momand, J., Syari'ati, A., et al. (2019). Chemical solution deposition of ordered 2D arrays of room-temperature ferrimagnetic cobalt ferrite nanodots. *Polymers* 11, 1598. doi:10.3390/polym11101598

Xu, X., Liu, R., Cui, Y., Liang, X., Lei, C., Meng, S., et al. (2017). PANI/FeUiO-66 nanohybrids with enhanced visible-light promoted photocatalytic activity for the selectively aerobic oxidation of aromatic alcohols. *Appl. Catal. B Environ.* 210, 484–494. doi:10.1016/j.apcatb.2017.04.021

Yang, Z., Tong, X., Feng, J., He, S., Fu, M., Niu, X., et al. (2019). Flower-like BiOBr/UiO-66-NH2 nanosphere with improved photocatalytic property for norfloxacin removal. *Chemosphere* 220, 98–106. doi:10.1016/j.chemosphere.2018.12.086

Yaseen, D., and Scholz, M. (2019). Textile dye wastewater characteristics and constituents of synthetic effluents: A critical review. *Int. J. Environ. Sci. Technol.* 16, 1193–1226. doi:10.1007/s13762-018-2130-z

Yassin, J. M., Taddesse, A. M., and Sánchez-Sánchez, M. (2022). Sustainable synthesis of semicrystalline Zr-BDC MOF and heterostructural Ag3PO4/Zr-BDC/g-C3N4 composite for photocatalytic dye degradation. *Catal. Today* 390, 162–175. doi:10.1016/j.cattod.2021.11.037

Yavari, S., Mahmodi, N. M., Teymouri, P., Shahmoradi, B., and Maleki, A. (2016). Cobalt ferrite nanoparticles: Preparation, characterization and anionic dye removal capability. *J. Taiwan Inst. Chem. Eng.* 59, 320–329. doi:10.1016/j.jtice.2015.08.011

Yi, X.-H., Ma, S.-Q., Du, X.-D., Zhao, C., Fu, H., Wang, P., et al. (2019). The facile fabrication of 2D/3D Z-scheme g-C3N4/UiO-66 heterojunction with enhanced photocatalytic Cr (VI) reduction performance under white light. *Chem. Eng. J.* 375, 121944. doi:10.1016/j.cej.2019.121944

Younes, H. A., Taha, M., Mahmoud, R., Mahmoud, H. M., and Abdelhameed, R. M. (2022). High adsorption of sodium diclofenac on post-synthetic modified zirconium-based metal-organic frameworks: Experimental and theoretical studies. *J. Colloid Interface Sci.* 607, 334–346. doi:10.1016/j.jcis.2021.08.158

Yuan, N., Gong, X., Sun, W., and Yu, C. (2021). Advanced applications of Zr-based MOFs in the removal of water pollutants. *Chemosphere* 267, 128863. doi:10.1016/j.chemosphere.2020.128863

Yuan, S., Feng, L., Wang, K., Pang, J., Bosch, M., Lollar, C., et al. (2018). Stable metal-organic frameworks: Stable metal-organic frameworks: Design, synthesis, and applications (adv. Mater. 37/2018). *Adv. Mater.* 30, 1870277. doi:10.1002/adma.201870277

Zeng, Y., Guo, N., Song, Y., Zhao, Y., Li, H., Xu, X., et al. (2018). Fabrication of Z-scheme magnetic MoS2/CoFe2O4 nanocomposites with highly efficient photocatalytic activity. *J. colloid interface Sci.* 514, 664–674. doi:10.1016/j.jcis.2017.12.079

Zhang, A., Liu, B., Liu, M., Xie, Z., Wang, D., and Feng, G. (2021a). The adsorption properties of defect controlled metal-organic frameworks of UiO-66. *Sep. Purif. Technol.* 270, 118842. doi:10.1016/j.seppur.2021.118842

Zhang, F., Cheng, W., Yu, Z., Ge, S., Shao, Q., Pan, D., et al. (2021b). Microwave hydrothermally synthesized WO3/UiO-66 nanocomposites toward enhanced photocatalytic degradation of rhodamine B. *Adv. Compos. Hybrid Mater.* 4, 1330–1342. doi:10.1007/s42114-021-00346-6

Zhang, G., Jin, L., Zhang, R., Bai, Y., Zhu, R., and Pang, H. (2021c). Recent advances in the development of electronically and ionically conductive metal-organic frameworks. *Coord. Chem. Rev.* 439, 213915. doi:10.1016/j.ccr.2021.213915

Zhang, L., Li, P., Feng, L., Chen, X., Jiang, J., Zhang, S., et al. (2020). Controllable fabrication of visible-light-driven CoSx/CdS photocatalysts with direct Z-scheme heterojunctions for photocatalytic Cr (VI) reduction with high efficiency. *Chem. Eng. J.* 397, 125464. doi:10.1016/j.cej.2020.125464

Zhang, R., Du, B., Li, Q., Cao, Z., Feng, G., and Wang, X. (2019a). α-Fe2O3 nanoclusters confined into UiO-66 for efficient visible-light photodegradation performance. *Appl. Surf. Sci.* 466, 956–963. doi:10.1016/j.apsusc.2018.10.048

Zhang, S., Zhao, Y., Shi, R., Waterhouse, G. I., and Zhang, T. (2019b). Photocatalytic ammonia synthesis: Recent progress and future. *EnergyChem* 1, 100013. doi:10.1016/j.enchem.2019.100013

Zhang, X., Tong, S., Huang, D., Liu, Z., Shao, B., Liang, Q., et al. (2021d). Recent advances of Zr based metal organic frameworks photocatalysis: Energy production and environmental remediation. *Coord. Chem. Rev.* 448, 214177. doi:10.1016/j.ccr.2021.214177

Zhang, X., Yang, Y., Lv, X., Wang, Y., Liu, N., Chen, D., et al. (2019c). Adsorption/desorption kinetics and breakthrough of gaseous toluene for modified microporous-mesoporous UiO-66 metal organic framework. *J. Hazard. Mater.* 366, 140–150. doi:10.1016/j.jhazmat.2018.11.099

Zhang, Y.-P., Han, W., Yang, Y., Zhang, H.-Y., Wang, Y., Wang, L., et al. (2022). S-scheme heterojunction of black TiO2 and covalent-organic framework for enhanced photocatalytic hydrogen evolution. *Chem. Eng. J.* 446, 137213. doi:10.1016/j.cej.2022.137213

Zhang, Y., Zhou, J., Feng, Q., Chen, X., and Hu, Z. (2018). Visible light photocatalytic degradation of MB using UiO-66/g-C3N4 heterojunction nanocatalyst. *Chemosphere* 212, 523–532. doi:10.1016/j.chemosphere.2018.08.117

Zhao, H., Liu, X., Dong, Y., Xia, Y., and Wang, H. (2019). A special synthesis of BiOCl photocatalyst for efficient pollutants removal: New insight into the band structure regulation and molecular oxygen activation. *Appl. Catal. B Environ.* 256, 117872. doi:10.1016/j.apcatb.2019.117872

Zhou, C., Lai, C., Huang, D., Zeng, G., Zhang, C., Cheng, M., et al. (2018). Highly porous carbon nitride by supramolecular preassembly of monomers for photocatalytic removal of sulfamethazine under visible light driven. *Appl. Catal. B Environ.* 220, 202–210. doi:10.1016/j.apcatb.2017.08.055

Zhou, C., Xia, W., Huang, D., Cheng, M., Zhang, H., Cai, T., et al. (2021). Strategies for enhancing the perylene diimide photocatalytic degradation activity: Method, effect factor, and mechanism. *Environ. Sci. Nano* 8, 602–618. doi:10.1039/d0en01245a

Zhou, G., Fu, Y., Zhou, R., Zhang, L., Zhang, L., Deng, J., et al. (2022). Efficient degradation of organic contaminants by magnetic cobalt ferrite combined with peracetic acid. *Process Saf. Environ. Prot.* 160, 376. doi:10.1016/j.psep.2022.02.031

Zhou, L., Ji, L., Ma, P.-C., Shao, Y., Zhang, H., Gao, W., et al. (2014). Development of carbon nanotubes/CoFe2O4 magnetic hybrid material for removal of tetrabromobisphenol A and Pb (II). *J. Hazard. Mater.* 265, 104–114. doi:10.1016/j.jhazmat.2013.11.058

Zou, X., Zhao, X., Zhang, J., Lv, W., Qiu, L., and Zhang, Z. (2021). Photocatalytic degradation of ranitidine and reduction of nitrosamine dimethylamine formation potential over MXene–Ti3C2/MoS2 under visible light irradiation. *J. Hazard. Mater.* 413, 125424. doi:10.1016/j.jhazmat.2021.125424

frontiers | Frontiers in Chemistry

TYPE Mini Review
PUBLISHED 20 January 2023
DOI 10.3389/fchem.2023.1119240

EDITED BY
Maria Vamvakaki,
University of Crete, Greece

REVIEWED BY
Tangxin Xiao,
Changzhou University, China
Bingbing Shi,
Northwest Normal University, China
Huangtianzhi Zhu,
University of Cambridge, United Kingdom

*CORRESPONDENCE
Zhenhui Qi,
✉ qi@nwpu.edu.cn
Qiangqiang Xu,
✉ skyee@mail.nwpu.edu.cn
Yan Ge,
✉ ge@nwpu.edu.cn

SPECIALTY SECTION
This article was submitted
to Nanoscience, a section of the journal
Frontiers in Chemistry

RECEIVED 08 December 2022
ACCEPTED 10 January 2023
PUBLISHED 20 January 2023

CITATION
Qi Z, Qin Y, Wang J, Zhao M, Yu Z, Xu Q, Nie H, Yan Q and Ge Y (2023), The aqueous supramolecular chemistry of crown ethers.
Front. Chem. 11:1119240.
doi: 10.3389/fchem.2023.1119240

The aqueous supramolecular chemistry of crown ethers

Zhenhui Qi[1]*, Yao Qin[1], Jijun Wang[1], Maojin Zhao[1], Zhuo Yu[1], Qiangqiang Xu[1]*, Hongqi Nie[2], Qilong Yan[2] and Yan Ge[1]*

[1]Sino-German Joint Research Lab for Space Biomaterials and Translational Technology, Synergetic Innovation Center of Biological Optoelectronics and Healthcare Engineering (BOHE), Shaanxi Provincial Synergistic Innovation Center for Flexible Electronics & Health Sciences (FEHS), School of Life Sciences, Northwestern Polytechnical University, Xi'an, Shaanxi, China, [2]Science and Technology on Combustion, Internal Flow and Thermostructure Laboratory, Northwestern Polytechnical University, Xi'an, China

This mini-review summarizes the seminal exploration of aqueous supramolecular chemistry of crown ether macrocycles. In history, most research of crown ethers were focusing on their supramolecular chemistry in organic phase or in gas phase. In sharp contrast, the recent research evidently reveal that crown ethers are very suitable for studying abroad range of the properties and applications of water interactions, from: high water-solubility, control of Hofmeister series, "structural water", and supramolecular adhesives. Key studies revealing more details about the properties of water and aqueous solutions are highlighted.

KEYWORDS

crown ethers, selenium, responsive materials, hofmeister series, structural water

Introduction

Supramolecular chemistry provides a powerful platform for achieving complex chemical/biological activities using non-covalent interactions. Water is significant for biomimetic chemistry and to achieve sustainability in both the natural environment and human societies. Thus, exploring aqueous supramolecular chemistry is essential for producing advanced functional materials for biomedical processing, energy, information technology, and environmental science applications (Zayed et al., 2010; Cremer et al., 2017; Zheng et al., 2018; Gatiatulin et al., 2019; Xiao et al., 2020a; Duan et al., 2020; WuXiao, 2020; Zhang et al., 2020; Zhang et al., 2021a; Zhang et al., 2021b; Ding et al., 2021; Liu et al., 2021; Zhu et al., 2021; Shi et al., 2022).

Crown ethers (CEs) are cyclic compounds comprising several ether linkages with a specifically sized cavity in their centers. The discovery of CEs was pivotal in the establishment of supramolecular chemistry. CE supramolecular chemistry is predominantly conducted in organic solvents (Qi et al., 2012; Qi et al., 2014; Qi and Schalley, 2014; Ali et al., 2019; Ge et al., 2019; Xiao et al., 2021) or partially in the gas phase (Weimann et al., 2009; Qi et al., 2013). The molecular structure of CEs indicates their great flexibility to adapt their conformation to interact with water molecules. In organic media, the lone electron pairs on the CE oxygen atoms create a region of high electron density in the ring cavity. CEs exhibit a rich conformational panorama and low energy barriers, and research in the past two decades has focused on fabricating CE-based threads or interlocking components for use in nanomachines. These reactions have primarily been conducted in organic solvents; however, in aqueous media, the polar surfaces of CE molecules are exposed, with a water-accessible surface area (ASA) originating from the ethylene glycol units. Therefore, it is reasonable to expect that CEs can be water-soluble macrocycles. However, the scientific community has long been skeptical of the solubility of CEs in water, resulting in few reported studies in the literature of water-soluble CEs (Zhang et al., 2022a; Wang et al., 2022) compared to those on other macrocycles, such as cucurbiturils (Das et al., 2019), calixarenes (Xu et al., 2019), cyclodextrins (Kwong et al., 2021; Li et al., 2021; Luo et al., 2021; Zhang et al., 2022b), and pillararenes (Yu et al., 2021). Recently, CEs have emerged as an intriguing host for studying water and aqueous supramolecular chemistry.

In this mini-review, we summarize applications that have capitalized on CE–water interactions to fabricate aqueous materials. Unexpectedly high water solubility, control of the Hofmeister cationic series, and "structural water" in supramolecular adhesives are highlighted.

CEs with water: A missing type of water-soluble macrocycle

In 2017, Qi et al. serendipitously discovered that benzo-21-crown-7 ether (**C7**) exhibits remarkably high water solubility (Dong et al., 2017a). The solubility of **C7** in water at room temperature reaches 1,500 g/L (4.21 M), which is superior to those of many classic water-soluble supramolecular macrocycles, such as cucurbit [n]urils and α-, β-, and γ-cyclodextrins (see comparison in Figure 1). Concentration-dependent nuclear Overhauser effect spectra (NOESY) revealed no significant intermolecular interactions between the **C7** molecules in solution. Diffusion-ordered NMR spectra (DOSY) indicated that the **C7** diffusion constants at high and low concentrations were similar. The solution was prepared using the **C7** monomer and no molecular aggregation was observed. The functional group on the benzo-moiety significantly affects the water-solubility of **C7** (Figure 1). The solubility of the derivatives follows the sequence: **C7** > **C7NH2** > **C7CN** > **C7COOH**. Entropic desolvation of the CE ethylene glycol units is known to increase the hydrophobicity of the cyclic chain, which results in separation from the aqueous solution. Therefore, the thermo-responsivity of **C7** and its derivatives in water is an intriguing topic of study (Zhang et al., 2021c). For example, low-molar-mass

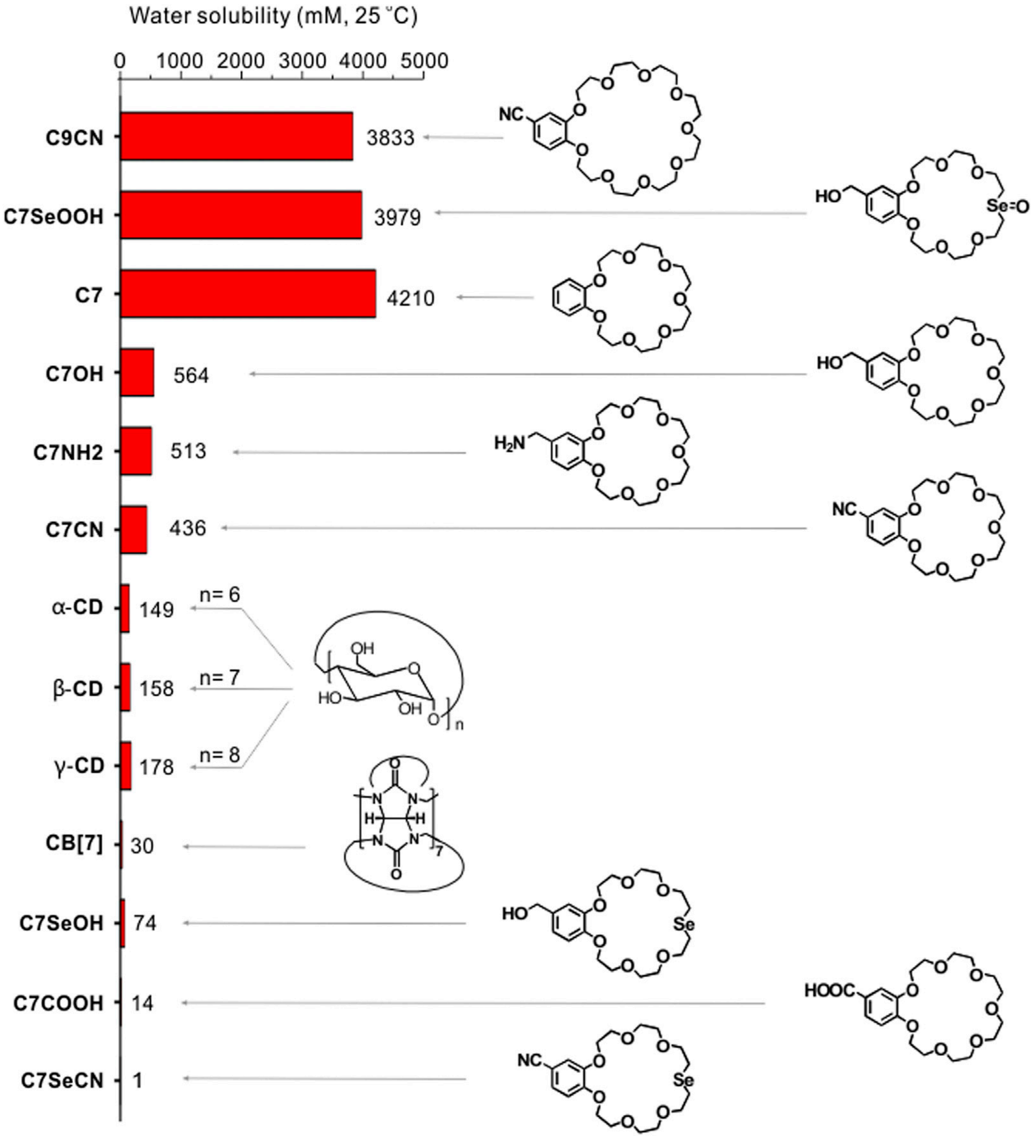

FIGURE 1
Comparison of the water-solubility of CEs and their derivatives with α-cyclodextrin, β-cyclodextrin, and γ-cyclodextrin and cucurbit[7]urils. Adapted and reproduced from Dong et al. (2017a), Jin et al. (2019), Xu et al. (2021) with kind permission from American Chemical Society and Elsevier.

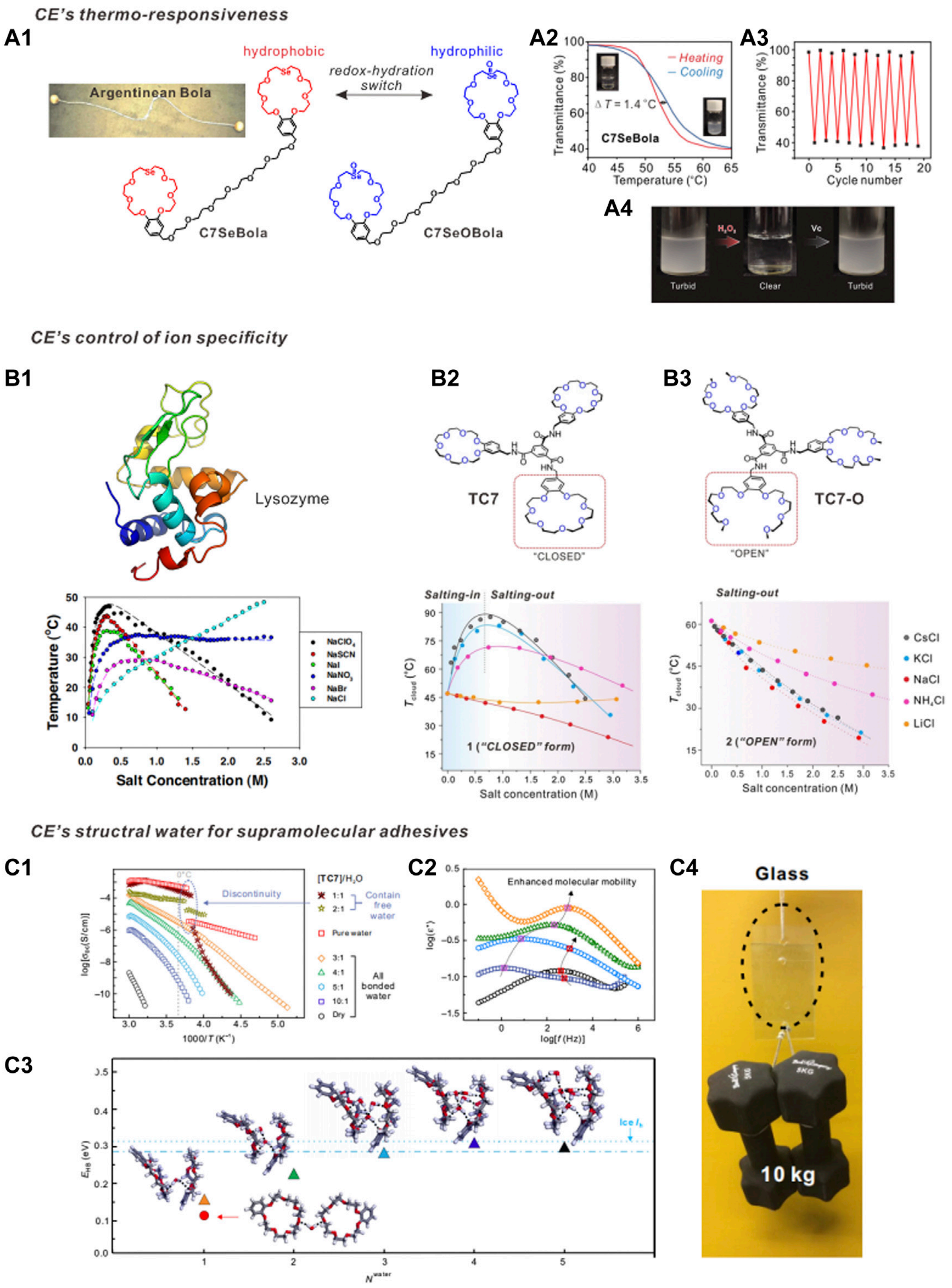

FIGURE 2
(A) The redox-controlled hydration of CE for design macrocyclic amphiphiles. **(A1)** the chemical structure of bolaamphiphile **C7SeBola**; **(A2) C7SeBola** exhibited rapid LCST behavior in water, **(A3)** The highly reversible LCST transition processes, **(A4)** turbid-to-clear and clear-to-turbid transitions can be controlled in an "ON-OFF" manner. **(B)** Hofmeister series reversal behavior. **(B1)** Hofmeister series reversal of anions for lysozyme reported by Cremer et al. The apparent association constants of anionic-lysozyme interaction for ClO_4^-, SCN^-, I^-, NO_3^-, Br^- and Cl^- are 0.10, 0.10, 0.09, 0.10, 0.18 and 0.12 M^{-1}, respectively. **(B2)** Hofmeister series reversal of cation for a triple-CE-molecule (**TC7**). The inverse Hofmeister series at low salt concentration regimes should be the cation−solute interaction at wok. The charge density is initially dominant and then decays due to the increase of the ionic radius, then the enhanced "size-fitting" induced molecular recognition dominants the system. **(B3)** Ring-open counterpart (**TC7-O**) showed no Hofmeister series reversal. **(C) TC7** generates structural water for fabricating supramolecular adhesive material. **(C1)** The dependence of DC conductivity σ_{dc} versus 1/T for **TC7**$_n$-**H** materials with different water content. **(C2)** Dielectric loss versus frequency for **TC7**$_n$-**H** materials with different water content at a temperature of −100°C; **(C3)** Averaged hydrogen-bond strengths (EHB) of CE-water systems with different number of water molecules (N_{water}) as obtained from the density functional theory (DFT) calculations; **(C4)** Application of **TC7**$_{10}$-**H**$_1$ materials as supramolecular adhesive materials. Adapted and reproduced from Xu et al. (2021), Qi et al. (2018), Zhang and Cremer (2009), Dong et al. (2017b) with kind permission by the Elsevier, National Academy of Science, Wiley-VCH and American Association for the Advancement of Science.

C7 and **C7CN** exhibit lower critical solution temperature (LCST) phenomena. Interestingly, **C7COOH** exhibits upper critical solution temperature (UCST) behavior followed by LCST phase behavior, implying that the benzo-group functionalization is instrumental in modulating the thermo-responsiveness of the CEs.

Substituting the O atom opposite the benzo-moiety on the CE with an Se atom transformed the **C7CN** from hydrophilic to strongly hydrophobic, and the aqueous solubility of **C7SeCN** decreased to 1 mM (Figure 1) (Jin et al., 2019). Using detailed computer modeling, the solvation free energies (ΔG_s^θ) of **C7CN** and **C7SeCN** were calculated to be −104.21 and −81.82 kJ/mol, respectively, which are in accordance with the experimentally determined solubility trend. By contrast, when the substituent on **C7CN** is a selenoxide moiety, the water-solubility of the CE is significantly enhanced. Both the crystal structure and theoretical modelling revealed that selenoxides are excellent hydrogen-bond (HB) acceptors, because the HB length of the selenoxide group (1.72 Å) is significantly shorter than that of the ether (-O-) group (1.90 Å). Qi et al. found that the water solubility of **C7SeOOH** reaches 3,979 mM (Xu et al., 2021). By contrast, the water solubility of **C7OH** is 564 mM and that of **C7SeOH** is merely 74 mM. Based on these results, the reversible transformation between the selenide- and selenoxide-containing CEs creates a switchable macrocycle pair (Figure 2A1) that differs dramatically in hydration and is controlled by redox stimuli. This constitutionally adaptive behavior of CEs offers an elegant platform for controlling and/or switching the hydration of bolaamphiphile skeletons (which are similar in structure to Argentinean boleadoras) (Xu et al., 2021). The resulting macrocyclic bolaamphiphile **C7SeBola** exhibited LCST behavior in water (Figure 2A2), and the overall LCST transition processes were highly reversible (Figure 2A3). Based on the redox-responsive transformation between **C7SeBola** and **C7SeOBola**, the chemically responsive, reversible, turbid-to-clear and clear-to-turbid transitions can be controlled in an "ON-OFF" manner (Figure 2A4). Based on these results, diverse CE-based macrocyclic amphiphiles with unique structures and responsiveness were subsequently developed (Zheng et al., 2019; Li et al., 2020a; Deng et al., 2020; Wu et al., 2020).

CEs with ions: Revisiting the Hofmeister series

The chemistry of aqueous salt solutions is rich in ambiguities and a prime example is the Hofmeister effect, which is a prominent example of a multilateral interactive relationship (Jungwirth and Cremer, 2014). As early as 1888, Franz Hofmeister, a Czech protein scientist, noticed specific cationic and anionic effects on the solubility of proteins and discovered that the effectiveness of simple ions in protein precipitation followed a specific order (the Hofmeister series). The effectiveness of the influence of positive ions on precipitating proteins is smaller than negative charged ions (Aoki et al., 2016). Subsequently, a wide variety of phenomena, from protein folding and enzymatic activity to colloidal assembly and bacterial growth, have been shown to follow the Hofmeister series (Wang et al., 2021). Recent evidence suggests that Hofmeister effects arise from direct interactions between ions and solutes and between ions and the first solvation shells of those solutes. However, several observations have challenged these theoretical ideas, such as the Hofmeister series reversal. The reversal of the Hofmeister series between low and high salt concentration regimes was initially reported in 1911. However, explanation and prediction of such phenomena are not possible using existing theories on specific ion effects. The current prevailing theory, the law of matching water affinities (LMWA), can only qualitatively explain and rank ion–ion and ion–solute interactions on charged surfaces. The rules and parameters that govern the reversal phenomena on a neutral polar surface, such as the uncharged hydrophilic regions on proteins or synthetic materials, have not yet been determined.

To address this issue, Qi and Dong developed a low-molecular-weight supramolecular system to reveal the underlying systematic relationships between ions, water, and solutes (Qi et al., 2018). A triple-CE-molecule (**TC7**) and its ring-opened counterpart (**TC7-O**) exhibit a distinctive topological effect (Figures 2B2, B3). When neutral polar groups are arranged in a crown geometry, the "size-fitting"-induced solute-cation recognition, though rather weak, efficiently tunes the Hofmeister series and results in a Hofmeister series reversal phenomenon with singly charged cations. The phase transition curve of **TC7** with cations (Figure 2B2, bottom) is quite similar to that of lysozyme with anions (Figure 2B1, bottom) reported by Cremer et al. (Zhang and Cremer, 2009). Interestingly, isothermal titration calorimetry measurements revealed unexpectedly low cation-solute interactions in this Hofmeister series reversal, with an apparent equilibrium association constant *Ka* of ~10 M^{-1}. Similar low binding affinities, from a supramolecular chemistry viewpoint, are observed in the majority of reported supramolecular recognition motifs (*Ka* > 10^3 M^{-1}). Therefore, CEs provide an elegant and simple model to control the Hofmeister series reversal behavior, which has long been a topic of debate in the physics community (Jungwirth and Cremer, 2014).

On-going research has further demonstrated the general principles of the spatial topology factor and site-fitting effect in CE-containing ionic systems (Huang et al., 2018; Luo et al., 2019; Pan et al., 2021). Chen et al. observed a similar coexisting salting-in and salting-out effect (Huang et al., 2018) when **C7** was functionalized on a poly (vinyl alcohol) polymer system, demonstrating that CEs can serve as general building blocks to control ion specificity in aqueous media. A benzo-27-crown-9 ether (**C9OH**) system was used to explore the "size-fitting"-induced host-guest complexation between **C9** and guanidinium. A similar coexisting salting-in and salting-out effect can be extended to guanidinium-type ions, such as guanidinium chloride and arginine (Pan et al., 2021).

CEs with structural water: Water act as an essential comonomer in supramolecular polymerization

Structural water molecules form strong HBs with the polar groups in proteins and are thought to tighten the protein matrix. These deeply-buried water molecules are considered an integral part of the folded protein structure. The concept of structural water bound within hydrophobic capsules that stabilize protein structures is well established in biology; however, the stabilization effects of water in materials science are rarely discussed. Supramolecular polymers are formed through non-covalent, directional interactions between monomeric building blocks. Assembly of these polymers is reversible, which enables functions such as coating, self-healing, and responsiveness (Wei et al., 2014; Xiao et al., 2020b; Lv et al., 2021). Water is typically regarded as a solvent in the assembly of supramolecular polymers; however, in 2017, Qi and Dong et al. reported a supramolecular polymer in which water acted as an indispensable comonomer in the supramolecular polymerization (Dong et al., 2017b).

In the dry state, **TC7** is a fragile, slippery solid that has an amorphous glassy structure. However, when exposed to the ambient environment (25°C, 40% relative humidity), the dry **TC7** quickly adsorbed the ambient water vapor, affording a **TC7**-water mixture with notable flexibility, elasticity, and adhesive properties (Figure 2C). Infrared spectra indicated that the **TC7** molecules self-assembled into one-dimensional supramolecular aggregates *via* amido-HBs. Broadband dielectric spectra (BDS) provided key evidence of the existence of structural water molecules (Figures 2C1, C2). The frequency-dependence of the conductivity spectra of **TC7**$_n$-water(**H**)$_1$ ($n = 1, 2, 3, 4, 5, 10$; n denotes the weight ratio of **TC7** to added water) presented the typical conductivity-frequency behavior observed in semiconducting materials (Zhang et al., 2021c). For weight ratios of **TC7**$_n$-**H**$_1$ above $n > 2$ (Figure 2C1), the σ_{dc} versus 1/T plots did not exhibit any discontinuity at the freezing temperature of water (273 K), indicating that up to this weight ratio, water molecules in this supramolecular polymer exist as structural water (which is distinct from free water in the bulk solvent). By contrast, the σ_{dc} versus 1/T plots of both **TC7**$_2$-**H**$_1$ and **TC7**$_1$-**H**$_1$ displayed a clear discontinuity close to the temperature at which water in the bulk solvent also displays a discontinuity. This result clearly indicates the presence of significant amounts of free water molecules within this supramolecular material that freeze at the temperature at which the discontinuity is observed. An *in situ* single crystal structure of frozen water was obtained from the high-water content sample **TC7**$_1$-**H**$_1$, which confirmed these findings. The average hydrogen bond energy (E_{HB}) between the **C7** and water molecules was calculated using density functional theory simulations and was similar to that of hydrogen bonds in the bulk ice (Figure 2C3). The adhesion strength of **TC7**$_{10}$-**H**$_1$ was 4.15 MPa (tensile rate 1.38 MPa/s), which is significantly higher than that of commercial PVA adhesives (0.43 MPa).

Inspired by this work, Dong et al. extended the structural water system to a pillararene-crown ether (**PC**) system (Li et al., 2020b) in which ten **C7** units were decorated on the upper and lower rims of pillar[5]arene. The frequency-dependence of the BDS conductivity spectra for **PC**$_{10}$-water (**W**)$_1$ exhibited a similar discontinuity around the freezing point of water, indicating the existence of structural water. Intriguingly, the resulting CE-structural water supramolecular polymer system exhibited low-temperature-resistant adhesive properties. The resulting **PC**$_{10}$-**W**$_1$ complex exhibited adhesion strengths up to 2.49 MPa at −18°C. By contrast, the adhesion strengths of samples with a high water content were between 0.37 and 0.46 MPa, which is comparable to that of pure water (0.36 MPa). Notably, the structural water in the **PC**$_{10}$-**W**$_1$ sample remained liquid down to −80°C, indicating that structural water imparts anti-icing properties to the adhesive material. The macroscopic adhesive strength was maintained between 1.12 and 1.46 MPa at −80°C. By contrast, high-water-content **PC** samples became turbid solids at low temperatures because the free water in these samples froze. These studies elegantly demonstrate the potential of CEs with structural water as supramolecular adhesive materials (Zhang et al., 2019; Li et al., 2020c).

Summaries and perspectives

This mini-review has highlighted selected, preeminent examples from the growing field of aqueous supramolecular chemistry of CEs. These studies have revealed new and unusual properties of CEs arising from their unique ability to interact with water molecules. These studies demonstrated the correlation between the hydration of CEs and the cyclic topological effect and the implications of cation affinities for neutral polar surfaces in the Hofmeister series. There is still much to explore and accomplish in this field; 1) CEs decorated with diverse functional groups make it easier to create diverse functional building blocks (Shen et al., 2019), thus enabling numerous opportunities for designing novel supramolecular materials in water; 2) To date, investigations into the aqueous behaviors of Se- or Te-containing CEs are scarce. The intrinsic catalytic roles and redox-responsiveness of Se and Te compounds significantly expand the functional range of CEs *via* substitution of a chalcogen atom on the CE with Se or Te (Shang et al., 2021a; Shang et al., 2021b; Li et al., 2022); 3) Revealing the interactions between water, CEs, and ions can benefit applied areas such as anti-icing materials (Ge et al., 2022; Hu et al., 2022) and aqueous metal-ion batteries (Wang et al., 2020). Aqueous CE supramolecular chemistry is an emerging research field and further studies will broaden our understanding of the properties and potential applications of aqueous CE systems.

Author contributions

ZQ and YQ first conceived the idea, framework and writing direction of the article. YQ performed a literature search and summary, and wrote the first draft of the manuscript. ZQ, YQ, and YG scrutinized the manuscript for scientific terminology and made important contributions to the revision of the literature. All authors have read and checked the submitted version before uploading.

Acknowledgments

We gratefully acknowledge financial support from the National Natural Science Foundation of China (22071196, 22007078), Key R&D Program of Shaanxi Province (2021KWZ-18), Aeronautical Science Foundation of China (ASFC-2020Z061053001), Opening Project of State Key Laboratory of Polymer Materials Engineering (Sichuan University) (Grant No. klpme 2021-05-03), Student Innovation and Entrepreneurship Education Center of the Student Work Department of the Party Committee of NPU (2021-cxcy-012), Higher Education Research Fund of NPU (CJGZMS202202), National Innovation Training Program for College Students (202210699005), the Fundamental Research Funds for the Central Universities, and Fellowship from CSC Innovative Team Program (CXXM2110141862). We thank the Analytical & Testing Center of NPU for the characterization of materials. We thank Dong Shengyi's scientific suggestion and assistance.

Conflict of interest

Publisher's note

References

Ali, M. C., Liu, R., Chen, J., Cai, T., Zhang, H., Li, Z., et al. (2019). New deep eutectic solvents composed of crown ether, hydroxide and polyethylene glycol for extraction of non-basic N-compounds. *Chin. Chem. Lett.* 30, 871–874. doi:10.1016/j.cclet.2019.02.025

Aoki, K., Shiraki, K., and Hattori, T. (2016). Salt effects on the picosecond dynamics of lysozyme hydration water investigated by terahertz time-domain spectroscopy and an insight into the Hofmeister series for protein stability and solubility. *Phys. Chem. Chem. Phys.* 18, 15060–15069. doi:10.1039/C5CP06324H

Cremer, P. S., Flood, A. H., Gibb, B. C., and Mobley, D. L. (2017). Collaborative routes to clarifying the murky waters of aqueous supramolecular chemistry. *Nat. Chem.* 10, 8–16. doi:10.1038/nchem.2894

Das, D., Assaf, K. I., and Nau, W. M. (2019). Applications of cucurbiturils in medicinal chemistry and chemical biology. *Front. Chem.* 7, 619. doi:10.3389/fchem.2019.00619

Deng, Y., Li, X., Han, C., and Dong, S. (2020). Supramolecular control over LCST behavior of hybrid macrocyclic system based on pillar[5]arene and crown ether. *Chin. Chem. Lett.* 31, 3221–3224. doi:10.1016/j.cclet.2020.03.074

Ding, M. H., Liao, J., Tang, L. L., Ou, G. C., and Zeng, F. (2021). High-yield synthesis of a novel water-soluble macrocycle for selective recognition of naphthalene. *Chin. Chem. Lett.* 32, 1665–1668. doi:10.1016/j.cclet.2020.11.019

Dong, S., Leng, J., Feng, Y., Liu, M., Stackhouse, C. J., Schonhals, A., et al. (2017). Structural water as an essential comonomer in supramolecular polymerization. *Sci. Adv.* 3, eaao0900. doi:10.1126/sciadv.aao0900

Dong, S., Wang, L., Wu, J., Jin, L., Ge, Y., Qi, Z., et al. (2017). Thermosensitive phase behavior of benzo-21-crown-7 and its derivatives. *Langmuir* 33, 13861–13866. doi:10.1021/acs.langmuir.7b03431

Duan, Q., Wang, L., Wang, F., Zhang, H., and Lu, K. (2020). Calix[n]arene/Pillar[n]arene-Functionalized graphene nanocomposites and their applications. *Front. Chem.* 8, 504. doi:10.3389/fchem.2020.00504

Gatiatulin, A. K., Ziganshin, M. A., and Gorbatchuk, V. V. (2019). Smart molecular recognition: From key-to-lock principle to memory-based selectivity. *Front. Chem.* 7, 933. doi:10.3389/fchem.2019.00933

Ge, Y., Gong, H., Shang, J., Jin, L., Pan, T., Zhang, Q., et al. (2019). Supramolecular gel based on crown-ether-appended dynamic covalent macrocycles. *Macromol. Rapid Commun.* 40, e1800731. doi:10.1002/marc.201800731

Ge, Y., Xu, Q., Yu, Z., Wang, R., Shen, X., and Qi, Z. (2022). Research progress of bioinspried-antifreeze protein material. *Chin. J. Chem. Edu* 43, 11–17. doi:10.13884/j.1003-3807hxjy.2021110017

Hu, B., Li, G., Ai, G., Zhang, M., Su, S., He, X., et al. (2022). Macrocycle molecule-based cryoprotectants for ice recrystallization inhibition and cell cryopreservation. *J. Mater Chem. B* 10, 6922–6927. doi:10.1039/d2tb01083f

Huang, D., Zhang, Q., Deng, Y., Luo, Z., Li, B., Shen, X., et al. (2018). Polymeric crown ethers: LCST behavior in water and stimuli-responsiveness. *Polym. Chem.* 9, 2574–2579. doi:10.1039/c8py00412a

Jin, L., Li, B., Cui, Z., Shang, J., Wang, Y., Shao, C., et al. (2019). Selenium substitution-induced hydration changes of crown ethers as tools for probing water interactions with supramolecular macrocycles in aqueous solutions. *J. Phys. Chem. B* 123, 9692–9698. doi:10.1021/acs.jpcb.9b09618

Jungwirth, P., and Cremer, P. S. (2014). Beyond hofmeister. *Nat. Chem.* 6, 261–263. doi:10.1038/nchem.1899

Kwong, C. H. T., Mu, J., Li, S., Fang, Y., Liu, Q., Zhang, X., et al. (2021). Reviving chloroquine for anti-SARS-CoV-2 treatment with cucurbit[7]uril-based supramolecular formulation. *Chin. Chem. Lett.* 32, 3019–3022. doi:10.1016/j.cclet.2021.04.008

Li, B., Xu, Q., Shen, X., Pan, T., Shang, J., Ge, Y., et al. (2022). Atom-economic macrocyclic amphiphile based on guanidinium-functionalized selenacrown ether acting as redox-responsive nanozyme. *Chin. Chem. Lett.*, 108015. doi:10.1016/j.cclet.2022.108015

Li, D., Zhang, Q., Zhao, W., Dong, S., Li, T., and Stang, P. J. (2020). Thermo/Anion dual-responsive supramolecular organoplatinum-crown ether complex. *Org. Lett.* 22, 4289–4293. doi:10.1021/acs.orglett.0c01333

Li, S., Gao, Y., Ding, Y., Xu, A., and Tan, H. (2021). Supramolecular nano drug delivery systems mediated via host-guest chemistry of cucurbit[n]uril (n = 6 and 7). *Chin. Chem. Lett.* 32, 313–318. doi:10.1016/j.cclet.2020.04.049

Li, T., Zhang, Q., Li, D., Dong, S., Zhao, W., and Stang, P. J. (2020). Rational design and bulk synthesis of water-containing supramolecular polymers. *ACS Appl. Mater Interfaces* 12, 38700–38707. doi:10.1021/acsami.0c11546

Li, X., Lai, J., Deng, Y., Song, J., Zhao, G., and Dong, S. (2020). Supramolecular adhesion at extremely low temperatures: A combined experimental and theoretical investigation. *J. Am. Chem. Soc.* 142, 21522–21529. doi:10.1021/jacs.0c10786

Liu, Y., Wang, H., Shangguan, L., Liu, P., Shi, B., Hong, X., et al. (2021). Selective separation of phenanthrene from aromatic isomer mixtures by a water-soluble azobenzene-based macrocycle. *J. Am. Chem. Soc.* 143, 3081–3085. doi:10.1021/jacs.1c01204

Luo, Y., Zhang, W., Liu, M., Zhao, J., Fan, Y., Bian, B., et al. (2021). A supramolecular fluorescent probe based on cucurbit[10]uril for sensing the pesticide dodine. *Chin. Chem. Lett.* 32, 367–370. doi:10.1016/j.cclet.2020.02.023

Luo, Z., Deng, Y., Li, X., Zhang, Q., Wu, J., Qi, Z., et al. (2019). LCST behavior controlled by size-matching selectivity from low molecular weight monomer systems. *New J. Chem.* 43, 6890–6896. doi:10.1039/c9nj00846b

Lv, P., Shen, X., Cui, Z., Li, B., Xu, Q., Yu, Z., et al. (2021). Mechanically strong and stiff supramolecular polymers enabled by fiber reinforced long-chain alkane matrix. *J. Polym. Sci.* 59, 3001–3008. doi:10.1002/pol.20210454

Pan, T., Li, J., Li, B., Xu, Q., Cui, Z., Shang, J., et al. (2021). Guanidinium-responsive crown ether-based macrocyclic amphiphile in aqueous medium. *J. Phys. Chem. Lett.* 12, 7418–7422. doi:10.1021/acs.jpclett.0c02994

Qi, Z., Chiappisi, L., Gong, H., Pan, R., Cui, N., Ge, Y., et al. (2018). Ion selectivity in nonpolymeric thermosensitive systems induced by water-attenuated supramolecular recognition. *Chem. Eur. J.* 24, 3854–3861. doi:10.1002/chem.201705838

Qi, Z., Malo de Molina, P., Jiang, W., Wang, Q., Nowosinski, K., Schulz, A., et al. (2012). Systems chemistry: Logic gates based on the stimuli-responsive gel–sol transition of a crown ether-functionalized bis(urea) gelator. *Chem. Sci.* 3, 2073–2082. doi:10.1039/C2SC01018F

Qi, Z., and Schalley, C. A. (2014). Exploring macrocycles in functional supramolecular gels: From stimuli responsiveness to systems chemistry. *Acc. Chem. Res.* 47, 2222–2233. doi:10.1021/ar500193z

Qi, Z., Schlaich, C., and Schalley, C. A. (2013). Multivalency in the gas phase: H/D exchange reactions unravel the dynamic "rock 'n' roll" motion in dendrimer-dendrimer complexes. *Chem. Eur. J.* 19, 14867–14875. doi:10.1002/chem.201301951

Qi, Z., Traulsen, N. L., Malo de Molina, P., Schlaich, C., Gradzielski, M., and Schalley, C. A. (2014). Self-recovering stimuli-responsive macrocycle-equipped supramolecular ionogels with unusual mechanical properties. *Org. Biomol. Chem.* 12, 503–510. doi:10.1039/c3ob41523f

Shang, J., Gong, H., Zhang, Q., Cui, Z., Li, S., Lv, P., et al. (2021). The dynamic covalent reaction based on diselenide-containing crown ether irradiated by visible light. *Chin. Chem. Lett.* 32, 2005–2008. doi:10.1016/j.cclet.2020.11.043

Shang, J., Li, B., Shen, X., Pan, T., Cui, Z., Wang, Y., et al. (2021). Selenacrown macrocycle in aqueous medium: Synthesis, redox-responsive self-assembly, and enhanced disulfide formation reaction. *J. Org. Chem.* 86, 1430–1436. doi:10.1021/acs.joc.0c02083

Shen, X., Li, B., Pan, T., Wu, J., Wang, Y., Shang, J., et al. (2019). Self-assembly behaviors of perylene- and naphthalene-crown macrocycle conjugates in aqueous medium. *Beilstein J. Org. Chem.* 15, 1203–1209. doi:10.3762/bjoc.15.117

Shi, B., Chai, Y., Qin, P., Zhao, X-X., Li, W., Zhang, Y-M., et al. (2022). Detection of aliphatic aldehydes by a pillar[5]arene-based fluorescent supramolecular polymer with vaporchromic behavior. *Chem. Asian. J.* 17, e202101421. doi:10.1002/asia.202101421

Wang, C., Zhang, Y. M., Li, H., Zhang, J., Zhou, Y., Liu, G., et al. (2022). Synergistic activation of photoswitchable supramolecular assembly based on sulfonated crown ether and dithienylethene derivative. *Chin. Chem. Lett.* 33, 2447–2450. doi:10.1016/j.cclet.2021.09.106

Wang, H., He, J., Liu, J., Qi, S., Wu, M., Wen, J., et al. (2020). Electrolytes enriched by crown ethers for lithium metal batteries. *Adv. Funct. Mater* 31, 2002578. doi:10.1002/adfm.202002578

Wang, P., Cao, S., Yin, T., and Ni, X. L. (2021). Unprecedented tunable hydrophobic effect and anion recognition triggered by AIE with Hofmeister series in water. *Chin. Chem. Lett.* 32, 1679–1682. doi:10.1016/j.cclet.2020.11.068

Wei, Q., Schlaich, C., Prevost, S., Schulz, A., Bottcher, C., Gradzielski, M., et al. (2014). Supramolecular polymers as surface coatings: Rapid fabrication of healable superhydrophobic and slippery surfaces. *Adv. Mater* 26, 7358–7364. doi:10.1002/adma.201401366

Weimann, D. P., Winkler, H. D. F., Falenski, J. A., Koksch, B., and Schalley, C. A. (2009). Highly dynamic motion of crown ethers along oligolysine peptide chains. *Nat. Chem.* 1, 573–577. doi:10.1038/nchem.352

Wu, S., Zhang, Q., Deng, Y., Li, X., Luo, Z., Zheng, B., et al. (2020). Assembly pattern of supramolecular hydrogel induced by lower critical solution temperature behavior of low-molecular-weight gelator. *J. Am. Chem. Soc.* 142, 448–455. doi:10.1021/jacs.9b11290

WuXiao, H. T. (2020). Supramolecular polymers with AIE property fabricated from a cyanostilbene motif-derived ditopic benzo-21-crown-7 and a ditopic dialkylammonium salt. *Front. Chem.* 8, 610093. doi:10.3389/fchem.2020.610093

Xiao, T., Elmes, R., and Yao, Y. (2020). Editorial: Host-Guest chemistry of macrocycles. *Front. Chem.* 8, 628200. doi:10.3389/fchem.2020.628200

Xiao, T., Wang, J., Shen, Y., Bao, C., Li, Z. Y., Sun, X. Q., et al. (2021). Preparation of a fixed-tetraphenylethylene motif bridged ditopic benzo-21-crown-7 and its application for constructing AIE supramolecular polymers. *Chin. Chem. Lett.* 32, 1377–1380. doi:10.1016/j.cclet.2020.10.037

Xiao, T., Zhou, L., Sun, X. Q., Huang, F., Lin, C., and Wang, L. (2020). Supramolecular polymers fabricated by orthogonal self-assembly based on multiple hydrogen bonding and macrocyclic host–guest interactions. *Chin. Chem. Lett.* 31, 1–9. doi:10.1016/j.cclet.2019.05.011

Xu, Q., Cui, Z., Yao, J., Li, B., Lv, P., Shen, X., et al. (2021). Constitutionally adaptive crown ether-based macrocyclic bolaamphiphile with redox-responsive switching of lower critical solution temperature behaviors. *Chin. Chem. Lett.* 32, 4024–4028. doi:10.1016/j.cclet.2021.05.058

Xu, Z., Jia, S., Wang, W., Yuan, Z., Jan Ravoo, B., and Guo, D. S. (2019). Heteromultivalent peptide recognition by co-assembly of cyclodextrin and calixarene amphiphiles enables inhibition of amyloid fibrillation. *Nat. Chem.* 11, 86–93. doi:10.1038/s41557-018-0164-y

Yu, S., Wang, Y., Chatterjee, S., Liang, F., Zhu, F., and Li, H. (2021). Pillar[5]arene-functionalized nanochannel platform for detecting chiral drugs. *Chin. Chem. Lett.* 32, 179–183. doi:10.1016/j.cclet.2020.11.055

Zayed, J. M., Nouvel, N., Rauwald, U., and Scherman, O. A. (2010). Chemical complexity—Supramolecular self-assembly of synthetic and biological building blocks in water. *Chem. Soc. Rev.* 39, 2806–2816. doi:10.1039/B922348G

Zhang, J., Qiu, H., He, T., Li, Y., and Yin, S. (2020). Fluorescent supramolecular polymers formed by crown ether-based host-guest interaction. *Front. Chem.* 8, 560. doi:10.3389/fchem.2020.00560

Zhang, K. R., Hu, M., Luo, J., Ye, F., Zhou, T. T., Yuan, Y. X., et al. (2022). Pseudo-crown ether having AIE and PET effects from a TPE-CD conjugate for highly selective detection of mercury ions. *Chin. Chem. Lett.* 33, 1505–1510. doi:10.1016/j.cclet.2021.08.072

Zhang, Q., Dong, S., Zhang, M., and Huang, F. (2021). Supramolecular control over thermo-responsive systems with lower critical solution temperature behavior. *Aggregate* 2, 35–47. doi:10.1002/agt2.12

Zhang, Q., Li, T., Duan, A., Dong, S., Zhao, W., and Stang, P. J. (2019). Formation of a supramolecular polymeric adhesive via water-participant hydrogen bond formation. *J. Am. Chem. Soc.* 141, 8058–8063. doi:10.1021/jacs.9b02677

Zhang, S., Boussouar, I., and Li, H. (2021). Selective sensing and transport in bionic nanochannel based on macrocyclic host-guest chemistry. *Chin. Chem. Lett.* 32, 642–648. doi:10.1016/j.cclet.2020.06.035

Zhang, W., Xiao, P., Lin, L., Guo, F., Wang, Q., Piao, Y., et al. (2022). Study of a water-soluble supramolecular complex of curcumin and β-cyclodextrin polymer with electrochemical property and potential anti-cancer activity. *Chin. Chem. Lett.* 33, 4043–4047. doi:10.1016/j.cclet.2021.12.037

Zhang, Y., and Cremer, P. S. (2009). The inverse and direct Hofmeister series for lysozyme. *Proc. Natl. Acad. Sci. U.S.A.* 106, 15249–15253. doi:10.1073/pnas.0907616106

Zhang, Y., Wang, L., Wang, J., Xin, S., and Sheng, X. (2021). Enzyme-responsive polysaccharide supramolecular nanoassembly for enhanced DNA encapsulation and controlled release. *Chin. Chem. Lett.* 32, 1902–1906. doi:10.1016/j.cclet.2021.01.032

Zheng, B., Luo, Z., Deng, Y., Zhang, Q., Gao, L., and Dong, S. (2019). A degradable low molecular weight monomer system with lower critical solution temperature behaviour in water. *Chem. Commun.* 55, 782–785. doi:10.1039/c8cc09160a

Zheng, X., Miao, Q., Wang, W., and Qu, D. H. (2018). Constructing supramolecular polymers from phototrigger containing monomer. *Chin. Chem. Lett.* 29, 1621–1624. doi:10.1016/j.cclet.2018.04.002

Zhu, H., Li, Q., Khalil-Cruz, L. E., Khashab, N. M., Yu, G., and Huang, F. (2021). Pillararene-based supramolecular systems for theranostics and bioapplications. *Sci. China Chem.* 64, 688–700. doi:10.1007/s11426-020-9932-9

frontiers | Frontiers in Chemistry

TYPE Review
PUBLISHED 24 January 2023
DOI 10.3389/fchem.2023.1115495

OPEN ACCESS

EDITED BY
Xing Li,
Beijing Institute of Life Science (CAS), China

REVIEWED BY
Ling Zhu,
National Center for Nanoscience and Technology (CAS), China
Xiao Xuan Liu,
China Pharmaceutical University, China
Jianfeng Liu,
Chinese Academy of Medical Sciences and Peking Union Medical College, China

*CORRESPONDENCE
Haiyan Xu,
✉ xuhy@pumc.edu.cn

SPECIALTY SECTION
This article was submitted to Nanoscience, a section of the journal Frontiers in Chemistry

RECEIVED 05 December 2022
ACCEPTED 09 January 2023
PUBLISHED 24 January 2023

CITATION
Zhang M and Xu H (2023), Peptide-assembled nanoparticles targeting tumor cells and tumor microenvironment for cancer therapy.
Front. Chem. 11:1115495.
doi: 10.3389/fchem.2023.1115495

Peptide-assembled nanoparticles targeting tumor cells and tumor microenvironment for cancer therapy

Meichen Zhang and Haiyan Xu*

Institute of Basic Medical Sciences, Chinese Academy of Medical Sciences and Peking Union Medical College, Beijing, China

Tumor cells and corrupt stromal cells in the tumor microenvironment usually overexpress cancer-specific markers that are absent or barely detectable in normal cells, providing available targets for inhibiting the occurrence and development of cancers. It is noticeable that therapeutic peptides are emerging in cancer therapies and playing more and more important roles. Moreover, the peptides can be self-assembled and/or incorporated with polymeric molecules to form nanoparticles *via* non-covalent bond, which have presented appealing as well as enhanced capacities of recognizing targeted cells, responding to microenvironments, mediating internalization, and achieving therapeutic effects. In this review, we will introduce the peptide-based nanoparticles and their application advances in targeting tumor cells and stromal cells, including suppressive immune cells, fibrosis-related cells, and angiogenic vascular cells, for cancer therapy.

KEYWORDS

peptide, nanoparticles, target, tumor microenvironment, cancer therapy

1 Introduction

Tumor cells can recruit and corrupt normal cells, and the interactions between them create the tumor microenvironment (TME) that affects cancer progression (Balkwill et al., 2012; Arneth, 2019). Tumor cells can invade healthy tissues and spread to other parts of the body through the lymphatic or circulatory system. Non-malignant cells, namely stromal cells, usually promote the cancer progress by sustaining proliferative signaling, evading growth suppressors, resisting cell death, inducing angiogenesis, activating invasion and metastasis, evading immune destruction, and reprogramming energy metabolism (Hanahan and Coussens, 2012). In the hypothesis of "seed and soil", tumor cells are considered as seed, and the microenvironment where the tumor cells live is soil that provides nutrition and survival guidance to the tumor cells, at the same time, the tumor cells educate the soil to become more friendly to the tumor cells (Paget, 1989). Stromal cells of the TME can be grouped into three general classes: angiogenic vascular cells, infiltrating immune cells, and tumor fibrosis-related cells (Hanahan and Coussens, 2012). Therefore, not only tumor cells but also the tumor microenvironment are available therapeutic targets in cancer treatment.

Up to date, some kinds of ligands have been developed for targeting tumor cells and stromal cells, such as antibody, peptide, and aptamer. In particular, peptides are emerging in cancer therapy in recent years and hold distinguished advantages compared with antibodies, such as low immunogenicity, structural variability, strong permeability, and more economic cost (Fosgerau and Hoffmann, 2015). Additionally, peptides can be carried by nanoparticles more easily than antibodies due to their low molecular weight and abundant amino residues, and nanoparticles-

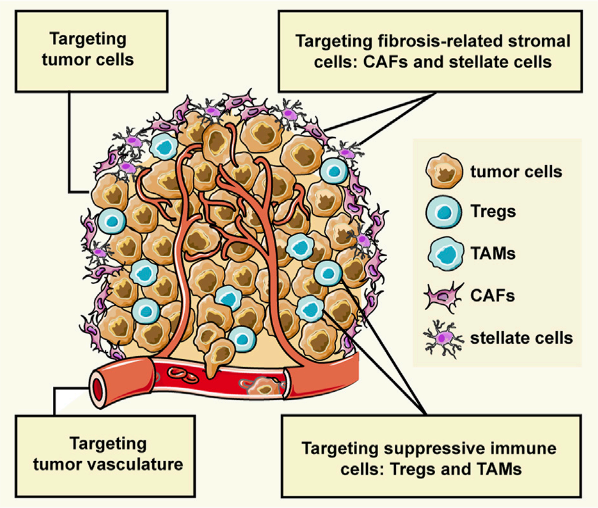

GRAPHICAL ABSTRACT
The interactions between tumor cells and stromal cells create the tumor microenvironment (TME) which largely affects the cancer progression. The stromal cells can be grouped into three general classes: angiogenic vascular cells, infiltrating immune cells, and tumor fibrosis-related cells. This review introduces the peptide-assembled nanoparticles targeting tumor cells and three types of stromal cells for cancer therapy.

loaded peptide can be carried into cells as well as interact with the targeted proteins locating in the cell membranes.

Functional peptides can be classified into four categories, which are targeting peptides, microenvironment-responsive peptides, cell-penetrating peptides (CPP), as well as therapeutic peptides. However, due to its inherent shortcomings of easy aggregation and short half-life of circulating plasma, the application of peptides has been facing challenges of poor soluble stability *in vivo*, easy degradation by protease, and easy clearance by the kidney and liver (Zafar et al., 2021; Wang et al., 2022).

It has been well documented that peptides themselves or with amphiphilic molecules, lipids, or hydrophobic drugs can be assembled into stable nanoparticles through intermolecular non-covalent interactions, including van der Waals force, hydrophobic, electrostatic, hydrogen bond, π-π aromatic stacking, and metal coordination. Factors affecting assembly include pH, temperature, solvent, ultrasound, and others. What's more, secondary structure of peptide also determines the self-assembly occurs or not. The secondary structure preferring peptide self-assembly includes *a*-Helices, *ß*-Sheets, and *ß*-Hairpins (Yadav et al., 2020; Li et al., 2022). Figure 1 provided the illustration of the assembly strategies. By utilizing these assembly properties, peptide-based nanoparticles with designated functions can be fabricated. For examples, targeting peptides modified NPs can specifically bind to tumors and promote cellular uptake, thereby reducing off-target effects and improving anti-tumor efficacy. Microenvironment-responsive peptide-based NPs are pH-dependent release or only cleaved by enzymes in the TME, thereby reducing accumulation in normal tissues as well as causing toxic side effects. What's more, the size of nanoparticles (NPs) is adjustable, and the appropriate particle size can not only avoid renal and hepatic clearance but also accumulate in the tumor site through the EPR effect (Chatterjee et al., 2014). More importantly, NPs can protect drugs from degradation and aggregation, and carry multiple therapeutic agents to achieve combined treatment and precisely resist tumor attacks in synchronize time and space manner (Yang et al., 2021).

Herein, we will describe the application of peptide-based nanoparticles that target tumor cells, suppressive immune cells, cancer-associated fibroblasts, stellate cells, and angiogenic cells in cancer therapies.

2 Therapeutic peptide-based nanoparticles targeting signaling proteins of the tumor cells

Tumor cells express tumor-associated protein that are low expressed in normal cells. These proteins can mediate tumor cells survival, proliferation, and migration through interacting with their ligands. Peptides can specifically bind to these protein targets, bring certain therapeutics to the tumor cells, or blocking the interactions between the proteins and their ligands (termed as to antagonist), which inhibit the activation of the down-stream signaling pathways. When antagonistic peptides are assembled with polymeric molecules and drugs, the peptide-based NPs combine the dual role of specifically targeting and antagonisms, which has showed promising potentials in the cancer treatment.

2.1 Targeting CXCR4

The C-X-C chemokine receptor 4 (CXCR4) is highly expressed in more than 23 kinds of human tumor cells and is a prognostic marker (Chatterjee et al., 2014). The interaction of CXCR4 and its ligand stromal-derived factor 1α (SDF-1α, also known as CXCL12) mainly secreted by stromal cells promotes several aspects of cancer progression including angiogenesis, metastasis, relapse, drug

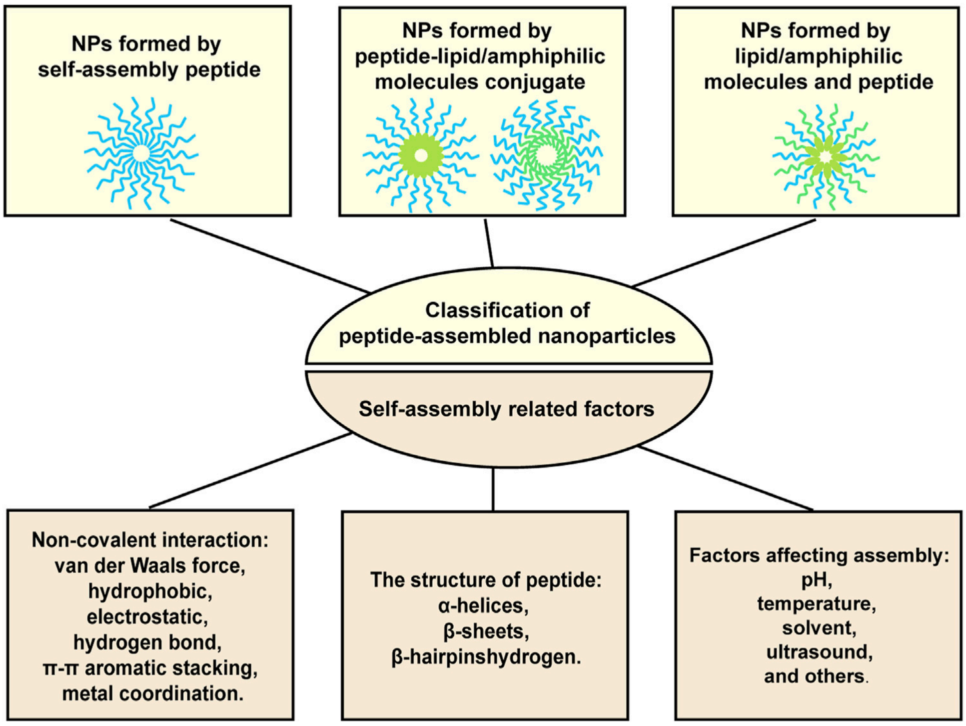

FIGURE 1
Illustration of the formation strategies for peptide-based nanoparticles.

resistance, and survival (Teicher and Fricker, 2010; Mortezaee, 2020). Some peptide sequences targeting CXCR4 have been developed and investigated in various tumors, and some review articles have made a comprehensive summary. Here we will focus on those that are fabricated to nanoparticles by self-assembly and/or assembled with other molecules, as the nanoparticles can provide a powerful platform to load various drugs as well as the peptide, which extends the capacity of the peptides.

X4-2-6, a PEG-modified 24-amino acid peptide analog of the second transmembrane helix of CXCR4, could be self-assembled into homogeneous nanoparticles in which the PEG extensions at the C-terminus preventing superaggregation (Tarasov et al., 2011). The nanoparticles adopted predominantly a *β*-Hairpin conformation in the aqueous solution, but folded into an *α*-Helix upon spontaneous fusion with the cell membrane. It was found that X4-2-6 peptide-based nanoparticles could inhibit CXCR4 function *in vitro* and hamper CXCR4-dependent bone metastasis of MDA-MB-231 cancer cells and prolong the survival in a mouse model of metastatic breast cancer. In addition, a hydrophobic drug HKH-40A was encapsulated by the nanoparticles with the *β*-Hairpin conformation, and the drug was released when the nanoparticles encountered with the cells membrane, thus providing an interesting delivery system.

The conjugate of peptides and other fragments can be efficiently produced by genetic engineering, which can spontaneously self assemble into nanoparticles. A cationic peptide T22, a known antagonist of CXCR4, bound to and penetrated CXCR4$^+$ cells efficiently *via* CXCR4-specific endocytosis (Nakashima et al., 1992). The researchers have constructed a CXCR4 targeted self-assembling nanoparticles by genetic engineering by combining peptide T22 with a polyhistidine H6 that has a strong dipolar charge distribution to support spontaneous self-organization (Céspedes et al., 2014). T22-GFP-H6 nanoparticles could effectively target and selectively internalize in several CXCR4$^+$ tumor cells, such as colorectal cancer, diffuse large B cell lymphoma and head and neck squamous cell carcinoma tumor. Moreover, when administered in CXCR4$^+$ tumor model, T22-GFP-H6 mostly accumulates in the tumor compared to other non-tumor bearing organs (Unzueta et al., 2012; Falgàs et al., 2020; Rioja-Blanco et al., 2022a). Furthermore, the active segments of the diphtheria toxin (DITOX) and the *Pseudomonas aeruginosa* exotoxin (PE24) were integrated with T22 and H6 to fabricate self-assembled toxin-based nanoparticles T22-DITOX-H6 and T22-PE24-H6, respectively, and they acted as toroid nanoparticles of 30–90 nm, penetrating the CXCR4$^+$ tumor cells and promote tumor cell killing *in vitro*. *In vivo*, the nanocarriers mainly accumulated in tumor tissues (>75% of the administered dose) compared to non-tumor bearing organs, displaying a potent CXCR4-dependant antitumor effect in the absence of systemic toxicity in several CXCR4$^+$ subcutaneous solid tumor mouse models (Sánchez-García et al., 2018; Serna et al., 2020; Voltà-Durán et al., 2021; Rioja-Blanco et al., 2022b; Falgàs et al., 2022). EPI-X4, a 16-residue fragment produced by proteolysis of human serum albumin, was the endogenous peptide inhibitor of CXCR4 (Zirafi et al., 2015). To form nanoparticles, the sequence was modified as EPIX4-(RK)-GFP-H6 that was efficiently produced in *Escherichia coli* by genetic engineering. The modified peptide was mixed with T22-GFP-H6 to form self-assembly biparatopic nanoparticles by divalent cation coordination through histidine-rich regions (Lee et al., 2011), which showed a dramatically improved biodistribution in the mouse models of CXCR4$^+$ human cancer, faster cell internalization and enhanced cell killing effect when compared to the version based on a single ligand.

Our group reported a *de novo* CXCR4 antagonistic peptide (named as E5) (Li et al., 2014; Li et al., 2015; Guo et al., 2017) and prepared a micelle formulation by using amphipathic polymer DSPE-mPEG2000 through a one-step self-assembly method to improve the soluble stability of E5 in the physiological environment. M-E5 achieved effective therapeutic effects on a refractory AML mouse model (Meng et al., 2020). Moreover, a co-delivery system of doxorubicin (Dox) and E5 with DSPE-mPEG2000 was constructed (Zhang et al., 2022), which can effectively bind to the CXCR4-expressing AML cells, downregulate the signaling proteins mediated by CXCR4/CXCL12 axis and increase the cellular uptake of Dox. Importantly, M-E5-Dox can improve the blood circulation time and blood concentration of Dox, and enhance the delivery of Dox to AML cells infiltrating tissues and organs. M-E5-Dox remarkably decreases the proportion of leukemic cells in the peripheral blood, bone marrow, spleen, liver, and lung of the refractory AML mice, which in turn prolongs the survival significantly. In another study, M-E5 has a higher affinity for CXCR4 overexpressing human solid tumor cells and a stronger ability to inhibit CXCL12-induced tumor cell migration compared with E5 (Fang et al., 2017). Furthermore, it has been confirmed that lymph node metastasis can be a source of tumor cells for distant metastases in solid tumors which was related to CXCR4/CXCL12 axis (Pereira et al., 2018). E5 is too small to accumulate in the lymphatic system, while the PEG-micelles M-E5 with a diameter of 20 nm showed lymph node tropism and prevented metastatic tumor cells from colonizing the lungs (Fang et al., 2021).

It should be noted that peptides can also be combined with nanozymes to enable the nanozyme with targeting and antagonistic functions. For example, CXCR4 and CD44 dual-targeted Prussian blue nanosystem and Fe_3O_4@Pt nanozymes combined with CXCR4 antagonists E5 were developed (Bai et al., 2021; Kong et al., 2021). The combination of E5 and nanozymes displayed a superior synergistic therapeutic efficacy against AML *in vitro* and *in vivo*, preventing AML cells from homing to bone marrow and migrating to the spleen, lung and liver, which in turn prolonged the survival period of AML mice.

2.2 Targeting CD123

The interleukin-3 receptor alpha chain (IL-3Rα), named as CD123, is widely overexpressed in various hematological malignancies, especially in the leukemic stem cells and more differentiated leukemic blasts, which makes CD123 a promising therapeutic target. Several drugs have been developed to target CD123 for the treatment of leukemia, such as anti-CD123 antibodies (CSL-360, talacotuzumab and KHK2823), CD3 × CD123 bispecific antibodies (flotetuzumab, vibecotamab, JNJ-63709178, APVO436, and SAR440234), antibody-drug conjugates (SGN-CD123A), and anti-CD123 chimeric antigen receptor T cell immunotherapy, but none of them have crossed the clinical trial due to serious side effect, including severe myelosuppression, infusion-related adverse reactions, infection, hemocytopenia, cardiotoxicity, and gastrointestinal dysfunction (Slade and Uy, 2020; Espinoza-Gutarra et al., 2021).

Our group has chemically synthesized a novel antagonistic peptide PO-6 targeting CD123 by using a lab-developed cell-based selection process of a fragmental screening method, which is the first reported peptide targeting CD123 (Xu et al., 2021; Xu et al., 2022). To increase the antagonistic ability as well as to improve the soluble stability of the peptide in the physiological environment, PO-6 was mixed with an amphipathic polymer (Soluplus) through a one-step self-assembly method to form micelles (^{m}PO-6) that were used as monotherapeutics in the animal model of refractory acute myeloid leukemia. Results showed that PO-6 could specifically bind to the CD123^{+} AML cells and the micellar formulation ^{m}PO-6 increased the dissolution stability and the specific binding capacity. In the AE and C-KIT^{D816V} mouse model, ^{m}PO-6 significantly reduced the percentage of AML cells infiltration and prolonged the median survival of AML mice by interfering CD123/IL-3 axis *via* regulating the activation of STAT5, PI3K/AKT, and NF-κB signaling pathways.

3 Targeting suppressive immune cells to enhance the anti-tumor effect

Immunosuppressive cells in TME are the main cause of tumor immune escape and are closely related to the poor prognosis of cancer patients. One of the current peptide-based immunotherapy methods is to synthesize peptide vaccines that are the same as tumor-associated antigens (TAAs) presented on the tumor cells to help cytotoxic T cells (CTL) produce a stronger immune response. However, this method is still limited by the downregulation of tumor cell TAAs and the instability of the peptide vaccine. It can be noticed there is another immunotherapy method that is to target immunosuppressive cells, such as tumor-associated macrophages (TAMs), regulatory T cells (Tregs) and myeloid-derived suppressor cells (MDSCs), to delivery therapeutic drugs. Among them, MDSCs is an immature cell group, and no specific biomarker of MDSCs for peptide binding has been found on its surface. In the following parts, we mainly introduced peptide-based self-assembled nanoparticles targeting Tregs and TAMs.

3.1 Targeting regulatory T cells

Regulatory T cells (Tregs) are a sub-type of CD4^{+} T cells which affect the activation of the immune system. Tregs inhibit the function of cytotoxic T cells by releasing cytokines, directly splitting and activating inhibitory receptors on the cell surface, thus promoting tumor immune escape in TME. Tregs are characterized by the expression of CD4, CD25, neuropilin-1 (NRP-1), and forkhead box P3 (FoxP3) (Bruder et al., 2004; Kelley and Parker, 2010).

Neuropilin-1 (NRP-1), a cell surface transmembrane glycoprotein, is regarded as the receptor for the class 3 semaphorins subfamily and vascular endothelial growth factor (VEGF) family members. NRP-1 is expressed on the majority of Tregs and promotes its activity, which was highly associated with Tregs-specific Foxp3^{+} expression (Bruder et al., 2004; Delgoffe et al., 2013; Glinka and Prud'homme, 2008). The tLyp-1 is a cell-penetrating peptide with a C-terminal R/KXXR/K consensus sequence, which has high affinity and specificity for NRP-1 receptor (Teesalu et al., 2009; Roth et al., 2012). The tLyp1 peptide-conjugated hybrid nanoparticles (tLyp-1-hNPs), incorporating tLyp-1-PEG-DSPE conjugate on the outer layer as the target ligand for the NRP-1 receptor and a PLGA core loading anti-CTLA-4 antibody and the tyrosine kinase inhibitor imatinib, was constructed by the oil-in-water (o/w) single-emulsion method (Ou et al., 2018). The tLyp-1-hNPs, which effectively targeted Tregs, presented good stability and enhanced suppressive effects against Tregs through inhibition of STAT3 and STAT5 phosphorylation and accumulation in Tregs. *In vivo*, tLyp1-hNPs mainly accumulated in the tumor areas *via* the enhanced

TABLE 1 Peptides targeting TAMs.

Peptide	Sequence	Receptor	Identification	Advantage/ Disadvantage	Ref
M2pep	YEQDPWGVKWWY	Unknown	Phage display *in vitro*	Targeted receptor was not identified	Li et al. (2020)
RP-182	KFRKAFKRFF	CD206	In silico biophysical homology screening	Also bound to RelB and CD47	Jaynes et al. (2020)
Melittin	GIGAVLKVLTTGLPALISWIKRKRQQ-NH2	CD206	In Lewis lung carcinoma mouse model	Had toxic to normal cells	Lee et al. (2017)
UNO	CSPGAKVRC	CD206	Phage display *in vitro*	Specifically targeted CD206 expressed on TAMs	Scodeller et al. (2017)
mUNO	(Linear version of UNO) CSPGAK	CD206	Phage display *in vitro*	Specifically targeted CD206 expressed on TAMs	Asciutto et al. (2019)
CRV	CRVLRSGSC, cyclic peptide	Retinoid X receptor beta (RXRB)	Phage display *in vitro*	RXRB may not be the surface marker of TAMs	Tang et al. (2019)
CSSTRESAC	CSSTRESAC	Vitamin D receptor	Phage display *in vitro*	Specifically bound to vitamin D receptor	Staquicini et al. (2021)
RVG	YTIWMPENPRPGTPCDIFTNSRGKRASNG	Nicotinic acetylcholine receptor (AchR)	Cell-based selection	AChR expressed on macrophage and microglia	Zou et al. (2017)

TABLE 2 Peptide-based assembling nanoparticles for CAFs.

Peptide	Sequence	Receptor	Nanoparticles	Function	Ref
DRGETGPAC	DRGETGPAC	FAP-α	F-SOS/DC/D NCs *via* the w/o/w double emulsion method	Depleted CAFs by the light assist; Remodeled TME; Improved the tumor penetration and anticancer efficacy *in vivo*	Yan et al. (2020b)
CAP	Ac-ATK(C18)DATGPAK(C18) TA-NH_2	FAP-α	Self-assembled micelles (CAP NPs) with hydrophobic drugs by hydrophobic interaction	Cleaved by FAP-α and release Dox to CAFs and tumor cells; Disrupted the stromal barrier and enhanced local drug accumulation; Inhibted the growth of tumor	Ji et al. (2016b)
RGD	RGD	Integrin $\alpha_v\beta_3$	RPM@NLQ	Inhibited matrix fibrosis; Enhanced the permeability of drugs	Duan et al. (2022)
TR	c (RGDfK) AGYLLGHINLHHLAHL (Aib)HHIL-NH_2	Integrin $\alpha_v\beta_3$	TR-PTX/HCQ-Lip by the thin film hydration method and the pH-gradient method	Recognized the integrin $\alpha_v\beta_3^+$ cells; Enhanced the cellular uptake; Inhibited stroma fibrosis; Killed tumor cells	Shi et al. (2015); Chen et al. (2019)
FH	FHKHKSPALSPVGGG	Tenascin-C	FH-SSLNav liposome by the thin film hydration method	Enhanced uptake and cytotoxicity; Targeted tumor stroma; CAFs depletion; Inhibited the growth of tumors	Kim et al. (2012); Chen et al. (2016)
			FH-NB-Dox nanobubble	Ultrasound contrast agent; Delivered more Dox into CAFs; Enhanced the Dox-induced eradication under ultrasound irradiation	Guo et al. (2019)
CFH	CFHKHKSPALSPVGGG	Tenascin-C	CFH/OM-L liposome by pH gradient method	Targeted and deactivated CAFs; Reversed the EMT process; Reduced collagen deposition	Guo et al. (2022)

permeability and retention (EPR) effect with decreased accumulation in the spleen and liver, owing to the suitable particle size, surface modification with DSPE-PEG and the NRP-1 targeted peptide, resulting in the significant reduction of the tumor volume and prolong of the survival of mice in the B16/BL6 tumor model.

3.2 Targeting tumor-associated macrophages

In different immune microenvironments, macrophages can display different phenotypes: M1 (anti-tumor) and M2 (tumor-promoting). Tumor-associated macrophages (TAMs) abundant in

TME, which usually display as M2 type, are usually associated with poor prognosis in most cancers (Cassetta and Kitamura, 2018). TAMs play a tumor-promoting role by stimulating tumor inflammation, promoting angiogenesis, suppressing antitumor immunity, resulting in adaptive resistance, and accelerating tumor cell metastasis (Xiao and Yu, 2021). TAMs are becoming a key target of immunotherapy. Several TAMs-targeted peptides have been reported (Table 1), such as CD206-targeted peptides [RP-182 (Jaynes et al., 2020), melittin (Lee et al., 2017), UNO (Scodeller et al., 2017) and mUNO (Asciutto et al., 2019)], retinoid X receptor beta-targeted peptide [CRV (Tang et al., 2019)], vitamin D receptor-targeted peptide (CSSTRESAC), M2pep (Cieslewicz et al., 2013) and RVG (Zou et al., 2017).

A peptide has been identified in 2013, termed M2pep (YEQDPWGVKWWY), which selectively bound to and internalized into M2-polarized TAMs as compared to M1 polarized mouse macrophages or other leukocytes (Cieslewicz et al., 2013). The CSF-1/CSF-1R pathway is crucial for the differentiation and survival of macrophages, providing a potential target of reprogramming TAMs from M2 to M1. PI3K-γ regulates a critical switch between immune stimulation and suppression and the blockade of PI3K-γ reprograms TAMs to stimulate $CD8^+$ T cell-mediated tumor suppression and to inhibit tumor cell invasion and metastasis. Li et al. (2020) have constructed M2pep-modified self-assembly nanomicelles co-encapsulating CSF-1R-siRNA and small molecule PI3K-γ inhibitor NVP-BEZ 235 to target TAMs and modulate its polarization. The nanomicelles have enhanced TAMs targeting efficiency compared with non-targeting micelles both *in vitro* and *in vivo*. After intravenous injection, the dual drug-loaded nanomicelles suppressed pancreatic tumor growth by re-building tumor immune microenvironment, which transformed the M2-like TAMs into the M1-like phenotype and consequently enhanced $CD8^+$ and $CD4^+$ T cell infiltration. The dual pathway inhibition by the TAMs-targeting nanomicelles provided an alternative approach for cancer immunotherapy. Another TAMs targeting nanoparticles (M2NPs) were constructed with anti-CSF-1R siRNA, modified by *α*-Peptide (a scavenger receptor B type 1 targeting peptide) and M2pep (Qian et al., 2017). *In vitro*, it had a higher affinity to TAMs than to tissue-resident macrophages in the liver, spleen, and lung after being administered to B16 melanoma mice. Compared with the control treatment groups, M2NPs-based siRNA delivery resulted in the effective elimination of TAMs (52%), decreased tumor size (87%), and prolonged survival with superior biocompatibility. Additionally, this molecular-targeted strategy reprogramed the cytokine secretion and restored the function of infiltrating $CD8^+$ T cells in the TME, providing a potential strategy of molecular-targeted cancer immunotherapy for clinical application.

RVG peptide, derived from a rabies virus glycoprotein, has been shown to bind specifically to macrophages *via* highly expressed AChR on the cell surface (Kim et al., 2010). In a study, self-assembly nanoparticles (RVG-PTX-NPs) were constructed by a modified nanoprecipitation method, with paclitaxel (PTX) encapsulated inside and RVG conjugated on the surface. RVG-PTX-NPs with desirable size (~140 nm) showed poor uptake by neurons, while were able to cross BBB and selectively target and were preferentially internalized in brain TAMs with controlled release and tumor-specific toxicity, resulting in an effective therapeutic effect in the human glioma mice model (Zou et al., 2017).

4 Targeting fibrosis-related stromal cells to improve tumor microenvironment

Unlike tumor cells, stromal cell types within the TME are genetically stable and thus represent an attractive therapeutic target with reduced risk of resistance and tumor recurrence (Quail and Joyce, 2013). There are a lot of fibrosis-related stromal cells in the tumor microenvironment such as cancer-associated fibroblasts (CAFs), stellate cells, and adipocytes, which lead to special pathological TME with high fibrosis and excessive connective tissue hyperplasia. Adipose stromal cells, the precursors of adipocytes, induce epithelial-mesenchymal transformation (EMT), and adipocytes can transdifferentiate into CAFs (Bochet et al., 2013; Su et al., 2019). Stellate cells are precursors of CAFs in many solid tumors, which can also transform into CAFs through EMT (Yan et al., 2020a). CAFs can deteriorate the TME and densify the cancer matrix, and hinder drug penetration in tumors, playing a major role in promoting tumor progression and metastasis. The peptide-based NPs targeting adipocytes have rarely been reported, so we will focus on CAFs and stellate cells.

4.1 Targeting stellate cells

In solid tumors, pancreatic stellate cells (PSCs) and hepatic stellate cells (HSCs), the precursors of CAFs, are the major stromal cell type presenting in tumor tissues and the principal source of ECM production and fibrosis in the stroma which provides physical barriers to inhibit the distribution and penetration of various antitumor drugs (Apte et al., 2013). Peptide-based self-assembly nanoparticles targeted to stellate cells have been reported.

Cell-penetrating peptides (CPP, VSRRRRRRGGRRRR) with positive charge enables them to spontaneously form non-covalent nanocomplexes with negatively charged oligonucleotides *via* electrostatic interactions (Lee et al., 2013). CPP-based nanocomplexes were constructed to delivery anti-miRNA-199a oligonucleotides to primary human pancreatic stellate cells (hPSCs) (Schnittert et al., 2017). Results showed that the uptake of dimeric CPP-based nanocomplexes (NC-2) by hPSCs was 130 times higher than that of monomer-based nanocomplexes (NC-1). NC-2 was efficiently transfected into hPSCs by clathrin-mediated endocytosis compared with normal human fibroblasts and human pancreatic tumor cells. The delivery of anti-miR-199a inhibited hPSC differentiation into CAFs and inhibited the size of 3D heterospheroids composed of hPSCs and tumor cells.

PSCs and tumor cells overexpressed matrix metalloproteinases (MMPs), which in turn provided opportunities to design responsive materials for pancreatic tumor drug delivery (Yokota et al., 2002). A peptide with a sequence of Ac-CSSSGPLGIAGQSSS-COOH was synthesized, in which a MMP-2 specifically cleavable sequence "-GPLGIAGQ-" was incorporated. Based on it, a *β*-Cyclodextrin (*β*-CD) modified matrix metalloproteinase-2 (MMP-2) responsive liposome (LRC-GEM-PFD) was constructed by a thin-film hydration method to regulate PSCs (Ji et al., 2016a), and RGD peptides were also modified onto the liposomes for targeting tumor cells. Pirfenidone (PFD), an antifibrotic and anti-inflammatory agent was inserted in the hydrophobic chamber of ß-CD, and the chemotherapeutic drug gemcitabine (GEM), was encapsulated in the liposomes. The liposomes were disassembled into two functional parts upon MMP-2 cleavage at the tumor site. The ß-CDs and PFD were kept in the stroma and inhibited the expression of collagen I and TGF-β in PSCs, down-regulating the fibrosis and decreasing the stromal barrier. The RGD peptide-modified-liposome loading GEM targeted and killed pancreatic tumor cells. Systemic administration of LRC-GEM-PFD into mice resulted in the alleviation of stromal fibrosis in pancreatic tumors and increased drug perfusion, ultimately showing an improved efficiency for pancreatic cancer therapy without overt side effects. MRP, another tailor-designed MMP-2 responsive amphiphilic peptide (sequence: SDK(C18)SGPLG-IAGQSK(C18)DS), tends to self-assemble to micrometer-long nanofibers. When it was mixed with the phospholipid, the co-assembly products transformed into stable hybrid liposomal nanospheres with uniform size distributions. Thus, a MMP-2 responsive peptide-hybrid liposome (MRPL) was constructed *via* co-assembly of phospholipids and MRP to deliver PFD to PSCs (Ji et al., 2017). The MRPL achieved tumor-specific delivery and release of PFD at the PSCs-enriched pancreatic tumors. The released PFD downregulated the multiple components of ECM secreted by the PSCs and increased the penetration of GEM into the tumor, thus enhancing the therapeutic efficacy of free GEM. Above all, the MMP-2 responsive nanomedicine may provide a potential strategy for improvement of the pancreatic cancer therapy.

4.2 Targeting cancer-associated fibroblasts

CAFs are one of the important types of stromal cells in solid tumor tissue, which highly express certain proteins, such as fibroblast activating proteins, αV-integrin family, and *a*-Smooth muscle actin (*α*-SMA). CAFs also secrete a series of factors and proteins, such as CXCL12 and Tenascin C, which promote tumor metastasis and densify the tumor matrix to build a barrier to prevent drug penetration. Peptide-based assembling NPs for targeting CAFs have been summarized in Table 2.

4.2.1 Targeting fibroblast activation protein-α

Fibroblast activation protein-α (FAP-α) is a transmembrane serine protein, which has been identified as a diagnostic marker to distinguish CAFs from normal fibroblasts.

Yan et al. (2020b) developed FAP-α-targeting peptide-modified, singlet oxygen ($^1O_2$)-sensitive, and Dox-loaded self-assembly nanoclusters (NCs) *via* a double emulsion method. After administration, the NCs specifically targeted CAFs, generated a large amount of $^1O_2$ under the assistance of light irradiation which depleted CAFs resulting in stroma attenuation and degrading the shell of NCs to release small-sized, positively charged Dox-loaded NCs. The Dox-loaded NCs could efficiently penetrate deeper regions of tumors to release Dox which played a synergistic role with $^1O_2$ in anti-tumor. This study provided a prospected way to promote the penetration of NCs in CAFs-rich tumors by simultaneously and spatiotemporally reconstructing the size and charge of NCs and remodeling TME. Other researchers constructed a FAP-α responsive peptide-based nanoparticles (CAP NPs) to target CAFs and encapsulate Dox (Ji et al., 2016b). The cleavable amphiphilic peptide (CAP) specifically responsive to FAP-α could self-assemble into nanofibers, which would transform into drug-loaded spherical NPs when the hydrophobic drug Dox was added. *In vitro*, the Dox of CAP NPs could efficiently and specifically take up by CAFs, while normal cells did not. However, when CAFs were co-cultured with tumor cells, both cells have taken Dox, implying that the specific response of CAP NPs to FAP-α could avoid off-target effects and allow the released Dox to CAFs and the co-existing tumor cells in TME. *In vivo*, the CAP NPs displayed outstanding tumor specificity and low non-specific organ accumulation. In the xenograft PC-3 prostate tumor model, MCF-7 breast tumor model, and Mia-paca-2 pancreatic tumor model, the CAP NPs were cleaved by FAP-α and disassembled to release free Dox to disrupt the stromal barrier and enhance local drug accumulation resulting in the completed inhibition of cancers. This stimulus-responsive nanocarrier was potentially applicable for the delivery of a broad spectrum of poorly soluble chemotherapeutic drugs, being able to greatly enhance tumor targeting and drug delivery efficacy. What's more, some researchers have constructed self-assembled nanoparticles based on anti-FAP-α antibodies and cell-penetrating peptides (CPP). Ji et al. (2015) designed and synthesized an amphiphilic peptide-cholesterol monomer (C2KG2R9) to deliver Dox to make CAFs depleted. The C2KG2R9 monomers, composed of CPP, oligo arginine and cholesterol, easily self-assembled to form positively charged core-shell NPs, in which hydrophobic Dox is encapsulated in the core, and anti-FAP-α antibody is modified on the surface through electrostatic binding. After administration in nude mice co-implanted with CAFs and PC-3 cells subcutaneously, the NPs bound to CAFs, enhanced the uptake of Dox by CAFs and led to the depletion of CAFs and the destruction of matrix barrier, resulting in improving the penetration of Dox to tumor tissues.

However, the strategy of CAFs depletion is controversial, because rapid elimination of CAFs may break the homeostasis of the TME and increase the risk of metastasis (Özdemir et al., 2014). CAFs inactivation, rather than depletion, reduces the risk of tumor cell metastasis. CXCL12, mainly secreted by activated CAFs in desmoplastic tumors, maintained the tumor-promoting phenotype of CAFs, which accelerated tumor growth and metastasis. When CXCL12 expression is knocked down, CAFs are inactivated (Kojima et al., 2010). The researchers constructed cell-penetrating peptide-based nanoparticles to deliver CXCL12 silencing siRNA (siCXCL12) to CAFs by targeting FAP-α (Lang et al., 2019). In short, the conjugate of cholesterol and cell-penetrating peptide R9 (Chol-R9) self-assembled to form nanoparticles *via* hydrophobic interaction, then siCXCL12 and anti-FAP-α antibody were adsorbed to the positive-charged surface of NPs in turn *via* electrostatic interactions. The NPs specifically delivered siCXCL12 into CAFs by binding the FAP-α on the cell membrane of CAFs, knocked down the expression of CXCL12, resulting in the CAFs inactivation, the CAFs-related malignant TME remodeling and the inhibition of migration, invasion, metastasis, and tumor angiogenesis *in vitro*. In an orthotopic prostate tumor model, the NPs prolonged the blood circulation time and improved antimetastasis efficacy with no toxicity and acute immunological reaction. The TME reshaping strategy *via* targeting and inactivated CAFs instead of killing it provided an alternative approach for malignant prostate tumor metastasis inhibition.

4.2.2 Targeting integrin

Integrin receptors are highly expressed in tumor cells and surrounding stromal cells, playing a role in promoting tumor progression.

Autophagy plays a significant role in pancreatic cancer, especially in activating CAFs. Chen et al. developed a multifunctional tandem peptide TH-RGD (TR) which consisted of integrin αvβ3-targeting cRGD peptide and the pH-sensitive TH peptide (Chen et al., 2019). Based on this, they constructed TR peptide-modified liposomes (TR-PTX/HCQ-Lip) loaded with hydroxychloroquine (HCQ), and paclitaxel (PTX) to inhibit the stroma fibrosis and tumor cell autophagy. The TR peptide-modified liposomes (TR Lip) had good targeting and permeability attributed to the electrostatic adsorption internalization caused by the positive charge under acidic conditions and the receptor-ligand interaction of integrin and peptide RGD *in vitro* and *in vivo*. TR-PTX/HCQ-Lip could effectively target and inhibit autophagy of pancreatic cells and CAFs, kill tumor cells and inhibit matrix fibrosis in allogeneic and *in situ* pancreatic cancer models.

Duan et al. (2022) developed an MMP-triggered dual-targeting co-assembly micelle-in-liposome NPs to sequentially deliver antifibrotic drugs quercetin (Que) and chemotherapeutic agents PTX to remodel fibrotic TME and enhance chemotherapy. The integrin αvβ3-targeting peptide RGD-modified and PTX-loading micelles and Que were co-encapsulated into MMP-sensitive liposomes, which were further modified with the NGR peptide binding to APN overexpressed on tumor vasculature. After administration in the 4T1/CAFs-bearing BALB/c mouse model, the NPs were aggregated at the tumor site through integrin αvβ3 and APN dual-targeting and disassembled into free Que and PTX-loaded micelles upon the cleavage of MMP in TME. Que entered CAFs and downregulated the expression of Wnt16 to inhibit fibrosis, which enhanced the permeability and killing ability of PTX-loaded micelles. The sequential delivery systems for fibrotic TME remodeling and chemotherapy potentiation may provide a promising therapeutic strategy for breast and other CAFs-rich tumors.

4.2.3 Targeting tenascin C

Tenascin C is a tumor-specific extracellular matrix glycoprotein mainly secreted by CAFs, which is highly expressed in most solid tumors TME, but not in normal adult tissues, and promotes tumor progression (Orend and Chiquet-Ehrismann, 2006). Tenascin C may exist on the cell membrane of CAFs before secretion, which may provide the possibility of targeting CAFs.

A small peptide FH screened by phage display peptide library that specifically binds to Tenascin C and can be used to target CAFs in TME to deliver drug and enhance drug accumulation (Kim et al., 2012). In a study, the researchers used FH peptide as CAFs targeting ligand, conjugated with DSPE-PEG$_{2000}$, and prepared tenascin C-targeting self-assembled liposomes (FH-SSLNav) loaded with Navitoclax, a Bcl-2 inhibitor, through the thin film hydration method (Chen et al., 2016). *In vitro*, FH-SSLNav showed more cellular uptake and toxicity. In Hep G2 tumor-bearing nude mice model, FH-SSLNav efficiently targeted tumor matrix and depleted CAFs to inhibit tumor growth. In another study, they constructed a CAFs-targeted and Dox-loaded ultrasonic nanobubble (FH-NB-Dox NB) consisting of the lipids as shell membrane, the FH peptide as CAFs targeting ligand and the perfluoropropan as core (Guo et al., 2019). FH-NB-Dox delivered more Dox into CAFs and enhanced the Dox-induced CAFs eradication under ultrasound irradiation and showed good contrast-enhanced ultrasound imaging *in vitro*. Another peptide targeting Tenascin C is the peptide CFH, which is obtained by connecting a cysteine at the end of the peptide FH (Guo et al., 2022). Based on it, a CAF targeting and oxymatrine-loaded liposome (CFH/OM-L) was developed by pH gradient method. CFH/OM-L could target and deactivate CAFs and reverse the EMT process accompanied by the upregulation of E-cadherin and downregulation of vimentin, N-cadherin, and snail protein *in vivo* and *in vitro*.

5 Targeting tumor vasculature

Angiogenesis plays a role in the growth, survival, metastasis and relapse of cancers. Angiogenic vascular cells, mainly endothelial cells, express specific molecular markers which are absent or barely detectable in the normal blood vessels, including integrins, aminopeptidase-N (APN or CD13), and VEGF receptors. Different from tumor cells, endothelial cells of tumor vasculature are genetically stable, and targeting it rather than tumor cells contributes to reducing drug resistance (Seyyednia et al., 2021). Therefore, tumor vasculature is a suitable site for cancer-targeted therapy. Most of the tumor vasculature-targeted peptides are also therapeutic peptides, which have the ability of anti-angiogenesis. The peptides targeting tumor vasculature are summarized in Supplementary Table S1.

5.1 Targeting integrin

Integrins are transmembrane-spanning receptors that play a critical role in tumor angiogenesis. RGD is the most classical peptide targeting integrin (Arap et al., 1998). Cyclized RGD is more stable and has a higher affinity (Kang et al., 2017). The tumor penetrating peptide iRGD synthesized by combining RGD with CendR motif not only binds to integrins αvβ3 and αvβ5, but also neuropilin-1 (NRP-1) (Kang et al., 2020; Li et al., 2021). Drug delivery systems based on RGD have been well summarized and will not be included in this review (Sadatmousavi et al., 2011; Danhier et al., 2012; Marelli et al., 2013; Sun et al., 2017; Sheikh et al., 2021a; Sheikh et al., 2021b; Cheng et al., 2021).

The C16Y peptide, which was derived from the laminin γ1 chain, bound to integrins αvβ3 and α5β1 strongly expressed on activated endothelial cells and tumor cells (Ponce et al., 2003). A study synthesized an amphiphilic chimeric peptide DEAP-C16Y that was able to self-assemble into spherical NPs at physiologic pH and dissociate to release individual peptides to target αvβ3 and α5β1 expressing cells in weakly acidic tumors (Ding et al., 2015). *In vitro*, DEAP-C16Y effectively inhibited endothelial cell migration, tubule formation and tumor cell invasion. In 4T1 breast cancer mouse models, the DEAP–C16Y NPs, with negligible cytotoxicity, were selectively located at the tumor site and suppressed tumor angiogenesis, growth, and metastasis. Through encapsulation of Dox, the DEAP-C16Y-Dox NPs have achieved more significant anti-tumor efficacy, due to the selective release and accumulation of Dox in tumor tissue. In another study, they prepared C16Y peptide-modified liposomes (C16Y-L) by a reverse-phase evaporation method, which could selectively target integrin αvβ3 and enhance intracellular uptake through energy-dependent endocytosis *in vitro* (Hamano et al., 2012).

AXT050, a collagen-IV derived peptide, bound to integrin αvβ3 with high affinity and had the ability to antitumor, anti-angiogenesis, and anti-lymphangiogenesis. An AXT050-modified PEGylated poly (lactic-co-glycolic acid) NPs was constructed (Bressler et al., 2018). The targeted NPs inhibited the adhesion and proliferation of tumor cells and endothelial cells through binding to integrin αvβ3 *in vitro* and showed two-fold greater accumulation in tumors and lower accumulation in the liver compared to non-targeted NPs in the triple-negative breast cancer mouse model.

Shroff et al. developed a fibronectin-mimetic peptide PR_b, which has been shown to bind specifically to integrin α5β1 (Shroff and Kokkoli, 2012). Based on this, they designed PR_b-functionalized PEGylated liposomes which could specifically bind to MDA-MB-231 cells through targeting integrin α5β1, and the binding could be controlled by varying the peptide concentration. The Dox-loaded liposomes were present in the early endosomes after 10 min incubation and in the late endosomes and lysosomes after long time incubation, which had equally cytotoxic as the free Dox, especially at higher doxorubicin concentrations. This study offered a promising strategy to deliver Dox to breast cancer cells.

5.2 Targeting aminopeptidase N

The enzyme aminopeptidase N (APN, also known as CD13) is related to angiogenesis, proliferation, invasion and metastasis, which is used as a diagnostic and prognostic factor for solid cancers (Wickström et al., 2011). NGR peptide was found to target APN by phage display in 1995 (Pasqualini et al., 1995). A tumor-penetrating peptide iNGR was screened out in 2013, composed of NGR motif and CendR motif (Alberici et al., 2013). iNGR initially bound to APN, with iNGR proteolytically cleaved to CRNGR, and then targeted NRP-1 to mediate deep penetration in the tumor parenchyma.

The major problem for glioma therapy is the poor extravasation and penetration of the nanodelivery system. The iNGR-modified nanodelivery system with the advantages of tumor blood vessel recognition and tumor penetration has been widely used in the treatment of glioblastoma, like iNGR-modified doxorubicin-loaded liposomes (Zhou et al., 2017), iNGR-modified PTX-loaded PEG-PLGA nanoparticles (Kang et al., 2014), and self-assembled RNAi nanoparticles functionalized with iNGR to siRNA delivery (An et al., 2015). All of them significantly facilitated the cellular uptake by HUVEC cells and glioma cells and enhanced the effect of drugs *in vitro*. In the glioblastoma-bearing mouse model, the iNGR-modified NPs displayed favorable pharmacokinetics, penetrated through tumor vasculature and into the deep tumor tissues and achieve the highest accumulation at the glioma sites.

iNGR-modified NPs also used in breast cancer for efficient drug delivery to tumor sites. In a study, the researchers constructed self-assembly ultrasmall micelles by the amphiphilic linear-dendritic PEG-PTX conjugate with a hydrated diameter of about 25 nm, which encapsulated PTX and linked with peptide iNGR (Zhang et al., 2017a). In triple-negative breast cancer mouse model, the micelles enhanced the accumulation in the tumor, displayed strong antitumor effect, and significantly extended the median survival time. In another study, the iNGR-modified Dox-loaded smart NPs with a PEGylated lipid monolayer shell and a pH-sensitive hydrophobic poly-l-histidine core was developed, which undergoed a two-step phase transition at two different pH values (Ye et al., 2018). In TME (pH_e: 7.0–6.5), the surface potential of the smart NPs turned neutral or positive, facilitating the cellular uptake. After internalization, due to the acid endolysosome (pH_{endo}: 6.5–4.5), the smart NPs dissociated and induced endolysosome escape to release Dox into the cytoplasm. The iNGR-modified smart NPs displayed higher cellular uptake *in vitro* and strongly inhibited tumor growth and prolonged the median survival time in late-stage aggressive breast carcinoma mouse model, providing a method for overcoming the problem of inefficient cellular uptake and intracellular drug release at the tumor site.

The angiogenesis-targeting iNGR peptide-modified TPGS-PLA nanoparticles co-encapsulating with chemotherapeutic agent docetaxel and photosensitizer verteporfin were constructed to treat drug-resistant human colorectal adenocarcinoma. The NPs promoted the cellular uptake and cytotoxicity of HUVEC cells and drug-resistant HCT-15 tumor cells and effectively inhibited tube formation under laser irradiation *in vitro*. In the drug-resistant HCT-15 mouse model, the NPs extravasated from the tumor vasculature and enhanced the inhibition of angiogenesis, selectively accumulated in the tumor site and penetrated deep site, and induced severe apoptosis and necrosis in tumor tissues under laser irradiation. It was evidenced that the NPs have great potential to treat drug-resistant tumors *via* efficient angiogenesis-targeted photo-chemotherapy.

5.3 Targeting VEGF receptor

Vascular endothelial growth factor (VEGF) and its receptors, such as VEGFR-1, VEGFR-2, and neuropilin-1 (NRP-1), have been implicated in pathological angiogenesis associated with tumors, intraocular neovascular disorders and other conditions, which were regarded as target molecules for the antiangiogenic approach (Ferrara et al., 2003).

Oku's team has identified angiogenic vessel-homing peptide APRPG binding to VEGFR-2 and utilized it in liposomal drug delivery. They constructed VEGFR-2-targeted liposomes modified with PEG and DSPE-PEG-APRPG to deliver Dox, with the ability of long-circulating characteristics, enhanced accumulation in tumor and efficient tumor growth suppression *in vivo* (Maeda et al., 2004). Next, they developed dual-targeting liposomes modified with APRPG targeting VEGFR-2 and GNGRG targeting APN to deliver Dox. Compared to single-targeting liposomes, the dual-targeting liposomes were remarkably associated with human umbilical vein endothelial cells (HUVEC) and suppressed the growth of it *in vitro* and strongly suppressed tumor growth by the disruption of tumor vasculature in carcinoma-bearing mice (Murase et al., 2010). They also developed APRPG-modified liposomes encapsulating insoluble angiogenesis inhibitor SU5416, with the advantages of the improvement of solubility, the enhancement of antiangiogenic and the suppression of tumor growth with no remarkable side effects (Katanasaka et al., 2008). Guo et al. (2015) conjugated APRPG to the amphipathic copolymer PLGA-PEG to synthesized copolymer APRPG-PEG-PLGA which could spontaneously self-assemble to micelles and it was used to encapsulate PTX. The micelles promoted the uptake by endothelial cells and enhanced the cytotoxicity of cancer cells *in vitro*. After intravenous injection, the micelles accumulated in the tumor tissues due to the passive accumulation and active targeting effects, leading to reducing the tumor volume and prolonging the survival time of tumor-bearing mice.

K237, isolated from the phage display peptide library, was found to target VEGFR-2 predominantly expressed on the surface of tumor neovasculature endothelial cells with high affinity and specificity and induce the inhibition of angiogenesis and tumor growth (Hetian et al., 2002). Fang's team developed K237-conjugated PTX-loaded nanoparticles (K237-PTX-NPs) for tumor neovasculature targeting drug delivery. *In vitro*, the K237-PTX-NPs could be significantly internalized by HUVEC by binding to VEGFR-2, thereby enhancing cytotoxicity and apoptosis. The K237-PTX-NPs with long-circulating property could accurately target tumor neovasculature, and induced the apoptosis of tumor neovasculature endothelial cells and necrosis of tumor tissues in MDA-MB-231 breast tumor-bearing mice (Yu et al., 2010). What's more, the anti-tumor effect of K237-PTX-NPs is consistent with that of an 8-fold dose of free PTX plus P-gp inhibitor XR9576 in P-gp expressing human colorectal resistant tumor model (Bai et al., 2013). Yao et al. (2017) developed neovasculature and circulating tumor cells (CTCs) dual-targeting NPs encapsulating PTX, which is conjugated with K237 peptide and CTCs-targeted Ep23 aptamer. The dual-targeting NPs enhanced the cellular uptake, cell apoptosis, cytotoxicity and antiangiogenesis activity *in vitro* and actively captured and eradicated CTCs *in vivo*. The NPs damaged the primary tumor site and eradicated CTCs simultaneously and achieved a synergistic anti-tumor therapeutic effect.

A7R and proteolytically stable ^{D}A7R, identified by phage display peptide library, showed high affinity for VEGFR-2 and NRP-1 and blocked VEGF-mediated angiogenesis and were commonly used as co-targeting ligands for anti-glioma targeted therapy (Binétruy-Tournaire et al., 2000). Several dual-targeted NPs have been reported, such as Dox and vincristine dual-loaded liposomes modified with ^{D}A7R and glioma-targeted peptide T7 (Zhang et al., 2017b), Dox-loaded liposomes functionalized by ^{D}A7R and nicotine acetylcholine receptor-targeting peptide ^{D}CDX (Ying et al., 2016), and PTX-loaded nanoparticles modified with A7R and heparan sulfates-targeting peptide CGKRK (Hu et al., 2016), which could cross the blood-brain barrier (BBB) and blood-brain tumor barrier (BBTB) and displayed high glioma localization and strong antiangiogenesis and antiglioma effect.

5.4 Targeting nucleolin

Some studies show that nucleolin, known as a nuclear and cytoplasmic protein, can express on the cell membrane of activated tumor cells and tumor-specific vascular endothelial cells. A research group developed peptide F3 that specifically targeted to this new marker and mediated nucleolin-dependent internalization of drug loaded NPs. (Christian et al., 2003).

Treatment of glioma with NPs is limited by its low vascular permeability and tumor penetrability. tLyp-1, a tumor homing and penetrating peptide, was able to mediate tissue penetration through the NRP-1-dependent internalization pathway. Researchers constructed F3-modified PTX-loaded PEG-PLA NPs (F3-NPs) by an emulsion/evaporation method and co-administered with tLyP-1 to achieve tumor targeting along with high cellular internalization and extensive vascular extravasation (Hu et al., 2013a). Results showed that the F3-NPs could effectively penetrate 3D multicell tumor spheroids and increased the cytotoxicity of PTX *in vitro*. The F3-NPs co-administered with tLyp-1 showed the highest accumulation at the tumor site and deep penetration into the glioma parenchyma and achieved the longest survival in mice bearing intracranial C6 glioma.

The CCL5/CCR5 cytokine-related pathways in TME could regulate VEGF in a variety of ways, resulting in the ineffectiveness of tumor vascular normalization therapy dependent on anti-VEGF. In order to overcome this problem, the researchers combined two nanoparticles for administration focusing to achieve the bi-directional modulation between tumor vasculature and TME (Deng et al., 2021). One self-assembly nanoparticle (FLG NP) was constructed by an amphiphilic conjugate, composed of F3 peptide and two VEGFR-2 inhibitors connected with acid-sensitive hydrazone bonds. The FLG NP could specifically degrade and release VEGFR-2 inhibitors to repair abnormal tumor vessels when entering acidic conditions in VECs. Another nanoparticle loading with CCL5/CCR5 blocker maraviroc was designed to inhibit the CCL5 functions of angiogenesis and TME deterioration. Results showed that the combination of two NPs synergistically induced vascular normalization and remodeled TME in Panc-1 pancreatic cancer nude model and increased infiltration of $CD4^{+}$ and $CD8^{+}$ T cells in the B16-F10 melanoma model, providing a new direction for cancer therapy based on the tumor vasculature normalization and TME remodeling.

Wan et al. found that the F3 peptide-modified NPs enhanced accumulation in normal tissues resulting in serious side effects. Then they synthesized a pH-sensitive peptide CF, only displaying penetration ability under acidic conditions, by conjugating the tumor homing peptide CREKA with nucleolin-targeting peptide F3 through the acidic sensitive linker-hydrazone (Wan et al., 2019). Then the peptide CF was modified on the surface of the NPs co-entrapped with EGFR inhibitor EB and Notch inhibitor GSI-DAPT. Compared with other groups, the pH-sensitive NPs displayed the lowest distribution in normal tissues and the highest accumulation in the tumor site and strongly inhibited tumor growth in triple-negative breast cancer, due to the cell penetration ability of F3 was sealed under normal physical conditions and recovered at the acidic tumor environment in which pH-sensitive linkage can be broken down.

5.5 Other targeting peptides

In addition to the above mentioned, there are also other self-assembled nanoparticles based on tumor vasculature targeting-peptides for cancer treatment.

GX1, the cyclic 7-mer peptide motif CGNSNPKSC, was identified as a human gastric tumor vasculature homing peptide at first and bound to transglutaminase-2 (TMG2) to inhibit angiogenesis (Lei et al., 2018). The GX1-modified liposomes have been used to treat gastric cancer, such as GX1-modified liposomes encapsulating PTX (GX1-PTX-NLCs) and GX1-mediated anionic liposomes carrying adenoviral vectors integrating with the tumor suppressor gene of PTEN (GX1-Ad5-AL), which all promoted the cellular uptake by HUVEC cells, enhanced the inhibition of HUVEC cells and significantly suppressed the migration of gastric cancer cell *in vitro* (Xiong et al., 2015; Jian et al., 2020). *In vivo* studies demonstrated that GX1-PTX-NLCs significantly inhibited tumor growth with lower toxicity in MKN45 tumor-bearing nude mice model (Jian et al., 2020). GX1-conjugated poly (lactic acid) nanoparticles encapsulating Endostar, a novel recombinant human endostatin, and labeled with the near-infrared dye were developed for colorectal cancer targeting and therapy *in vivo*, which accumulated in tumor site and improved antitumor efficacy in the colorectal mouse model (Du et al., 2015).

E-selectin was exclusively expressed on the endothelial cells of tumor vasculature. The researchers designed a peptide (IELLQAR) to target E-selectin, and developed a PEGylated peptide-drug conjugate (PEGylated PDC) as a nano-prodrug, which was able to assemble into nanoparticles in aqueous conditions, by conjugating PEG and E-selectin targeting peptide to the antitumor molecule SN38 (Hao et al., 2021). The self-assembly NPs increased drug accumulation and retention at the tumor site by the EPR effect and improved tumor growth inhibition and prolonged the survival of mice bearing primary HCT116 tumors.

CGKRK peptide was specially bound to both neovascular endothelial cells and tumor cells and its receptor was reported to be heparan sulfate in 2007 (Järvinen and Ruoslahti, 2007) and mitochondrial protein p32 in 2013 (Agemy et al., 2013). CGKRK peptide functionalized and PTX loaded PEG-co-PCL NPs were developed by the emulsion/solvent evaporation technique, aiming to achieve tumor cells and tumor angiogenic blood vessels dual-targeting (Hu et al., 2013b). The dual-targeting NPs enhanced cytotoxicity and apoptosis on both HUVEC cells and U87MG cells and improved its inhibition effect on the growth of U87MG tumor spheroids *in vivo*. The dual-targeting NPs selectively accumulated at the tumor site and achieved the smallest tumor volume in mice bearing subcutaneous U87MG tumors. Above all, the tumor cells and tumor angiogenic blood vessels dual-targeting system might provide a great promising approach for reducing the disadvantages of antiangiogenic therapy alone.

IF7 peptide was designed to bind to the annexin 1 (Anxa 1), a novel specific biomarker of the tumor vasculature endothelial cells, with high affinity and specificity. IF7-PTX-NP nanoparticles modified with IF7 peptide and loading with PTX were developed by the emulsion/solvent evaporation method to treat resistant cancers (Yu et al., 2015). IF7-PTX-NP was significantly internalized by HUVEC through the IF7-Anxa 1 interaction and inhibited the tumor angiogenesis ability of HUVEC. IF7-PTX-NP prolonged circulation, accumulated in the tumor site, induced significant apoptosis of the tumor vascular endothelial cells and necrosis of the tumor tissues, and showed significant anticancer efficacy with a low dose (1 mg/kg) in the MCF-7/ADR xenografts in female nude mice. The same efficacy was only obtained with an 8-fold dose of PTX (8 mg/kg) or PTX plus P-gp inhibitor XR9576, which showed that targeting the tumor vasculature rather than the resistant tumor cells offered a promising strategy for the treatment of multidrug-resistant cancer.

The abundant presence of tumor vasculature and cancer stem cells (CSCs) promotes cancer metastasis. CD105 is a specific co-biomarker for tumor neovascular endothelial cells and CSCs, providing a potential target for inhibiting both cells simultaneously. An amphiphilic peptide based on the CD105 recognition motif was constructed, which could self-assemble into nanoparticles under physiological conditions (Wang et al., 2020). When nanoparticles bound to CD105, they transformed into nanofiber barriers on the cell membrane *in situ*, resulting in reducing endothelial permeability and angiogenesis and inhibiting the stemness and metastasis of CSCs in renal cancer. The NPs significantly inhibited the tumorigenesis and angiogenesis and reduced the metastatic nodules in lung in the patient-derived xenograft renal cancer mouse model, providing a promising method for inhibiting the metastasis of cancer.

6 Conclusion and prospect

Cancer is a multi-component entity, including tumor cells, stromal cells. This review described the advances of peptide-based nanoparticles in the cancer targeted therapies and summarized the currently existing peptides in tables. It should be noticeable that therapeutic peptides have evolved and played a notable role in the cancer treatment in recent years. Hence, it can be expected that peptide-assembled nanoparticles would provide alternative treatment strategies for cancer treatment in the future. Besides, peptide-drug conjugates (PDCs) that combine therapeutic molecules with a peptide through a biodegradable linker are emerging and developed rapidly in recent years, which will become an appealing direction in the peptide field. It should be noted that most PDCs can self-assemble to different nanostructures, such as nanotubes, nanoparticles, and nanofibers, with the advantage of easy synthesis, alternative modes of administration, providing the means to tune the physicochemical properties, and a precise loading capacity (Wang et al., 2017; Fang and Wang, 2022).

Nevertheless, so far there have been no active-targeting carriers approved by FDA (Pérez-Herrero and Fernández-Medarde, 2015). Some concerns may be the potential blockades for successful translation of peptide-assembled nanoparticles into clinic. Firstly, tumor heterogeneity, multidrug resistance, inappropriate target and upregulation compensation in other ways may lead to the failure of targeted therapy. Secondly, the behavior of the peptide-based nanoparticles after entering the blood circulation cannot be completely tracked. Another issue is that all the transient metabolites and their potential toxicities should be identified and manifested, while there is no mature method to evaluate the biocompatibility and toxicity of peptide-assembled nanoparticles yet.

Above all, peptide-based assembling nanoparticles for cancer therapy has broad prospects and strong trends of sustainability.

Author contributions

All authors listed have made a substantial, direct, and intellectual contribution to the work, and approved it for publication.

Funding

This work was supported by the National Key R&D Program of China (2017YFA0205504) and the National Natural Science Foundation of China (Grant Nos. 81870133).

Conflict of interest

The authors declare that the research was conducted in the absence of any commercial or financial relationships that could be construed as a potential conflict of interest.

Publisher's note

organizations, or those of the publisher, the editors and the reviewers. Any product that may be evaluated in this article, or claim that may be made by its manufacturer, is not guaranteed or endorsed by the publisher.

Supplementary material

The Supplementary Material for this article can be found online at: https://www.frontiersin.org/articles/10.3389/fchem.2023.1115495/full#supplementary-material

References

Agemy, L., Kotamraju, V. R., Friedmann-Morvinski, D., Sharma, S., Sugahara, K. N., and Ruoslahti, E. (2013). Proapoptotic peptide-mediated cancer therapy targeted to cell surface p32. *Mol. Ther.* 21 (12), 2195–2204. doi:10.1038/mt.2013.191

Alberici, L., Roth, L., Sugahara, K. N., Agemy, L., Kotamraju, V. R., Teesalu, T., et al. (2013). De novo design of a tumor-penetrating peptide. *Cancer Res.* 73 (2), 804–812. doi:10.1158/0008-5472.can-12-1668

An, S., Jiang, X., Shi, J., He, X., Li, J., Guo, Y., et al. (2015). Single-component self-assembled RNAi nanoparticles functionalized with tumor-targeting iNGR delivering abundant siRNA for efficient glioma therapy. *Biomaterials* 53, 330–340. doi:10.1016/j.biomaterials.2015.02.084

Apte, M. V., Wilson, J. S., Lugea, A., and Pandol, S. J. (2013). A starring role for stellate cells in the pancreatic cancer microenvironment. *Gastroenterology* 144 (6), 1210–1219. doi:10.1053/j.gastro.2012.11.037

Arap, W., Pasqualini, R., and Ruoslahti, E. (1998). Cancer treatment by targeted drug delivery to tumor vasculature in a mouse model. *Science* 279 (5349), 377–380. doi:10.1126/science.279.5349.377

Arneth, B. (2019). Tumor microenvironment. *Med. Kaunas.* 56 (1), 15. doi:10.3390/medicina56010015

Asciutto, E. K., Kopanchuk, S., Lepland, A., Simón-Gracia, L., Aleman, C., Teesalu, T., et al. (2019). Phage-display-derived peptide binds to human CD206 and modeling reveals a new binding site on the receptor. *J. Phys. Chem. B* 123 (9), 1973–1982. doi:10.1021/acs.jpcb.8b11876

Bai, F., Wang, C., Lu, Q., Zhao, M., Ban, F. Q., Yu, D. H., et al. (2013). Nanoparticle-mediated drug delivery to tumor neovasculature to combat P-gp expressing multidrug resistant cancer. *Biomaterials* 34 (26), 6163–6174. doi:10.1016/j.biomaterials.2013.04.062

Bai, H., Wang, T., Kong, F., Zhang, M., Li, Z., Zhuang, L., et al. (2021). CXCR4 and CD44 dual-targeted Prussian blue nanosystem with daunorubicin loaded for acute myeloid leukemia therapy. *Chem. Eng. J.* 405, 126891. doi:10.1016/j.cej.2020.126891

Balkwill, F. R., Capasso, M., and Hagemann, T. (2012). The tumor microenvironment at a glance. *J. Cell Sci.* 125 (23), 5591–5596. doi:10.1242/jcs.116392

Binétruy-Tournaire, R., Demangel, C., Malavaud, B., Vassy, R., Rouyre, S., Kraemer, M., et al. (2000). Identification of a peptide blocking vascular endothelial growth factor (VEGF)-mediated angiogenesis. *Embo J.* 19 (7), 1525–1533. doi:10.1093/emboj/19.7.1525

Bochet, L., Lehuédé, C., Dauvillier, S., Wang, Y. Y., Dirat, B., Laurent, V., et al. (2013). Adipocyte-derived fibroblasts promote tumor progression and contribute to the desmoplastic reaction in breast cancer. *Cancer Res.* 73 (18), 5657–5668. doi:10.1158/0008-5472.can-13-0530

Bressler, E. M., Kim, J., Shmueli, R. B., Mirando, A. C., Bazzazi, H., Lee, E., et al. (2018). Biomimetic peptide display from a polymeric nanoparticle surface for targeting and antitumor activity to human triple-negative breast cancer cells. *J. Biomed. Mater Res. A* 106 (6), 1753–1764. doi:10.1002/jbm.a.36360

Bruder, D., Probst-Kepper, M., Westendorf, A. M., Geffers, R., Beissert, S., Loser, K., et al. (2004). Frontline: Neuropilin-1: A surface marker of regulatory T cells. *Eur. J. Immunol.* 34 (3), 623–630. doi:10.1002/eji.200324799

Cassetta, L., and Kitamura, T. (2018). Macrophage targeting: Opening new possibilities for cancer immunotherapy. *Immunology* 155 (3), 285–293. doi:10.1111/imm.12976

Céspedes, M. V., Unzueta, U., Tatkiewicz, W., Sánchez-Chardi, A., Conchillo-Solé, O., Álamo, P., et al. (2014). *In vivo* architectonic stability of fully de novo designed protein-only nanoparticles. *ACS Nano* 8 (5), 4166–4176. doi:10.1021/nn4055732

Chatterjee, S., Behnam Azad, B., and Nimmagadda, S. (2014). The intricate role of CXCR4 in cancer. *Adv. Cancer Res.* 124, 31–82. doi:10.1016/B978-0-12-411638-2.00002-1

Chen, B., Wang, Z., Sun, J., Song, Q., He, B., Zhang, H., et al. (2016). A tenascin C targeted nanoliposome with navitoclax for specifically eradicating of cancer-associated fibroblasts. *Nanomedicine* 12 (1), 131–141. doi:10.1016/j.nano.2015.10.001

Chen, X., Yu, Q., Liu, Y., Sheng, Q., Shi, K., Wang, Y., et al. (2019). Synergistic cytotoxicity and co-autophagy inhibition in pancreatic tumor cells and cancer-associated fibroblasts by dual functional peptide-modified liposomes. *Acta Biomater.* 99, 339–349. doi:10.1016/j.actbio.2019.09.003

Cheng, T. M., Chang, W. J., Chu, H. Y., De Luca, R., Pedersen, J. Z., Incerpi, S., et al. (2021). Nano-strategies targeting the integrin αvβ3 network for cancer therapy. *Cells* 10 (7), 1684. doi:10.3390/cells10071684

Christian, S., Pilch, J., Akerman, M. E., Porkka, K., Laakkonen, P., and Ruoslahti, E. (2003). Nucleolin expressed at the cell surface is a marker of endothelial cells in angiogenic blood vessels. *J. Cell Biol.* 163 (4), 871–878. doi:10.1083/jcb.200304132

Cieslewicz, M., Tang, J., Yu, J. L., Cao, H., Zavaljevski, M., Motoyama, K., et al. (2013). Targeted delivery of proapoptotic peptides to tumor-associated macrophages improves survival. *Proc. Natl. Acad. Sci. U. S. A.* 110 (40), 15919–15924. doi:10.1073/pnas.1312197110

Danhier, F., Le Breton, A., and Préat, V. (2012). RGD-based strategies to target alpha(v) beta(3) integrin in cancer therapy and diagnosis. *Mol. Pharm.* 9 (11), 2961–2973. doi:10.1021/mp3002733

Delgoffe, G. M., Woo, S. R., Turnis, M. E., Gravano, D. M., Guy, C., Overacre, A. E., et al. (2013). Stability and function of regulatory T cells is maintained by a neuropilin-1-semaphorin-4a axis. *Nature* 501 (7466), 252–256. doi:10.1038/nature12428

Deng, Y., Jiang, Z., Jin, Y., Qiao, J., Yang, S., Xiong, H., et al. (2021). Reinforcing vascular normalization therapy with a bi-directional nano-system to achieve therapeutic-friendly tumor microenvironment. *J. Control Release* 340, 87–101. doi:10.1016/j.jconrel.2021.10.016

Ding, Y., Ji, T., Zhao, Y., Zhang, Y., Zhao, X., Zhao, R., et al. (2015). Improvement of stability and efficacy of C16Y therapeutic peptide via molecular self-assembly into tumor-responsive nanoformulation. *Mol. Cancer Ther.* 14 (10), 2390–2400. doi:10.1158/1535-7163.mct-15-0484

Du, Y., Zhang, Q., Jing, L., Liang, X., Chi, C., Li, Y., et al. (2015). GX1-conjugated poly(lactic acid) nanoparticles encapsulating Endostar for improved *in vivo* anticolorectal cancer treatment. *Int. J. Nanomedicine* 10, 3791–3802. doi:10.2147/IJN.S82029

Duan, H., Liu, C., Hou, Y., Liu, Y., Zhang, Z., Zhao, H., et al. (2022). Sequential delivery of quercetin and paclitaxel for the fibrotic tumor microenvironment remodeling and chemotherapy potentiation via a dual-targeting hybrid micelle-in-liposome system. *ACS Appl. Mater Interfaces* 14 (8), 10102–10116. doi:10.1021/acsami.1c23166

Espinoza-Gutarra, M. R., Green, S. D., Zeidner, J. F., and Konig, H. (2021). CD123-targeted therapy in acute myeloid leukemia. *Expert Rev. Hematol.* 14 (6), 561–576. doi:10.1080/17474086.2021.1935855

Falgàs, A., Garcia-León, A., Núñez, Y., Serna, N., Sánchez-Garcia, L., Unzueta, U., et al. (2022). A diphtheria toxin-based nanoparticle achieves specific cytotoxic effect on CXCR4(+) lymphoma cells without toxicity in immunocompromised and immunocompetent mice. *Biomed. Pharmacother.* 150, 112940. doi:10.1016/j.biopha.2022.112940

Falgàs, A., Pallarès, V., Unzueta, U., Céspedes, M. V., Arroyo-Solera, I., Moreno, M. J., et al. (2020). A CXCR4-targeted nanocarrier achieves highly selective tumor uptake in diffuse large B-cell lymphoma mouse models. *Haematologica* 105 (3), 741–753. doi:10.3324/haematol.2018.211490

Fang, X., Xie, H., Duan, H., Li, P., Yousaf, M., Xu, H., et al. (2017). Anti-tumor activity of nanomicelles encapsulating CXCR4 peptide antagonist E5. *PLoS One* 12 (8), e0182697. doi:10.1371/journal.pone.0182697

Fang, X., Zhang, K., Jiang, M., Ma, L., Liu, J., Xu, H., et al. (2021). Enhanced lymphatic delivery of nanomicelles encapsulating CXCR4-recognizing peptide and doxorubicin for the treatment of breast cancer. *Int. J. Pharm.* 594, 120183. doi:10.1016/j.ijpharm.2020.120183

Fang, Y., and Wang, H. (2022). Molecular engineering of peptide-drug conjugates for therapeutics. *Pharmaceutics* 14 (1), 212. doi:10.3390/pharmaceutics14010212

Ferrara, N., Gerber, H. P., and LeCouter, J. (2003). The biology of VEGF and its receptors. *Nat. Med.* 9 (6), 669–676. doi:10.1038/nm0603-669

Fosgerau, K., and Hoffmann, T. (2015). Peptide therapeutics: Current status and future directions. *Drug Discov. Today* 20 (1), 122–128. doi:10.1016/j.drudis.2014.10.003

Glinka, Y., and Prud'homme, G. J. (2008). Neuropilin-1 is a receptor for transforming growth factor beta-1, activates its latent form, and promotes regulatory T cell activity. *J. Leukoc. Biol.* 84 (1), 302–310. doi:10.1189/jlb.0208090

Guo, H., Ge, Y., Li, X., Yang, Y., Meng, J., Liu, J., et al. (2017). Targeting the CXCR4/CXCL12 axis with the peptide antagonist E5 to inhibit breast tumor progression. *Signal Transduct. Target Ther.* 2, 17033. doi:10.1038/sigtrans.2017.33

Guo, J., Zeng, H., Shi, X., Han, T., Liu, Y., Liu, Y., et al. (2022). A CFH peptide-decorated liposomal oxymatrine inactivates cancer-associated fibroblasts of hepatocellular carcinoma through epithelial-mesenchymal transition reversion. *J. Nanobiotechnology* 20 (1), 114. doi:10.1186/s12951-022-01311-1

Guo, L., Shi, D., Meng, D., Shang, M., Sun, X., Zhou, X., et al. (2019). New FH peptide-modified ultrasonic nanobubbles for delivery of doxorubicin to cancer-associated fibroblasts. *Nanomedicine (Lond)* 14 (22), 2957–2971. doi:10.2217/nnm-2019-0302

Guo, P., Song, S., Li, Z., Tian, Y., Zheng, J., Yang, X., et al. (2015). *In vitro* and *in vivo* evaluation of APRPG-modified angiogenic vessel targeting micelles for anticancer therapy. *Int. J. Pharm.* 486 (1-2), 356–366. doi:10.1016/j.ijpharm.2015.03.067

Hamano, N., Negishi, Y., Fujisawa, A., Manandhar, M., Sato, H., Katagiri, F., et al. (2012). Modification of the C16Y peptide on nanoparticles is an effective approach to target endothelial and cancer cells via the integrin receptor. *Int. J. Pharm.* 428 (1-2), 114–117. doi:10.1016/j.ijpharm.2012.02.006

Hanahan, D., and Coussens, L. M. (2012). Accessories to the crime: Functions of cells recruited to the tumor microenvironment. *Cancer Cell* 21 (3), 309–322. doi:10.1016/j.ccr.2012.02.022

Hao, T., Fu, Y., Yang, Y., Yang, S., Liu, J., Tang, J., et al. (2021). Tumor vasculature-targeting PEGylated peptide-drug conjugate prodrug nanoparticles improve chemotherapy and prevent tumor metastasis. *Eur. J. Med. Chem.* 219, 113430. doi:10.1016/j.ejmech.2021.113430

Hetian, L., Ping, A., Shumei, S., Xiaoying, L., Luowen, H., Jian, W., et al. (2002). A novel peptide isolated from a phage display library inhibits tumor growth and metastasis by blocking the binding of vascular endothelial growth factor to its kinase domain receptor. *J. Biol. Chem.* 277 (45), 43137–43142. doi:10.1074/jbc.m203103200

Hu, Q., Gao, X., Kang, T., Feng, X., Jiang, D., Tu, Y., et al. (2013). CGKRK-modified nanoparticles for dual-targeting drug delivery to tumor cells and angiogenic blood vessels. *Biomaterials* 34 (37), 9496–9508. doi:10.1016/j.biomaterials.2013.09.001

Hu, Q., Gu, G., Liu, Z., Jiang, M., Kang, T., Miao, D., et al. (2013). F3 peptide-functionalized PEG-PLA nanoparticles co-administrated with tLyp-1 peptide for anti-glioma drug delivery. *Biomaterials* 34 (4), 1135–1145. doi:10.1016/j.biomaterials.2012.10.048

Hu, Q., Kang, T., Feng, J., Zhu, Q., Jiang, T., Yao, J., et al. (2016). Tumor microenvironment and angiogenic blood vessels dual-targeting for enhanced anti-glioma therapy. *ACS Appl. Mater Interfaces* 8 (36), 23568–23579. doi:10.1021/acsami.6b08239

Järvinen, T. A., and Ruoslahti, E. (2007). Molecular changes in the vasculature of injured tissues. *Am. J. Pathol.* 171 (2), 702–711. doi:10.2353/ajpath.2007.061251

Jaynes, J. M., Sable, R., Ronzetti, M., Bautista, W., Knotts, Z., Abisoye-Ogunniyan, A., et al. (2020). Mannose receptor (CD206) activation in tumor-associated macrophages enhances adaptive and innate antitumor immune responses. *Sci. Transl. Med.* 12 (530), eaax6337. doi:10.1126/scitranslmed.aax6337

Ji, T., Ding, Y., Zhao, Y., Wang, J., Qin, H., Liu, X., et al. (2015). Peptide assembly integration of fibroblast-targeting and cell-penetration features for enhanced antitumor drug delivery. *Adv. Mater* 27 (11), 1865–1873. doi:10.1002/adma.201404715

Ji, T., Lang, J., Wang, J., Cai, R., Zhang, Y., Qi, F., et al. (2017). Designing liposomes to suppress extracellular matrix expression to enhance drug penetration and pancreatic tumor therapy. *ACS Nano* 11 (9), 8668–8678. doi:10.1021/acsnano.7b01026

Ji, T., Li, S., Zhang, Y., Lang, J., Ding, Y., Zhao, X., et al. (2016). An MMP-2 responsive liposome integrating antifibrosis and chemotherapeutic drugs for enhanced drug perfusion and efficacy in pancreatic cancer. *ACS Appl. Mater Interfaces* 8 (5), 3438–3445. doi:10.1021/acsami.5b11619

Ji, T., Zhao, Y., Ding, Y., Wang, J., Zhao, R., Lang, J., et al. (2016). Transformable peptide nanocarriers for expeditious drug release and effective cancer therapy via cancer-associated fibroblast activation. *Angew. Chem. Int. Ed. Engl.* 55 (3), 1062–1067. doi:10.1002/ange.201506262

Jian, Y., Zhao, M., Cao, J., Fan, T., Bu, W., Yang, Y., et al. (2020). <p>A gastric cancer peptide GX1-modified nano-lipid carriers encapsulating paclitaxel: Design and evaluation of anti-tumor activity</p>. *Drug Des. Devel Ther.* 14, 2355–2370. doi:10.2147/dddt.s233023

Kang, S., Lee, S., and Park, S. (2020). iRGD peptide as a tumor-penetrating enhancer for tumor-targeted drug delivery. *Polym. (Basel)* 12 (9), 1906. doi:10.3390/polym12091906

Kang, T., Gao, X., Hu, Q., Jiang, D., Feng, X., Zhang, X., et al. (2014). iNGR-modified PEG-PLGA nanoparticles that recognize tumor vasculature and penetrate gliomas. *Biomaterials* 35 (14), 4319–4332. doi:10.1016/j.biomaterials.2014.01.082

Kang, W., Svirskis, D., Sarojini, V., McGregor, A. L., Bevitt, J., and Wu, Z. (2017). Cyclic-RGDyC functionalized liposomes for dual-targeting of tumor vasculature and cancer cells in glioblastoma: An *in vitro* boron neutron capture therapy study. *Oncotarget* 8 (22), 36614–36627. doi:10.18632/oncotarget.16625

Katanasaka, Y., Ida, T., Asai, T., Shimizu, K., Koizumi, F., Maeda, N., et al. (2008). Antiangiogenic cancer therapy using tumor vasculature-targeted liposomes encapsulating 3-(3, 5-dimethyl-1H-pyrrol-2-ylmethylene)-1, 3-dihydro-indol-2-one, SU5416. *Cancer Lett.* 270 (2), 260–268. doi:10.1016/j.canlet.2008.05.009

Kelley, T. W., and Parker, C. J. (2010). CD4 CD25 Foxp3 regulatory T cells and hematologic malignancies. *Front. Biosci. Sch. Ed.* 2 (3), 114–192. doi:10.2741/s114

Kim, M. Y., Kim, O. R., Choi, Y. S., Lee, H., Park, K., Lee, C. T., et al. (2012). Selection and characterization of tenascin C targeting peptide. *Mol. Cells* 33 (1), 71–77. doi:10.1007/s10059-012-2214-4

Kim, S. S., Ye, C., Kumar, P., Chiu, I., Subramanya, S., Wu, H., et al. (2010). Targeted delivery of siRNA to macrophages for anti-inflammatory treatment. *Mol. Ther.* 18 (5), 993–1001. doi:10.1038/mt.2010.27

Kojima, Y., Acar, A., Eaton, E. N., Mellody, K. T., Scheel, C., Ben-Porath, I., et al. (2010). Autocrine TGF-beta and stromal cell-derived factor-1 (SDF-1) signaling drives the evolution of tumor-promoting mammary stromal myofibroblasts. *Proc. Natl. Acad. Sci. U. S. A.* 107 (46), 20009–20014. doi:10.1073/pnas.1013805107

Kong, F., Bai, H., Ma, M., Wang, C., Xu, H., Gu, N., et al. (2021). Fe3O4@Pt nanozymes combining with CXCR4 antagonists to synergistically treat acute myeloid leukemia. *Nano Today* 37, 101106. doi:10.1016/j.nantod.2021.101106

Lang, J., Zhao, X., Qi, Y., Zhang, Y., Han, X., Ding, Y., et al. (2019). Reshaping prostate tumor microenvironment to suppress metastasis via cancer-associated fibroblast inactivation with peptide-assembly-based nanosystem. *ACS Nano* 13 (11), 12357–12371. doi:10.1021/acsnano.9b04857

Lee, C., Bae, S. S., Joo, H., and Bae, H. (2017). Melittin suppresses tumor progression by regulating tumor-associated macrophages in a Lewis lung carcinoma mouse model. *Oncotarget* 8 (33), 54951–54965. doi:10.18632/oncotarget.18627

Lee, S. H., Castagner, B., and Leroux, J. C. (2013). Is there a future for cell-penetrating peptides in oligonucleotide delivery? *Eur. J. Pharm. Biopharm.* 85 (1), 5–11. doi:10.1016/j.ejpb.2013.03.021

Lee, Y., Chen, Y., Tarasova, N. I., and Gaponenko, V. (2011). The structure of monomeric components of self-assembling CXCR4 antagonists determines the architecture of resulting nanostructures. *Nanotechnology* 22 (50), 505101. doi:10.1088/0957-4484/22/50/505101

Lei, Z., Chai, N., Tian, M., Zhang, Y., Wang, G., Liu, J., et al. (2018). Novel peptide GX1 inhibits angiogenesis by specifically binding to transglutaminase-2 in the tumorous endothelial cells of gastric cancer. *Cell Death Dis.* 9 (6), 579. doi:10.1038/s41419-018-0594-x

Li, C., Chen, Z., Zheng, D., Zhao, J., and Lei, J. (2021). Targeted delivery of dual anticancer drugs based on self-assembled iRGD-modified soluble drug-polymer pattern conjugate nanoparticles. *ACS Appl. Bio Mater* 4 (2), 1499–1507. doi:10.1021/acsabm.0c01388

Li, M., Li, M., Yang, Y., Liu, Y., Xie, H., Yu, Q., et al. (2020). Remodeling tumor immune microenvironment via targeted blockade of PI3K-γ and CSF-1/CSF-1R pathways in tumor associated macrophages for pancreatic cancer therapy. *J. Control Release* 321, 23–35. doi:10.1016/j.jconrel.2020.02.011

Li, T., Lu, X. M., Zhang, M. R., Hu, K., and Li, Z. (2022). Peptide-based nanomaterials: Self-assembly, properties and applications. *Bioact. Mater* 11, 268–282. doi:10.1016/j.bioactmat.2021.09.029

Li, X., Guo, H., Duan, H., Yang, Y., Meng, J., Liu, J., et al. (2015). Improving chemotherapeutic efficiency in acute myeloid leukemia treatments by chemically synthesized peptide interfering with CXCR4/CXCL12 axis. *Sci. Rep.* 5, 16228. doi:10.1038/srep16228

Li, X., Guo, H., Yang, Y., Meng, J., Liu, J., Wang, C., et al. (2014). A designed peptide targeting CXCR4 displays anti-acute myelocytic leukemia activity *in vitro* and *in vivo*. *Sci. Rep.* 4, 6610. doi:10.1038/srep06610

Maeda, N., Takeuchi, Y., Takada, M., Sadzuka, Y., Namba, Y., and Oku, N. (2004). Anti-neovascular therapy by use of tumor neovasculature-targeted long-circulating liposome. *J. Control Release* 100 (1), 41–52. doi:10.1016/j.jconrel.2004.07.033

Marelli, U. K., Rechenmacher, F., Sobahi, T. R., Mas-Moruno, C., and Kessler, H. (2013). Tumor targeting via integrin ligands. *Front. Oncol.* 3, 222. doi:10.3389/fonc.2013.00222

Meng, J., Ge, Y., Xing, H., Wei, H., Xu, S., Liu, J., et al. (2020). Synthetic CXCR4 antagonistic peptide assembling with nanoscaled micelles combat acute myeloid leukemia. *Small* 16 (31), e2001890. doi:10.1002/smll.202001890

Mortezaee, K. (2020). CXCL12/CXCR4 axis in the microenvironment of solid tumors: A critical mediator of metastasis. *Life Sci.* 249, 117534. doi:10.1016/j.lfs.2020.117534

Murase, Y., Asai, T., Katanasaka, Y., Sugiyama, T., Shimizu, K., Maeda, N., et al. (2010). A novel DDS strategy, "dual-targeting", and its application for antineovascular therapy. *Cancer Lett.* 287 (2), 165–171. doi:10.1016/j.canlet.2009.06.008

Nakashima, H., Masuda, M., Murakami, T., Koyanagi, Y., Matsumoto, A., Fujii, N., et al. (1992). Anti-human immunodeficiency virus activity of a novel synthetic peptide, T22 ([Tyr-5, 12, lys-7]polyphemusin II): A possible inhibitor of virus-cell fusion. *Antimicrob. Agents Chemother.* 36 (6), 1249–1255. doi:10.1128/aac.36.6.1249

Orend, G., and Chiquet-Ehrismann, R. (2006). Tenascin-C induced signaling in cancer. *Cancer Lett.* 244 (2), 143–163. doi:10.1016/j.canlet.2006.02.017

Ou, W., Thapa, R. K., Jiang, L., Soe, Z. C., Gautam, M., Chang, J. H., et al. (2018). Regulatory T cell-targeted hybrid nanoparticles combined with immuno-checkpoint blockage for cancer immunotherapy. *J. Control Release* 281, 84–96. doi:10.1016/j.jconrel.2018.05.018

Özdemir, B. C., Pentcheva-Hoang, T., Carstens, J. L., Zheng, X., Wu, C. C., Simpson, T. R., et al. (2014). Depletion of carcinoma-associated fibroblasts and fibrosis induces immunosuppression and accelerates pancreas cancer with reduced survival. *Cancer Cell* 25 (6), 719–734. doi:10.1016/j.ccr.2014.04.005

Paget, S. (1989). The distribution of secondary growths in cancer of the breast. 1889. *Cancer Metastasis Rev.* 8 (2), 98–101.

Pasqualini, R., Koivunen, E., and Ruoslahti, E. (1995). A peptide isolated from phage display libraries is a structural and functional mimic of an RGD-binding site on integrins. *J. Cell Biol.* 130 (5), 1189–1196. doi:10.1083/jcb.130.5.1189

Pereira, E. R., Kedrin, D., Seano, G., Gautier, O., Meijer, E. F. J., Jones, D., et al. (2018). Lymph node metastases can invade local blood vessels, exit the node, and colonize distant organs in mice. *Science* 359 (6382), 1403–1407. doi:10.1126/science.aal3622

Pérez-Herrero, E., and Fernández-Medarde, A. (2015). Advanced targeted therapies in cancer: Drug nanocarriers, the future of chemotherapy. *Eur. J. Pharm. Biopharm.* 93, 52–79. doi:10.1016/j.ejpb.2015.03.018

Ponce, M. L., Hibino, S., Lebioda, A. M., Mochizuki, M., Nomizu, M., and Kleinman, H. K. (2003). Identification of a potent peptide antagonist to an active laminin-1 sequence that blocks angiogenesis and tumor growth. *Cancer Res.* 63 (16), 5060–5064.

Qian, Y., Qiao, S., Dai, Y., Xu, G., Dai, B., Lu, L., et al. (2017). Molecular-targeted immunotherapeutic strategy for melanoma via dual-targeting nanoparticles delivering small interfering RNA to tumor-associated macrophages. *ACS Nano* 11 (9), 9536–9549. doi:10.1021/acsnano.7b05465

Quail, D. F., and Joyce, J. A. (2013). Microenvironmental regulation of tumor progression and metastasis. *Nat. Med.* 19 (11), 1423–1437. doi:10.1038/nm.3394

Rioja-Blanco, E., Arroyo-Solera, I., Álamo, P., Casanova, I., Gallardo, A., Unzueta, U., et al. (2022). CXCR4-targeted nanotoxins induce GSDME-dependent pyroptosis in head and neck squamous cell carcinoma. *J. Exp. Clin. Cancer Res.* 41 (1), 49. doi:10.1186/s13046-022-02267-8

Rioja-Blanco, E., Arroyo-Solera, I., Álamo, P., Casanova, I., Gallardo, A., Unzueta, U., et al. (2022). Self-assembling protein nanocarrier for selective delivery of cytotoxic polypeptides to CXCR4(+) head and neck squamous cell carcinoma tumors. *Acta Pharm. Sin. B* 12 (5), 2578–2591. doi:10.1016/j.apsb.2021.09.030

Roth, L., Agemy, L., Kotamraju, V. R., Braun, G., Teesalu, T., Sugahara, K. N., et al. (2012). Transtumoral targeting enabled by a novel neuropilin-binding peptide. *Oncogene* 31 (33), 3754–3763. doi:10.1038/onc.2011.537

Sadatmousavi, P., Soltani, M., Nazarian, R., Jafari, M., and Chen, P. (2011). Self-assembling peptides: Potential role in tumor targeting. *Curr. Pharm. Biotechnol.* 12 (8), 1089–1100. doi:10.2174/138920111796117409

Sánchez-García, L., Serna, N., Álamo, P., Sala, R., Céspedes, M. V., Roldan, M., et al. (2018). Self-assembling toxin-based nanoparticles as self-delivered antitumoral drugs. *J. Control Release* 274, 81–92. doi:10.1016/j.jconrel.2018.01.031

Schnittert, J., Kuninty, P. R., Bystry, T. F., Brock, R., Storm, G., and Prakash, J. (2017). Anti-microRNA targeting using peptide-based nanocomplexes to inhibit differentiation of human pancreatic stellate cells. *Nanomedicine (Lond)* 12 (12), 1369–1384. doi:10.2217/nnm-2017-0054

Scodeller, P., Simón-Gracia, L., Kopanchuk, S., Tobi, A., Kilk, K., Säälik, P., et al. (2017). Precision targeting of tumor macrophages with a CD206 binding peptide. *Sci. Rep.* 7 (1), 14655. doi:10.1038/s41598-017-14709-x

Serna, N., Álamo, P., Ramesh, P., Vinokurova, D., Sánchez-García, L., Unzueta, U., et al. (2020). Nanostructured toxins for the selective destruction of drug-resistant human CXCR4(+) colorectal cancer stem cells. *J. Control Release* 320, 96–104. doi:10.1016/j.jconrel.2020.01.019

Seyyednia, E., Oroojalian, F., Baradaran, B., Mojarrad, J. S., Mokhtarzadeh, A., and Valizadeh, H. (2021). Nanoparticles modified with vasculature-homing peptides for targeted cancer therapy and angiogenesis imaging. *J. Control Release* 338, 367–393. doi:10.1016/j.jconrel.2021.08.044

Sheikh, A., Alhakamy, N. A., Shadab, M., and Kesharwani, P. (2021). Recent progress of RGD modified liposomes as multistage rocket against cancer. *Front. Pharmacol.* 12, 803304. doi:10.3389/fphar.2021.803304

Sheikh, A., Shadab, M., and Kesharwani, P. (2021). RGD engineered dendrimer nanotherapeutic as an emerging targeted approach in cancer therapy. *J. Control Release* 340, 221–242. doi:10.1016/j.jconrel.2021.10.028

Shi, K., Li, J., Cao, Z., Yang, P., Qiu, Y., Yang, B., et al. (2015). A pH-responsive cell-penetrating peptide-modified liposomes with active recognizing of integrin αvβ3 for the treatment of melanoma. *J. Control Release* 217, 138–150. doi:10.1016/j.jconrel.2015.09.009

Shroff, K., and Kokkoli, E. (2012). PEGylated liposomal doxorubicin targeted to α5β1-expressing MDA-MB-231 breast cancer cells. *Langmuir* 28 (10), 4729–4736. doi:10.1021/la204466g

Slade, M. J., and Uy, G. L. (2020). CD123 bi-specific antibodies in development in AML: What do we know so far? *Best. Pract. Res. Clin. Haematol.* 33 (4), 101219. doi:10.1016/j.beha.2020.101219

Staquicini, F. I., Hajitou, A., Driessen, W. H., Proneth, B., Cardó-Vila, M., Staquicini, D. I., et al. (2021). Targeting a cell surface vitamin D receptor on tumor-associated macrophages in triple-negative breast cancer. *Elife* 10, e65145. doi:10.7554/eLife.65145

Su, F., Ahn, S., Saha, A., DiGiovanni, J., and Kolonin, M. G. (2019). Adipose stromal cell targeting suppresses prostate cancer epithelial-mesenchymal transition and chemoresistance. *Oncogene* 38 (11), 1979–1988. doi:10.1038/s41388-018-0558-8

Sun, Y., Kang, C., Liu, F., Zhou, Y., Luo, L., and Qiao, H. (2017). RGD peptide-based target drug delivery of doxorubicin nanomedicine. *Drug Dev. Res.* 78 (6), 283–291. doi:10.1002/ddr.21399

Tang, T., Wei, Y., Kang, J., She, Z. G., Kim, D., Sailor, M. J., et al. (2019). Tumor-specific macrophage targeting through recognition of retinoid X receptor beta. *J. Control Release* 301, 42–53. doi:10.1016/j.jconrel.2019.03.009

Tarasov, S. G., Gaponenko, V., Howard, O. M., Chen, Y., Oppenheim, J. J., Dyba, M. A., et al. (2011). Structural plasticity of a transmembrane peptide allows self-assembly into biologically active nanoparticles. *Proc. Natl. Acad. Sci. U. S. A.* 108 (24), 9798–9803. doi:10.1073/pnas.1014598108

Teesalu, T., Sugahara, K. N., Kotamraju, V. R., and Ruoslahti, E. (2009). C-end rule peptides mediate neuropilin-1-dependent cell, vascular, and tissue penetration. *Proc. Natl. Acad. Sci. U. S. A.* 106 (38), 16157–16162. doi:10.1073/pnas.0908201106

Teicher, B. A., and Fricker, S. P. (2010). CXCL12 (SDF-1)/CXCR4 pathway in cancer. *Clin. Cancer Res.* 16 (11), 2927–2931. doi:10.1158/1078-0432.ccr-09-2329

Unzueta, U., Céspedes, M. V., Ferrer-Miralles, N., Casanova, I., Cedano, J., Corchero, J. L., et al. (2012). Intracellular CXCR4⁺ cell targeting with T22-empowered protein-only nanoparticles. *Int. J. Nanomedicine* 7, 4533–4544. doi:10.2147/IJN.S34450

Voltà-Durán, E., Serna, N., Sánchez-García, L., Aviñó, A., Sánchez, J. M., López-Laguna, H., et al. (2021). Design and engineering of tumor-targeted, dual-acting cytotoxic nanoparticles. *Acta Biomater.* 119, 312–322. doi:10.1016/j.actbio.2020.11.018

Wan, X., Liu, C., Lin, Y., Fu, J., Lu, G., and Lu, Z. (2019). pH sensitive peptide functionalized nanoparticles for co-delivery of erlotinib and DAPT to restrict the progress of triple negative breast cancer. *Drug Deliv.* 26 (1), 470–480. doi:10.1080/10717544.2019.1576801

Wang, L., Lv, Y., Li, C., Yang, G., Fu, B., Peng, Q., et al. (2020). Transformable dual-inhibition system effectively suppresses renal cancer metastasis through blocking endothelial cells and cancer stem cells. *Small* 16 (40), e2004548. doi:10.1002/smll.202004548

Wang, X. J., Cheng, J., Zhang, L. Y., and Zhang, J. G. (2022). Self-assembling peptides-based nano-cargos for targeted chemotherapy and immunotherapy of tumors: Recent developments, challenges, and future perspectives. *Drug Deliv.* 29 (1), 1184–1200. doi:10.1080/10717544.2022.2058647

Wang, Y., Cheetham, A. G., Angacian, G., Su, H., Xie, L., and Cui, H. (2017). Peptide-drug conjugates as effective prodrug strategies for targeted delivery. *Adv. Drug Deliv. Rev.* 110, 112–126. doi:10.1016/j.addr.2016.06.015

Wickström, M., Larsson, R., Nygren, P., and Gullbo, J. (2011). Aminopeptidase N (CD13) as a target for cancer chemotherapy. *Cancer Sci.* 102 (3), 501–508. doi:10.1111/j.1349-7006.2010.01826.x

Xiao, Y., and Yu, D. (2021). Tumor microenvironment as a therapeutic target in cancer. *Pharmacol. Ther.* 221, 107753. doi:10.1016/j.pharmthera.2020.107753

Xiong, D., Liu, Z., Bian, T., Li, J., Huang, W., Jing, P., et al. (2015). GX1-mediated anionic liposomes carrying adenoviral vectors for enhanced inhibition of gastric cancer vascular endothelial cells. *Int. J. Pharm.* 496 (2), 699–708. doi:10.1016/j.ijpharm.2015.11.019

Xu, S., Zhang, M., Fang, X., Hu, X., Xing, H., Yang, Y., et al. (2022). CD123 antagonistic peptides assembled with nanomicelles act as monotherapeutics to combat refractory acute myeloid leukemia. *ACS Appl. Mater Interfaces* 14 (34), 38584–38593. doi:10.1021/acsami.2c11538

Xu, S., Zhang, M., Fang, X., Meng, J., Xing, H., Yan, D., et al. (2021). A novel CD123-targeted therapeutic peptide loaded by micellar delivery system combats refractory acute myeloid leukemia. *J. Hematol. Oncol.* 14 (1), 193. doi:10.1186/s13045-021-01206-y

Yadav, S., Sharma, A. K., and Kumar, P. (2020). Nanoscale self-assembly for therapeutic delivery. *Front. Bioeng. Biotechnol.* 8, 127. doi:10.3389/fbioe.2020.00127

Yan, J., Wu, Q., Zhao, Z., Wu, J., Ye, H., Liang, Q., et al. (2020). Light-assisted hierarchical intratumoral penetration and programmed antitumor therapy based on tumor microenvironment (TME)-amendatory and self-adaptive polymeric nanoclusters. *Biomaterials* 255, 120166. doi:10.1016/j.biomaterials.2020.120166

Yan, M., Shen, M., Xu, L., Huang, J., He, G., An, M., et al. (2020). Inactivation of pancreatic stellate cells by exendin-4 inhibits the migration and invasion of pancreatic cancer cells</p>. *Onco Targets Ther.* 13, 9455–9463. doi:10.2147/ott.s259853

Yang, M., Li, J., Gu, P., and Fan, X. (2021). The application of nanoparticles in cancer immunotherapy: Targeting tumor microenvironment. *Bioact. Mater* 6 (7), 1973–1987. doi:10.1016/j.bioactmat.2020.12.010

Yao, J., Feng, J., Gao, X., Wei, D., Kang, T., Zhu, Q., et al. (2017). Neovasculature and circulating tumor cells dual-targeting nanoparticles for the treatment of the highly-invasive breast cancer. *Biomaterials* 113, 1–17. doi:10.1016/j.biomaterials.2016.10.033

Ye, G., Jiang, Y., Yang, X., Hu, H., Wang, B., Sun, L., et al. (2018). Smart nanoparticles undergo phase transition for enhanced cellular uptake and subsequent intracellular drug release in a tumor microenvironment. *ACS Appl. Mater Interfaces* 10 (1), 278–289. doi:10.1021/acsami.7b15978

Ying, M., Zhan, C., Wang, S., Yao, B., Hu, X., Song, X., et al. (2016). Liposome-based systemic glioma-targeted drug delivery enabled by all-d peptides. *ACS Appl. Mater Interfaces* 8 (44), 29977–29985. doi:10.1021/acsami.6b10146

Yokota, T., Denham, W., Murayama, K., Pelham, C., Joehl, R., and Bell, R. H., Jr. (2002). Pancreatic stellate cell activation and MMP production in experimental pancreatic fibrosis. *J. Surg. Res.* 104 (2), 106–111. doi:10.1006/jsre.2002.6403

Yu, D. H., Liu, Y. R., Luan, X., Liu, H. J., Gao, Y. G., Wu, H., et al. (2015). IF7-Conjugated nanoparticles target annexin 1 of tumor vasculature against P-gp mediated multidrug resistance. *Bioconjug Chem.* 26 (8), 1702–1712. doi:10.1021/acs.bioconjchem.5b00283

Yu, D. H., Lu, Q., Xie, J., Fang, C., and Chen, H. Z. (2010). Peptide-conjugated biodegradable nanoparticles as a carrier to target paclitaxel to tumor neovasculature. *Biomaterials* 31 (8), 2278–2292. doi:10.1016/j.biomaterials.2009.11.047

Zafar, S., Beg, S., Panda, S. K., Rahman, M., Alharbi, K. S., Jain, G. K., et al. (2021). Novel therapeutic interventions in cancer treatment using protein and peptide-based targeted smart systems. *Semin. Cancer Biol.* 69, 249–267. doi:10.1016/j.semcancer.2019.08.023

Zhang, M., Ge, Y., Xu, S., Fang, X., Meng, J., Yu, L., et al. (2022). Nanomicelles co-loading CXCR4 antagonist and doxorubicin combat the refractory acute myeloid leukemia. *Pharmacol. Res.* 185, 106503. doi:10.1016/j.phrs.2022.106503

Zhang, Y., Lu, Y., Zhang, Y., He, X., Chen, Q., Liu, L., et al. (2017). Tumor-targeting micelles based on linear-dendritic PEG-PTX(8) conjugate for triple negative breast cancer therapy. *Mol. Pharm.* 14 (10), 3409–3421. doi:10.1021/acs.molpharmaceut.7b00430

Zhang, Y., Zhai, M., Chen, Z., Han, X., Yu, F., Li, Z., et al. (2017). Dual-modified liposome codelivery of doxorubicin and vincristine improve targeting and therapeutic efficacy of glioma. *Drug Deliv.* 24 (1), 1045–1055. doi:10.1080/10717544.2017.1344334

Zhou, J. E., Yu, J., Gao, L., Sun, L., Peng, T., Wang, J., et al. (2017). iNGR-modified liposomes for tumor vascular targeting and tumor tissue penetrating delivery in the treatment of glioblastoma. *Mol. Pharm.* 14 (5), 1811–1820. doi:10.1021/acs.molpharmaceut.7b00101

Zirafi, O., Kim, K. A., Ständker, L., Mohr, K. B., Sauter, D., Heigele, A., et al. (2015). Discovery and characterization of an endogenous CXCR4 antagonist. *Cell Rep.* 11 (5), 737–747. doi:10.1016/j.celrep.2015.03.061

Zou, L., Tao, Y., Payne, G., Do, L., Thomas, T., Rodriguez, J., et al. (2017). Targeted delivery of nano-PTX to the brain tumor-associated macrophages. *Oncotarget* 8 (4), 6564–6578. doi:10.18632/oncotarget.14169

frontiers | Frontiers in Chemistry

TYPE Original Research
PUBLISHED 30 January 2023
DOI 10.3389/fchem.2023.1122333

OPEN ACCESS

EDITED BY
Hua Wang,
Beihang University, China

REVIEWED BY
Zhaohui Xiao,
Hainan University, China
Guoru Li,
Changzhou University, China
Wei Wei,
Shangqiu Normal University, China
Yu Dandan,
China Jiliang University, China

*CORRESPONDENCE
Mingshang Jin,
✉ jinm@mail.xjtu.edu.cn
Ruiyun Guo,
✉ guoruiyun@stu.xjtu.edu.cn

SPECIALTY SECTION
This article was submitted to Nanoscience, a section of the journal Frontiers in Chemistry

RECEIVED 12 December 2022
ACCEPTED 16 January 2023
PUBLISHED 30 January 2023

CITATION
Zheng Y, Guo R, Li X, He T, Wang W, Zhan Q, Li R, Zhang K, Ji S and Jin M (2023), Synthesis of amorphous trimetallic PdCuNiP nanoparticles for enhanced OER. *Front. Chem.* 11:1122333.
doi: 10.3389/fchem.2023.1122333

Synthesis of amorphous trimetallic PdCuNiP nanoparticles for enhanced OER

Yangzi Zheng[1], Ruiyun Guo[2]*, Xiang Li[3], Tianou He[1], Weicong Wang[1], Qi Zhan[1], Rui Li[1], Ke Zhang[1], Shangdong Ji[1] and Mingshang Jin[1]*

[1]State Key Laboratory of Multiphase Flow in Power Engineering, Frontier Institute of Science and Technology, Xi'an Jiaotong University, Xi'an, Shaanxi, China, [2]School of Materials Science and Engineering, Xi'an University of Science and Technology, Xi'an, Shaanxi, China, [3]Shaanxi Key Laboratory of Optoelectronic Functional Materials and Devices, School of Materials Science and Chemical Engineering, Xi'an Technological University, Xi'an, Shaanxi, China

Metal phosphides with multi-element components and amorphous structure represent a novel kind of electrocatalysts for promising activity and durability towards the oxygen evolution reaction (OER). In this work, a two-step strategy, including alloying and phosphating processes, is reported to synthesize trimetallic amorphous PdCuNiP phosphide nanoparticles for efficient OER under alkaline conditions. The synergistic effect between Pd, Cu, Ni, and P elements, as well as the amorphous structure of the obtained PdCuNiP phosphide nanoparticles, would boost the intrinsic catalytic activity of Pd nanoparticles towards a wide range of reactions. These obtained trimetallic amorphous PdCuNiP phosphide nanoparticles exhibit long-term stability, nearly a 20-fold increase in mass activity toward OER compared with the initial Pd nanoparticles, and 223 mV lower in overpotential at 10 mA cm^{-2}. This work not only provides a reliable synthetic strategy for multi-metallic phosphide nanoparticles, but also expands the potential applications of this promising class of multi-metallic amorphous phosphides.

KEYWORDS

palladium, phosphide, amorphous, core-shell, electrocatalysis

1 Introduction

The rapid consumption of fossil fuels with more and more population has caused serious social and ecological problems, including climate change, the greenhouse effect, sea level rise, and environmental pollution (Chu et al., 2012; Shih et al., 2018). Developing sustainable and clean energy conversion and storage technologies is vital to address the above-mentioned problems. Especially, electrochemical energy conversion technologies, such as water electrolysis for hydrogen production, fuel cells, and carbon dioxide conversion, have attracted numerous attention in the past few decades by virtue of the high energy conversion efficiency (He et al., 2021a; Wang et al., 2021a; Liu et al., 2021; Zhang et al., 2022; Zhou et al., 2022). Oxygen evolution reaction (OER) is evinced as one of the main rate-determining steps for clean energy production *via* electrochemical process (Li et al., 2014a; Hong et al., 2015; Xia et al., 2016). By far, the application of renewable energy conversion and storage processes is still hindered by the sluggish kinetics and low efficiency of OER originating from the four-electron process (Koper et al., 2013; Li et al., 2014b; Trotochaud et al., 2014; Chen et al., 2015; Jiao et al., 2015; Hunter et al., 2016; Reier et al., 2017; Song et al., 2018). The rational design and synthesis of electrocatalysts with high electrocatalytic activity and stability remain critical issues in the construction of high-performance electrochemical energy production systems. Extensive attempts have been made to develop advanced OER electrocatalysts to date (McCrory et al., 2013; Antolini et al., 2014; Trotochaud et al., 2014; Yu et al., 2015; Suen et al., 2017; Song et al., 2018; Zhang et al., 2018). Many types of nanomaterials, such as metal oxides, hydroxides, and layered double hydroxides (LDHs), have been reported to exhibit excellent electrocatalytic performances towards OER under alkaline conditions (McCrory et al., 2013; Trotochaud et al., 2014; Yu et al., 2015; Suen et al., 2017; Zhang et al., 2018). Nevertheless, low electrical conductivity is a crucial drawback for most oxides and hydroxides OER electrocatalysts, which may impede the ability of electron transport and cause sluggish reaction kinetics and low yields (Xu et al., 2016).

Recently, many researchers have developed doping strategies for high-efficiency electrocatalysts, which could principally modulate the electronic structure, thus enhancing the electrocatalytic activity (Xiao et al., 2022). Considering the important role of phosphorus (P) doping in improving the electrical conductivity and enhancing the intrinsic activity of metal catalysts, works related to monometallic and bimetallic phosphides, including the engineering of heterojunctions for potential TMP catalysts and phosphated bimetallic clusters on macroporous nitrogen-doped carbon, have been explored in recent years (Ryu et al., 2015; Stern et al., 2015; Liu et al., 2018a; Qin et al., 2018; Chu et al., 2019; Lv et al., 2020; Wang et al., 2021b; Guo et al., 2022). Meanwhile, according to the recently reported references, many electrocatalysts with amorphous structure have been proven to be more efficient than their crystalline counterparts (Wang et al., 2021c; Wang et al., 2022). Inspired by these, the combination of constructing an amorphous structure and P atom doping strategy is an excellent way to improve electrocatalytic performance. In recent years, it has been reported that Pd-based electrocatalysts can exhibit outstanding electrocatalytic performance for OER, especially in alkaline media (Kwon et al., 2013; Li et al., 2014a; Alegre et al., 2015). Particularly, alloying with other transition metals can effectively enhance the intrinsic catalytic activity by modulating the electronic structure of the Pd sites (Yu et al., 2016; Feng et al., 2017; Tang et al., 2017; Xu et al., 2018; Park et al., 2019; Zhu et al., 2019), thus reducing the usage of Pd catalysts. Therefore, there have been many mono- and bi-metallic phosphide nanoparticles reported in the literature previously, which can deliver superior catalytic activities relative to Pd nanoparticles. Compared with mono- and bi-metallic phosphide nanoparticles, alloying Pd with more transition metal elements can further tune the electronic structure of the Pd sites, and thus an even better catalytic performance could be expected for tri-metallic phosphide nanoparticles (Kim et al., 2018; Xu et al., 2020). However, trimetallic phosphide nanoparticles have rarely been reported, since the phase separation would be likely happened during the synthesis process due to the coexistence of trimetallic transition metal elements. Furthermore, multiple metal X-ides (including phosphides, sulfides, nitrides, and carbides) have been demonstrated increasingly to be better OER catalysts thanks to their lower free energy barrier in DFT calculations (Zheng et al., 2018; Luo et al., 2021). Therefore, the development of ternary metal phosphide catalysts for efficient electrocatalytic reactions is challenging and significant.

Herein, an effective approach has been developed for the preparation of trimetallic PdCuNiP phosphide nanoparticles with an amorphous structure based on the phosphorization treatment of Pd@PdCuNi core-shell nanoparticles. Impressively, these obtained trimetallic amorphous PdCuNiP phosphide nanoparticles exhibit long-term stability, with nearly a 20-fold increase in mass activity toward OER compared with the initial Pd nanoparticles. Moreover, the PdCuNiP nanoparticles possess an overpotential as small as 314 mV @ 10 mA cm^{-2}, much smaller than that of the commercial RuO_2 (391.5 mV) and the original Pd nanocubes (537 mV).

2 Materials and methods

2.1 Chemicals and reagents

Sodium tetrachloropalladate (Na_2PdCl_4, 98%), poly-(vinyl pyrrolidone) (PVP, M_w ≈55,000), ascorbic acid (AA, 99%), potassium bromide (KBr, 99%), $CuCl_2{\cdot}2H_2O$, $Ni(acac)_2$, oleylamine (OAm, 80%–90%), tri-n-octylphosphine (TOP, 90%), nafion-117 (5%), Pd/C (10 wt%) were all purchased from Sigma-Aldrich and utilized as received. KOH (85%) were purchased from Alfa Aesar. Isopropyl alcohol (C_3H_8O, AR) was bought from Macklin to use. Ketjen Black (ECP600JD) was purchased from Sinero. Milli-Q ultrapure water and ethanol absolute (AR, 0.79 g/mL) were used throughout all the experiments.

2.2 Synthesis

Synthesis of Pd nanocubes. Pd nanocubes were prepared according to the approach reported previously (Jin et al., 2011). For a typical synthesis, 11 mL of an aqueous solution containing poly-(vinylpyrrolidone) (PVP, Mw ≈55,000, 105 mg, Aldrich), L-ascorbic acid (AA, 60 mg, Aldrich), KBr (300 mg, Fisher), and sodium tetrachloropalladate (Na_2PdCl_4, 57 mg, Aldrich) was placed in a vial and heated at 80°C in the air under magnetic stirring for 3 h. The obtained product was collected by centrifugation and washed 4 times with water and ethanol, and then re-dispersed in 10 mL of oleylamine.

Synthesis of Pd@PdCuNi core-shell nanocrystals. Pd@PdCuNi core-shell nanocrystals were based on a modified two-step approach reported by our group previously (Li et al., 2018). (1) 4 mg of $CuCl_2{\cdot}2H_2O$, 3 mL of OAm, and 1 mL of an OAm solution of Pd nanocubes were mSixed in a 50-mL round-bottomed flask and heated in an oil bath with magnetic stirring at 200°C for 2 h under nitrogen gas. The sediments were collected by centrifugation at 8,000 rpm, washed three times with a mixture of ethanol and n-hexane (1:1, v/v) and twice with ethanol, and ultimately re-dispersed in 1 mL of OAm; (2) 2 mg of $Ni(acac)_2$, 3 mL of OAm, and 1 mL of an OAm solution of the product in step one were mixed in a 50-mL three-neck round-bottom flask and heated with magnetic stirring at 220°C for 2 h under the flow of nitrogen gas until the temperature decreased to room temperature. The precipitates were separated by centrifugation at 8,000 rpm, washed three times with a mixture of ethanol and n-hexane (1:1, v/v) and twice with ethanol, and eventually re-dispersed in 1 mL of OAm.

Synthesis of amorphous PdCuNiP nanoparticles. 1 mL of an OAm solution of Pd@PdCuNi core-shell nanocrystals, 1 mL of OAm, and 500 μL of TOP were mixed in a 50-mL three-neck round-bottom flask and heated under magnetic stirring at 290°C for 15 min under the flow of nitrogen gas until the temperature dropped to room temperature. The final product was initially centrifuged at 5,000 rpm followed by washing three times with a mixture of ethanol and n-hexane (1:1, v/v) and twice with ethanol.

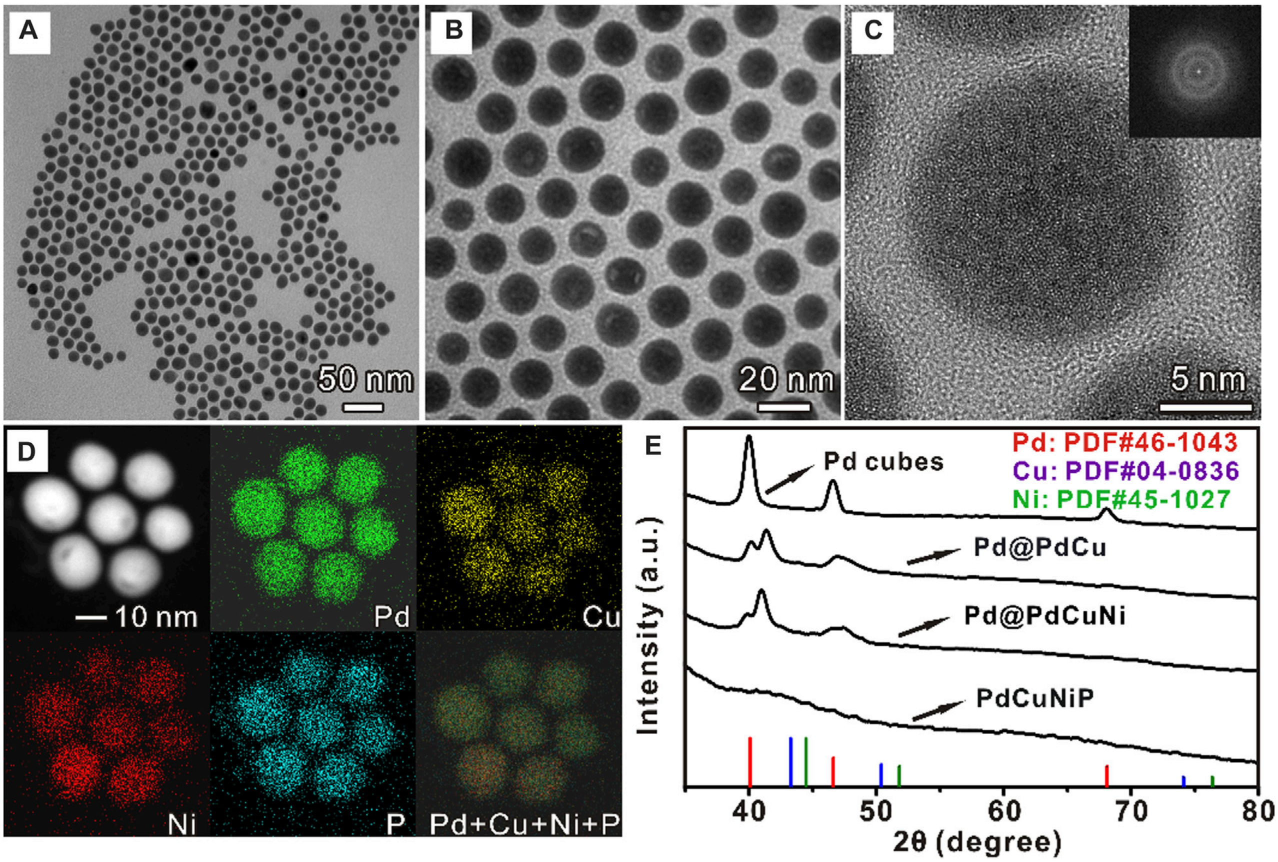

FIGURE 1
(A, B) TEM image, **(C)** HRTEM image, **(D)** EDS mappings of PdCuNiP nanoparticles, and **(E)** XRD patterns of Pd nanocubes, Pd@PdCu, Pd@PdCuNi, and PdCuNiP nanoparticles.

2.3 Characterizations

Transmission electron microscopy (TEM) images were carried out on a Hitachi HT-7700 microscope equipped with a tungsten filament, operating at 100 kV. High-resolution TEM (HRTEM) imaging, high-angle annular dark-field scanning transmission microscopy (HAADF-STEM) imaging and energy-dispersive X-ray spectroscopy (EDS) elemental mapping were performed on a JEM-2100F (JEOL) equipped with a built-in EDS at 200 kV. The powder X-ray diffraction (XRD) patterns were recorded using an X-ray diffractometer (SmartLab (3), Rigaku) operated at 3 kW. X-ray photoelectron spectroscopy (XPS) was conducted using a Thermo Scientific K-Alpha spectrometer equipped with monochromatic Al Kα radiation. The contents of Pd, Cu, Ni, and P in the samples were received by inductively coupled plasma mass spectrometry (ICP-MS) with a PerkinElmer NexION 300X.

2.4 Electrocatalytic OER measurement

All the electrocatalysis tests were accomplished at 25°C in O_2-saturated 1.0 M KOH electrolyte, using a typical three-electrode cell controlled by an electrochemical workstation (CHI 760E) with a catalyst-modified glassy carbon rotating disk electrode (RDE, diameter: 5 mm) as the working electrode, a platinum (Pt) foil as the counter electrode and a Hg/HgO (1.0 M KOH) as the reference electrode. It is worth noting that the electrochemical and chemical dissolution of a platinum foil counter electrode could take place in an alkaline electrolyte during catalysis, and cause redeposition of Pt on the working electrode, which has no obvious effect on the OER catalytic performance except for a small amount Pt dissolution and redeposition (Chen et al., 2017; Su et al., 2022). To prepare the working electrode, PdCuNiP, Pd@PdCuNi, Pd nanocubes, and commercial RuO_2 catalysts were all deposited onto Ketjen Carbon (C) (EC300J) in ethanol with a noble metal loading of 20% (determined by ICP-MS). The products were separated by centrifugation and redispersed in a mixture of water, isopropanol, and 5 wt% Nafion (volume ratio, 1:1:0.02) under ultrasonication for 20 min to form a homogeneous ink. 10 μL catalyst ink was then loaded onto a precleaned RDE. All the potentials were calibrated in reference with the reversible hydrogen electrode (RHE) by the open circuit voltage test in 1 M KOH using the following equation:

$$E\left(\mathrm{vs.}\,RHE\right) = E\left(\mathrm{vs.}\,HgO\right) + 0.904\,V \tag{1}$$

where 0.904 V is the potential difference between the Hg/HgO reference electrode and RHE in 1.0 M KOH. The OER activity was studied *via* linear sweep voltammetry (LSV) in the range of 1.3–1.8 V vs. RHE at 10 mV s^{-1} scan rate and 1,600 rpm rotation speed with 95% iR compensation. The overpotential (η) for OER could be calculated using the following equation:

$$\eta = E\left(\mathrm{vs.}\,RHE\right) - 1.23\,V \tag{2}$$

The electrochemical active surface area (ECSA) of the electrocatalysts was estimated from the double-layer capacitance (C_{dl}). The C_{dl} depended on the cyclic voltammograms (CVs) measured in a non-faradaic potential region (0.9–1.0 V vs. RHE) in O_2-saturated 1 M KOH at a series of different scan rates (10, 20, 30, 40, 50, and 60 mV s^{-1}). And C_{dl} was calculated according to the following equation:

$$C_{dl} = \frac{\Delta J}{2v} \tag{3}$$

where ΔJ is the current difference between the anode and cathode at 0.95 V vs. RHE, and v is the potential scan rate. Then, ECSA was obtained by the following equation:

$$ECSA = \frac{C_{dl}}{C_s} \tag{4}$$

where C_s is the specific capacitance of an atomically smooth planar surface [0.04 mF cm^{-2} in alkaline media (McCrory et al., 2013)]. Additionally, the roughness factor (R_f) was estimated based on the equation below:

$$R_f = \frac{\text{ECSA}}{0.196\, cm^2} \tag{5}$$

where 0.196 cm^2 is the geometric area of the electrode. Moreover, the specific current density (j_{ECSA}) was normalized by ECSA value as the equation below:

$$j_{ECSA} = \frac{j_{Geo}}{R_f} \tag{6}$$

where j_{Geo} is the current density per geometric area of the electrode at a given overpotential. Electrochemical impedance spectroscopy (EIS) was tested at 1.5 V vs. RHE over a frequency range of 0.1–100K Hz with an amplitude of 5 mV at a rotation rate of 1,600 rpm. The catalytic stabilities were assessed by chronopotentiometry measurements at a current density of 10 mA cm^{-2} for 22 h.

3 Results and discussion

In a typical synthesis of PdCuNiP nanoparticles, Pd nanocubes were first prepared by the method reported previously (Jin et al., 2011). Supplementary Figure S1 shows a typical TEM image of the obtained Pd nanocubes, with sizes around 11 nm. Then, the ions of Cu and Ni were gradually added to the Pd solutions to reduce the second metals, and deposited onto the surface of Pd nanocubes, which subsequently diffused into the crystal lattices at the reaction temperature, finally resulting in the formation of Pd@PdCu and Pd@PdCuNi nanoparticles, respectively. Supplementary Figures S2, S3 show the TEM images of Pd@PdCu and Pd@PdCuNi nanoparticles, as well as the corresponding diagrams of the particle size distribution. As we can see, with the incorporation of Cu and Ni, the average size of the nanoparticles increases from 11 to 16 nm gradually, and the shape also slowly changes from cube to cuboctahedron. Then, the obtained Pd@PdCuNi nanoparticles were further subjected to the phosphorization treatment with TOP at 290°C. During the reaction, Phosphorus (P) atoms generated from the decomposition of TOP can insert into the lattice of nanoparticles, and thus the original crystalline core-shell nanoparticles would transform into amorphous spherical solid trimetallic PdCuNiP phosphide nanoparticles, as shown in Figure 1, Supplementary Figure S4. The average size of the PdCuNiP nanoparticles is ~17 nm, slightly larger than that of the Pd@PdCuNi core-shell nanoparticles. Figure 1C reveals the HRTEM image of the PdCuNiP nanoparticles, where the amorphous structure of the products can be identified. Such an amorphous nature can also be evidenced by Fourier transformation (inset in Figure 1C). To further investigate the elemental composition and distribution, the Energy-dispersive X-ray spectroscopy (EDS) elemental mappings analysis was carried out (Figure 1D). PdCuNiP nanoparticles are composed of Pd, Cu, Ni, and P elements, while all the elements distribute homogeneously within the nanoparticles. The atomic ratio of Pd:Cu:Ni:P determined by inductively coupled plasma mass spectrometry (ICP-MS) is 44.2:16.2:25.2:14.4 for the amorphous trimetallic phosphide nanoparticles. Additionally, the chemical composition ratio of amorphous PdCuNiP nanoparticles can be further demonstrated by XPS test results listed in Supplementary Table S1, and these groups of atomic ratios are no different from each other. Figure 1E shows the XRD patterns of the Pd nanocubes, Pd@Cu, Pd@CuNi, and PdCuNiP nanoparticles. As can be seen in the XRD pattern, peak shifts could be observed for Pd@Cu and Pd@CuNi nanoparticles relative to the original Pd nanocubes (black line) due to the formation of alloy surfaces. Two peaks can be observed near 40° for Pd@PdCu and Pd@PdCuNi nanoparticles, which indicates the co-existence of Pd cores and shells and the formation of PdCu and PdCuNi alloy shells. However, the XRD pattern of PdCuNiP phosphide nanoparticles suggests that the Pd@PdCuNi core-shell nanocrystals have turned into an amorphous phase after phosphorization treatment, consistent with the HRTEM and Fourier transformation analysis. To further prove amorphous of PdCuNiP nanoparticles, the XRD pattern was presented with a wider 2θ range (Supplementary Figure S5).

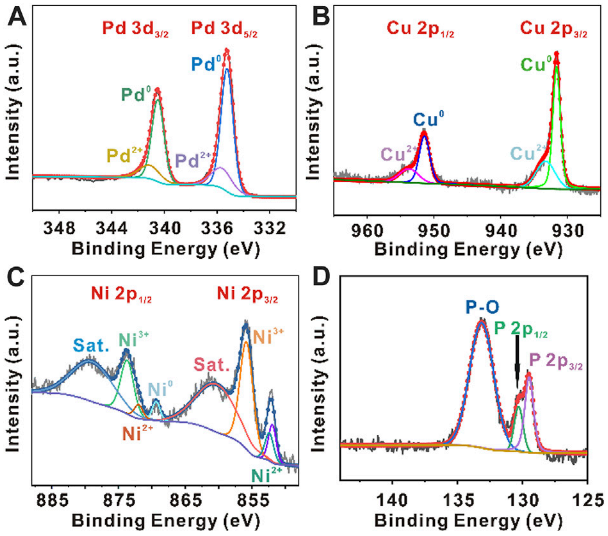

FIGURE 2
XPS survey spectra of sample PdCuNiP: **(A)** Pd 3d XPS spectra; **(B)** Cu 2p XPS spectra; **(C)** Ni 2p XPS spectra; and **(D)** P 2p XPS spectra.

XPS analysis was performed to investigate the chemical states and compositions of PdCuNiP nanoparticles (Figure 2). Figure 2A represents the Pd $3d_{5/2}$ and Pd $3d_{3/2}$ signals. As can be seen, the peaks can be deconvoluted into Pd^0 and Pd^{2+} peaks. The peaks located at 335.2 and 340.5 eV could be attributed to metallic Pd (Pd^0) and the

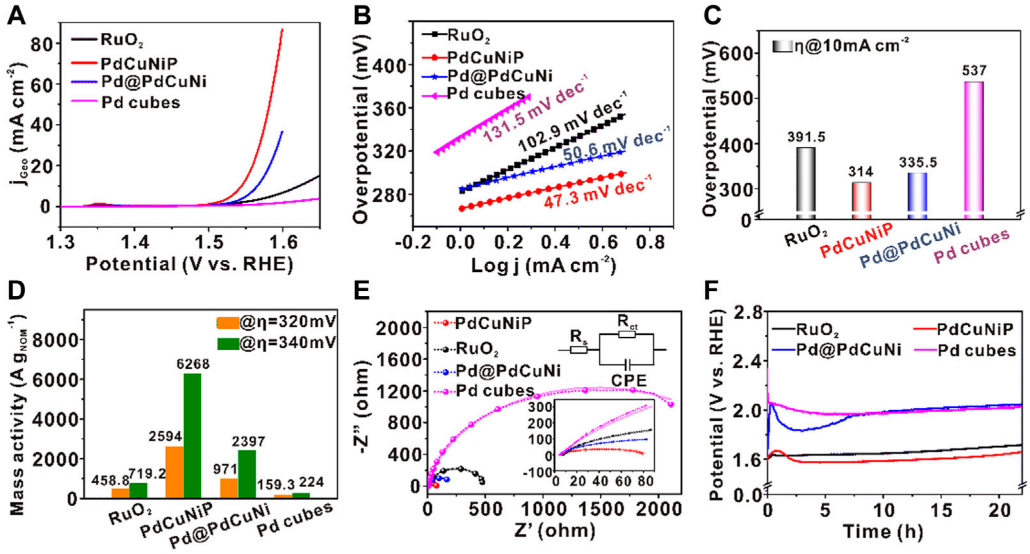

FIGURE 3
(A) LSV curves of PdCuNiP, Pd@PdCuNi, Pd nanocubes and commercial RuO_2 for OER in 1 M KOH. **(B)** Corresponding Tafel plots derived from the data in **(A)**. **(C)** Comparison of the overpotentials among PdCuNiP, Pd@PdCuNi, Pd nanocubes, and commercial RuO_2. **(D)** Mass activity of all catalysts at the overpotentials of 320 and 340 mV. **(E)** Nyquist plots of different catalysts. **(F)** Chronopotentiometry test of all catalysts for 22 h at the current densities of 10 mA cm^{-2}.

peaks at 335.6 and 341.1 eV are from Pd^{2+}. The peak intensity suggested that Pd^0 is dominant in the product. Compared with the original Pd nanocubes, the Pd $3d_{5/2}$ and Pd $3d_{3/2}$ binding energy values of PdCuNiP nanoparticles shift by + 0.4 eV (Supplementary Figure S6). Figure 2B shows the high-resolution Cu 2p spectra. The binding energies 931.6 and 951.4 eV corresponds to zero-valance Cu, while the peaks at 933.2 and 951.4 eV correspond to Cu^{2+}, respectively (Zhang et al., 2020). In the Ni 2p range, the XPS curves can be deconvoluted into three types of Ni species, including zero-valance Ni (Ni^0), Ni^{2+}, and Ni^{3+} (Figure 2C). In general, the binding energies at 852.0 and 869.4 eV could be attributed to Ni^0, and the binding energies at 852.4, 855.8, 872.0, and 873.7 eV with shake-up satellite peaks (abbreviated as "Sat.") at 860.3 and 878.9 eV correspond to the oxidized nickel species (Ni^{2+} and Ni^{3+}), suggesting the existence of bi- and tri-valance nickel species on the surface of PdCuNiP nanoparticles (Hengne et al., 2018; Wang et al., 2019a; Jin et al., 2019; Lei et al., 2019; Qiu et al., 2019). In Figure 2D, the XPS P 2p spectra show two peaks at 129.5 and 130.3 eV corresponding to P $2p_{3/2}$ and P $2p_{1/2}$, respectively, which can be ascribed to the phosphide. This result further confirms the successful synthesis of trimetallic PdCuNiP phosphide nanoparticles in this work. The peak 133.1 eV assigned to P-O is mainly due to the inevitable surface binding of P with oxygen in the air. The coexisted Cu^{2+}, Ni^{2+}, Ni^{3+}, and P-O could benefit the formation of oxygen-containing species (OH^-_{ads}) (Miao et al., 2014; Lv et al., 2019). According to the reports, this process can accelerate the reaction kinetics during OER, and thus improve the catalytic performance of the catalysts (Wang et al., 2017; Ibrahim et al., 2019). The increase of Pd, Cu, and Ni valence states is the result of electronic regulation between different elements, which is an important factor for improved OER performance. Also, valence states changes indicate the phenomenon of vast electron transfer from Pd, Cu, and Ni to P during the phosphorization treatment, contributing to the strong linkages between metal and P atoms, along with decreased 3d electron density and lower d-band energy of Pd, Cu, and Ni. Therefore, the electronic regulation weakened the bonding strength between the catalyst surface and the intermediate on the catalytic interface for enhanced OER catalytic performance (Zhou et al., 2006; Yang et al., 2010; He et al., 2021b). In addition, the positive shift of Pd 3d binding energies would also result in a stronger interaction with OH^-_{ads}, thereby enhancing the catalytic activity of Pd sites towards OER (Du et al., 2012; Bhowmik et al., 2016). Collectively, the above results reveal the chemical valence states and synergetic effects of Pd, Cu, Ni, and P elements in trimetallic amorphous phosphide nanoparticles.

The obtained trimetallic PdCuNiP amorphous nanoparticles were then evaluated as catalysts towards OER in 1.0 M O_2-saturated KOH aqueous solution, benchmarking against the commercial RuO_2, Pd@PdCuNi core-shell nanoparticles, and the original Pd nanocubes. Figure 3A shows the linear sweep voltammetry (LSV) normalized with the geometrical area of the electrode (0.196 cm^2) at a scan rate of 5 mV s^{-1}. The total mass of the noble metal loading was kept the same (5.1 μg cm^{-2}) for all the catalysts. As shown in Figure 3A, in an alkaline medium, the activity sequence of the catalysts is PdCuNiP > Pd@PdCuNi > RuO_2 > Pd nanocubes. The corresponding Tafel slopes of the catalysts are shown in Figure 3B. Different from the original Pd nanocubes (131.5 mV dec^{-1}), RuO_2 (102.9 mV dec^{-1}), and Pd@PdCuNi (50.6 mV dec^{-1}), the Tafel slope of PdCuNiP sharply decreased to 47.3 mV dec^{-1}, which should be ascribed to the synergistic of trimetallic component, the modified electronic structure, and the amorphous structure of the catalyst, which helps to lower the energy barrier and thus accelerate the reaction kinetics. Figure 3C further shows that the prepared trimetallic PdCuNiP phosphide nanoparticles possess the lowest overpotential (314 mV) to afford a current density of 10 mA cm^{-2} in OER, which is 223, 77.5, and 21.5 mV lower than those of the original Pd nanocubes,

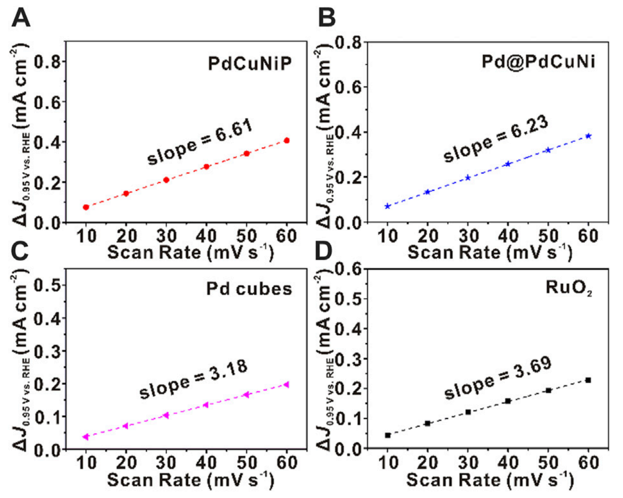

FIGURE 4
Measurements for electrochemical double-layer capacitance. Corresponding Δ*J* as a function of scan rates of **(A)** PdCuNiP, **(B)** Pd@PdCuNi, **(C)** Pd nanocubes and **(D)** RuO_2 catalysts.

commercial RuO_2 catalysts, and the Pd@PdCuNi core-shell catalysts, respectively. The above experiment results manifest that the synergistic effect between the trimetallic component and the amorphous structure, as well as the introduction of P, can significantly enhance the electrocatalytic performance. Moreover, the mass activities of the catalysts normalized to noble metal loadings (measured by ICP-MS, Supplementary Figure S7), which is a vital indicator of electrocatalytic activity in practical applications (Zhao et al., 2017), were further calculated based on the values measured at the overpotentials of 320 and 340 mV (Figure 3D). As can be seen, the mass activity of PdCuNiP achieves 2,594 and 6268 A $g^{-1}{}_{Pd}$ at overpotentials of 320 and 340 mV, respectively, which is 5.7 and 8.7 times as high as that of the commercial RuO_2 catalyst. The electrochemical reaction kinetics were further investigated using electrochemical impedance spectroscopy (EIS). Figure 3E illustrates the Nyquist plots fitting the equivalent circuit diagram at the potential of 1.50 V vs. RHE for different electrocatalysts, in which solid lines represent experimental data and dotted lines with circles represent fitting curves. The obtained solution resistance (R_s) is almost equivalent for all the catalysts, and the diameters of the fitting semicircles accord with the charge transfer resistance (R_{ct}). Compared with other samples, the R_{ct} of PdCuNiP is much lower, suggesting a faster transport rate of electrons and reaction kinetics towards oxygen evolution reaction (Supplementary Table S2). Unambiguously, the results further confirm the enhanced intrinsic activity for amorphous PdCuNiP nanoparticles. The stability of the catalysts is another important parameter. As shown in Figure 3F, the chronoamperometry measurements were employed to test the stability of the catalysts. After testing for 22 h, the overpotential decrease of PdCuNiP is 66 mV, which is much smaller than those of Pd@PdCuNi nanoparticles (412 mV), Pd cubes (84 mV), and commercial RuO_2 (180 mV). The reason that the activity of PdCuNiP catalysts decreased first and then increased significantly in Figure 3F is caused by the oxidation of the oleylamine and other organic compounds adsorbed by the catalysts during the stability test. In addition, it was found that the PdCuNiP catalyst did not undergo structural reconstruction by testing the HRTEM and XRD of the catalyst after the stability test, and the amorphous structure is well maintained (Supplementary Figure S9). This is different from the previously reported surface reconstruction process of some metal phosphides and metal-based compounds (PdCuNiP, cobalt pnictide, and defect-rich Co_3O_4) during OER (Kim et al., 2018; Lyu et al., 2020; Huang et al., 2022). Worthy, the PdCuNiP catalyst exhibits outstanding performance compared to other reported catalysts listed in Supplementary Table S3 for OER (Bai et al., 2016; Guan et al., 2017; He et al., 2017; Liyanage et al., 2017; Ren et al., 2017; Wang et al., 2019b).

To better illustrate the intrinsic activity of the catalysts towards OER, the electrochemical activity surface area (ECSA) and roughness factor (R_f) were calculated by measuring the electrochemical double-layer capacitance (C_{dl}) of corresponding electrocatalysts. As shown in Supplementary Figure S10, cyclic voltammetry (CV) curves were carried out at a fixed potential (0.90–1.0 V vs. RHE) from the non-faradaic potential with various scan rates from 10 to 60 mV s^{-1}. As evidenced in Figure 4, the curves of the difference between anodic and cathodic current densities (Δ*J*) against scan rate were plotted, in which the fitting slops represent twice of C_{dl}. The calculated results summarized in Supplementary Table S4 show that the C_{dl} and ECSA of PdCuNiP nanoparticles were 3.31 mF cm^{-2} and 82.75 cm^2 $g^{-1}{}_{Pd}$, respectively, which were superior to that of Pd@PdCuNi (3.12 mF cm^{-2} and 78 cm^2 $g^{-1}{}_{Pd}$), Pd nanocubes (1.59 mF cm^{-2} and 39.75 cm^2 $g^{-1}{}_{Pd}$) and RuO_2 (1.85 mF cm^{-2} and 46.25 cm^2 $g^{-1}{}_{Ru}$). It turns out that PdCuNiP nanoparticles would possess more active sites, which could be attributed to the low coordination surface of amorphous structure (Tsuji et al., 2011; Bergmann et al., 2015; Zhao et al., 2017; Liu et al., 2018b; Anantharaj et al., 2020). Additionally, to reduce the impact of the different ECSAs, we further compared the intrinsic activity by recording the ECSAs normalized polarization curves and a diagram of the specific activity versus different overpotentials of 320 and 340 mV for all the samples (Supplementary Figure S11; Supplementary Table S4). As can be seen, the trends of the C_{dl}, ECSA, and R_f were found to be consistent with that of the activity. As well, the computed C_{dl} increased with the growth of the particle size, which agreed with our theoretical predictions, and means the trend of the C_{dl}, ECSA and R_f coincide with that of MA, SA, and the particle sizes (Supplementary Table S4; Supplementary Figures S2–S4). Collectively, the prepared trimetallic amorphous PdCuNiP nanoparticles exhibit the largest ECSA, and the highest specific and mass activities among the four catalysts, showing the important role of the synergistic effect of multi-elements and the amorphous structure in improving the catalytic performance of noble-metal based electrocatalysts.

4 Conclusion

In summary, amorphous structured trimetallic PdCuNiP nanoparticles with enhanced OER performance under an alkaline solution have been synthesized through alloying Cu and Ni into the surface lattice of Pd nanocubes and the subsequent phosphorization treatment. Catalytic performance evaluation reveals that both the synergistic effect between four kinds of elements and the advantage of amorphous structure can enhance the catalytic performance of the Pd-based catalysts. Hence, trimetallic amorphous PdCuNiP phosphide nanoparticles can show a mass activity nearly 20-fold enhancement compared with the initial Pd nanocubes towards OER, and an overpotential 223 mV lower. This work may shed new light on both the fabrication of novel amorphous multi-metallic phosphide electrocatalysts and their catalytic applications in a set of electrocatalysis, thereby promoting the practical applications of electrocatalysis in renewable energy conversion systems.

Data availability statement

The original contributions presented in the study are included in the article/Supplementary Material, further inquiries can be directed to the corresponding authors.

Author contributions

MJ designed and guided the research project and wrote the paper. YZ carried out the preparation of catalysts, electrocatalytic test, and data analysis, and wrote parts of the paper. RG, XL, TH, WW, QZ, RL, KZ, and SJ assisted in laboratory operation and electrochemical testing. All listed authors are involved in this work and have made many useful contributions to this paper.

Funding

This work is sponsored by the National Natural Science Foundation of China (NSFC, 22171217, 51888103, and 21773180), the Distinguished Young Scholars in Shaanxi Province (no:2023-JC-JQ-12), the Fundamental Research Funds for the Central Universities, the China Postdoctoral Science Foundation (No. 2021M692547), the Natural Science Basic Research Program of Shaanxi (2022JQ-105, 2023-JC-QN-0161), and the Science Research Program Funded by Shaanxi Provincial Education Department (22JK0461).

Acknowledgments

We would like to thank J. Li and C. Li from the Instrument Analysis Center at Xi'an Jiaotong University for their assistance with HRTEM analysis. We also thank M. Sun. and X. Wen. from Shiyanjia Lab (www.shiyanjia.com) for the ICP-OES/MS and XPS tests.

Conflict of interest

The authors declare that the research was conducted in the absence of any commercial or financial relationships that could be construed as a potential conflict of interest.

Publisher's note

Supplementary material

The Supplementary Material for this article can be found online at: https://www.frontiersin.org/articles/10.3389/fchem.2023.1122333/full#supplementary-material

References

Alegre, C., Stassi, A., Modica, E., Lo Vecchio, C., Arico, A. S., and Baglio, V. (2015). Investigation of the activity and stability of Pd-based catalysts towards the oxygen reduction (ORR) and evolution reactions (OER) in iron–air batteries. *RSC Adv.* 5 (32), 25424–25427. doi:10.1039/c4ra15578e

Anantharaj, S., Noda, S., et al. (2020). Amorphous catalysts and electrochemical water splitting: An untold story of harmony. *Small* 16 (2), 1905779. doi:10.1002/smll.201905779

Antolini, E., et al. (2014). Iridium as catalyst and cocatalyst for oxygen evolution/reduction in acidic polymer electrolyte membrane electrolyzers and fuel cells. *ACS Catal.* 4 (5), 1426–1440. doi:10.1021/cs4011875

Bai, Y., Zhang, H., Feng, Y., Fang, L., and Wang, Y. (2016). Sandwich-like CoP/C nanocomposites as efficient and stable oxygen evolution catalysts. *J. Mater. Chem. A* 4 (23), 9072–9079. doi:10.1039/c6ta03392j

Bergmann, A., Martinez-Moreno, E., Teschner, D., Chernev, P., Gliech, M., de Araujo, J. F., et al. (2015). Reversible amorphization and the catalytically active state of crystalline Co_3O_4 during oxygen evolution[J]. *Nat. Commun.* 6 (1), 8625. doi:10.1038/ncomms9625

Bhowmik, T., Kundu, M., Barman, S., et al. (2016). Palladium nanoparticle–graphitic carbon nitride porous synergistic catalyst for hydrogen evolution/oxidation reactions over a broad range of pH and correlation of its catalytic activity with measured hydrogen binding energy. *ACS Catal.* 6 (3), 1929–1941. doi:10.1021/acscatal.5b02485

Chen, D., Chen, C., Baiyee, Z., Shao, Z., and Ciucci, F. (2015). Nonstoichiometric oxides as low-cost and highly-efficient oxygen reduction/evolution catalysts for low-temperature electrochemical Devices. *Chem. Rev.* 115 (18), 9869–9921. doi:10.1021/acs.chemrev.5b00073

Chen, R., Yang, C., Cai, W., Wang, H. Y., Miao, J., Zhang, L., et al. (2017). Use of platinum as the counter electrode to study the activity of nonprecious metal catalysts for the hydrogen evolution reaction. *ACS energy Lett.* 2 (5), 1070–1075. doi:10.1021/acsenergylett.7b00219

Chu, S., Chen, W., Chen, G., Huang, J., Zhang, R., Song, C., et al. (2019). Holey Ni-Cu phosphide nanosheets as a highly efficient and stable electrocatalyst for hydrogen evolution. *Appl. Catal. B Environ.* 243, 537–545. doi:10.1016/j.apcatb.2018.10.063

Chu, S., Majumdar, A., et al. (2012). Opportunities and challenges for a sustainable energy future. *Nature* 488 (7411), 294–303. doi:10.1038/nature11475

Du, W., Mackenzie, K., Milano, D., Deskins, N. A., Su, D., and Teng, X. (2012). Palladium–tin alloyed catalysts for the ethanol oxidation reaction in an alkaline medium. *ACS Catal.* 2 (2), 287–297. doi:10.1021/cs2005955

Feng, J., Lv, F., Zhang, W., Wang, K., Yang, C., et al. (2017). Iridium-based multimetallic porous hollow nanocrystals for efficient overall-water-splitting catalysis. *Adv. Mater.* 29 (47), 1703798. doi:10.1002/adma.201703798

Guan, B. Y., Yu, L., Lou, X. W., et al. (2017). General synthesis of multishell mixed-metal oxyphosphide particles with enhanced electrocatalytic activity in the oxygen evolution reaction. *Angew. Chem. Int. Ed.* 56 (9), 2386–2389. doi:10.1002/anie.201611804

Guo, X., Wan, X., and Liu, Q. (2022). *Phosphated IrMo bimetallic cluster for efficient hydrogen evolution reaction[J].* Amsterdam, Holland: Elsevier.

He, P., Yu, X. Y., Lou, X. W., et al. (2017). Carbon-incorporated nickel-cobalt mixed metal phosphide nanoboxes with enhanced electrocatalytic activity for oxygen evolution. *Angew. Chem. Int. Ed.* 56 (14), 3897–3900. doi:10.1002/anie.201612635

He, T., Wang, W., Shi, F., Yang, X., Li, X., Wu, J., et al. (2021). Mastering the surface strain of platinum catalysts for efficient electrocatalysis. *Nature* 598 (7879), 76–81. doi:10.1038/s41586-021-03870-z

He, T., Wang, W., Yang, X., Shi, F., Ye, Z., Zheng, Y., et al. (2021). Deposition of atomically thin Pt shells on amorphous palladium phosphide cores for enhancing the electrocatalytic durability. *ACS Nano* 15 (4), 7348–7356. doi:10.1021/acsnano.1c00602

Hengne, A., Samal, A., Enakonda, L., Harb, M., Gevers, L. E., Anjum, D. H., et al. (2018). Ni-Sn-supported ZrO2 catalysts modified by indium for selective CO_2 hydrogenation to methanol[J]. *ACS Omega* 3 (4), 3688–3701. doi:10.1021/acsomega.8b00211

Hong, W., Risch, M., Stoerzinger, K., Grimaud, A., Suntivich, J., and Shao-Horn, Y. (2015). Toward the rational design of non-precious transition metal oxides for oxygen electrocatalysis. *Energy Environ. Sci.* 8 (5), 1404–1427. doi:10.1039/c4ee03869j

Huang, Y. C., Chen, W., Xiao, Z., Hu, Z., Lu, Y. R., Chen, J. L., et al. (2022). Situ/operando soft X-ray spectroscopic identification of a Co^{4+} intermediate in the oxygen evolution reaction of defective Co_3O_4 nanosheets[J]. *J. Phys. Chem. Lett.* 13 (35), 8386–8396. doi:10.1021/acs.jpclett.2c01557

Hunter, B., Gray, H., Muller, A., et al. (2016). Earth-abundant heterogeneous water oxidation catalysts. *Chem. Rev.* 116 (22), 14120–14136. doi:10.1021/acs.chemrev.6b00398

Ibrahim, K. B., Tsai, M. C., Chala, S. A., Berihun, M. K., Kahsay, A. W., Berhe, T. A., et al. (2019). A review of transition metal-based bifunctional oxygen electrocatalysts. *J. Chin. Chem. Soc.* 66 (8), 829–865. doi:10.1002/jccs.201900001

Jiao, Y., Zheng, Y., Jaroniec, M., and Qiao, S. Z. (2015). Design of electrocatalysts for oxygen- and hydrogen-involving energy conversion reactions. *Chem. Soc. Rev.* 44 (8), 2060–2086. doi:10.1039/c4cs00470a

Jin, M., Liu, H., Zhang, H., Xie, Z., Liu, J., and Xia, Y. (2011). Synthesis of Pd nanocrystals enclosed by {100} facets and with sizes <10 nm for application in CO oxidation. *Nano Res.* 4 (1), 83–91. doi:10.1007/s12274-010-0051-3

Jin, Z., Lv, J., Jia, H., Liu, W., Li, H., Chen, Z., et al. (2019). Nanoporous Al-Ni-Co-Ir-Mo high-entropy alloy for record-high water splitting activity in acidic environments. *Small* 15 (47), 1904180. doi:10.1002/smll.201904180

Kim, B. K., Kim, S. K., Cho, S. K., and Kim, J. J. (2018). Enhanced catalytic activity of electrodeposited Ni-Cu-P toward oxygen evolution reaction. *Appl. Catal. B Environ.* 237, 409–415. doi:10.1016/j.apcatb.2018.05.082

Koper, M., et al. (2013). Theory of multiple proton–electron transfer reactions and its implications for electrocatalysis. *Chem. Sci.* 4 (7), 2710–2723. doi:10.1039/c3sc50205h

Kwon, G., Ferguson, G. A., Heard, C. J., Tyo, E. C., Yin, C., DeBartolo, J., et al. (2013). Size-dependent subnanometer Pd cluster (Pd_4, Pd_6, and Pd_{17}) water oxidation electrocatalysis[J]. *ACS Nano* 7 (7), 5808–5817. doi:10.1021/nn400772s

Lei, C., Wang, Y., Hou, Y., Liu, P., Yang, J., Zhang, T., et al. (2019). Efficient alkaline hydrogen evolution on atomically dispersed Ni-N_x species anchored porous carbon with embedded Ni nanoparticles by accelerating water dissociation kinetics[J]. *Energy & Environ. Sci.* 12 (1), 149–156. doi:10.1039/c8ee01841c

Li, X., Wang, X., Liu, M., Liu, H., Chen, Q., Yin, Y., et al. (2018). Construction of Pd-M (M = Ni, Ag, Cu) alloy surfaces for catalytic applications. *Nano Res.* 11 (2), 780–790. doi:10.1007/s12274-017-1687-z

Li, Y., Selloni, A., et al. (2014). Mechanism and activity of water oxidation on selected surfaces of pure and Fe-doped NiO_x[J]. *ACS Catal.* 4 (4), 1148–1153. doi:10.1021/cs401245q

Li, Z., Liu, Z., Liang, J., Xu, C. W., and Lu, X. (2014). Facile synthesis of Pd-Mn_3O_4/C as high-efficient electrocatalyst for oxygen evolution reaction[J]. *J. Mater. Chem. A* 2 (43), 18236–18240. doi:10.1039/c4ta04110k

Liu, J., Nai, J., You, T., An, P., Zhang, J., Ma, G., et al. (2018). The flexibility of an amorphous cobalt hydroxide nanomaterial promotes the electrocatalysis of oxygen evolution reaction. *Small* 14 (17), 1703514. doi:10.1002/smll.201703514

Liu, K., Zhang, C., Sun, Y., Zhang, G., Shen, X., Zou, F., et al. (2018). High-performance transition metal phosphide alloy catalyst for oxygen evolution reaction. *ACS Nano* 12 (1), 158–167. doi:10.1021/acsnano.7b04646

Liu, Z., Zheng, F., Xiong, W., Li, X., Yuan, A., and Pang, H. (2021). Strategies to improve electrochemical performances of pristine metal-organic frameworks-based electrodes for lithium/sodium-ion batteries. *SmartMat* 2 (4), 488–518. doi:10.1002/smm2.1064

Liyanage, D. R., Li, D., Cheek, Q. B., Baydoun, H., and Brock, S. L. (2017). Synthesis and oxygen evolution reaction (OER) catalytic performance of $Ni_{2-x}Ru_xP$ nanocrystals: Enhancing activity by dilution of the noble metal[J]. *J. Mater. Chem. A* 5 (33), 17609–17618. doi:10.1039/c7ta05353c

Luo, R., Qian, Z., Xing, L., Du, C., Yin, G., Zhao, S., et al. (2021). Re-Looking into the active moieties of metal X-ides (X- = phosph-, sulf-, nitr-, and carb-) toward oxygen evolution reaction. *Adv. Funct. Mater.* 31 (37), 2102918. doi:10.1002/adfm.202102918

Lv, H., Sun, L., Xu, D., Ma, Y., and Liu, B. (2019). When ternary PdCuP alloys meet ultrathin nanowires: Synergic boosting of catalytic performance in ethanol electrooxidation. *Appl. Catal. B Environ.* 253, 271–277. doi:10.1016/j.apcatb.2019.04.066

Lv, X., Li, X., Yang, C., Ding, X., Zhang, Y., Zheng, Y., et al. (2020). Large-size, porous, ultrathin NiCoP nanosheets for efficient electro/photocatalytic water splitting. *Adv. Funct. Mater.* 30 (16), 1910830. doi:10.1002/adfm.201910830

Lyu, Y., Zheng, J., Xiao, Z., Zhao, S., Jiang, S. P., and Wang, S. (2020). Identifying the intrinsic relationship between the restructured oxide layer and oxygen evolution reaction performance on the cobalt pnictide catalyst. *Small* 16 (14), 1906867. doi:10.1002/smll.201906867

McCrory, C., Jung, S., Peters, J., and Jaramillo, T. F. (2013). Benchmarking heterogeneous electrocatalysts for the oxygen evolution reaction. *J. Am. Chem. Soc.* 135 (45), 16977–16987. doi:10.1021/ja407115p

Miao, Y., Ouyang, L., Zhou, S., Xu, L., Yang, Z., Xiao, M., et al. (2014). Electrocatalysis and electroanalysis of nickel, its oxides, hydroxides and oxyhydroxides toward small molecules. *Biosens. Bioelectron.* 53, 428–439. doi:10.1016/j.bios.2013.10.008

Park, J., Choi, S., Oh, A., Jin, H., Joo, J., Baik, H., et al. (2019). Hemi-core@frame AuCu@IrNi nanocrystals as active and durable bifunctional catalysts for the water splitting reaction in acidic media. *Nanoscale Horizons* 4 (3), 727–734. doi:10.1039/c8nh00520f

Qin, Q., Jang, H., Chen, L., Nam, G., Liu, X., and Cho, J. (2018). Low loading of Rh_xP and RuP on N, P codoped carbon as two trifunctional electrocatalysts for the oxygen and hydrogen electrode reactions[J]. *Adv. Energy Mater.* 8 (29), 1801478. doi:10.1002/aenm.201801478

Qiu, H., Fang, G., Wen, Y., Liu, P., Xie, G., Liu, X., et al. (2019). Nanoporous high-entropy alloys for highly stable and efficient catalysts. *J. Mater. Chem. A* 7 (11), 6499–6506. doi:10.1039/c9ta00505f

Reier, T., Nong, H., Teschner, D., Schlogl, R., and Strasser, P. (2017). Electrocatalytic oxygen evolution reaction in acidic environments - reaction mechanisms and catalysts. *Adv. Energy Mater.* 7 (1), 1601275. doi:10.1002/aenm.201601275

Ren, X., Zhou, J., Qi, X., Liu, Y., Huang, Z., Li, Z., et al. (2017). Few-layer black phosphorus nanosheets as electrocatalysts for highly efficient oxygen evolution reaction. *Adv. Energy Mater.* 7 (19), 1700396. doi:10.1002/aenm.201700396

Ryu, J., Jung, N., Jang, J., Kim, H. J., and Yoo, S. J. (2015). *In situ* transformation of hydrogen-evolving CoP nanoparticles: Toward efficient oxygen evolution catalysts bearing dispersed morphologies with Co-oxo/hydroxo molecular units. *ACS Catal.* 5 (7), 4066–4074. doi:10.1021/acscatal.5b00349

Shih, C. F., Zhang, T., Li, J., and Bai, C. (2018). Powering the future with liquid sunshine. *Joule* 2 (10), 1925–1949. doi:10.1016/j.joule.2018.08.016

Song, F., Bai, L., Moysiadou, A., Lee, S., Hu, C., Liardet, L., et al. (2018). Transition metal oxides as electrocatalysts for the oxygen evolution reaction in alkaline solutions: An application-inspired renaissance. *J. Am. Chem. Soc.* 140 (25), 7748–7759. doi:10.1021/jacs.8b04546

Stern, L., Feng, L., Song, F., and Hu, X. (2015). Ni_2P as a Janus catalyst for water splitting: The oxygen evolution activity of Ni_2P nanoparticles[J]. *Energy & Environ. Sci.* 8 (8), 2347–2351. doi:10.1039/c5ee01155h

Su, H., Soldatov, M. A., Roldugin, V., and Liu, Q. (2022). Platinum single-atom catalyst with self-adjustable valence state for large-current-density acidic water oxidation. *eScience* 2 (1), 102–109. doi:10.1016/j.esci.2021.12.007

Suen, N., Hung, S., Quan, Q., Zhang, N., Xu, Y. J., and Chen, H. M. (2017). Electrocatalysis for the oxygen evolution reaction: Recent development and future perspectives. *Chem. Soc. Rev.* 46 (2), 337–365. doi:10.1039/c6cs00328a

Tang, C., Zhang, R., Lu, W., He, L., Jiang, X., Asiri, A. M., et al. (2017). Fe-doped CoP nanoarray: A monolithic multifunctional catalyst for highly efficient hydrogen generation. *Adv. Mater.* 29 (2), 1602441. doi:10.1002/adma.201602441

Trotochaud, L., Young, S., Ranney, J., and Boettcher, S. W. (2014). Nickel–Iron oxyhydroxide oxygen-evolution electrocatalysts: The role of intentional and incidental iron incorporation. *J. Am. Chem. Soc.* 136 (18), 6744–6753. doi:10.1021/ja502379c

Tsuji, E., Imanishi, A., Fukui, K., and Nakato, Y. (2011). Electrocatalytic activity of amorphous RuO_2 electrode for oxygen evolution in an aqueous solution[J]. *Electrochimica Acta* 56 (5), 2009–2016. doi:10.1016/j.electacta.2010.11.062

Wang, J., Bai, Z., et al. (2017). Fe-based catalysts for heterogeneous catalytic ozonation of emerging contaminants in water and wastewater. *Chem. Eng. J.* 312, 79–98. doi:10.1016/j.cej.2016.11.118

Wang, Q., Shang, L., Sun-Waterhouse, D., Zhang, T., and Waterhouse, G. (2021). Engineering local coordination environments and site densities for high-performance Fe-N-C oxygen reduction reaction electrocatalysis. *SmartMat* 2 (2), 154–175. doi:10.1002/smm2.1033

Wang, S., Jang, H., Wang, J., Wu, Z., Liu, X., and Cho, J. (2019). Cobalt-tannin-Framework-derived amorphous Co−P/Co−N−C on N, P Co-doped porous carbon with abundant active moieties for efficient oxygen reactions and water splitting. *ChemSusChem* 12 (4), 830–838. doi:10.1002/cssc.201802909

Wang, T., Cao, X., Jiao, L., et al. (2021). Ni_2P/NiMoP heterostructure as a bifunctional electrocatalyst for energy-saving hydrogen production[J]. *eScience* 1 (1), 69–74. doi:10.1016/j.esci.2021.09.002

Wang, T., Guo, X., Zhang, J., Xiao, W., Xi, P., Peng, S., et al. (2019). Electronic structure modulation of NiS_2 by transition metal doping for accelerating the hydrogen evolution reaction[J]. *J. Mater. Chem. A* 7 (9), 4971–4976. doi:10.1039/c8ta11286j

Wang, W., He, T., Yang, X., Liu, Y., Wang, C., Li, J., et al. (2021). General synthesis of amorphous PdM (M = Cu, Fe, Co, Ni) alloy nanowires for boosting HCOOH dehydrogenation. *Nano Lett.* 21 (8), 3458–3464. doi:10.1021/acs.nanolett.1c00074

Wang, W., Shi, X., He, T., Zhang, Z., Yang, X., Guo, Y. J., et al. (2022). Tailoring amorphous PdCu nanostructures for efficient C–C cleavage in ethanol electrooxidation. *Nano Lett.* 22 (17), 7028–7033. doi:10.1021/acs.nanolett.2c01870

Xia, B., Yan, Y., Li, N., Wu, H. B., Lou, X. W., and Wang, X. (2016). A metal–organic framework-derived bifunctional oxygen electrocatalyst. *Nat. Energy* 1 (1), 15006. doi:10.1038/nenergy.2015.6

Xiao, Z., Luo, S., Duan, W., Zhang, X., Han, S., Liu, Y., et al. (2022). Doughty-electronegative heteroatom-induced defective MoS_2 for the hydrogen evolution reaction[J]. *Front. Chem.* 10, 1064752. doi:10.3389/fchem.2022.1064752

Xu, J., Li, J., Xiong, D., Zhang, B., Liu, Y., Wu, K. H., et al. (2018). Trends in activity for the oxygen evolution reaction on transition metal (M = Fe, Co, Ni) phosphide pre-catalysts. *Chem. Sci.* 9 (14), 3470–3476. doi:10.1039/c7sc05033j

Xu, K., Ding, H., Lv, H., Chen, P., Lu, X., Cheng, H., et al. (2016). Dual electrical-behavior regulation on electrocatalysts realizing enhanced electrochemical water oxidation. *Adv. Mater.* 28 (17), 3326–3332. doi:10.1002/adma.201505732

Xu, S., Gao, X., Deshmukh, A., Zhou, J., Chen, N., Peng, W., et al. (2020). Pressure-promoted irregular $CoMoP_2$ nanoparticles activated by surface reconstruction for oxygen evolution reaction electrocatalysts[J]. *J. Mater. Chem. A* 8 (4), 2001–2007. doi:10.1039/c9ta11775j

Yang, G., Chen, Y., Zhou, Y., Tang, Y., and Lu, T. (2010). Preparation of carbon supported Pd–P catalyst with high content of element phosphorus and its electrocatalytic performance for formic acid oxidation. *Electrochem. Commun.* 12 (3), 492–495. doi:10.1016/j.elecom.2010.01.029

Yu, J., Li, Q., Li, Y., Xu, C. Y., Zhen, L., Dravid, V. P., et al. (2016). Ternary metal phosphide with triple-layered structure as a low-cost and efficient electrocatalyst for bifunctional water splitting. *Adv. Funct. Mater.* 26 (42), 7644–7651. doi:10.1002/adfm.201603727

Yu, X., Zhang, M., Yuan, W., and Shi, G. (2015). A high-performance three-dimensional Ni–Fe layered double hydroxide/graphene electrode for water oxidation. *J. Mater. Chem. A* 3 (13), 6921–6928. doi:10.1039/c5ta01034a

Zhang, J., Liu, J., Xi, L., Yu, Y., Chen, N., Sun, S., et al. (2018). Single-atom Au/NiFe layered double hydroxide electrocatalyst: Probing the origin of activity for oxygen evolution reaction. *J. Am. Chem. Soc.* 140 (11), 3876–3879. doi:10.1021/jacs.8b00752

Zhang, J., Liu, X., Chen, W., Fang, H., Zheng, Y., and Yuan, Y. (2020). N configuration control of N-doped carbon for stabilizing Cu nanoparticles: The synergistic effects on oxy-carbonylation of methanol. *Carbon* 158, 836–845. doi:10.1016/j.carbon.2019.11.064

Zhang, K., He, Y., Guo, R., Wang, W., Zhan, Q., Li, R., et al. (2022). Interstitial carbon-doped PdMo bimetallene for high-performance oxygen reduction reaction. *ACS Energy Lett.* 7 (10), 3329–3336. doi:10.1021/acsenergylett.2c01734

Zhao, B., Zhang, L., Zhen, D., Yoo, S., Ding, Y., Chen, D., et al. (2017). A tailored double perovskite nanofiber catalyst enables ultrafast oxygen evolution. *Nat. Commun.* 8 (1), 14586. doi:10.1038/ncomms14586

Zheng, X., Zhang, B., De Luna, P., Liang, Y., Comin, R., Voznyy, O., et al. (2018). Theory-driven design of high-valence metal sites for water oxidation confirmed using *in situ* soft X-ray absorption. *Nat. Chem.* 10 (2), 149–154. doi:10.1038/nchem.2886

Zhou, W. P., Lewera, A., Larsen, R., Masel, R. I., Bagus, P. S., and Wieckowski, A. (2006). Size effects in electronic and catalytic properties of unsupported palladium nanoparticles in electrooxidation of formic acid. *J. Phys. Chem. B* 110 (27), 13393–13398. doi:10.1021/jp061690h

Zhou, X., Liu, H., Xia, B. Y., Ostrikov, K. K., Zheng, Y., and Qiao, S. (2022). Customizing the microenvironment of CO_2 electrocatalysis via three-phase interface engineering. *J. SmartMat* 3 (1), 111–129. doi:10.1002/smm2.1109

Zhu, J., Chen, Z., Xie, M., Lyu, Z., Chi, M., Mavrikakis, M., et al. (2019). Iridium-based cubic nanocages with 1.1-nm-Thick walls: A highly efficient and durable electrocatalyst for water oxidation in an acidic medium. *Angew. Chem.* 131 (22), 7322–7326. doi:10.1002/ange.201901732

Frontiers in Chemistry

TYPE Original Research
PUBLISHED 01 February 2023
DOI 10.3389/fchem.2023.1115377

OPEN ACCESS

EDITED BY
Xingxing Gu,
Chongqing Technology and Business University, China

REVIEWED BY
Ya Han,
Hebei GEO University, China
Yinghua Song,
Chongqing Technology and Business University, China

*CORRESPONDENCE
Hemmat A. Elbadawy,
Hemmatabdelfattah@alexu.edu.eg

†These authors have contributed equally to this work

SPECIALTY SECTION
This article was submitted to Nanoscience, a section of the journal Frontiers in Chemistry

RECEIVED 03 December 2022
ACCEPTED 03 January 2023
PUBLISHED 01 February 2023

CITATION
Elbadawy HA, El-Dissouky A, Hussein SM, El-Kewaey SR, Elfeky SA and El-Ghannam G (2023), A novel terpolymer nanocomposite (carboxymethyl β-cyclodextrin–nano chitosan–glutaraldehyde) for the potential removal of a textile dye acid red 37 from water.
Front. Chem. 11:1115377.
doi: 10.3389/fchem.2023.1115377

A novel terpolymer nanocomposite (carboxymethyl β-cyclodextrin–nano chitosan–glutaraldehyde) for the potential removal of a textile dye acid red 37 from water

Hemmat A. Elbadawy[1]*, Ali El-Dissouky[1†], Seham M. Hussein[1], Sara R. El-Kewaey[1], Souad A. Elfeky[2†] and Gamal El-Ghannam[2]

[1]Chemistry Department, Faculty of Science, Alexandria University, Alexandria, Egypt, [2]Department of Laser Applications in Metrology, Photochemistry, and Agriculture, National Institute of Laser Enhanced Sciences (NILES), Cairo University, Cairo, Egypt

Carboxymethyl β-cyclodextrin–nanochitosan–glutaraldehyde (CM-βCD:nChi:Glu) terpolymer was prepared as a nano-adsorbent for the removal of the anionic textile dye, acid red 37. The terpolymer nanocomposite formation and characterization were clarified by FTIR, XRD, scanning electron microscopy, TEM, Brunauer–Emmett–Teller specific surface area (BET-SSA), and zeta potential. The removal of the textile dye was investigated by using the batch adsorption method, investigating the effect of pH, dye concentration, adsorbent dose, contact time, and temperature. The results revealed that the maximum removal efficiency of 102.2 mg/L of the dye is about 99.67% under pH 6.0, the optimal contact time is 5 min, and the adsorbent dosage is 0.5 g/L. At 29°C; the adsorption capacity increased from 81.29 to 332.60 mg/g when the initial concentration of the dye was increased from 40.97 to 212.20 mg/L. Adsorption kinetics fitted well with the pseudo–second-order model with a good correlation (R^2 = 0.9998). The Langmuir isotherm model can best describe the adsorption isotherm model. Based on the experimental results, the CM-βCD:nChi:Glu terpolymer has a promising potential as an efficient novel adsorbent for the removal of textile dye acid red 37 from contaminated water. This study's preparation techniques and demonstrated mechanisms offer valuable insights into the adsorbent–adsorbate interactions mechanism, analysis, challenges, and future directions of beta-cyclodextrin/chitosan–based adsorbents in wastewater treatment.

KEYWORDS

terpolymer, CM-βCD:nChi:Glu, acid red 37, textile dye, adsorption capacity, % removal

1 Introduction

Water is one of the most valuable reserves among all natural resources that have economic, social, political, and environmental importance worldwide (Shin et al., 2020; Ibrahim et al., 2022). Recently, water pollution has triggered significant concerns due to its adverse environmental impact. As a result of rapid industrialization and the fastest modernization, numerous pollutants are introduced into the aquatic ecosystem (Kaur and Jindal, 2019). Thus, human activities play an ever-greater part in increasing water incompetence by polluting natural water supplies. Among various water pollutants, dyes are considered the most common contaminants that have the most hazardous chemical classes. Globally, about 0.8 million tons of dyes are produced annually, making them one of the greatest important groups of industrial chemicals (Pandey et al., 2020). Synthetic dyes are produced by many industries, especially textile industries, which are the main contributors to water pollution. Moreover, many synthetic dyes are lost during the dyeing process and released into the textile effluents (Subramani and Thinakaran, 2017; Crini et al., 2019). Consequently, massive dye production, along with large-scale applications, creates significant environmental contamination, causes serious health risks, exacerbates the water crisis, and negatively influences plant and animal lives, human health, and the entire living ecosystem (Altaher et al., 2014). Because of this expanding environmental issue, color removal from sewage has received much attention. As a result, with the basic concern for protecting and conserving natural water resources, one of the major difficulties confronting the scientific community is the control of water contamination. Several physicochemical and biological techniques have been developed and have gained great attention in removing dyes from wastewater, which may or may not be safe, robust, low-cost, or capable of tackling persistent organic pollutants of low concentrations (Katheresan et al., 2018; Hynes et al., 2020; Dassanayake et al., 2021; Senousy et al., 2022). Among these techniques, the adsorption process has gained considerable attention due to its remarkable efficiency, innovation, operational simplicity, and economic and non-destructive technique (Crini et al., 2018). The critical challenge in applying the adsorption method for dye elimination is in finding a fast adsorption rate and high-adsorption-capacity adsorbent. Hence, the necessary evidence that controls the efficiency of adsorption includes the attraction force between the adsorbent and adsorbate, the active sites on the adsorbent surface, low-cost adsorbents, concentration and particle size of the adsorbent, temperature, pH, and contact time. Here comes the role of choosing a suitable adsorbent that can achieve economic and effective conditions (Pourhakkak et al., 2021; Zaimee et al., 2021). β-Cyclodextrin (β-CD) is a cyclic oligosaccharide made up of seven α-D-glucose units linked through α-(1,4) linkages. Their basket-like structure contains a hydrophobic polar chamber lined on both sides with hydroxyl groups on the inside and outside of the cavity (Badruddoza et al., 2011). β-Cyclodextrin (β-CD) has an interesting ability to create attachment complexes with a wide variety of organic and inorganic compounds through its hydrophobic cavity and hydroxyl groups in solution through host–guest interactions (Li et al., 2018; Tang et al., 2018). It is an ecofriendly and biodegradable polysaccharide that has gained significant care in environmental cleaning (Sikder et al., 2019; Blach et al., 2008; Yadav et al.). The high concentration of hydroxyl groups shows high activity and can be easily functionalized. Even though dyes can be removed, the only adsorption sites are CD cavities, resulting in a long adsorption process and equilibrium time (Yuan et al., 2017). Therefore, carboxymethyl β-cyclodextrin (CM-β-CD) has been developed to increase the adsorption capacity of β-CD by grafting it with active functional groups, such as the carboxyl groups, which may serve as highly active adsorption sites. The high adsorption efficiency of CM-β-CD can be gained by increasing the number of adsorption sites thereby being considered a potential and highly efficient adsorbent for the removal of dyes from wastewater (Pu et al., 2020; Ghazimokri et al., 2022). Chitosan (Chi) is a natural biopolymer produced by the deacetylation of chitin of the shells of crabs and shrimps. Chi is effectively renewable, highly available, biodegradable, and biocompatible and does not generate toxic products (Azlan et al., 2009; Wu et al., 2010; Santos et al., 2019). Thus, Chi as the adsorbent is suitable for removing anionic dyes. Furthermore, different physical and chemical modifications have been made to its molecular structure by the addition of crosslinking agents. For example, crosslinking chitosan with crosslinking agents such as glutaraldehyde (Glu) allows for better physical and chemical properties and improves the adsorption capacity that maximizes the removal efficiency (Filipkowska, 2012; Galan et al., 2021). Some studies have used glutaraldehyde as the flexible grafting and crosslinking agent for the reaction between chitosan and β-CD or carboxymethyl β-cyclodextrin (CM-βCD) in the preparation of two- and three-component polymers. Thus, the resulting terpolymer gains a range of sorption-based applications (Wilson et al., 2013).

The innovative aspect of this research is the development of a novel terpolymer (three-component) adsorbent material by crosslinking CM-βCD and nanochitosan with glutaraldehyde (CM-β-CD:nChi:Glu), to employ it for the removal of toxic textile dye pollutants from aqueous systems. Several tools were utilized to fully characterize the produced material, such as FTIR, XRD, SEM, TEM, BET–specific surface area (BET-SSA), and zeta potential. Then, by applying the product as a potential adsorbent material, a textile dye model to remove acid red 37 dye from the aqueous medium was developed. To our knowledge, the simultaneous removal of acid red 37 from water using such a terpolymer adsorbent has not been reported in the available literature. The adsorption behavior, mechanism, characteristics, and thermodynamics of CM-βCD:nChi:Glu have also been evaluated in this study.

2 Materials and methods

2.1 Reagents and chemicals

Materials, chemicals, and their sources are described in the Supplementary Material.

2.2 Methods

2.2.1 Synthesis of carboxymethyl β-cyclodextrin

CM-βCD was synthesized according to the reported steps with some essential modifications (Mohamadi Zahedi and Mansourpanah, 2018; Emara et al., 2020). First, 5.0 g of β-cyclodextrin was dissolved in 50.0 mL of 10% (w/v) NaOH by constant stirring for complete mixing. After that, 10.0 mL of epichlorohydrin was added dropwise with vigorous stirring for 8.0 h. Then, 5.0 mL of epichlorohydrin was added more, and the mixture was continuously stirred for another 3 h and left overnight at room temperature. Then, the solution was concentrated to a volume of about 15.0 mL and cleansed with cold ethanol while the mixture was vigorously stirred to obtain a gummy precipitate. Washing again with cold acetone produced a durable precipitate. Thus, an excellent yield of β-CD/epichlorohydrin copolymer (12 g) was obtained. To gain our target polymer, 300 mL of 5% (W/V) NaOH solution was used to dissolve 12 g of the β-CD/epichlorohydrin copolymer, and then, 12 g of monochloroacetic acid was added gently. The mixture was vigorously stirred for 24 h. Excess NaOH was neutralized by adding 2 M HCl

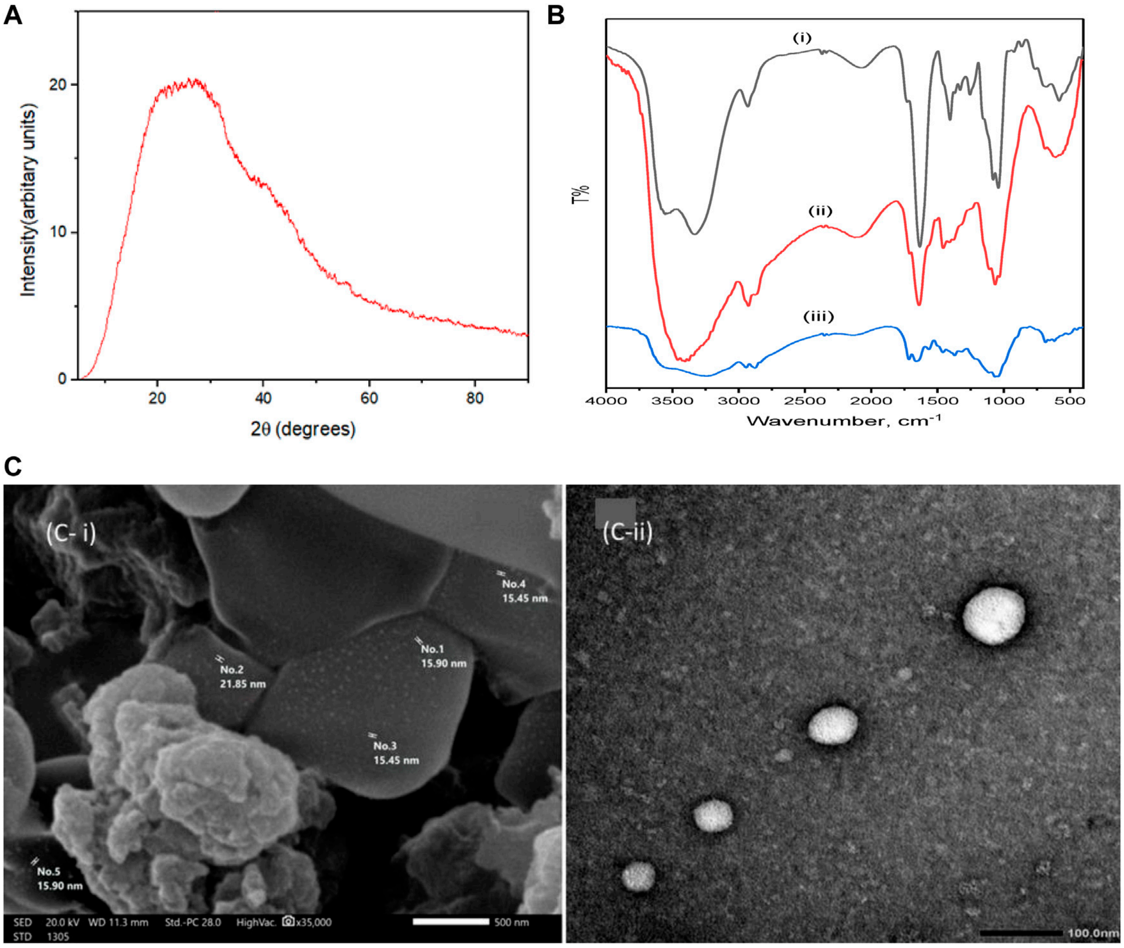

FIGURE 1
X-ray diffraction pattern of (CM-βCD:nChi:Glu), **(A)**, FTIR spectra of CM-βCD **(B i)**, CM-βCD:nChi:Glu **(B ii)**, and CM-βCD:nChi:Glu- after adsorption **(B iii)**, SEM image **(C i)** and TEM image of CM-βCD:nChi:Glu **(C ii)**.

dropwise until neutral pH. The mixture was cooled to 4°C after being concentrated to 45 mL using an ice bath. It was filtered to remove the precipitated NaCl. Hence, the supernatant was precipitated by stirring vigorously with cold ethanol. Finally, a highly pure yield of CM-βCD was obtained by washing several times with ethanol.

2.2.2 Synthesis of nanochitosan

Nanochitosan was prepared as in the literature (Taghizadeh et al., 2019) with some modifications. 2.0 g of chitosan was dissolved in 200 mL of 25% aqueous acetic acid solution and stirred for 24 h at room temperature till the solution became clear (solution A). 1.0 g of trisodium citrate was dissolved in 100.0 mL of deionized water (solution B). Solution B was gradually added to solution A, with constant stirring till a pale yellow nanochitosan solution was formed.

2.2.3 Synthesis of carboxymethyl β-cyclodextrin–nanochitosan–glutaraldehyde terpolymer

CM-CD polymer (0.7506 g) was dissolved in 35.0 mL of 8.6 × 10^{-2} M acetic acid, then 25.0 mL of nanochitosan solution was added, and the mixture was stirred overnight. The mixture turned into gel by rapid addition of 25.12 mL of 25% (w/v) glutaraldehyde. After 1.5 h of continuous stirring, the temperature was raised to 60°C and the mixture was continuously stirred for another 2 h to complete the reaction. A dark orange-yellow hydrogel was obtained that was washed several times with deionized water and finally dried after about 2 h at 50°C (Wilson et al., 2013).

2.2.4 Batch adsorption method for removal of acid red 37 dye from aqueous medium

Batch adsorption experiments were followed to study the adsorption behavior of the synthesized composite (CM-βCD:nChi:Glu) toward acid red 37 dye in terms of i) pH, ii) contact time, iii) initial dye concentration, iv) the adsorbent dosage, and v) temperature. Each parameter was investigated at least thrice to ensure consistent results. The concentrations of the remaining pollutant (acid red 37 dye) were determined by measuring the dye absorbance before and after the adsorption process, using a UV-Vis spectrophotometer at a wavelength of 504 nm. 250 mg/L of acid red 37 dye was prepared as the stock solution, and different concentrations were obtained by diluting in deionized water.

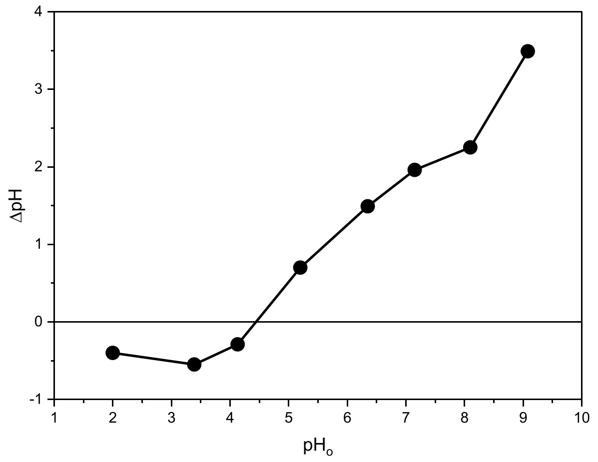

FIGURE 2
Point of zero charge of CM-βCD:nChi:Glu.

The adsorption capacity of acid red 37 dye on the adsorbent (CM-βCD:nChi:Glu) was determined using Equation 1 (Mittal et al., 2009)

$$q_e = \frac{(C_0 - C_e)\,V}{m} \tag{1}$$

where q_e is the amount of dye (mg) that is adsorbed by 1.0 g of the adsorbent, C_O and C_e are the concentrations (mg/L) of the dye at zero time and equilibrium, respectively. V is the volume of dye solution in a liter, and m is the mass (g) of the adsorbent.

The batch experiments were done at 29°C at a shaking rate of 250 rpm to study the following effects:

(i) pH: the effect of pH was studied in the range of 2.0–9.3, applying 25.0 mg of CM-βCD:nChi:Glu to remove 102.0 mg/L of the polluting dye in 50 mL solution. 1.0 M hydrochloric acid and 1.0 M sodium hydroxide solution were used to adjust the pH using a pH meter for 10 min;
(ii) contact time: appropriate time intervals in the range of 20–600 s at the optimum pH of 6.0; the amount of acid red 37 dye was 50.0 mL of 102.0 mg/L and that of CM-βCD:nChi:Glu was 25.0 mg;
(iii) initial dye concentrations, C_O: this was studied varying from 80.30 to 214.72 mg/L at pH 6, with 25.0 mg of the adsorbent; and
(iv) adsorbent dosage: this was studied in the range 8.0–50.0 mg.

Furthermore, the effect of temperature on the adsorption process was studied in the range of 293–313 K under the optimum pH of 6.0, 50.0 mL of the dye solution (102.21 mg/L), and 25.0 mg of the adsorbent.

The removal percentage (% R) was calculated using Equation 2:

$$\%R = \frac{C_0 - C_e}{C_0} \times 100 \tag{2}$$

where C_O and C_e are the initial and equilibrium dye concentrations (mg/L).

To determine the point of zero charge (pH PZC), eight 125-mL stoppered glass bottles containing 0.1 N NaCl were prepared and adjusted to different pH values (2.0–9.3) using 0.1 N of either HCl and/or NaOH. 25.0 mg of the adsorbent (CM-βCD:nChi:Glu) was added to every bottle and the mixtures were shaken for 48 h, at room temperature, at 250 rpm shaking rate. The calculated ΔpH $(= pH_{after\,48h} - pH_0)$ was plotted *versus* the starting pH (pH_0). The pH PZC was then derived from the intersection of the resulting plot with the pH_0 axis.

The desorption experiments were examined using 50.0 mL of 1 M NaCl prepared in 60% ethanol as the eluent solution (Xing et al., 2012) and applied to the adsorbent carrying the acid red 37 dye. The adsorbent was then washed with deionized water, and the process was repeated several times. The resulting solution was examined spectroscopically every time. The recycling experiment was repeated five times.

2.3 Instrumentation

A double-beam UV-Vis spectrophotometer (T80+ UV/vis spectrometer, PG Instruments Ltd, UK) was used to measure the concentration of the dye at λ = 504 nm, while FT-IR spectra (FT-IR, KBr pellets; 3 mm thickness) were validated on a Perkin-Elmer FT-IR spectrophotometer (FT-IR 1650). Energy dispersive X-ray spectroscopy (EDX) FEI (QUANTA-250) was utilized to identify the chemical composition of the synthesized terpolymer. X-ray diffraction (XRD) analysis was used to determine the crystalline structure by (XRD-7000, Shimadzu, Japan) Cu kα radiation (λ = 1.54060 Å). The surface morphology was examined using a scanning electron microscope JEOL JSM-5300LV. The specific surface area of the adsorbents was calculated with the Brunauer–Emmett–Teller (BET) equation using a BELSORP-mini X (S/N: 149, Version 1.0.9.0). The zeta potential (ζ-potential) measurements of the diluted samples were determined using a Zetasizer (NANO, μV, APS) software v7.13.

3 Results and discussion

3.1 Characterization of synthesized terpolymer nano-adsorbent CM-βCD:nChi:Glu

The XRD spectrum of the amorphous structure of the nanocomposite CM-βCD:nChi:Glu is shown in Figure 1i. The spectral pattern reflects the amorphous nature of the cross-linked terpolymer (Mohamadi Zahedi and Mansourpanah, 2018; Yang et al., 2020).

The FTIR spectra of CM-βCD and CM-βCD:nChi:Glu terpolymer in the 400–4,000 cm^{-1} wave number range are shown in Figure 1ii. The spectrum of CM-βCD exhibits bands at 3,330; 2,930; 1,634; and 1,405 cm^{-1} attributed to ν_{OH}, ν_{CH}, $\nu_{asy\ C=O}$, and $\nu_{sy\ C=O}$, respectively. The bands at 1,060 and 1,040 cm^{-1} are attributed to ν C–O. The spectrum of CM-βCD:nChi:Glu terpolymer shows a broadening in 3,100–3,550 cm^{-1} that may be attributed to the cross-linkage bonding between nanochitosan and CM-βCD. The broad band appearing at 2,927 cm^{-1} corresponds to the νCH that overlaps with the OH stretching peak (Chen and Park, 2003). The bonding between the carboxylic group of CM-βCD and the amino group of chitosan is evidenced in the shifts from 1,639 cm^{-1} and 1,457 cm^{-1} to 1,633 cm^{-1} and 1,405 cm^{-1}, respectively (Wang et al., 2016).

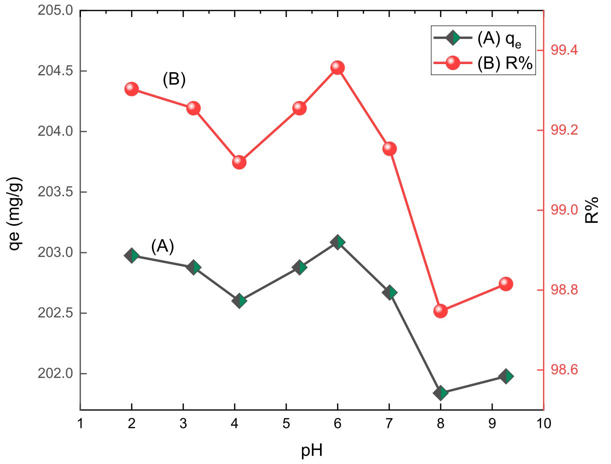

FIGURE 3
Effect of pH on **(A)** adsorption capacity (q_e) and **(B)** % removal (R%) of acid red 37 dye by CM-βCD:nChi:Glu.

The surface morphology of CM-βCD:nChi:Glu is determined by scanning electron microscopy, showing a heterogeneous surface due to the non-uniform cross-linking interactions. Figure 1Aiii shows an irregular surface structure with holes and high cavities increasing the surface area and can be the reason for the effective adsorption properties (Pu et al., 2020). The TEM image in Figure 1Biii shows the highly stable and well-dispersed spherical CM-βCD:nChi:Glu nanoparticles in the size range 30–72 nm.

CM-βCD:nChi:Glu was exposed to BET technique to determine the surface area and pore distribution *via* a nitrogen adsorption–desorption method. As can be predicted, this terpolymer shows the low specific surface area (2.903 $m^2 g^{-1}$), poor pore volume (0.002 $cm^3 g^{-1}$), and average pore diameter (3.078 nm).

The surface charge density of the adsorbent is explained based on the point of zero charges, at which the charge on the adsorbent surface is zero (Behbahani et al., 2020; Elbadawy et al., 2021). Plotting the relationship between ΔpH and pH_0, the point of zero charges was found to be 4.5 after 48 h (Figure 2). Thus, a positive charge was formed on the CM-βCD:nChi:Glu surface when the solution pH was less than the calculated zero-point charge value (4.5), while a negative charge was developed when the pH was more than 4.5. The free negative charge on the CM-CD:nChi:Glu attracts the dye, promoting the adsorption process (Islam et al., 2019). Furthermore, the zeta potential was measured and showed a surface potential of 20.8 mV, confirming the positivity of the adsorbent's surface. Also, this high positive charge reflects the electrical stability of CM-CD:nChi:Glu because the surface charge inhibits particle aggregation and becomes coagulation-resistant.

3.2 Factors affecting adsorption behavior

The adsorption behavior of the synthesized nano-composite CM-βCD:nChi:Glu toward acid red 37 dye was studied using batch adsorption techniques. The main parameters studied are i) pH, ii) contact time, iii) initial dye concentration, and iv) adsorbent dosage.

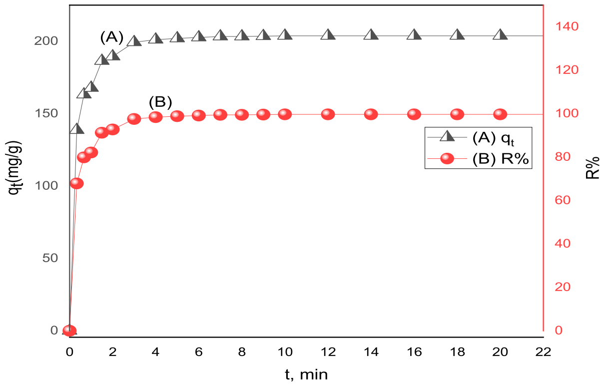

FIGURE 4
Effect of contact time on **(A)** adsorption capacity (q_t) and **(B)** % removal (R%) of acid red 37 dye on CM-βCD:nChi:Glu (25 mg of adsorbent with dye initial concentration C_o = 102.2 mg L^{-1}, the optimum pH, and shaking rate of 250 rpm).

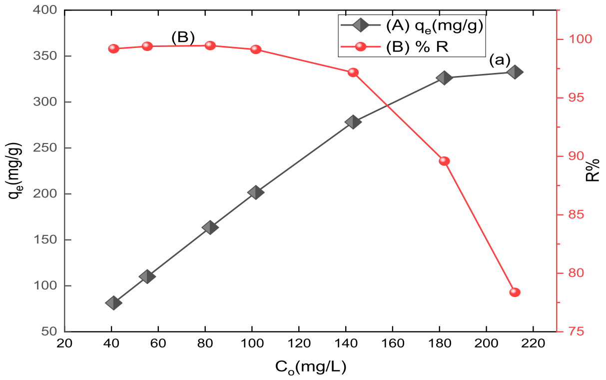

FIGURE 5
Effect of initial concentration on **(A)** adsorption capacity (q_t) and **(B)** % removal (R%) of acid red 37 dye on CM-βCD:nChi:Glu (25 mg of the adsorbent for 5.0 min and pH 6.0).

3.2.1 pH Effect

The pH of a solution is one of the essential variables affecting the adsorption process related to the adsorbate and surface characteristics of the adsorbents. The acid red 37 dye removal by CM-βCD:nChi:Glu adsorbent was explored in the pH range of 2.0–10.0 by shaking 25 mg of adsorbent with 102.2 mg L^{-1} of the dye solution for 10 min at 250 rpm. The % removal of the dye and the adsorption capacity onto CM-βCD:nChi:Glu as a function of the pH are presented in Figure 3. The highest adsorption efficiency was found at pH 6.0. Some variations in the adsorption efficiency were noticed in the applied pH range (Wu et al., 2018). This can be attributed to the pH impact of the medium on the surface charge of the adsorbent. As deduced from the zeta potential and PZC tests, the charge on the surface of the adsorbent is positive, which attracts the negatively charged dye at pH 2.0, showing relatively high

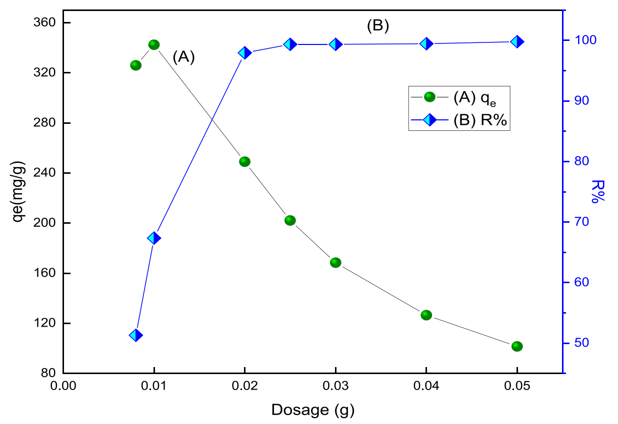

FIGURE 6
Effect of adsorbent, CM-βCD:nChi:Glu, dosage on **(A)** the adsorption capacity and **(B)** % removal (R%) of acid red 37 (102.2 mg L^{-1} dye solution for 30 min at 250 rpm and optimum pH).

adsorption of 99.3%, then a decrease is noticed till pH 4.5, where the adsorbent charge becomes zero after which its surface becomes negative, attracting the protonated dye till pH 6.0, with the highest efficiency of 99.8%. Increasing the pH of the medium stabilizes the dye and adsorbent as negatively charged species, decreasing the adsorption efficiency. Previous reports on the adsorption of anionic dyes such as methyl orange or Congo red using chi- and βCD-based adsorbents, separately or mixed, have shown that the pH of the medium has different impacts, with a higher capacity at low to moderate pH values but lower adsorption at higher pH (Ozmen and Yilmaz, 2007; Jiang et al., 2018; Jiang et al., 2020) which is consistent with the behavior of βCM-CD:nChi:Glu toward acid red 37 textile dye. However, the adsorption efficiency ranges from 98.75 to 99.36% all over the pH range of 2.0–9.3.

3.2.2 Contact time effect

The adsorption of acid red 37 dye by the synthesized adsorbent CM-βCD:nChi:Glu was investigated at different adsorption times from 20 s to 10 min. The effect of the contact time on dye adsorption onto the prepared adsorbents is displayed in Figure 4. The results indicated that the effectiveness of dye removal increases with increasing contact time until an equilibrium is achieved. An instantaneous increase in the adsorption capacity is observed up to 5.0 min, and then it slowly increases to become almost constant at 10 min with a removal efficiency of 99.67% (Jawad et al., 2021). The rapid adsorption at the beginning can be explained on the basis of the vacant active adsorption sites on CM-βCD:nChi:Glu, but eventually this slows down with time and remains almost the same. The optimum time of contact for the adsorbents was 3–5 min (Islam et al., 2019).

3.2.3 Initial dye concentration effect

The dye adsorption by CM-βCD:nChi:Glu has been carried out as a function of the initial concentration of the dye from 40.97 mg/L to 212.20 mg/L (Figure 5). Increasing the initial dye concentration led to a greater adsorption capacity for CM-βCD:nChi:Glu, but a lower percentage of removal. If more dye was present at the onset, more binding sites would become occupied, resulting in a higher adsorption capacity. It is also likely that the initial high concentration of the adsorbate molecules will result in a more direct contact between the dye and adsorbent particles. There exists the possibility that an insufficiency in the number of available active sites on the adsorbent surface could be responsible for the decrease in dye removal that occurs when the initial dye concentration is increased (Si et al., 2015).

3.2.4 Adsorbent dosage effect

The % removal of acid red 37 dye and its adsorption capacity onto the prepared adsorbent as a function of the adsorbent dosage varying from 8.0 mg to 50.0 mg are shown in Figure 6. The result reveals that the percentage removal increases as the mass of the adsorbent increases till the optimum dosage. The optimum dosage that can be used for the adsorption process is 25 mg for CM-βCD:nChi:Glu. On the other hand, the adsorption capacity decreases relative to the dosage of the adsorbent. The increase in adsorption removal efficiency with increasing dosage of the adsorbents is expected due to the availability of additional surface area in the adsorption process. Moreover, no significant increment in adsorption is observed after the addition of a certain amount of the adsorbent, and this point is known as the optimum dose (25 mg). This is because of the equilibrium condition as the number of dye anions attached to the surface of the adsorbent and the number of mobile anions remains constant. Hence, any further addition of the adsorbent does not change adsorption significantly (Abdulhameed et al., 2019).

3.3 Adsorption kinetics

The adsorption kinetics of acid red 37 dye onto the surface of the synthesized adsorbent CM-βCD:nChi:Glu was investigated at a pH of 6.0°C and temperature of 29°C, applying the pseudo–first- and second-order, Elovich, and intraparticle diffusion kinetic models (Ho and Mckay, 1999; Yuh-Shan, 2004; Priscila et al., 2013; Wang et al., 2019). Supplementary Table S1 summarizes the examined adsorption kinetic models in Supplementary Equations S1–S4.

To determine whether the type of adsorption is physio-sorption or chemisorption, the pseudo–first-order and second-order kinetic models are applied. Figures 7A, B shows the experimentally determined values of rate constants K_1 and K_2 obtained from plotting the two models. The second-order model appears to be more favorable for the dye adsorption process, indicating its chemical adsorption by CM-βCD:nChi:Glu (Eltaweil et al., 2020). The K_1 and K_2 values for CM-βCD:nChi:Glu and the other parameters obtained from the linear form of pseudo–first-order and second-order are listed in Table 1.

In addition, the Elovich kinetic model is examined to identify if the adsorption mechanism is chemisorption. The chemisorption mechanism usually involves energetically heterogeneous adsorbent surfaces. The Elovich constants (initial adsorption rate, α: 115.9 mg g^{-1} min^{-1} and the surface coverage and activated energy, β: 0.0201 g mg^{-1}) give an insight into the energetic heterogeneity of the surface (Figure 7C).

Furthermore, the adsorption of the targeted material onto the active sites of the adsorbent, mass transfer across the liquid film surrounding the surface, and intra-particle diffusion onto the pores of the surface make up the three stages of the intra-particle diffusion

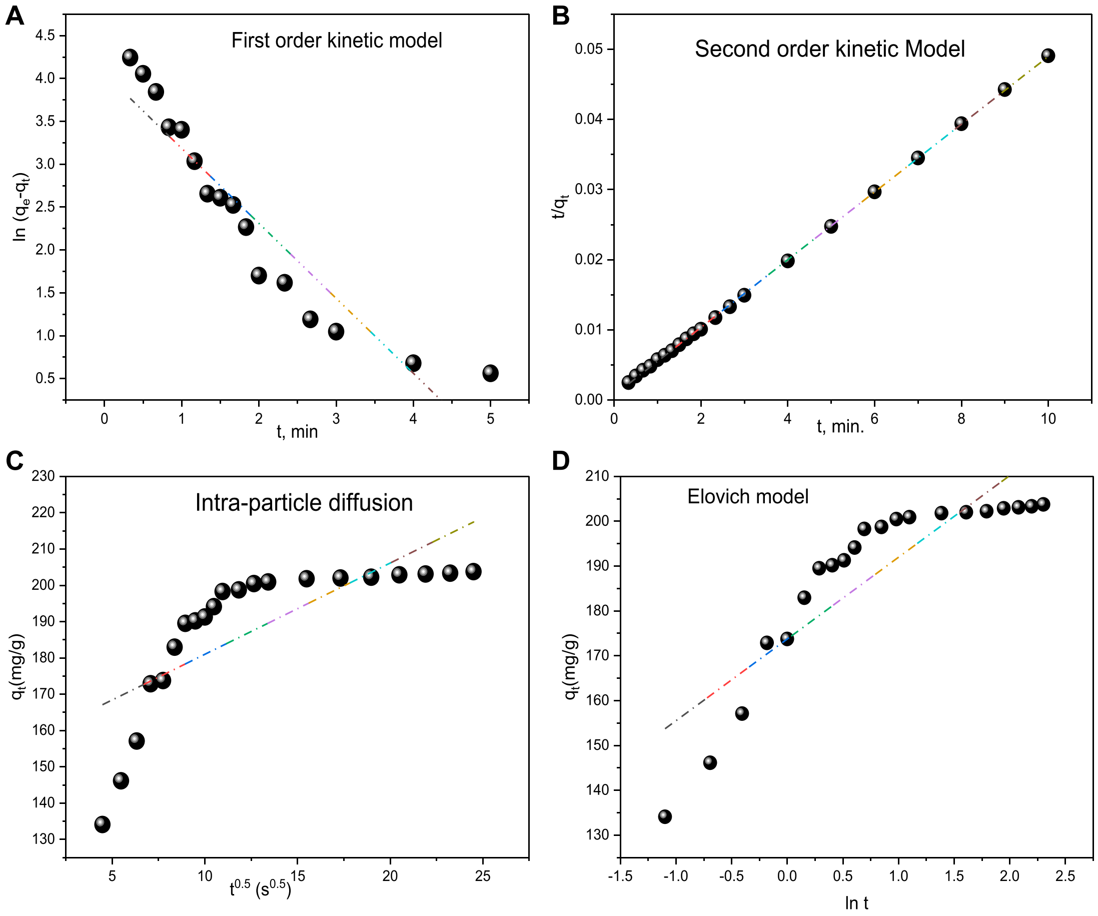

FIGURE 7
Kinetic models **(A)** First order kinetic model, **(B)** Second order kinetic model, **(C)** Intra-particle diffusion and **(D)** Elovich model for acid red 37 dye adsorption onto CM-βCD:nChi:Glu.

TABLE 1 Kinetic parameters of the sorption of acid red 37 dye by CM-βCD:nChi:Glu.

Kinetic model	Parameters		Equation
Pseudo–first order	q_e (mg g^{-1}) (Exp./Calc.)	203.76/57.92	$y = -0.8745x + 4.0592$
	k_1 (min^{-1})	0.876	$R^2 = 0.8852$
Pseudo–second order	q_e (mg g^{-1}) (Exp./Calc.)	203.76/208.33	$y = 0.0048x + 0.0007$
	k_2 (g mg^{-1} min^{-1})	3.2×10^{-2}	$R^2 = 0.9998$
Elovich	β (g mg^{-1})	0.0549	$y = 18.221x + 173.74$
	α(mg g^{-1} min^{-1})	2.5×10^5	$R^2 = 0.775$
Intra-particle diffusion	C_i (mg g^{-1})	155.84	$y = 2.5146x + 155.84$
	k_{id} (mg g^{-1} $min^{-0.5}$)	19.48	$R^2 = 0.5715$

C_i; External film resistance.

model. The processes that make use of the active sites in the adsorbents are thought to go faster. Now, if the model fits, the plot of q_t *versus* $t^{0.5}$ should show a straight line, either i) passing through the origin, when the intra-particle diffusion is the only controlling step or ii) with an intercept with the *y*-axis (Figure 7C) (Özer et al., 2006; Singh et al., 2012; Haerifar and Azizian, 2013). However, after fitting the data to the intra-particle diffusion model, a multi-linear plot was seen, indicating that intra-particle diffusion and bulk-to-surface transit of acid red 37 dye interact together producing the observed response. Intra-particle diffusion is not the rate-limiting phase since the plot does not pass through the origin. k_{id} and C_i were found to be 2.514 mg g^{-1} $s^{-0.5}$ and 155 mg g^{-1}, respectively.

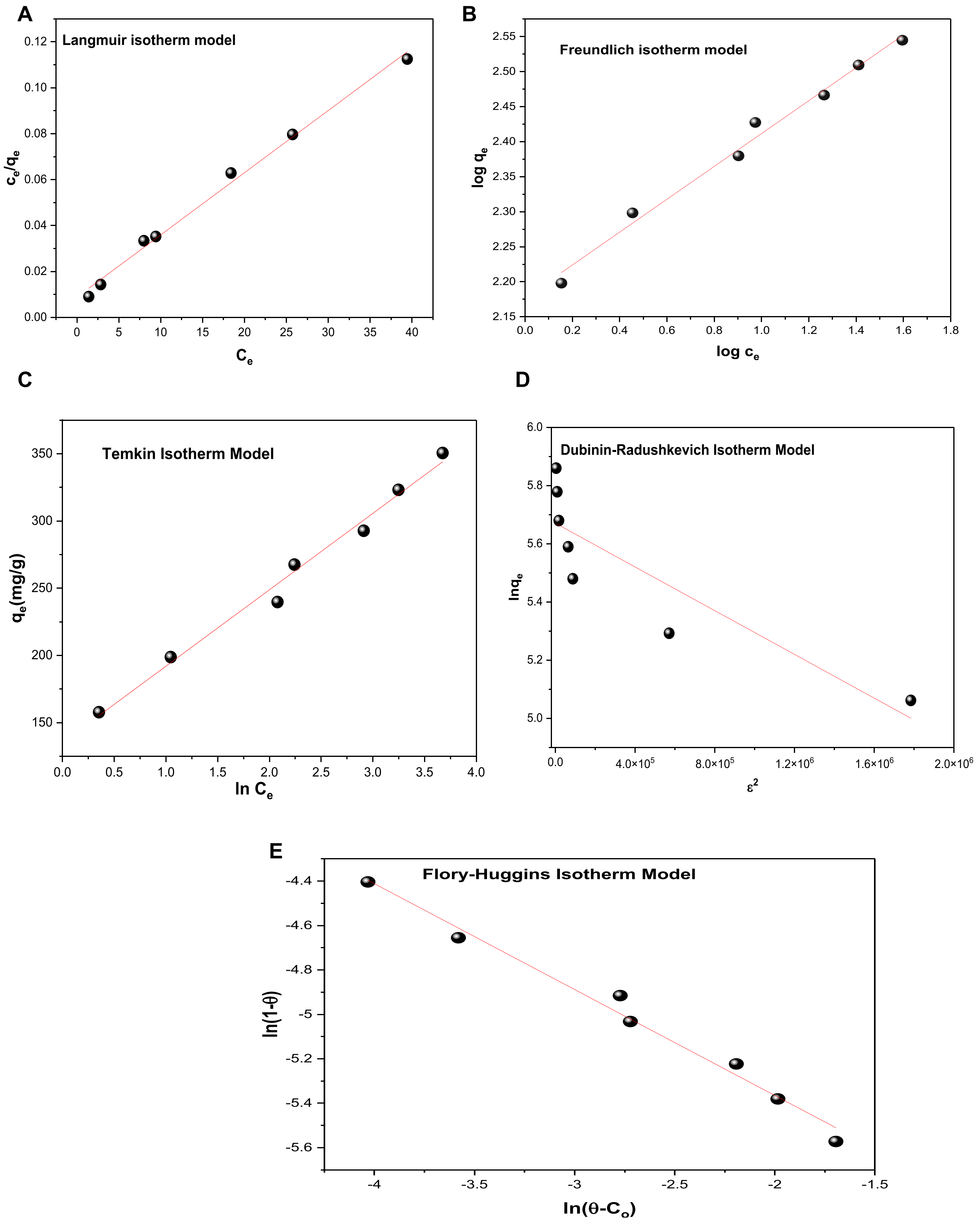

FIGURE 8
Isotherm models **(A)** Langmuir isotherm model, **(B)** Freundlich isotherm model, **(C)** Temkin isotherm model, **(D)** Dubinin–Radushkevich isotherm model and **(E)** Flory–Huggins isotherm model for dye adsorption onto CM-βCD:nChi:Glu.

3.4 Adsorption equilibrium isotherm models

The adsorption isotherm models are applied to relate the equilibrium and adsorbed concentrations of acid red 37 dye (Figure 8) and thus estimate the adsorption efficiency of the adsorbent CM-βCD:nChi:Glu. The linear equations of the applied isotherm models are given in Supplementary Table S2, expressed as Supplementary Equations S5–S9.

TABLE 2 Adsorption isotherm parameters of the sorption of acid red 37 dye by CM-βCD:nChi:Glu.

Isotherm model	Parameters		Equation
Langmuir	q_m (mg g^{-1})	370.37	y = 0.0027x + 0.0088
	K_L (Lmg^{-1})	0.3068	R^2 = 0.9933
	R_L	(0.0390–0.0149)	—
Freundlich	1/n	0.2345	y = 0.2345x + 2.1771
	K_F	150.349	R^2 = 0.987
Temkin	$ß_T$ (J mol^{-1})	44.608	y = 56.846x + 135.11
	K_T (L g^{-1})	10.770	R^2 = 0.9874
Dubinin–Radushkevich	q_m (mg g^{-1})	290.122	y = −4.0 × 10^{-7}x + 5.6703
	$ß_{DR}$ (mol^2/J^2)	4.0 × 10^{-7}	R^2 = 0.773
	E (J mol^{-1})	1,118.034	—
Flory–Huggins	n_{FH}	−0.4766	y = −0.4766x − 6.3182
	k_{FH} ($Lmol^{-1}$)	0.0018	R^2 = 0.9848
	ΔG°($Jmol^{-1}$)	−15863.91	—

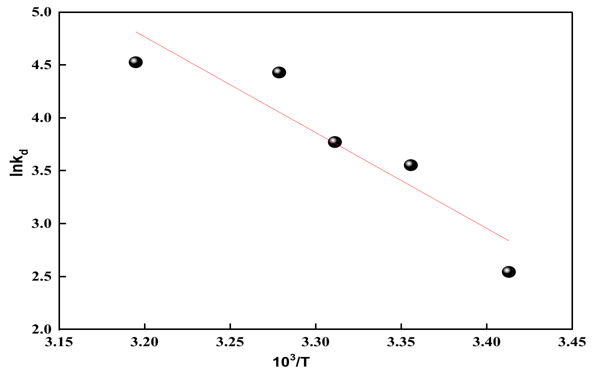

FIGURE 9
Representation of Van't Hoff equation for acid red 37 dye adsorption onto CM-βCD:nChi:Glu.

The values of the correlation coefficients R^2 of the linear plots of the applied models are typically compared for the evaluation of the best fit (Table 2). The R^2 values can be arranged as: Langmuir > Freundlich> Temkin > Flory–Huggins > Dubinin–Radushkevich.

From the Langmuir isotherm model, the values of the maximum adsorption capacity ($q_{m)}$ and Langmuir isotherm constant ($K_{L)}$ were calculated to be 370.37 mg g^{-1} and 0.3068 L mg^{-1}, respectively. The equilibrium parameter R_L = (0.0390–0.0149) values postulate an advantageous adsorption behavior of the CM-βCD:nChi:Glu adsorbent toward the acid red 37 dye, leading to the assumption that sorption sites are energetically equivalent, and the acid dye removal occurs on a homogeneous surface by monolayer adsorption. The Freundlich model was also applied, and the experimental results revealed a linear association between log q_e and log C_e; the adsorption intensity (1/n) = 0.2345 < 1 (n = 4.264) and adsorption capacity (K_f) = 150.35 mg/g.

In order to examine if the adsorption possesses a uniform bond energy distribution, the Temkin isotherm model was applied (Tempkin and Pyzhev, 1940). With values of the Temkin isotherm constant (K_{Te}) and Temkin constant related to the heat of sorption (b_{Te}) being 10.77 L g^{-1} and 44.61 J mol^{-1}, respectively, the Temkin isotherm fits the adsorption process well.

On the other hand, Dubinin–Radushkevich isotherm shows R^2 is equal to 0.773, which is less fitting with the experimental data. While the Flory–Huggins model (Supplementary Equation S11) is better fitting with R^2 equal to 0.9848, with the Flory–Huggins constants (n_{FH}, k_{FH}) being equal to −0.4766 and 0.0643 $Lmol^{-1}$, respectively, and the ΔG° value being −15863.91 $Jmol^{-1}$. The Flory–Huggins isotherm describes the adsorbate's surface coverage patterns on the adsorbent.

3.5 Thermodynamics of acid red dye adsorption

The thermodynamic parameters such as the change in free energy ΔG°, kJ/mole; change in enthalpy ΔH°, kJ/mole; and change in entropy ΔS°, kJ/mole/K) provide valued information about the type and mechanism of the adsorption process. The change in Gibbs free energy (ΔG°) of an adsorption process denotes its spontaneity. A negative ΔG° value indicates spontaneous adsorption. Equations applied to deduce the thermodynamic parameters are given in Supplementary Table S3, expressed as Supplementary Equations S10–S12 (Dizge et al., 2008; Tanhaei et al., 2019).

By applying the Van 't Hoff equation (Supplementary Equation S13) in plotting ln K_d against 1/T as shown in Figure 9, a straight line is obtained with a slope equal to ΔH°/R and an intercept of ΔS°/R (Anush and Vishalakshi, 2019). Table 3 presents the thermodynamic parameters for acid red 37 dye adsorption onto the CM-βCD:nChi:Glu adsorbent studied at the temperature range

TABLE 3 Thermodynamic parameters for dye adsorption onto CM-βCD:nChi:Glu.

Temperature (K)	$\ln K_d$	ΔG° ($KJmol^{-1}$)	ΔH° ($KJmol^{-1}$)	ΔS° ($Jmol^{-1}K^{-1}$)
293	2.543	−6.195	75.289	280.556
298	3.552	−8.800		
302	3.771	−9.469		
305	4.429	−11.230		
313	4.525	−11.775		

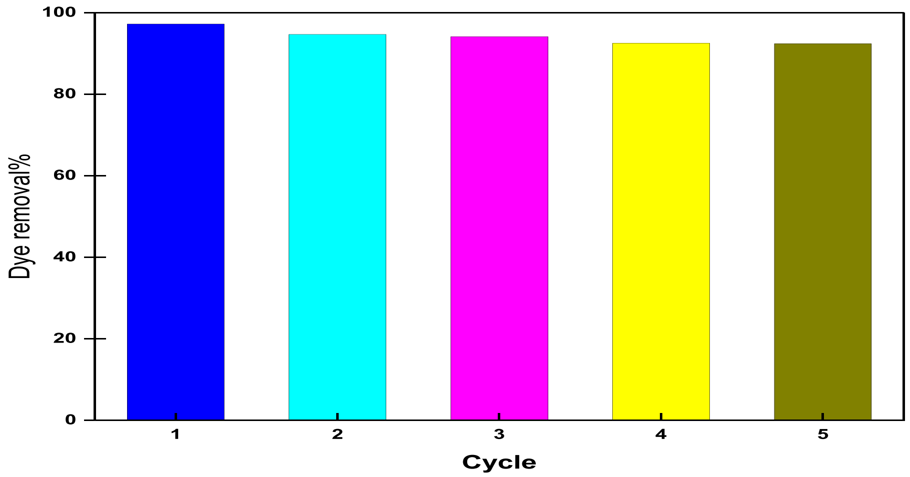

FIGURE 10
Reusability of CM-βCD:nChi:Glu for the adsorption of acid red dye 37 (dye concentration, 102.21 mg L^{-1}; adsorbent dose, 0.025 g; time, 5 min; volume of dye solution, 50 mL; the optimum pH, and shaking rate, 250 rpm).

293–313 K. The negative values of ΔG° indicate the spontaneous nature of the adsorption processes, which are adjusted by chemical adsorption, whereas decreases in ΔG° with rising temperatures show more favorable adsorption at higher temperatures. Also, the positive values of ΔH° and ΔS° reflect endothermic adsorption with additional randomness states existing at the solid–liquid interfaces.

3.6 Desorption and reusability study

From the point of view of economical, ecological, and material science, the reusability of adsorbents is a fundamental issue. Consequently, it is desirable to adsorb pollutants and regenerate the adsorbent for many cycles. Desorption is accomplished by incubating the terpolymer adsorbent with a solution of 60% ethanol and 1 M NaCl for 20 min; the regenerated adsorbents are then washed many times with distilled water. The regenerated adsorbents were used for five successive adsorption–desorption cycles and are presented in Figure 10. It has been observed that the dye removal efficiency of CM-βCD:nChi:Glu after five cycles decreased from 97.2 to 92.4%. This decrease may be attributed to the possibility of breakage of the polymer chains as a result of repeated base treatment during the reusability process. Since the examined acid red 37 dye is of the anionic type, CM-βCD:nChi:Glu can be considered an efficient adsorbent for anionic dyes.

3.7 Suggested adsorption mechanism of acid red 37 dye by CM-βCD:nChi:Glu

The adsorption mechanism of acid red 37 dye on the surface of CM-βCD:nChi:Glu is displayed in Scheme 1. A comparison between the FTIR analysis of the adsorbent before and after the adsorption process shows the interaction of acid red 37 dye with CM-βCD:nChi:Glu (Figures 1B, C, ii). The adsorbent band centered at 3425 cm^{-1} corresponds to O-H and N-H stretching, showing different features with more broadening (3,000–3,600 cm^{-1}), indicating their interactions with the adsorbed dye. Moreover, a peak appears at 1,554 cm^{-1} (Figure 1Cii), attributed to the vibration of the aromatic ring of the dye molecules. However, the adsorption mechanism could be explained by the synergistic effect of the electrostatic attraction of the amino groups from nanochitosan with host–guest interactions from β-cyclodextrin. Thus, cyclodextrin cavities are responsible for capturing organic pollutant molecules *via* the host–guest inclusion interaction (Zhao et al., 2017; Pu et al., 2020; Shi et al., 2022). Also, the negatively charged sulfonate groups ($-SO_3^-$) of acid red 37 dye facilitate electrostatic attractions with the

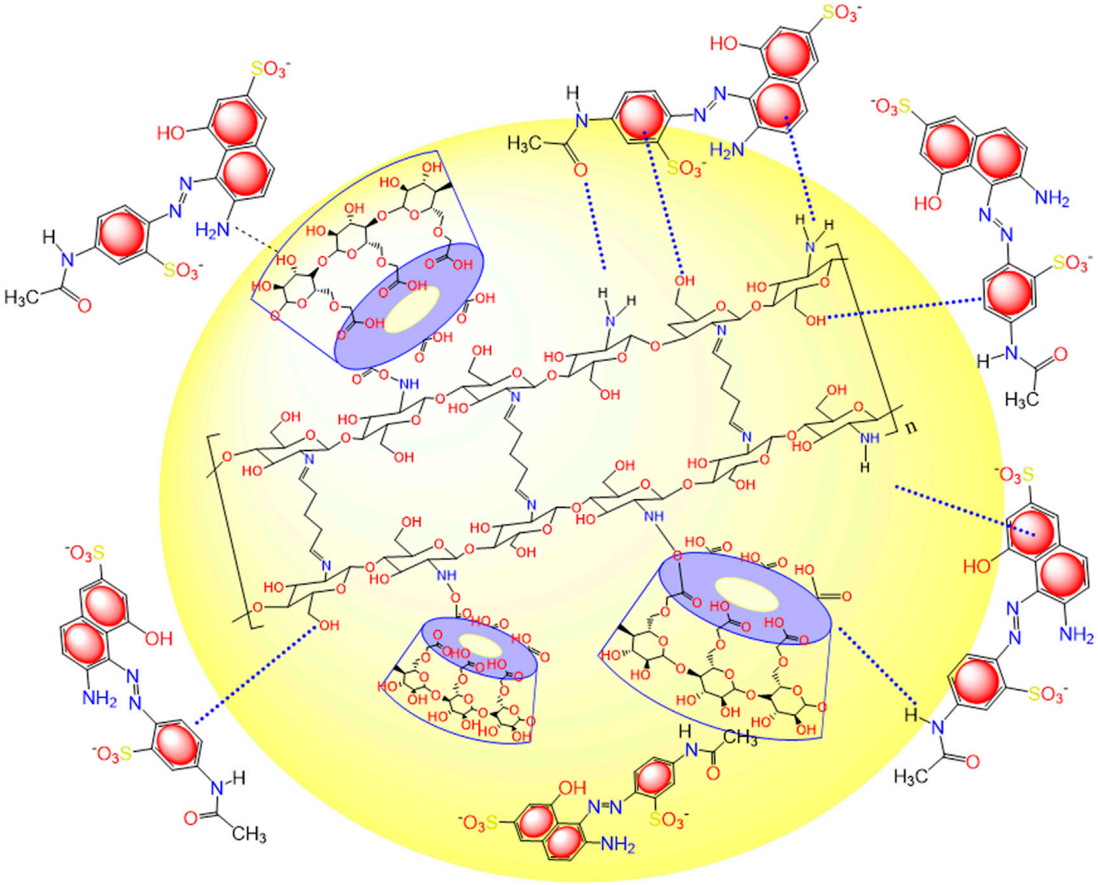

SCHEME 1
Illustration of the probable interactions between CM-βCD:nChi:Glu and acid red 37 dye.

amino and hydroxyl groups of chitosan. Moreover, other interactions may take place, but with lesser opportunity, such as dipole–dipole bonds, hydrogen bonding, electrostatic, Van der Waals, hydrophobic, n–pi interactions, and porous network capture (Jiang et al., 2020; Galan et al., 2021). We also found that the adsorption process followed pseudo–second-order kinetics, suggesting chemical sorption. The affinity of CM-βCD:nChi:Glu as the adsorbent for the acid red 37 dye was verified by negative values of free energy change (ΔG°). The high adsorption efficiency may be attributed to the triple adsorption effect of CM-βCD:nChi:Glu (Jiang et al., 2020).

4 Conclusion

Terpolymer nano-adsorbent carboxymethyl β-cyclodextrin–nanochitosan–glutaraldehyde (CM-βCD:nChi:Glu) was successfully prepared with holes and high cavities surface structure that was characterized by FTIR, XRD, SEM, TEM, BET, and zeta potential analysis. CM-βCD:nChi:Glu composite was found to be highly efficient in removing the toxic textile acid red 37 dye. Based on the results, the adsorbent dose, pH, and initial dye concentration had significant effects on dye removal. The normal pH of 6.0, adsorbent dose of 0.5 g/L, and initial dye concentration of 102.2 mg/L were found to be the optimal conditions for dye removal with an optimum contact time of only 5 min, showing a maximum removal efficiency of 99.67%. Kinetically, the dye removal fitted best with the pseudo–second-order model with a good correlation (R^2 = 0.9998). Among the applied equilibrium isothermal models, the Langmuir isotherm model showed good agreement with the experimental data, with high R^2 and maximum adsorption capacity (332.60 mg/g). The negative values of Gibbs free energy (ΔG°) calculated from the thermodynamic data indicated that the adsorption process was spontaneous in nature. The positive values of ΔH° and ΔS^{o} reflect the endothermic adsorption process with an additional randomness state. It can therefore be said that the CM-βCD:nChi:Glu terpolymer nanocomposite has high efficacy in anionic dye removal with the benefit of low cost for easier reusing or recycling for 5 cycles. The incorporation of nanochitosan in addition to the cone structure of βCD combined together by Glu gave the adsorbent splendid properties as a highly efficient adsorbent toward the acid red 37 dye which is an example of a highly toxic anionic dye.

Data availability statement

The original contributions presented in the study are included in the article/Supplementary Material; further inquiries can be directed to the corresponding author.

Author contributions

HE: conception, methodology, discussion, writing, and reviewing the article; AE-D and SE: equal contributions in conception and following and reviewing the final manuscript; SH: methodology, calculations, writing original draft; SE-K: methodology, calculations, writing results, and data; GE-G: preparation of nanochitosan.

Conflict of interest

The authors declare that the research was conducted in the absence of any commercial or financial relationships that could be construed as a potential conflict of interest.

Publisher's note

Supplementary material

The Supplementary Material for this article can be found online at: https://www.frontiersin.org/articles/10.3389/fchem.2023.1115377/full#supplementary-material

References

Abdulhameed, A. S., Mohammad, A., and Jawad, A. H. (2019). Modeling and mechanism of reactive orange 16 dye adsorption by chitosan-glyoxal/TiO2 nanocomposite: Application of response surface methodology. *Desalination Water Treat.* 164, 346–360. doi:10.5004/dwt.2019.24384

Altaher, H., Khalil, T. E., and Abubeah, R. (2014). The effect of dye chemical structure on adsorption on activated carbon: A comparative study. *Color. Technol.* 130, 205–214. doi:10.1111/cote.12086

Anush, S., and Vishalakshi, B. (2019). Modified chitosan gel incorporated with magnetic nanoparticle for removal of Cu (II) and Cr (VI) from aqueous solution. *Int. J. Biol. Macromol.* 133, 1051–1062. doi:10.1016/j.ijbiomac.2019.04.179

Azlan, K., Saime, W. N. W., and Liew, L. (2009). Chitosan and chemically modified chitosan beads for acid dyes sorption. *J. Environ. Sci.* 21, 296–302. doi:10.1016/s1001-0742(08)62267-6

Badruddoza, A., Tay, A., Tan, P., Hidajat, K., and Uddin, M. (2011). Carboxymethyl-β-cyclodextrin conjugated magnetic nanoparticles as nano-adsorbents for removal of copper ions: Synthesis and adsorption studies. *J. Hazard. Mater.* 185, 1177–1186. doi:10.1016/j.jhazmat.2010.10.029

Behbahani, E. S., Dashtian, K., and Ghaedi, M. (2020). Fe/Co-chalcogenide-stabilized Fe3O4 nanoparticles supported MgAl-layered double hydroxide as a new magnetically separable sorbent for the simultaneous spectrophotometric determination of anionic dyes. *Microchem. J.* 152, 104431. doi:10.1016/j.microc.2019.104431

Chen, X.-G., and Park, H.-J. (2003). Chemical characteristics of O-carboxymethyl chitosans related to the preparation conditions. *Carbohydr. Polym.* 53, 355–359. doi:10.1016/s0144-8617(03)00051-1

Crini, G., Lichtfouse, E., Wilson, L. D., and Morin-Crini, N. (2018). *Green adsorbents for pollutant removal*. Springer.Adsorption-oriented processes using conventional and non-conventional adsorbents for wastewater treatment

Crini, G., Torri, G., Lichtfouse, E., Kyzas, G. Z., Wilson, L. D., and Morin-Crini, N. (2019). Dye removal by biosorption using cross-linked chitosan-based hydrogels. *Environ. Chem. Lett.* 17, 1645–1666. doi:10.1007/s10311-019-00903-y

Dassanayake, R. S., Acharya, S., and Abidi, N. (2021). Recent advances in biopolymer-based dye removal technologies. *Molecules* 26, 4697. doi:10.3390/molecules26154697

Dizge, N., Aydiner, C., Demirbas, E., Kobya, M., and Kara, S. (2008). Adsorption of reactive dyes from aqueous solutions by fly ash: Kinetic and equilibrium studies. *J. Hazard. Mater.* 150, 737–746. doi:10.1016/j.jhazmat.2007.05.027

Elbadawy, H. A., Abdel-Salam, A. H., and Khalil, T. E. (2021). The impact of an Amberlite XAD-16-based chelating resin for the removal of aqueous Cd(II) and Pb(II) ions. *Microchem. J.* 165, 106097. doi:10.1016/j.microc.2021.106097

Eltaweil, A. S., Elgarhy, G. S., El-Subruiti, G. M., and Omer, A. M. (2020). Carboxymethyl cellulose/carboxylated graphene oxide composite microbeads for efficient adsorption of cationic methylene blue dye. *Int. J. Biol. Macromol.* 154, 307–318. doi:10.1016/j.ijbiomac.2020.03.122

Emara, N. A., Amin, R. M., Youssef, A. F., and Elfeky, S. A. (2020). Recycling of steel industry waste acid in the preparation of Fe3O4 nanocomposite for heavy metals remediation from wastewater. *Rev. Chim.* 71, 34–46. doi:10.37358/rc.20.12.8384

Filipkowska, U. (2012). Effectiveness of dye adsorption onto non-cross-linked and cross-linked chitosan beads. *Prog. Chem. Appl. Chitin its Deriv.* 17, 43–52.

Galan, J., Trilleras, J., Zapata, P. A., Arana, V. A., and Grande-Tovar, C. D. (2021). Optimization of chitosan glutaraldehyde-crosslinked beads for reactive blue 4 anionic dye removal using a surface response methodology. *Life* 11, 85. doi:10.3390/life11020085

Ghazimokri, H. S., Aghaie, H., Monajjemi, M., and Gholami, M. R. (2022). Removal of methylene blue dye from aqueous solutions using carboxymethyl-β-cyclodextrin-Fe3O4 nanocomposite: Thermodynamics and kinetics of adsorption process. *Russ. J. Phys. Chem. A* 96, 371–380. doi:10.1134/s0036024422020108

Haerifar, M., and Azizian, S. (2013). Mixed surface reaction and diffusion-controlled kinetic model for adsorption at the solid/solution interface. *J. Phys. Chem. C* 117, 8310–8317. doi:10.1021/jp401571m

Ho, Y.-S., and Mckay, G. (1999). Pseudo-second order model for sorption processes. *Process Biochem.* 34, 451–465. doi:10.1016/s0032-9592(98)00112-5

Hynes, N. R. J., Kumar, J. S., Kamyab, H., Sujana, J. a. J., Al-Khashman, O. A., Kuslu, Y., et al. (2020). Modern enabling techniques and adsorbents based dye removal with sustainability concerns in textile industrial sector-A comprehensive review. *J. Clean. Prod.* 272, 122636. doi:10.1016/j.jclepro.2020.122636

Ibrahim, Q., Creedon, L., and Gharbia, S. (2022). A literature review of modelling and experimental studies of water treatment by adsorption processes on nanomaterials. *Membranes* 12, 360. doi:10.3390/membranes12040360

Islam, M. N., Khan, M. N., Mallik, A. K., and Rahman, M. M. (2019). Preparation of bio-inspired trimethoxysilyl group terminated poly (1-vinylimidazole)-modified-chitosan composite for adsorption of chromium (VI) ions. *J. Hazard. Mater.* 379, 120792. doi:10.1016/j.jhazmat.2019.120792

Jawad, A. H., Abdulhameed, A. S., Wilson, L. D., Syed-Hassan, S. S. A., Alothman, Z. A., and Khan, M. R. (2021). High surface area and mesoporous activated carbon from KOH-activated dragon fruit peels for methylene blue dye adsorption: Optimization and mechanism study. *Chin. J. Chem. Eng.* 32, 281–290. doi:10.1016/j.cjche.2020.09.070

Jiang, H.-L., Xu, M.-Y., Xie, Z.-W., Hai, W., Xie, X.-L., and He, F.-A. (2020). Selective adsorption of anionic dyes from aqueous solution by a novel β-cyclodextrin-based polymer. *J. Mol. Struct.* 1203, 127373. doi:10.1016/j.molstruc.2019.127373

Jiang, Y., Liu, B., Xu, J., Pan, K., Hou, H., Hu, J., et al. (2018). Cross-linked chitosan/β-cyclodextrin composite for selective removal of methyl orange: Adsorption performance and mechanism. *Carbohydr. Polym.* 182, 106–114. doi:10.1016/j.carbpol.2017.10.097

Katheresan, V., Kansedo, J., and Lau, S. Y. (2018). Efficiency of various recent wastewater dye removal methods: A review. *J. Environ. Chem. Eng.* 6, 4676–4697. doi:10.1016/j.jece.2018.06.060

Kaur, K., and Jindal, R. (2019). Comparative study on the behaviour of Chitosan-Gelatin based Hydrogel and nanocomposite ion exchanger synthesized under microwave conditions towards photocatalytic removal of cationic dyes. *Carbohydr. Polym.* 207, 398–410. doi:10.1016/j.carbpol.2018.12.002

Li, X., Xie, L., Yang, X., and Nie, X. (2018). Adsorption behavior and mechanism of β-cyclodextrin–styrene-based polymer for cationic dyes. *RSC Adv.* 8, 40321–40329. doi:10.1039/c8ra07709f

Mittal, A., Kaur, D., Malviya, A., Mittal, J., and Gupta, V. (2009). Adsorption studies on the removal of coloring agent phenol red from wastewater using waste materials as adsorbents. *J. colloid interface Sci.* 337, 345–354. doi:10.1016/j.jcis.2009.05.016

Mohamadi Zahedi, S., and Mansourpanah, Y. (2018). Construction of chitosan-carboxymethyl β-cyclodextrin silver nanocomposite hydrogel to improve antibacterial activity. *Plastics, Rubber Compos.* 47, 273–281. doi:10.1080/14658011.2018.1475166

Özer, A., Akkaya, G., and Turabik, M. (2006). Biosorption of acid blue 290 (AB 290) and acid blue 324 (AB 324) dyes on spirogyra rhizopus. *J. Hazard. Mater.* 135, 355–364. doi:10.1016/j.jhazmat.2005.11.080

Ozmen, E. Y., and Yilmaz, M. (2007). Use of β-cyclodextrin and starch based polymers for sorption of Congo red from aqueous solutions. *J. Hazard. Mater.* 148, 303–310. doi:10.1016/j.jhazmat.2007.02.042

Pandey, S., Do, J. Y., Kim, J., and Kang, M. (2020). Fast and highly efficient removal of dye from aqueous solution using natural locust bean gum based hydrogels as adsorbent. *Int. J. Biol. Macromol.* 143, 60–75. doi:10.1016/j.ijbiomac.2019.12.002

Pourhakkak, P., Taghizadeh, A., Taghizadeh, M., Ghaedi, M., and Haghdoust, S. (2021). *Interface science and Technology*. Elsevier.Fundamentals of adsorption technology

Priscila, F., Magriotis, Z. M., Rossi, M. A., Resende, R. F., and Nunes, C. A. (2013). Optimization by response surface methodology of the adsorption of coomassie blue dye on natural and acid-treated clays. *J. Environ. Manag.* 130, 417–428. doi:10.1016/j.jenvman.2013.08.067

Pu, H., Tang, P., Zhao, L., Sun, Q., Zhai, Y., Li, Z., et al. (2020). Preparation of a carboxymethyl β-cyclodextrin polymer and its rapid adsorption performance for basic fuchsin. *RSC Adv.* 10, 20905–20914. doi:10.1039/c9ra10797e

Santos, P. B., Santos, J. J., Correa, C. C., Corio, P., and Andrade, G. F. (2019). Plasmonic photodegradation of textile dye reactive black 5 under visible light: A vibrational and electronic study. *J. Photochem. Photobiol. A Chem.* 371, 159–165. doi:10.1016/j.jphotochem.2018.11.005

Senousy, H. H., Khairy, H. M., El-Sayed, H. S., Sallam, E. R., El-Sheikh, M. A., and Elshobary, M. E. (2022). Interactive adverse effects of low-density polyethylene microplastics on marine microalga Chaetoceros calcitrans. *Chemosphere* 311, 137182. doi:10.1016/j.chemosphere.2022.137182

Shi, Y., Chang, Q., Zhang, T., Song, G., Sun, Y., and Ding, G. (2022). A review on selective dye adsorption by different mechanisms. *J. Environ. Chem. Eng.* 10, 108639. doi:10.1016/j.jece.2022.108639

Shin, H., Tiwari, D., and Kim, D.-J. (2020). Phosphate adsorption/desorption kinetics and P bioavailability of Mg-biochar from ground coffee waste. *J. Water Process Eng.* 37, 101484. doi:10.1016/j.jwpe.2020.101484

Si, J., Yuan, T.-Q., and Cui, B.-K. (2015). Exploring strategies for adsorption of azo dye Congo Red using free and immobilized biomasses of Trametes pubescens. *Ann. Microbiol.* 65, 411–421. doi:10.1007/s13213-014-0874-3

Singh, S. K., Townsend, T. G., Mazyck, D., and Boyer, T. H. (2012). Equilibrium and intra-particle diffusion of stabilized landfill leachate onto micro- and meso-porous activated carbon. *Water Res.* 46, 491–499. doi:10.1016/j.watres.2011.11.007

Subramani, S., and Thinakaran, N. (2017). Isotherm, kinetic and thermodynamic studies on the adsorption behaviour of textile dyes onto chitosan. *Process Saf. Environ. Prot.* 106, 1–10. doi:10.1016/j.psep.2016.11.024

Taghizadeh, M. T., Ashassi-Sorkhabi, H., Afkari, R., and Kazempour, A. (2019). Cross-linked chitosan in nano and bead scales as drug carriers for betamethasone and tetracycline. *Int. J. Biol. Macromol.* 131, 581–588. doi:10.1016/j.ijbiomac.2019.03.094

Tang, P., Sun, Q., Zhao, L., Pu, H., Yang, H., Zhang, S., et al. (2018). Mesalazine/hydroxypropyl-β-cyclodextrin/chitosan nanoparticles with sustained release and enhanced anti-inflammation activity. *Carbohydr. Polym.* 198, 418–425. doi:10.1016/j.carbpol.2018.06.106

Tanhaei, B., Ayati, A., and Sillanpää, M. (2019). Magnetic xanthate modified chitosan as an emerging adsorbent for cationic azo dyes removal: Kinetic, thermodynamic and isothermal studies. *Int. J. Biol. Macromol.* 121, 1126–1134. doi:10.1016/j.ijbiomac.2018.10.137

Tempkin, M., and Pyzhev, V. (1940). Kinetics of ammonia synthesis on promoted iron catalyst. *Acta Phys. Chim. USSR* 12, 327.

Wang, A., Jin, W., Chen, E., Zhou, J., Zhou, L., and Wei, S. (2016). Drug delivery function of carboxymethyl-β-cyclodextrin modified upconversion nanoparticles for adamantine phthalocyanine and their NIR-triggered cancer treatment. *Dalton Trans.* 45, 3853–3862. doi:10.1039/c5dt04900h

Wang, D., Chen, G., Li, X., and Jia, Q. (2019). Hypercrosslinked β-cyclodextrin porous polymer as adsorbent for effective uptake towards albendazole from aqueous media. *Sep. Purif. Technol.* 227, 115720. doi:10.1016/j.seppur.2019.115720

Wilson, L. D., Pratt, D. Y., and Kozinski, J. A. (2013). Preparation and sorption studies of β-cyclodextrin–chitosan–glutaraldehyde terpolymers. *J. colloid interface Sci.* 393, 271–277. doi:10.1016/j.jcis.2012.10.046

Wu, D., Hu, L., Wang, Y., Wei, Q., Yan, L., Yan, T., et al. (2018). EDTA modified β-cyclodextrin/chitosan for rapid removal of Pb(II) and acid red from aqueous solution. *J. Colloid Interface Sci.* 523, 56–64. doi:10.1016/j.jcis.2018.03.080

Wu, F.-C., Tseng, R.-L., and Juang, R.-S. (2010). A review and experimental verification of using chitosan and its derivatives as adsorbents for selected heavy metals. *J. Environ. Manag.* 91, 798–806. doi:10.1016/j.jenvman.2009.10.018

Yang, Y., Liu, Y., Chen, S., Cheong, K.-L., and Teng, B. (2020). Carboxymethyl β-cyclodextrin grafted carboxymethyl chitosan hydrogel-based microparticles for oral insulin delivery. *Carbohydr. Polym.* 246, 116617. doi:10.1016/j.carbpol.2020.116617

Yuan, J., Qiu, F., and Li, P. (2017). Synthesis and characterization of β-cyclodextrin–carboxymethyl cellulose–graphene oxide composite materials and its application for removal of basic fuchsin. *J. Iran. Chem. Soc.* 14, 1827–1837. doi:10.1007/s13738-017-1122-0

Yuh-Shan, H. (2004). Citation review of Lagergren kinetic rate equation on adsorption reactions. *Scientometrics* 59, 171–177. doi:10.1023/b:scie.0000013305.99473.cf

Zaimee, M. Z. A., Sarjadi, M. S., and Rahman, M. L. (2021). Heavy metals removal from water by efficient adsorbents. *Water* 13, 2659. doi:10.3390/w13192659

Zhao, F., Repo, E., Yin, D., Chen, L., Kalliola, S., Tang, J., et al. (2017). One-pot synthesis of trifunctional chitosan-EDTA-β-cyclodextrin polymer for simultaneous removal of metals and organic micropollutants. *Sci. Rep.* 7, 15811–15814. doi:10.1038/s41598-017-16222-7

frontiers | Frontiers in Chemistry

TYPE Review
PUBLISHED 09 February 2023
DOI 10.3389/fchem.2023.1036715

Recent advances in lanthanide-doped up-conversion probes for theranostics

Danyang Xu†, Chenxu Li†, Wenjing Li†, Bi Lin and Ruichan Lv*

Engineering Research Center of Molecular and Neuro Imaging, Ministry of Education, School of Life Science and Technology, Xidian University, Xi'an, Shaanxi, China

OPEN ACCESS

EDITED BY
Preston Todd Snee,
University of Illinois at Chicago,
United States

REVIEWED BY
Yahong Jin,
Guangdong University of Technology,
China
Mikhail Zamkov,
Bowling Green State University,
United States

*CORRESPONDENCE
Ruichan Lv,
✉ rclv@xidian.edu.cn

†These authors have contributed equally to this work

SPECIALTY SECTION
This article was submitted to
Nanoscience,
a section of the journal
Frontiers in Chemistry

RECEIVED 05 September 2022
ACCEPTED 31 January 2023
PUBLISHED 09 February 2023

CITATION
Xu D, Li C, Li W, Lin B and Lv R (2023), Recent advances in lanthanide-doped up-conversion probes for theranostics. *Front. Chem.* 11:1036715.
doi: 10.3389/fchem.2023.1036715

Up-conversion (or anti-Stokes) luminescence refers to the phenomenon whereby materials emit high energy, short-wavelength light upon excitation at longer wavelengths. Lanthanide-doped up-conversion nanoparticles (Ln-UCNPs) are widely used in biomedicine due to their excellent physical and chemical properties such as high penetration depth, low damage threshold and light conversion ability. Here, the latest developments in the synthesis and application of Ln-UCNPs are reviewed. First, methods used to synthesize Ln-UCNPs are introduced, and four strategies for enhancing up-conversion luminescence are analyzed, followed by an overview of the applications in phototherapy, bioimaging and biosensing. Finally, the challenges and future prospects of Ln-UCNPs are summarized.

KEYWORDS

lanthanide-doped, probes for theranostics, up-conversion, up-conversion luminescence, biomedicine

1 Introduction

Rare earth-based nanomaterials have attracted attention due to their superior fluorescence properties. Because of their dense energy levels that enable complex electronic transitions, rare Earth elements have become a treasure house of luminescence (Li et al., 2015a; Binnemans, 2015). Rare earth-based nanomaterials require specific wavelength of excitation to photoluminese (Tsang et al., 2015; Adachi, 2018; Quan et al., 2018; Mintz et al., 2019; Mir et al., 2020; Gierschner et al., 2021). The emission can be characterized as up-conversion or downconversion luminescence (Reddy et al., 2018). For example, Ln- UCNPs can be excited by infrared light to emit visible light. If modified properly, they can become good candidates for tumor diagnosis and treatment.

Phototherapy (PT) (Li et al., 2018; Lan et al., 2019; Zhen et al., 2019; Xie et al., 2020), as a new type of treatment with good targeting and low toxicity, is often classified as photodynamic therapy (PDT) or photothermal therapy (PTT). Phototherapy is gradually becoming an important supplement for tumor treatment. Therefore, Ln-UCNPs can serve as a substrate for composition with other materials for phototherapy, to aid surgical navigation, to enhance the precision of imaging, and for efficient treatment (Shanmugam et al., 2014; Liu et al., 2019a).

In addition to therapy, Ln-UCNPs also have potential for use in bioimaging and biosensing (Zhang et al., 2016; Zhang et al., 2019). Functionalized Ln-UCNPs can be applied in Computed Tomography (CT) and Magnetic Resonance Imaging (MRI) among others, which adds value to the bioimaging field (Zhang et al., 2011; Sun et al., 2013; Li et al., 2019). Regardless, Ln-UCNP-based biological imaging has shortcomings and there is significant room for improvement. Ln-UCNPs also perform well in biosensing (Guo

TABLE 1 **Typical methods of Ln-UCNPs synthesis (Li and Lin, 2010; Du et al., 2011; Lin et al., 2012).**

Method	Morphology	Reaction condition	Product stability	Synthetic cost
Thermal decomposition	Controllable	Harsh	Stable	Higher
Hydrothermal/solvothermal	Controllable	Simple	Stable	Lower
Co-precipitation	Uncontrollable	Simple	Stable	Lower

et al., 2016; Mahata et al., 2017). Ln-UCNPs can be used as pH and temperature sensors as well as gas and DNA sensors, to name a few, due to temperature sensitivity and other optical properties. It is foreseeable that the use of Ln-UCNPs will expand in the sensor field (Wang et al., 2014a; Cui et al., 2014; Dong et al., 2015; Pan et al., 2017).

This manuscript reviews research on the synthesis, luminescence modulation, and the latest achievements in phototherapy, bioimaging and biosensing of Ln-UCNPs. Synthetic methods are summarized in Section 2, research on luminescence modulation is outlined in Section 3, and then applications for Ln-UCNPs in phototherapy, bioimaging and biosensing are introduced in Section 4. Finally, the current challenges of Ln-UCNPs and their prospects for the future are discussed.

2 Synthesis methods of Ln-UCNPs

Many challenges concerning the morphology and performance of Ln-UCNPs must be addressed for successful application in biomedicine. Fortunately, many kinds of Ln-UCNPs have been synthesized that enable the potential for applications. Rare Earth luminescent materials have attracted much attention because of their flexibility and easy modulation. Different nanoparticles can be synthesized by controlling the reaction conditions; these include the temperature, pH, precursor concentrations, etc. Researchers have successively realized several luminescence mechanisms such as excited state absorption (ESA), energy transfer up-conversion (ETU), cooperative sensitization up-conversion (CSU), photon avalanche (PA), and energy transfer-mediated up-conversion (EMU). This section introduces the most common methods, specifically thermal decomposition and hydrothermal/solvothermal, as well as several other synthetic approaches. A brief comparison of these methods is provided in Table 1.

2.1 Thermal decomposition method

The thermal decomposition method is the most facile to create high-quality Ln-UCNPs. Thermal decomposition is the process of pyrolyzing organometallic precursors in an organic solvent under an oxygen-free environment. In general, the precursors are organic salts of rare Earth ions, such as trifluoroacetate and acetate among others. Octadecene (ODE) is the most frequently used high-boiling organic solvent. Oleic acid (OA) and oleylamine (OM) can serve dual roles as solvents and as ligands that adsorbed onto the nanoparticles to control their size and shape. It is worth noting that the crystal nucleation and growth process that control the nanoparticle uniformity can be adjusted with the temperature, heating rate, and precursor concentrations during synthesis.

Yan and co-authors first synthesized LaF_3 crystals by thermal decomposition using a single-source precursor (Zhang et al., 2005). Later they pioneered the use of multi-source precursors to prepare high quality nanocrystals through thermal decomposition, which greatly promoted the development of Ln-UCNPs (Yin et al., 2010). Murray and collaborators studied the influence of reaction time and the ratio of sodium to lanthanide precursors on the morphology of β-$NaYF_4$-based Ln-UCNPs in detail, thereby obtaining beautiful rare earth-based nanocrystals (Ye et al., 2010). We applied $LnCl_3$ (Ln = Y and Er) as precursors in an OA and ODE mixture that was heated to a high temperature, next NH4F and NaOH were added to obtain core nanoparticles of $NaYF_4$:Er. Finally $Lu(CF_3COO)_3$ and CF_3COONa mixed with $NaYF_4$: Er were further processed under high temperature and oxygen-free environment to obtain stable $NaYF_4$:x%Er@NaLuF4 (Feng et al., 2018).

Ln-UCNPs synthesized using the thermal decomposition method are highly monodisperse and uniform in shape. They also display greater up-conversion emission intensity; however, the syntheses are complicated and the products are lipophilic and not stable, which limits the application of thermal decomposition in Ln-UCNPs synthesis.

2.2 Hydrothermal/solvothermal method

The hydrothermal/solvothermal method is facile for synthesizing Ln-UCNPs under mild conditions at a low cost. Generally, hydrothermal syntheses are carried out in a reactor to provide a high-pressure environment. Simple rare Earth nitrates or chlorides are used as precursors for the preparation of Ln-UCNPs. The most common solvents are water, ethanol, glycol and other simple hydrophilic inorganic/organic solvents (Rafique et al., 2019). Li and co-workers introduced oleic acid into solvothermal synthesis. As an oleophilic organic solvent, it broadened the range of materials and structures that can be realized using this method (Wang et al., 2005). The selection of organic additives has a significant impact on the morphology and size of the product. Hydrophilic organic ligands that can adhere to the surface of products and inhibit particle aggregation can endow the nanocrystals with good hydrophilicity, biocompatibility, and functionalizability with biomolecules. It was reported that ethylene diamine tetra acetic acid (EDTA), polyvinyl pyrrolidone (PVP), hexadecyl trimethyl ammonium bromide (CTAB) and polyacrylic acid (PAA)/poly ethylenimine (PEI) as additives improve the morphology and dispersion of Ln-UCNPs (Mousavand et al., 2010; Li et al., 2020a). A mixed solution of $Ln(NO_3)_3$, Y:Yb:Tm = 70:30:0.5, was used as a rare Earth precursor with EDTA as an organic additive. $NaYF_4$: Yb^{3+}, Tm^{3+} were synthesized by high temperature and pressure

TABLE 2 Typical cases of Ln-UCNPs for sensing.

No	Sensor system	Excitation (nm)	Emission	Sensor type	Recent advances	References
1	NaYF$_4$:Yb,Tm-T (Thymine)	980	475 nm	ECL sensor	In the presence of Hg^{2+}, the T monolayer-modified Au electrode (AuE/T) absorbed Hg^{2+}and T-Ln-UCNPs by T-Hg^{2+}-T matching. Surface-tethered T-Ln-UCNPs further recruited more Hg^{2+}, as well as T-Ln-UCNPs, thus forming a Ln-UCNPs-T-Hg^{2+}-T-Ln-UCNPs reticular architecture on the surface of the electrode	Dhal et al. (2020)
2	ssDNA-NaYF$_4$:Yb,Er@SiO$_2$	980	549, 654 nm	miRNA sensor	In the absence of complementary miRNA sequences, the ssDNA functionalized particles interact with the GQD leading to an enhancement of the up-conversion emission. In the presence of the target miRNA sequences, the hybridization process yields dsDNA on the surface of the Ln-UCNPs that hinders the interaction with GQD and reduces the up-conversion fluorescence enhancement.	Zhou et al. (2020)
3	NaLuGdF$_4$:Yb,Er-Fe^{3+}, C u^{2+}, and Li^{+}	980	543 nm	CAs sensor	It was found that catecholamines could be more effectively detected in the presence of Ln-UCNPs-Fe^{3+}, whereas, dopamine and epinephrine were detected selectively using Ln-UCNPs-Li^{+} and Ln-UCNPs-Cu^{2+} sensors.	Hu et al. (2020)
4	APTEs-NaYF4:Yb,Er-Pt	980	543 nm	TNT sensor	The Janus capsule motors were fabricated by layer-by-layer assembly of Ln-UCNPs-functionalized polyelectrolyte microcapsules, followed by sputtering of a platinum layer onto one half of the capsule.	Zhang et al. (2020)
5	NaGdF$_4$:Yb,Er@SiO$_2$–Spiropyran	980	540 nm	HIS fluorescent nanosensor	HIS could specifically bind to SP, which could cause the isomerization of SP. His will lead to fluorescence quenching of the sensor based on inner filter effects (IFE)	Wu et al. (2019)
6	NaYF$_4$:Yb,Er-pHrodo	980	550, 590 nm	pH sensor	A nanosensor based on up-conversion resonance energy transfer (UC-RET) between an upconverting nanoparticle (Ln-UCNPs) and a fluorogenic pH-dependent dye PHrodo ™ Red that was covalently bound to the aminosilane surface of the nanoparticles. The sensitized fluorescence of the pHrodo™ Red dye increases strongly with decreasing PH.	Liu et al. (2018b)
7	NaYF$_4$:Yb,Tm-BODIPY	980	451, 475, 64 8 nm	pH sensor	The blue UCL of NaYF4:Yb^{3+},Tm^{3+}Ln-UCNPs excited at 980 nm, that overlaps with the absorption of the pH-sensitive fluorophore, provides reabsorption based excitation of the dye, the spectrally distinguishable green fluorescence of which is switched ON upon protonation, preventing photoinduced electron transfer within the dye moiety, and the pH-inert red UCL act as reference.	Park et al. (2018)

(Continued on following page)

TABLE 2 (*Continued*) Typical cases of Ln-UCNPs for sensing.

No	Sensor system	Excitation (nm)	Emission	Sensor type	Recent advances	References
8	NaGdF4:Yb,Er-mOrange	980	540 nm	pH sensor	The Ln-UCNPs-mOrange nanoprobe could be fluorescently imaged with 980 nm excitation, having deep penetration depth, by a fluorescence microscope on a coverslip, or uptaken in a single HeLa cell. Nigericin mediated intracellular pH (3.0, 5.0, and 7.0) could be accurately estimated from the CLSM derived FRET ratio.	Qiu et al. (2017)
9	La_2MoO_6:Er	379	555 nm	Temperature Sensor	By means of a fluorescence intensity ratio (FIR) technique, the temperature sensing performances in the temperature range of 303–463 K were investigated based on thermally coupled levels, ^{2}H11/2 and ^{4}S3/2, of Er^{3+} ions. The sensor sensitivity of Er^{3+}-activated La_2MoO_6 nanoparticles can be greatly affected by the doping concentration and the maximum sensor sensitivity was determined to be about 0.0097 K^{-1} at 463 K.	Du et al. (2020)
10	$NaGdF_4$:1%Tm/49%Yb@$NaGdF_4$:15%Tb/1.5%Eu	980	545 nm	Temperature sensor	The large difference in energy between the emission of $Tb^{3+}$and Eu^{3+}made the spectra easier to be detected and calculated based on relative intensity measurement compared to single-ion based systems.	Zhao et al. (2020)
11	$NaLuF_4$:Mn,Ln-PNIPAM-Au	980	544, 660,	Temperature sensor	By utilizing red/near-infrared dual emitting NaLuF4:Mn^{2+},Ln^{3+}(Ln^{3+} = Yb^{3+}, Er^{3+}, Tm^{3+}) Ln-UCNPs as the energy donor and Au nanoparticles as the acceptor, the temperature resolution of the Ln-UCNPs is significantly increased from 3.1°C to 0.9°C in the physiological temperature range.	Luo et al. (2020)
12	$NaY(WO_4)_2$:Er,Yb	980	552, 655 nm	Temperature sensor	The maximum relative sensitivity (Srel) and absolute sensitivity (Sabs) were determined to be ~1.2% K^{-1} at 293 K and ~0.9% K^{-1} at 503 K, respectively. The excellent repeatability of fluorescence intensity ration (FIR) and low temperature uncertainty ΔTmin of ~0.4 K at 293 K make this optical nanothermometry cover a wide temperature range of 293–503 K.	Li et al. (2014)
13	$Bi_2Ti_2O_7$:Yb,Ho	980	550,665,750 nm	Temperature sensor	The maximum relative sensitivity is calculated to be 2.44% at 498 K, obtained from the temperature-dependent spectra by recording in the range of 298–498 K. The samples also provide excellent repeatability and chromaticity stability.	Tse et al. (2019)
14	$NaYF_4$:Yb,Er	980	525,548 nm	Temperature sensor	The spider silks were drawn directly from Araneus ventricosus and were decorated with core–shell Ln-UCNPs *via* a photophoretic effect. By measuring the fluorescence spectra of the Ln-UCNPs on the spider silks, the membrane temperature of a single breast cancer cell was obtained with absolute and relative sensitivities ranging from 3.3 to 4.5 × $10^{-3}K^{-1}$and 0.2–0.8% $K^{-1.}$	Yang et al. (2016)

(Continued on following page)

TABLE 2 (*Continued*) Typical cases of Ln-UCNPs for sensing.

No	Sensor system	Excitation (nm)	Emission	Sensor type	Recent advances	References
15	$NaYF_4$:Yb,Er-polystyrene	980	542,657 nm	Gas sensor	PS is chosen as a matrix because it displays permeation selectivity for CO_2 and rejects protons. The luminescence intensities of the Ln-UCNPs at 542 and 657 nm increase with increasing concentration of CO_2, and the detection limit is 0.11% of CO_2.	Cao et al. (2013)
16	$NaYF_4$:Yb,Tm@PEP	980	474 nm	Fe^{3+} sensor	Limit of detections (LOD) of 0.2 μM and recoveries of 94.5–102.5%, Ln-UCNPs@PEP was shown to have low cytotoxicity and was used for monitoring Fe^{3+} in HeLa cells by fluorescence microscopy.	Gerelkhuu et al. (2019)

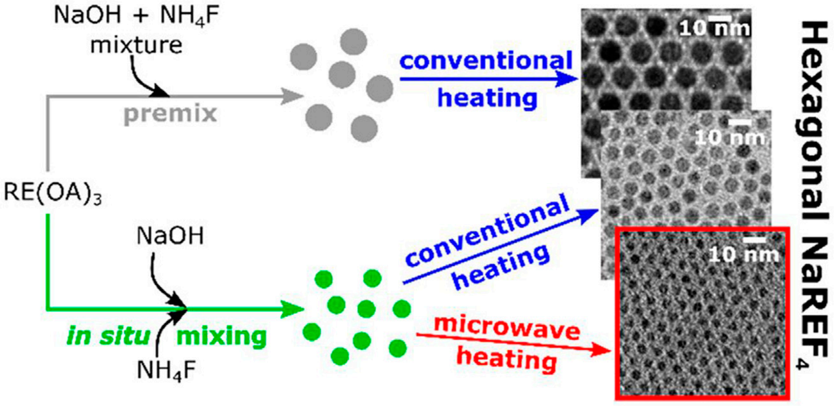

FIGURE 1
Mixing and high-temperature heating steps are important processes in the controlled thermal coprecipitation synthesis of sub-5-nm Na(Gd–Yb)F4: Tm. [Reprinted with permission from Ref. (Amouroux et al., 2019) Copyright 2019: American Chemical Society].

in a reactor (Xu et al., 2020). The advantages of hydrothermal/solvothermal method include the potential for large-scale production. Moreover, the reaction is always carried out under closed conditions without harmful gas leakage, so it is environmentally friendly and non-toxic. However, these conditions also make it impossible to observe the crystal growth process, which impede the studies into the reaction mechanisms.

2.3 Co-precipitation methods

The products of the co-precipitation method are usually chemically homogeneous and uniformly distributed; however, the surfaces are rough and difficult to control. Coudret et al. obtained ultra-small Na(Gd-Yb)F_4:Tm through an improved co-precipitation method (Figure 1). In addition to the synthesis of specific precursors and microwave-assisted heating, the influence of oleic acid content on heating efficiency was discussed (Amouroux et al., 2019). In 2014, Liu and co-workers demonstrated a simpler co-precipitation method to prepare core-shell NaGdF4 nanoparticles doped with luminescent lanthanide ions that did not require precise control of the feeding rate of shell precursors. However, the large core-shell nanocrystals had a low up-conversion efficiency (Wang et al., 2014b). Jin and co-workers synthesized a near-infrared (NIR) fluorescence "turn-on" kit based on rare Earth ion-doped nanoparticles and gold nanoparticles, which created an HIV-1 based DNA detection system that was simple, homogeneous, and highly selective (Zhou et al., 2019). Chen and co-workers were the first to report the synthesis of CaS:Eu^{2+},Sm^{3+} near infrared photostimulated luminescence nanocrystals by a high temperature co-precipitation method. The materials exhibited a fast response to stimuli over 800–1,600 nm (Gao et al., 2019). In conclusion, the application of the co-precipitation method creates products that have biomedical applications; however, they are limited by defects. Regardless, this simple process is conducive to industrial production.

2.4 Other methods

In addition to the processes discussed previously, several novel methods have been developed for the synthesis of Ln-UCNPs. For instance, microemulsions and ionic liquids have been applied, and Ln-UCNPs have been prepared using microwave heating. The microemulsion method creates materials in droplets that contains the surfactant, cosurfactant, solvent and water. Few product nanoparticles are prepared this way; furthermore, the dispersion is poor because the growth of the particles is affected by the size of the micelle. Li and colleagues reported a method of microemulsion assisted synthesis of functionalized Ln-UCNPs. The nanoparticles was synthesized in a heterogeneous oil-water microemulsion phase, and the product had a high cross-section and adjustable pore size (Dai et al., 2020).

Microwave synthesis has unique properties, including increased speed and heating efficiency, which contributes to energy savings and environmental protection. It was reported that $NaGdF_4$:Yb, Er can be directly synthesized using a microwave digestion/extraction system; furthermore, the produced have good biomedical application prospects (Li et al., 2012).

3 Up-conversion luminescence modulation

Key issues concerning the optical properties of Ln-UCNPs include the small absorption cross-section, fluorescence quenching, and the electronic structure that may result in multiple emission lines despite excitation at a single wavelength. As a result, Ln-UCNPs should be classified according to the requirements of applications (Li et al., 2015b). In recent years, a series of Ln-UCNPs with enhanced up-conversion luminescence (UCL) have been obtained by adjusting the composition and structure. This provides a deeper understanding of the characteristics and nature of rare Earth luminescence and broadens the potential for applications (Wu et al., 2016; Garfield et al., 2018).

3.1 Species and concentration of doping ions

Up-conversion is the process of converting low-energy photons into high-energy luminescence, which relies on energy transfer within the 4f electron manifold of the luminescent ions. Luminescence mechanisms include excited state absorption (ESA), energy transfer up-conversion (ETU), and cooperative sensitization up-conversion (CSU). The ESA process occurs within a single ion that continuously absorbs photons to create upconverted luminescence. The ETU process involved in a pair of neighboring rare Earth ions, a sensitizer as energy donor, and an activator as energy acceptor. After excitation, the ground state sensitizer ion becomes electronically excited, the energy from which is transmitted to activators. In turn the activator ion transitions to a higher electronic state, and then luminesces to the ground state. The CSU process requires at least three ion centers. Two of them are the same element that act as sensitizers. They can interact with activators simultaneously in the excited state, which in turn transfers energy to activators. Consequently, the doping of rare Earth ions is closely related to the up-conversion luminescence ability of the nanoparticles, and the luminescence intensity can be regulated by adjusting the species and concentration of rare Earth ions.

Ln-UCNPs are composed of activators and sensitizers within a matrix. For up-conversion, the matrix must have excellent optical properties and stability. The most studied are fluoride materials $NaYF_4$, LaF_3, $LiYF_4$, and $NaGdF_4$ among others (Wang et al., 2011; Liu et al., 2012; Wang et al., 2014b; Zhang et al., 2015). To achieve up-conversion luminescence, the energy difference between at least three adjacent energy levels of the activator should be in close proximity. Therefore, Er^{3+}, Tm^{3+} and Ho^{3+} are the most important due to their step-like energy levels. Sensitizer ions are usually introduced due to the fact that the luminous efficiency of single-doped Ln-UCNPs is not high. Yb^{3+} has become the most common sensitizer due to its unique energy level structure (Han et al., 2014).

We synthesized highly doped Er^{3+} core-shell nanoparticles of $NaYF_4$:x%Er@$NaXF_4$ (x = 5, 25, 50, and 100; X = Lu and Y). The effect on luminescence as a function of Er^{3+} concentration was studied. There was a significant enhancement of red emission at 100% Er^{3+} doping (Feng et al., 2018). In a sensitizer and activator co-doped system, the concentration of activator generally does not exceed 5% while the sensitizer concentration is relatively high, on the order of 15%–40%. The emission of Yb^{3+}/Er^{3+} co-doped systems range from 510 nm to 560 nm (green) and 640 nm–670 nm (red). This system can emit with multiple colors as a combination of green and red can produce yellow light. Er^{3+}/Yb^{3+} co-doped $Na_{0.5}Gd_{0.5}Mo_{O4}$ was reported to emit with characteristic peaks at 531/552/667 nm; furthermore, the intensity of UCL increased with higher Yb^{3+} concentration over a certain range (Du et al., 2016). Similarly, the intense emission of the Yb^{3+}/Tm^{3+} co-doped system was in the blue region, while the Yb^{3+}/Ho^{3+} co-doped system mostly emitted green light with improved efficiency due to the sensitizer. Rare Earth ions have further utility. For example, multi-doped systems empower enhanced luminescence modulation. Liu et al. reported white light emission from $Er^{3+}/Tm^{3+}/Yb^{3+}$ triple-doped SrLu2O4. The Yb^{3+} concentration and pump power can be tuned to modulate the emission color. The optimal doping ratio of 0.5% Er^{3+}, 0.5% Tm^{3+}, and 20% Yb^{3+} created the best balance of red, green and blue luminescence to produce bright white light emission (Liu et al., 2018a). Dammak and coworkers designed a white light modulation system, $Yb^{3+}/Er^{3+}/Tm^{3+}$ doped $GdPO_4$ at a high concentration of Yb^{3+} (35%mol), which emitted white light with excitation by an appropriate laser power (Hassairi et al., 2018). β-$NaYF_4$: Yb^{3+}, Ho^{3+}, Tm^{3+} triple-doped Ln-UCNPs can create multicolor UCL by adjusting the doping concentration and excitation power, which resulted in both white and red light output (Gao et al., 2017).

3.2 Surface plasmon resonance modulation

Metal nanoparticles exhibit a strong plasmon resonance intensity due to electron delocalization over a large surface area. The surface plasmon resonance (SPR) effect will occur when the frequency of the incident photon is the same as the surface plasma oscillation. At this time, a strong local electric field is generated around the metal nanostructure, which further increases the excitation and radiation decay rates of Ln-UCNPs and thus enhances the up-conversion luminescence. UCL can be enhanced by SPR (Thariani and Yager, 2010), which prompted us to theoretically explore the effects of metal nanoparticles on Ln-

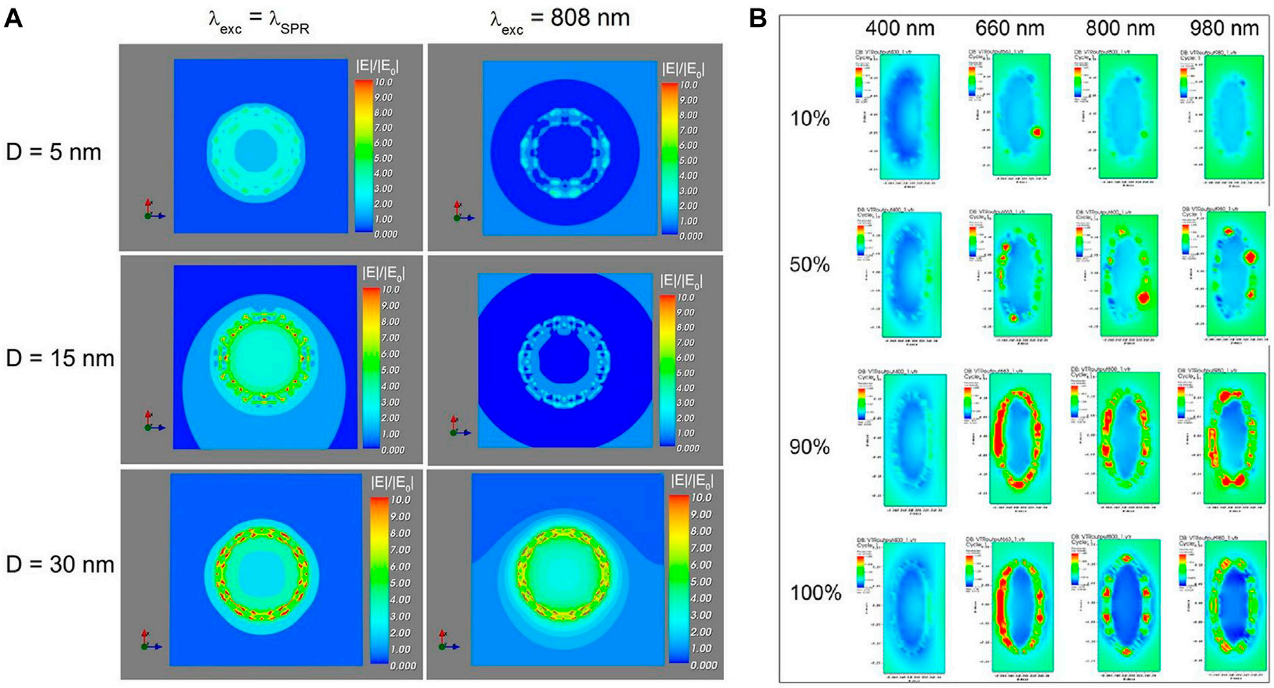

FIGURE 2
(A) Simulation of the electric field strength (|E|/|E0|) of Ln-UCNPs@mSiO2-Au NPs (15 nm–D–5 nm geometry) under irradiation at λexc = λSPR and λexc = 800 nm, with different silica spacers with thickness D of 5, 15, and 30 nm |E|/|E0| is the enhancement factor. The electric field is amplified as |E| > |E0|. [Reprinted with permission from Ref. (Lv et al., 2018a) Copyright 2018: Lv et al. (2018a)]. **(B)** DDSCAT simulation results. Extinction spectra of the corresponding electronic strength images of SPS@Au. [Reprinted with permission from Ref. (Lin et al., 2020) Copyright 2020: American Chemical Society].

UCNPs luminescence using the Discrete Dipole Approximation (DDA). The DDA algorithm can calculate the electromagnetic properties of nanoparticles as a function of shape. We synthesized La2O3:Yb/Er@Au, the gold coating of which significantly enhanced the emission intensity of La_2O_3:Yb/Er@Au by 16.8 times. Experiments demonstrated that the amount of Au added affects the particle spacing and the intensity of UCL. The increase in the electric field simulated by DDA was in good agreement with the observations made in the presence of an Au coating (Lv et al., 2014a). Light exposure and heating of the metal were shown to result in drug release in $Na_5Lu_9F_{32}$:Yb/Er@Au. Both DDA simulation and experimental studies of Ln-UCNPs revealed that the coating of Au enhanced the absorptivity, which in turn resulted in a temperature increase upon excitation that facilitated the release of doxorubicin (DOX). Therefore, this system can be used for controlled drug release by the photothermal effect (Lv et al., 2014b). In the first two systems, we only performed electromagnetic calculations on single Au nanoparticles. DDA was used for the first time to perform extinction calculations on the rare earth-metal model of Ln-UCNPs@SiO_2-Au (Figure 2A) (Lv et al., 2018a). The results revealed the potential to use DDA to guide the construction of rare earth-metal composite materials.

Although considerable progress has been made, many issues remain to be addressed. In the simulations discussed above, gold shells were used to simulate gold coatings. To obtain more accurate results, the Au shells were replaced with randomly distributed gold spheres to simulate Ln-UCNPs@mSiO_2-Au. Both DDA simulation and experiments demonstrated that the presence of 5 nm Au spheres results in enhancements; however the experimental results on 20 nm Au sphere were inconsistent with the DDA simulations due to insufficient uniformity and aggregation. Regardless, the overall accuracy of the model on the modulation of the luminescence was improved (Lv et al., 2020). Next, we synthesized Au/Ag@Ln-UCNPs, and used DDA to simulate the enhancement on UCL due to the presence of gold nanocages of different sizes and thicknesses. Optical characterizations revealed that the luminous intensity of Au/Ag@Ln-UCNPs is twice that of Ln-UCNPs alone. In addition, Au/Ag@Ln-UCNPs were also effective for PTT/PDT treatment of tumors (Liu et al., 2019b). Additionally, Ln-UCNPs@SiO_2@Au (SPS@Au) was synthesized and coated with ZnPc (zinc phthalocyanine) to produce SPS@Au/ZnPc. DDA was used to simulate the extinction of SPS@Au/ZnPc as a function of gold particle content (Figure 2B), the results from which revealed enhanced luminescence properties (Lin et al., 2020).

The finite difference time domain (FDTD) method can be used to simulate the enhancement of UCL due to metal SPR. Song and coworkers used FDTD to simulate $NaYF_4$: Yb^{3+}, Er^{3+} up-conversion luminescence in the presence of a gold rod. Single-layer gold nanorod (GNRs) and Ln-UCNPs were assembled on both sides of an isolating MoO_3 layer to demonstrate a luminescence enhancement effect of more than 35 times (Yin et al., 2016). Zhou and coworkers used FDTD to model Ag@SiO_2 to calculate the optimal Ag particle size and silicon layer thickness. The prepared Ag@SiO_2@YF_3:Ho^{3+} nanoparticles exhibited better luminous

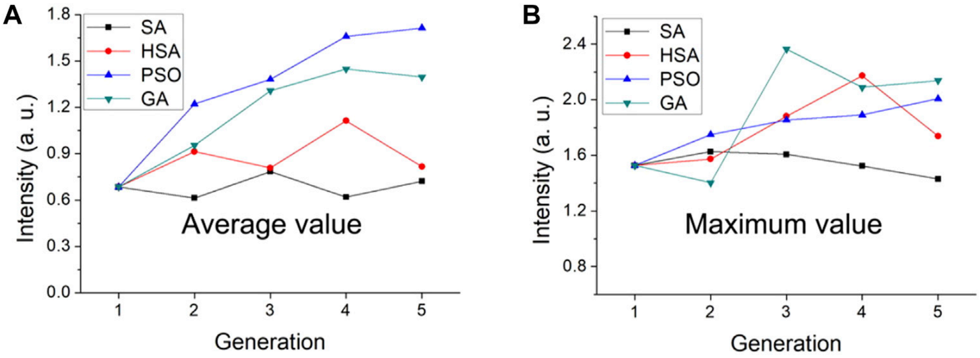

FIGURE 3
Comparison of SA, HSA, PSO, and GA algorithms to the final average and maximum luminescence intensity. Variance of **(A)** all concentrations and **(B)** the Ce/Tb concentrations in different generations. [Reprinted with permission from Ref. (Lv et al., 2019) Copyright 2019: American Chemical Society].

intensity (Xu et al., 2019). Although enhancements are realized using the current strategy of metal modulation to enhance UCL, the effects are actually quite modest. Methods to achieve greater optical enhancements is a problem to be solved in the future.

3.3 Algorithm optimization

A large number of experiments are usually required to determine the optimal doping concentration for Ln-UCNPs.

However, computer technology has revolutionized the traditional screening method. Using algorithms to guide this process can greatly simplify experimental realization. The doping optimization of rare Earth luminescent powder is essentially a combination optimization problem. A product can be designed on a computer and then experimentally realized; these steps are repeated to obtain a material with the best properties. In this process, heuristic algorithms based on natural body algorithms, have been used to guide the synthesis of rare earth-doped luminescent powders with high quantum yield. Heuristic algorithms include the genetic algorithm (GA), particle swarm optimization (PSO), and simulated annealing (SA) (Hopper and Turton, 2001; Hamza et al., 2017; Ozdemir and Karaboga, 2019). GA is a global random search optimization algorithm that uses the “survival of the fittest” mechanism to derive relationships between the material properties and the mole percentage of each raw material, and is often used to guide chemical synthesis optimization problems (Katoch et al., 2021). PSO simulates “bird predation.” The algorithm is easy to understand and program, has global search ability; as a result it has been applied in the field of combinatorial chemistry. Annealing is the process in which the temperature of the system decreases with time (Thangaraj et al., 2011). SA continuously iterates a simulated annealing process to find a solution that meets design specifications (Suman and Kumar, 2006). This algorithm has not yet been applied to combinatorial chemistry problems. Therefore, the most widely used optimization algorithm is the genetic algorithm (Lv et al., 2018b).

Our group has studied the pros and cons of SA, the improved SA of harmony search, PSO, and GA for guiding the synthesis of luminescent powders (Figure 3). The efficacy of the four algorithms were evaluated by taking the same first-generation luminescent powder as the starting point for optimization and performing 5 iterations. SA had no obvious optimization effect; however, better results were obtained when combined with the harmony search. The genetic algorithm was better than PSO; however, generational analysis found that the brightness of the luminous powders as guided by PSO was more gradual (Lv et al., 2019).

In recent years, it was reported that the regression equation was built through the experimental results, which showed the relationship between luminescence and doping concentration. Then genetic algorithm was used to get the doping concentration corresponding to the maximum luminescence intensity (Sun et al., 2015). Coincidentally, Zhao et al. (2019) used the genetic algorithm to modulate Er^{3+}/Yb^{3+} co-doped Ba5Gd8Zn4O21, resulting in efficient red light emission.

3.4 Dye sensitization

Ln-UCNPs are challenged with weak absorptions and narrow optical excitation regions. These issues can be addressed using the dye sensitization strategy in which organic near-infrared chromophores are coordinated to the surface of Ln-UCNPs. Examples include IR783, IR806, IR808, and indocyanine green (ICG) which act as “antennas” to capture photons and transfer energy to the up-conversion rare Earth particles to improve UCL (Hazra et al., 2018). In 2012, Zou et al. (2012) used IR806 to sensitize β-$NaYF_4$: Yb, Er for the first time. In this study, the intensity of up-conversion luminescence *via* excitation with an 800 nm laser increased by 1,100 times compared to that realized from excitation at 980 nm. This work prompted widespread application of this strategy for up-conversion luminescence enhancement. Han and coworkers synthesized (β-$NaYF_4$: 20% Yb^{3+}, 2% Er^{3+}) Ln-UCNPs without hydrophobic organic ligands, and then explored the best ratio of near-infrared dyes to Ln-UCNPs to enhance luminescence. They coordinated IR783, IR808, IR820 and IR845 to Ln-UCNPs, and found enhancements of 80, 200, 70 and 10, respectively. To explore the sensitization effect of multiple dyes, IR783 and IR845 were simultaneously coordinated to

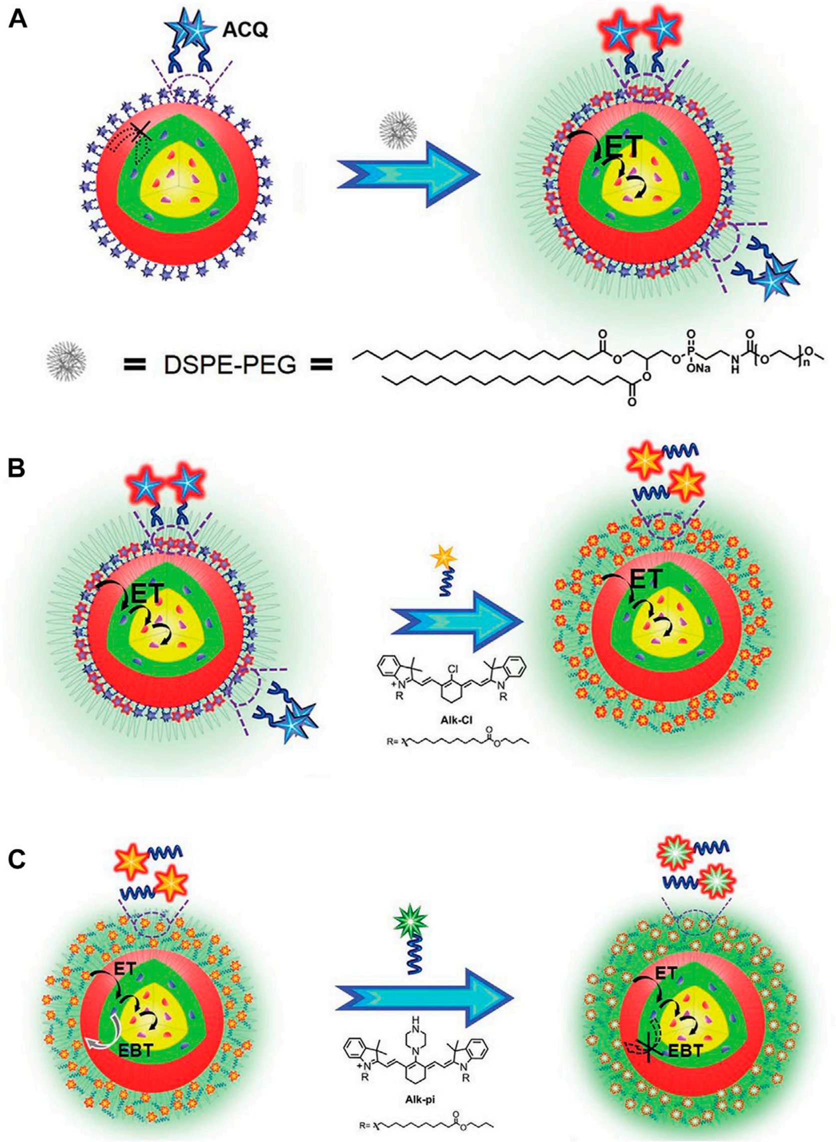

FIGURE 4
(A) Schematic illustration of the alleviation of Aggregation-Caused Quenching (ACQ) and promotion of dye sensitization in aqueous phase by coating with DSPE-PEG. **(B)** Schematic illustration of improving dye-sensitization performance through eliminating ACQ of dye molecules. **(C)** Schematic illustration of improving dye sensitization performance through alleviating EBT from Nd^{3+} to dyes. [Reprinted with permission from Ref. (Liang et al., 2020a) Copyright 2020: John Wiley & Sons, Inc.].

the same Ln-UCNPs. The multidye-sensitized Ln-UCNPs showed a wider wavelength range and were applied for orthogonal bioimaging (Wu et al., 2015). Chen et al. proposed a new concept of energy-cascaded up-conversion (ECU) through the design of an IR808-sensitized core/shell Ln-UCNPs. IR808 was coordinated to the Ln-UCNPs and acted as an antenna to collect excitation energy that was transferred to Nd^{3+}, Tm^{3+} and Yb^{3+} through a multi-step process. This approach achieved a high up-conversion quantum efficiency of 19% (Chen et al., 2015).

Although the sensitization strategy can significantly enhance UCL, the dyes are quenched in water which greatly limits potential applications. Researchers have explored the synthesis of more stable and brighter dye-sensitized Ln-UCNPs. It was reported that Ln-UCNPs sensitized with Cy7 enhanced UCL in ethanol by ~30 times, although the effect was limited in water by ~2 times. To address this problem phosphatidylcholine was introduced to improve water dispersibility, which resulted in an increase of 17 times efficiency and enabled lymphatic imaging (Zou et al., 2016). Liu and coworkers revealed that quenching of dye sensitized Ln-UCNPs in water is the result of dye aggregation. Generally, near-infrared dyes are coupled to Ln-UCNPs through chemical coordination; in contrast, Liu and coworkers constructed dye-sensitized systems through hydrophobic interactions. The amphiphilic molecule DSPE-PEG (1,2-distearoyl-n-glycerol-3-phosphoethanolamine-N-[(polyethyleneglycol)-methoxy]) was used to coat the dye Car-Cl. As a result, the sensitization was improved 85 times in water. Unfortunately, aggregation-induced quenching was nonetheless observed at high concentrations.

To further eliminate strong coordination between the dye and rare Earth ions, Liu and coworkers used two long hydrophobic alkyl chains to replace the carboxyl group of the dye Car-Cl to produce a new dye (Alk-Cl), the use of which achieved enhancement of UCL of 215 times (Figure 4) (Liang et al., 2020a). In addition, NIR-II dye (IR-1061) was used to sensitize core-shell Ln-UCNPs and solve the problem of quenching in water. It was worth noting that the purpose of this research was not to enhance up-conversion, rather, to obtain a strong near-infrared signal. Application of this strategy resulted in an increase in the 800 nm emission of Tm^{3+} ions by 2.83 times. Furthermore, the near-infrared emission had a deeper tissue penetration depth, which is more conducive for biological imaging compared to visible emitters (Hazra et al., 2018). Although Ln-UCNPs have multicolor emission, it should be noted that red light has the advantages of deep penetration depth and imparts minimal damage to tissues in biological application.

3.5 Surface modification

During the synthesis of nanoparticles, long-chain polymers like oleic acid always were wrapped on the surface of Ln-UCNPs. In this way, the stability and luminescence intensity in aqueous are decreased compared with organic solvents, which limits the application in organisms. The following methods are usually used to deal with synthesized Ln-UCNPs. 1) Acid or excess ethanol was added. The ligands on the surface of Ln-UCNPs can be removed under the ultrasound. Capobianco and co-workers successfully removed the oleic acid ligands on the surface of $NaGdF_4$: Yb^{3+},Er^{3+} by the means of acid treatment (Bogdan et al., 2011) 2). The hydrophobic ligands were replaced by hydrophilic ligands, such as PEI, PAMAM, and PAA, to increase the water solubility of the nanoparticles. (Kovalenko et al., 2009; Kovalenko et al., 2010; Tangirala et al., 2010) 3) Inorganic material shells were coated on the surface of Ln-UCNPs, such as SiO_2. This method can improve the water solubility of the nanoparticles effectively. It is worth noting that, thickness of the SiO_2 needs to be determined by multiple experiments. Since too thick or too thin SiO_2 layers may affect the luminescence intensity of Ln-UCNPs and make the synthesis process more difficult. (Li and Zhang, 2006)

4 Ln-UCNPs-based theranostics

The traditional treatment for tumors, chemotherapy and surgical resection, have disadvantages that must be addressed. Several new therapies have attracted recent attention (Atmaca et al., 2021; Kobayashi et al., 2021; Lu et al., 2021; Pedziwiatr-Werbicka et al., 2021; Zhu et al., 2021). PT mainly includes photodynamic therapy and photothermal therapy. In PDT, irradiating a photosensitizer produces reactive oxygen species (ROS) that cause oxidative damage to cells (Yan et al., 2021a). In PTT, light-induced heating damages cancer cells (Shi et al., 2021). Combining photosensitizer or photothermal agent with Ln-UCNPs can achieve PT with near-infrared light.

4.1 Ln-UCNPs-based drug delivery

Drug delivery is an important part of cancer treatment. Generally, Ln-UCNPs can be used as a vehicle for drug delivery to achieve a specific therapy. Mechanisms for drug delivery using Ln-UCNPs include passive, active, and physical targeting. In the passive targeting strategy, drugs are combined with Ln-UCNPs to achieve targeted therapy with the help of the enhanced permeability and retention (EPR) effect. In the active targeting strategy, drugs are combined with Ln-UCNPs, and the interaction between a ligand and receptor, or antigen and antibody, is used to specifically recognize cells to achieve the targeted delivery of drugs. Chen et al. (2017) designed Tm^{3+}-doped UCNPs and combined them with light-activated Ru complexes, so that enzyme inhibitors can be released by NIR excitation. In the physical targeting strategy, designer nanoparticles can be used to release drugs in specific locations by external environmental stimulus, such as changes in pH or temperature, photoexcitation, or magnetic targeting. Lin and coworkers designed Ln-UCNPs doped with Yb^{3+} and Tm^{3+} with additional modification of hydrazine monohydrate on the surface. In an acidic environment, the hydrogen bonds in the nanoparticles dissociate, enabling drug release (Yang et al., 2014). Mykhaylyk et al. (2001) designed magnetic nanoparticles that can deliver drugs to penetrate the blood-brain barrier and enter the mouse brain (Mykhaylyk et al., 2001). De et al. designed a polyelectrolyte complex based on Yb^{3+} and Er^{3+} to deliver pharmaceutical grade protein (De et al., 2022). The modified nanosystem overcame the problem of protein aggregation in the cell membrane and protected the protein drugs from destruction by proteases and the action of heat. At the same time, the nanoscale drug carrier system responded to the 980-nm NIR light, and realized the imaging of the protein delivery process.

4.2 Ln-UCNPs-based phototherapy

PDT has been clinically applied as a supplement to traditional therapy. Porphyrin is the first photosensitizer approved for this purpose (Tian et al., 2020), and mTHPC (meso-tetra hydroxy phenyl chlorin), a second generation photosensitizer, has shown many excellent characteristics in photodynamic therapy (Pinto et al., 2021; Yakavets et al., 2021; Yuan et al., 2021). In addition, chlorin dihydrogen E6 (Chlorin e6, Ce6), ZnPc and other photosensitizers have been widely used in scientific research although they have not been clinically approved (Chen et al., 2021a; Zhang et al., 2021a; Chen et al., 2021b; Hu et al., 2021; Lee et al., 2021; Shen et al., 2021; Zheng et al., 2021). Most photosensitizers are hydrophobic and easily aggregate in solution, which introduces practical difficulties (Liu et al., 2021a; Lin et al., 2021; Wei et al., 2021; Wu et al., 2021). Compared with PDT, there are less examples of the clinical application of PTT for tumor treatment. ICG is a dye that has been widely used in clinical diagnosis (Lutken et al., 2021; Teng et al., 2021). It can absorb in the near-infrared (600–900 nm) which enhances tissue penetration. In addition to its use in imaging and diagnosis, ICG has high photothermal conversion efficiency for photothermal therapy which is helpful for follow-up treatment of tumors (Ravichandran et al., 2020; Zhang et al., 2021b).

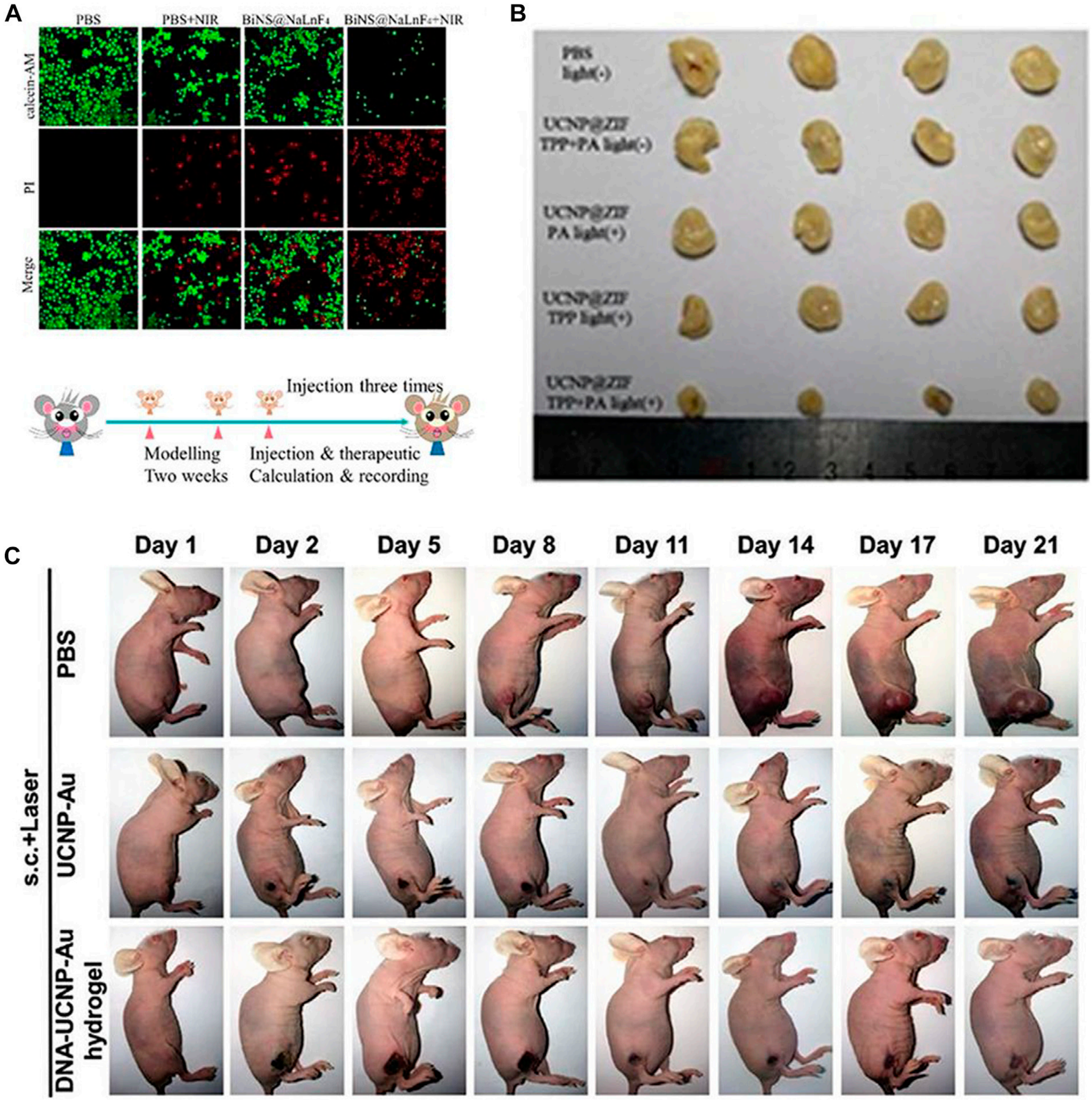

FIGURE 5
(A) *In vitro* PTT confocal images of ECA109 cells treated with PBS and BiNS@NaLnF4, with or without NIR irradiation. [Reprinted with permission from Ref. (Ma et al., 2021a) Copyright 2021: Royal Society of Chemistry]. **(B)** Images of tumor after treatment. [Reprinted with permission from Ref. (Wang et al., 2020) Copyright 2020: Royal Society of Chemistry]. **(C)** Photographs of female BALB/c nude mice bearing T24 tumors when treated with DNA–Ln-UCNPs-Au hydrogel, Ln-UCNPs-Au, and PBS samples over a period of 21 days after NIR irradiation in 3 min (1 W cm^{-2}); s.c., subcutaneous injection. [Reprinted with permission from Ref. (Liu et al., 2020) Copyright 2020: John Wiley & Sons, Inc.].

Currently, most of the photothermal agents are still applied in preclinical or early clinical research due to the fact that photothermal reaction cannot not completely eradicate a tumor; furthermore, there are additional risks due to overheating caused by laser ablation (Gao et al., 2020; Guo et al., 2021; Li et al., 2021; Pang et al., 2021; Zhao et al., 2021).

Ln-UCNPs are candidates for phototherapy due to their low toxicity and ability to be excited by near-infrared light. Ln-UCNPs are often used to deliver other molecules or add modifiers, for which the ability to upconvert expands the range of usable therapeutic agents making it more suitable for cancer phototherapy. In most cases, PDT and PTT effects exist simultaneously (Yang et al., 2021a; Bian et al., 2021; Yang et al., 2021b).

Generally, Ln-UCNPs is used in phototherapy to convert near infrared into visible light to trigger a photodynamic response. Guang and co-workers synthesized BiNS@NaLnF$_4$(Ln = Gd) using a solvothermal method (Figure 5A). Specifically, NaGdF4 was loaded onto Bi ultra-thin nanosheets, and up-conversion was observed under 980 nm laser irradiation to stimulate ROS generation. NaLnF$_4$ has a light-to-heat conversion efficiency of

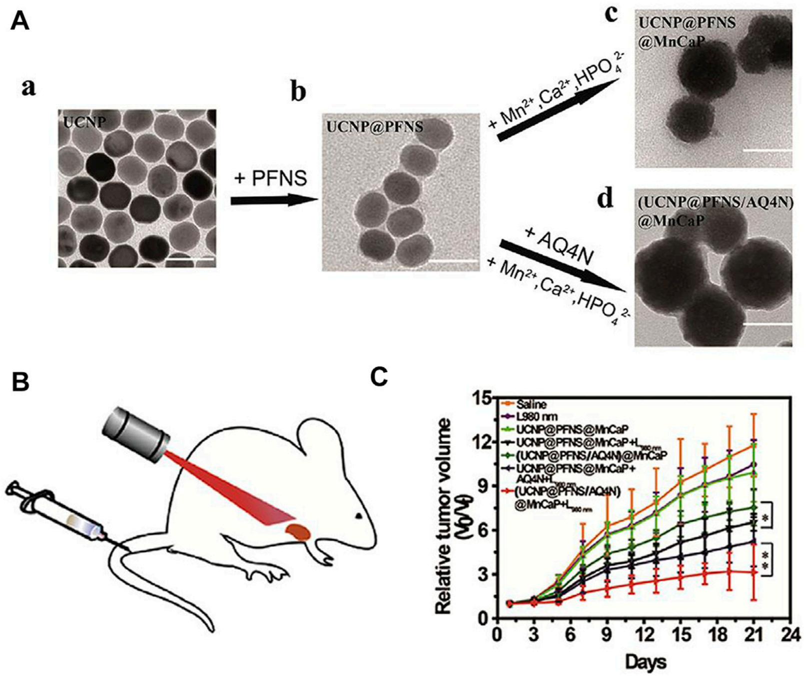

FIGURE 6
(A) Transmission electron microscope (TEM) images of Ln-UCNPs (a), Ln-UCNPs@PFNS (b), Ln-UCNPs@PFNS@MnCaP (c) and (Ln-UCNPs@PFNS/AQ4N) @MnCaP (d). **(B)** Schematic of the treatment of mice with intravenously injected (Ln-UCNPs@PFNS/AQ4N)@MnCaP and treatment by illumination. **(C)** The tumor growth curves for different treatments. Error bars indicate SD (*n* = 6). [Reprinted with permission from Ref. (Ji et al., 2019) Copyright 2019: Elsevier].

35.3% (Ma et al., 2021a). Ln-UCNPs can also be used as a light energy converter to participate in the reconstruction of a tumor's microenvironment (Figure 5B). The emitted light of a Ln-UCNPs can activate a photoacid to release H^+, which reduced the pH value of the tumor environment and improved the release of ROS in the cell in response to acid environment (Wang et al., 2020). Liu et al. (2020) synthesized an injectable DNA-Ln-UCNPs-Au hydrogel, which enhanced the aggregation of Ln-UCNPs-Au through electrostatically complexed DNA strands and achieved a photothermal conversion efficiency of 42.7% (Figure 5C). In *in vivo* experiments, DNA-Ln-UCNPs-Au showed good stability and anti-cancer activity. In these preclinical studies, Ln-UCNPs have played an important role for tumor treatment. Since the excitation wavelength is in near-infrared band, phototherapy based on Ln-UCNPs can avoid the self-absorption problem of biological tissues and increase the penetration depth.

4.3 Ln-UCNPs-based phototherapy with chemotherapy

Chemotherapy can address the shortcomings of phototherapy, while phototherapy can more accurately target tumors and can be used to visually monitor drug release when combined with bioimaging (Andre et al., 2020; Birtle et al., 2020; Zheng and Xu, 2020; Yan et al., 2021b). A Ln-UCNPs-based multifunctional platform, Ln-UCNPs@PDA@Cy3-pep, that has treatment and real-time monitoring functions was reported (Liu et al., 2021b). The Ln-UCNPs comprised the core, while the chemotherapeutic drug staurosporine (STS) was loaded on the polydopamine (PDA) shell. The complex was shown to be effective for both photothermal therapy and chemotherapy under near infrared light irradiation. The quenching and restoration of Cy3 fluorescence was used to monitor the anti-cancer efficiency of the complex in real time (Liu et al., 2021b). Ju and coworkers reported a combination of chemical-photodynamic therapy based on a dual emitting Ln-UCNPs that was functionalized with a photosensitizer and the prodrug camptothecin. The surface was modified to enhance water solubility and targeting. Near-infrared excitation resulted in ultraviolet emission that activated the toxicity of CPT, and additional blue emission activated the photosensitizer to produce singlet oxygen to kill cancer cells (He et al., 2021). Huang and coworkers modified the photosensitizer to the surface of Ln-UCNPs to obtain Ln-UCNPs@PFNS. AQ4N, a hypoxia-activated prodrug that displays high toxicity selectively to hypoxic environment, was added to the pH-sensitive surface coating for chemotherapy (Figure 6). The surface coating decomposed at the tumor site due to the acidic environment, resulting in exposure of AQ4N and the photosensitizer. Under near-infrared excitation the photosensitizer generated ROS and aggravated the hypoxia at the tumor site which enhanced the therapeutic effect of hypoxia-activated AQ4N (Ji et al., 2019). It is promising to actively explore therapies that can assist chemotherapy given its role as the dominant cancer treatment. It is foreseeable that the structure and optical properties of Ln-UCNPs will add value in chemotherapeutic approaches to treat cancer more effectively (Liang et al., 2020b).

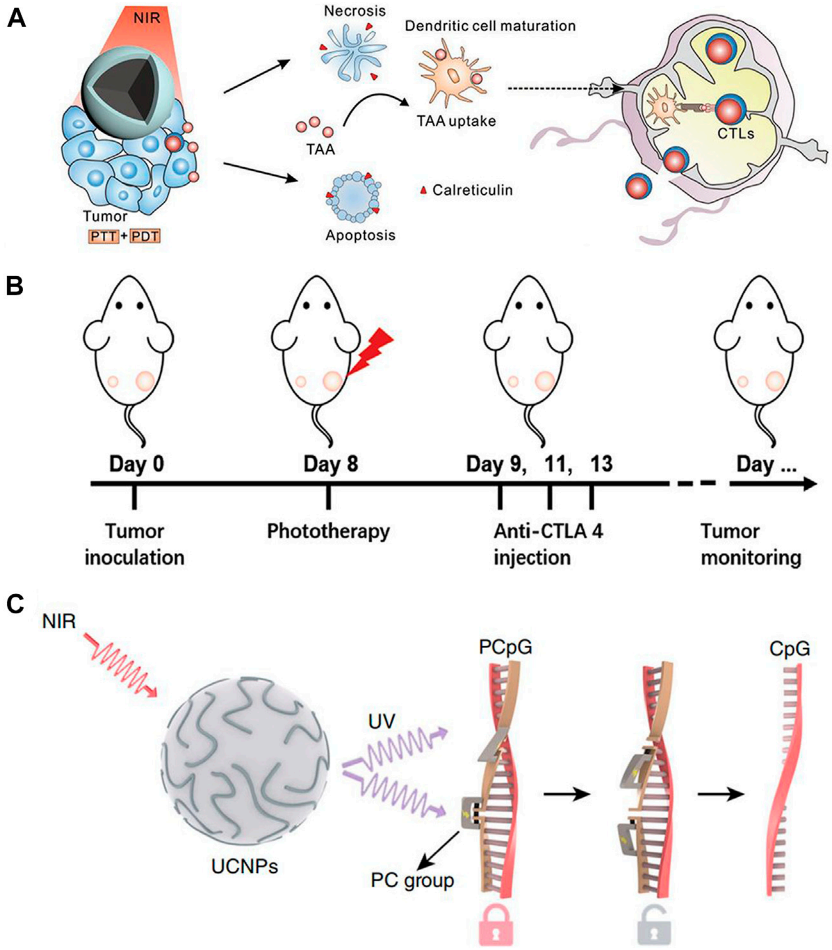

FIGURE 7
(A) Scheme of synergistic phototherapy for augmentation of antitumor immunity. Upon laser irradiation, nanoparticles ablate the primary tumor through phototherapy. (Reprinted with permission from Ref. (Yan et al., 2019) Copyright 2019: John Wiley & Sons, Inc.). **(B)** Schematic depiction of the experimental approach for the evaluation of the abscopal effects induced by Ln-UCNPs/ICG/RB-mal based phototherapy. (Reprinted with permission from Ref. (Wang et al., 2019a) Copyright 2019: John Wiley & Sons, Inc.). **(C)** Schematic of the design of a photoactivatable immunodevice through the integration of Ln-UCNPs with the UV light-responsive photoactivatable CpG (PCpG). Ln-UCNPs act as transducer to upconvert NIR light into UV light locally, thus liberate CpG oligonucleotides (ODN) from PCpG to achieve refined temporal control on its immunoactivity. [Reprinted with permission from Ref. (Chu et al., 2019) Copyright 2019: Nature Publishing Group].

4.4 Ln-UCNPs-based phototherapy with immunotherapy

In recent years, immunotherapy has attracted attention due to the targeting capability and increased safety. Tumor immunotherapy does not reply on external stimuli, rather, it activates the immune response and cultivates immune cells to attack cancer cells (Tan et al., 2020a). Unlike traditional therapies, cancer cells can be removed continuously and quickly. Due to the efficacious anti-cancer effects of anti-CTLA-4 and anti-PD-1 antibodies, immunotherapy has the potential to revolutionize tumor treatment (Kamata-Sakurai et al., 2021; Tay et al., 2021). Many studies have demonstrated the potential for immunotherapy to improve the survival rate of patients and improving quality of life (Borcoman et al., 2019; Wallis et al., 2019; Mpekris et al., 2020). The combination of Ln-UCNPs-based phototherapy and immunotherapy may augment each other's therapeutic effects. Liu et al. prepared a core-shell structure with a core PDA, a $NaGdF_4$:Yb/Er shell, and modified it with the photosensitizer Ce6 (Figure 7A). When irradiated with a 980 nm laser, the PDA component of the PDA@Ln-UCNPs-PEG/Ce6 acted as a photothermal agent while the Ce6 functioned as a photodynamic therapy agent. Phototherapy stimulated the body to produce an immune response, activated T lymphocytes and T memory cells, and helped to inhibit tumor metastasis and recurrence. However, it did not protect the mice from death threats caused by cancer. When combined with the immunosuppressant PD-1, the survival rate of mice was significantly improved to 77.8%, demonstrating the advantages of immunotherapy in long-term survival (Yan et al., 2019). Similarly, Chen and co-authors constructed a Ln-UCNPs/ICG/rose bengal (RB-mal) system (Figure 7B) that triggered enhanced phototherapy by ICG under near-infrared irradiation. Tumor-derived protein antigen was captured by the nano-platform and kept in place to trigger a systemic anti-tumor immune response.

Experiments in mice proved that Ln-UCNPs/ICG/RB-mal can not only cure tumors *in situ*, but also inhibits the growth of distant tumors, illustrating the generation of a tumor-specific immune response (Wang et al., 2019a). In addition, Ln-UCNPs can stimulate the immune response. Li and co-workers combined Ln-UCNPs with PCpG for immunotherapy (Figure 7C). The core-shell nanoparticles $NaGdF_4$:70%Yb, 1%Tm@$NaGdF_4$ emitted at 313, 363, 453 and 478 nm under 980 nm laser excitation. The UV light activated PCpG to release the immunotherapy agent CpG. In mouse experiments, it was worth noting that the CpG/UCs conjugate proved more effective compared to PCpG/UCs + NIR; however, the former caused severe systemic toxicity which reveals the advantages of using Ln-UCNPs in this process (Chu et al., 2019).

When combining phototherapy with immunotherapy, both the near-infrared irradiation and phototherapy reagents elicit the body's immune response (Hou et al., 2018; Dai et al., 2020; Sun et al., 2020). However, the process is not clear, and as such exploring complex systems that can cause an immune response is still an urgent issue to be solved.

5 Ln-UCNPs-based bioimaging

Recent research in biological imaging has centered on the design of new optical molecular probes (Yao et al., 2020).

Since biological tissue is a high-scattering medium, current imaging technology has disadvantages such as low penetration depth, interference from biological autofluorescence, and may cause tissue damage which greatly limits the application of biological imaging (Jia et al., 2020). Ln-UCNPs have a strong anti-Stokes shift, and the ability to absorb near-infrared light helps avoid biological background fluorescence interference (Dhal et al., 2020). Furthermore, near-infrared light has a deep tissue penetration depth. However, Ln-UCNPs cannot be directly applied to biological imaging due to fluorescence quenching, hydrophobicity, biological toxicity and other problems. Addressing these issues requires modification to their structure (Zhou et al., 2020).

5.1 Ln-UCNPs-based fluorescence imaging

Fluorescence imaging generally uses photoluminescence probes, for which Ln-UCNPs are excellent candidates as their application does not result in tissue damage (Hu et al., 2020; Zhang et al., 2020). Recently, Hao and co-workers synthesized polyacrylic acid-modified NaLnF4: 40Gd/20Yb/2Er, (Ln = Y, Yb, Lu, PAA-Ln-NRs). PAA-Ln-NRs with bright NIR II emission were injected into the tail vein of mice, and under excitation from a 980 nm laser they achieved high-precision imaging of small tumors and metastases that enabled early cancer diagnosis (Wu et al., 2019). Liu et al. synthesized dye-sensitized Ln-UCNPs with a reduced propensity for aggregation in water through hydrophobic coordination. Issues with the quenching of Ln-UCNPs luminescence in water was addressed by adjusting the dye absorption band (Liang et al., 2020a). Chen et al. designed an ingenious $NaYF_4$@$NaYbF_4$@$NaYF_4$:Yb^{3+}/Tm^{3+}@$NaYF_4$ structure for multi-channel fluorescence imaging. After intravenous and subcutaneous injection of the Ln-UCNPs, clear *in vivo* color imaging was obtained (Li et al., 2020b). The Fuyou group (Qiu et al., 2017; Liu et al., 2018b; Park et al., 2018) recently synthesized a rare-earth probe with NIR-II imaging capability. Ce^{3+} doping significantly increased the intensity of NIR-II luminescence, resulting a higher resolution in *in vivo* tumor imaging (Cao et al., 2020).

There are some interesting new studies for Ln-UCNPs outside *in vivo* imaging. Giri et al. coated Ln-UCNPs with oleylamine to obtain OA-Ln-UCNPs, and then further processed it to make a Ln-UCNPs oleogel with better skin permeability. The loading of Ln-UCNPs in the oleogels was varied to study the relationship between concentration and fluorescence intensity. For *in vitro* experiments, the Ln-UCNPs oleogel could penetrate the skin more deeply than free OA-Ln-UCNPs and be used as a skin tissue imaging agent under near-infrared excitation. Xu and co-workers reported the application of Ln-UCNPs in plant cell imaging, whereby LiErF4:1%Tm^{3+}@LiYF4 with a core-shell structure could enter the cell membrane easily and emit bright red light (Qiao et al., 2021).

5.2 Ln-UCNPs-based computed tomography

Computed tomography (CT) is based on the difference in the absorption and transmittance of X-rays among various tissues of the human body. The data is scanned by an instrument and processed to determine the pathological condition (Pfeiffer, 2018). Lanthanides have high X-ray attenuation coefficients (Issa et al., 2018), for example, the atomic number and electron density of Lu and Yb are greater than iodine which is currently used in CT. Du et al. reported the synthesis of core-shell nanoparticles $NaYF_4$:Yb/Er@$NaLuF_4$:Nd/Yb@$NaLuF_4$ and surface modification of chitosan. Next, Ag_2Se was grown *in situ* to form $NaYF_4$:Yb/Er@$NaLuF_4$:Nd/Yb@$NaLuF_4$@CS@Ag_2Se. *In vivo* imaging experiments with these agents demonstrated potential for clinical CT (Du et al., 2020). Bismuth doping of materials significantly improves CT imaging as Bi has better X-ray attenuation ability compared to lanthanides. You et al. reported the synthesis of a porous BiF3:Yb, Er nanomaterial that generated an *in vivo* CT signal as demonstrated with concentration dependence. The CT value curve showed that the Hounsfield unit (HU) value of the sample was higher than observed in commercial Iohexol (Zhao et al., 2020). Gao and co-workers reported the synthesis of BaYF5 with different bismuth doping ratios: Yb, Er, Bi-x (x = 0–3). Under the excitation of a 980 nm laser, the up-conversion luminescence was enhanced with increasing Bi content, reaching a maximum at x = 2.5. Then Ln-UCNPs was coated with citrate for biological imaging. Both *in vitro* and *in vivo* experiments demonstrated that the Ln-UCNPs can be successfully used in X-ray CT imaging by accumulating at the tumor site (Luo et al., 2020).

5.3 Ln-UCNPs-based magnetic resonance imaging

Magnetic resonance imaging is a technique in which radio frequency pulses are applied to generate structural information

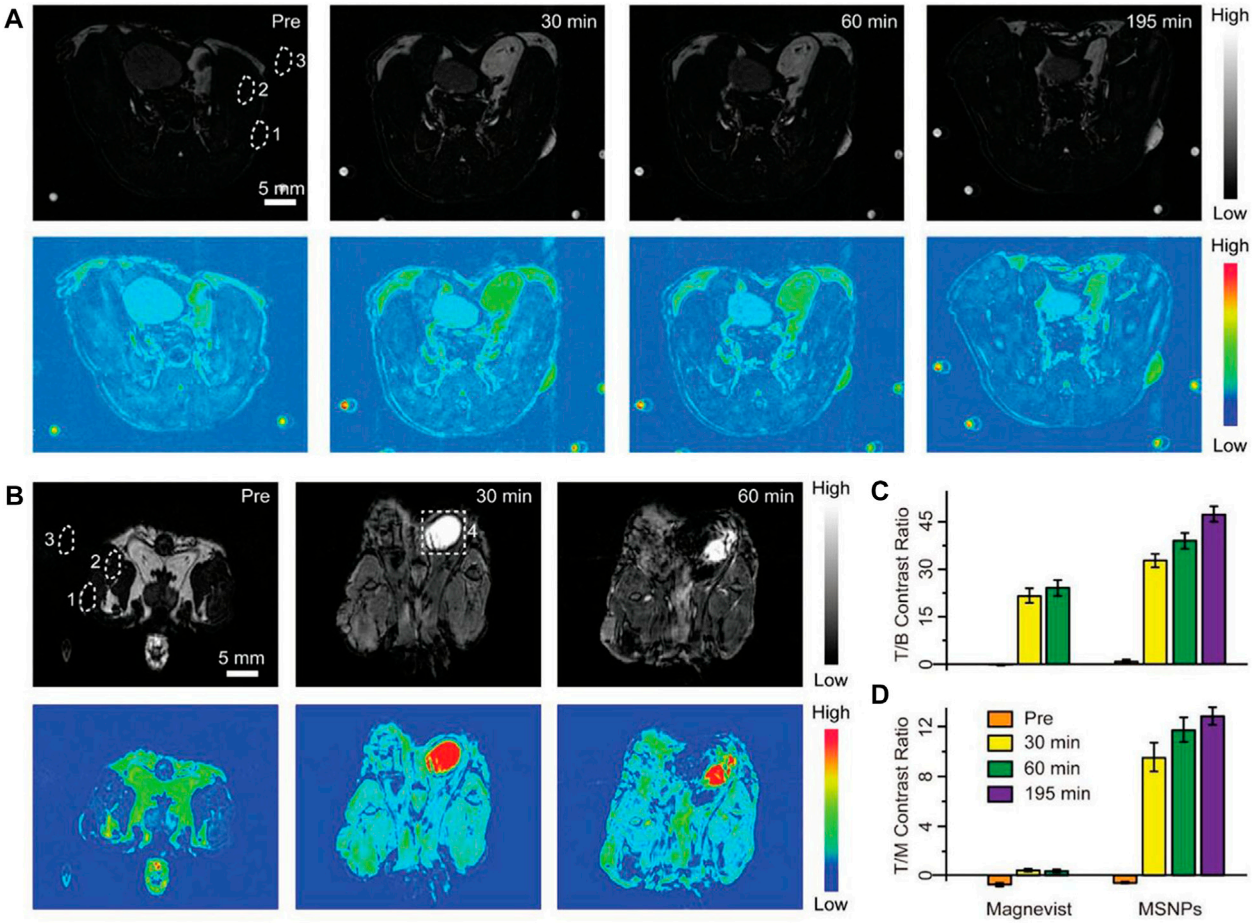

FIGURE 8
Positive contrast enhancement evaluation *in vivo*. **(A, B)** T1-weighted MRI and corresponding pseudocolor images of tumor-bearing mice after intravenous injection of cell membrane coated-BSNPs (MSNPs) **(A)** and Magnevist **(B)** with the same dosage (2.5 μmol of Gd^{3+} for each mouse). Images were captured before and at different time points after the administration of contrast agents. The time points were collected at the midpoint of the time interval during each imaging acquisition. The dotted circles represent the regions of interest: 1) tumor, 2) muscle, 3) background, and 4) bladder. Scale bars are 5 mm for all images. The small spots on the corners are from the circulation apparatus in the MRI scanner. **(C, D)** Tumor-to-background (T/B) and tumor-to-muscle (T/M) contrast ratios based on the corresponding MRI images. Values represented as means ± s.d. (*n* = 3). [Reprinted with permission from Ref. (Yi et al., 2019) Copyright 2019: John Wiley & Sons, Inc.].

(Tirotta et al., 2015; Clough et al., 2019). The signal is generated from relaxation of nuclei from the excited state to equilibrium over the relaxation time. There are two relaxation times, labeled T1 and T2, where T1 is the spin-lattice or longitudinal relaxation time and T2 is the spin-spin or transverse relaxation time. Therefore, MRI is divided into T1 MRI and T2 MRI. The lanthanide gadolinium is the main contrast agent for T1 MRI due to its paramagnetic properties (Li et al., 2014; Yang et al., 2016; Tse et al., 2019). Liu et al. reported a T1-weighted nanocontrast agent with smart MRI switch based on $NaGdF_4$. Ultra-small $NaGdF_4$ and pH-sensitive $CaCO_3$ generated self-assembled bare self-assembled nanoparticles (BSNPs) in organic solvents (Figure 8). The addition of a tumor targeting coating on the surface effectively guided the BNSPs to the tumor location, and then $CaCO_3$ reacted with the acidic environment to release $NaGdF_4$ to achieve MRI with 60 times higher contrast compared to the commercial contrast agent Magnevist (Yi et al., 2019). Superparamagnetic Fe_3O_4 nanoparticles combined with Ln-UCNPs are often used in T2 MRI. Li et al. synthesized Fe_3O_4@$NaGdF_4$:Yb:Er-HMME with a core-shell structure, which was used for both treatment and imaging. The super paramagnetism of the sample was first confirmed, and its T2-weighted MRI performance was studied. Compared with the commercial T2 contrast agent Feridex, the samples performed better, and were effective for use in *in vivo* T2 MRI (Wang et al., 2019b).

5.4 Other imaging based on Ln-UCNPs

Single-Photon Emission Computed Tomography (SPECT) and Positron Emission Tomography (PET) are two techniques in nuclear medicine. PET is the only imaging technique that can interrogate biomolecular metabolism, receptors, and neuromediator activity *in vivo*. Generally, substances necessary for metabolism, such as glucose, are labeled with short-lived radionuclides such as ^{18}F and ^{11}C. After injection into the human body, metabolic activities are reflected by the accumulation of the radiolabeled probes to enable diagnosis. Fang et al. (2020) used cancer cell membrane-modified $NaGdF_4$:Yb,Tm@ $NaGdF_4$ for UCL/MRI/PET trimodal tumor imaging and successfully differentiated triple-negative breast cancer subtypes MDA-MB-231 and MCF-7. Sun et al. (2011) used an efficient strategy for labeling Ln-UCNPs with ^{18}F, and successfully applied the materials in sentinel lymph nodes mapping with PET imaging and detection. The materials were realized by the reaction between rare Earth cations and fluoride ions. The process was simple, fast, and efficient as no organic reagents were applied.

The principle of SPECT is to label probes with short half-life nuclides and inject them intravenously. The nuclides emit γ-rays through decay, and the γ-rays are then converted into electrical signals and input into a computer for tomography reconstruction. A cross-section or three-dimensional image reflecting the physiological condition of organs in the human body can be obtained. Li et al. (2020b) prepared radioactive PEG-modified $NaYF_4$:Yb, Er, Sm. These 10-nm nanoparticles were detected in kidney and urine by SPECT imaging and gamma counter analysis, confirming the potential for these probes as a biodistribution markers (Cao et al., 2013). Ma et al. (2021b) prepared a platelet membrane-coated nanostructure (PM-PAAO-Ln-UCNPs) containing Ln-UCNPs and Ce6 photosensitizer (PAAO = poly(noctylamine) acrylate), and injected them into mice models. SPECT/CT dual-mode imaging was performed and the precise location of an atherosclerotic plaque was demonstrated.

6 Ln-UCNPs-based biosensing

The unique optical properties of Ln-UCNPs make them effective for biological analysis and sensing. First, they are easily incorporated into a fluorescence analysis scheme due to their robust emission properties and high chemical stability. Second, the near-infrared excitation of Ln-UCNPs can effectively avoids autofluorescence of biological tissues. The use of Ln-UCNPs as fluorescent sensors has been extensively studied (Laurenti et al., 2016; Gerelkhuu et al., 2019; Yuan et al., 2019; Su et al., 2020; Gu et al., 2021). This section introduces the application of Ln-UCNPs-based pH and temperature sensors, as well as gas and ion sensors and some other platforms. And the typical cases of Ln-UCNPs for sensing are shown in Table 2.

6.1 Ln-UCNPs-based pH sensors

The pH of the cell can reflect its condition; for example, abnormal cells are acidic. Furthermore, as some viruses and germs are most active under acidic conditions, (White et al., 2017) it is important to monitor intracellular pH. Ratiometric (dual color) Ln-UCNPs-based pH ratiometric sensors can be prepared by first analyzing the emission spectrum of Ln-UCNPs to ensure that it has a pH-insensitive component to serve as a reference, and then coupling it to a fluorescent pH indicator. Proper spectral matching results in fluorescence resonance energy transfer that can generate pH-dependent emission. The Schaferling group coupled Ln-UCNPs to a fluorescent pH-dependent dye pHrodoTM Red. The $NaYF_4$:Yb^{3+}, Er^{3+} material emits at 550 and 660 nm under laser excitation at 980 nm. As the emission peak at 550 nm was found to be invariant to changes in pH, it was used as a reference signal. The dye pHrodoTM Red emitted at 590 nm with an intensity that is dependent on pH. As a result, the combination of the two chromophores created a ratiometric fluorescence probe that displayed a linear response to pH over the range 3–6.7 (Arppe et al., 2014). Likewise Resch-Genger et al. combined NaYF4:Yb^{3+}, Tm^{3+} with a pH-sensitive BODIPY dye to create a ratiometric pH sensor (Figure 9). Excitation at 980 nm resulted in 475 nm emission of Tm^{3+} that was absorbed by the dye, while the pH-insensitive 648 nm emission of Tm^{3+} was used as a calibrant against the 528 nm emission of BODIPY. This two-component sensor was successfully applied for pH monitoring in *Escherichia coli* (Radunz et al., 2019). Ln-UCNPs can also be coupled to pH-dependent fluorescent proteins to create ratiometric sensors. Recently, it was reported that Ln-UCNPs were combined with mOrange fluorescent protein. Excitation at 980 nm resulted in UCL green emission by the Ln-UCNPs, which subsequently excited the mOrange fluorescent protein. The ratio of the pH independent Ln-UCNPs emission at 655 nm to the pH- dependent emission of mOrange fluorescent protein was a quantifiable metric that was shown to have good stability and reversibility (Ghosh et al., 2020).

6.2 Ln-UCNPs-based temperature sensors

Sensitive, convenient, and biocompatible temperature sensors are needed for biological studies (Tran Quang et al., 2016; Ge et al., 2020). Some rare Earth particles have temperature sensitive luminescence properties, which makes them good candidates for biological thermal sensing (Du et al., 2014; Zheng et al., 2014; Wang et al., 2015; Du and Yu, 2017). Lin et al. synthesized doubly-doped NaLuF4:Mn^{2+}, Ln^{3+}(Ln^{3+} = Yb^{3+}, Er^{3+}, Tm^{3+}), which have red/NIR dual emission that can be enhanced by the SPR effect of proximal Au nanoparticles. Embedding both these materials into the thermoresponsive polymer poly(N-isopropylacrylamide) (PNIPAM) resulted in a temperature dependent modulation of the Ln-UCNPs and Au nanoparticle distance. The effect was to modulate the red to NIR emission ratio, which was the metric of the temperature-sensitive sensor that had a resolution of 0.9°C (Xiao et al., 2014). Shahzad et al. (2019) co-doped microfibers with $LiYF_4$:Yb^{3+}/Er^{3+}, polymethyl methacrylate, and silver to create temperature sensors. The temperature dependent ratio of the emission intensity at 522 nm and 541 nm of the Ln-UCNPs was quantified over the range of 303–348 K. Doping with Ag was shown to significantly improve the photostability and temperature response of the composite (Shahzad et al., 2019). A study on the temperature sensitivity of ZnO:Yb^{3+}/Tm^{3+} has been reported. The Ln-UCNPs was excited using a 980 nm laser to produce blue and red UCL emission. The UCL decreased at lower temperatures in the range of 300°C–780°C. The ratio of the intensities of the blue and red emission was modulated by 2.1% K^{-1} at 293 K (Li et al., 2017a). Zhong et al. synthesized a new type of 8.5 nm × 12.5 nm nanoparticle of NaY(WO4)2:Er^{3+}, Yb^{3+} that were shown to be temperature sensitive over the range 293 K–503 K (Lin et al., 2019). In addition to explore the relationship between luminescence of Ln-UCNPs and temperature, researchers have combined various fiber optic probes and temperature-sensitive Ln-UCNPs. Kumar et al. designed Ln-UCNPs coated with polydimethylsiloxane (PDMS) to obtain better fluorescence emission. The pure Ln-UCNPs and Ln-UCNPs-PDMS composite materials were coated on optical fibers for temperature sensing. The sensor coated with composite material displayed a linear response from 295 to 473 K

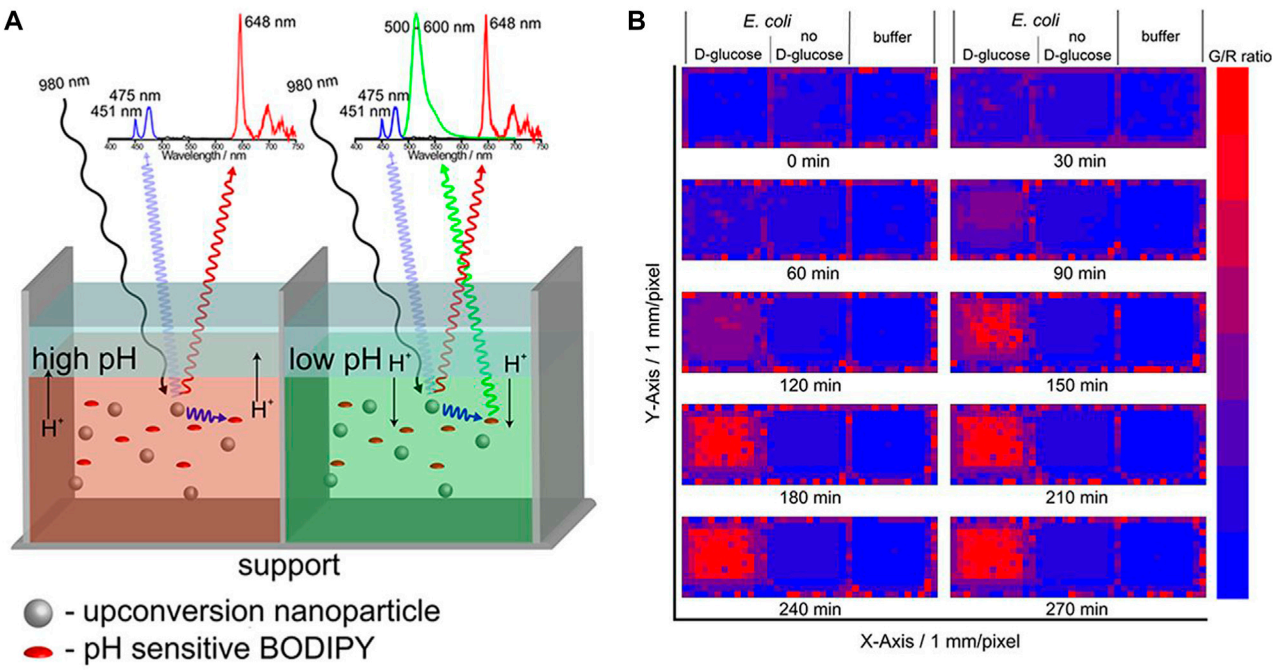

FIGURE 9
(A) Simple self-referenced luminescent pH sensors based on up-conversion nanocrystals and pH-sensitive fluorescent BODIPY dyes. **(B)** Time-dependent changes of the G/R ratio of the pH sensor layers treated with a suspension of E. coli with D-glucose and a suspension of E. coli without D-glucose or pure buffer. [Reprinted with permission from Ref. (Radunz et al., 2019) Copyright 2019: American Chemical Society].

(Kumar et al., 2020). A recent report demonstrated the coating of a temperature-dependent Ln-UCNPs onto the surface of spider silk, a natural optical fiber, to construct a temperature sensor with good biocompatibility. The change in fluorescence intensity of Ln-UCNPs reflected the temperature change of cancer cells. In addition, the sensor successfully detected temperature changes during apoptosis (Gong et al., 2021). Meiling et al. designed a lanthanide nanoscale temperature measurement system that can be used for the diagnosis of *in vivo* inflammation. The structure included an inert core, an active shell and an inert shell. The thermosensitive lanthanide elements were localized in the intermediate shell to shield from interference of the bioactive environment. This ternary structure enabled nanothermometers to continuously measure temperature changes of up to 4 mm depth in biological tissues, with high temperature sensitivity over a physiological temperature range of 10°C–64°C (Tan et al., 2020b). Although Ln-UCNPs are not the only material used for temperature sensors, their use imparts unique advantages. Ln-UCNPs have adjustable excitation wavelengths and can be excited by near-infrared light, making such temperature sensors beneficial for *in vivo* applications. Additionally, Ln-UCNPs have multi-color luminescence, which enables a wide selection of emission for construction of a temperature sensor.

6.3 Ln-UCNPs-based gas sensors

Gas molecules are of great significance in many biological processes. For example, O_2 is important for maintaining metabolism (Mates et al., 2012). CO_2 can regulate breathing and the acid-base balance in the body. NO regulates cardiovascular function and improves the immunity of white blood cells (Carpenter and Schoenfisch, 2012; Lundberg et al., 2015; Farah et al., 2018). As a result, the sensing of gas molecules can elucidate the internal physiological behaviors of organisms. In 2010, Achatz et al. (2011) reported a CO_2 gas sensor based on Ln-UCNPs for the first time. In their system bromothymol blue was used as the luminescence intensity modifier of Ln-UCNPs on polystyrene. Specifically, bromothymol blue the absorption of bromothymol blue quenched the emission of the Ln-UCNPs; however, the presence of acidic CO_2 changed the pH which instigated a color change. Thus, when the CO_2 concentration increased, the absorption of bromothymol blue was minimized which resulted in higher intensity Ln-UCNPs fluorescence that enabled a quantitative detection of CO_2 with a detection limit of 0.11% (Ali et al., 2010). The same group created other gas sensors using Ln-UCNPs. They reported the first application of $NaYF_4$:Yb, Tm excited by near-infrared light as an O_2 sensor. First, an iridium (III) oxygen probe, Ln-UCNPs, and ethyl cellulose were dissolved in tetrahydrofuran. The solvent was evaporated to yield a sensor film. The Ln-UCNPs was excited by a 980 nm laser and emitted at 455 nm and 475 nm. These two emission peaks overlapped the absorption of the iridium complex at 468 nm. Therefore, Ln-UCNPs acted as a nanolamp in the sensor. The fact that the iridium complex's emission at 568 nm is quenched by O_2 enabled quantitatively oxygen detection (Achatz et al., 2011).

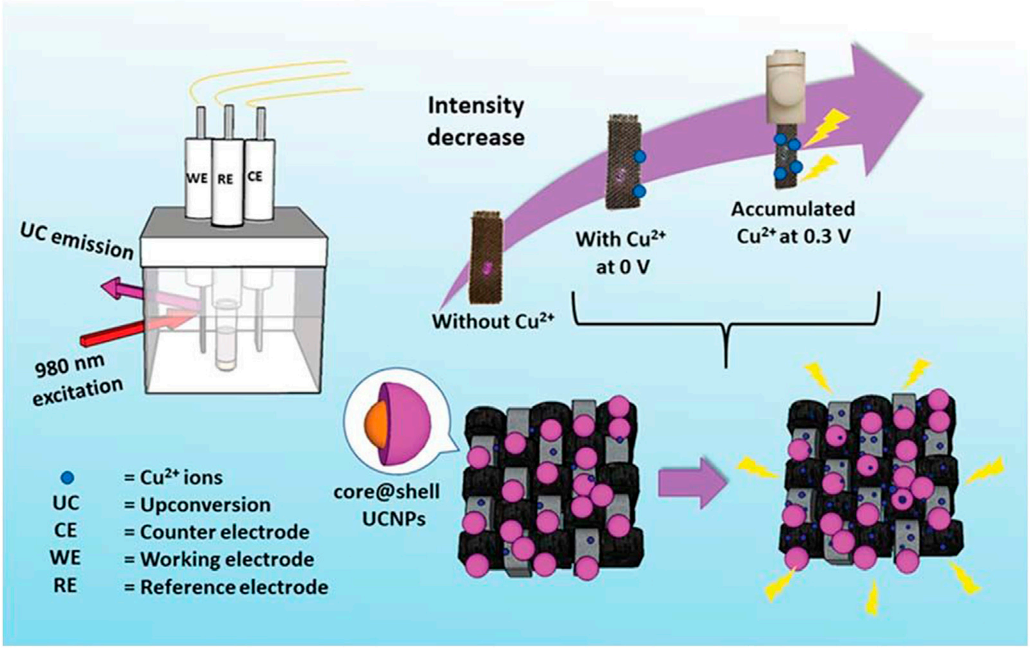

FIGURE 10
A schematic diagram showing the CFC-Ln-UCNPs probe for Cu^{2+} ion sensing with electrochemical assistance. [Reprinted with permission from Ref. (Wong et al., 2019) Copyright 2019: Royal Society of Chemistry].

6.4 Ln-UCNPs-based ion sensors

Although the content of metal ions in organisms is small, they play an important role in maintaining the acid-base balance of cells and organisms and other metabolic activities, and are components of many complex biological compounds. The luminescence properties of Ln-UCNPs show great advantages for metal ion detection. Many studies have demonstrated that ion sensors based on Ln-UCNPs have high sensitivity and selectivity, the results from which can be visualized for convenient operation. Iron directly participates in the transport and storage of oxygen. It is a component of hemoglobin, myoglobin and cytochrome, and is necessary for many metabolic processes (Abbaspour et al., 2014; Sangkhae and Nemeth, 2017). The Lee group reported that adrenaline-modified $NaYF_4$:Yb, Tm was used for intracellular Fe^{3+} detection. PEP can complex with Fe^{3+}, and the energy transfer with the Ln-UCNPs occurred through non-radiative electron transfer and energy return (EBT), resulting in reduced Ln-UCNPs emission at 474 nm. The detection limit of the Fe^{3+} sensor was 0.2 μM over a range of 1–10 μM (Gerelkhuu et al., 2021). The content of zinc in the human body can affect the activity of many enzymes, and as a result Zn^{2+} has an important role in human health (Maret, 2013). Chang et al. synthesized a Zn^{2+} sensor composed of a Ln-UCNPs and a Zn^{2+} sensitive dye.

$NaYF_4$:Yb/Tm@$NaYF_4$ has a multi-peak emission; the blue component at 475 nm was within in the absorption range of the dye while the 654 nm emission was not affected. When Zn^{2+} was added, the absorption of the dye shifted to 360 nm, which led to an increase in the ratio of I475 nm/I654 nm. The sensor successfully detected Zn^{2+} in a live animal model of zebrafish (Peng et al., 2015).

Copper is an indispensable component in blood and participates in hematopoietic process and iron metabolism. It was reported that core-shell Ln-UCNPs were electrostatically adsorbed onto flexible carbon fiber cloth (CFC) to create Cu^{2+} sensors (Figure 10). The absorption of Cu^{+} and Cu^{2+} coincided with the emission of Ln-UCNPs, which is a sensing mechanism. It was the first time that electrochemical technology was used to improve the sensing performance. Cu^{2+} accumulated when a voltage of 0.3 eV was applied. CFC reduced the quenching of Ln-UCNPs in water. The synergy of the electrochemical technology and the CFC protective layer resulted in a detection limit of 82 ppb (Wong et al., 2019). Trace fluoride can promote the normal development of teeth and bones, but excessive fluoride causes dental and skeletal fluorosis. Dual-functional gallic acid-Fe(III) modified Ln-UCNPs was reported with a 654 nm emission that was quenched by the Fe-complex. The presence of F^{-} destroyed the Fe-complex, which imparted a sensing mechanism between the UCL and F^{-} ion analyte (Ma et al., 2017).

6.5 Other new sensors

Recently there have been many reports on the use of Ln-UCNPs for the detection of miRNA and other biologically active molecules (Yuan et al., 2015; Li et al., 2016). Trypsin is an activating enzyme that plays an important role in food digestion and has anti-inflammatory and swelling functions (Plattner and Noe, 2015; Wattanasiritham et al., 2016). Guo et al. synthesized Ln-UCNPs-peptide-AuNP for the detection of trypsin and its

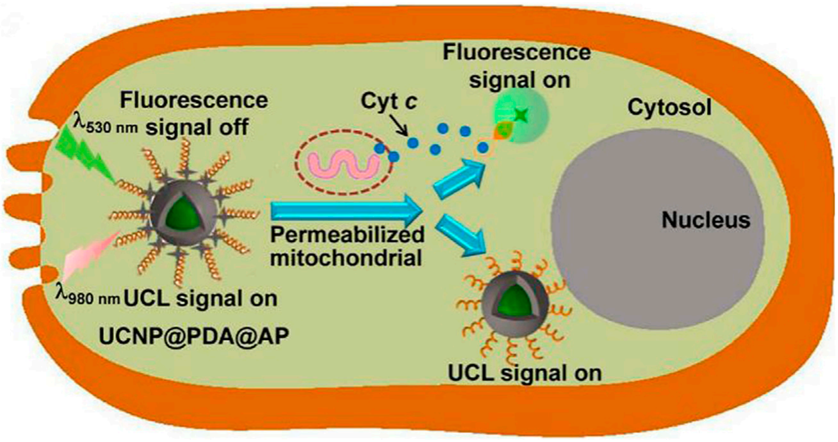

FIGURE 11
Illustration of the Ln-UCNPs@PDA@AP application for sensing intracellular Cyt c. The illustration is not drawn to scale. [Reprinted with permission from Ref. (Ma et al., 2017) Copyright 2017: Elsevier].

inhibitors. The peptide, DDDDARC, is sensitive to trypsin. In the initial state, the emission of UCL was quenched by the Au NP due to Förster Resonance Energy Transfer (FRET) energy transfer. After adding trypsin the peptide was cleaved and UCL was restored. The detection limit of the trypsin sensor was 4.15 ng/mL (Wu et al., 2017). Cytochromes are involved in cell redox reactions and take part in cell energy transfer (Zanger and Schwab, 2013). Wang et al. attached a Cy3-labeled aptamer to the surface of a Ln-UCNPs wrapped with PDA (Figure 11). The aptamer responded to cytochrome c to trigger changes in the fluorescence intensity of Cy3, and the internal UCL served as a reference signal. The sensor reflected the level of Cytc through a ratiometric fluorescence signal, with a detection limit of 20 nM over a range of 50 nM to 10 μM (Ma et al., 2017).

Recent studies have demonstrated that a single sensor can be used for the simultaneous detection multiple biomolecules. Xu et al. developed an Au-Au-Ln-UCNPs with an aptamer with sensitivity for both alpha-fetoprotein (AFP) and mucin 1. The sensor generated both Raman and fluorescence signals. Mucin 1 concentration was detected through the change of surface enhanced Raman scattering intensity, and AFP was sensed by the change of fluorescence intensity. The detection limits of both proteins were at an attomolar level (Qu et al., 2017).

Thrombin acts on the last step of the blood coagulation process. It can be used to stop bleeding and is a relevant marker for tumor diagnosis. Prostate-specific antigens are abundantly present in prostate tissue and semen, with extremely high tissue organ specificity, and are currently the first-choice marker for the diagnosis of prostate cancer. Kuang et al. used a Raman signal and fluorescence of Au-Ln-UCNPs in conjunction with aptamers to respond to thrombin and prostate specific antigen (PSA). The signal intensity of SERS was affected by the concentration of thrombin. The fluorescence signal was affected by PSA, and the detection limit was 3.2×10^{-20} M (Hao et al., 2017).

7 Biological toxicity of Ln-UCNPs

Despite the great potential in applications such as biotherapy, biological imaging and biosensing, the biotoxicity remains a major problem hindering the clinical application of Ln-UCNP. Most of the current studies on *in vivo* toxicity of Ln-UCNPs focus on mice. Ln-UCNPs enter mice in tail vein injection and reach the whole body by blood circulation. Due to the high permeability effect of capillaries to nanoparticles, the liver and spleen become the main aggregate organs of Ln-UCNPs (Li et al., 2017b; Abualrejal et al., 2019; Chen et al., 2019; Guryev et al., 2019; Shan et al., 2020). Chen and co-workers designed targeted contrast agents modified by PEI and FA (Chen et al., 2019). At 24 h and 18 days after the injection, the aggregation of nanoions in liver was higher than that in other tissues. Ln-UCNPs injected into the body can be eliminated by the hepatobiliary and renal metabolic systems. Tian and co-workers (Tian et al., 2019) found that the rate of excretion of Ln-UCNPs is independent of the modified groups. Other studies have shown that the modified group species can influence the toxicity of Ln-UCNPs. Chen and co-workers (Chen et al., 2018) designed a kind of unmodified nanoparticles ($NaYF_4$:Er and $NaGdF_4$:Yb,Er), which caused mild liver toxicity and nephritis. This can be considered as the unmodified Ln-UCNPs would release rare Earth ions under biological conditions, which will react with the phosphate group of ATP, cause ATP inactivation and tissue damage. Vedunova and co-workers (Vedunova et al., 2016) polymaleic anhydride octadecene, PEI, tetramethyl ammonium hydroxide modified Ln-UCNPs ($NaYF_4$:Yb,Tm@$NaYF_4$) respectively. The nanoparticles caused the morphological changes of the hippocampal cells, reduction in Ca^{2+} activity and cellular damage. Moreover, the nanoparticle size, concentration, and treatment time can also affect the biotoxicity of Ln-UCNPs (Xu et al., 2016; Chen et al., 2018; Rafique et al., 2018).

8 Conclusion and future prospects

In this review, we summarize the latest progress in the synthesis, optimization and application (especially for therapy) of Ln-UCNPs. The high-temperature pyrolysis method and hydrothermal/solvothermal procedure are still the most widespread protocols for their syntheses. In terms of improving up-conversion emission, through algorithm optimization, dye sensitization and other methods, the up-conversion emission intensity can be increased by multiple orders of magnitude. The fluorescent properties of lanthanide upconverting nanoparticles have also advanced the field of biomedicine. Near-infrared excitation addresses the limitations of ultraviolet to visible light excitation, penetrates deeper into tissue, and makes nanotherapeutic materials with light as the main excitation source a strong competitor for clinical drugs. Although lanthanide up-conversion has advanced significantly, there are still a large number of obstacles to address. We posit that the future direction of Ln-UCNPs research in the field of biology consists of: 1) Existing luminescence enhancement strategies are either ineffective or easily quenched when exposed to water. Better results may be obtained starting from the principle of up-conversion luminescence to explore optimization methods. 2) Cancer treatment drugs based on Ln-UCNPs have not been reported clinically, which may be related to long term toxicity in the body. It may be possible to extend the *in vivo* experiment period and minimize other factors that affect drug metabolism to simulate the therapeutic effects to the greatest extent. 3) Although the synthesis technology of Ln-UCNPs is very mature, the products are often hydrophobic. Surface modification for *in vivo* application will improve biocompatibility; however, this process will affect the luminescence efficiency. Finding the balance between biocompatibility and luminescence is a difficult problem. 4) Ln-UCNPs-based biosensors have been developed. However, few studies have evaluated the sensitivity and stability of Ln-UCNPs sensors for *in vivo* sensing. The *in vivo* environment is complex, and how to accurately deliver nanosensors to the detected cellular locations is also a major challenge.

Author contributions

RL, DX, and BL contributed to conception and design of the study. DX organized the database. CL performed the statistical analysis. DX wrote the first draft of the manuscript. BL, CL, and WL wrote sections of the manuscript. All authors contributed to manuscript revision, read, and approved the submitted version.

Funding

This work was supported by the Natural Science Foundation of China (NSFC Nos. 81801744 and 91859202), the National Key R&D Program of China Grant (No. 2017YFA0205202) and the Fundamental Research Funds for the Central Universities.

Conflict of interest

The authors declare that the research was conducted in the absence of any commercial or financial relationships that could be construed as a potential conflict of interest.

Publisher's note

References

Abbaspour, N., Hurrell, R., and Kelishadi, R. (2014). Review on iron and its importance for human health. *J. Res. Med. Sci.* 19 (2), 164–174.

Abualrejal, M. M. A., Eid, K., Tian, R., Liu, L., Chen, H., Abdullah, A. M., et al. (2019). Rational synthesis of three-dimensional core-double shell upconversion nanodendrites with ultrabright luminescence for bioimaging application. *Chem. Sci.* 10 (32), 7591–7599. doi:10.1039/c9sc01586h

Achatz, D. E., Meier, R. J., Fischer, L. H., and Wolfbeis, O. S. (2011). Luminescent sensing of oxygen using a quenchable probe and upconverting nanoparticles. *Angew. Chemie-International Ed.* 50 (1), 274–277. doi:10.1002/ange.201004902

Adachi, S. (2018). Photoluminescence properties of Mn4+-activated oxide phosphors for use in white-LED applications: A review. *J. Luminescence* 202, 263–281. doi:10.1016/j.jlumin.2018.05.053

Ali, R., Saleh, S. M., Meier, R. J., Azab, H. A., Abdelgawad, I. I., and Wolfbeis, O. S. (2010). Upconverting nanoparticle based optical sensor for carbon dioxide. *Sensors Actuators B-Chemical* 150 (1), 126–131. doi:10.1016/j.snb.2010.07.031

Amouroux, B., Roux, C., Marty, J. D., Pasturel, M., Bouchet, A., Sliwa, M., et al. (2019). Importance of the mixing and high-temperature heating steps in the controlled thermal coprecipitation synthesis of sub-5-nm Na(Gd-Yb)F-4:Tm. *Inorg. Chem.* 58 (8), 5082–5088. doi:10.1021/acs.inorgchem.9b00143

Andre, T., Shiu, K. K., Kim, T. W., Jensen, B. V., Jensen, L. H., Punt, C., et al. (2020). Pembrolizumab in microsatellite-instability-high advanced colorectal cancer. *N. Engl. J. Med.* 383 (23), 2207–2218. doi:10.1056/nejmoa2017699

Arppe, R., Nareoja, T., Nylund, S., Mattsson, L., Koho, S., Rosenholm, J. M., et al. (2014). Photon upconversion sensitized nanoprobes for sensing and imaging of pH. *Nanoscale* 6 (12), 6837–6843. doi:10.1039/c4nr00461b

Atmaca, G. Y., Aksel, M., Keskin, B., Bilgin, M. D., and Erdogmus, A. (2021). The photo-physicochemical properties and *in vitro* sonophotodynamic therapy activity of Di-axially substituted silicon phthalocyanines on PC3 prostate cancer cell line. *Dyes Pigments* 184, 108760. doi:10.1016/j.dyepig.2020.108760

Bian, H., Ma, D., Zhang, X., Xin, K., Yang, Y., Peng, X., et al. (2021). Tailored engineering of novel xanthonium polymethine dyes for synergetic PDT and PTT triggered by 1064 nm laser toward deep-seated tumors. *Small* 17 (21), 2100398. doi:10.1002/smll.202100398

Binnemans, K. (2015). Interpretation of europium(III) spectra. *Coord. Chem. Rev.* 295, 1–45. doi:10.1016/j.ccr.2015.02.015

Birtle, A., Johnson, M., Chester, J., Jones, R., Dolling, D., Bryan, R. T., et al. (2020). Adjuvant chemotherapy in upper tract urothelial carcinoma (the POUT trial): A phase 3, open-label, randomised controlled trial. *Lancet* 395 (10232), 1268–1277. doi:10.1016/s0140-6736(20)30415-3

Bogdan, N., Vetrone, F., Ozin, G. A., and Capobianco, J. A. (2011). Synthesis of ligand-free colloidally stable water dispersible brightly luminescent lanthanide-doped upconverting nanoparticles. *Nano Lett.* 11 (2), 835–840. doi:10.1021/nl1041929

Borcoman, E., Kanjanapan, Y., Champiat, S., Kato, S., Servois, V., Kurzrock, R., et al. (2019). Novel patterns of response under immunotherapy. *Ann. Oncol.* 30 (3), 385–396. doi:10.1093/annonc/mdz003

Cao, C., Wu, N., Yuan, W., Gu, Y. Y., Ke, J. M., Feng, W., et al. (2020). Ln(3+)-doped nanoparticles with enhanced NIR-II luminescence for lighting up blood vessels in mice. *Nanoscale* 12 (15), 8248–8254. doi:10.1039/d0nr01098g

Cao, T., Yang, Y., Sun, Y., Wu, Y., Gao, Y., Feng, W., et al. (2013). Biodistribution of sub-10 nm PEG-modified radioactive/upconversion nanoparticles. *Biomaterials* 34 (29), 7127–7134. doi:10.1016/j.biomaterials.2013.05.028

Carpenter, A. W., and Schoenfisch, M. H. (2012). Nitric oxide release: Part II. Therapeutic applications. *Chem. Soc. Rev.* 41 (10), 3742–3752. doi:10.1039/c2cs15273h

Chen, G., Damasco, J., Qiu, H., Shao, W., Ohulchanskyy, T. Y., Valiev, R. R., et al. (2015). Energy-cascaded upconversion in an organic dye-sensitized core/shell fluoride nanocrystal. *Nano Lett.* 15 (11), 7400–7407. doi:10.1021/acs.nanolett.5b02830

Chen, J., Li, S., Liu, X., Liu, S., Xiao, C., Zhang, Z., et al. (2021). Transforming growth factor-beta blockade modulates tumor mechanical microenvironments for enhanced antitumor efficacy of photodynamic therapy. *Nanoscale* 13 (22), 9989–10001. doi:10.1039/d1nr01552d

Chen, J. P., Shi, S. S., Liu, G. F., Chen, Y., Zheng, S. S., Wang, X. B., et al. (2018). Potential clinical risk of inflammation and toxicity from rare-earth nanoparticles in mice. *Chin. Med. J. Engl.* 131 (13), 1591–1597. doi:10.4103/0366-6999.235105

Chen, Q., Ma, X., Xie, L., Chen, W., Xu, Z., Song, E., et al. (2021). Iron-based nanoparticles for MR imaging-guided ferroptosis in combination with photodynamic therapy to enhance cancer treatment. *Nanoscale* 13 (9), 4855–4870. doi:10.1039/d0nr08757b

Chen, Y., Fei, X., Ye, C., Qian, Q., Ye, Z., Xie, S., et al. (2019). Acute hepatotoxicity of multimodal targeted imaging contrast agent NaLuF<sub>4</sub>:Gd,Yb,Er-PEG/PEI-FA in mice. *J. Toxicol. Sci.* 44 (9), 621–632. doi:10.2131/jts.44.621

Chen, Z. J., Thiramanas, R., Schwendy, M., Xie, C. M., Parekh, S. H., Mailander, V., et al. (2017). Upconversion nanocarriers encapsulated with photoactivatable Ru complexes for near-infrared light-regulated enzyme activity. *SMALL* 13 (46), 1700997. doi:10.1002/smll.201700997

Chu, H., Zhao, J., Mi, Y., Di, Z., and Li, L. (2019). NIR-light-mediated spatially selective triggering of anti-tumor immunity via upconversion nanoparticle-based immunodevices. *Nat. Commun.* 10, 2839. doi:10.1038/s41467-019-10847-0

Clough, T. J., Jiang, L., Wong, K.-L., and Long, N. J. (2019). Ligand design strategies to increase stability of gadolinium-based magnetic resonance imaging contrast agents. *Nat. Commun.* 10, 1420. doi:10.1038/s41467-019-09342-3

Cui, Y., Chen, B., and Qian, G. (2014). Lanthanide metal-organic frameworks for luminescent sensing and light-emitting applications. *Coord. Chem. Rev.* 273, 76–86. doi:10.1016/j.ccr.2013.10.023

Dai, Y., Yang, D. P., Yu, D. P., Xie, S. H., Wang, B. W., Bu, J., et al. (2020). Engineering of monodisperse core-shell up-conversion dendritic mesoporous silica nanocomposites with a tunable pore size. *Nanoscale* 12 (8), 5075–5083. doi:10.1039/c9nr10813k

De, R., Song, Y. H., Mahata, M. K., and Lee, K. T. (2022). pH-responsive polyelectrolyte complexation on upconversion nanoparticles: a multifunctional nanocarrier for protection, delivery, and 3D-imaging of therapeutic protein. *J. Mater Chem. B* 10 (18), 3420–3433. doi:10.1039/d2tb00246a

Dhal, S., Pal, K., Banerjee, I., and Giri, S. (2020). Upconversion nanoparticle incorporated oleogel as probable skin tissue imaging agent. *Chem. Eng. J.* 379, 122272. doi:10.1016/j.cej.2019.122272

Dong, H., Sun, L.-D., and Yan, C.-H. (2015). Energy transfer in lanthanide upconversion studies for extended optical applications. *Chem. Soc. Rev.* 44 (6), 1608–1634. doi:10.1039/c4cs00188e

Du, H., Zhang, W., and Sun, J. (2011). Structure and upconversion luminescence properties of BaYF5:Yb3+, Er3+ nanoparticles prepared by different methods. *J. Alloys Compd.* 509 (7), 3413–3418. doi:10.1016/j.jallcom.2010.12.101

Du, K., Lei, P., Dong, L., Zhang, M., Gao, X., Yao, S., et al. (2020). *In situ* decorating of ultrasmall Ag2Se on upconversion nanoparticles as novel nanotheranostic agent for multimodal imaging-guided cancer photothermal therapy. *Appl. Mater. Today* 18, 100497. doi:10.1016/j.apmt.2019.100497

Du, P., Luo, L., Li, W., Yue, Q., and Chen, H. (2014). Optical temperature sensor based on upconversion emission in Er-doped ferroelectric 0.5Ba(Zr0.2Ti0.8)O-3-0.5(Ba0.7Ca0.3) TiO3 ceramic. *Appl. Phys. Lett.* 104 (15), 152902. doi:10.1063/1.4871378

Du, P., Luo, L., Park, H.-K., and Yu, J. S. (2016). Citric-assisted sol-gel based Er3+/Yb3+-codoped Na0.5Gd0.5MoO4: A novel highly-efficient infrared-to-visible upconversion material for optical temperature sensors and optical heaters. *Chem. Eng. J.* 306, 840–848. doi:10.1016/j.cej.2016.08.007

Du, P., and Yu, J. S. (2017). Near-ultraviolet light induced visible emissions in Er3+-activated La2MoO6 nanoparticles for solid-state lighting and non-contact thermometry. *Chem. Eng. J.* 327, 109–119. doi:10.1016/j.cej.2017.06.069

Fang, H., Li, M., Liu, Q., Gai, Y., Yuan, L., Wang, S., et al. (2020). Ultra-sensitive nanoprobe modified with tumor cell membrane for UCL/MRI/PET multimodality precise imaging of triple-negative breast cancer. *Nano-Micro Lett.* 12 (1), 62. doi:10.1007/s40820-020-0396-4

Farah, C., Michel, L. Y. M., and Balligand, J.-L. (2018). Nitric oxide signalling in cardiovascular health and disease. *Nat. Rev. Cardiol.* 15 (5), 292–316. doi:10.1038/nrcardio.2017.224

Feng, M., Lv, R., Xiao, L., Hu, B., Zhu, S., He, F., et al. (2018). Highly erbium-doped nanoplatform with enhanced red emission for dual-modal optical-imaging-guided photodynamic therapy. *Inorg. Chem.* 57 (23), 14594–14602. doi:10.1021/acs.inorgchem.8b02257

Gao, G., Jiang, Y.-W., Guo, Y., Jia, H.-R., Cheng, X., Deng, Y., et al. (2020). Enzyme-mediated tumor starvation and phototherapy enhance mild-temperature photothermal therapy. *Adv. Funct. Mater.* 30 (16), 1909391. doi:10.1002/adfm.201909391

Gao, X., Li, T., He, J., Ye, K., Song, X., Wang, N., et al. (2017). Synthesis of Yb3+, Ho3+ and Tm3+ co-doped beta-NaYF4 nanoparticles by sol-gel method and the multi-color upconversion luminescence properties. *J. Mater. Science-Materials Electron.* 28 (16), 11644–11653. doi:10.1007/s10854-017-6967-6

Gao, Y., Li, R., Zheng, W., Shang, X., Wei, J., Zhang, M., et al. (2019). Broadband NIR photostimulated luminescence nanoprobes based on CaS:Eu2+, Sm3+ nanocrystals. *Chem. Sci.* 10 (21), 5452–5460. doi:10.1039/c9sc01321k

Garfield, D. J., Borys, N. J., Hamed, S. M., Torquato, N. A., Tajon, C. A., Tian, B., et al. (2018). Enrichment of molecular antenna triplets amplifies upconverting nanoparticle emission. *Nat. Photonics* 12 (7), 402–407. doi:10.1038/s41566-018-0156-x

Ge, G., Lu, Y., Qu, X., Zhao, W., Ren, Y., Wang, W., et al. (2020). Muscle-inspired self-healing hydrogels for strain and temperature sensor. *Acs Nano* 14 (1), 218–228. doi:10.1021/acsnano.9b07874

Gerelkhuu, Z., Huy, B. T., Jung, D., Sharipov, M., and Lee, Y.-I. (2021). Selective optosensing of iron(III) ions in HeLa cells using NaYF4:Yb3+/Tm3+ upconversion nanoparticles coated with polyepinephrine. *Anal. Bioanal. Chem.* 413 (5), 1363–1371. doi:10.1007/s00216-020-03099-1

Gerelkhuu, Z., Jung, D., Bui The, H., Tawfik, S. M., Conte, M. L., Conte, E. D., et al. (2019). Highly selective and sensitive detection of catecholamines using NaLuGdF4: Yb3+/Er3+ upconversion nanoparticles decorated with metal ions. *Sensors Actuators B-Chemical* 284, 172–178. doi:10.1016/j.snb.2018.12.135

Ghosh, S., Chang, Y.-F., Yang, D.-M., and Chattopadhyay, S. (2020). Upconversion nanoparticle-mOrange protein FRET nanoprobes for self-ratiometric/ratiometric determination of intracellular pH, and single cell pH imaging. *Biosens. Bioelectron.* 155, 112115. doi:10.1016/j.bios.2020.112115

Gierschner, J., Shi, J., Milian-Medina, B., Roca-Sanjuan, D., Varghese, S., and Park, S. (2021). Luminescence in crystalline organic materials: From molecules to molecular solids. *Adv. Opt. Mater.* 9 (13), 2002251. doi:10.1002/adom.202002251

Gong, Z., Wu, T., Chen, X., Guo, J., Zhang, Y., and Li, Y. (2021). Upconversion nanoparticle decorated spider silks as single-cell thermometers. *Nano Lett.* 21 (3), 1469–1476. doi:10.1021/acs.nanolett.0c04644

Gu, Y., Jiang, Z., Ren, D., Shang, Y., Hu, Y., and Yi, L. (2021). Electrochemiluminescence sensor based on the target recognition-induced aggregation of sensing units for Hg2+ determination. *Sensors Actuators B-Chemical* 337, 129821. doi:10.1016/j.snb.2021.129821

Guo, S., Xie, X., Huang, L., and Huang, W. (2016). Sensitive water probing through nonlinear photon upconversion of lanthanide-doped nanoparticles. *Acs Appl. Mater. Interfaces* 8 (1), 847–853. doi:10.1021/acsami.5b10192

Guo, T., Tang, Q., Guo, Y., Qiu, H., Dai, J., Xing, C., et al. (2021). Boron quantum dots for photoacoustic imaging-guided photothermal therapy. *Acs Appl. Mater. Interfaces* 13 (1), 306–311. doi:10.1021/acsami.0c21198

Guryev, E. L., Shilyagina, N. Y., Kostyuk, A. B., Sencha, L. M., Balalaeva, I. V., Vodeneev, V. A., et al. (2019). Preclinical study of biofunctional polymer-coated upconversion nanoparticles. *Toxicol. Sci.* 170 (1), 123–132. doi:10.1093/toxsci/kfz086

Hamza, M. F., Yap, H. J., and Choudhury, I. A. (2017). Recent advances on the use of meta-heuristic optimization algorithms to optimize the type-2 fuzzy logic systems in intelligent control. *Neural Comput. Appl.* 28 (5), 979–999. doi:10.1007/s00521-015-2111-9

Han, S., Deng, R., Xie, X., and Liu, X. (2014). Enhancing luminescence in lanthanide-doped upconversion nanoparticles. *Angew. Chemie-International Ed.* 53 (44), 11702–11715. doi:10.1002/anie.201403408

Hao, T., Wu, X., Xu, L., Liu, L., Ma, W., Kuang, H., et al. (2017). Ultrasensitive detection of prostate-specific antigen and thrombin based on gold-upconversion nanoparticle assembled pyramids. *Small* 13 (19), 1603944. doi:10.1002/smll.201603944

Hassairi, M. A., Garrido Hernandez, A., Dammak, M., Zambon, D., Chadeyron, G., and Mahiou, R. (2018). Tuning white upconversion emission in GdPO4:Er/Yb/Tm phosphors. *J. Luminescence* 203, 707–713. doi:10.1016/j.jlumin.2018.07.024

Hazra, C., Ullah, S., Serge Correales, Y. E., Caetano, L. G., and Ribeiro, S. J. L. (2018). Enhanced NIR-I emission from water-dispersible NIR-II dye-sensitized core/active shell upconverting nanoparticles. *J. Mater. Chem. C* 6 (17), 4777–4785. doi:10.1039/c8tc00335a

He, Y., Guo, S., Zhang, Y., Liu, Y., and Ju, H. (2021). Near-infrared photo-controlled permeability of a biomimetic polymersome with sustained drug release and efficient tumor therapy. *Acs Appl. Mater. Interfaces* 13 (13), 14951–14963. doi:10.1021/acsami.1c00842

Hopper, E., and Turton, B. C. H. (2001). A review of the application of meta-heuristic algorithms to 2D strip packing problems. *Artif. Intell. Rev.* 16 (4), 257–300. doi:10.1023/a:1012590107280

Hou, X., Tao, Y., Pang, Y., Li, X., Jiang, G., and Liu, Y. (2018). Nanoparticle-based photothermal and photodynamic immunotherapy for tumor treatment. *Int. J. Cancer* 143 (12), 3050–3060. doi:10.1002/ijc.31717

Hu, C., He, X., Chen, Y., Yang, X., Qin, L., Lei, T., et al. (2021). Metformin mediated PD-L1 downregulation in combination with photodynamic-immunotherapy for treatment of breast cancer. *Adv. Funct. Mater.* 31 (11), 2007149. doi:10.1002/adfm.202007149

Hu, Z., Fang, C., Li, B., Zhang, Z., Cao, C., Cai, M., et al. (2020). First-in-human liver-tumour surgery guided by multispectral fluorescence imaging in the visible and near-infrared-I/II windows. *Nat. Biomed. Eng.* 4 (3), 259–271. doi:10.1038/s41551-019-0494-0

Issa, S. A. M., Sayyed, M. I., Zaid, M. H. M., and Matori, K. A. (2018). Photon parameters for gamma-rays sensing properties of some oxide of lanthanides. *Results Phys.* 9, 206–210. doi:10.1016/j.rinp.2018.02.039

Ji, Y., Lu, F., Hu, W., Zhao, H., Tang, Y., Li, B., et al. (2019). Tandem activated photodynamic and chemotherapy: Using pH-Sensitive nanosystems to realize different tumour distributions of photosensitizer/prodrug for amplified combination therapy. *Biomaterials* 219, 119393. doi:10.1016/j.biomaterials.2019.119393

Jia, T., Wang, Z., Sun, Q., Dong, S., Xu, J., Zhang, F., et al. (2020). Intelligent Fe-Mn layered double hydroxides nanosheets anchored with upconversion nanoparticles for oxygen-elevated synergetic therapy and bioimaging. *Small* 16 (46), 2001343. doi:10.1002/smll.202001343

Kamata-Sakurai, M., Narita, Y., Hori, Y., Nemoto, T., Uchikawa, R., Honda, M., et al. (2021). Antibody to CD137 activated by extracellular adenosine triphosphate is tumor selective and broadly effective *in vivo* without systemic immune activation. *Cancer Discov.* 11 (1), 158–175. doi:10.1158/2159-8290.cd-20-0328

Katoch, S., Chauhan, S. S., and Kumar, V. (2021). A review on genetic algorithm: Past, present, and future. *Multimedia Tools Appl.* 80 (5), 8091–8126. doi:10.1007/s11042-020-10139-6

Kobayashi, H., Furusawa, A., Rosenberg, A., and Choyke, P. L. (2021). Near-infrared photoimmunotherapy of cancer: A new approach that kills cancer cells and enhances anti-cancer host immunity. *Int. Immunol.* 33 (1), 7–15. doi:10.1093/intimm/dxaa037

Kovalenko, M. V., Scheele, M., and Talapin, D. V. (2009). Colloidal nanocrystals with molecular metal chalcogenide surface ligands. *Science* 324 (5933), 1417–1420. doi:10.1126/science.1170524

Kovalenko, M. V., Spokoyny, B., Lee, J. S., Scheele, M., Weber, A., Perera, S., et al. (2010). Semiconductor nanocrystals functionalized with antimony telluride zintl ions for nanostructured thermoelectrics. *J. Am. Chem. Soc.* 132 (19), 6686–6695. doi:10.1021/ja909591x

Kumar, R., Binetti, L., Nguyen, T. H., Alwis, L. S. M., Sun, T., and Grattan, K. T. V. (2020). Optical fibre thermometry using ratiometric green emission of an upconverting nanoparticle-polydimethylsiloxane composite. *Sensors Actuators a-Physical* 312, 112083. doi:10.1016/j.sna.2020.112083

Lan, G., Ni, K., and Lin, W. (2019). Nanoscale metal-organic frameworks for phototherapy of cancer. *Coord. Chem. Rev.* 379, 65–81. doi:10.1016/j.ccr.2017.09.007

Laurenti, M., Paez-Perez, M., Algarra, M., Alonso-Cristobal, P., Lopez-Cabarcos, E., Mendez-Gonzalez, D., et al. (2016). Enhancement of the upconversion emission by visible-to-near-infrared fluorescent graphene quantum dots for miRNA detection. *Acs Appl. Mater. Interfaces* 8 (20), 12644–12651. doi:10.1021/acsami.6b02361

Lee, H. R., Kim, D. W., Jones, V. O., Choi, Y., Ferry, V. E., Geller, M. A., et al. (2021). Sonosensitizer-functionalized graphene nanoribbons for adhesion blocking and sonodynamic ablation of ovarian cancer spheroids. *Adv. Healthc. Mater.* 10, 2001368. doi:10.1002/adhm.202001368

Li, C., and Lin, J. (2010). Rare Earth fluoride nano-/microcrystals: Synthesis, surface modification and application. *J. Mater. Chem.* 20 (33), 6831–6847. doi:10.1039/c0jm00031k

Li, F., Li, C., Liu, X., Chen, Y., Bai, T., Wang, L., et al. (2012). Hydrophilic, upconverting, multicolor, lanthanide-doped NaGdF4 nanocrystals as potential multifunctional bioprobes. *Chemistry-a Eur. J.* 18 (37), 11641–11646. doi:10.1002/chem.201201309

Li, G., Tian, Y., Zhao, Y., and Lin, J. (2015). Recent progress in luminescence tuning of Ce3+ and Eu2+-activated phosphors for pc-WLEDs. *Chem. Soc. Rev.* 44 (23), 8688–8713. doi:10.1039/c4cs00446a

Li, H., Tan, M., Wang, X., Li, F., Zhang, Y., Zhao, L., et al. (2020). Temporal multiplexed *in vivo* upconversion imaging. *J. Am. Chem. Soc.* 142 (4), 2023–2030. doi:10.1021/jacs.9b11641

Li, H., Wang, C., Jiang, Y., Cui, Z., and Lin, Q. (2014). One-step synthesis of biocompatible chitosan/nagdf4:Eu3+ nanocomposite with fluorescent and magnetic properties for bioimaging. *Nano* 9 (1), 1450007. doi:10.1142/s1793292014500076

Li, J., Rao, J., and Pu, K. (2018). Recent progress on semiconducting polymer nanoparticles for molecular imaging and cancer phototherapy. *Biomaterials* 155, 217–235. doi:10.1016/j.biomaterials.2017.11.025

Li, N., Tan, H., Xie, S., Liu, S., Tong, C., Ouyang, M., et al. (2020). Hexadecylpyridinium chloride mediated hydrothermal synthesis of NaYF4:Yb,Er nanocrystal and their luminescent properties. *J. Nanosci. Nanotechnol.* 20 (3), 1866–1872. doi:10.1166/jnn.2020.17348

Li, Q., Wang, Z., Chen, Y., and Zhang, G. (2017). Elemental bio-imaging of PEGylated NaYF4:Yb/Tm/Gd upconversion nanoparticles in mice by laser ablation inductively coupled plasma mass spectrometry to study toxic side effects on the spleen, liver and kidneys. *Metallomics* 9 (8), 1150–1156. doi:10.1039/c7mt00132k

Li, S., Xu, L., Ma, W., Wu, X., Sun, M., Kuang, H., et al. (2016). Dual-mode ultrasensitive quantification of MicroRNA in living cells by chiroplasmonic nanopyramids self-assembled from gold and upconversion nanoparticles. *J. Am. Chem. Soc.* 138 (1), 306–312. doi:10.1021/jacs.5b10309

Li, X., Zhang, F., and Zhao, D. (2015). Lab on upconversion nanoparticles: Optical properties and applications engineering via designed nanostructure. *Chem. Soc. Rev.* 44 (6), 1346–1378. doi:10.1039/c4cs00163j

Li, Y., Li, Y., Wang, R., Xu, Y., and Zheng, W. (2017). Enhancing upconversion luminescence by annealing processes and the high-temperature sensing of ZnO:Yb/Tm nanoparticles. *New J. Chem.* 41 (15), 7116–7122. doi:10.1039/c7nj01358b

Li, Y., Liu, J., Qin, X., Deng, Y., Zhang, J., and Sun, Y. (2019). Ultrafast synthesis of fluorine-18 doped bismuth based upconversion nanophosphors for tri-modal CT/PET/UCL imaging *in vivo*. *Chem. Commun.* 55 (50), 7259–7262. doi:10.1039/c9cc02677k

Li, Z.-H., Chen, Y., Sun, Y., and Zhang, X.-Z. (2021). Platinum-doped prussian blue nanozymes for multiwavelength bioimaging guided photothermal therapy of tumor and anti-inflammation. *Acs Nano* 15 (3), 5189–5200. doi:10.1021/acsnano.0c10388

Li, Z., and Zhang, Y. (2006). Monodisperse silica-coated polyvinylpyrrolidone/NaYF(4) nanocrystals with multicolor upconversion fluorescence emission. *Angew. Chem. Int. Ed. Engl.* 45 (46), 7732–7735. doi:10.1002/anie.200602975

Liang, T., Wang, Q., Li, Z., Wang, P., Wu, J., Zuo, M., et al. (2020). Removing the obstacle of dye-sensitized upconversion luminescence in aqueous phase to achieve high-contrast deep imaging *in vivo*. *Adv. Funct. Mater.* 30 (16), 1910765. doi:10.1002/adfm.201910765

Liang, X., Fan, J., Zhao, Y., and Jin, R. (2020). Core-shell structured NaYF4:Yb,Er nanoparticles with excellent upconversion luminescent for targeted drug delivery. *J. Clust. Sci.* 32, 1683–1691. doi:10.1007/s10876-020-01929-x

Lin, B., Liu, J., Wang, Y., Yang, F., Huang, L., and Lv, R. (2020). Enhanced upconversion luminescence-guided synergistic antitumor therapy based on photodynamic therapy and immune checkpoint blockade. *Chem. Mater.* 32 (11), 4627–4640. doi:10.1021/acs.chemmater.0c01031

Lin, M., Xie, L., Wang, Z., Richards, B. S., Gao, G., and Zhong, J. (2019). Facile synthesis of mono-disperse sub-20 nm NaY(WO4)(2):Er3+,Yb3+ upconversion nanoparticles: A new choice for nanothermometry. *J. Mater. Chem. C* 7 (10), 2971–2977. doi:10.1039/c8tc05669b

Lin, M., Zhao, Y., Wang, S., Liu, M., Duan, Z., Chen, Y., et al. (2012). Recent advances in synthesis and surface modification of lanthanide-doped upconversion nanoparticles for biomedical applications. *Biotechnol. Adv.* 30 (6), 1551–1561. doi:10.1016/j.biotechadv.2012.04.009

Lin, M., Zou, S., Liao, X., Chen, Y., Luo, D., Ji, L., et al. (2021). Ruthenium(ii) complexes as bioorthogonal two-photon photosensitizers for tumour-specific photodynamic therapy against triple-negative breast cancer cells. *Chem. Commun.* 57 (36), 4408–4411. doi:10.1039/d1cc00661d

Liu, B., Sun, J., Zhu, J., Li, B., Ma, C., Gu, X., et al. (2020). Injectable and NIR-responsive DNA-inorganic hybrid hydrogels with outstanding photothermal therapy. *Adv. Mater.* 32 (39), 2004460. doi:10.1002/adma.202004460

Liu, J., Yang, F., Feng, M., Wang, Y., Peng, X., and Lv, R. (2019). Surface plasmonic enhanced imaging-guided photothermal/photodynamic therapy based on lanthanide-metal nanocomposites under single 808 nm laser. *Acs Biomaterials Sci. Eng.* 5 (10), 5051–5059. doi:10.1021/acsbiomaterials.9b01112

Liu, K., Liu, X., Zeng, Q., Zhang, Y., Tu, L., Liu, T., et al. (2012). Covalently assembled NIR nanoplatform for simultaneous fluorescence imaging and photodynamic therapy of cancer cells. *Acs Nano* 6 (5), 4054–4062. doi:10.1021/nn300436b

Liu, L., Li, X. T., Zhang, H., Chen, H. D., Abualrejal, M. M. A., Song, D. Q., et al. (2021). Six-in-one peptide functionalized upconversion@polydopamine nanoparticle-based ratiometric fluorescence sensing platform for real-time evaluating anticancer efficacy through monitoring caspase-3 activity. *Sensors Actuators B-Chemical* 333, 129554. doi:10.1016/j.snb.2021.129554

Liu, Q., Xu, M., Yang, T., Tian, B., Zhang, X., and Li, F. (2018). Highly photostable near-IR-excitation upconversion nanocapsules based on triplet-triplet annihilation for *in vivo* bioimaging application. *Acs Appl. Mater. Interfaces* 10 (12), 9883–9888. doi:10.1021/acsami.7b17929

Liu, S., Liu, S., Ming, H., Du, F., Peng, J., You, W., et al. (2018). Tunable multicolor and bright white upconversion luminescence in Er3+/Tm3+/Yb3+ tri-doped SrLu2O4 phosphors. *J. Mater. Sci.* 53 (20), 14469–14484. doi:10.1007/s10853-018-2632-6

Liu, Y., Chen, M., Zhao, Y., Lv, S., Zheng, D., Liu, D., et al. (2021). A novel D-A-D photosensitizer for efficient NIR imaging and photodynamic therapy. *Chembiochem* 22, 2161–2167. doi:10.1002/cbic.202100107

Liu, Y., Meng, X., and Bu, W. (2019). Upconversion-based photodynamic cancer therapy. *Coord. Chem. Rev.* 379, 82–98. doi:10.1016/j.ccr.2017.09.006

Lu, C., Guan, J., Lu, S., Jin, Q., Rousseau, B., Lu, T., et al. (2021). DNA sensing in mismatch repair-deficient tumor cells is essential for anti-tumor immunity. *Cancer Cell* 39 (1), 96–108.e6. doi:10.1016/j.ccell.2020.11.006

Lundberg, J. O., Gladwin, M. T., and Weitzberg, E. (2015). Strategies to increase nitric oxide signalling in cardiovascular disease. *Nat. Rev. Drug Discov.* 14 (9), 623–641. doi:10.1038/nrd4623

Luo, R., Chen, L., Li, Q., Zhou, J., Mei, L., Ning, Z., et al. (2020). Bi3+-Doped BaYF5: Yb,Er upconversion nanoparticles with enhanced luminescence and application case for X-ray computed tomography imaging. *Inorg. Chem.* 59 (24), 17906–17915. doi:10.1021/acs.inorgchem.0c01818

Lutken, C. D., Achiam, M. P., Osterkamp, J., Svendsen, M. B., and Nerup, N. (2021). Quantification of fluorescence angiography: Toward a reliable intraoperative assessment of tissue perfusion-A narrative review. *Langenbecks Archives Surg.* 406 (2), 251–259. doi:10.1007/s00423-020-01966-0

Lv, R., Feng, M., and Parak, W. J. (2018). Up-conversion luminescence properties of lanthanide-gold hybrid nanoparticles as analyzed with Discrete Dipole approximation. *Nanomaterials* 8 (12), 989. doi:10.3390/nano8120989

Lv, R., Xiao, L., Jiang, X., Feng, M., Yang, F., and Tian, J. (2018). Optimization of red luminescent intensity in Eu3+-doped lanthanide phosphors using genetic algorithm. *Acs Biomaterials Sci. Eng.* 4 (12), 4378–4384. doi:10.1021/acsbiomaterials.8b00513

Lv, R., Xiao, L., Wang, Y., Yang, F., Tian, J., and Lin, J. (2019). Searching for the optimized luminescent lanthanide phosphor using heuristic algorithms. *Inorg. Chem.* 58 (9), 6458–6466. doi:10.1021/acs.inorgchem.9b00667

Lv, R., Yang, F., Jiang, X., Hu, B., Zhang, X., Chen, X., et al. (2020). Plasmonic modulated upconversion fluorescence by adjustable distributed gold nanoparticles. *J. Luminescence* 220, 116974. doi:10.1016/j.jlumin.2019.116974

Lv, R., Yang, G., Dai, Y., Gai, S., He, F., and Yang, P. (2014). Self-produced bubble-template synthesis of La2O3:Yb/Er@Au hollow spheres with markedly enhanced luminescence and release properties. *Crystengcomm* 16 (41), 9612–9621. doi:10.1039/c4ce01063a

Lv, R., Yang, P., Dai, Y., Gai, S., He, F., and Lin, J. (2014). Lutecium fluoride hollow mesoporous spheres with enhanced up-conversion luminescent bioimaging and light-triggered drug release by gold nanocrystals. *ACS Appl. Mater. interfaces* 6 (17), 15550–15563. doi:10.1021/am504347e

Ma, L., Liu, F., Lei, Z., and Wang, Z. (2017). A novel upconversion@polydopamine core@shell nanoparticle based aptameric biosensor for biosensing and imaging of cytochrome c inside living cells. *Biosens. Bioelectron.* 87, 638–645. doi:10.1016/j.bios.2016.09.017

Ma, S., Wang, L., Liu, Z., Luo, X., Zhou, Z., Xie, J., et al. (2021). One stone, two birds": Engineering 2-D ultrathin heterostructure nanosheet BiNS@NaLnF(4) for dual-modal computed tomography/magnetic resonance imaging guided, photonic synergetic theranostics. *Nanoscale* 13 (1), 185–194. doi:10.1039/d0nr07590f

Ma, Y., Ma, Y., Gao, M., Han, Z., Jiang, W., Gu, Y., et al. (2021). Platelet-mimicking therapeutic system for noninvasive mitigation of the progression of atherosclerotic plaques. *Adv. Sci.* 8 (8), 2004128. doi:10.1002/advs.202004128

Mahata, M. K., Bae, H., and Lee, K. T. (2017). Upconversion luminescence sensitized pH-nanoprobes. *Molecules* 22 (12), 2064. doi:10.3390/molecules22122064

Maret, W. (2013). Zinc biochemistry: From a single zinc enzyme to a Key element of life. *Adv. Nutr.* 4 (1), 82–91. doi:10.3945/an.112.003038

Mates, J. M., Segura, J. A., Alonso, F. J., and Marquez, J. (2012). Oxidative stress in apoptosis and cancer: An update. *Archives Toxicol.* 86 (11), 1649–1665. doi:10.1007/s00204-012-0906-3

Mintz, K. J., Zhou, Y., and Leblanc, R. M. (2019). Recent development of carbon quantum dots regarding their optical properties, photoluminescence mechanism, and core structure. *Nanoscale* 11 (11), 4634–4652. doi:10.1039/c8nr10059d

Mir, W. J., Sheikh, T., Arfin, H., Xia, Z., and Nag, A. (2020). Lanthanide doping in metal halide perovskite nanocrystals: Spectral shifting, quantum cutting and optoelectronic applications. *Npg Asia Mater.* 12 (1), 9. doi:10.1038/s41427-019-0192-0

Mousavand, T., Ohara, S., Naka, T., Umetsu, M., Takami, S., and Adschiri, T. (2010). Organic-ligand-assisted hydrothermal synthesis of ultrafine and hydrophobic ZnO nanoparticles. *J. Mater. Res.* 25 (2), 219–223. doi:10.1557/jmr.2010.0037

Mpekris, F., Voutouri, C., Baish, J. W., Duda, D. G., Munn, L. L., Stylianopoulos, T., et al. (2020). Combining microenvironment normalization strategies to improve cancer immunotherapy. *Proc. Natl. Acad. Sci. U. S. A.* 117 (7), 3728–3737. doi:10.1073/pnas.1919764117

Mykhaylyk, O., Cherchenko, A., Ilkin, A., Dudchenko, N., Ruditsa, V., Novoseletz, M., et al. (2001). Glial brain tumor targeting of magnetite nanoparticles in rats. *J. MAGNETISM MAGNETIC Mater.* 225 (1-2), 241–247. doi:10.1016/s0304-8853(00)01264-6

Ozdemir, G., and Karaboga, N. (2019). A review on the cosine modulated filter bank studies using meta-heuristic optimization algorithms. *Artif. Intell. Rev.* 52 (3), 1629–1653. doi:10.1007/s10462-017-9595-x

Pan, G., Bai, X., Yang, D., Chen, X., Jing, P., Qu, S., et al. (2017). Doping lanthanide into perovskite nanocrystals: Highly improved and expanded optical properties. *Nano Lett.* 17 (12), 8005–8011. doi:10.1021/acs.nanolett.7b04575

Pang, H., Tian, C., He, G., Zhang, D., Yang, J., Zhang, Q., et al. (2021). NIR-absorbing Prussian blue nanoparticles for transarterial infusion photothermal therapy of VX2 tumors implanted in rabbits. *Nanoscale* 13 (18), 8490–8497. doi:10.1039/d1nr01394g

Park, J., Xu, M., Li, F., and Zhou, H.-C. (2018). 3D long-range triplet migration in a water-stable metal-organic framework for upconversion-based ultralow-power *in vivo* imaging. *J. Am. Chem. Soc.* 140 (16), 5493–5499. doi:10.1021/jacs.8b01613

Pedziwiatr-Werbicka, E., Horodecka, K., Shcharbin, D., and Bryszewska, M. (2021). Nanoparticles in combating cancer: Opportunities and limitations: A brief review. *Curr. Med. Chem.* 28 (2), 346–359. doi:10.2174/1875533xmta0kmdkhw

Peng, J., Xu, W., Teoh, C. L., Han, S., Kim, B., Samanta, A., et al. (2015). High-efficiency *in vitro* and *in vivo* detection of Zn2+ by dye-assembled upconversion nanoparticles. *J. Am. Chem. Soc.* 137 (6), 2336–2342. doi:10.1021/ja5115248

Pfeiffer, F. (2018). X-ray ptychography. *Nat. Photonics* 12 (1), 9–17. doi:10.1038/s41566-017-0072-5

Pinto, A., Marangon, I., Mereaux, J., Nicolas-Boluda, A., Lavieu, G., Wilhelm, C., et al. (2021). Immune reprogramming precision photodynamic therapy of peritoneal metastasis by scalable stem-cell-derived extracellular vesicles. *Acs Nano* 15 (2), 3251–3263. doi:10.1021/acsnano.0c09938

Plattner, N., and Noe, F. (2015). Protein conformational plasticity and complex ligand-binding kinetics explored by atomistic simulations and Markov models. *Nat. Commun.* 6, 7653. doi:10.1038/ncomms8653

Qiao, Y. F., Qiao, S. Q., Yu, X., Min, Q. H., Pi, C. J., Qiu, J. B., et al. (2021). Plant tissue imaging with bipyramidal upconversion nanocrystals by introducing Tm3+ ions as energy trapping centers. *Nanoscale* 13 (17), 8181–8187. doi:10.1039/d0nr07399g

Qiu, X., Zhu, X., Xu, M., Yuan, W., Feng, W., and Li, F. (2017). Hybrid nanoclusters for near-infrared to near-infrared upconverted persistent luminescence bioimaging. *Acs Appl. Mater. Interfaces* 9 (38), 32583–32590. doi:10.1021/acsami.7b10618

Qu, A., Wu, X., Xu, L., Liu, L., Ma, W., Kuang, H., et al. (2017). SERS- and luminescence-active Au-Au-UCNP trimers for attomolar detection of two cancer biomarkers. *Nanoscale* 9 (11), 3865–3872. doi:10.1039/c6nr09114h

Quan, L. N., de Arquer, F. P. G., Sabatini, R. P., and Sargent, E. H. (2018). Perovskites for light emission. *Adv. Mater.* 30 (45), 1801996. doi:10.1002/adma.201801996

Radunz, S., Andresen, E., Wuerth, C., Koerdt, A., Tschiche, H. R., and Resch-Genger, U. (2019). Simple self-referenced luminescent pH sensors based on upconversion nanocrystals and pH-sensitive fluorescent BODIPY dyes. *Anal. Chem.* 91 (12), 7756–7764. doi:10.1021/acs.analchem.9b01174

Rafique, R., Baek, S. H., Le Minh Tu, P., Chang, S.-J., Gul, A. R., and Park, T. J. (2019). A facile hydrothermal synthesis of highly luminescent NaYF4:Yb3+/Er3+ upconversion nanoparticles and their biomonitoring capability. *Mater. Sci. Eng. C-Materials Biol. Appl.* 99, 1067–1074. doi:10.1016/j.msec.2019.02.046

Rafique, R., Baek, S. H., Park, C. Y., Chang, S. J., Gul, A. R., Ha, S., et al. (2018). Morphological evolution of upconversion nanoparticles and their biomedical signal generation. *Sci. Rep.* 8 (1), 17101. doi:10.1038/s41598-018-35513-1

Ravichandran, V., Thuy Giang Nguyen, C., Dae Gun, C., Han Chang, K., and Min Suk, S. (2020). Non-ionic polysorbate-based nanoparticles for efficient combination chemo/photothermal/photodynamic therapy. *J. Industrial Eng. Chem.* 88, 260–267. doi:10.1016/j.jiec.2020.04.023

Reddy, K. L., Balaji, R., Kumar, A., and Krishnan, V. (2018). Lanthanide doped near infrared active upconversion nanophosphors: Fundamental concepts, synthesis strategies, and technological applications. *Small* 14 (37), 1801304. doi:10.1002/smll.201801304

Sangkhae, V., and Nemeth, E. (2017). Regulation of the iron homeostatic hormone hepcidin. *Adv. Nutr.* 8 (1), 126–136. doi:10.3945/an.116.013961

Shahzad, M. K., Zhang, Y., Raza, A., Ikram, M., Qi, K., Khan, M. U., et al. (2019). Polymer microfibers incorporated with silver nanoparticles: A new platform for optical sensing. *Nanoscale Res. Lett.* 14 (1), 270. doi:10.1186/s11671-019-3108-6

Shan, X., Chen, Q., Yin, X., Jiang, C., Li, T., Wei, S., et al. (2020). Polypyrrole-based double rare Earth hybrid nanoparticles for multimodal imaging and photothermal therapy. *J. Mater Chem. B* 8 (3), 426–437. doi:10.1039/c9tb02254f

Shanmugam, V., Selvakumar, S., and Yeh, C.-S. (2014). Near-infrared light-responsive nanomaterials in cancer therapeutics. *Chem. Soc. Rev.* 43 (17), 6254–6287. doi:10.1039/c4cs00011k

Shen, Y., Wu, T., Wang, Y., Zhang, S.-L., Zhao, X., Chen, H.-Y., et al. (2021). Nucleolin-targeted ratiometric fluorescent carbon dots with a remarkably large emission wavelength shift for precise imaging of cathepsin B in living cancer cells. *Anal. Chem.* 93 (8), 4042–4050. doi:10.1021/acs.analchem.0c05046

Shi, M., Fu, Z., Pan, W., Chen, Y., Wang, K., Zhou, P., et al. (2021). A protein-binding molecular photothermal agent for tumor ablation. *Angew. Chemie-International Ed.* 60 (24), 13676–13680. doi:10.1002/ange.202101009

Su, J., Li, Y., Gu, W., and Liu, X. (2020). Spiropyran-modified upconversion nanocomposite as a fluorescent sensor for diagnosis of histidinemia. *Rsc Adv.* 10 (45), 26664–26670. doi:10.1039/d0ra03711g

Suman, B., and Kumar, P. (2006). A survey of simulated annealing as a tool for single and multiobjective optimization. *J. Operational Res. Soc.* 57 (10), 1143–1160. doi:10.1057/palgrave.jors.2602068

Sun, J.-S., Li, S.-W., Shi, L.-L., Zhou, T.-M., Li, X.-P., Zhang, J.-S., et al. (2015). Experimental optimal design of the Er3+/Yb3+ codoped BaGd2ZnO5 phosphor and its upconversion luminescence properties. *Acta Phys. Sin.* 64 (24), 243301. doi:10.7498/aps.64.243301

Sun, Y., Peng, J., Feng, W., and Li, F. (2013). Upconversion nanophosphors naluf(4): Yb, Tm for lymphatic imaging *in vivo* by real-time upconversion luminescence imaging under ambient light and high-resolution X-ray CT. *Theranostics* 3 (5), 346–353. doi:10.7150/thno.5137

Sun, Y., Yu, M. X., Liang, S., Zhang, Y. J., Li, C. G., Mou, T. T., et al. (2011). Fluorine-18 labeled rare-Earth nanoparticles for positron emission tomography (PET) imaging of sentinel lymph node. *Biomaterials* 32 (11), 2999–3007. doi:10.1016/j.biomaterials.2011.01.011

Sun, Y., Zhang, Y., Gao, Y., Wang, P., He, G., Blum, N. T., et al. (2020). Six birds with one stone: Versatile nanoporphyrin for single-laser-triggered synergistic phototheranostics and robust immune activation. *Adv. Mater.* 32 (48), 2004481. doi:10.1002/adma.202004481

Tan, M., Li, F., Cao, N., Li, H., Wang, X., Zhang, C., et al. (2020). Accurate *in vivo* nanothermometry through NIR-II lanthanide luminescence lifetime. *Small* 16 (48), 2004118. doi:10.1002/smll.202004118

Tan, S., Li, D., and Zhu, X. (2020). Cancer immunotherapy: Pros, cons and beyond. *Biomed. Pharmacother.* 124, 109821. doi:10.1016/j.biopha.2020.109821

Tangirala, R., Baker, J. L., Alivisatos, A. P., and Milliron, D. J. (2010). Modular inorganic nanocomposites by conversion of nanocrystal superlattices. *Angew. Chem. Int. Ed. Engl.* 49 (16), 2878–2882. doi:10.1002/anie.200906642

Tay, R. E., Richardson, E. K., and Toh, H. C. (2021). Revisiting the role of CD4(+) T cells in cancer immunotherapy-new insights into old paradigms. *Cancer Gene Ther.* 28 (1-2), 5–17. doi:10.1038/s41417-020-0183-x

Teng, C. W., Huang, V., Arguelles, G. R., Zhou, C., Cho, S. S., Harmsen, S., et al. (2021). Applications of indocyanine green in brain tumor surgery: Review of clinical evidence and emerging technologies. *Neurosurg. Focus* 50 (1), E4. doi:10.3171/2020.10.focus20782

Thangaraj, R., Pant, M., Abraham, A., and Bouvry, P. (2011). Particle swarm optimization: Hybridization perspectives and experimental illustrations. *Appl. Math. Comput.* 217 (12), 5208–5226. doi:10.1016/j.amc.2010.12.053

Thariani, R., and Yager, P. (2010). Imaging of surfaces by concurrent surface plasmon resonance and surface plasmon resonance-enhanced fluorescence. *Plos One* 5 (3), e9833. doi:10.1371/journal.pone.0009833

Tian, J., Huang, B., Nawaz, M. H., and Zhang, W. (2020). Recent advances of multi-dimensional porphyrin-based functional materials in photodynamic therapy. *Coord. Chem. Rev.* 420, 213410. doi:10.1016/j.ccr.2020.213410

Tian, R., Zhao, S., Liu, G., Chen, H., Ma, L., You, H., et al. (2019). Construction of lanthanide-doped upconversion nanoparticle-Uelx Europaeus Agglutinin-I bioconjugates with brightness red emission for ultrasensitive *in vivo* imaging of colorectal tumor. *Biomaterials* 212, 64–72. doi:10.1016/j.biomaterials.2019.05.010

Tirotta, I., Dichiarante, V., Pigliacelli, C., Cavallo, G., Terraneo, G., Bombelli, F. B., et al. (2015). ^{19}F magnetic resonance imaging (MRI): From design of materials to clinical applications. *Chem. Rev.* 115 (2), 1106–1129. doi:10.1021/cr500286d

Tran Quang, T., Ramasundaram, S., Hwang, B.-U., and Lee, N.-E. (2016). An all-elastomeric transparent and stretchable temperature sensor for body-attachable wearable electronics. *Adv. Mater.* 28 (3), 502–509. doi:10.1002/adma.201504441

Tsang, M.-K., Bai, G., and Hao, J. (2015). Stimuli responsive upconversion luminescence nanomaterials and films for various applications. *Chem. Soc. Rev.* 44 (6), 1585–1607. doi:10.1039/c4cs00171k

Tse, W. H., Chen, L., McCurdy, C. M., Tarapacki, C. M., Chronik, B. A., and Zhang, J. (2019). Development of biocompatible NaGdF4: Er3+, Yb3+ upconversion nanoparticles used as contrast agents for bio-imaging. *Can. J. Chem. Eng.* 97 (10), 2678–2684. doi:10.1002/cjce.23510

Vedunova, M. V., Mishchenko, T. A., Mitroshina, E. V., Ponomareva, N. V., Yudintsev, A. V., Generalova, A. N., et al. (2016). Cytotoxic effects of upconversion nanoparticles in primary hippocampal cultures. *RSC Adv.* 6 (40), 33656–33665. doi:10.1039/c6ra01272h

Wallis, C. J. D., Butaney, M., Satkunasivam, R., Freedland, S. J., Patel, S. P., Hamid, O., et al. (2019). Association of patient sex with efficacy of immune checkpoint inhibitors and overall survival in advanced cancers A systematic review and meta-analysis. *Jama Oncol.* 5 (4), 529–536. doi:10.1001/jamaoncol.2018.5904

Wang, C., Zhao, P., Yang, G., Chen, X., Jiang, Y., Jiang, X., et al. (2020). Reconstructing the intracellular pH microenvironment for enhancing photodynamic therapy. *Mater. Horizons* 7 (4), 1180–1185. doi:10.1039/c9mh01824g

Wang, F., Deng, R., and Liu, X. (2014). Preparation of core-shell NaGdF4 nanoparticles doped with luminescent lanthanide ions to be used as upconversion-based probes. *Nat. Protoc.* 9 (7), 1634–1644. doi:10.1038/nprot.2014.111

Wang, G., Peng, Q., and Li, Y. (2011). Lanthanide-doped nanocrystals: Synthesis, optical-magnetic properties, and applications. *Accounts Chem. Res.* 44 (5), 322–332. doi:10.1021/ar100129p

Wang, M., Song, J., Zhou, F., Hoover, A. R., Murray, C., Zhou, B., et al. (2019). NIR-triggered phototherapy and immunotherapy via an antigen-capturing nanoplatform for metastatic cancer treatment. *Adv. Sci.* 6 (10), 1802157. doi:10.1002/advs.201802157

Wang, X., Chang, H., Xie, J., Zhao, B., Liu, B., Xu, S., et al. (2014). Recent developments in lanthanide-based luminescent probes. *Coord. Chem. Rev.* 273, 201–212. doi:10.1016/j.ccr.2014.02.001

Wang, X., Liu, Q., Bu, Y., Liu, C.-S., Liu, T., and Yan, X. (2015). Optical temperature sensing of rare-Earth ion doped phosphors. *Rsc Adv.* 5 (105), 86219–86236. doi:10.1039/c5ra16986k

Wang, X., Zhuang, J., Peng, Q., and Li, Y. D. (2005). A general strategy for nanocrystal synthesis. *Nature* 437 (7055), 121–124. doi:10.1038/nature03968

Wang, Z., Liu, C., Zhao, Y., Hu, M., Ma, D., Zhang, P., et al. (2019). Photomagnetic nanoparticles in dual-modality imaging and photo-sonodynamic activity against bacteria. *Chem. Eng. J.* 356, 811–818. doi:10.1016/j.cej.2018.09.077

Wattanasiritham, L., Theerakulkait, C., Wickramasekara, S., Maier, C. S., and Stevens, J. F. (2016). Isolation and identification of antioxidant peptides from enzymatically hydrolyzed rice bran protein. *Food Chem.* 192, 156–162. doi:10.1016/j.foodchem.2015.06.057

Wei, R., Dong, Y., Tu, Y., Luo, S., Pang, X., Zhang, W., et al. (2021). Bioorthogonal pretargeting strategy for anchoring activatable photosensitizers on plasma membranes for effective photodynamic therapy. *Acs Appl. Mater. Interfaces* 13 (12), 14004–14014. doi:10.1021/acsami.1c01259

White, K. A., Grillo-Hill, B. K., and Barber, D. L. (2017). Cancer cell behaviors mediated by dysregulated pH dynamics at a glance. *J. Cell Sci.* 130 (4), 663–669. doi:10.1242/jcs.195297

Wong, Y.-T., Pang, S.-Y., Tsang, M.-K., Liu, Y., Huang, H., Yu, S.-F., et al. (2019). Electrochemically assisted flexible lanthanide upconversion luminescence sensing of heavy metal contamination with high sensitivity and selectivity. *Nanoscale Adv.* 1 (1), 265–272. doi:10.1039/c8na00012c

Wu, C., Huang, X., Tang, Y., Xiao, W., Sun, L., Shao, J., et al. (2019). Pyrrolopyrrole aza-BODIPY near-infrared photosensitizer for dual-mode imaging-guided photothermal cancer therapy. *Chem. Commun.* 55 (6), 790–793. doi:10.1039/c8cc07768a

Wu, M., Liu, X., Chen, H., Duan, Y., Liu, J., Pan, Y., et al. (2021). Activation of pyroptosis by membrane-anchoring AIE photosensitizer design: New prospect for photodynamic cancer cell ablation. *Angew. Chemie-International Ed.* 60 (16), 9175–9180. doi:10.1002/ange.202016399

Wu, M., Wang, X., Wang, K., and Guo, Z. (2017). An ultrasensitive fluorescent nanosensor for trypsin based on upconversion nanoparticles. *Talanta* 174, 797–802. doi:10.1016/j.talanta.2017.07.013

Wu, X., Lee, H., Bilsel, O., Zhang, Y., Li, Z., Chen, T., et al. (2015). Tailoring dye-sensitized upconversion nanoparticle excitation bands towards excitation wavelength selective imaging. *Nanoscale* 7 (44), 18424–18428. doi:10.1039/c5nr05437k

Wu, X., Zhang, Y., Takle, K., Bilsel, O., Li, Z., Lee, H., et al. (2016). Dye-sensitized core/active shell upconversion nanoparticles for optogenetics and bioimaging applications. *Acs Nano* 10 (1), 1060–1066. doi:10.1021/acsnano.5b06383

Xiao, Q., Li, Y., Li, F., Zhang, M., Zhang, Z., and Lin, H. (2014). Rational design of a thermalresponsive-polymer-switchable FRET system for enhancing the temperature sensitivity of upconversion nanophosphors. *Nanoscale* 6 (17), 10179–10186. doi:10.1039/c4nr02497d

Xie, Z., Fan, T., An, J., Choi, W., Duo, Y., Ge, Y., et al. (2020). Emerging combination strategies with phototherapy in cancer nanomedicine. *Chem. Soc. Rev.* 49 (22), 8065–8087. doi:10.1039/d0cs00215a

Xu, D., Liu, J., Wang, Y., Jian, Y., Wu, W., and Lv, R. (2020). Black phosphorus nanosheet with high thermal conversion efficiency for photodynamic/photothermal/immunotherapy. *Acs Biomaterials Sci. Eng.* 6 (9), 4940–4948. doi:10.1021/acsbiomaterials.0c00984

Xu, J., Lv, R., Du, S., Gai, S., He, F., Yang, D., et al. (2016). UCNPs@gelatin-ZnPc nanocomposite: Synthesis, imaging and anticancer properties. *J. Mater Chem. B* 4 (23), 4138–4146. doi:10.1039/c6tb00714g

Xu, X., Sun, Y., Zhang, Q., Cai, H., Li, Q., and Zhou, S. (2019). Synthesis and photocatalytic activity of plasmon-enhanced core-shell upconversion luminescent photocatalytic Ag@SiO2@YF3:Ho3+@TiO2 nanocomposites. *Opt. Mater.* 94, 444–453. doi:10.1016/j.optmat.2019.05.038

Yakavets, I., Francois, A., Lamy, L., Piffoux, M., Gazeau, F., Wilhelm, C., et al. (2021). Effect of stroma on the behavior of temoporfin-loaded lipid nanovesicles inside the stroma-rich head and neck carcinoma spheroids. *J. Nanobiotechnology* 19 (1), 3. doi:10.1186/s12951-020-00743-x

Yan, C., Zhang, Y., and Guo, Z. (2021). Recent progress on molecularly near-infrared fluorescent probes for chemotherapy and phototherapy. *Coord. Chem. Rev.* 427, 213556. doi:10.1016/j.ccr.2020.213556

Yan, J., Gao, T., Lu, Z., Yin, J., Zhang, Y., and Pei, R. (2021). Aptamer-targeted photodynamic platforms for tumor therapy. *ACS Appl. Mater. interfaces* 13, 27749–27773. doi:10.1021/acsami.1c06818

Yan, S., Zeng, X., Tang, Y. a., Liu, B.-F., Wang, Y., and Liu, X. (2019). Activating antitumor immunity and antimetastatic effect through polydopamine-encapsulated core-shell upconversion nanoparticles. *Adv. Mater.* 31 (46), 1905825. doi:10.1002/adma.201905825

Yang, C., Su, M., Luo, P., Liu, Y., Yang, F., and Li, C. (2021). A photosensitive polymeric carrier with a renewable singlet oxygen reservoir regulated by two NIR beams for enhanced antitumor phototherapy. *Small* 17, e2101180.

Yang, C., Zhu, Y., Li, D., Liu, Y., Guan, C., Man, X., et al. (2021). Red phosphorus decorated TiO2 nanorod mediated photodynamic and photothermal therapy for renal cell carcinoma. *Small* 17, e2101837.

Yang, D., Dai, Y., Liu, J., Zhou, Y., Chen, Y., Li, C., et al. (2014). Ultra-small BaGdF5-based upconversion nanoparticles as drug carriers and multimodal imaging probes. *Biomaterials* 35 (6), 2011–2023. doi:10.1016/j.biomaterials.2013.11.018

Yang, L., Shao, B., Zhang, X., Cheng, Q., Lin, T., and Liu, E. (2016). Multifunctional upconversion nanoparticles for targeted dual-modal imaging in rat glioma xenograft. *J. Biomaterials Appl.* 31 (3), 400–410. doi:10.1177/0885328216658779

Yao, J., Huang, C., Liu, C., and Yang, M. (2020). Upconversion luminescence nanomaterials: A versatile platform for imaging, sensing, and therapy. *Talanta* 208, 120157. doi:10.1016/j.talanta.2019.120157

Ye, X., Collins, J. E., Kang, Y., Chen, J., Chen, D. T. N., Yodh, A. G., et al. (2010). Morphologically controlled synthesis of colloidal upconversion nanophosphors and their shape-directed self-assembly. *Proc. Natl. Acad. Sci. U. S. A.* 107 (52), 22430–22435. doi:10.1073/pnas.1008958107

Yi, Z., Luo, Z., Barth, N. D., Meng, X., Liu, H., Bu, W., et al. (2019). *In vivo* tumor visualization through MRI off-on switching of $NaGdF_4$–$CaCO_3$ nanoconjugates. *Adv. Mater.* 31 (37), 1901851. doi:10.1002/adma.201901851

Yin, A., Zhang, Y., Sun, L., and Yan, C. (2010). Colloidal synthesis and blue based multicolor upconversion emissions of size and composition controlled monodisperse hexagonal NaYF4: Yb,Tm nanocrystals. *Nanoscale* 2 (6), 953–959. doi:10.1039/b9nr00397e

Yin, Z., Zhou, D., Xu, W., Cui, S., Chen, X., Wang, H., et al. (2016). Plasmon-enhanced upconversion luminescence on vertically aligned gold nanorod monolayer supercrystals. *Acs Appl. Mater. Interfaces* 8 (18), 11667–11674. doi:10.1021/acsami.5b12075

Yuan, J., Cen, Y., Kong, X.-J., Wu, S., Liu, C.-L., Yu, R.-Q., et al. (2015). MnO2-Nanosheet-Modified upconversion nanosystem for sensitive turn-on fluorescence detection of H2O2 and glucose in blood. *Acs Appl. Mater. Interfaces* 7 (19), 10548–10555. doi:10.1021/acsami.5b02188

Yuan, Y., Gao, C., Wang, D., Zhou, C., Zhu, B., and He, Q. (2019). Janus-micromotor-based on-off luminescence sensor for active TNT detection. *Beilstein J. Nanotechnol.* 10, 1324–1331. doi:10.3762/bjnano.10.131

Yuan, Z., Fan, G., Wu, H., Liu, C., Zhan, Y., Qiu, Y., et al. (2021). Photodynamic therapy synergizes with PD-L1 checkpoint blockade for immunotherapy of CRC by multifunctional nanoparticles. *Mol. Ther. J. Am. Soc. Gene Ther.* 29, 2931–2948. doi:10.1016/j.ymthe.2021.05.017

Zanger, U. M., and Schwab, M. (2013). Cytochrome P450 enzymes in drug metabolism: Regulation of gene expression, enzyme activities, and impact of genetic variation. *Pharmacol. Ther.* 138 (1), 103–141. doi:10.1016/j.pharmthera.2012.12.007

Zhang, C., Zhao, K., Bu, W., Ni, D., Liu, Y., Feng, J., et al. (2015). Marriage of scintillator and semiconductor for synchronous radiotherapy and deep photodynamic therapy with diminished oxygen dependence. *Angew. Chemie-International Ed.* 54 (6), 1790–1794. doi:10.1002/ange.201408472

Zhang, G., Li, K., He, S., Wang, L., Guan, S., Zhou, S., et al. (2021). Electron donor-acceptor effect-induced organic/inorganic nanohybrids with low energy gap for highly efficient photothermal therapy. *Acs Appl. Mater. Interfaces* 13 (15), 17920–17930. doi:10.1021/acsami.1c00554

Zhang, G., Liu, Y., Yuan, Q., Zong, C., Liu, J., and Lu, L. (2011). Dual modal *in vivo* imaging using upconversion luminescence and enhanced computed tomography properties. *Nanoscale* 3 (10), 4365–4371. doi:10.1039/c1nr10736d

Zhang, J., Cheng, F., Li, J., Zhu, J.-J., and Lu, Y. (2016). Fluorescent nanoprobes for sensing and imaging of metal ions: Recent advances and future perspectives. *Nano Today* 11 (3), 309–329. doi:10.1016/j.nantod.2016.05.010

Zhang, Y., Schroeder, L. K., Lessard, M. D., Kidd, P., Chung, J., Song, Y., et al. (2020). Nanoscale subcellular architecture revealed by multicolor three-dimensional salvaged fluorescence imaging. *Nat. Methods* 17 (2), 225–231. doi:10.1038/s41592-019-0676-4

Zhang, Y. W., Sun, X., Si, R., You, L. P., and Yan, C. H. (2005). Single-crystalline and monodisperse LaF3 triangular nanoplates from a single-source precursor. *J. Am. Chem. Soc.* 127 (10), 3260–3261. doi:10.1021/ja042801y

Zhang, Z., Shikha, S., Liu, J., Zhang, J., Mei, Q., and Zhang, Y. (2019). Upconversion nanoprobes: Recent advances in sensing applications. *Anal. Chem.* 91 (1), 548–568. doi:10.1021/acs.analchem.8b04049

Zhang, Z., Wang, R., Luo, R., Zhu, J., Huang, X., Liu, W., et al. (2021). An activatable theranostic nanoprobe for dual-modal imaging-guided photodynamic therapy with self-reporting of sensitizer activation and therapeutic effect. *Acs Nano* 15 (3), 5366–5383. doi:10.1021/acsnano.0c10916

Zhao, S., Tian, R., Shao, B., Feng, Y., Yuan, S., Dong, L., et al. (2020). One-pot synthesis of Ln(3+)-doped porous BiF3@PAA nanospheres for temperature sensing and pH-responsive drug delivery guided by CT imaging. *Nanoscale* 12 (2), 695–702. doi:10.1039/c9nr09401f

Zhao, Y., He, Z., Zhang, Q., Wang, J., Jia, W., Jin, L., et al. (2021). 880 nm NIR-triggered organic small molecular-based nanoparticles for photothermal therapy of tumor. *Nanomaterials* 11 (3), 773. doi:10.3390/nano11030773

Zhao, Y., Yang, F., Sun, J.-S., Li, X.-P., Zhang, J.-S., Zhang, X.-Z., et al. (2019). Experimental optimal design of Er<sup>3+</sup>/Yb<sup>3+</sup> co-doped Ba<sub>5</sub>Gd<sub>8</sub>Zn<sub>4</sub>O<sub>21</sub> phosphor and red upconversion luminescence properties. *Acta Phys. Sin.* 68 (21), 213301. doi:10.7498/aps.68.20191192

Zhen, X., Cheng, P., and Pu, K. (2019). Cancer phototherapy: Recent advances in cell membrane-camouflaged nanoparticles for cancer phototherapy (small 1/2019). *Small* 15 (1), 1970002. doi:10.1002/smll.201970002

Zheng, F., and Xu, R. (2020). CircPVT1 contributes to chemotherapy resistance of lung adenocarcinoma through miR-145-5p/ABCC1 axis. *Biomed. Pharmacother.* 124, 109828. doi:10.1016/j.biopha.2020.109828

Zheng, K., Liu, X., Liu, H., Dong, D., Li, L., Jiang, L., et al. (2021). Novel pH-triggered doxorubicin-releasing nanoparticles self-assembled by functionalized beta-cyclodextrin and amphiphilic phthalocyanine for anticancer therapy. *Acs Appl. Mater. Interfaces* 13 (9), 10674–10688. doi:10.1021/acsami.0c19027

Zheng, S., Chen, W., Tan, D., Zhou, J., Guo, Q., Jiang, W., et al. (2014). Lanthanide-doped NaGdF4 core-shell nanoparticles for non-contact self-referencing temperature sensors. *Nanoscale* 6 (11), 5675–5679. doi:10.1039/c4nr00432a

Zhou, H., Zeng, X., Li, A., Zhou, W., Tang, L., Hu, W., et al. (2020). Upconversion NIR-II fluorophores for mitochondria-targeted cancer imaging and photothermal therapy. *Nat. Commun.* 11 (1), 6183. doi:10.1038/s41467-020-19945-w

Zhou, Y., Chen, Y., He, H., Liao, J., Duong, H. T. T., Parviz, M., et al. (2019). A homogeneous DNA assay by recovering inhibited emission of rare Earth ions-doped upconversion nanoparticles. *J. Rare Earths* 37 (1), 11–18. doi:10.1016/j.jre.2018.05.008

Zhu, S., Yu, Q., Huo, C., Li, Y., He, L., Ran, B., et al. (2021). Ferroptosis: A novel mechanism of artemisinin and its derivatives in cancer therapy. *Curr. Med. Chem.* 28 (2), 329–345. doi:10.2174/1875533xmtazlnzkj1

Zou, W., Visser, C., Maduro, J. A., Pshenichnikov, M. S., and Hummelen, J. C. (2012). Broadband dye-sensitized upconversion of near-infrared light. *Nat. Photonics* 6 (8), 560–564. doi:10.1038/nphoton.2012.158

Zou, X., Xu, M., Yuan, W., Wang, Q., Shi, Y., Feng, W., et al. (2016). A water-dispersible dye-sensitized upconversion nanocomposite modified with phosphatidylcholine for lymphatic imaging. *Chem. Commun.* 52 (91), 13389–13392. doi:10.1039/c6cc07180e

Frontiers in Chemistry

TYPE Original Research
PUBLISHED 13 April 2023
DOI 10.3389/fchem.2023.1167701

OPEN ACCESS

EDITED BY
Ziying Wang,
Hebei University of Technology, China

REVIEWED BY
Abdelazeem Eltaweil,
Alexandria University, Egypt
Buzuayehu Abebe,
Adama Science and Technology
University, Ethiopia

*CORRESPONDENCE
Muhammad Ikram,
dr.muhammadikram@gcu.edu.pk
Walid Nabgan,
walid.nabgan@urv.cat

RECEIVED 22 February 2023
ACCEPTED 03 April 2023
PUBLISHED 13 April 2023

CITATION
Ikram M, Shahzadi A, Bilal M, Haider A, Ul-Hamid A, Nabgan W, Haider J, Ali S, Medina F and Imran M (2023), Strontium-doped chromium oxide for RhB reduction and antibacterial activity with evidence of molecular docking analysis. *Front. Chem.* 11:1167701.
doi: 10.3389/fchem.2023.1167701

Strontium-doped chromium oxide for RhB reduction and antibacterial activity with evidence of molecular docking analysis

Muhammad Ikram[1]*, Anum Shahzadi[2], Muhammad Bilal[1], Ali Haider[3], Anwar Ul-Hamid[4], Walid Nabgan[5]*, Junaid Haider[6], Salamat Ali[7], Francisco Medina[5] and Muhammad Imran[8]

[1]Solar Cell Applications Research Lab, Department of Physics, Government College University Lahore, Lahore, Pakistan, [2]Faculty of Pharmacy, The University of Lahore, Lahore, Pakistan, [3]Department of Clinical Sciences, Faculty of Veterinary and Animal Sciences, Muhammad Nawaz Shareef University of Agriculture, Multan, Pakistan, [4]Core Research Facilities, King Fahd University of Petroleum and Minerals, Dhahran, Saudi Arabia, [5]Departament d'Enginyeria Química, Universitat Rovira i Virgili, Tarragona, Spain, [6]Chinese Academy of Sciences, Tianjin Institute of Industrial Biotechnology, Tianjin, China, [7]Department of Physics, The University of Lahore, Lahore, Pakistan, [8]Government College University Faisalabad, Sahiwal, Punjab, Pakistan

The emergence of multi-drug resistance (MDR) in aquatic pathogens and the presence of cationic dyes are the leading causes of water contamination on a global scale. In this context, nanotechnology holds immense promise for utilizing various nanomaterials with catalytic and antibacterial properties. This study aimed to evaluate the catalytic and bactericidal potential of undoped and Sr-doped Cr_2O_3 nanostructures (NSs) synthesized through the co-precipitation method. In addition, the morphological, optical, and structural properties of the resultant NSs were also examined. The optical bandgap energy of Cr_2O_3 has been substantially reduced by Sr doping, as confirmed through extracted values from absorption spectra recorded by UV-Vis studies. The field-emission scanning electron microscopy (FE-SEM) and transmission electron microscopy (TEM) micrographs illustrate that the composition of Cr_2O_3 primarily consisted of agglomerated, irregularly shaped NSs with a morphology resembling nanoflakes. Moreover, the presence of Sr in the lattice of Cr_2O_3 increased the roughness of the resulting NSs. The catalytic activity of synthesized NSs was analyzed by their reduction ability of Rhodamine B (RhB) dye in the dark under different pH conditions. Their antibacterial activity was evaluated against MDR *Escherichia coli* (*E. coli*). Sr doping increased antibacterial efficiency against MDR *E. coli*, as indicated by inhibition zone measurements of 10.15 and 11.75 mm at low and high doses, respectively. Furthermore, a molecular docking analysis was conducted to determine the binding interaction pattern between NSs and active sites in the target cell protein. The findings corroborated antimicrobial test results indicating that Sr-Cr_2O_3 is the most effective inhibitor of FabH and DHFR enzymes.

KEYWORDS

dye degradation, MDR *E. coli*, RhB, antibacterial, Cr_2O_3

1 Introduction

The development of multi-drug resistance (MDR) in pathogenic bacteria has evolved significantly in recent years (Franci et al., 2015). A team from the University of Alberta has discovered that a strain of *E. coli* (*Escherichia coli*) bacterium can survive and flourish in wastewater treatment plants. Although oxygenation, chlorine, and other treatments in sewage facilities are effective in eradicating the majority of *E. coli*, researchers have identified certain pathogenic strains of *E. coli* that exhibit significant resistance to these treatments. The efficacy of conventional antibiotics diminishes over time as bacteria resist them (Wise and BSAC Working Party on The Urgent Need: Regenerating Antibacterial Drug Discovery and Development, 2011). This poses a significant threat to the health and lives of millions of people each year. In addition, the progress of industrialization and urbanization generates a significant volume of waste in the form of dyes, heavy metals, and microorganisms continuously discharged into rivers and soil (Chen et al., 2015; Sallam et al., 2018). Every year, numerous types of dyes released from different sectors worldwide are dumped into aquatic systems (He et al., 2019). These are colored chemicals, and their pollution is primarily attributed to their high stability, which stems from the presence of numerous aromatic rings. Rhodamine B (RhB) is an amino xanthene dye that finds widespread applications in the colored glass industry, as well as in the fields of textiles, biology, and fluorescent staining. RhB is commonly detected in dye effluent as it is widely used in the textile industry (Qamar et al., 2020; Nguyen et al., 2021). Textile dyes have been shown to increase toxicity, reduce photosynthesis, impair plant growth, enter the food chain, and promote carcinogenic effects in water (Magureanu et al., 2008; Hameed and Ismail, 2019; He et al., 2019; Eltaweil et al., 2022). Consequently, the simultaneous eradication of organic contaminants prevalent in industrial wastewater, including chemicals, phenolic compounds, colorful dyes, and microorganisms, could effectively replace typical phased treatment methods.

Recently, metal and metal oxide nanoparticles (NPs) gained significant medical and health applications due to their superior stability at higher temperatures and pressures than conventional organic antimicrobials (Liu et al., 2009; Di et al., 2017). Transition metal NPs have been the subject of extensive research due to their potent antibacterial properties. Consequently, nanostructured chromium oxide (Cr_2O_3) with large surface areas attracted researchers worldwide (El-Sheikh et al., 2009). In contrast to traditional polycrystalline materials, they display advantageous and unique features. Shafi et al. reported Cr_2O_3 NPs with Brunauer–Emmett–Teller (BET) area of 219.9 m^2g^{-1} and pore width of 4.2 nm (Shafi et al., 2021). The majority of research conducted on the antibacterial properties of Cr_2O_3 NPs has focused on their effectiveness against Gram-negative bacteria, using *E. coli* as a representative model (Ramesh et al., 2012; Almontasser et al., 2021; Ghotekar et al., 2021). Chromium and supported chromium oxides have been utilized in various catalytic processes such as the dehydrogenation of toluene, the decomposition of ammonia, and the oxidation of toluene. Calcined chromia catalysts, both supported and unsupported, exhibit excellent activity in redox processes (El-Sheikh et al., 2009). Additionally, supported chromium oxide catalysts have found applications in selective catalytic reduction of NOx with ammonia, polymerization reactions, and oxidative dehydrogenation of isobutene (Abu-Zied, 2000). Studies on chromium oxide catalysts have shown that the type and concentration of surface Cr-O species play a significant role in controlling their adsorptive and catalytic characteristics (Fouad et al., 1991; Gabr et al., 1994). Doping Cr_2O_3 with metals has enhanced its catalytic and antibacterial properties. Rare Earth metals can readily form strong bonds with functional groups when used as dopants in metal oxides, owing to the availability of 4f empty orbitals (Mehtab et al., 2022). Strontium (Sr) is a chemically highly reactive alkaline Earth metal that exhibits chemical similarity with calcium and can be utilized to enhance the properties of Cr_2O_3. The utilization of Sr in various applications has been extensively investigated, revealing its potential for beneficial effects through doping with metal oxides (Akihide et al., 2004; Li et al., 2007; Ramam and Chandramouli, 2009; Suresh and Roy, 2012; Kiani et al., 2020).

Numerous methods, including solid thermal decomposition (Li et al., 2008), hydrothermal (Pei et al., 2009), bio-method (Bai et al., 2009), nano casting method (Xia and Mokaya, 2005), sol-gel (Pinna et al., 2004), combustion (Lima et al., 2006), laser-induced deposition (Zhong et al., 2001), precipitation-gelation (Kim et al., 2004), mechanochemical reaction and subsequent heat treatment (Tsuzuki and McCormick, 2000), chromium oxidation in oxygen (Mougin et al., 2001), and sonochemical methods (Balachandran et al., 1995) have been successfully developed to synthesize Cr_2O_3 nanomaterials. However, most of these complex techniques involve specialized lab equipment, high temperatures and are environmentally sensitive (Singh et al., 2019a). Among these methods, co-precipitation is low-cost, convenient, time-saving, and ecologically beneficial synthesis method (Yazid and Joon, 2019; Asha et al., 2021).

This study aims to synthesize pure and Sr (2, 4, and 6 wt%) doped Cr_2O_3 nanostructures (NSs) using co-precipitation and analyze their optical, morphological, and structural features, as well as their ability to function as catalyst and antibacterial agent. The catalytic activity of as-prepared NSs was tested against RhB dye reduction, and the bactericidal potential of NSs was examined for MDR *E. coli* (a G-ve bacteria).

2 Experimental part

2.1 Materials

Chromium acetate ($Cr(CH_3COO)_3$, 99.0%) was purchased from Uni-Chem Chemical Reagents, and strontium chloride hexahydrate ($SrCl_2.6H_2O$, puriss≥99%), sodium hydroxide (NaOH) were purchased from Sigma-Aldrich and used without further purification.

2.2 Synthesis of Sr-doped chromium oxide

The co-precipitation method was used to synthesize the Cr_2O_3 NSs, with 0.5 M of $Cr(CH_3COO)_3$ serving as the precursor material. The pH of the solution was maintained at 12 by adding NaOH drop by drop while constantly stirring at 80 °C. After centrifugation at

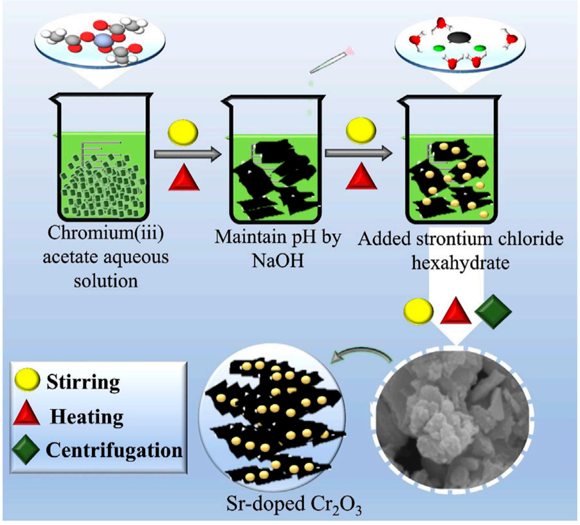

FIGURE 1
Schematic illustration for synthesis route of pristine and Sr-doped Cr_2O_3.

7,500 rpm for 6 min to remove impurities, the resulting product was dried at 200°C for 12 h, and a fine powder was obtained using a mortar and pestle. To synthesize Sr-doped Cr_2O_3, the same procedure was followed, adding various concentrations of Sr (2, 4, and 6%) in Cr_2O_3. The preparation method is illustrated schematically in Figure 1.

2.3 Catalytic activity

To assess the catalytic performance of undoped and Sr-doped Cr_2O_3 in the presence of the reducing agent sodium borohydride ($NaBH_4$), the synthesized NSs were utilized for the reduction of RhB dye, which acts as an oxidizing agent. All the reagents, including RhB and $NaBH_4$, were used immediately after preparation to maintain the experimental integrity. Initially, a freshly made 400 μL of 0.1 M $NaBH_4$ solution was combined with a 1.5 mL aqueous RhB solution. Subsequently, 400 μL of synthetic nanocatalyst was added and thoroughly mixed with the solution. RhB has a peak absorption at 555 nm, which was chosen to measure the reduction in UV-vis absorption. Adding $NaBH_4$ led to a change in RhB to its leuco form, indicating dye reduction. The % reduction was calculated as follows:

$$\% \text{ reduction} = \left(\frac{C_0 - C_t}{C_0}\right) \times 100$$

where C_o and C_t are the initial and specific time absorptions.

2.4 Isolation and identification of MDR *Escherichia coli*

2.4.1 Isolation of *Escherichia coli*

To collect unpasteurized milk samples from lactating dairy cows of different farmlands and veterinary clinics in Punjab, Pakistan, prompt milking in a sterile glass container was used. The milk specimen's transportation proceeded at the temperature of 4°C. The coliform pathogen found in unpasteurized milk was quantified using MacConkey agar. Each plate endured 48 h of incubation at 37°C.

2.4.2 Identification and characterization of bacterial isolates

The variety of Gram stain colonial morphology and biochemical tests were used in conjunction with Bergey's Manual of Determinative Bacteriology (Holt et al., 1994) to make a preliminary determination of the identity of *E. coli*.

The disc diffusion approach was employed on Mueller Hinton agar (MHA) to investigate antibiotic susceptibility (Bauer, 1966). The test was made to evaluate the antibiotic resistance of gram-ve *E. coli bacteria* against the following antibiotics (classes); Ceftriaxone (Cro) 30 μg (Cephalosporins), Gentamicin (Gm) 10 μg (Aminoglycosides), Ciprofloxacin (Cip) 5 μg (Quinolones), Tetracycline (Te) 30 μg (Tetracyclines), Imipenem (Imi) 10 μg (Carbapenem), Amoxycillin (A) 30 μg (Penicillins), and Azithromycin (Azm) 15 μg (Macrolides). The *E. coli* resistant to 5 μg of the antibiotic ciprofloxacin was conducted through various experiments (Adzitey et al., 2022). Purified cultures of *E. coli* were grown to a turbidity level of 0.5, as determined by the MacFarland standard. Following this, the bacteria were spread out on MHA (Oxoid Limited, Basingstoke, United Kingdom), and antibiotic discs were placed at a distance on the inoculation plate surface. This avoided disrupting inhibition zones. The plates were incubated at 37°C for 48 h while being cultivated, and the data were then examined in accordance with the guidelines provided by the Diagnostic, Therapeutic, and Laboratory Standard Institute (Wayne, 2008). At least three drugs were shown to be ineffective against MDR bacteria (Iwalokun et al., 2004).

2.5 Molecular docking analysis

To comprehend the mechanism behind bactericidal action, molecular docking research was conducted on synthetic Cr_2O_3 and Sr-doped Cr_2O_3 NPs. This was accomplished by focusing on proteins essential for bacterial survival and proliferation. The molecular docking investigation selected several protein targets from biosynthetic pathways, such as dihydrofolate reductase and beta-ketoacyl-acyl carrier protein synthase III (FabH). The dihydrofolate reductase plays a crucial part in synthesizing folic acid, which is essential for the survival of bacteria. FabH enzymes catalyze critical stages in bacterial cells' fatty acid biosynthesis pathway (Li et al., 2009; Altaf et al., 2020). *E. coli* target protein crystal structures of the high resolution were acquired from the Protein Data Bank. The protein DHFR identified by PDB ID 2ANQ; Resolution: 2.6 (Summerfield et al., 2006) $FabH_{E.\ Coli}$ with PDB ID 5BNR; Resolution: 1.9 (McKinney et al., 2016) was chosen to comprehend molecular interactions between NPs and protein active pocket residues.

Sybyl-X2.0 was used for molecular docking investigations (Mehmood et al., 2022; Shahzadi et al., 2022). Water molecules and co-crystallized ligands were eliminated to create a protein structure. The protein structures were optimized for energy reduction using default settings and a force field. Following this,

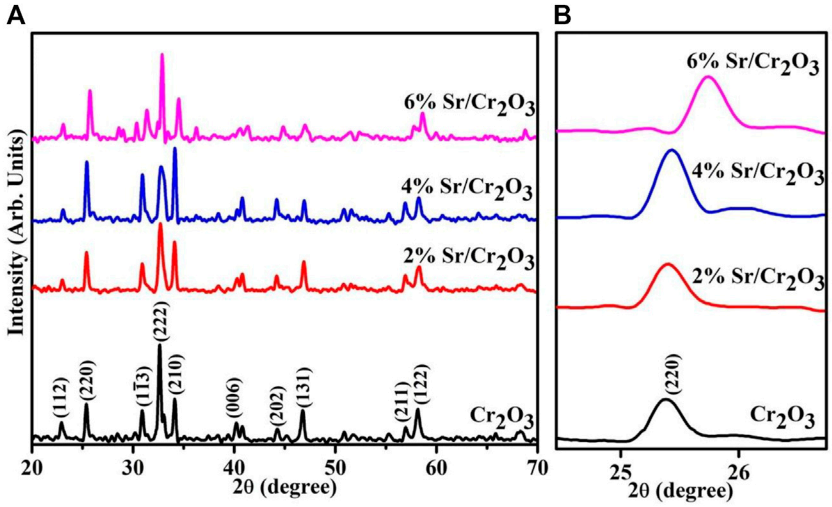

FIGURE 2
(A) XRD patterns of Cr_2O_3 and Sr-doped Cr_2O_3 **(B)** zoomed area of (220) plane.

a protomol was generated to characterize the binding pocket, and the 10 best-docked conformations were created to investigate the interaction pattern between NPs and active site residues (Ikram et al., 2023).

2.6 Characterizations

To analyze the crystal structure and phase information of the NSs, a PANalytical XPert PRO X-ray diffraction (XRD) system was utilized with Cu Kα radiation (λ ~ 0.0154 nm) within the 2θ range of 20°–70°. The optical properties within the 200–700 nm range were examined using a UV-Vis spectrophotometer (Genesys 10S). The morphology and microstructure of the samples were observed with a JSM-6460LV FE-SEM system with an EDX spectrometer. The PL spectra were collected using a JASCO FP-8300 system. Inter-planar d-spacing of the NSs was measured using the HR-TEM equipment JEOL JEM 2100F.

3 Results and discussion

The XRD analysis pattern for the phase purity, crystallographic plane structure, and crystallite size of the synthesized products are shown in Figure 2A. The spectra show well-defined peaks at 23.0°, 25.6°, 31.1°, 32.3°, 34.1°, 39.7°, 44.1, 46.9°, 57.1°, and 58.3°, which correspond to the (112), (220), $(1\ \bar{1}\ 3)$, (222), (210), (006), (202), (131), (211), and (122) facets that are well matched with standard spectrums (00-038-1479/00-036-1329/80-2473). These planes belong to polycrystalline Cr_2O_3, Cr_2O_5, and Cr_8O_{13}, which have been previously reported (Ivanov et al., 2001; Panda et al., 2018). Norby et al. examined the crystal structure of Cr_8O_{13} in detail (Norby et al., 1991). Cr_8O_{21} is composed of two CrO_6 octahedra that share a standard edge. Two chromate groups (CrO_4, tetrahedra) connected the double octahedra to form a sheet. Finally, tetrachromate groups (Cr_4O_{13}) link these sheets to construct a three-dimensional structure. Upon Sr doping, the slight shift of peaks is caused by extensive dispersion of the dopant element between the interlayers of the host sample. The size of the crystallite affects the crystallinity-dependent properties of the crystal. Moreover, larger crystallites produce sharper peaks in the XRD pattern for a particular crystal plane. The shift in a peak that occurs due to doping is attributed to the presence of Sr in the host of the Cr_2O_3 matrix (see Figure 2B). Crystallite size is correlated with the width of a peak. Using the following Debby-Scherrer formula (Abdullah et al., 2014), the crystallite size (D) of pristine Cr_2O_3 and (2, 4, and 6%) Sr-doped Cr_2O_3 was found to be 37.5 nm, 28.1 nm, 33.9 nm, and 56.6 nm respectively.

The absorption spectra of the synthesized Cr_2O_3 and Sr-doped Cr_2O_3 nanomaterials from the UV-Vis spectrophotometer are presented in Figure 3A. On the graph, two significant absorption peaks were demonstrated at 260 nm and 360 nm wavelengths. The peak showed a Cr_2O_3 NSs band gap transition at 360 nm (Singh et al., 2019b). In optical characteristics, the estimate of band gap energy is an essential factor. There are numerous ways to calculate the optical band gap. Among them, the optical procedure is the most precise and simple way to detect the band gap energy of materials (Ashiri et al., 2009). The Tauc equation interprets the relationship between the absorption coefficient (α) and the incident energy (hν), which was used to obtain the optical band gap energy of the materials. The optical band gap was determined using the Tauc relation:

$$(\alpha h\nu)^2 = B(h\nu - Eg)$$

where hν is the photon energy, E.g., represents the optical band gap, and B is constant and takes on different values depending on the transitions. Therefore, the band gap can be determined by extrapolating the linear portion of the curve intersecting the hν axis. The Cr_2O_3 NSs prepared by co-precipitation contain a direct band gap (Singh et al., 2019b). As it is obvious from Figure 3B, doping substantially redshifted the band gap energy from 3.3 eV in pristine Cr_2O_3 to around 3.0 eV in the case of (2,4% and 6%) Sr-

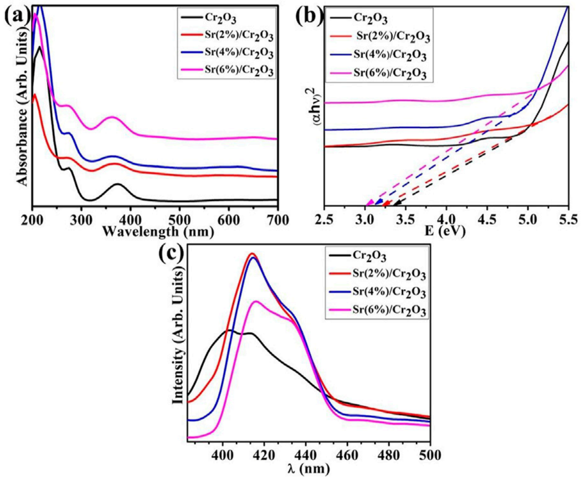

FIGURE 3
(A) optical spectra, **(B)** band gap energy determination, and **(C)** PL emission spectra of Cr_2O_3 and Sr-doped Cr_2O_3.

doped Cr_2O_3 attributed to quantum confinement effect. The incorporation of dopants into Cr_2O_3 has modified the optical band gap and crystallinity, indicating the interaction and complexation of dopants with the Cr_2O_3.

The Cr_2O_3 NSs photoluminescence (PL) spectra are displayed in Figure 3C. The PL spectra were used to analyze the charge recombination of the NSs. The broad emission peaks could be observed in all samples, attributed to higher crystallinity of the as-synthesized NSs. It is shown that the Sr-doped Cr_2O_3 powders have a greater PL signal than pure Cr_2O_3 (Figure 5), demonstrating increased charge recombination. The most prevalent defect sites in oxide materials are oxygen vacancies, that produce PL emission by recombining with an electron. The Sr doping causes increased PL intensities compared to Cr_2O_3 (Kamari et al., 2019). The transition involving the $3d^3$ electrons of the Cr^{3+} ions causes the peak to appear at ~425 nm. The oxygen interstitials, oxygen vacancies, chromium interstitials, dangling surface bonds, and chromium vacancies may all be responsible for the broad emission peaks in the visible spectrum range that are centered at roughly 415 nm (violet PL) and 435 nm (blue emission) (Almontasser and Parveen, 2020).

The morphology of as-grown material was assessed using the FE-SEM and TEM techniques. Figure 4 illustrates the typical morphology of Cr_2O_3 and Sr (2%, 4%, and 6%) doped Cr_2O_3. The FE-SEM and TEM micrographs demonstrate that most of Cr_2O_3 consist of strongly agglomerated NPs with a morphology resembling nanoflakes, as depicted in Figure 4(A-A′). Nanoflakes are preferable for various applications demanding higher redox-active sites since they tend to give more surface area for interfacial contact (Rashad et al., 2020). Sr doping caused NPs to agglomerate further, as shown in Figure 4(B-B′, D-D′). Consequently, the presence of Sr in the lattice of Cr_2O_3 increased the roughness of resulting NSs. As reported earlier, the agglomeration of NPs is caused by high surface area and high surface energy (Anbu et al., 2022). This rise in NSs surface area, caused by Sr doping, promotes the formation of reactive oxygen species (ROS), thereby improving the antibacterial activity (Yarahmadi et al., 2021).

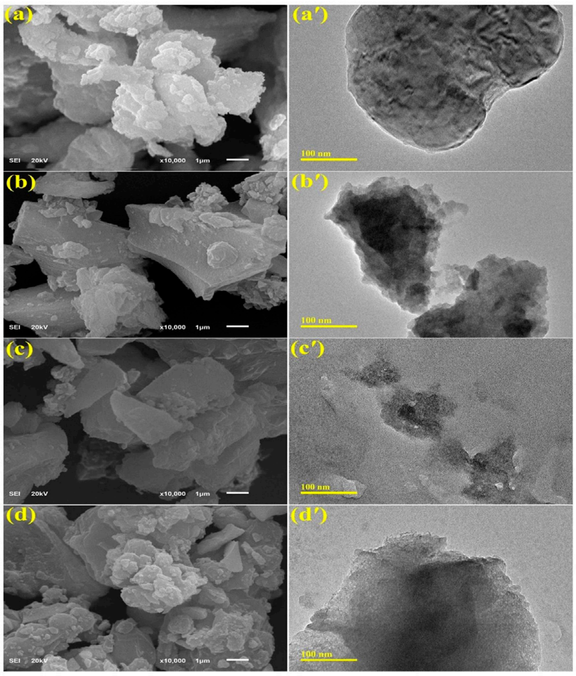

FIGURE 4
FE-SEM and TEM images of **(A, A′)** Cr_2O_3, **(B, B′)** 2% Sr/Cr_2O_3, **(C, C′)** 4% Sr/Cr_2O_3, **(D, D′)** 6% Sr/Cr_2O_3.

The number of layers can be microscopically estimated using a high-resolution TEM (HR-TEM) study of edge regions. HR-TEM pictures show many atomic planes exhibiting periodic atomic configurations on a single grain, as illustrated in Figures 5A–D. Moreover, planes are well arranged to form a single layer at particular points, with an interplanar spacing of 0.16 nm. This correlates with the XRD-determined (2 1 1) facet of the rhombohedral Cr_2O_3 phase. The addition of dopants resulted in samples with d-spacings of 0.19, 0.23, and 0.26 nm, as indicated by XRD analysis.

Energy dispersive spectroscopy (EDS) was used to investigate the elemental composition of as-prepared Cr_2O_3 NSs (Figure 6). The spectrum demonstrates the corresponding peaks for chromium and oxygen, along with minor Au peaks. Additional Na peaks were also noticed, which could have resulted from using NaOH during the synthesis process. Furthermore, no Sr peaks were observed in EDS attributed to low concentration of dopants.

The catalytic activity of nanocatalysts against RhB dye was investigated utilizing $NaBH_4$ as a reducing agent. The visible absorption spectra of RhB solution during the reduction process are displayed in Figures 7A–C. The absorption peak at 555 nm is reduced after the nanocatalyst is added, indicating that the dye molecules have undergone reduction.

UV–vis absorption spectra of the RhB solution treated in the three different pH (acidic, basic, and neutral) show that dye reduction was significant at pH = 4, well matched with previous observations (Cui et al., 2015). The pristine Cr_2O_3 and (2,4% and 6%) Sr-doped Cr_2O_3 NSs showed maximum % reduction of 68.19%,

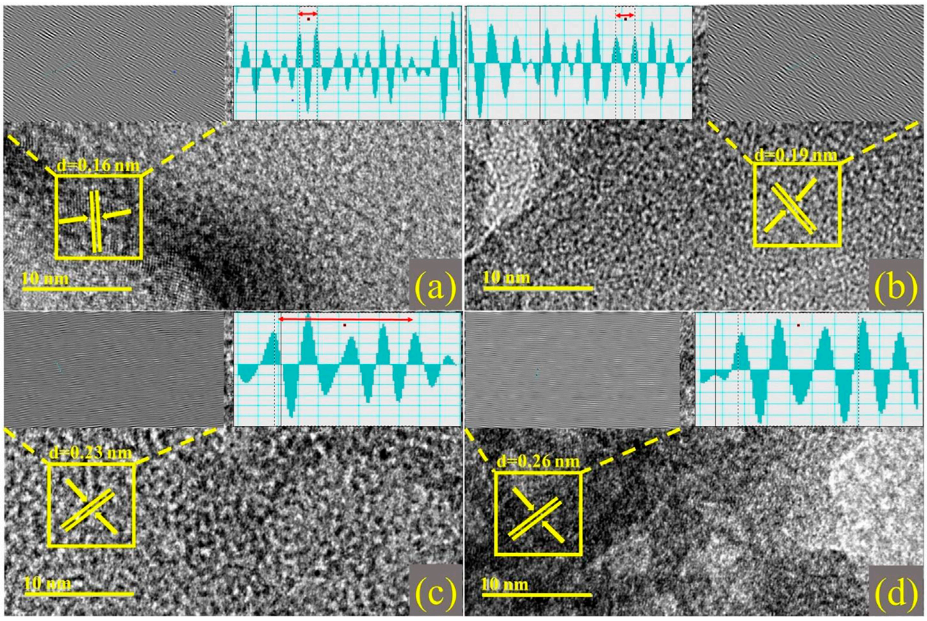

FIGURE 5
d-spacing calculated from HR-TEM images with Inverse Fast Fourier Transform (IFFT) and IFFT image profile of **(A)** Cr_2O_3 **(B)** 2% Sr/Cr_2O_3 **(C)** 4% Sr/Cr_2O_3 **(D)** 6% Sr/Cr_2O_3.

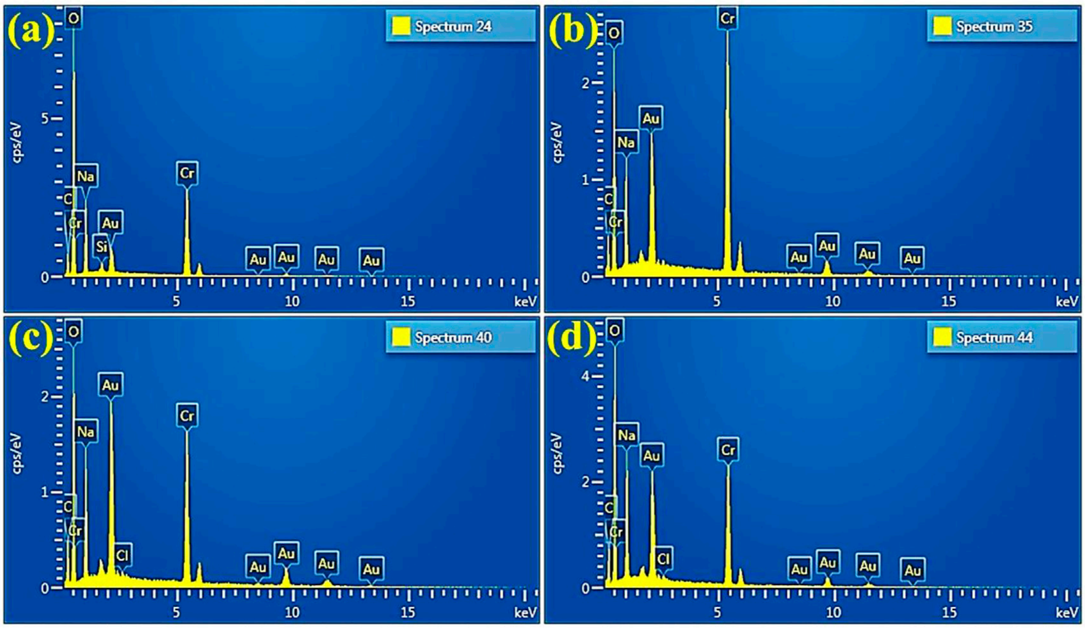

FIGURE 6
EDS of **(A)** Cr_2O_3 **(B)** 2% Sr/Cr_2O_3 **(C)** 4% Sr/Cr_2O_3 **(D)** 6% Sr/Cr_2O_3.

65.26%, 52.28%, and 62.88% in acidic medium (pH = 4), 60.72% 59.63%, 63.45%, 54.72% in basic medium (pH = 12) and 46.41%, 55.01%, 46.95% and 54.48% in neutral medium (pH = 7) respectively as shown in Figures 8A–C. In the absence of a catalyst, the reduction process occurred at a slow rate, resulting in only 25.22%, 21.81%, and 17.02% reduction in acidic, basic, and neutral environments, respectively. The effects of Sr as dopant reduced the effects of Cr_2O_3 as nanocatalyst in acidic and basic mediums. At pH = 8, 6% Sr-doped Cr_2O_3 causes an increase in catalytic activity from 46.41% to 54.48%. The shape, size, and surface area of nanocatalysts

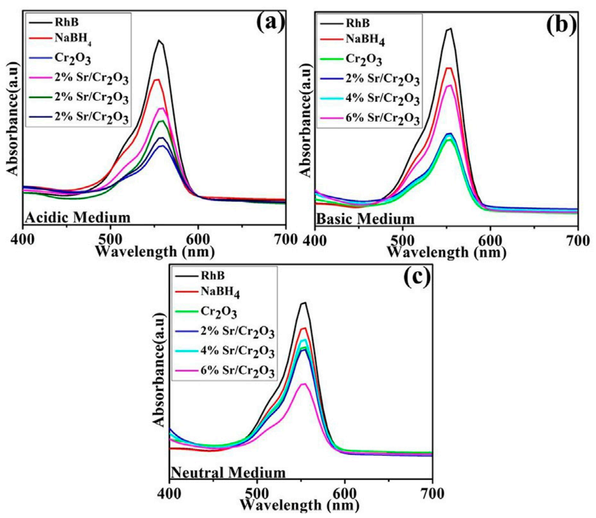

FIGURE 7
UV-Visible absorption spectra of RhB in the presence of nanocatalysts. **(A)** Acidic Medium, **(B)** Basic Medium, **(C)** Neutral Medium.

significantly impact performance reduction by generating substantial active sites. The undoped catalyst showed a better reduction rate than the Sr-doped nanomaterial. Due to their various placements within the host lattice, dopants may not have identical impacts on trapping electrons on the interface or during interfacial charge transfer (Munusamy et al., 2013). Moreover, dopants take up residence in the host material active sites, reducing the adsorption process—consequently, the catalytic efficiency change with the choice of dopant and morphology. The decolorization mechanism of RhB by Cr$_2$O$_3$ depends on the crystal structure of the oxides and the solution pH.

The electrochemical mechanism can explain the catalytic process of the reduction reaction using NSs. The reduction process begins with the migration of BH^{4-} from NaBH$_4$ and RhB molecules via aquatic solution to the exterior of Sr-doped Cr$_2$O$_3$. Afterward, the nanocatalysts on the top of the heterogeneous catalyst act as an electron relay system to accelerate the flow of electrons from the donor to the acceptor, i.e., from BH^{4-} to RhB. The next step entails a nanocatalyst's catalytic decomposition of the hydrogen source NaBH$_4$ to deliver hydrogen atoms. The produced reactive hydrogens subsequently react with dye molecules, causing the breakdown of RhB molecules into its luco form (Alani et al., 2021), as shown in Figure 9. The nanocatalysts enhanced the reduction of RhB with NaBH$_4$, resulting in significant reduction efficiency.

In-vitro antibacterial activity of Cr$_2$O$_3$ and (2, 4, and 6%) Sr-doped Cr$_2$O$_3$ was evaluated by assessing inhibitory zones against Gram-negative bacteria MDR *E. coli* with agar-based diffusion technique (see Table 1). Significant inhibitory zones were found at lower and higher doses (8.65—10.15 mm) and (9.65—11.75 mm) against MDR *E. coli,* respectively. Ciprofloxacin showed an 11.85 mm inhibition zone compared to DI water (0 mm). The formation of ROS is enhanced by the Sr-doping, that increases the specific surface area of Cr2O3 NPs, thereby improving the antibacterial activity of the NSs. Additionally, the uptake of positively charged metal ions Cr3+ following their release from

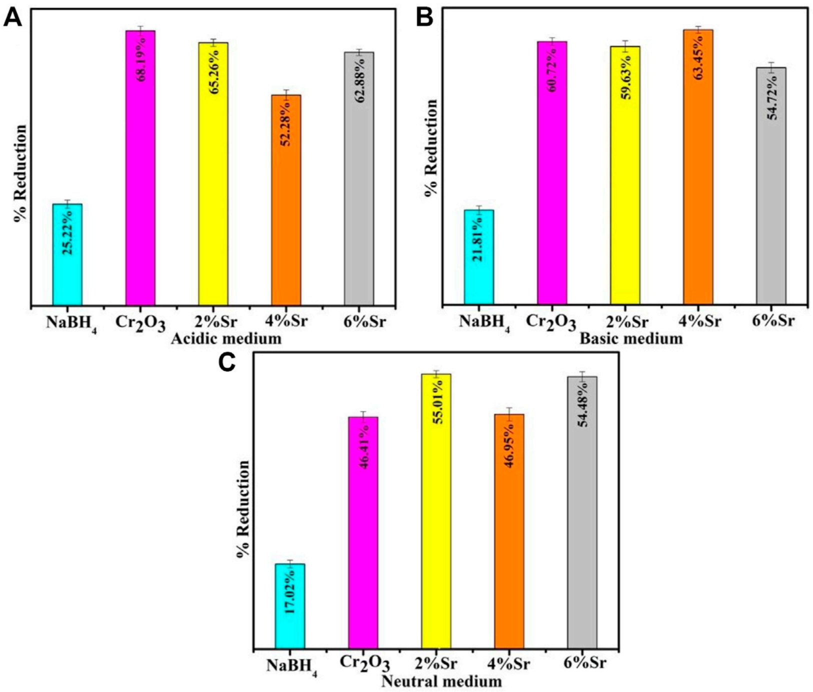

FIGURE 8
Catalytic activity of Cr$_2$O$_3$ and Sr-doped Cr$_2$O$_3$ in the presence of NaBH$_4$. **(A)** Acidic Medium, **(B)** Basic Medium, **(C)** Neutral Medium.

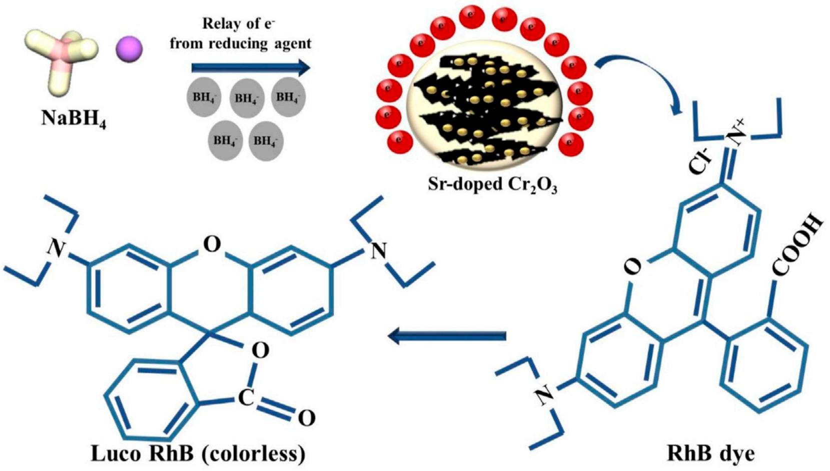

FIGURE 9
Schematic illustration of catalytic activity.

TABLE 1 The bactericidal potential of Cr_2O_3 and Sr-doped Cr_2O_3.

	Inhibition zone (mm)	
Samples	0.5 mg/50 µL	1.0 mg/50 µL
Cr_2O_3	8.65	9.65
2% Sr/Cr_2O_3	9.05	10.45
4% Sr/Cr_2O_3	9.55	10.95
6% Sr/Cr_2O_3	10.15	11.75
Ciprofloxacin	11.85	11.85
DI water	0	0

Cr2O3 at the cell boundary might lead to bacterial cell death by increasing their localized concentration. The outcomes of the current study are consistent with previous research that revealed metal oxide NPs have superior action against Gram-negative pathogens (Ahmad et al., 2014; Yarahmadi et al., 2021). This is due to the fast passage of smaller-sized NPs through the cell wall of *E. coli* (a Gram-negative bacterium), which has a single peptidoglycan layer, in contrast to the cell wall of Gram-positive bacteria, which has multiple peptidoglycan layers. Consequently, the outer membrane of bacteria enables greater NPs penetration to the bacterial cell wall.

Numerous mechanisms have been recognized as being responsible for antibacterial action. In the vicinity of air and metallic nanoclusters (as Cr_2O_3 in our case), reactive oxygen species (ROS), including reactive nitrogen species and hydrogen peroxide, are generated. Examples of ROS include free radicals (•OH, $^1O_2$), small molecules (such as H_2O_2), and superoxide ions (such as $-O_2$) (Rashad et al., 2020). It has also been observed that physicochemical properties, such as crystal structure, defects, surface charge, and composition, are directly correlated with the improved antimicrobial effect of materials. Specifically, it has been discovered that NPs of smaller size are substantially more effective antibacterial agents. As a result of their disintegration, harmful metal ions can infiltrate bacterial cells, making them a more effective tool against bacteria. NPs with a high metal oxide content, such as Sr-doped Cr_2O_3 NSs, may accumulate on the surface of bacteria if they are encased in nanoflakes. During contact, the rough surface of Sr-doped Cr_2O_3 encloses the bacterial surface.

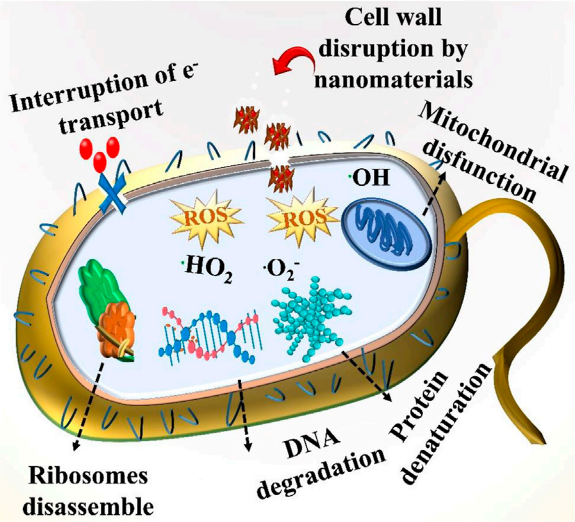

FIGURE 10
Antibacterial action mechanism of synthesized NSs.

The Sr-doped Cr_2O_3 NSs react oxygen molecules with electrons to produce superoxide ions ($\cdot O_2^-$). The $\cdot HO_2$ can be produced by reacting $\cdot O_2^-$ with hydrogen ions. Hydrogen peroxide (H_2O_2) can be produced by the interaction of $\cdot HO_2$ with hydrogen ions. Following this, $\cdot HO_2$ and H_2O_2 can react to generate extremely reactive hydroxyl radicals ($\cdot OH$). The presence of such particles leads to protein dysfunction, DNA damage, cell membrane deterioration, and an increase in death receptor gene expression. The interaction of

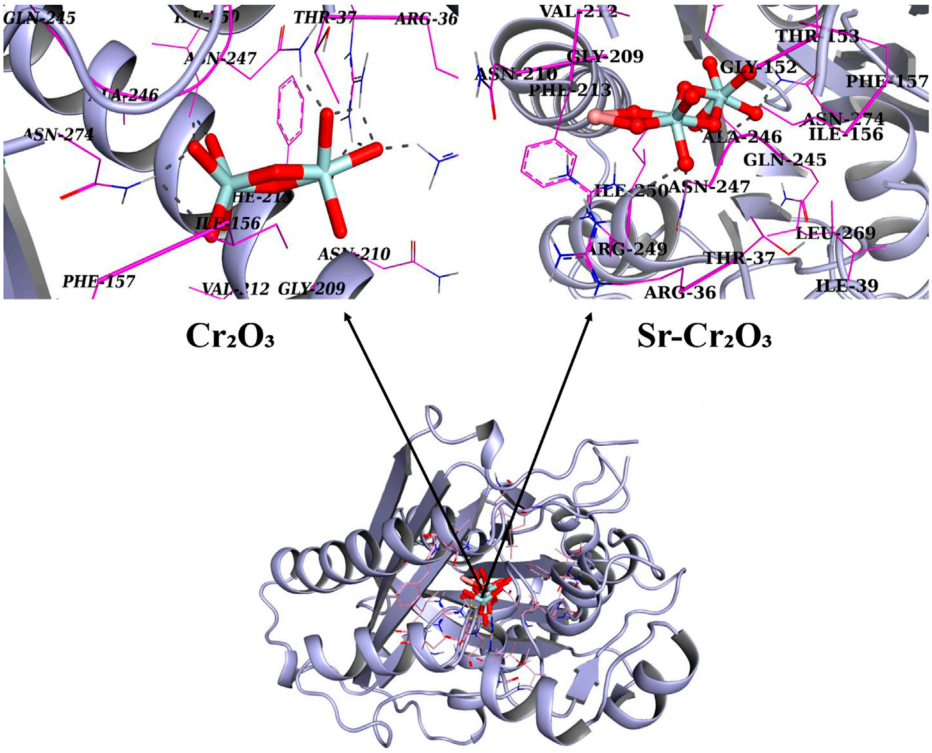

FIGURE 11
3D graphical representation of binding interaction patterns of Cr_2O_3 and Sr-doped Cr_2O_3 nanocomposites inside active pockets of FabH from *E. Coli* ($FabH_{E.\ Coli}$).

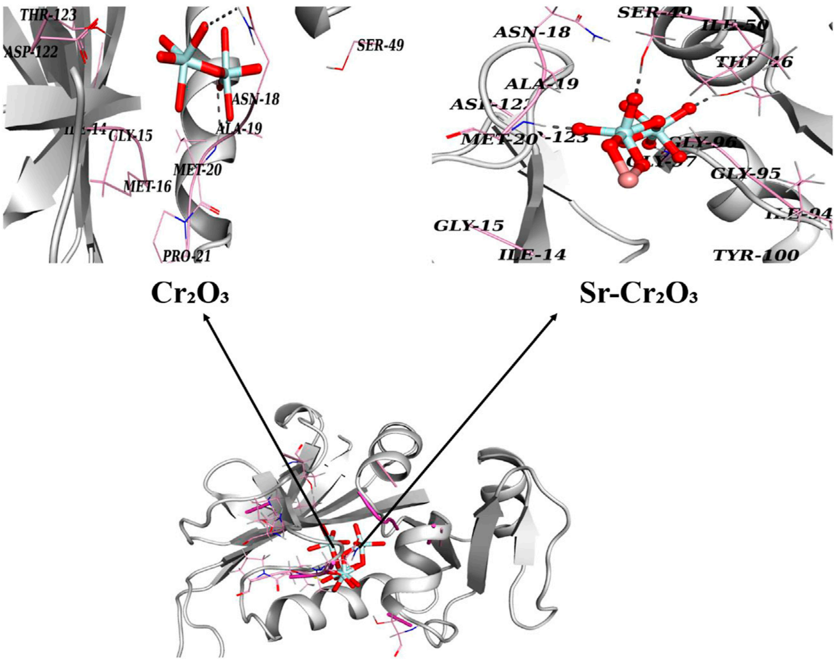

FIGURE 12
3D graphical representation of binding interaction patterns of Cr_2O_3 and Sr-doped Cr_2O_3 nanocomposites inside active pockets of DHFR from *E. Coli* ($DHFR_{E.\ Coli}$).

metal oxide NPs with the thiol groups present in essential enzymes for bacterial survival results in the death of bacterial cells, as shown in Figure 10. Antibacterial action also involves the inhibition of membrane function. The electrostatic interaction of metal NPs with the exterior of the microorganisms also triggers this process. This results in the accumulation of NPs on the cell's surface and a change in the structure of the cell, both of which inhibit the growth of bacterial cells (Alahmadi et al., 2017; Almontasser et al., 2021).

To understand the possible molecular and atomic-level mechanisms responsible for the antibacterial activity of NPs, it is essential to examine their binding interactions with potential protein targets. The enzyme targets for this investigation relate to metabolic pathways critical for bacterial survival and growth. Molecular docking analysis was conducted to determine the binding interaction pattern of Cr_2O_3 and Sr-doped Cr_2O_3 with different *E. coli* enzyme targets. β-ketoacyl-acyl carrier protein synthetase III $(FabH)_{E.\ coli}$ formed the best-docked complexes with Cr_2O_3 (see Figure 1). The optimal Cr_2O_3-$FabH_{E.\ Coli}$ docking arrangement has a docking score of 7.07. Cr_2O_3 established H-bonding interactions with Arg36, Thr37, Asn247, and Asn274, as seen in Figure. In addition, Sr-doped Cr_2O_3 NPs exhibit H-bonding interaction with Asn247, Arg249, and Asn274, leading to a bind score of 8.62 when docked into the active pocket of FabH, as shown in Figure 11.

In the case of $DHFR_{E.\ Coli}$, Cr_2O_3 exhibited hydrogen-bonding interactions with Asn18 and Met20, with a binding score of 8.78. Similarly, Sr-doped Cr_2O_3 nanocomposites also showed comparable binding interactions and scores with active site residues. In the case of Sr-doped Cr_2O_3, residues interacting through H-bonds were Met20, Thr46, Ser49, and Gly97, with active pockets having an overall binding score of 9.88, as depicted in Figure 12.

4 Conclusion

The co-precipitation technique was used to prepare pristine and Sr-doped Cr_2O_3 NSs for catalytic and antibacterial applications. The properties of synthesized NSs were investigated using various structural and optical characterization techniques. The XRD analysis endorsed the polycrystalline planes of pristine Cr_2O_3 and crystalline size increases from 37.5 nm to 56.6 nm in the case of 6% Sr-doped Cr_2O_3. FE-SEM and TEM micrographs indicate that the presence of Sr in the lattice of Cr_2O_3 increased the roughness of resulting NSs attributed to high surface area and high surface energy. Sr doping enhances the surface area of NPs, leading to a more significant formation of reactive oxygen species and, ultimately, a higher antibacterial effect. The interlayer spacing (0.16–0.26 nm) in pure and Sr-doped materials was consistent with HR-TEM. The optical spectra of the samples indicate a redshift after doping, causing a reduction in, $E_{g.}$, from 3.3 to 3.0 eV, as revealed by UV–vis spectroscopy. Regarding the reduction efficiency against RhB, the synthesized nanocatalysts demonstrated that the pristine Cr_2O_3 exhibited superior catalytic activity compared to the Sr-doped nanomaterials. *In-vitro* antibacterial activity of NSs using an agar-based diffusion technique shows that significant inhibition zone measurements were 8.65—10.15 mm and 9.65—11.75 mm for lower and higher concentrations against MDR *E. coli,* respectively. Cr_2O_3 and Sr-doped Cr_2O_3 were shown to have an impressive binding score and interaction mechanism within the active region of targeted proteins, indicating that they may be employed as a possible inhibitor of FabH and DHFR enzymes and warranting further exploration into their inhibitory properties. The superior inhibitory activity observed against MDR bacteria classifies these samples as viable candidates for wastewater treatment systems.

Data availability statement

The original contributions presented in the study are included in the article/supplementary material, further inquiries can be directed to the corresponding authors.

Author contributions

MIk: Conceptualization, Investigation, Writing—original draft preparation, Supervision, Funding acquisition, Visualization. AS: Methodology, Formal analysis, Writing—review and editing, MB: Conceptualization, Resources. AH: Investigation, Data Curation. AU-H: Methodology, Investigation. WN: Conceptualization, Writing—review and editing, Investigation. JH: Formal analysis, Resources. SA: Conceptualization, Data Curation. FM: data analysis, interpretation, conceptualization, review and editing, investigation, formal analysis, and fund acquisition. MIm: Methodology, Formal analysis.

Acknowledgments

The authors express their gratitude to the Higher Education Commission (HEC), Pakistan, for the support through NRPU 20-17615 (MIk) and to the Universitat Rovira i Virgili for the support under the Maria Zambrano Programme (Reference number: 2021URV-MZ-10). Authors are also thankful to Proyectos de Generación de Conocimiento AEI/MCIN (PID2021-123665OB-I00) the project reference number of TED2021-129343B-I00 Grant PID2021-123665OB-I00 and TED2021-129343BI00 funded by MCIN/AEI/ 10.13039/501100011033 and, as appropriate, by "ERDF A way of making Europe", by the "European Union" or by the "European Union NextGenerationEU/PRTR".

Conflict of interest

The authors declare that the research was conducted in the absence of any commercial or financial relationships that could be construed as a potential conflict of interest.

Publisher's note

References

Abdullah, M. M., Rajab, F. M., and Al-Abbas, S. M. (2014). Structural and optical characterization of Cr2O3 nanostructures: Evaluation of its dielectric properties. *AIP Adv.* 4 (2), 027121. doi:10.1063/1.4867012

Abu-Zied, B. M. (2000). Structural and catalytic activity studies of silver/chromia catalysts. *Appl. Catal. A General.* 198 (1), 139–153. doi:10.1016/s0926-860x(99)00508-6

Adzitey, F., Yussif, S., Ayamga, R., Zuberu, S., Addy, F., Adu-Bonsu, G., et al. (2022). Antimicrobial susceptibility and molecular characterization of *Escherichia coli* recovered from milk and related samples. *Microorganisms* 10 (7), 1335. doi:10.3390/microorganisms10071335

Ahmad, S., Farrukh, M. A., Khan, M., Khaleeq-ur-Rahman, M., and Tahir, M. A. (2014). Synthesis of iron oxide–tin oxide nanoparticles and evaluation of their activities against different bacterial strains. *Can. Chem. Trans.* 2 (2), 122–133.

Akihide, I., Hideki, K., Hiroaki, O., and Akihiko, K. (2004). formation of surface nano-step structures and improvement of photocatalytic activities of NaTaO3 by doping of alkaline earth metal ions. *Chem. Lett.* 33 (10), 1260–1261. doi:10.1246/cl.2004.1260

Alahmadi, N., Betts, J., Cheng, F., Francesconi, M., Kelly, S., Kornherr, A., et al. (2017). Synthesis and antibacterial effects of cobalt–cellulose magnetic nanocomposites. *RSC Adv.* 7 (32), 20020–20026. doi:10.1039/c7ra00920h

Alani, O. A., Ari, H. A., Offiong, N-A. O., Alani, S. O., Li, B., Zeng, Q-r., et al. (2021). Catalytic removal of selected textile dyes using zero-valent copper nanoparticles loaded on filter paper-chitosan-titanium oxide heterogeneous support. *J. Polym. Environ.* 29 (9), 2825–2839. doi:10.1007/s10924-021-02062-0

Almontasser, A., Parveen, A., Hashim, M., Ul-Hamid, A., and Azam, A. (2021). Structural, optical, and antibacterial properties of pure and doped (Ni, Co, and Fe) Cr2O3 nanoparticles: A comparative study. *Appl. Nanosci.* 11 (2), 583–604. doi:10.1007/s13204-020-01590-w

Almontasser, A., and Parveen, A. (2020). Preparation and characterization of chromium oxide nanoparticles. *AIP Conf. Proc.* 2220 (1), 020010.

Altaf, S., Haider, A., Naz, S., Ul-Hamid, A., Haider, J., Imran, M., et al. (2020). Comparative study of selenides and tellurides of transition metals (Nb and Ta) with respect to its catalytic, antimicrobial, and molecular docking performance. *Nanoscale Res. Lett.* 15 (1), 144. doi:10.1186/s11671-020-03375-0

Anbu, P., Gopinath, S. C., Salimi, M. N., Letchumanan, I., and Subramaniam, S. (2022). Green synthesized strontium oxide nanoparticles by Elodea canadensis extract and their antibacterial activity. *J. Nanostructure Chem.* 12 (3), 365–373. doi:10.1007/s40097-021-00420-x

Asha, S., Hentry, C., Bindhu, M. R., Al-Mohaimeed, A. M., AbdelGawwad, M. R., and Elshikh, M. S. (2021). Improved photocatalytic activity for degradation of textile dyeing waste water and thiazine dyes using PbWO4 nanoparticles synthesized by co-precipitation method. *Environ. Res.* 200, 111721. doi:10.1016/j.envres.2021.111721

Ashiri, R., Nemati, A., Sasani Ghamsari, M., and Aadelkhani, H. (2009). Characterization of optical properties of amorphous BaTiO3 nanothin films. *J. Non-Crystalline Solids* 355 (50), 2480–2484. doi:10.1016/j.jnoncrysol.2009.08.030

Bai, B., Wang, P., Wu, L., Yang, L., and Chen, Z. (2009). A novel yeast bio-template route to synthesize Cr2O3 hollow microspheres. *Mater. Chem. Phys.* 114 (1), 26–29. doi:10.1016/j.matchemphys.2008.10.030

Balachandran, U., Siegel, R. W., Liao, Y. X., and Askew, T. R. (1995). Synthesis, sintering, and magnetic properties of nanophase Cr2O3. *Nanostructured Mater.* 5 (5), 505–512. doi:10.1016/0965-9773(95)00266-h

Bauer, A. (1966). Antibiotic susceptibility testing by a standardized single disc method. *Am. J. Clin. Pathol.* 45, 149–158.

Chen, W., Hong, J., and Xu, C. (2015). Pollutants generated by cement production in China, their impacts, and the potential for environmental improvement. *J. Clean. Prod.* 103, 61–69. doi:10.1016/j.jclepro.2014.04.048

Cui, H-J., Huang, H-Z., Yuan, B., and Fu, M-L. (2015). Decolorization of RhB dye by manganese oxides: Effect of crystal type and solution pH. *Geochem. Trans.* 16 (1), 10. doi:10.1186/s12932-015-0024-2

Di, L., Yang, H., Xian, T., and Chen, X. (2017). Enhanced photocatalytic activity of NaBH4 reduced BiFeO3 nanoparticles for rhodamine B decolorization. *Mater. [Internet]* 10 (10), 1118. doi:10.3390/ma10101118

El-Sheikh, S. M., Mohamed, R. M., and Fouad, O. A. (2009). Synthesis and structure screening of nanostructured chromium oxide powders. *J. Alloys Compd.* 482 (1), 302–307. doi:10.1016/j.jallcom.2009.04.011

Eltaweil, A. S., Abdelfatah, A. M., Hosny, M., and Fawzy, M. (2022). Novel biogenic synthesis of a Ag@biochar nanocomposite as an antimicrobial agent and photocatalyst for methylene blue degradation. *ACS Omega* 7 (9), 8046–8059. doi:10.1021/acsomega.1c07209

Fouad, N. E., Knözinger, H., Zaki, M. I., and Mansour, S. A. A. (1991). Chromia on silica and alumina catalysts. *Z. für Phys. Chem.* 171 (1), 75–96. doi:10.1524/zpch.1991.171.part_1.075

Franci, G., Falanga, A., Galdiero, S., Palomba, L., Rai, M., Morelli, G., et al. (2015). Silver nanoparticles as potential antibacterial agents. *Molecules* 20 (5), 8856–8874. doi:10.3390/molecules20058856

Gabr, R. M., Girgis, M. M., El-Awad, A. M., and Abou-Zeid, B. M. (1994). Effect of spinel (ZnCr2O4) formation on the texture, electrical conduction and catalytic behaviour of the ZnO Cr2O3 system. *Mater. Chem. Phys.* 39 (1), 53–62. doi:10.1016/0254-0584(94)90131-7

Ghotekar, S., Pansambal, S., Bilal, M., Pingale, S. S., and Oza, R. (2021). Environmentally friendly synthesis of Cr2O3 nanoparticles: Characterization, applications and future perspective— a review. *Case Stud. Chem. Environ. Eng.* 3, 100089. doi:10.1016/j.cscee.2021.100089

Hameed, B. B., and Ismail, Z. Z. (2019). Decolorization, biodegradation and detoxification of reactive blue azo dye using immobilized mixed cells. *J. Eng.* 25 (6), 53–66. doi:10.31026/j.eng.2019.06.05

He, X., Yang, D-P., Zhang, X., Liu, M., Kang, Z., Lin, C., et al. (2019). Waste eggshell membrane-templated CuO-ZnO nanocomposites with enhanced adsorption, catalysis and antibacterial properties for water purification. *Chem. Eng. J.* 369, 621–633. doi:10.1016/j.cej.2019.03.047

Holt, J. G., Krieg, N. R., Sneath, P. H., Staley, J. T., and Williams, S. T. (1994). *Bergey's Manual of determinate bacteriology*. Philadelphia, PA, USA: Lippincott Williams and Wilkins.

Ikram, M., Haider, A., Imran, M., Haider, J., Ul-Hamid, A., Shahzadi, A., et al. (2023). Graphitic-C3N4/chitosan-doped NiO nanostructure to treat the polluted water and their bactericidal with *in silico* molecular docking analysis. *Int. J. Biol. Macromol.* 227, 962–973. doi:10.1016/j.ijbiomac.2022.11.273

Ivanov, P., Watts, S., and Lind, D. (2001). Epitaxial growth of CrO 2 thin films by chemical-vapor deposition from a Cr 8 O 21 precursor. *J. Appl. Phys.* 89 (2), 1035–1040. doi:10.1063/1.1331343

Iwalokun, B., Ogunledun, A., Ogbolu, D., Bamiro, S., and Jimi-Omojola, J. (2004). *In vitro* antimicrobial properties of aqueous garlic extract against multidrug-resistant bacteria and Candida species from Nigeria. *J. Med. food* 7 (3), 327–333. doi:10.1089/jmf.2004.7.327

Kamari, H. M., Al-Hada, N. M., Baqer, A. A., Shaari, A. H., and Saion, E. (2019). Comprehensive study on morphological, structural and optical properties of Cr 2 O 3 nanoparticle and its antibacterial activities. *J. Mater. Sci. Mater. Electron.* 30, 8035–8046. doi:10.1007/s10854-019-01125-2

Kiani, F. A., Shamraiz, U., and Badshah, A. (2020). Enhanced photo catalytic activity of Ag2O nanostructures through strontium doping. *Mater. Res. Express* 7 (1), 015035. doi:10.1088/2053-1591/ab608c

Kim, D-W., Shin, S-I., Lee, J-D., and Oh, S-G. (2004). Preparation of chromia nanoparticles by precipitation–gelation reaction. *Mater. Lett.* 58 (12), 1894–1898. doi:10.1016/j.matlet.2003.11.023

Li, H-Q., Shi, L., Li, Q-S., Liu, P-G., Luo, Y., Zhao, J., et al. (2009). Synthesis of C(7) modified chrysin derivatives designing to inhibit β-ketoacyl-acyl carrier protein synthase III (FabH) as antibiotics. *Bioorg. Med. Chem.* 17 (17), 6264–6269. doi:10.1016/j.bmc.2009.07.046

Li, L., Zhu, Z., Yao, X., Lu, G., and Yan, Z. (2008). Synthesis and characterization of chromium oxide nanocrystals via solid thermal decomposition at low temperature. *Microporous Mesoporous Mater.* 112 (1), 621–626. doi:10.1016/j.micromeso.2007.10.044

Li, Y., Peng, S., Jiang, F., Lu, G., and Li, S. (2007). Effect of doping TiO2 with alkaline-Earth metal ions on its photocatalytic activity. *J. Serbian Chem. Soc.* 72 (4), 393–402. doi:10.2298/jsc0704393l

Lima, M. D., Bonadimann, R., de Andrade, M. J., Toniolo, J. C., and Bergmann, C. P. (2006). Nanocrystalline Cr2O3 and amorphous CrO3 produced by solution combustion synthesis. *J. Eur. Ceram. Soc.* 26 (7), 1213–1220. doi:10.1016/j.jeurceramsoc.2005.01.042

Liu, Y., He, L., Mustapha, A., Li, H., Hu, Z. Q., and Lin, M. (2009). Antibacterial activities of zinc oxide nanoparticles against *Escherichia coli* O157:H7. *J. Appl. Microbiol.* 107 (4), 1193–1201. doi:10.1111/j.1365-2672.2009.04303.x

Suresh, M. B., and Roy, J. (2012). The effect of strontium doping on densification and electrical properties of Ce0.8Gd0.2O2−δelectrolyte for IT-SOFC application. *Ionics* 18 (3), 291–297. doi:10.1007/s11581-011-0633-4

Magureanu, M., Piroi, D., Mandache, N. B., and Parvulescu, V. (2008). Decomposition of methylene blue in water using a dielectric barrier discharge: Optimization of the operating parameters. *J. Appl. Phys.* 104 (10), 103306. doi:10.1063/1.3021452

McKinney, D. C., Eyermann, C. J., Gu, R-F., Hu, J., Kazmirski, S. L., Lahiri, S. D., et al. (2016). Antibacterial FabH inhibitors with mode of action validated in Haemophilus influenzae by *in vitro* resistance mutation mapping. *ACS Infect. Dis.* 2 (7), 456–464. doi:10.1021/acsinfecdis.6b00053

Mehmood, Z., Ikram, M., Imran, M., Shahzadi, A., Haider, A., Ul-Hamid, A., et al. (2022). Z. officinale-doped silver/calcium oxide nanocomposites: Catalytic activity and antimicrobial potential with molecular docking analysis. *Process Biochem.* 121, 635–646. doi:10.1016/j.procbio.2022.07.035

Mehtab, A., Ahmed, J., Alshehri, S. M., Mao, Y., and Ahmad, T. (2022). Rare Earth doped metal oxide nanoparticles for photocatalysis: A perspective. *Nanotechnology* 33 (14), 142001. doi:10.1088/1361-6528/ac43e7

Mougin, J., Le Bihan, T., and Lucazeau, G. (2001). High-pressure study of Cr2O3 obtained by high-temperature oxidation by X-ray diffraction and Raman spectroscopy. *J. Phys. Chem. Solids* 62 (3), 553–563. doi:10.1016/s0022-3697(00)00215-8

Munusamy, S., Rsl, A., and Prasad, R. (2013). Photocatalytic effect of TiO2and the effect of dopants on degradation of brilliant green. *Sustain. Chem. Process.* 1 (1), 4. doi:10.1186/2043-7129-1-4

Nguyen, H-T. T., Tran, K-N. T., Van Tan, L., Tran, V. A., Doan, V-D., Lee, T., et al. (2021). Microwave-assisted solvothermal synthesis of bimetallic metal-organic framework for efficient photodegradation of organic dyes. *Mater. Chem. Phys.* 272, 125040. doi:10.1016/j.matchemphys.2021.125040

Norby, P., Christensen, A. N., Fjellvåg, H., and Nielsen, M. (1991). The crystal structure of Cr8O21 determined from powder diffraction data: Thermal transformation and magnetic properties of a chromium-chromate-tetrachromate. *J. Solid State Chem.* 94 (2), 281–293. doi:10.1016/0022-4596(91)90193-l

Panda, A. K., Singh, A., Divakar, R., Krishna, N. G., Reddy, V. R., Thirumurugesan, R., et al. (2018). Crystallographic texture study of pulsed laser deposited Cr2O3 thin films. *Thin Solid Films* 660, 328–334. doi:10.1016/j.tsf.2018.06.030

Pei, Z., Xu, H., and Zhang, Y. (2009). Preparation of Cr2O3 nanoparticles via C2H5OH hydrothermal reduction. *J. Alloys Compd.* 468 (1), L5–L8. doi:10.1016/j.jallcom.2007.12.086

Pinna, N., Garnweitner, G., Antonietti, M., and Niederberger, M. (2004). Non-aqueous synthesis of high-purity metal oxide nanopowders using an ether elimination process. *Adv. Mater.* 16 (23-24), 2196–2200. doi:10.1002/adma.200400460

Qamar, S. A., Ashiq, M., Jahangeer, M., Riasat, A., and Bilal, M. (2020). Chitosan-based hybrid materials as adsorbents for textile dyes–A review. *Case Stud. Chem. Environ. Eng.* 2, 100021. doi:10.1016/j.cscee.2020.100021

Ramam, K., and Chandramouli, K. (2009). Dielectric and piezoelectric properties of combinatory effect of A-site isovalent and B-site acceptor doped PLZT ceramics. *Ceram. Silik* 53 (3), 189.

Ramesh, C., Mohan Kumar, K., Latha, N., and Ragunathan, V. (2012). Green synthesis of Cr2O3 nanoparticles using Tridax procumbens leaf extract and its antibacterial activity on *Escherichia coli*. *Curr. Nanosci.* 8 (4), 603–607. doi:10.2174/157341312801784366

Rashad, M., Ali, A. M., Sayyed, M. I., Somaily, H. H., Algarni, H., and Rammah, Y. S. (2020). Radiation attenuation and optical features of lithium borate glasses containing barium: B2O3.Li2O.BaO. *Ceram. Int.* 46 (13), 21000–21007. doi:10.1016/j.ceramint.2020.05.165

Sallam, S. A., El-Subruiti, G. M., and Eltaweil, A. S. (2018). Facile synthesis of Ag–γ-Fe2O3 superior nanocomposite for catalytic reduction of nitroaromatic compounds and catalytic degradation of methyl orange. *Catal. Lett.* 148 (12), 3701–3714. doi:10.1007/s10562-018-2569-z

Shafi, I., Liang, E., and Li, B. (2021). Ultrafine chromium oxide (Cr2O3) nanoparticles as a pseudocapacitive electrode material for supercapacitors. *J. Alloys Compd.* 851, 156046. doi:10.1016/j.jallcom.2020.156046

Shahzadi, I., Islam, M., Saeed, H., Haider, A., Shahzadi, A., Haider, J., et al. (2022). Formation of biocompatible MgO/cellulose grafted hydrogel for efficient bactericidal and controlled release of doxorubicin. *Int. J. Biol. Macromol.* 220, 1277–1286. doi:10.1016/j.ijbiomac.2022.08.142

Singh, J., Verma, V., and Kumar, R. (2019). Preparation and structural, optical studies of Al substituted chromium oxide (Cr2O3) nanoparticles. *Vacuum* 159, 282–286. doi:10.1016/j.vacuum.2018.09.033

Singh, J., Verma, V., Kumar, R., Sharma, S., and Kumar, R. (2019). Effect of structural and thermal disorder on the optical band gap energy of Cr2O3 nanoparticles. *Mater. Res. Express* 6 (8), 085039. doi:10.1088/2053-1591/ab195c

Summerfield, R. L., Daigle, D. M., Mayer, S., Mallik, D., Hughes, D. W., Jackson, S. G., et al. (2006). A 2.13 Å structure of *E. coli* dihydrofolate reductase bound to a novel competitive inhibitor reveals a new binding surface involving the M20 loop region. *J. Med. Chem.* 49 (24), 6977–6986. doi:10.1021/jm060570v

Tsuzuki, T., and McCormick, P. G. (2000). Synthesis of Cr2O3 nanoparticles by mechanochemical processing. *Acta Mater.* 48 (11), 2795–2801. doi:10.1016/s1359-6454(00)00100-2

Wayne, P. (2008). *Performance standards for antimicrobial susceptibility testing*. Villanova, PA, USA: National Committe for Clinical Laboratory Standards.

Wise, R., BSAC Working Party on The Urgent Need: Regenerating Antibacterial Drug Discovery and Development (2011). The urgent need for new antibacterial agents. *J. Antimicrob. Chemother.* 66 (9), 1939–1940. doi:10.1093/jac/dkr261

Xia, Y., and Mokaya, R. (2005). Hollow spheres of crystalline porous metal oxides: A generalized synthesis route via nanocasting with mesoporous carbon hollow shells. *J. Mater. Chem.* 15 (30), 3126–3131. doi:10.1039/b502558c

Yarahmadi, M., Maleki-Ghaleh, H., Mehr, M. E., Dargahi, Z., Rasouli, F., and Siadati, M. H. (2021). Synthesis and characterization of Sr-doped ZnO nanoparticles for photocatalytic applications. *J. Alloys Compd.* 853, 157000. doi:10.1016/j.jallcom.2020.157000

Yazid, N. A., and Joon, Y. C. (2019). Co-precipitation synthesis of magnetic nanoparticles for efficient removal of heavy metal from synthetic wastewater. *AIP Conf. Proc.* 2124 (1), 020019.

Zhong, Z. C., Cheng, R. H., Bosley, J., Dowben, P. A., and Sellmyer, D. J. (2001). Fabrication of chromium oxide nanoparticles by laser-induced deposition from solution. *Appl. Surf. Sci.* 181 (3), 196–200. doi:10.1016/s0169-4332(01)00346-4

Frontiers in Chemistry

TYPE Original Research
PUBLISHED 14 April 2023
DOI 10.3389/fchem.2023.1152501

EDITED BY
Ziying Wang,
Hebei University of Technology, China

REVIEWED BY
Shailajha Sathiyaseelan,
Manonmaniam Sundaranar University,
India
Sabari Girisun T. C.,
Bharathidasan University, India

*CORRESPONDENCE
Ehsan Koushki,
ehsan.koushki@yahoo.com,
ehsan.koushki@hsu.ac.ir
Behrooz Maleki,
malekibehrooz@gmail.com,
b.maleki@umz.ac.ir

RECEIVED 27 January 2023
ACCEPTED 03 April 2023
PUBLISHED 14 April 2023

CITATION
Jalili Z, Koushki E, Ehsanian AH,
Tayebee R and Maleki B (2023), Synthesis,
band gap structure and third order non-linear optical properties of zinc tungsten
oxide nanocomposite using a single CW
laser beam.
Front. Chem. 11:1152501.
doi: 10.3389/fchem.2023.1152501

Synthesis, band gap structure and third order non-linear optical properties of zinc tungsten oxide nanocomposite using a single CW laser beam

Zahra Jalili[1], Ehsan Koushki[2]*, Amir Hossein Ehsanian[2],
Reza Tayebee[1] and Behrooz Maleki[3]*

[1]Department of Chemistry, Faculty of Sciences, Hakim Sabzevari University, Sabzevar, Iran, [2]Department of Physics, Faculty of Sciences, Hakim Sabzevari University, Sabzevar, Iran, [3]Department of Organic Chemistry, Faculty of Chemistry, University of Mazandaran, Babolsar, Iran

In this study, a composite of zinc tungsten oxide nanoparticles (W-ZnO NPs) has been synthesized via mixing Na_2WO_4 and zinc acetate in water, followed by dropwise addition of NaOH. The synthesized W-ZnO NPs were characterized using measurement methods such as XRD, dynamic light scattering (DLS), Scanning electron microscopy (SEM) and UV-Vis. Also, the results were compared with the pure synthesized ZnO and WO_3 NPs. Non-linear optical properties of the synthesized composite were measured using the Z-scan technique with a continuous wave Nd-Yag laser. The negative non-linear absorption coefficient of the components was obtained which indicates that the saturation absorption occurred in this composite. In comparison with pure ZnO NPs, non-linear absorption decreases which can be attributed to the negligible optical response of WO_3 structures. Also, the negative value of the close aperture Z-scan curve shows that the thermal lensing effect is the main reason for the third-order non-linear refraction.

KEYWORDS

zinc tungsten oxide, Z-scan measurement, saturation absorption, thermal lensing, third order non-linear optical

1 Introduction

Recently, the use of inorganic materials in electronic and optical devices as active elements, such as light-emitting diodes, photovoltaic devices, and field-effect transistors has received much attention from the outlook of potential technological applications as well as fundamental science (Cao et al., 2011; Akherat Doost et al., 2021; Ashfaq et al., 2022). Meanwhile, metal oxide NPs (MONPs) are more important in technology because of their unique semiconducting properties (Silva et al., 2019) and play a considerable role in a multitude of fields of chemistry, physics and material sciences. MONPs are commonly known as catalysts, gas sensors, absorbents, superconductors, semiconductors and ceramics (Naseem and Durrani, 2021). Due to the effect of morphology and size on the properties of metal oxide NPs, their synthesis techniques mainly focus on these two parameters (Maduraiveeran et al., 2019). Among MONPs, the transition metal oxides have drawn much notice due to their outer electron configuration (Velmurugan and Incharoensakdi, 2018)

Among various classes of metal oxide NPs, II-VI class inorganic semiconductor nanomaterials like Zinc Oxide (ZnO), Cadmium Sulfide (CdS) and Zinc Sulfide (ZnS) have emerged as important materials for the applications in photovoltaic and optoelectronics devices (Abbasi et al., 2017). High chemical stability, inexpensive and easy synthesis methods and fast optical response speed lead to the use of them in non-linear optical devices such as optical switchers (Koushki et al., 2014a).

Zinc oxide (ZnO) and tungsten oxide (WO_3) are among the most widely used transition metal oxides. ZnO is a semiconductor with a wide band gap, good electrical conductivity and high transmittance (Nakahara et al., 2001). ZnO is one of the most highly used materials in catalysts and photocatalysts, optical materials, solar cells, UV absorbers in cosmetics, biosensors and nanogenerators (Gao et al., 2005; Srivastava et al., 2013). In addition to the above features, ZnO NPs have the potential for applications as non-linear optical devices, optical switchers, and have been studied extensively (Baedi et al., 2021). Being a member of group II-VI compounds, ZnO NPs have been extensively used in photovoltaic and optoelectronic devices. On the other hand, WO_3 NPs also have far-reaching usages in various fields such as batteries, gas sensors, catalysts and photocatalysts, illumination and electronics (Widenkvist et al., 2008; Hariharan et al., 2019). The synthesis of ZnO NPs doped WO_3 has also been investigated in a few articles, from the viewpoint of structure and photocatalytic properties (Arshad et al., 2020).

In the present work, WO_3, ZnO and zinc tungsten oxide NPs (W-ZnO NPs) have been synthesized through hydrothermal and chemical methods, and characterized using some measurement methods such as XRD, DLS, SEM and UV-Vis. After the evaluation of the band gap structure, the third-order non-linear optical properties of the synthesized composite were measured using the Z-scan method (Sheik-Bahae et al., 1990), and interesting results about the origin of non-linear absorption and refraction were offered at low laser irradiations regimes. Z scan technique was first discovered by Sheik-Bahae and his colleagues, and it is still used because of simplicity and highly sensitivity in measuring non-linear optical properties of materials (Sharma et al., 2012). To obtain the non-linear optical information of the material, it is enough to move the sample along the laser beam and detect the transmitting power through the sample. This experiment found that WO 3 doping can reduce the non-linear absorption coefficient and consequently the saturation of absorption of W-ZnO NPs [18] while increasing the absorption of the composite. It was directly related to the band gap structure of the synthesized composite, and discussed from the viewpoint of the physical properties of the charge carriers. The main novelty of this study is the investigation of tungsten dopant effects on the optical properties, bandgap and subsequently non-linear optical properties of ZnO nanoparticles.

2 Experiments

2.1 Experimental methods

The synthesized nanostructures were characterized by X-ray diffraction (XRD, DMAX2500, Rigaku X-ray diffractometer) in the 2θ domain at 30 mA and 40 keV and a scanning rate of 3° min^{-1} from 10° to 80° with Cu Kα radiation. The morphology and size of NPs were studied using a scanning electron microscope (SEM, MIRA3, TESCAN, Czech Republic) and a DynaPro NanoStar dynamic light scattering (DLS) detector (WYATT Technology). UV-visible spectra were recorded with a EU_ 2200 spectrophotometer.

Z scan setup contains a continuing wave (CW) Nd-Yag laser, a convergence lens, and a detector. The laser beam, which has a Gaussian distribution, propagates along the Z direction. The lens is placed perpendicular to the Z direction. After the lens, the laser beam is focused, and the sample containing the nano-colloid scans the z-axis before and after the focus. The beam falls completely into the detector to measure the transmitted power. In a close aperture setup which is due to the non-linear refraction, a finite aperture is placed before the detector, as shown in Figure 1.

The wavelength of the used green laser in close and open aperture Z-scan curves was 532.8 nm (CNIlaser/MSL-S-532-S). The output power of the laser was about 5mW, and the beam was focused using a convergence lens with a focal length of 8 cm. The beam waist at the focal point was measured at about $w_0 = 35\mu m$ using the well-known edge-scan technique (Suzaki and Tachibana, 1975), and the power after focusing on the lens was 4.35 mW. Also, the Rayleigh range and the on-axis peak intensity were obtained $z_0 = 7.2mm$ and $I_0 = 228\, {}^{W}\!/_{cm^2}$, respectively. Transmitted powers were measured using a semiconductor photo-detector (Ashabeam/PMB-101/IRAN). Colloidal solutions of NPs with a concentration of 0.01M in water have been prepared and poured into a 1 mm thickness quartz cell that was used as an optical sample. In a close aperture setup, a circular aperture with a radius of $r_a = 0.2mm$ was used.

3 Theory of Z-scan method

In the presence of the laser beam, the absorption coefficient (β) and also the refractive index (n_2) of non-linear materials would change according to (Sheik Bahae et al., 1990; Tsigaridas et al., 2003):

$$n = n_0 + n_2 I \text{ and } \alpha = \alpha_0 + \beta I \tag{1}$$

where n_0 and α_0 are refractive index and absorption coefficient in low intensities, respectively. In the close aperture Z-scan experiment, the sample scans the z-axes (parallel to beam direction) before and after the focal point and, the transmitted power through an optical aperture (radius of r_a) is plotted via the sample position (z). It gives rise to the close aperture Z-scan curve, and by curve fitting, experimental curves with theoretical one, n_2 would be obtained. The focal point is considered the origin of the z-axis ($z = 0$). The far-field at the aperture plane ($z + D$) is given by (Sheik Bahae et al., 1990; Koushki and Majles Ara, 2011):

$$E(r, z + D) = E_{in}(r = 0, z)e^{-\alpha L/2} \sum_{m=0}^{\infty} \frac{[-i\Delta\varphi(z, r = 0)]^m}{m!} \frac{w_{m0}}{w_m} \exp\left(-\frac{r^2}{w_m^2} - \frac{ikr^2}{2R_m} + i\theta_m\right) \tag{2}$$

In this relation, D is the distance between the aperture and the sample, and $E_{in}(r = 0, z)$ is the electric field of the incident beam on the sample plane. We also have r as the radial coordinates, K, the wave number, $\Delta\varphi(z, r = 0)$, the phase change of the beam at the

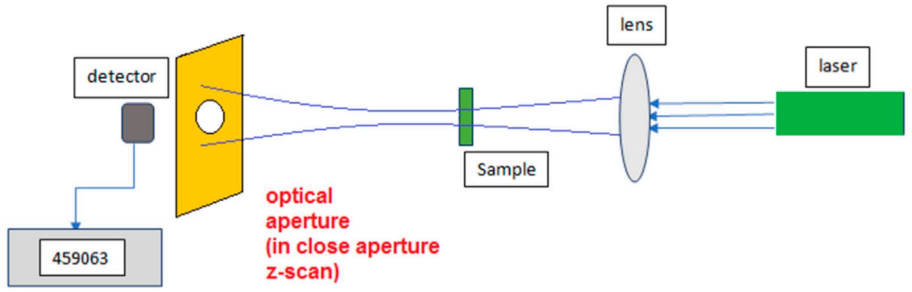

FIGURE 1
Schematic of Z-scan technique.

center of the beam, and L, the thickness of the sample. Now, we will have the optical phase change as follows:

$$\Delta\varphi(z,r) = \frac{kn_2 I_0 L_{eff}}{1+\left(\frac{z}{z_0}\right)^2}\exp\left(-2r^2/w^2(z)\right) \tag{3}$$

and also $L_{eff} = {(1-e^{-\alpha L})}/{\alpha}$, z_0 and I_0 are the effective length of the sample, the Rayleigh length and the intensity at the center of the beam waist, respectively. By defining $g = 1 + D/R(z)$, we will have other terms in Eq. 2 as below:

$$w_{m0}^2 = \frac{w^2(z)}{2m+1}, d_m = \frac{kw_{m0}^2}{2}, w_m^2 = w_{m0}^2\left[g^2 + \frac{D^2}{d_m^2}\right],$$

$$R_m = D\left[1 - \frac{g}{g^2 + D^2/d_m^2}\right]^{-1}$$

$$\theta_m = \tan^{-1}\left[\frac{D/d_m}{g}\right] \tag{4}$$

where $w(z)$ is the radius of the beam at z position, we can obtain the transmitted power, which obeys the following relation:

$$P(z) = \int_0^{r_a} I(r,z)2\pi r dr \tag{5}$$

So, at any point of z, the normalized transmittance follows:

$$T(z) = \frac{\int_0^{\infty} P(z,\Delta\varphi_0(t))dt}{\int_0^{\infty} P(z,\Delta\varphi_0 = 0)dt} \tag{6}$$

Eq. 6 gives close aperture Z-scan curve which is sensitive to the non-linear refractive index and, it can be evaluated by the suitable curve fitting with experimental data n_2. To evaluate the non-linear absorption coefficient, it is enough to match the experimental data with the theoretical curve. But when we want to perform the open aperture experiment, the aperture should be removed, and the sample should be directly exposed to the laser beam. The related relations are given as (Sheik Bahae et al., 1990);

$$P(z) = P_0 e^{-\alpha L}\frac{Ln(1+q_0(z))}{q_0(z)} \tag{7}$$

where $q_0(z) = \frac{\beta I_0 L_{eff}}{(1+(z/z_0)^2)}$. By curve fitting, the normalized curve with Eq. 7, β would be obtained.

4 Synthesis of NPs

Here, the experimental routes for the synthesis of NPs were offered.

4.1 Synthesis of WO_3

We used a reliable technique based on the recommendations of Hassani et al., 2011 to synthesize WO_3. A mixture of $Na_2WO_4.2H_2O$ (0.4 g) and NaCl (0.15 g) was dissolved in deionized water (2 mL) under magnetic stirring. HCl (3 M) was added dropwise to the stirring solution until the solution became acidic. The solution was heated into in an autoclave at 180°C for 2 h. Being under room temperature for a time span of 1 day, the precipitate was centrifuged (2 min, 30,000 rpm) with ethanol and distilled water, and then dried at 60°C for 8 h.

4.2 Synthesis of ZnO

ZnO was prepared as described by Liu et al., 2014. For this purpose, a mixture of zinc acetate ($Zn(AC)_2$, 0.75 g) and sodium peroxide (Na_2O_2, 0.4 g) was dissolved into 40 mL of deionized water under stirring. 20 min later, the mixture was centrifuged, and the separated final white product was washed with distilled water several times, and then dried at 50°C for 8 h.

4.3 Preparation of W-ZnO NPs

As reported in the previous work (Chen et al., 2021), W-ZnO was synthesized via mixing 2.5 mL sodium tungstate ($Na_2WO_4.2H_2O$, 0.5 M) and 22 mL zinc acetate dihydrate ($Zn(CH_3CO_2)_2{\cdot}2H_2O$, 1 M) in water, followed by dropwise addition of 35 mL NaOH (4 M) and stirring at room temperature (for 3 hours) to form the precursor. The suspension was then transferred into a glass conical flask (250 mL) with a ground glass stopper, and then water was added up to the marked line, and the temperature was maintained at 95 C for 10 h. The produced

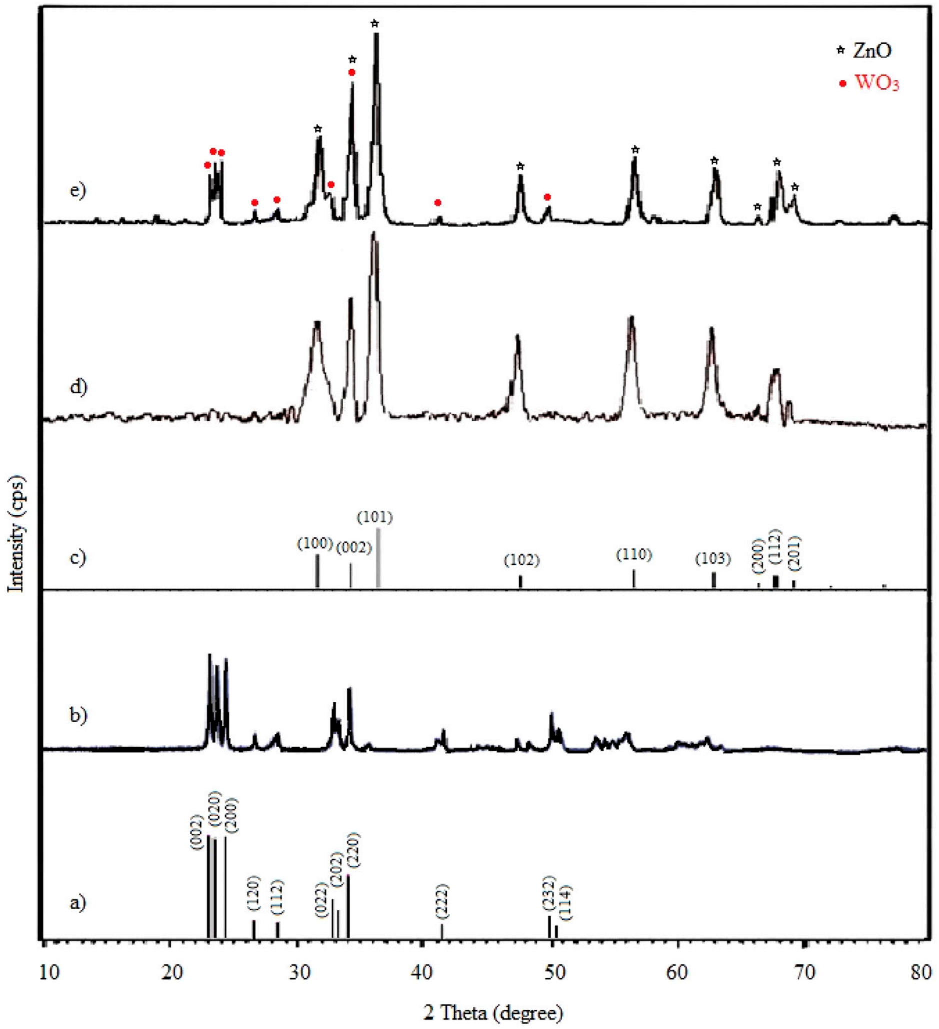

FIGURE 2
Wide-angle XRD pattern of **(A)** simulated standard WO_3, **(B)** synthesized WO_3, **(C)** simulated standard ZnO, **(D)** synthesized ZnO and **(E)** synthesized W-ZnO.

precipitate was collected, washed with deionized water, and dried at ambient temperature in the air.

5 Results and discussion

5.1 Characterization and structural identification of NPs

As carefully described in the experimental section, WO_3, ZnO and W-ZnO NPs were synthesized through reliable techniques. The resulting nanomaterial was characterized by means of various techniques including XRD, DLS, ESM and UV-Vis as follows.

To demonstrate the successful synthesis of NPs and to investigate their crystal phase, XRD measurements have been performed. Figure 2B reveals the monoclinic structure of synthesized WO_3 by matching it with the standard patterns (JCPDS card no. 83-0950, Figure 2A). Main strong diffraction peaks at $2\theta = 23.1°$, 23.5°, 24.3°, 26.6°, 28.3°,32.8°, 33.2°, 34.0°, 41.4°, 49.8°, 50,4° are assigned as (002), (020), (200), (120), (112), (022), (202), (220), (222), (232) and (114). The XRD pattern for the synthesized ZnO NPs is shown in Figure 2D. The XRD peaks at $2\theta =$ 31.5°, 34.2°, 36.4°, 47.8°, 56.7°, 62.9°, 66.3°, 67.8° and 69.2° are associated with the (100), (002), (101), (102), (110), (103), (200), (112) and (201) crystalline planes of hexagonal crystal geometry of ZnO, which is associated with JCPSD card no. 01-007-2551 (Figure 2C). In the XRD pattern of W-ZnO (Figure 2E), the diffraction peaks at the 2θ of 23.0°, 23.45°, 24.2°, 26.5°, 28.3°,32.5°, 41.2° and 49.8° corresponded to the (002), (020), (200), (120), (112), (022), (222) and (232) crystal planes of WO_3. In addition, the diffraction peaks at the 2θ of 31.5°, 34.2°, 36.1°, 47.7°, 56.8°, 63.1°, 66.2°, 68° and 69.1° corresponded to (100), (002), (101), (102), (110), (103), (200), (112) and (201) planes of ZnO, respectively. These results confirmed that W-ZnO was properly synthesized.

Size is an important factor to describe NPs, hereupon the DLS as a widely used technique for the determination of particle size in colloidal solution was used in this study. Figure 3 shows the particle size

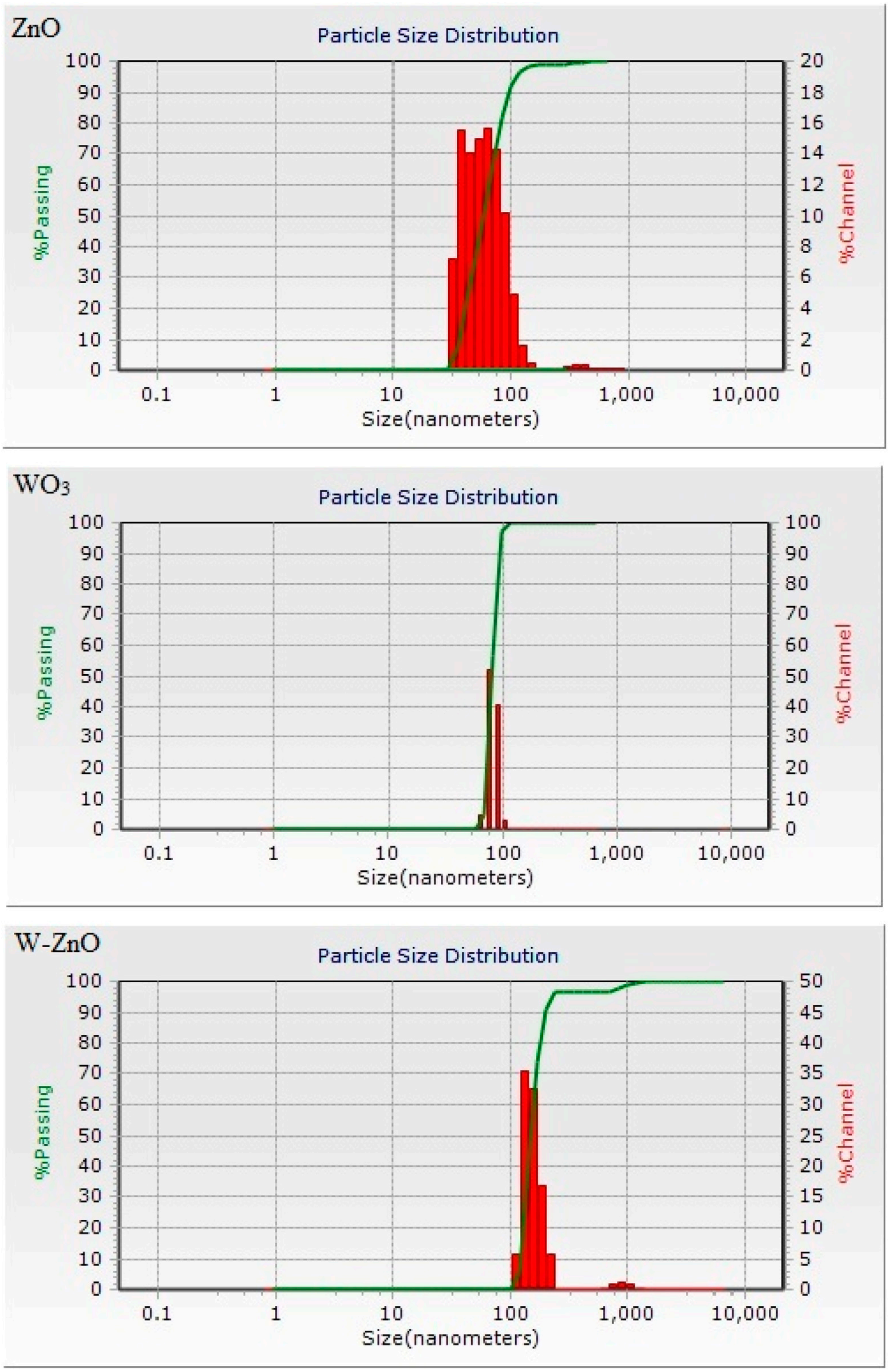

FIGURE 3
The size distribution charts of ZnO, WO_3 and W-ZnO particles.

distribution graph for the ZnO, WO_3 and W-ZnO NPs. According to the data obtained from the DLS analysis, the average size of synthesized NPs is 75, 91 and 183 for ZnO, WO_3 and W-ZnO particles, respectively.

To evaluate the precise and dispersion of measurement values for DLS analysis result, we calculate the standard deviation (σ) of the particles. Standard deviation can be calculated using:

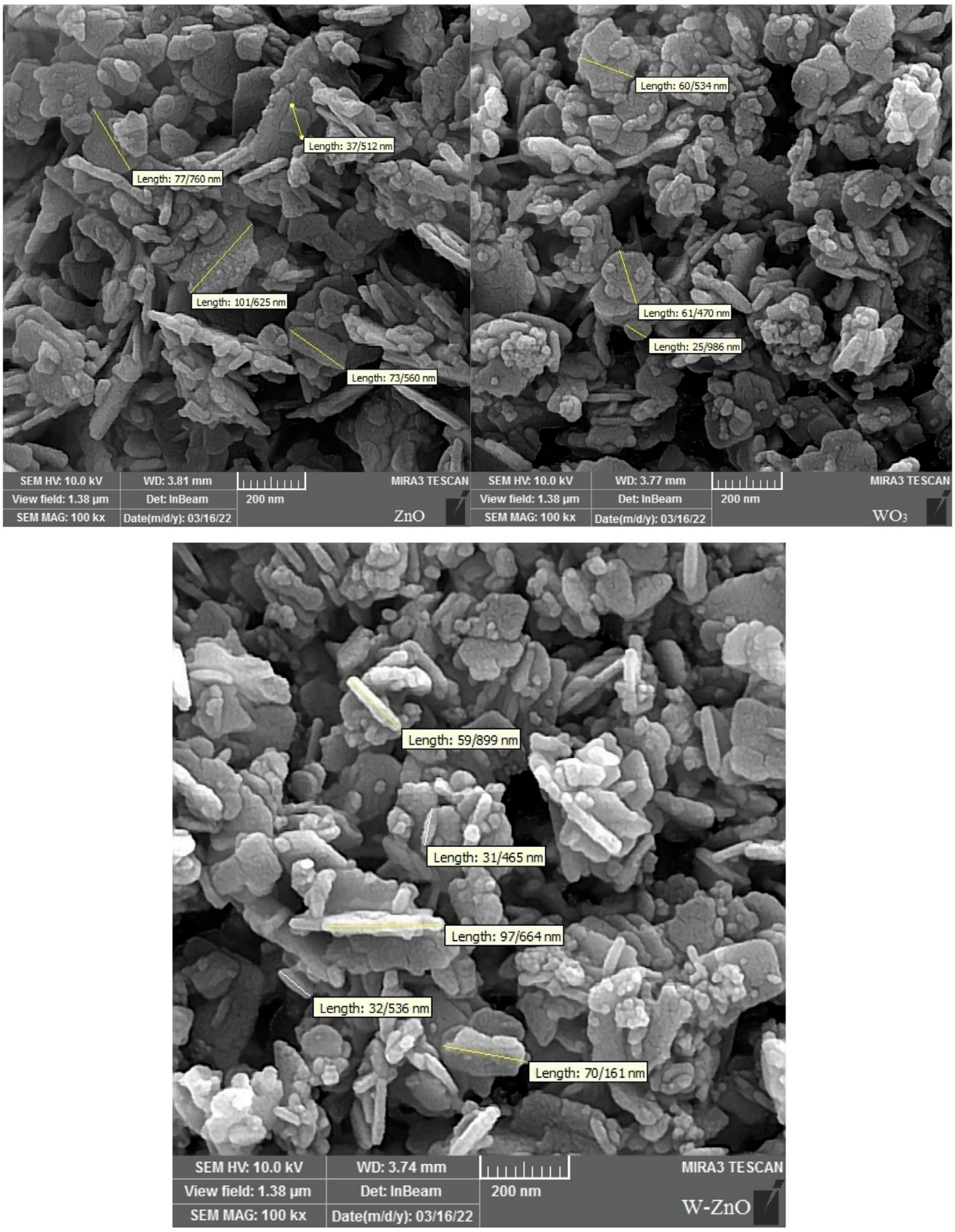

FIGURE 4
SEM images of ZnO, WO_3 and W-ZnO.

$$\sigma = \sqrt{\frac{\sum f_i (x_i - \bar{x})^2}{n - 1}} \tag{8}$$

where f_i, $\bar{x}$ and n are the frequency (percent of passing particles), average size and summation of frequencies, respectively. Standard deviations of ZnO, WO3 and W-ZnO NPs were obtained 33, 9 and 17 nm, respectively.

Unlike range and interquartile range, variance is a measure of dispersion that takes into account the spread of all data points in a data set. It's the measure of dispersion the most often used, along with the standard deviation, which is simply the square root of the variance. The variance is mean squared difference between each data point and the centre of the distribution measured by the mean.

Scanning electron microscopy (SEM) was used as a powerful technique to describe the morphological characteristics of the synthesized structures (Figure 4). According to the SEM images, it can be concluded that the synthesized W-ZnO has almost a

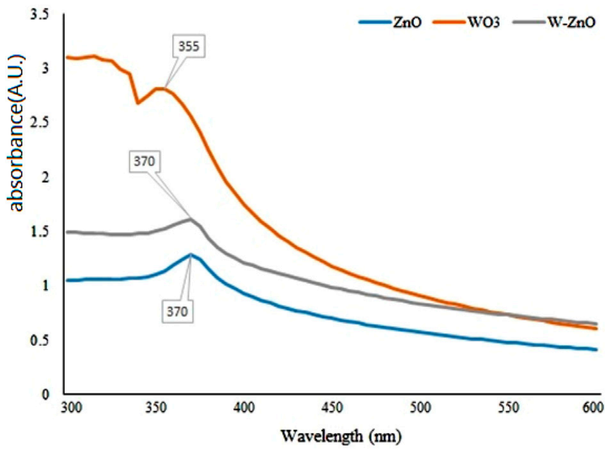

FIGURE 5
UV–Vis absorption spectra of ZnO, WO_3 and W-ZnO.

nanosheet framework. By consideration of this figure, it is clear that WO_3 and ZnO particles have dimensions below 100 nm. It is well recognizable that adding WO_3 to ZnO did not cause a noticeable change in the particle size and most of the W-ZnO particles have dimensions below 100 nm. In addition, there is approximately no agglomeration in synthesized structures.

For a more analytical investigation of the synthesized samples, the amount of absorption with the wavelength of 300–600 nm was observed by UV-Vis spectroscopy. As can be seen in Figure 5, the SPR band cantered 370 nm confirms the formation of ZnO NPs (Ghorbani et al., 2015). The excitonic feature of W-ZnO has also appeared at 370 nm. There is a lack of unanimous value for the excitonic point of WO_3 in the literature (Baishya et al., 2018), However, Figure 5 shows adsorption at 335 nm for WO_3 which can be consigned to the intrinsic band-gap absorption of WO_3 (Ramar and Balasubramanian, 2018).

In Figure 6, the colloidal absorption spectrum of ZnO, WO_3 and W-ZnO NPs in water is plotted in the ultraviolet-visible region. With the help of the Tauc method, the optical energy band gap of NPs can be obtained. In this method, the following relation is used (Eq.3) (Arun et al., 2015).

In Figure 6, the Tauc plot of colloidal ZnO, WO_3 and W-ZnO NPs in water is plotted. With the help of the Tauc method, the optical energy band gap of NPs can be obtained. In this method, the following relation is used (Arun et al., 2015; Koushki et al., 2019).

$$(\alpha h\nu)^{0.5} = A\left(h\nu - E_g\right) \tag{9}$$

where A is a constant value, h is Planck constant, ν is the photon frequency and α is the absorption value. The value on the left side of this equation is plotted against $h\nu$. By drawing a tangent line to the curve, a bang gap value would be achieved. As can be seen in the table 1 the band gap energy of 3.04 eV was obtained for ZnO NPs and, therefore, it can be considered as semiconductors with relatively high band gap energy, but other NPs have a smaller bandgap (Koushki, 2021), and their higher conductivity can be attributed to the presence of tungsten structures.

5.2 The study of non-linear optical properties of synthesized NPs

The curves of the closed aperture Z-scan measurement of the NPs have been obtained and fitted with Eq. 6. No trustworthy non-linear signal was obtained in the WO_3 nano colloid according to the measurements made with the Z-scan. For ZnO and W-ZnO NPs, we have the peak-valley distortion according to Figure 7, which indicates the non-linear refractive index n_2 is negative, as is shown in Table 1. As we know, the negative n_2 is a result of the thermal lensing effect because, at low laser intensities, non-linearity rather is not related to the electronic transition of energy levels, or at least it can be concluded that the origin of non-linear optical properties is expressed electronically with a very small percentage. In the thermal lensing effect, if we increase the light intensity, it causes the material gets hotter, and we will have a local expansion at the point of light irradiation, so the material will be diluted and the refractive index will decrease (negative in Eq. 1) (Koushki and Majles Ara, 2014). Therefore, the greater the absorption of the material, the more the expansion of the sample, that is, they are directly related to each other. We expect a high refraction change at the wavelength of 532.8 nm because of high absorption in this wavelength (Figure 5). As shown in table 1, there is a direct relation between the non-linear refractive index n_2 and the absorption coefficient.

Figure 8 shows open aperture curves for the synthesized NPs that are plotted with numerical curves (Eq. 7), and non-linear absorption coefficients (β) were reported in Table 1 which are negative, and indicate saturation in absorption (SA) is the origin of non-linear absorption. In SA, photons absorbed by NPs enhance the relative population of NPs in exited states and therefore, absorption of new photons experience a decrease, and transmitted power from the particles increases (Purohit, 2020). SA has many applications in the light modulation and laser mode locking. Saturation intensity can be approximately obtained by $I_s \approx -\alpha/\beta$ (Sharma et al., 2012; Koushki et al., 2014b), as reported in table 1. Decreasing the saturation intensity for W-ZnO can be related to decreasing the band gap. The smaller the bandgap, the less the probability of electrons staying at a high level, and the creation of population inversion and saturation in absorption will be reduced.

It should be considered that optical non-linearity of metal base nanocolloids and nanocomposites are highly sensitive on the environmental factors around the NPs, and one should not expect completely stable non-linear behavior with the change of these factors. Changes in beam intensity, wavelength, surface agents and dopants can all change the non-linear optical behavior of metal base nanocomposites. The effects of dopants on the change in size of NPs, lattice structure and energy gap and consequently the non-linear optical properties have been proven (Babeela et al., 2019). Also, the effects of surface agents on defect states and morphology can change the amount and even the mechanism type of non-linear response (Sabari Girisun et al., 2018; Monisha et al., 2020). Non-linear optical responses can be tunable and varies with change of beam wavelengths. For example, two photons absorption can be replaced with SA in different wavelengths (Sabari Girisun et al., 2018; Hegde et al., 2019). This response for metal NPs is not only a defect but they can be effective in tunable optical designs such as broadband ultrafast optical limiters.

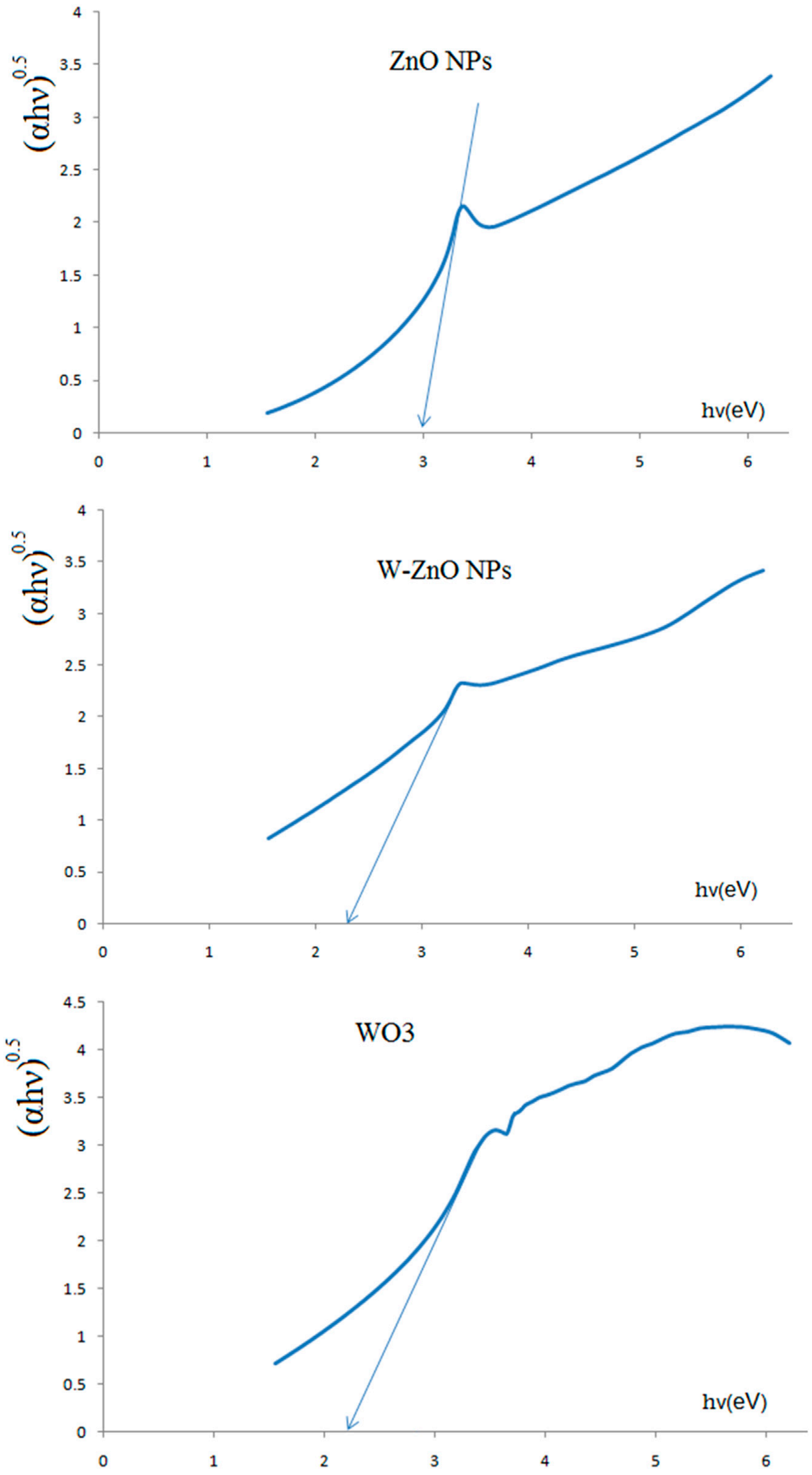

FIGURE 6
Tauc plots of ZnO, WO_3 and W-ZnO.

TABLE 1 Optical coefficients of synthesized NPs, measured using a CW Nd-Yag (green) laser.

Component	α(1/cm) at 532nm	n_2 (cm^2/W)	β (cm/W)	Is (W/cm2)	Band gap energy (eV)
ZnO NPs	0.6	-7.5×10^{-8}	-1.71×10^{-3}	350	3.04
WO3 NPs	0.9	-1.5×10^{-9}	—	—	2.2
W-ZnO NPs	0.9	-9.3×10^{-8}	-1.46×10^{-3}	610	2.3

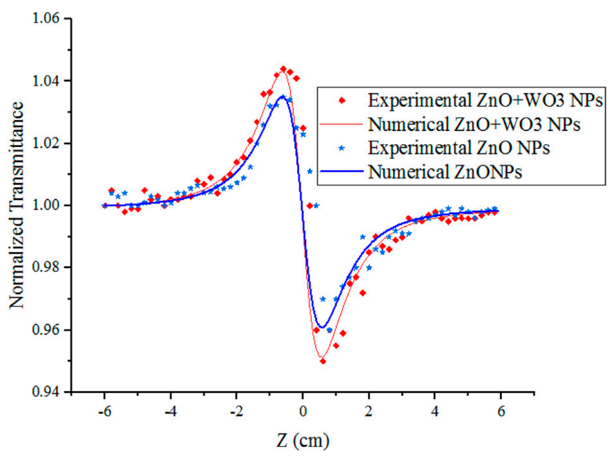

FIGURE 7
Curves of NPs in close aperture experiment.

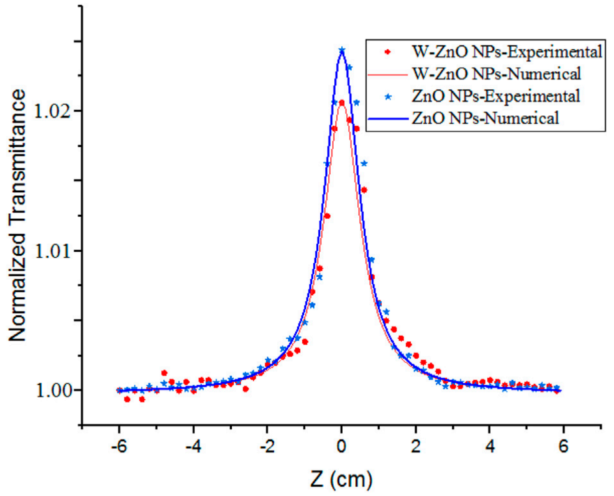

FIGURE 8
Open aperture curves of ZnO and ZnO-WO_3NPs.

6 Conclusion

In summary, the nanocomposite of zinc tungsten oxide (W-ZnO NPs) was synthesized and characterized using measurement methods such as XRD, DLS, SEM and UV-Vis. Also, the results were compared with pure synthesized ZnO and WO_3 NPs. Non-linear optical properties of the synthesized composite were measured using the Z-scan technique with a continuous wave 5 mW Nd-Yag laser beam. A negative non-linear absorption coefficient of the components was obtained, and it shows that saturation absorption occurred in this composite. In comparison with pure ZnO NPs, non-linear absorption decreases that can be attributed to the negligible optical response of WO_3 structures. Also, the negative value of the close aperture Z-scan curve shows that the thermal lensing effect is the main reason for the third-order non-linear refraction.

Data availability statement

The raw data supporting the conclusion of this article will be made available by the authors, without undue reservation.

Author contributions

All authors listed have made a substantial, direct, and intellectual contribution to the work and approved it for publication.

Funding

This research was supported by the Research Council of the University of Mazandaran and the hakim Sabzevari University, Iran.

Acknowledgments

The authors would like to thank the peer reviewers of this paper who improved it with their comments.

Conflict of interest

The authors declare that the research was conducted in the absence of any commercial or financial relationships that could be construed as a potential conflict of interest.

Publisher's note

References

Abbasi, F., Koushki, E., Majles Ara, M. H., and Sahraei, R. (2017). Optical dispersion, permittivity spectrum and thermal-lensing effect in nickel-doped zinc sulfide nanoparticles. *J. Electron. Mater.* 46, 6473–6479. doi:10.1007/s11664-017-5678-3

Akherat Doost, H., Majles Ara, M. H., Ghasedi, A., and Koushki, E. (2021). Effects of gold and silver nanoparticles on optical bistabilityof titanium dioxide nanocolloid. *Phys. Solid State.* 63, 318–323. doi:10.1134/S1063783421020062

Arshad, M., Ehtisham-ul-Haque, S., Bilal, M., Ahmad, N., Ahmad, A., Abbas, M., et al. (2020). A ghaffar and M iqbal, synthesis and characterization of Zn doped WO_3 nanoparticles: Photocatalytic, antifungal and antibacterial activities evaluation. *Mater. Res. Express.* 7, 015407. doi:10.1088/2053-1591/ab6380

Arun, K. J., Batra, A. K., Krishna, A., Bhat, K., Aggarwal, M. D., and Joseph Francis, P. J. (2015). Surfactant free hydrothermal synthesis of copper oxide nanoparticles. *Am. J. Mater. Sci.* 5 (3A), 36–38. doi:10.5923/s.materials.201502.06

Ashfaq, M. H., Shahid, S., Javed, M., Iqbal, S., Hakami, O., Aljazzar, S. O., et al. (2022). Controlled growth of TiO_2/Zeolite nanocomposites for simultaneous removal of ammonium and phosphate ions to prevent eutrophication. *Front. Mater.* 9, 1007485. doi:10.3389/fmats.2022.1007485

Babeela, C., Narendran, N. K. S., Pannipara, M., Al-Sehemi, A. G., and Sabari Girison, T. C. (2019). Excited state absorption assisted optical limiting action of Fe decorated γ-BBO nanorods. *Mater. Chem. Phys.* 237, 121827. doi:10.1016/j.matchemphys.2019.121827

Baedi, J., Ghasedi, A., Koushki, E., and Akrami, B. (2021). Nonlinear response of sodium and potassium doped ZnO along with improvement in bandgap structure: A combined physicochemical study. *Phys. B Condens. Matter* 620, 413279. doi:10.1016/j.physb.2021.413279

Baishya, K., Ray, J. S., Dutta, P., and Das, S. K. (2018). Graphene-mediated band gap engineering of WO_3 nanoparticle and a relook at Tauc equation for band gap evaluation. *Appl. Phys. A* 124 (10), 704–706. doi:10.1007/s00339-018-2097-0

Cao, J., Wang, Y., Ma, T., Liu, Y., and Yuan, Z. (2011). Synthesis of porous hematite nanorods loaded with CuO nanocrystals as catalysts for CO oxidation. *J. Nat. Gas. Chem.* 20 (6), 669–676. doi:10.1016/S1003-9953(10)60238-1

Chen, R., Jalili, Z., and Tayebee, R. (2021). UV-visible light-induced photochemical synthesis of benzimidazoles by coomassie brilliant blue coated on W–ZnO@NH_2 nanoparticles. *RSC Adv.* 11 (27), 16359–16375. doi:10.1039/D0RA10843J

Gao, P. X., Ding, Y., Mai, W., Hughes, W. L., Lao, C. S., and Wang, Z. L. (2005). Conversion of zinc oxide nanobelts into superlattice-structured nanohelices. *Science* 309, 1700–1704. doi:10.1126/science.1116495

Ghorbani, H. R., Parsa Mehr, F., Pazoki, H., and Mosavar Rahmani, B. (2015). Synthesis of ZnO nanoparticles by precipitation method. *Orient. J. Chem.* 31 (2), 1219–1221. doi:10.13005/ojc/310281

Hariharan, V., Gnanavel, B., Sathiyapriya, R., and Aroulmoji, V. (2019). A review on tungsten oxide (WO_3) and their derivatives for sensor applications. *Int. J. Adv. Sci. Eng.* 5 (4), 1163–1168. doi:10.29294/IJASE.5.4.2019.1163-1168

Hassani, H., Marzbanrad, E., Zamani, C., and Raissi, B. (2011). Effect of hydrothermal duration on synthesis of WO_3 nanorods. *J. Mater. Sci. Mater. Electron.* 22 (9), 1264–1268. doi:10.1007/s10854-011-0297-x

Hegde, T. A., Dutta, A., Sabari Girisun, T. C., Abith, M., and Vinitha, G. (2019). Intensity tunable optical limiting behavior of an organometallic cesium hydrogen tartrate single crystal. *J. Mater. Sci. Mater. Electron.* 30, 18885–18896. doi:10.1007/s10854-019-02245-5

Koushki, E., Baedi, J., and Tasbandi, A. (2019). Sodium doping effect on optical permittivity, band gap structure, nonlinearity and piezoelectric properties of PZT nano-colloids and nanostructures. *J. Electron Mater* 48 (2), 1066–1073. doi:10.1007/s11664-018-6834-0

Koushki, E. (2021). Effect of conjugation with organic molecules on the surface plasmon resonance of gold nanoparticles and application in optical biosensing. *RSC Adv.* 11 (38), 23390–23399. doi:10.1039/D1RA01842F

Koushki, E., Farzaneh, A., and Majles Ara, M. H. (2014a). Modeling absorption spectrum and saturation intensity of ZnO nano-colloid. *Optik* 125, 220–223. doi:10.1016/j.ijleo.2013.06.007

Koushki, E., Majles Ara, M. H., and Akherat Doost, H. (2014b). Z-scan technique for saturable absorption using diffraction method in γ-alumina nanoparticles. *Appl. Phys. B* 115 (2), 279–284. doi:10.1007/s00340-013-5602-3

Koushki, E., and Majles Ara, M. H. (2011). Comparison of the Gaussian-decomposition and the Fresnel–Kirchhoff diffraction methods in circular and elliptic Gaussian beams. *Opt. Commun.* 284, 5488–5494. doi:10.1016/j.optcom.2011.08.028

Koushki, E., and Majles Ara, M. H. (2014). Modeling electrical and optical spectral responses of homogeneous nanocomposites. *Phys. E Amst. Neth.)* 61, 111–117. doi:10.1016/j.physe.2014.03.021

Liu, H., Li, M., Wei, Y., Liu, Z., Hu, Y., and Ma, H. (2014). A facile surfactant-free synthesis of flower-like ZnO hierarchical structure at room temperature. *Mater. Lett.* 137, 300–303. doi:10.1016/j.matlet.2014.09.023

Maduraiveeran, G., Sasidharan, M., and Jin, W. (2019). Earth-abundant transition metal and metal oxide nanomaterials: Synthesis and electrochemical applications. *Prog. Mater. Sci.* 106, 100574. doi:10.1016/j.pmatsci.2019.100574

Monisha, M., Priyadarshani, N., Durairaj, M., and Sabari Girisun, T. C. (2020). 2PA induced optical limiting behaviour of metal (Ni, Cu, Zn) niobate decorated reduced graphene oxide. *Opt. Mater.* 101, 109775. doi:10.1016/j.optmat.2020.109775

Nakahara, K., Takasu, H., Fons, P., Yamada, A., Matsubara, K., Hunger, R., et al. (2001). Interactions between gallium and nitrogen dopants in ZnO films grown by radical-source molecular-beam epitaxy. *Appl. Phys. Lett.* 79, 4139–4141. doi:10.1063/1.1424066

Naseem, T., and Durrani, T. (2021). The role of some important metal oxide nanoparticles for wastewater and antibacterial applications: A review. *Environ. Chem. Ecotoxicol.* 3, 59–75. doi:10.1016/j.enceco.2020.12.001

Purohit, G. (2020). *Overview of lasers*. India: NISCAIR-CSIR.

Ramar, V., and Balasubramanian, K. (2018). Charge transfer induced tunable bandgap and enhanced saturable absorption behavior in rGO/WO_3 composites. *Appl. Phys. A* 124 (11), 779–811. doi:10.1007/s00339-018-2191-3

Sabari Girisun, T. C., Saravanan, M., and Venugopal Rao, S. (2018). Enhanced broadband optical limiting and switching of nonlinear absorption in functionalized solar exfoliated reduced graphene oxide–Ag-Fe_2O_3 nanocomposites. *J. Appl. Phys.* 124, 193101. doi:10.1063/1.5050478

Sharma, D., Gaur, P., Pal Malik, B., Singh, N., and Gaur, A. (2012). Intensity dependent nonlinear absorption in direct and indirect band gap crystals under nano and picosecond Z-scan. *Opt. Photonics J.* 2 (2), 98–104. doi:10.4236/opj.2012.22013

Sheik-Bahae, M., Said, A. A., Wei, T. H., Hagan, D. J., and Van Stryland, E. W. (1990). Sensitive measurement of optical nonlinearities using a single beam. *IEEE J. Quantum Electron.* 26 (4), 760–769. doi:10.1109/3.53394

Silva, N., Ramírez, S., Díaz, I., Garcia, A., and Hassan, N. (2019). Easy, quick, and reproducible sonochemical synthesis of CuO nanoparticles. *Materials* 12 (5), 804. doi:10.3390/ma12050804

Srivastava, V., Gusain, D., Sharma, Y. C., Hao, Y., Liu, X., Li, M., et al. (2013). Simple preparation of WO3–ZnO composites with UV–Vis photocatalytic activity and energy storage ability. *Ceram. Int.* 40, 12519–12524. doi:10.1016/j.ceramint.2014.04.106

Suzaki, Y., and Tachibana, A. (1975). Measurement of the μm sized radius of Gaussian laser beam using the scanning knife-edge. *Appl. Opt.* 14, 2809–2810. doi:10.1364/AO.14.002809

Tsigaridas, G., Fakis, M., Polyzos, I., Persephonis, P., and Giannetas, V. (2003). Z-scan analysis for high order nonlinearities through Gaussian decomposition. *Opt. Commun.* 225, 253–268. doi:10.1016/j.optcom.2003.08.025

Velmurugan, R., and Incharoensakdi, A. (2018). Nanoparticles and organic matter. *Nanoparticles Org. Matter* 1, 407–428. doi:10.1016/B978-0-12-811487-2.00018-9

Widenkvist, E., Quinlan, R. A., Holloway, B. C., Grennberg, H., and Jansson, U. (2008). Synthesis of nanostructured tungsten oxide thin films. *Cryst. Growth Des.* 8, 3750–3753. doi:10.1021/cg800383c

frontiers | Frontiers in Chemistry

TYPE Original Research
PUBLISHED 23 June 2023
DOI 10.3389/fchem.2023.1207984

Polymer-coated hexagonal upconverting nanoparticles: chemical stability and cytotoxicity

Vitalii Patsula[1], Dana Mareková[2,3], Pavla Jendelová[2,3], Mykhailo Nahorniak[1], Oleksandr Shapoval[1], Petr Matouš[4], Viktoriia Oleksa[1], Rafał Konefał[1], Magda Vosmanská[5], Lucia Machová-Urdziková[2] and Daniel Horák[1]*

[1]Institute of Macromolecular Chemistry, Czech Academy of Sciences, Prague, Czechia, [2]Institute of Experimental Medicine, Czech Academy of Sciences, Prague, Czechia, [3]Department of Neurosciences, Second Faculty of Medicine, Charles University, Prague, Czechia, [4]Center for Advanced Preclinical Imaging, First Faculty of Medicine, Charles University, Prague, Czechia, [5]Department of Analytical Chemistry, University of Chemistry and Technology Prague, Prague, Czechia

OPEN ACCESS

EDITED BY
Borislav Angelov,
Institute of Physics (ASCR), Czechia

REVIEWED BY
Emma Martín Rodríguez,
Autonomous University of Madrid, Spain
Bartosz Krajnik,
Wrocław University of Technology,
Poland

*CORRESPONDENCE
Daniel Horák,
horak@imc.cas.cz

RECEIVED 18 April 2023
ACCEPTED 15 June 2023
PUBLISHED 23 June 2023

CITATION
Patsula V, Mareková D, Jendelová P, Nahorniak M, Shapoval O, Matouš P, Oleksa V, Konefał R, Vosmanská M, Machová-Urdziková L and Horák D (2023), Polymer-coated hexagonal upconverting nanoparticles: chemical stability and cytotoxicity. *Front. Chem.* 11:1207984. doi: 10.3389/fchem.2023.1207984

Large (120 nm) hexagonal $NaYF_4$:Yb, Er nanoparticles (UCNPs) were synthesized by high-temperature coprecipitation method and coated with poly(ethylene glycol)-alendronate (PEG-Ale), poly (*N*,*N*-dimethylacrylamide-*co*-2-aminoethylacrylamide)-alendronate (PDMA-Ale) or poly(methyl vinyl ether-*co*-maleic acid) (PMVEMA). The colloidal stability of polymer-coated UCNPs in water, PBS and DMEM medium was investigated by dynamic light scattering; UCNP@PMVEMA particles showed the best stability in PBS. Dissolution of the particles in water, PBS, DMEM and artificial lysosomal fluid (ALF) determined by potentiometric measurements showed that all particles were relatively chemically stable in DMEM. The UCNP@Ale-PEG and UCNP@Ale-PDMA particles were the least soluble in water and ALF, while the UCNP@PMVEMA particles were the most chemically stable in PBS. Green fluorescence of FITC-Ale-modified UCNPs was observed inside the cells, demonstrating successful internalization of particles into cells. The highest uptake was observed for neat UCNPs, followed by UCNP@Ale-PDMA and UCNP@PMVEMA. Viability of C6 cells and rat mesenchymal stem cells (rMSCs) growing in the presence of UCNPs was monitored by Alamar Blue assay. Culturing with UCNPs for 24 h did not affect cell viability. Prolonged incubation with particles for 72 h reduced cell viability to 40%–85% depending on the type of coating and nanoparticle concentration. The greatest decrease in cell viability was observed in cells cultured with neat UCNPs and UCNP@PMVEMA particles. Thanks to high upconversion luminescence, high cellular uptake and low toxicity, PDMA-coated hexagonal UCNPs may find future applications in cancer therapy.

KEYWORDS

luminescence, upconversion, nanoparticles, lanthanides, dissolution, cell viability, uptake

1 Introduction

Upconverting nanoparticles (UCNPs) have attracted much attention already since 1966, when the general principles of photon upconversion were first discovered (Auzel, 2004). Currently, luminescent lanthanide-doped upconverting nanoparticles (UCNPs) are widely used in medicine for biological imaging and diagnosis of serious diseases (Li et al., 2020). UCNPs have the advantage that they can be excited by relatively long wavelengths, namely, near-infrared (NIR) light, typically in the 700–1,000 nm spectral range, which penetrates deep into tissues and converts low-energy NIR photons into high-energy UV-visible light (Hamblin, 2018; Wen et al., 2018). UCNPs typically consist of $NaYF_4$ as a host matrix, which is usually co-doped with a sensitizer (Yb^{3+} or Nd^{3+}) and an activator (Er^{3+}, Tm^{3+} or Ho^{3+}) (Ye et al., 2015). $NaYF_4$ can exist under normal pressure in two polymorphic phases, cubic and hexagonal, the latter showing an order of magnitude higher upconversion efficiency than the former (Park et al., 2013). The crystallinity of UCNPs, and thus the lattice structure, is also affected by size, resulting in a change in luminescent properties (Sun et al., 2014). A strong dependence on the size of upconversion $NaYF_4$:Yb^{3+},Er^{3+} nanocrystals was observed; the larger the particles, the higher the emission (Schietinger et al., 2009), which also affects the synthesis strategy of UCNPs. Methods developed for the preparation of hexagonal-phase UCNPs with uniform size (Wang et al., 2012), which is advantageous for biomedical applications, include thermal decomposition (Xie et al., 2013), hydrothermal/solvothermal synthesis with phase transfer (Wang et al., 2009), microemulsion (Shan et al., 2011), sol-gel processing (Yao et al., 2016) and microwave synthesis (Egatz-Gomez et al., 2022).

Despite the many undeniable advantages of UCNPs, such as large anti-Stokes shift, narrow emission bandwidth, no photobleaching, no blinking, deep detection ability, and low damage to biological tissues, these particles also have some pitfalls. For example, they have relatively low quantum yields that need to be increased for future applications in PDT, bioimaging, sensing, theranostics and optogenetics (Jones et al., 2021). In contrast to bulk materials, higher photoluminescence efficiency of UCNPs can be achieved, for example, by better selection of the host lattice (Fischer et al., 2014), combination and appropriate concentration of rare earth dopants (Kaiser et al., 2017), improvement of nanoparticle crystallinity (Zhou et al., 2015), or introduction of core-shell structures (Fischer et al., 2016) to suppress the surface quenching characteristic of lanthanide nanoparticles (Wang et al., 2010); plasmonic and photonic structures (Park et al., 2015) and dye sensitizers can also be used (Wisser et al., 2018). In addition, UCNPs used in a living organism must be biocompatible, hydrophilic, dispersible in biological media, poorly soluble and, last but not least, chemically and colloidally stable (Liang et al., 2020). Initially, UCNPs were thought to be chemically inert, but recently an increasing number of studies have demonstrated their dissolution in aqueous media at high dilution (Abdul Jalil and Zhang, 2008), leading to the release of F^- and Ln^{3+} ions (Barbier et al., 2010; Lisjak et al., 2016; Plohl et al., 2017). This highlights the need for more detailed studies addressing the chemical stability and toxicity of UCNPs (Oliveira et al., 2019). In particular, the effect of particles size on their dissolution is only reported for UCNPs <50 nm in diameter and data on the degradation of larger UCNPs are lacking. The dissolution of large UCNPs (>100 nm) can be expected to be lower compared to small particles (<50 nm), which are characterized by a larger surface-to-volume ratio than large particles. As a result, the upconversion fluorescence intensity of the latter particles can be maintained for longer periods of time, which significantly affects their use in biomedical applications. To the best of our knowledge, so far, only a minimum of works has dealt with monodisperse UCNPs of 100–200 nm in size, except for hollow microtubes, rods and peanut-shaped particles. It can be assumed that they will dissolve mainly in the cell and their dissolution will then depend on their cellular uptake and on the surface-to-volume ratio, which will be different for various particle morphologies. In view of the above facts, subsequent surface protection of UCNPs against aggregation, precipitation or dissolution is necessary, consisting of their treatment with hydrophilic polymers, chelating agents, bioconjugations, hybrid materials, etc. (Boyer et al., 2006; Li et al., 2015). Examples of polymers that provide colloidal stability of UCNPs are poly (ethylene glycol) (PEG) (Pichaandi et al., 2011), silica (Johnson et al., 2010), polyvinylpyrrolidone (MacKenzie et al., 2022), poly (acrylic acid) (Jin et al., 2011), polyethyleneimine (Shao et al., 2018), etc. The conjugation of specific biomolecules such as antibodies (Ramírez-García et al., 2018), nucleic acids (Mao et al., 2017) or proteins (Kamimura et al., 2008) required for a given bioanalytical application is facilitated by functional, often hydroxyl, carboxyl or amino groups of the polymers (Mi et al., 2010; Wilhelm et al., 2015). The surface coating influences the physicochemical properties of nanoparticles, especially their chemical and colloidal stability, interactions with biological systems, and ultimately affects their cellular uptake and toxicity. The coating can reduce cell viability by facilitating cellular uptake by changing the ξ-potential or improving colloidal stability; in contrast, if uncoated particles aggregate, they are less likely to enter cells. If surface coatings are not firmly bound to particles, they may be released into body fluids during application, increasing toxicity.

The aim of this work was to prepare highly sensitive multicolor fluorescent nanoparticles combining upconversion luminescence and fluorescence imaging using fluorescein-5-isothiocyanate (FITC) to follow particle uptake during cell culture. The combination of two luminescent agents with excitation and emission in the visible to NIR region makes these particles an ideal contrast for *in vitro* and *in vivo* visualization of various biological processes. Multicolor particles were prepared by attaching FITC to neat and poly(ethylene glycol)-alendronate (PEG-Ale)-, poly (*N*,*N*-dimethylacrylamide-*co*-2-aminoethylacrylamide)-alendronate (PDMA-Ale)- and/or poly (methyl vinyl ether-*co*-maleic acid) (PMVEMA)-modified hexagonal-phase $NaYF_4$:Yb^{3+},Er^{3+} UCNPs that were larger than 100 nm in size. The stability of these nanomaterials was studied under various conditions in aqueous media like water, 0.01 M phosphate buffered saline (PBS; pH 7.4), Dulbecco's modified Eagle's medium (DMEM) or artificial lysosomal fluid (ALF). The concentrations of released F^- and Y^{3+} ions were determined by combined fluoride electrode, UV-Vis spectroscopy and inductively coupled plasma mass spectrometry (ICP-MS). Internalization of UCNPs into rMSCs or C6 cells was monitored using a multiphoton laser scanning microscope, epifluorescent microscopy and cytotoxicity was tested using the Alamar Blue.

2 Experimental

2.1 Materials

Octadec-1-ene (OD; 90%), NH_4F (99.99%), anhydrous YCl_3 and $YbCl_3$ (99%), $ErCl_3{\cdot}6\ H_2O$ (99%), *N*,*N*-dimethylacrylamide

(DMA; 99%), fluorescein isothiocyanate (FITC), and phosphate buffered saline (PBS) were purchased from Sigma-Aldrich (St Louis, MO, United States). Sodium trihydrate of (4-amino-1-hydroxy-1-phosphonobutyl)phosphonic acid (alendronate; Ale) was obtained from TCI (Tokyo, Japan). Poly (methyl vinyl ether-*co*-maleic acid) (PMVEMA; M_w = 60,000 g/mol) was obtained from Scientific Polymer Products (Ontario, NY, United States). Oleic acid (OA; 98%), methanol (99.5%), hexane (99.5%), dichloromethane (99.9%), and paraformaldehyde were from Lach-Ner (Neratovice, Czech Republic). Ale-modified PEG (PEG-Ale) and poly (*N*,*N*-dimethylacrylamide-*co*-2-aminoethylacrylamide)-alendronate (PDMA-Ale) were prepared as described in literature (Kostiv et al., 2017; Oleksa et al., 2020; Nahorniak et al., 2023). Dulbecco's modified Eagle's medium (DMEM), Alamar Blue assay and 4′,6-diamidino-2-phenylindole (DAPI) were purchased from Thermo Fischer Scientific (Waltham, MA, United States). Fetal bovine serum (FBS) was from Merck (Darmstadt, Germany) and primocin and penicillin streptomycin were from Gibco, Life Technologies (Grand Island, NY, United States). Artificial lysosomal fluid (ALF, pH 4.5) was prepared as previously reported (Colombo et al., 2008). Suprapur® nitric acid was purchased from Merck (Kenilworth, NJ, United States). Mesenchymal stromal cells (rMSCs) were isolated from rat bone marrow according to the previous report (Nahorniak et al., 2023). C6 cells were kindly provided by Dr. Čestmír Altaner from the Cancer Research Institute SAS (Bratislava, Slovakia). All other reagent grade chemicals were purchased from Sigma-Aldrich and used as received. Polyethersufone filter (MWCO 30 kg/mol) was obtained from VWR (Radnor, PA, United States). Ultrapure water (conductivity ˂0.1 μS/cm) was obtained on a Milli-Q Gradient A10 purification system (Millipore; Molsheim, France) and used throughout the experimental work.

2.2 Synthesis of hexagonal NaYF$_4$:Yb^{3+},Er^{3+} nanoparticles (UCNPs)

UCNPs with hexagonal-phase were prepared by high-temperature coprecipitation method. To a solution of OA (6 mL) in OD (15 mL), YCl_3 (0.78 mmol), $YbCl_3$, (0.2 mmol) and $ErCl_3 \cdot 6\ H_2O$ (0.02 mmol) were added under magnetic stirring. The reaction mixture was heated to 160°C under vacuum (2.1 kPa) and maintained at this temperature for 30 min. The solution was then cooled to room temperature (RT) under Ar atmosphere and a solution of NH_4F (148 mg; 4 mmol) and NaOH (100 mg; 2.5 mmol) in methanol (8 mL) was added. To evaporate the methanol, the reactor pressure was slowly reduced to 2.1 kPa while stirring and the mixture was heated to 65°C. The reaction temperature was then slowly raised to 120°C and maintained at this value for 30 min to evaporate the residual water. Finally, the mixture was heated at 300°C for 1.5 h under Ar atmosphere and cooled to RT. The UCNPs were separated by centrifugation (3,460 rcf) for 1 h, washed twice with a hexane/ethanol (1:1 v/v) mixture, three times with ethanol, twice with ethanol/water (1:1 v/v), and twelve times with water (14 mL each), and redispersed in water.

2.3 Surface modification of hexagonal UCNPs with PEG-Ale, P(DMA-AEA)-Ale, and PMVEMA

Modification of UCNPs with polymers was performed according to a previously published procedure (Nahorniak et al., 2023). Briefly, a dispersion of UCNPs (30 mg) in water (1.64 mL) was added dropwise to an aqueous solution (2 mL) of PEG-Ale (M_w = 5,000 g/mol) or PDMA-Ale (15 mg; M_w = 11,000 g/mol) under sonication (Ultrasonic Homogenizer UP200S Hielscher; 20% power) for 1 min. The mixture was magnetically stirred at RT for 24 h. The resulting polymer-coated UCNPs denoted as UCNP@Ale-PEG and UCNP@Ale-PDMA were sedimented by centrifugation and washed twice with water (1.5 mL) followed by centrifugation (14,100 rcf).

UCNP@PMVEMA nanoparticles were prepared by adding aqueous dispersion of UCNPs (15 mg; 1 mL) to aqueous PMVEMA solution (50 mg/mL; 15 mL; pH 7.4 adjusted by adding 2 M NaOH) with shaking at RT for 30 min and further stirring at 70°C for 16 h. Nanoparticles were sedimented by centrifugation (14,100 rcf) and washed with water three times.

2.4 Synthesis of FITC-alendronate and modification of hexagonal UCNPs

For the preparation of FITC-alendronate (FITC-Ale), FITC (105 mg) was dissolved in dimethyl sulfoxide (1 mL), a solution of Ale (70 mg) in 0.2 M sodium carbonate-bicarbonate buffer (3 mL; pH 10.4) was added, and the mixture was stirred at RT for 72 h in the dark. Then, the resulting FITC-alendronate (FITC-Ale) was purified by gel filtration on a Sephadex G-25 column with water as eluent and the solution was passed through a column filled with sulfonated polystyrene to replace Na^+ with H^+ ions in the phosphonate groups of FITC-Ale. Finally, water was removed at 40°C on a vacuum rotary evaporator. The structure of FITC-Ale was confirmed by ^{1}H NMR (SI Supporting Information, Supplementary Figure S1); the purity was 52% and the yield was 29 mg.

In the next step, neat UCNPs or UCNPs coated with PEG-Ale and PDMA-Ale were functionalized with FITC-Ale. An aqueous solution of FITC-Ale (0.05 mg; 0.5 mL) was added to an aqueous dispersion (3.64 mL) of particles (30 mg) and the mixture was stirred at RT for 21 h in the dark. In the case of UCNP@PMVEMA particles, an aqueous solution of FITC-Ale (0.5 mg; 0.225 mL) was added 30 min after the addition of the PMVEMA solution to the neat UCNPs under the same conditions as described above. The resulting FITC-modified particles were separated by centrifugation and washed twice with water (1.5 mL) followed by centrifugation (14,100 rcf).

2.5 Dissolution of hexagonal UCNPs

Dispersion of UCNPs in water, 0.01 M PBS (pH 7.4), DMEM or ALF (1 mg/mL) was placed in a plastic vial sealed with a rubber septum and allowed to age at 25 or 37°C for a period of time with agitation (250 rpm). Subsequently, the dispersion was centrifuged

(14,129 rcf) for 30 min to separate UCNPs and the supernatant was filtered (MWCO 30 kg/mol) to remove residual particles. A combined fluoride electrode (Thermo Fisher Scientific; Waltham, MA, United States) was used to measure the dissolution of UCNPs expressed as the concentration of released F^- ions in the medium according to the manufacturer's instructions. The molar fraction of F^- ions was expressed as the mean ± standard error of the mean ($n = 3$).

The concentration of Y^{3+}, Yb^{3+} and Er^{3+} ions leached from neat and polymer-coated UCNPs was determined spectrophotometrically according to our previous publication (Nahorniak et al., 2023). Briefly, supernatants from particle dispersions were separated via centrifugation (14,010 rcf) for 30 min and mixed with xylenol orange buffer solution (2 mL; pH 5.8). The concentration of free Y^{3+}, Yb^{3+} and Er^{3+} released from the UCNPs was measured by UV-Vis spectroscopy at 350–650 nm from the ratio of absorbance at 570 and 443 nm. The calibration curve was obtained as the dependence of the integrated intensity ratios of absorption bands from 18 μM xylenol orange in acetate buffer (pH 5.8) at different concentrations of YCl_3 (0–70 μM Y^{3+}).

2.6 Inductively coupled plasma mass spectrometry (ICP-MS)

ICP-MS measurements were performed on a PerkinElmer NexION 350D ICP-MS instrument (Woodbridge, Canada) equipped with Universal Cell Technology™. The sample system consisted of an internal peristaltic pump with Tygon® tubing (0.38 mm inner diameter), a polytetrafluoroethylene concentric nebulizer and a 100-mL glass cyclone spray chamber.

After 24 h incubation with all tested UCNPs at a concentration of 20 μg/mL, rMSCs or C6 cells were treated with concentrated nitric acid (3 mL) and the mixture was placed in a Teflon digestion vessel (Speedwave 4; Berghof, Germany). After dilution, digested sample was spiked with internal standard solution (^{100}Rh) and placed in a 50-mL volumetric flask. Calibration solution and internal standard solution were prepared from a starting concentration of 1.000 ± 0.002 g/L (Merck, Darmstadt, Germany).

2.7 Determination of cytotoxicity

The cell cultures were prepared as previously reported (Nahorniak et al., 2023) and the cytotoxicity of all prepared UCNPs was determined by Alamar Blue assay. Briefly, rMSCs and C6 cell line were incubated with UCNPs for 24 h in complete culture medium, after which the medium was aspirated and a 10% Alamar Blue solution in culture medium was added and incubation continued for 3 h. The solution was pipetted into 96-well plates and fluorescence was measured using a FLUOstar Omega reader (BMG LABTECH; Ortenberg, Germany) at an excitation of 530 nm and emission of 590 nm. In the meantime, fresh culture medium was added to the cells and left for another 48 h; fluorescence was measured after 72 h as a percentage of control (readouts of nanoparticle-free cells).

2.8 Microscopy imaging

Cells grown on coverslips were incubated with UCNPs (20 μg/mL) for 24 h, fixed with 4% paraformaldehyde for 20 min, stained with DAPI and mounted. The presence of UCNPs in rMSCs or C6 cells was monitored using an Olympus FV1200 MPE multiphoton laser scanning microscope (Tokyo, Japan). Briefly, cells were fixed with 4% paraformaldehyde in PBS, stained with DAPI and light-field images were taken at 980 nm excitation and 540 nm emission using an infrared pulsed laser with negative chirp for multiphoton excitation. DAPI-stained cells were observed in the blue channel using a 405 nm laser diode and the bright field and the blue channel were superimposed. FITC-modified UCNPs were imaged using a Zeiss fluorescence microscope (Oberkochen, Germany) in a green filter (488 nm).

2.9 Equipment

Micrographs of the synthesized UCNPs were recorded with a Tecnai Spirit G2 transmission electron microscopy (TEM; FEI; Brno, Czech Republic). The TEM was coupled with energy-dispersive X-ray (EDX) detector (Mahwah, NJ, United States). Particles were also characterized using a Thermo Nicolet 870 FTIR spectrometer (Madison, WI, United States) equipped with a liquid nitrogen-cooled mercury cadmium telluride detector using a GoldenGate single reflection diamond ATR system (Specac; Orpington, United Kingdom). Hydrodynamic size, polydispersity (*PD*) and ξ-potential were measured using dynamic light scattering (DLS; ZSU 5700 Zetasizer Ultra Instrument; Malvern Instruments; Malvern, United Kingdom). ^1H NMR spectra were measured on a Bruker Avance III 600 spectrometer (Billerica, MA, United States). Thermogravimetric analysis (TGA) was conducted on a Perkin Elmer TGA 7 analyzer (Norwalk, CT, United States); the particles were heated in air from RT to 650°C at 10°C/min. UV-Vis spectra were recorded on a Specord 250 Plus UV-Vis spectrophotometer (Analytik; Jena, Germany). Emission and excitation spectra were recorded using a FS5 Edinburgh Instruments spectrofluorometer (Livingston, United Kingdom) coupled with UV-Vis Xe lamp and 980 nm CW laser with 2 W output power (MDL-III-980).

3 Results and discussion

3.1 Polymer-coated hexagonal UCNPs

The UCNPs were synthetized by a high temperature coprecipitation method with rigorous removal of volatile solvents, which resulted in the formation of fewer nuclei than in the preparation of small (25 nm) spherical particles (Nahorniak et al., 2023). The TEM image showed that the UCNPs consisted of larger particles transformed into hexagonal plates that had the uniform size with dispersity $Đ$ ~1 (Figure 1A; Table 1). The average diameter of the plates was ~120 nm and their thickness was 68 nm. The hydrodynamic size was 174 nm and the ξ-potential was positive (28 mV; Table 1, Supplementary Figure S2). The presence of Y, Yb

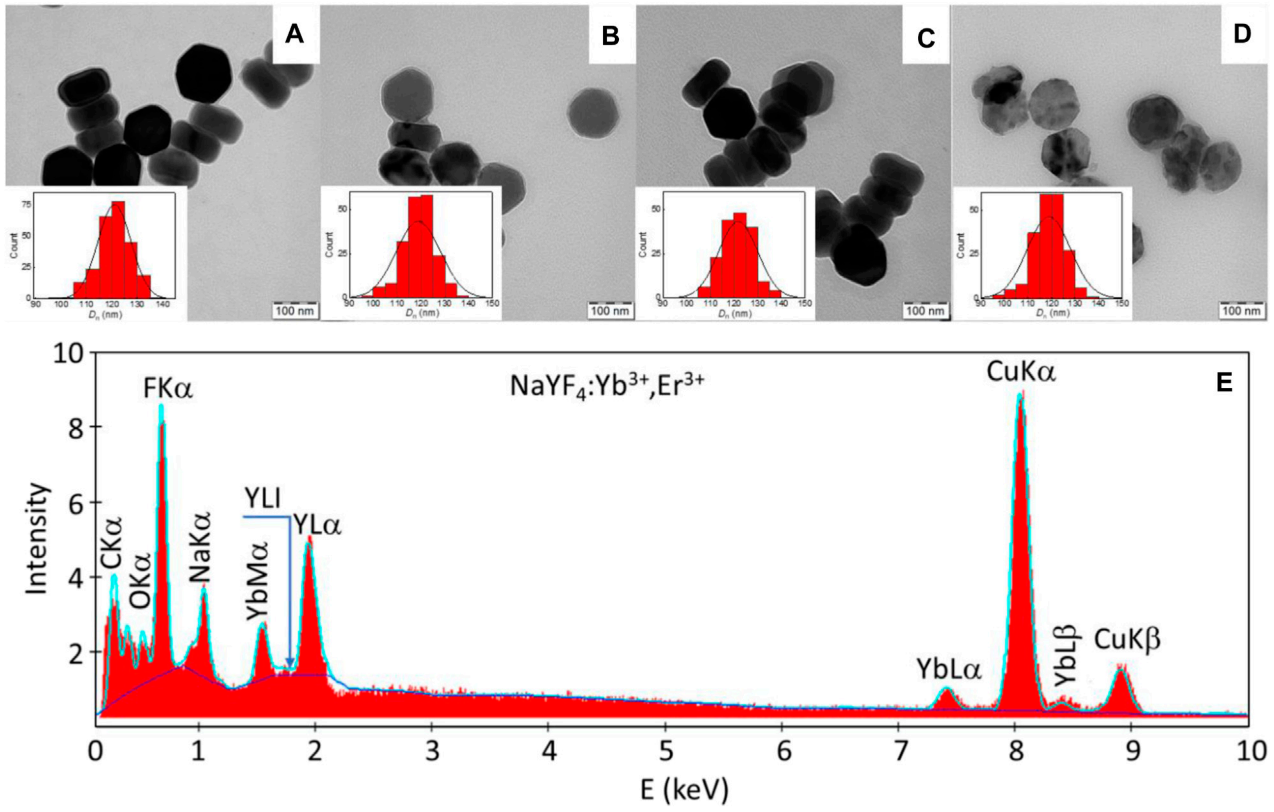

FIGURE 1
(A) TEM micrographs of **(A)** UCNPs, **(B)** UCNP@Ale-PEG, **(C)** UCNP@Ale-PDMA, **(D)** UCNP@PMVEMA and **(E)** TEM/EDX analysis of hexagonal UCNPs.

TABLE 1 Characterization of differently coated UCNPs and their dissolution rates in PBS.

Particles	D_n (nm)	*Đ*	D_h (nm)	*PD*	ζ-potential (mV)	Coating^a (wt%)	Dissolution rate (mol%/h)	
							25°C	37°C
UCNPs	121	1.01	174 ± 1	0.11	28 ± 3	0.2	0.54 ± 0.06	1.3 ± 0.3
UCNP@Ale-PEG	119	1.02	158 ± 3	0.09	4 ± 1	1.5	0.32 ± 0.02	0.8 ± 0.2
UCNP@Ale-PDMA	122	1.01	160 ± 3	0.07	22 ± 2	3.3	0.31 ± 0.01	1.0 ± 0.2
UCNP@PMVEMA	119	1.01	234 ± 7	0.10	−46 ± 6	14.4	0.08 ± 0.01	0.5 ± 0.1

UCNPs, upconverting NaYF$_4$:Yb^{3+}, Er^{3+}. Nanoparticles; PEG-Ale, poly(ethylene glycol)-alendronate; PDMA-Ale, poly(N,N-dimethylacrylamide)-alendronate; PMVEMA, poly (methyl vinyl ether-*co*-maleic acid); D_n, number-average diameter (TEM); *Đ*, dispersity D_w/D_n (TEM); D_h, hydrodynamic diameter (DLS); *PD*, polydispersity (DLS).
[a] According to TGA.

and F in the particles was confirmed by TEM/EDX spectra, which showed large peaks at ~0.68, 1.04 and 1.91 keV corresponding to F, Na and Y atoms, respectively (Figure 1E). Peaks at 0.23 and 8.04 keV were attributed to C and Cu atoms from the supporting TEM grid. The smaller peaks at 1.54, 7.4 and 8.42 keV belonged to Yb atoms, while the signal of Er atoms (~6.9 keV) was not visible due to their low concentration.

To ensure the chemical and colloidal stability of hexagonal UCNPs in aqueous media used in biological experiments, the particles were protected against dissolution by coating with polymers, namely, PEG-Ale, PDMA-Ale and PMVEMA; the hydrodynamic particle size then reached ~160–230 nm and the polydispersity *PD* was ~0.1, characterizing a narrow particle size distribution (Figures 1B-D, Table 1, Supplementary Figure S2A). Compared to UCNP@PMVEMA particles, the correlation functions of UCNP@Ale-PEG and UCNP@Ale-PDMA decayed faster confirming their smaller size (Supplementary Figure S2B). The ξ-potential of UCNP@Ale-PEG, UCNP@Ale-PDMA and UCNP@PMVEMA particles was 4, 22 and −46 mV, respectively, (Table 1, Supplementary Figure S2C). This was due the electroneutrality of PEG and the positive and negative charges of PDMA and PMVEMA, respectively. At the same time, negatively charged

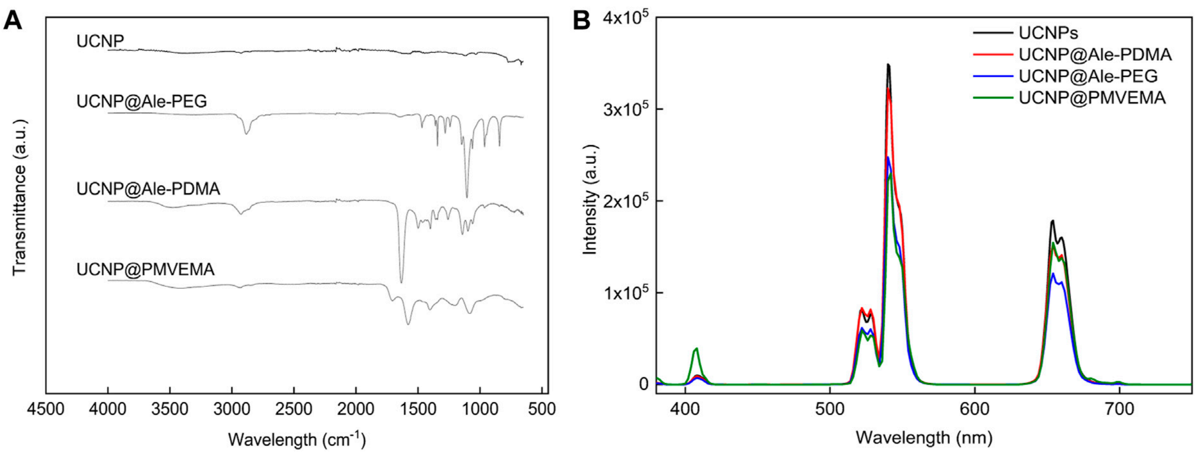

FIGURE 2
(A) ATR FTIR spectra and **(B)** upconversion photoluminescence emission spectra of uncoated and polymer-coated hexagonal UCNPs. The upconversion spectra were measured at concentration of 4 mg of particles/mL of water, excitation at 980 nm and laser power density of 0.25 W/cm^2.

particles are known to have a lower frequency of binding to plasma proteins, i.e., they avoid clearance by the reticuloendothelial system. According to TGA, the amount of PEG, PDMA and PMVEMA coating was ~2, 3 and 14 wt% (Table 1). It should still be noted that PDMA contained a reactive *N*-(2-aminoethyl)acrylamide comonomer suitable for potential attachment of biomolecules. The ATR FTIR spectra of hexagonal UCNPs, UCNP@Ale-PEG, UCNP@Ale-PDMA and UCNP@PMVEMA particles confirmed the presence of polymers on the nanoparticle surface, where the characteristic ν(OH), ν(C-H) symmetric and asymmetric, ν(CH_2) symmetric and C-O stretching vibrations were observed at ~3,450–3,300, 2,927–2,884, 2,850–2,860 and 1,105–1,080 cm^{-1}, respectively (Figure 2A). The spectrum of hexagonal UCNPs@Ale-PDMA exhibited absorption band at 1,633 cm^{-1}, which was attributed to ν(C=O) stretching vibrations of the amide DMA (Oleksa et al., 2020). Then, after modification of the hexagonal UCNPs by PMVEMA, the asymmetric (1,578 cm^{-1}) and symmetric (1,403 cm^{-1}) stretching vibrations of the COOH groups of PMVEMA were found in the spectrum (Ahmad et al., 2020).

3.2 Luminescence of UCNPs

The upconversion luminescence of the neat and polymer-coated hexagonal UCNPs in water was determined under excitation in the near-infrared region at a wavelength of 980 nm (Figure 2B). The characteristic upconversion emission of Er^{3+} was observed, which was attributed to the transitions $^2H_{11/2} \rightarrow {}^2I_{15/2}$ (409 nm), $^4S_{3/2} \rightarrow {}^2I_{15/2}$ (525 nm), $^2H_{9/2} \rightarrow {}^4I_{15/2}$ (542 nm), and $^4F_{9/2} \rightarrow {}^2I_{15/2}$ (656 nm). The upconversion emission spectra of the hexagonal nanoparticles (120 nm in diameter) showed similar peaks and emission intensities to those observed for previously described spherical 25-nm particles (Supplementary Figure S3) (Nahorniak et al., 2023). However, the uncoated large hexagonal UCNPs exhibited ~30 times higher emission intensity at 542 nm than the small spherical UCNPs, making them more attractive and useful for bioassays and biological imaging. Uncoated and PEG-Ale- and PDMA-Ale-coated UCNPs exhibited weaker upconversion emission intensity than UCNP@PMVEMA, independent of the thickness of the PDMA and PEG coating. This demonstrated the quenching effect caused by irregularities in the coating of these particle that allowed direct access of water to the particle surface. The UCNP@PMVEMA particles had the highest upconversion emission intensity due to their largest hydrodynamic diameter of all particles.

3.3 Colloidal stability of UCNPs

The colloidal stability of neat and polymer-modified UCNPs in water, PBS and DMEM was monitored by analyzing their D_h and ζ-potential as a function of time. No significant changes in D_h and ζ-potential were observed for any of the polymer-coated nanoparticles incubated in water at 25°C and 37°C for 168 h, demonstrating their good colloidal stability (Supplementary Figures S4A, B and Supplementary Figures S5A, B). Similar results were observed for neat UCNPs, but after 168 h at 37°C the particles started to aggregate and their hydrodynamic diameter increased from 120 to 220 nm. This was attributed to a decrease in their ζ-potential, as these nanoparticles were only stabilized by electrostatic repulsions (Supplementary Figure S5A). In PBS, the D_h of UCNP@Ale-PEG increased after 24 and 6 h of incubation at 25°C and 37°C, respectively. UCNP@Ale-PDMA particles started to aggregate immediately after contact with PBS, and their D_h was >1,000 nm. In both cases, the aggregation was probably due to the small amount and rapid exchange of polymer coatings with phosphate ions, as previously observed for PEG-phosphate-modified UCNPs (Boyer et al., 2010). The ζ-potential of both UCNP@Ale-PEG and UCNP@Ale-PDMA approached zero due to the formation of the counterion layer (Supplementary Figure S5C, D). UCNP@PMVEMA particles showed very good colloidal stability in PBS at both temperatures for 168 h, as there were no noticeable changes in their D_h and ζ-potential. Also, neat UCNPs, UCNP@Ale-PEG and UCNP@PMVEMA particles were colloidally stable in DMEM at 37°C and their D_h and *PD* were constant for 168 h (Supplementary Figure

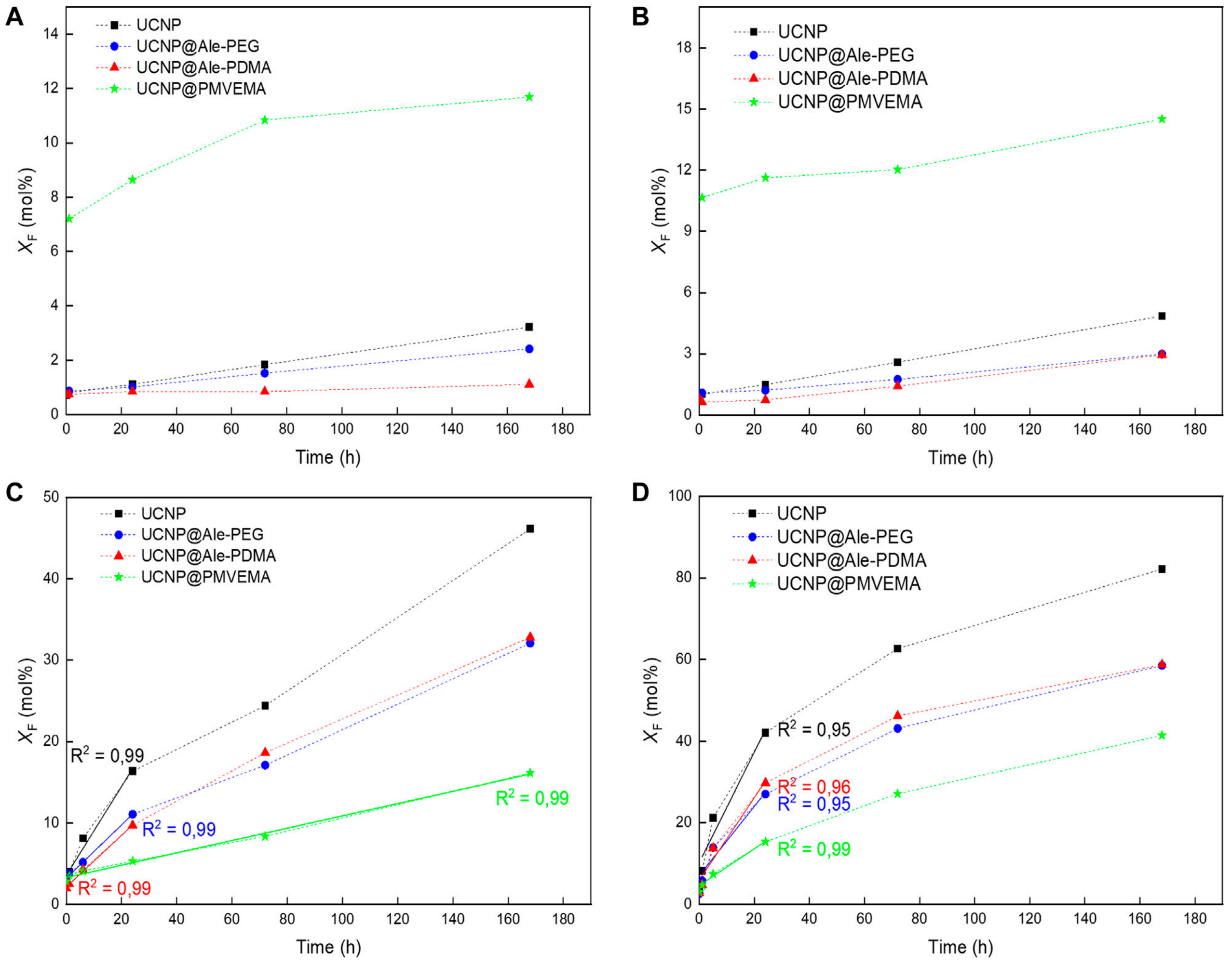

FIGURE 3
Time dependences of F⁻ion molar fraction (X_F) in supernatants. Hexagonal UCNPs were stored in **(A, B)** water and **(C, D)** PBS (pH 7.4) at **(A, C)** 25 and **(B, D)** 37°C. The standard errors of the means of X_F in water ranged from 0.02 to 0.026 and in PBS from 0.02 to 0.24 mol%.

S6A, B). In contrast, UCNP@Ale-PDMA particles were unstable in DMEM and their D_h and *PD* increased due to opsonization with proteins and aggregation.

3.4 Dissolution of UCNPs

The dissolution of neat and polymer-coated hexagonal UCNPs in water and PBS at 25°C and 37°C was measured with a fluoride ion selective electrode from time-depended changes in the concentration of F^-ions in the supernatants. The F^-ion leakage was determined as the molar fraction of dissolved F^- ions (X_F) relative to the total amount of fluorine in the nanoparticles with a nominal composition of NaF_4:$Y_{0.78}$:$Yb_{0.20}$,$Er_{0.02}$ (Figures 3A–D). It can be seen that at higher temperatures, X_F increased (Figures 3B, D) due to the better solubility of $NaYF_4$ (Lisjak et al., 2016). It is also interesting to note that the UCNP@PMVEMA particles dissolved more in water compared to the neat particles (Figures 3 A, B). This phenomenon has been previously described for small 25-nm UCNPs and also for other polymer coatings probably due to their complexation with lanthanides (Plohl et al., 2017; Nahorniak et al., 2023). In contrast to water, dissolution of all particle types was significantly higher in PBS (Figure 3) because the reaction of phosphates with lanthanides accelerated the hydrolysis of surface atoms (Lisjak et al., 2016; Saleh et al., 2020). The F^-leakage from neat UCNPs reached 20 mol% after 44 and 7 h of incubation in PBS at 25°C and 37°C, respectively (Figures 3C, D). UCNP@Ale-PEG and UCNP@Ale-PDMA particles were more resistant to dissolution in PBS; at 25°C, X_F reached 20 mol% after 94 and 81 h, respectively (Figure 3C). In the case of UCNP@PMVEMA particles in PBS, X_F reached only 16 mol% even after 168 h. When the temperature was increased to 37°C, 20 mol% $F^-$was released from UCNP@Ale-PEG, UCNP@Ale-PDMA and UCNP@PMVEMA after 15, 14 and 43 h of incubation, respectively (Figure 3D). As a result, the dissolution rate of UCNP@PMVEMA in PBS at 37°C was lower (0.45 mol%/h) than that of UCNP@Ale-PEG (0.8 mol%/h), UCNP@Ale-PDMA (1 mol%/h) and neat UCNPs (1.3 mol%/h; Table 1). Similar results were also obtained at 25°C, but the dissolution rate of all particles was 2.5–6 times slower than that at 37°C due to the poor solubility of

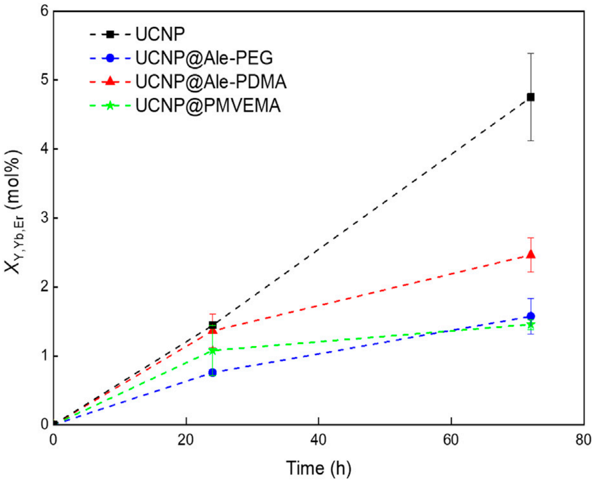

FIGURE 4
Time dependence of Y^{3+}, Yb^{3+} and Er^{3+} ion molar fraction ($X_{Y,Yb,Er}$) in supernatants. Hexagonal UCNPs (1 mg/mL) were aged in PBS at 37°C.

$NaYF_4$. Thus, all protective coatings retarded the dissolution of UCNPs in PBS. Moreover, the determination of the molar fraction of released Y^{3+}, Yb^{3+} and Er^{3+} ions ($X_{Y,Yb,Er}$) supported the above statement that UCNP@PMVEMA particles were the most resistant to dissolution in PBS at 37°C. $X_{Y,Yb,Er}$ of UCNP@PMVEMA, UCNP@Ale-PEG, UCNP@Ale-PDMA and UCNPs after 72 h of incubation was 1.46 ± 0.07, 1.57 ± 0.25, 2.46 ± 0.25 and 4.75 ± 0.63 mol%, respectively (Figure 4).

Furthermore, DMEM culture medium and ALF simulating the environment inside lysosomes with which the particles come into contact after endocytosis were used to model the dissolution of UCNPs under different *in vitro* conditions (pH, ionic strength and the presence of biomolecules). In DMEM, 1.9, 1.8, 1.8 and 3.3 mol% of F^-ions were released from UCNPs, UCNPs@Ale-PEG, UCNPs@Ale-PDMA, and UCNPs@PMVEMA particles, respectively, after 168 h of aging at 37°C (Supplementary Figure S7A). The nanoparticle dissolution in ALF was more pronounced than in DMEM, with X_F reaching ~13, 8, 9 and 16 mol% for neat, Ale-PEG-coated, Ale-PDMA-coated and PMVEMA-coated UCNPs, respectively, after 168 h at 37°C (Supplementary Figure S7B). The slower dissolution in DMEM that in ALF was due to the formation of a protein corona on the particle surface, which inhibited their dissolution (Saleh et al., 2020). Thus, UCNPs can be expected to dissolve predominantly intracellularly and their toxicity will be related to the number of internalized nanoparticles and protective polymer coating.

When comparing the dissolution of particles in PBS, the UCNP@PMVEMA with the highest amount of coating were the most resistant to dissolution. However, in water these particles demonstrated the highest F^- release, suggesting that not only the amount of polymer but rather chemistry of coating and surface ζ-potential influenced the rate of particle dissolution. In contrast to PMVEMA with many carboxyl groups that can act as attachment sites of polymer with the particle, Ale-PEG and Ale-PDMA contained only one phosphonate group for binding with UCNPs. Therefore, a polymer with one anchoring group on the particle surface can more easily exchange with phosphate ions, which accelerates the hydrolysis of surface atoms and induces faster particles dissolution. This agreed with earlier report, where ligand containing four anchoring groups provided higher protection of UCNPs against dissolution than those with only two (Andresen et al., 2020). On the other hand, the negative ζ-potential of UCNP@PMVEMA particles can suppress the diffusion of phosphate ions to the nanoparticle surface due to Coulomb repulsions, inhibiting exchange reaction and particle dissolution. Moreover, the particle size seems to influence the rate of dissolution in aqueous media. In comparison to earlier report on the dissolution of 25-nm particles with the same coatings, the dissolution of hexagonal UCNPs in water and PBS at 37°C was lower (Nahorniak et al., 2023). In PBS, the dissolution of 120-nm particles was lower by ~14 and 20%–24% for neat and all polymer-coated UCNPs, respectively. In water, the decrease in solubility was lower by 31, 37, 65% and 9% for UCNPs, UCNPs@Ale-PEG, UCNPs@Ale-PDMA and UCNPs@PMVEMA, respectively (Table 2). This was attributed to a smaller surface-to-volume ratio of 120-nm UCNPs, which agrees with the literature (Saleh et al., 2020). As a result, the dissolution of UCNPs is a complex phenomenon dependent on many parameters such as temperature, type of aqueous medium, nanoparticle size, surface chemistry and charge.

3.5 Cytotoxicity of polymer-coated hexagonal UCNPs

To assess the suitability of UCNPs for biological applications, it is necessary to determine whether the individual particle types, specifically UCNPs, UCNP@Ale-PEG, UCNP@Ale-PDMA and UCNP@PMVEMA both without and with bound FITC are toxic to cells. Two cell types were used to assess cytotoxicity, rMSCs serving as a model of healthy non-tumorigenic cells and a C6 rat tumor cell line representing diseased tumorigenic cells. Cells in cell culture medium were incubated with particles at a concentration of 1–1,000 μg/mL for 24 and 72 h, and cell viability was examined using the Alamar Blue assay, one of the best *in vitro* assays for the determination of cell viability, cytotoxicity and cell proliferation. It is an alternative to tetrazolium dyes such as 3-(4,5-dimethylthiazol-2-yl)-2,5-diphenyltetrazolium bromide (MTT), and because it is non-toxic, it can also be used for long-term cell proliferation studies. Alamar Blue is based on the fluorometric redox indicator resazurin (7-hydroxy-3H-phenoxazin-3-one 10-oxide), a blue-colored non-fluorescent compound. After intracellular uptake, the oxidized resazurin is reduced to the fluorescent resorufin (7-hydroxy-3H-phenoxazin-3-one) due to the reducing environment of the cell cytosol. Resorufin produces bright red fluorescence with an excitation of 530–570 nm and emission of 580–610 nm; the fluorescence intensity is then used to quantify cell viability (Longhin et al., 2022).

The presence of nanoparticles in the medium for 24 h did not affect the proliferation of C6 cells regardless of the type of particle coating (Figure 5). Similarly, the viability rMSCs cultured for 24 h in the presence of different UCNPs at two highest concentrations (500 and 1,000 μg/mL) decreased only slightly (to 80%). Culturing C6 cells for 72 h in the presence of uncoated UCNPs and UCNP@PMVEMA particles at a concentration of

TABLE 2 Molar fraction of F^- ions (X_F) dissolved in water or PBS at 37°C for 168 h and percentage of X_F from large (120 nm) versus small (25 nm) nanoparticles.

	X_F (mol%)				1-($X_{F\ 120\ nm}/X_{F\ 25nm}$) 100 (%)	
	Water		PBS			
Particles	25 nm	120 nm	25 nm	120 nm	Water	PBS
UCNPs	5.8	4.0	90.6	78.3	31.4	13.6
UCNP@Ale-PEG	3.3	2.1	73.1	55.9	36.9	23.5
UCNP@Ale-PDMA	6.2	2.2	73.8	56.0	65.1	24.1
UCNP@PMVEMA	4.9	4.5	48.4	38.4	8.7	20.7

X_F values for 25-nm UCNPs were taken from (Nahorniak et al., 2023).

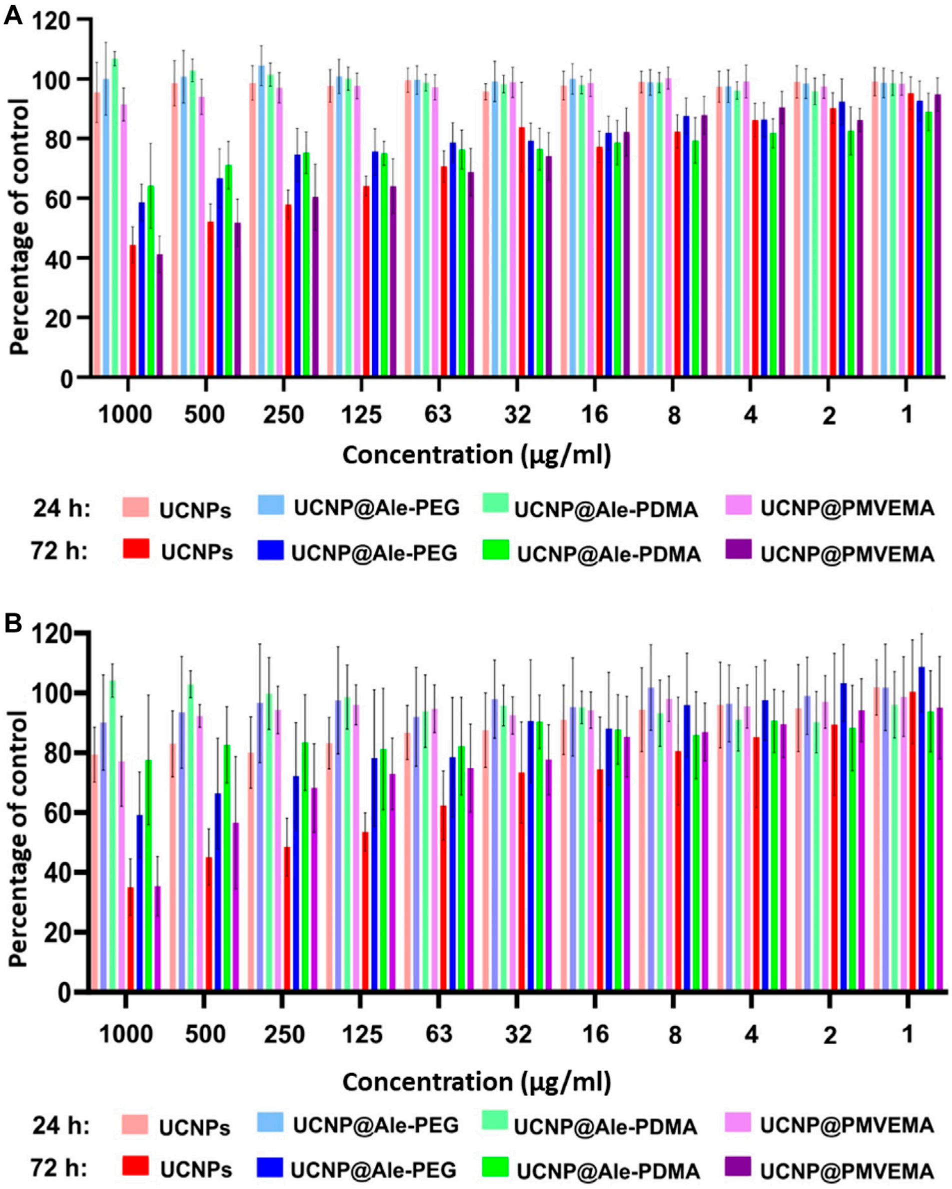

FIGURE 5
(A) C6 cell line and **(B)** rMSC viability in the presence of different concentrations of various UCNPs for 24 and 72 h.

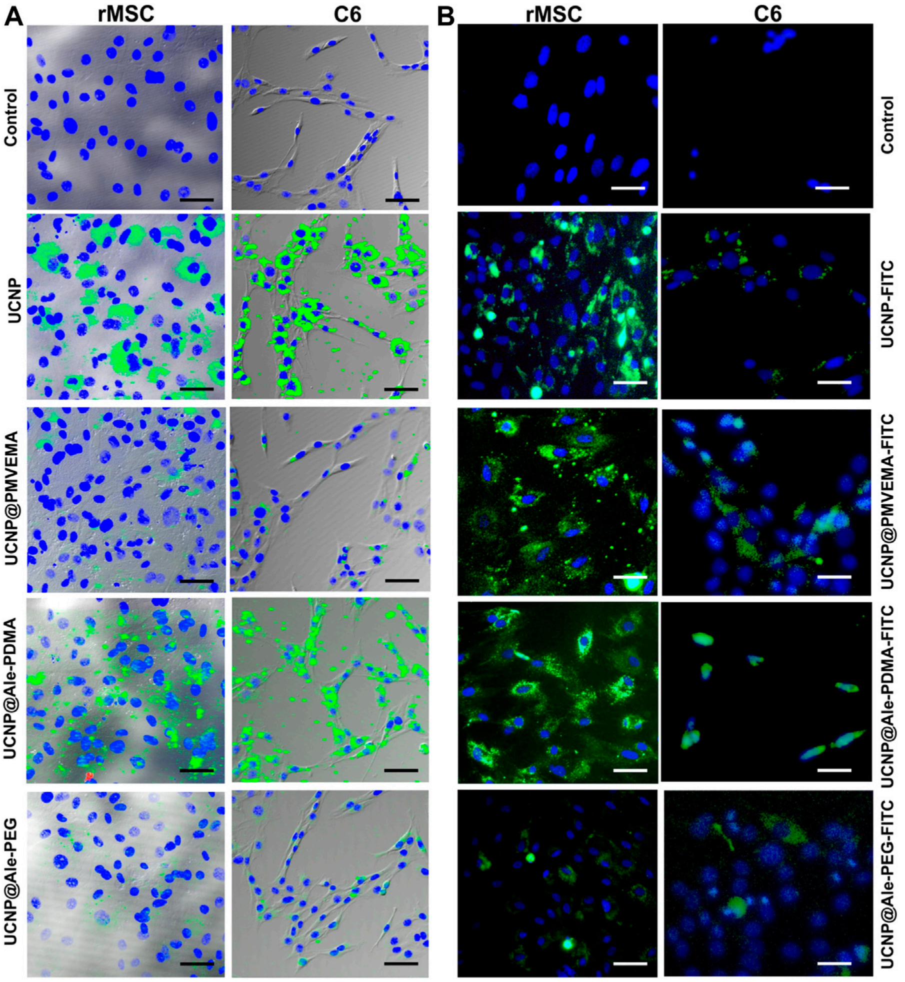

FIGURE 6
C6 and rMSC cells imaged by confocal microscope and overlaid with brightfield images **(A)** after 1 day of incubation with UCNPs, UCNP@PMVEMA, UCNP@Ale-PDMA, and UCNP@Ale-PEG particles (green). **(B)** FITC-modified UCNPs, UCNP@PMVEMA, UCNP@Ale-PDMA, and UCNP@Ale-PEG particles visualized in C6 and rMSC cells by fluorescence microscope after 24 h of incubation. The cell nuclei were stained with DAPI (blue). Cells not incubated with nanoparticles served as a control. Scale bar 50 μm.

1,000 μg/mL resulted in a decrease in cell viability to 40%; with decreasing particle concentration, viability slowly increased to values reaching 80%–90%. Toxicity of UCNP@PMVEMA particles can be ascribed to their high solubility in water (Figures 3A, B) as well as in AFL. In contrast, cells cultured in the presence of UCNP@Ale-PDMA or UCNP@Ale-PEG nanoparticles at the two highest concentrations of 500 and 1,000 μg/mL maintained viability between 70% and 58%, while at lower concentrations cell viability was between 70% and 90%. Likewise, the viability of rMSCs cultured for 72 h in the presence of UCNPs and UCNP@PMVEMA particles was reduced to 30% and maintained <60% up to a concentration of 63 μg/mL. At lower concentrations of neat UCNPs and UCNP@PMVEMA, the viability ranged between 80%–90%. The rMSCs incubated with UCNP@Ale-PDMA maintained 80%–90% viability regardless of particle concentration. For the same cells incubated with UCNP@Ale-PEG at a concentration of 63–1,000 μg/mL, viability gradually decreased from 80% to 60%; at lower concentrations, rMSC viability was ~90%. In addition, there was no difference in the viability of cells incubated with UCNPs either with or without FITC. These findings corresponded to the results of dissolution of UCNPs in ALF, as the best viability was achieved for particles coated with PEG and PDMA, which protected them well. In our previous study, a significant decrease in rMSCs and C6 cell viability (<20%; MTT assay) was observed already after 24 h of incubation with uncoated small spherical UCNPs at a concentration 1,000 μg/mL (Nahorniak et al., 2023). It should be mentioned that the toxicity of particles is generally influenced by a number of factors, including the ζ-potential, the particle size and the amount of lanthanide and fluoride ions released into the medium. A limitation of our study was that we did not have non-toxic polymer-coated particles with the same ζ-potential as the control. However, the ζ-potential of UCNP@Ale-PDMA particles was comparable to that of uncoated UCNPs, but the cytotoxicity of the former was significantly lower. Thus, it can be

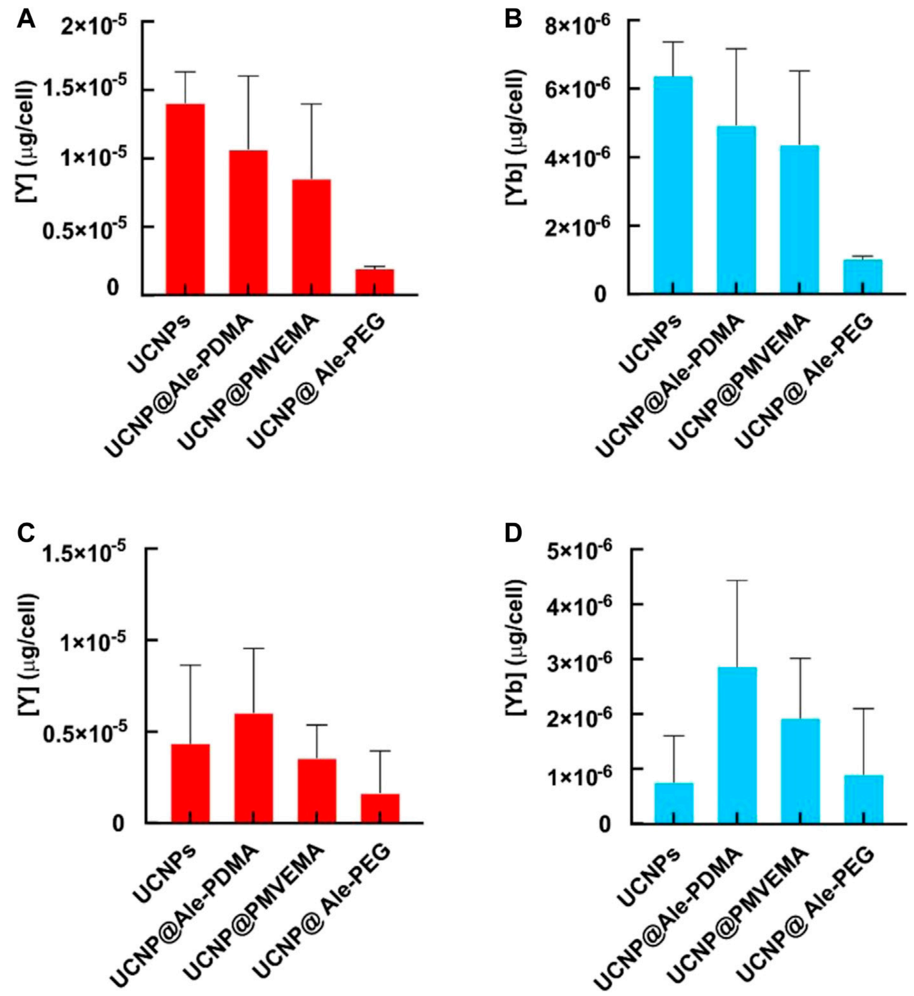

FIGURE 7
Amount of Y and Yb in **(A, B)** rMSCs and **(C, D)** C6 cell line after incubation with differently coated hexagonal UCNPs for 1 day according to ICP-MS.

concluded that the cytotoxicity of UCNPs is not only determined by the ζ-potential but also by the dissolution of the particles.

3.6 Monitoring the internalization of polymer-coated hexagonal UCNPs by confocal microscopy

To demonstrate the concept of dual imaging, i.e., to visualize particle internalization in cells and particle distribution in the cytoplasm by confocal microscopy, a commonly used fluorescent dye, fluorescein isothiocyanate (FITC), was attached to UCNPs, which is useful for prospective *in vivo* animal control and histology. In addition, optical imaging allows for independent control, where nanoparticles can be excited throughout the organism to easily verify their biodistribution. The FITC was first modified with Ale to complex it with lanthanide ions on the particle surface. Its normalized photoluminescence spectrum and spectra of FITC-modified polymer-coated UCNPs under excitation and emission at 492 and 517 nm, respectively, were shown in Supplementary Figure S8. The main advantage of fluorescent particles is that they are visible in an epifluorescence microscope, which is part of the equipment of every culture laboratory, and therefore their uptake by cells can be monitored during cell culturing; it is also easier to detect particles in histological tissue sections. In addition, with excitation at 980 nm and emission at 542 and 656 nm, UCNPs enable deep tissue *in vivo* imaging.

To examine the uptake of all differently coated UCNPs, rMSC and C6 cells were cultured in the presence of particles at a concentration of 20 μg/mL for 24 h. Cells were then fixed with paraformaldehyde and imaged under confocal and epifluorescent microscope (Figure 6). Our results confirmed that particle uptake can be visualized by both confocal and fluorescence microscopy. The strongest signal in both confocal and fluorescence microscopy was observed in cells incubated with uncoated UCNPs. Of the coated particles, UCNP@Ale-PDMA were the most abundant in the cells, followed by UCNP@PMVEMA. UCNP@Ale-PEG particles were the least abundant in the cells because PEG is bioinert to a number of biological components found in the human body including proteins and does not exhibit cell-adhesive properties. There were generally more particles in the cytoplasm of rMCSs because they are usually larger than C6 cells. The signal was brightest in cells incubated with uncoated UCNPs, probably due to their high internalization (Figure 6). These findings are consistent with the results obtained by ICP-MS, which determined the concentration of Y and Yb in rMSCs and C6 cells after 24 h of culture with nanoparticles (Figure 7). The highest concentrations of Y and Yb were found in rMSCs containing uncoated UCNPs; Y and Yb concentrations ranged from 11.3 to 15.4 and from 5.2 to 7.0 pg per cell, respectively. The amount of Y per cell ranged from 4.9 to 15.5 pg and from 5.6 to 12.3 pg for UCNP@Ale-PDMA and UCNP@PMVEMA nanoparticles, respectively; similarly, the amount of Yb per cell was 2.6–7.0 pg and 2.8–5.9 pg for UCNP@Ale-PDMA and UCNP@PMVEMA nanoparticles, respectively. The only difference was found for UCNP@Ale-PEG particles, as PEG prevented their internalizing into cells and the concentrations of Y and Yb were in the range of 1.7–2.0 and 0.9–1.1 pg per cell, respectively.

In general, slightly lower concentrations of Y and Yb were found in C6 cells than in rMSCs (Figure 7). The highest amounts of Y and Yb were in C6 cells incubated with UCNP@Ale-PDMA nanoparticles for 24 h, 3.5–10.1 pg and 1.6–4.6 pg per cell, respectively. The average levels of Y and Yb in C6 cells labeled with uncoated particles were 4.4 and 0.7 pg/cell, respectively, while C6 cells incubated with UCNP@PMVEMA particles contained 3.6 and 1.9 pg of Y and Yb per cell, respectively. As in rMSCs, the lowest concentrations of Y (1.7 pg) and Yb (0.9 pg) were found in C6 cells containing UCNP@Ale-PEG nanoparticles. Comparison of the results of hexagonal UCNPs with previously published data on spherical nanoparticles coated with the same polymers (Nahorniak et al., 2023) shows that C6 cells cultured with hexagonal UCNPs contain orders of magnitude more Y and Yb than after culture with small spherical UCNPs. This difference was not observed for rMSCs, where Y and Yb concentrations were in a similar range, probably due to the larger size of rMSCs and their higher capacity for particle endocytosis. The size of the nanoparticles may also play a role; large particles contain higher amounts of Y and Yb, although their total number in the cell may not be greater than that of small spherical nanoparticles.

4 Conclusion

In this report, we present the design of uniform hexagonal $NaYF_4$:Yb^{3+},Er^{3+} nanoparticles with a size of 120 nm that were coated with PEG-Ale, PDMA-Ale and PMVEMA polymers. The uniform size means that the particles have the same physicochemical properties, thus providing reproducible results in biomedical applications. After loading UCNPs with FITC, a two-color optical image with excitation at 494 or 980 nm can be obtained. This combination of two luminescence properties allows convenient and easy monitoring of biological processes *in vitro* and *in vivo*, such as particle uptake, tissue and tumor perfusion, or vascular leakage. Both colloidal stability and long-term dissolution of particles were systematically investigated in various aqueous media such as water, PBS, DMEM cell culture medium or ALF at 25°C and 37°C. Particle dissolution and colloidal stability were determined by potentiometry and DLS, respectively. To our knowledge, this is the first comprehensive study on the dissolution of UCNPs >100 nm in size. In contrast to small (25 nm) particles, the dissolution of large ones (120 nm) in water and PBS at 37°C was lower due to the smaller surface-to-volume ratio. PEG-Ale-and PDMA-Ale polymers provided a relatively good protection against particle dissolution in all tested media. While the UCNP@Ale-PEG particles were colloidally stable in water and DMEM, the UCNP@Ale-PDMA particles were stable only in water. Both particle types were unstable in PBS due to the exchange of polymer coatings with phosphates. In contrast, PMVEMA provided excellent colloidal stability of UCNPs in water, PBS and DMEM but suppressed their dissolution only in PBS, while accelerating dissolution in water, DMEM and ALF. Last but not least the cytotoxicity of particles was determined by Alamar Blue assay using C6 cells and rMSCs. Short-term (24 h) incubation of cells with UCNPs even at the highest concentration did not significantly affect cell viability. However, the viability of cells incubated with different types of particles for 72 h decreased to 40%–85% depending on the concentration. Neat UCNPs and UCNP@PMVEMA particles caused the greatest decrease. The highest particle uptake was seen with neat UCNPs, followed by UCNP@Ale-PDMA and UCNP@PMVEMA. Successful particle internalization and cell visualization was documented by green fluorescence of FITC-Ale-modified UCNPs inside the cells. Thus, it can be concluded that UCNP@Ale-PDMA and UCNP@Ale-PEG nanoparticles are the most promising in terms of further applications. Both particles were the least toxic but differed in their uptake into cells. While UCNP@Ale-PEG may find applications with prolonged circulation time when internalization into cells is not required, UCNP@Ale-PDMA is suitable for accumulation into, for example, tumor cells. In addition, surface-modified UCNPs can be prospectively loaded with various bioactive agents such as drugs or photosensitizers.

Data availability statement

The original contributions presented in the study are included in the article/Supplementary Material, further inquiries can be directed to the corresponding author.

Author contributions

DH, PJ, and LM-U contributed to conception and design of the study. VP conducted basic research, DM, MN, OS, PM, and VO participated in specific investigations, RK performed NMR analysis, MV elemental analysis. DH, VP, and PJ wrote the manuscript. All authors contributed to the article and approved the submitted version.

Funding

Support of the Czech Science Foundation (No. 21-04420S) is acknowledged. Microscopy was done at the Microscopy Service Centre of the Institute of Experimental Medicine CAS supported by the MEYS CR (LM2023050 Czech-Bioimaging). Support of The Ministry of Education, Youth and Sports (No. CZ.02.1.01/0.0/0.0/15_003/0000419) is acknowledged.

Conflict of interest

The authors declare that the research was conducted in the absence of any commercial or financial relationships that could be construed as a potential conflict of interest.

Publisher's note

Supplementary material

The Supplementary Material for this article can be found online at: https://www.frontiersin.org/articles/10.3389/fchem.2023.1207984/full#supplementary-material

References

Abdul Jalil, R., and Zhang, Y. (2008). Biocompatibility of silica coated $NaYF_4$ upconversion fluorescent nanocrystals. *Biomaterials* 29, 4122–4128. doi:10.1016/j.biomaterials.2008.07.012

Ahmad, M. Y., Ahmad, M. W., Yue, H., Ho, S. L., Park, J. A., Jung, K.-H., et al. (2020). *In vivo* positive magnetic resonance imaging applications of poly(methyl vinyl ether-*alt*-maleic acid)-coated ultra-small paramagnetic gadolinium oxide nanoparticles. *Molecules* 25, 1159. doi:10.3390/molecules25051159

Andresen, E., Würth, C., Prinz, C., Michaelis, M., and Resch-Genger, U. (2020). Time-resolved luminescence spectroscopy for monitoring the stability and dissolution behaviour of upconverting nanocrystals with different surface coatings. *Nanoscale* 12, 12589–12601. doi:10.1039/D0NR02931A

Auzel, F. (2004). Upconversion and anti-Stokes processes with f and d ions in solids. *Chem. Rev.* 104, 139–174. doi:10.1021/cr020357g

Barbier, O., Arreola-Mendoza, L., and Del Razo, L. M. (2010). Molecular mechanisms of fluoride toxicity. *Biol. Interact.* 188, 319–333. doi:10.1016/j.cbi.2010.07.011

Boyer, J.-C., Vetrone, F., Cuccia, L. A., and Capobianco, J. A. (2006). Synthesis of colloidal upconverting $NaYF_4$ nanocrystals doped with Er^{3+}, Yb^{3+} and Tm^{3+}, Yb^{3+} via thermal decomposition of lanthanide trifluoroacetate precursors. *J. Am. Chem. Soc.* 128, 7444–7445. doi:10.1021/ja061848b

Boyer, J. C., Naseaou, M. P., Morray, J. I., and van Veggel, F. C. J. M. (2010). Surface modification of upconverting $NaYF_4$ nanoparticles with PEG-phosphate ligands for NIR (800 nm) biolabeling within the biological window. *Langmuir* 26, 1157–1164. doi:10.1021/la902260j

Colombo, C., Monhemius, A. J., and Plant, J. A. (2008). Platinum, palladium and rhodium release from vehicle exhaust catalysts and road dust exposed to simulated lung fluids. *Ecotoxicol. Environ. Saf.* 71, 722–730. doi:10.1016/j.ecoenv.2007.11.011

Egatz-Gomez, A., Asher, M., Peterson, R., Roldan, M. A., and Ros, A. (2022). Microwave synthesis of upconverting nanoparticles with bis(2-ethylhexyl) adipate. *RSC Adv.* 12, 23026–23038. doi:10.1039/D2RA03262G

Fischer, S., Bronstein, N. D., Swabeck, J. K., Chan, E. M., and Alivisatos, A. P. (2016). Precise tuning of surface quenching for luminescence enhancement in core–shell lanthanide-doped nanocrystals. *Nano Lett.* 16, 7241–7247. doi:10.1021/acs.nanolett.6b03683

Fischer, S., Martín-Rodríguez, R., Fröhlich, B., Krämer, K. W., Meijerink, A., and Goldschmidt, J. C. (2014). Upconversion quantum yield of Er^{3+}-doped β-$NaYF_4$ and Gd_2O_2S: The effects of host lattice, Er^{3+} doping, and excitation spectrum bandwidth. *J. Lumin.* 153, 281–287. doi:10.1016/j.jlumin.2014.03.047

Hamblin, M. R. (2018). Upconversion in photodynamic therapy: Plumbing the depths. *Dalton Trans.* 47, 8571–8580. doi:10.1039/c8dt00087e

Jin, J., Gu, Y.-J., Man, C. W.-Y., Cheng, J., Xu, Z., Zhang, Y., et al. (2011). Polymer-coated $NaYF_4$:Yb^{3+}, Er^{3+} upconversion nanoparticles for charge-dependent cellular imaging. *ACS Nano* 5, 7838–7847. doi:10.1021/nn201896m

Johnson, N. J. J., Sangeetha, N. M., Boyer, J.-C., and van Veggel, F. C. J. M. (2010). Facile ligand-exchange with polyvinylpyrrolidone and subsequent silica coating of hydrophobic upconverting β-$NaYF_4$:Yb^{3+}/Er^{3+} nanoparticles. *Nanoscale* 2, 771–777. doi:10.1039/b9nr00379g

Jones, C. M. S., Gakamsky, A., and Marques-Hueso, J. (2021). The upconversion quantum yield (ucqy): A review to standardize the measurement methodology, improve comparability, and define efficiency standards. *Sci. Technol. Adv. Mat.* 22, 810–848. doi:10.1080/14686996.2021.1967698

Kaiser, M., Würth, C., Kraft, M., Hyppänen, I., Soukka, T., and Resch-Genger, U. (2017). Power-dependent upconversion quantum yield of $NaYF_4$:Yb^{3+},Er^{3+} nano- and micrometer-sized particles – measurements and simulations. *Nanoscale* 9, 10051–10058. doi:10.1039/c7nr02449e

Kamimura, M., Miyamoto, D., Saito, Y., Soga, K., and Nagasaki, Y. (2008). Design of poly(ethylene glycol)/streptavidin coimmobilized upconversion nanophosphors and their application to fluorescence biolabeling. *Langmuir* 24, 8864–8870. doi:10.1021/la801056c

Kostiv, U., Lobaz, V., Kučka, J., Švec, P., Sedláček, O., Hrubý, M., et al. (2017). A simple neridronate-based surface coating strategy for upconversion nanoparticles: Highly colloidally stable ^{125}I-radiolabeled $NaYF_4$:Yb^{3+}/Er^{3+}@PEG nanoparticles for multimodal *in vivo* tissue imaging. *Nanoscale* 9, 16680–16688. doi:10.1039/c7nr05456d

Li, S., Wei, X., Li, S., Zhu, C., and Wu, C. (2020). Up-Conversion luminescent nanoparticles for molecular imaging, cancer diagnosis and treatment. *Int. J. Nanomed.* 15, 9431–9445. doi:10.2147/IJN.S266006

Li, X., Zhang, F., and Zhao, D. (2015). Lab on upconversion nanoparticles: Optical properties and applications engineering *via* designed nanostructure. *Chem. Soc. Rev.* 44, 1346–1378. doi:10.1039/c4cs00163j

Liang, G., Wang, H., Shi, H., Wang, H., Zhu, M., Jing, A., et al. (2020). Recent progress in the development of upconversion nanomaterials in bioimaging and disease treatment. *J. Nanobiotechnol.* 18, 154. doi:10.1186/s12951-020-00713-3

Lisjak, D., Plohl, O., Vidmar, J., Majaron, B., and Ponikvar-Svet, M. (2016). Dissolution mechanism of upconverting AYF4:Yb,Tm (A = Na or K) nanoparticles in aqueous media. *Langmuir* 32, 8222–8229. doi:10.1021/acs.langmuir.6b02675

Longhin, E. M., El Yamani, N., Rundén-Pran, E., and Dusinska, M. (2022). The alamar blue assay in the context of safety testing of nanomaterials. *Front. Toxicol.* 4, 981701. doi:10.3389/ftox.2022.981701

MacKenzie, L. E., Alvarez-Ruiz, D., and Pal, R. (2022). Low-temperature open-air synthesis of PVP-coated $NaYF_4$:Yb,Er,Mn upconversion nanoparticles with strong red emission. *R. Soc. Open Sci.* 9, 211508. doi:10.1098/rsos.211508

Mao, L., Lu, Z., He, N., Zhang, L., Deng, Y., and Duan, D. (2017). A new method for improving the accuracy of miRNA detection with $NaYF_4$:Yb,Er upconversion nanoparticles. *Sci. China Chem.* 60, 157–162. doi:10.1007/s11426-016-0021-0

Mi, C., Zhang, J., Gao, H., Wu, X., Wang, M., Wu, Y., et al. (2010). Multifunctional nanocomposites of superparamagnetic (Fe_3O_4) and NIR-responsive rare Earth-doped up-conversion fluorescent ($NaYF_4$: Yb,Er) nanoparticles and their applications in biolabeling and fluorescent imaging of cancer cells. *Nanoscale* 2, 1141–1148. doi:10.1039/c0nr00102c

Nahorniak, M., Patsula, V., Mareková, D., Matouš, P., Shapoval, O., Oleksa, V., et al. (2023). Chemical and colloidal stability of polymer-coated $NaYF_4$:Yb,Er nanoparticles in aqueous media and viability of cells: The effect of a protective coating. *Int. J. Mol. Sci.* 24, 2724. doi:10.3390/ijms24032724

Oleksa, V., Macková, H., Patsula, V., Dydowitzová, A., Janoušková, O., and Horák, D. (2020). Doxorubicin-conjugated iron oxide nanoparticles: Surface engineering and biomedical investigation. *ChemPlusChem* 85, 1156–1163. doi:10.1002/cplu.202000360

Oliveira, H., Bednarkiewicz, A., Falk, A., Fröhlich, E., Lisjak, D., Prina-Mello, A., et al. (2019). Critical considerations on the clinical translation of upconversion nanoparticles (UCNPs): Recommendations from the European upconversion network (COST Action CM1403). *Adv. Healthc. Mat.* 8, 1801233. doi:10.1002/adhm.201801233

Park, W., Lu, D., and Ahn, S. (2015). Plasmon enhancement of luminescence upconversion. *Chem. Soc. Rev.* 44, 2940–2962. doi:10.1039/c5cs00050e

Park, Y. I., Nam, S. H., Kim, J. H., Bae, Y. M., Yoo, B., Kim, H. M., et al. (2013). Comparative study of upconverting nanoparticles with various crystal structures, core/shell structures, and surface characteristics. *J. Phys. Chem. C* 117, 2239–2244. doi:10.1021/jp3105248

Pichaandi, J., Boyer, J.-C., Delaney, K. R., and van Veggel, F. C. J. M. (2011). Two-photon upconversion laser (scanning and wide-field) microscopy using Ln^{3+}-doped $NaYF_4$ upconverting nanocrystals: A critical evaluation of their performance and potential in bioimaging. *J. Phys. Chem. C* 115, 19054–19064. doi:10.1021/jp206345j

Plohl, O., Kralj, S., Majaron, B., Fröhlich, E., Ponikvar-Svet, M., Makovec, D., et al. (2017). Amphiphilic coatings for the protection of upconverting nanoparticles against dissolution in aqueous media. *Dalton Trans.* 46, 6975–6984. doi:10.1039/c7dt00529f

Ramírez-García, G., Panikar, S. S., López-Luke, T., Piazza, V., Honorato-Colin, M. A., Camacho-Villegas, T., et al. (2018). An immunoconjugated up-conversion nanocomplex for selective imaging and photodynamic therapy against HER2-positive breast cancer. *Nanoscale* 10, 10154–10165. doi:10.1039/c8nr01512k

Saleh, M. I., Rühle, B., Wang, S., Radnik, J., You, Y., and Resch-Genger, U. (2020). Assessing the protective effects of different surface coatings on $NaYF_4:Yb^{3+}$, Er^{3+} upconverting nanoparticles in buffer and DMEM. *Sci. Rep.* 10, 19318. doi:10.1038/s41598-020-76116-z

Schietinger, S., Menezes, L. S., Lauritzen, B., and Benson, O. (2009). Observation of size dependence in multicolor upconversion in single Yb^{3+}, Er^{3+} codoped $NaYF_4$ nanocrystals. *Nano Lett.* 9, 2477–2481. doi:10.1021/nl901253t

Shan, S. N., Wang, X. Y., and Jia, N. Q. (2011). Synthesis of $NaYF_4:Yb^{3+}$, Er^{3+} upconversion nanoparticles in normal microemulsions. *Nanoscale Res. Lett.* 6, 539. doi:10.1186/1556-276x-6-539

Shao, H., Xu, D., Ding, Y., Hong, X., and Liu, Y. (2018). An "off-on" colorimetric and fluorometric assay for Cu(II) based on the use of $NaYF_4$:Yb(III),Er(III) upconversion nanoparticles functionalized with branched polyethylenimine. *Microchim. Acta* 185, 211. doi:10.1007/s00604-018-2740-7

Sun, L.-D., Wang, Y.-F., and Yan, C.-H. (2014). Paradigms and challenges for bioapplication of rare Earth upconversion luminescent nanoparticles: Small size and tunable emission/excitation spectra. *Acc. Chem. Res.* 47, 1001–1009. doi:10.1021/ar400218t

Wang, F., Wang, J., and Liu, X. (2010). Direct evidence of a surface quenching effect on size-dependent luminescence of upconversion nanoparticles. *Angew. Chem. Int. Ed.* 49, 7456–7460. doi:10.1002/anie.201003959

Wang, M., Liu, J.-L., Zhang, Y.-X., Hou, W., Wu, X.-L., and Xu, S.-K. (2009). Two-phase solvothermal synthesis of rare-Earth doped $NaYF_4$ upconversion fluorescent nanocrystals. *Mat. Lett.* 63, 325–327. doi:10.1016/j.matlet.2008.10.028

Wang, Z.-L., Hao, J., Chan, H. L. W., Wong, W.-T., and Wong, K.-L. (2012). A strategy for simultaneously realizing the cubic-to-hexagonal phase transition and controlling the small size of $NaYF_4:Yb^{3+},Er^{3+}$ nanocrystals for *in vitro* cell imaging. *Small* 8, 1863–1868. doi:10.1002/smll.201102703

Wen, S., Zhou, J., Zheng, K., Bednarkiewicz, A., Liu, X., and Jin, D. (2018). Advances in highly doped upconversion nanoparticles. *Nat. Commun.* 9, 2415. doi:10.1038/s41467-018-04813-5

Wilhelm, S., Kaiser, M., Würth, C., Heiland, J., Carrillo-Carrion, C., Muhr, V., et al. (2015). Water dispersible upconverting nanoparticles: Effects of surface modification on their luminescence and colloidal stability. *Nanoscale* 7, 1403–1410. doi:10.1039/c4nr05954a

Wisser, M. D., Fischer, S., Siefe, C., Alivisatos, A. P., Salleo, A., and Dionne, J. A. (2018). Improving quantum yield of upconverting nanoparticles in aqueous media *via* emission sensitization. *Nano Lett.* 18, 2689–2695. doi:10.1021/acs.nanolett.8b00634

Xie, X., Gao, N., Deng, R., Sun, Q., Xu, Q.-H., and Liu, X. (2013). Mechanistic investigation of photon upconversion in Nd^{3+}-sensitized core–shell nanoparticles. *J. Am. Chem. Soc.* 135, 12608–12611. doi:10.1021/ja4075002

Yao, W., Tian, Q., Liu, J., Wu, Z., Cui, S., Ding, J., et al. (2016). Large-scale synthesis and screen printing of upconversion hexagonal-phase $NaYF_4:Yb^{3+},Tm^{3+}/Er^{3+}/Eu^{3+}$ plates for security applications. *J. Mat. Chem. C* 4, 6327–6335. doi:10.1039/c6tc01513a

Ye, S., Chen, G., Shao, W., Qu, J., and Prasad, P. N. (2015). Tuning upconversion through a sensitizer/activator-isolated $NaYF_4$ core/shell structure. *Nanoscale* 7, 3976–3984. doi:10.1039/c4nr07678h

Zhou, J., Liu, Q., Feng, W., Sun, Y., and Li, F. (2015). Upconversion luminescent materials: Advances and applications. *Chem. Rev.* 115, 395–465. doi:10.1021/cr400478f

frontiers | Frontiers in Chemistry

TYPE Review
PUBLISHED 14 July 2023
DOI 10.3389/fchem.2023.1227843

OPEN ACCESS

EDITED BY
Rita Petrucci,
Sapienza University of Rome, Italy

REVIEWED BY
Zhimei He,
Nanjing University of Posts and Telecommunications, China
Luís Pinto Da Silva,
University of Porto, Portugal
Qi Zhao,
Technical Institute of Physics and Chemistry (CAS), China

*CORRESPONDENCE
Sandeep Sheth,
✉ ssheth@larkin.edu

[†]These authors have contributed equally to this work and share first authorship

RECEIVED 23 May 2023
ACCEPTED 05 July 2023
PUBLISHED 14 July 2023

CITATION
Kaurav H, Verma D, Bansal A, Kapoor DN and Sheth S (2023), Progress in drug delivery and diagnostic applications of carbon dots: a systematic review.
Front. Chem. 11:1227843.
doi: 10.3389/fchem.2023.1227843

Progress in drug delivery and diagnostic applications of carbon dots: a systematic review

Hemlata Kaurav[1†], Dhriti Verma[1†], Amit Bansal[2],
Deepak N. Kapoor[1] and Sandeep Sheth[3]*

[1]School of Pharmaceutical Sciences, Shoolini University of Biotechnology and Management Sciences, Solan, Himachal Pradesh, India, [2]Formulation Research and Development, Perrigo Company Plc, Allegan, MI, United States, [3]Department of Pharmaceutical Sciences, College of Pharmacy, Larkin University, Miami, FL, United States

Carbon dots (CDs), which have particle size of less than 10 nm, are carbon-based nanomaterials that are used in a wide range of applications in the area of novel drug delivery in cancer, ocular diseases, infectious diseases, and brain disorders. CDs are biocompatible, eco-friendly, easy to synthesize, and less toxic with excellent chemical inertness, which makes them very good nanocarrier system to deliver multi-functional drugs effectively. A huge number of researchers worldwide are working on CDs-based drug delivery systems to evaluate their versatility and efficacy in the field of pharmaceuticals. As a result, there is a tremendous increase in our understanding of the physicochemical properties, diagnostic and drug delivery aspects of CDs, which consequently has led us to design and develop CDs-based theranostic system for the treatment of multiple disorders. In this review, we aim to summarize the advances in application of CDs as nanocarrier including gene delivery, vaccine delivery and antiviral delivery, that has been carried out in the last 5 years.

KEYWORDS

carbon dots, drug delivery, gene delivery, nanocarriers, bioimaging

1 Introduction

First discovered by Walter Scrivens and his colleagues in 2004 (Xu et al., 2004), carbon dots (CDs) possess properties of good photostability, biocompatibility, adaptability, less cytotoxicity, high chemical inertness, easy method of synthesis, eco-friendliness, easy functionalization, non-blinking photoluminescence, and better water solubility. These properties make CDs suitable for use in various fields like drug delivery, bioimaging, and optoelectronics (Ren et al., 2019). In pharmaceuticals, CDs are mainly used as a nanomaterial for drug delivery in various disorders such as cancer, neurological disorders, eye diseases, infectious diseases and for gene delivery (Figure 1) (Zhang et al., 2019a). CDs have functional groups on their surfaces to enhance their water solubility and allow conjugation with organic, inorganic polymers and biomolecules for different applications (Singh et al., 2017). Functional groups, specifically amino, carboxyl, and hydroxyl groups on CDs surface also help further modifications that improve their biocompatibility, optical properties, target ability while increasing their sensitivity and selectivity (Zuo et al., 2016).

The application of CDs depends upon their interaction with the analytes. The interaction of analyte with CDs either decreases fluorescence by quenching or increases fluorescence by inhibiting the quenching effect. The CDs quenching mechanism consists of static quenching, energy transfer, dynamic quenching, photoinduced electron transferred, and inner filter

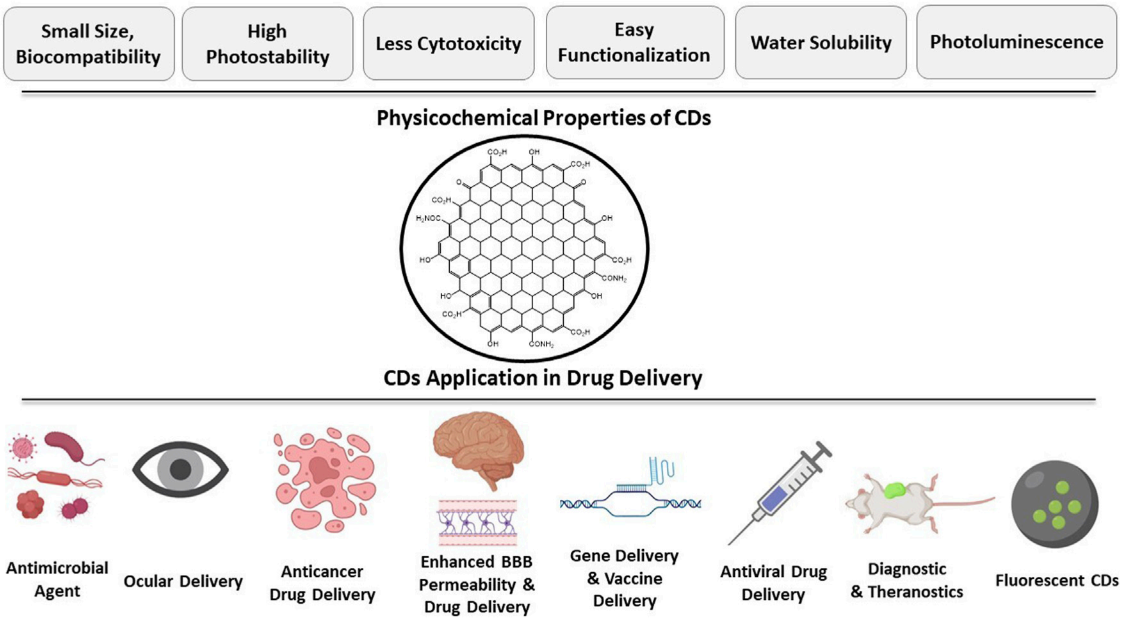

FIGURE 1
Applications of CDs in therapeutic drug delivery.

effect. Energy transfer further includes dexter energy transfer, fluorescence resonance energy transfer, and static energy transfer (Zu et al., 2017). CDs gives the advantage to choose surface functionality through electrostatic interaction for selective drug molecules (Singh et al., 2017). To date, different types of CDs have been synthesized for multiple purposes such as for therapeutic drug delivery, drug targeting, gene delivery, biosensing, chemical sensing, bioimaging electrolysis, etc. Researchers also discovered that under near infrared (NIR) light stimulation, CDs emit in the NIR spectral range, expanding its applicability in drug administration, bioimaging, photoacoustic imaging, and anticancer treatment. Due to the excellent photostability and fluorescent property, CDs can also be used as probes in analytical field (Zuo et al., 2016). Recently, green and red-emitting CDs are synthesized to characterize the normal cell and cancer cell through bioimaging (Zeng et al., 2016; An et al., 2021).

Reportedly, research shows that CDs can suppress growth of HepG2 human hepatocellular carcinoma cells (Li et al., 2014). It can also suppress breast cancer cells by generating a huge amount of reactive oxygen species (Hsu et al., 2013). CDs can pass the blood-brain barrier (BBB), which helps in treating brain-related diseases like Alzheimer's and brain tumor (Dong, 2018; Zhang W. et al., 2021). Worldwide, a significant number of researchers are working on CDs-based drug delivery systems to evaluate their versatility and efficacy in the field of pharmaceuticals. As per the reported scientific data, there is a tremendous increase in our understanding of the physicochemical properties, diagnostic and drug delivery aspects of CDs, which has helped researchers to design and develop CDs-based theranostic system for the treatment of multiple disorders. CDs has potential application in antimicrobial delivery, gene delivery, ocular delivery, cancer targeted delivery, vaccine delivery, antiviral delivery, drug targeting to neurological conditions and enhancing BBB penetration. In this review, we have discussed recent advances in CDs research with special emphasis on their drug delivery applications for different diseases.

2 Structure, method of synthesis and properties of CDs

2.1 Structure

Structurally, the average size of CDs is reported to be less than 10 nm and they may be either graphitic or amorphous in nature (El-Shafey, 2021). CDs exhibit dot like structure with varying size and surface morphology depending up on the selection of precursor and method of synthesis (Wang B. et al., 2022). Amorphous core shell structure with mixed sp^2/sp^3 hybridization is suggested by some researchers while others have suggested graphitic crystalline structure with sp^2 carbon (Mintz et al., 2021; Yadav et al., 2023). CDs are endowed with various functional groups on their surface, which may include hydroxyl (–OH), carboxyl (–COOH), aldehyde (–CHO), amino ($-NH_2$) and sulfhydryl (–SH) group. The type of functional group present on the surface is governed by the precursor used for the preparation of CDs which can further affect their properties. For example, oxygen containing functional groups imparts negative charge to CDs, whereas nitrogen containing functional groups give positive charge, and the difference in charge affects the passivation capabilities of CDs. Therefore, it is important to know the functional groups present on the surface of CDs that can be determined using various conventional techniques such as ninhydrin colorimetry for the determination of amino groups and Boehm titration for carboxyl group determination. The analytical attributes of CDs can be characterized by using transmission electron microscopy (TEM) and X-ray diffraction (XRD).

2.2 Synthesis of CDs

A wide range of methods are available for the preparation of CDs. An ideal method is the one that can synthesize CDs of uniform size, with high quantum yield (QY), scalable, and cost effective. CDs are generally synthesized by two methods, i.e., top-down and bottom-up.

2.2.1 Top-down method

The top-down approach for synthesis of CDs involves breakdown of large carbon precursors (graphene, ash, or soot) to generate nanosized particles (Carbonaro et al., 2019). Different top-down methods include arc discharge, oxidative cracking, laser ablation and electrochemical oxidation (Lim et al., 2015). The arc discharge method of making CDs has the limitation of forming non-uniform size CDs and purification. Other methods such as laser ablation and oxidative cracking uses toxic reagents passivation and are therefore not the preferred choice. The electrochemical oxidation method uses electrolytic graphite rods that can produce crystalline CDs with high photocatalytic activity (Ming et al., 2012). Moreover, the CDs produced by electrochemical oxidation method confer protection from immune-mediated hepatitis due to the interference with activation of T cells and macrophages and their inherent accumulation in liver. The CDs produced by electrolysis have fewer surface functional groups resulting in its poor water dispersibility. This deficiency can be overcome by adding surface functional groups via refluxing.

Top-down approaches provide the advantage of scalability and availability of abundant raw materials for the synthesis of CDs. However, it suffers from the limitation of producing CDs of non-uniform morphology with a wider size distribution. It may also introduce impurities in CDs that can affect its fluorescence property (Wang B. et al., 2022).

2.2.2 Bottom-up method

The bottom-up approach involves production of CDs using carbon precursors that are small organic molecules and polymers containing -OH, -COOH, and -NH_2 functional groups. The common procedure used involves dehydration followed by carbonization resulting in formation of CDs with stable properties and uniform morphology with narrow particle size distribution. The bottom-up approach for making CDs includes synthesis via microwave, hydrothermal method, template assisted, cage opening, etc. (Wang B. et al., 2022). Among these, microwave and hydrothermal methods have gained more attraction and are discussed in more detail herein.

2.2.2.1 Microwave

The microwave method used to synthesize CDs provides an efficient route due to its fast heating rate and reaction kinetics. This method produces CDs that are uniform in size and the size obtained can be controlled using microwave power and treatment time. Microwave causes the dehydration and pyrolysis of reaction precursor followed by carbonization to form CDs (Xu et al., 2016). Despite the benefits that microwave method offers, it suffers from the limitation of making unwanted byproducts and needs extensive purification process. Tables 1 and 2 shows several studies in which microwave method was used to make CDs that were later used for biomedical application.

2.2.2.2 Hydrothermal

This is the most commonly used method for CDs synthesis as it is reported to be ecofriendly and inexpensive. This method has gained a lot of popularity and is found to surpass the benefits of microwave methods. The CDs produced by hydrothermal method are endowed with hydrophilic surface functional groups such as -OH, -COOH, or -NH_2 groups and thus imparts good water dispersibility (Wang et al., 2019).

In the past few years, the synthetic procedures for the fabrication of fluorescent CDs have become significantly advanced. However, developing simple methods for the synthesis of multifunctional CDs with high QY is still challenging due to limited availability of raw materials and multiple variables involved in the process (Zuo et al., 2016; An et al., 2021). Recently, fabrication of CDs using plant material as a carbon source, such as orange juice (Sahu et al., 2012), beetroot extract (Singh et al., 2018), bread, jaggery and sugar (Sk et al., 2012), has been reported.

2.3 Properties of CDs

CDs have gained a lot of attraction in recent years due to their unique optical properties and biocompatibility. CDs possess optical properties which include absorption and photoluminescence. Due to these properties, CDs are reported to have potential application in the field of bioimaging and theranostics (Naik et al., 2022). CDs are also reported to have biocompatibility and low toxicity which allows the application of CDs as nanocarrier in the field of drug delivery and diagnostics (Biswal and Bhatia, 2021).

2.3.1 Absorption

The absorption behavior of CDs depends on its method of preparation and precursor carbon source. CDs show strong absorbance in the UV region of 200–400 nm and that further extends to visible range. The absorption bands in the visible region are assigned π- π^* *of* C=C bond or n- π^* transition of C=O/C=N bond (Adrita et al., 2020; Liu et al., 2020). Some CDs that emit red or near infrared (NIR) emission possess conjugated π domains that allow absorption in the range of 50–800 nm. Moreover, CDs absorption properties are further affected by the size of π conjugated domains, type and content of surface functional groups, and the oxygen/nitrogen content of the carbon cores (Biswal and Bhatia, 2021).

2.3.2 Photoluminescence

Photoluminescence is one of the most important properties of CDs finding wide range of applications especially in the field of biomedical sciences. Various parameters such as size, morphology, internal structure, and composition affect the photoluminescence of CDs. Moreover, the method of synthesis, surface passivation, and the precursor used regulates

TABLE 1 Recently reported CDs as antimicrobials and their applications for delivery of antimicrobials.

No.	Nanomaterial	Precursor	Method of preparation	Applications	Ref.
1	Nitrogen co-doped CDs-genipin covalent conjugate (N-CDs-GP)	Genipin	Hydrothermal Method; QY was 4.7%	Antibacterial agent, Selective Gram-positive bacterial	Chu et al. (2020)
2	Nitrogen-doped CDs (N-CDs)	Meta-phenylenediamine	Hydrothermal Method; QY was 12%	Eradication of Gram-negative and Gram-positive bacteria	Saravanan et al. (2020)
3	Nitrogen-doped CDs (N-CDs)	polyethylenimine (PEI) and citric acid (CA)	Hydrothermal Method; QY was 53%	Inhibition of bacteria and good topical delivery	Demirci et al. (2020)
4	Nanofiltration Membrane Nitrogen-doped CDs (N-CDs)	Polyethersulfone (PES)	Hydrothermal technique	Improved anti-microbial results as compared to the plain PES	Koulivand et al. (2020)
5	Photoluminescent CDs	Wheat bran conjugated with amoxicillin	Hydrothermal method; QY was 33.23%	Minimal cytotoxic, Increased Drug Loading Efficiency, Drug Delivery of Amoxicillin	John et al. (2020)
6	Nitrogen, sulphur co-doped graphene quantum dots (N, S-GQDs	Octa-imine substitution of zinc phthalocyanine (ZnPc)	π-π stacking	Antimicrobial PDT	Sen and Nyokong (2021)
7	CDs	Citric acid	One-pot microwave-assisted synthesis	Photodynamic antimicrobial action, useful for treating wounds infected with Gram-positive bacteria	Romero et al. (2021)
8	Fluorescent surface-quaternized CDs (JB-CDs)	Jute caddies, benzalkonium chloride	Sonochemical method of preparation	Chemical sensing, Antibacterial Activity, Nanocarrier for ciprofloxacin delivery	Das et al. (2020)
9	Fluorescent CDs	Levofloxacin hydrochloride	Hydrothermal method	Antibacterial activity, Synergetic mechanism of CDs with Levofloxacin hydrochloride	Liang et al. (2021)
10	CDs	*Curcuma longa*	Hydrothermal method	Antibacterial activity against Gram-positive and Gram-negative bacteria	Saravanan et al. (2021)
11	Chlorhexidine gluconate CDs (CGCDs)	Chlorhexidine gluconate	Hydrothermal method	Antibacterial effect against both Gram-positive and Gram-negative bacteria	Sun et al. (2021)
12	Blue–green emitting CDs (CDs)	Glucose, citric acid, polyethylenimine	Hydrothermal method; QY was found to be 14%	Antibacterial activity against Gram-negative and Gram-positive Bacteria	Zhao et al. (2021)
13	Negative-charge CDs (CDs)	Citric acid, Urea	Microwave assisted synthesis	Antimicrobial therapy	Kung et al. (2020)
14	Fluorescent blue/green CDs	Oyster mushroom (*Pleurotus species*)	Hydrothermal method	Antibacterial activity against Gram-negative and Gram-positive Bacteria	Boobalan et al. (2020)
15	CDs	*P*-phenylenediamine	One-step hydrothermal method	Antibacterial activity for both Gram-negative and Gram-positive Bacteria	Ye et al. (2020)
16	CDs	Citric acid and β-alanine	One-pot microwave-assisted synthesis	CDs are a viable alternative to commercially supplied antibiotics	Pandey et al. (2021)
17	Xylitol CDs (XCDs)	Xylitol (XLT) conjugated with ketoconazole and tetracycline	Microwave-assisted carbonization	Good drug carrier and at low dose high inhibition was reported	Ahuja et al. (2021)
18	Levofloxacin-basedCDs (LCDs)	Levofloxacin hydrochloride	One-step hydrothermal method	Greater antibacterial activities and low drug resistance	Wu et al. (2022)

the photoluminescence of CDs. Among the methods, synthesis via hydrothermal carbonization and microwave are found to augment the photoluminescence of CDs. For passivation, polyethylene glycol (PEG) and polyethylenimine (PEI) are some of the commonly used passivating agents (Biswal and Bhatia, 2021). Studies have shown that imparting chirality to CDs results in enhanced light stability and provides long term imaging. The addition of L-cysteine to the surface of CDs forming L-CDs allows precise imaging of dynamic changes in the Golgi apparatus in the early stages of an infection (Li et al., 2017).

2.3.3 Toxicity of CDs

The increased possibility of the use of CDs in humans has mandated the evaluation of its toxicity profile. The toxicity of CDs can be evaluated by *in vitro* and *in vivo* methods. For *in vitro* methods, assays such as MTT or WST-1 are frequently used in which cultured cells are exposed to CDs and cell viability is determined and compared with the positive control and naïve group (Zhang M. et al., 2021). For *in vivo* study, CDs are administered to mice or zebra fish and toxicity is assessed through blood analysis, hematological analysis, and inflammatory analysis on various organs such as kidney, spleen, liver, etc (Singh

TABLE 2 Drug delivery application of carbon dots in treatment and diagnosis of cancer.

No.	CD type	Precursor	Method of preparation	Anticancer drug	Applications	Ref.
1	Fluorescent CDs	κ-carrageenan and folic acid	Facile hydrothermal process; quantum yield (QY) obtained was 76.12%.	Capecitabine (cap)	Can be used as nano-vehicle for anticancer drug, biomedical studies and cancer cell targeting	Das et al. (2019)
2	Fluorescent CDs	Polyethylene glycol (PEG), gelatin	Microwave carbonization; QY obtained was 34%.	Methotrexate (MTX)	CDs-PEG showed good antitumor efficacy than free MTX	Arsalani et al. (2019)
3	Mesoporous silica nanoparticles (MSNs) coated with CDs and poly-N-vinylcaprolactam (PNVCL)	Poly (N-vinylcaprolactam) (PNVCL)	Schiff base reaction	Doxorubicin (DOX)	Controlled drug release; CDs showed low toxicity and killed cancer cells without affecting normal cells	Li et al. (2020a)
4	Red-emissive carbon quantum dots (CQDs)	Nitrogen	One-step solvothermal method; QY was 20%	DOX	CQDs can be targeted to nuclei of the cancer cells and cancer stem cells	Su et al. (2020a)
5	5-ALA-CQD-Glub-CD based nanocarrier system	5-aminolevulinic acid, mono-(5-BOC-protected-glutamine-6-deoxy) β-cyclodextrin (COD-Glu-β-CD)	Hydrothermal method	DOX	Chemo/photodynamic synergistic effects on cancer therapy, ROS production causes cell damage and morphological alterations in breast MCF-7 cell line	Li et al. (2020b)
6	Fluorescent CDs	Polyethylenimine (PEI)	Microwave hydrothermal carbonization	DOX	Improved and prolonged drug release, CD-PEI-DOX showed better cytotoxic effect in liver cancer cells (MHCC-97L and Hep3B) as compared to plain DOX	Hailing et al. (2020)
7	DOX-CDs	Citrate and urea	Hydrothermal method	DOX	Biomedical imaging showed excellent aqueous stability, photoluminescence property, and a high quantum yield of 93%. Intracellular drug delivery, DOX-CDs showed cytotoxicity in ovarian cancer cell line H0-8910	Sun et al. (2020)
8	CDs	Folic acid	Hydrothermal method; QY was 97%.	DOX	Potential in biological imaging and in drug delivery, better targeting ability and stronger fluorescence intensity of FA-CDs-DOX makes it easy to penetrate tumor tissue and skin	Wang et al. (2020)
9	Nitrogen doped carbon quantum dots (CQD)	Citric acid and urea	Hydrothermal method	5-Fluorouracil (5-FU)	5-FU-CQD nanoconjugate can improve effectiveness and reduced side effects of 5-FU	Cutrim et al. (2021)
10	Fluorescent CQD	o-phenylenediamine	Synthetic microplasma liquid method	---	Good solubility, non-toxic, and high biocompatibility, photodynamic therapy for treating cancer. Yellow fluorescence can be used for marking HeLa cancer cells	Qin et al. (2021)
11	Red emissive polymer CDs	Thiophene phenylpropionic acid	Hydrothermal method	Coptisine	High drug loading efficiency (>96%), prolonged drug release and improved effectiveness against cancer cells, tumor-targeting potential and drug release tracer	Ren et al. (2021)
12	CQDs	Gallic acid (GA) used as carbon resource, folic acid was used as the nitrogen resource and citric acid monohydrate (CA) was used as the auxiliary carbon source.	Microwave-assisted method	Gallic acid	Showed good targeting imaging and antitumor abilities towards HeLa cells	Lv et al. (2021)

(Continued on following page)

TABLE 2 (*Continued*) **Drug delivery application of carbon dots in treatment and diagnosis of cancer.**

No.	CD type	Precursor	Method of preparation	Anticancer drug	Applications	Ref.
13	CDs	Ethylenediamine	Hydrothermal method	Curcumin (Cur)	Excellent solubility, Improved stability and enhanced bioavailability of CurCDs as compared with plain curcumin	Sharma et al. (2021)
14	CDs	Aldehyde precursors, chitosan	Solvothermal method	Chitosan nanocomp-osite hydrogels	3D nanocomposite prepared for microRNA-21 detection in MCF-7 breast cancer cells (LOD—0.03fM) showed low probe cytotoxicity	Mohammadi et al. (2021)
15	CDs	GSH-sensitive carbonyl vinyl sulfide linkage, and surface decoration with biotin	Direct conjugation	6-Mercaptopu-rine (6-MP)	Showed excellent stability, lower cellular toxicity and good activity against MCF-7 and HepG2	Talib and Mohammed (2021)
16	CDs	Folic acid	Microwave assisted method	DOX	Excellent therapeutic and diagnostic capability	Fahmi et al. (2021)
17	Nitrogen and sulphur co-doped fluorescent CDs	Methyl-β-cyclodextrin (Me-β-CD)	Hydrothermal method	Mitoxantr-one (MTO)	CDs exhibited biocompatibility and greater photobleaching which can be used in cell imaging and drug tracking	Wen et al. (2020)

et al., 2018). The prevalence of reports on the toxicity of CDs suggests that CDs are either non-toxic or minimally toxic. The toxicity of CDs depends on their individual physicochemical properties such as surface charge, concentration, photolysis, etc. It has been found that a positive charge on CDs is mainly responsible for its toxicity. Further studies have revealed that increased surface charge density causes significant oxidative stress, IL-8 release, and mitochondrial dysfunction resulting in airway inflammation or allergen-induced immune response (Weiss et al., 2021).

One of the *in-vitro* studies used HeLa cells for toxicity evaluation of reactive red 2 (RR2), a raw material used for the synthesis of CDs. The results obtained showed that CDs prepared from RR2 showed 70% more cell viability than its precursor, RR2. The *in vivo* studies performed on zebra fish showed reduced cytotoxicity of CDs and thus further confirmed its safety at preclinical level (Chen W. et al., 2021; Wang B. et al., 2022). Furthermore, to evaluate the biological distribution of CDs in mammals, radiolabeling of CDs was done and the results revealed that CDs were eliminated via kidney and fecal excretion (Tao et al., 2012). This indicates that CDs does not get accumulated and have negligible toxicity *in vivo*.

3 CDs applications in drug delivery

3.1 CDs in antimicrobial drug delivery

Microbial infection is caused by a number of microorganisms such as *Escherichia. coli, Salmonella typhimurium, Streptococcal pneumoniae Bacillus cereus, Mycobacterium tuberculosis, clostridium perfringens, and Staphylococcus aureus* (Cui et al., 2020). There is a wide range of antibiotics which are used against these infectious diseases. Inconsistent and regular use of antibiotics are now the main cause of developing antimicrobial resistance (AMR) among humans. Due to AMR, small injuries and common infections will become life-threatening diseases (Zhao et al., 2019). Thus, it is necessary to develop an antimicrobial substrate against resistant bacteria. CDs have significant potential for microbial imaging and itself acts as antimicrobial agents owing to their physicochemical and optical properties which includes simple method of preparation, low toxicity, excellent photostability, good water dispersibility, and flexible surface functionalization (Dong et al., 2020). Antibacterial mechanism of CDs occurs via electrostatic interaction between negatively charged bacterial cell walls and positively charged CDs. It will cause bacterial cell wall lysis and cell apoptosis. CDs acts as a photosensitizer nanomaterial for detection and photodynamic inhibition of bacterial strains, which is a one of the most prominent approaches to fight against multidrug resistance (MDR) pathogens (Figure 2) (Ghirardello et al., 2021).

3.1.1 Antimicrobial applications of nitrogen-doped CDs

Antibacterial activity of CDs mainly depends upon the nitrogen (N) content and their surface charges. In this context, many studies utilized amines or quaternary ammonium salts as precursors for cationic group-based CDs probes synthesis. Also, phosphorus and sulphur-doped CDs were reported as antimicrobials (Ghirardello et al., 2021). Chu et al. (2020), produced nitrogen co-doped CDs-genipin covalent conjugate (N-CDs-GP) for Gram-positive bacterial bioimaging and as antibacterial agents. Saravanan et al. (2020), synthesized nitrogen-doped CDs (N-CDs) in which meta-phenylenediamine was used as a source of carbon and nitrogen. The N-CDs showed bright blue color fluorescence emission with a quantum yield of 12% and inhibited the Gram-negative *E. coli* and Gram-positive *S. aureus* at a minimum inhibitory concentration (MIC) of 1 and 0.75 mg/mL, respectively. N-CDs were also used as nanocarrier for ciprofloxacin that was used as a model drug and its

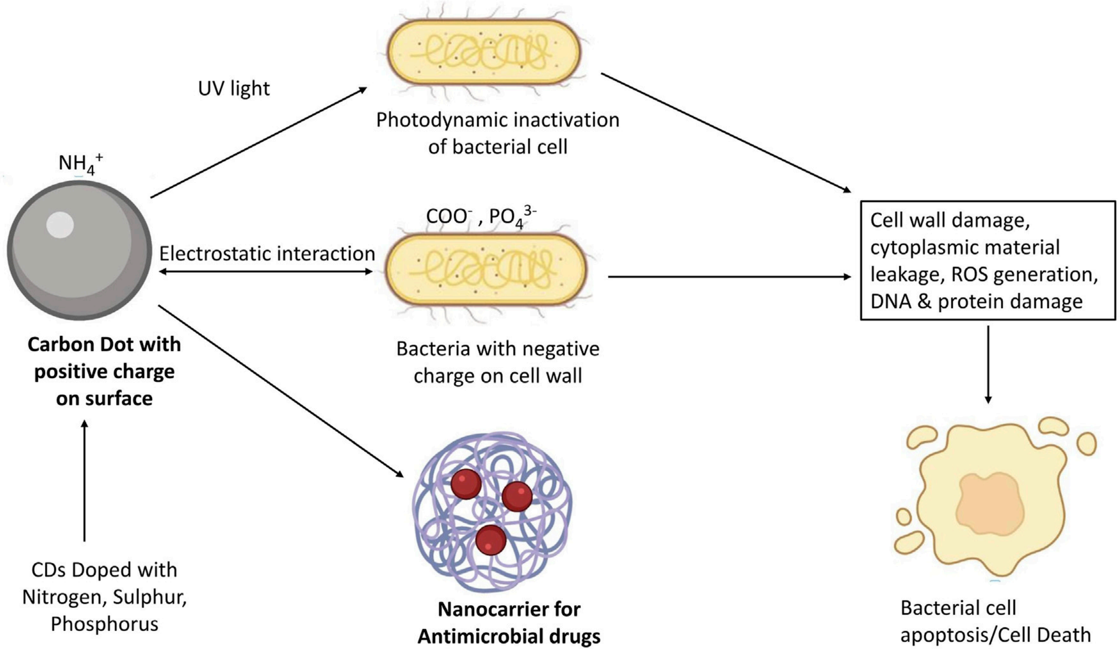

FIGURE 2
Mechanism of CDs for antimicrobial activity.

release was proven time-dependent. The release kinetics followed Korsmeyer-Peppas model at the physiological pH. Also, trinitrophenol (TNP), an explosive, was analyzed by using N-CDs via fluorescence quenching (Saravanan et al., 2020). Zhao et al. (2019), developed nitrogen and phosphorus co-doped CDs (N, P-CDs), which were used as effective antibacterial material against *S. aureus* and *E. coli*. The developed CDs were also utilized for fluorescence imaging of *S. aureus*, and as a fluorescence probe for the detection of Sudan Red I (Zhao et al., 2019). Demirci et al. (2020), prepared N-CDs using PEI and citric acid (CA) as starting material. The N-CDs were prepared at a yield of 53% ± 4.8% as per quinine sulfate standard using PEI:CA in 1:1 wt. ratio. These N-CDs inhibited the development of both Gram-negative and Gram-positive bacteria without any toxicity to *in vitro* mammalian cells. Additionally, skin permeation studies indicated good permeation of CDs into and through the dermis, showing their topical administration potential (Demirci et al., 2020). Koulivand et al. (2020), prepared N-CDs added to polyethersulfone (PES) to create new antifouling and antibacterial nanofiltration membranes using hydrothermal technique. All the N-CD-blended membranes displayed improved performance compared to the plain PES when evaluated. It also showed a flux recovery ratio (*FRR*) of 73.1% revealing its antifouling properties. Membrane showed inhibition of both Gram-positive and Gram-negative bacteria in antibacterial assessment showing antibacterial potential of N-CD-blended membranes (Koulivand et al., 2020).

John et al. (2020), developed photoluminescent CDs from wheat bran using hydrothermal method in which they conjugated CDs with amoxicillin (AMX) in order to assess the application of CDs for delivery of antimicrobial drug. CDs showed blue-green fluorescence emission and higher drug loading efficacy of 69.8% particularly in CD-AMX: 2-800. CD-AMX release profile was tested in different pH conditions (5, 6.8, and 7.2) and showed initial rapid release followed by sustained release up to 70 h. The CD-AMX conjugate showed faster release in acidic conditions (pH-5.0) due to protonation of AMX β-lactam ring in acidic conditions, and thus showed that the conjugate CD-AMX confer sustained pH-sensitive drug delivery. MTT assay was performed at various dilution of CD-AMX prepared using ratio of CD-AMX:2-400 and results showed higher survival rate of 92.23% using 25% diluted CD-AMX. Prepared CDs showed effectiveness against Gram- negative and Gram- positive bacteria with causing significant toxicity, showing its potential as a promising carrier for antibacterial drug delivery (John et al., 2020). Antimicrobial photodynamic therapy (PDT) is an alternate therapeutic technique which is cost-effective and practicable. For this objective, octa-imine substituted zinc phthalocyanine (ZnPc) was synthesised and attached to nitrogen, sulphur co-doped graphene quantum dots (N, S-GQDs) through π-π stacking. Prior to *in vitro* cell studies, the photochemical and photophysical properties of Pc alone and Pc-conjugated to the GQD nanomaterial were investigated in solutions, including fluorescence, absorption, fluorescence lifetime, singlet oxygen quantum yields, triplet state quantum yields, and excited state lifetimes. Results showed that photodynamic inactivation increased with ZnPc conjugation to N, S-GQDs (Sen and Nyokong, 2021).

3.1.2 CDs-mediated delivery of antimicrobials

Romero et al. (2021), studied antimicrobial photodynamic effect of CDs developed from citric acid against *S. aureus* suspension and biofilm. *In vivo* studies were conducted in mice with wounds contaminated with *S. aureus*. The viability test showed 10^4 log reduction in bacterial count on the skin lesions via CDs-mediated photodynamic inactivation. These findings showed promising application of CDs based antibacterial PDT in the treatment of wounds infected with Gram-positive bacteria (Romero et al., 2021). Das et al. (2020), prepared fluorescent surface-quaternized CDs (JB-CDs) sonochemically from jute caddies and modified their surface characteristics by adding benzalkonium chloride (BZC). Results showed that JB-CDs exhibited good water solubility, photostability and excitation-dependent emission. These JB-CDs were used as a fluorescent nano switch for the detection of inorganic pollutants in aqueous solutions, such as chromium (VI) [Cr (VI)] ions. To confirm antibacterial activity, JB-CDs were tested against *S. aureus* and *E. coli* indicating substantial inhibition of bacterial growth. Apart from this, JB-CDs were studied as nanocarrier for drug delivery of ciprofloxacin. *In vitro* release study results showed pH-responsive controlled release behavior of JB-CDs at physiological pH (Das et al., 2020). In another study, Liang et al. (2021), reported antibacterial activity of CDs incorporated with levofloxacin hydrochloride. CDs showed capable antibacterial properties against both Gram-positive and Gram-negative bacteria without causing any cytotoxicity. Mechanism of antibacterial action of CDs included their physical/chemical attachment to cell membrane, surface wrapping and then cell membrane breakdown, which caused increased production of reactive oxygen species (ROS) within the cell without the use of additional light or oxidant (Liang et al., 2021). Saravanan et al. (2021), prepared CDs from *Curcuma longa*, which were examined for their antibacterial efficacy against Gram-positive bacteria, *S. aureus* and *S. epidermidis*, and Gram-negative bacteria, *E. coli* and *K. pneumoniae*. Sun et al. (2021), performed a study in which chlorhexidine gluconate-derived CDs were divided into three groups on the basis of their particle size by applying different molecular weight cut-off membranes. Their findings revealed that antibacterial activity against Gram-negative bacteria and Gram-positive bacteria improves as CDs size decreases. This phenomenon might be caused by changes in the cellular absorption and CDs distribution in the cell membrane, or by a limitation between the polar functional group and the DNA molecule (Sun et al., 2021). Zhao et al. (2021), synthesized CDs with blue-green fluorescence under low reaction temperature (30 min, 60°C). The inhibitory action of developed CDs against diverse microbes, including bacteria and fungus, were compared using inhibition zone tests and minimum inhibitory concentration (MIC) studies (Zhao et al., 2021). In another study, negative charge CDs were prepared from citric acid and urea as precursors and evaluated for their antibacterial action against MDR bacteria. Results revealed that the developed CDs have the potential to be effective against MDR *S. aureus* and can be used as an alternative to antibacterial treatment (Kung et al., 2020). Boobalan et al. (2020), developed fluorescent blue/green CDs using oyster mushroom and demonstrated their antibacterial activity. Ye et al. (2020), developed CDs for antibacterial action against *S. aureus* and *E. coli* using *p*-phenylenediamine as carbon source through a simple hydrothermal method. The minimum bactericidal concentrations of the CDs were found to be 2 and 30 μg/mL, against *S. aureus* and *E. coli*, respectively (Ye et al., 2020). Similarly, Pandey et al. (2021), prepared CDs from citric acid and β-alanine. Its antimicrobial activity was studied against several Gram-negative bacteria, including *E. coli*, *Salmonella*, *Agrobacterium*, *Pseudomonas*, and *Pectobacterium* species. Results from this showed that CDs can act as an effective alternate to commercially available antibiotics (Pandey et al., 2021). Ahuja et al. (2021), synthesized CDs using xylitol (XCDs) which were conjugated with antimicrobial drugs ketoconazole and tetracycline for fungi and bacteria, respectively. Results showed higher inhibitory potential with reduced dose of antimicrobials using XCDs as compared to xylitol against *C. neoformans, C. albicans, S. pyogenes*, *E. coli*, *L. monocytogenes* and *S. typhi.* Drug delivery was also improved in the presence of XCDs showing drug carrier potential of CDs (Ahuja et al., 2021). Levofloxacin-based CDs (LCDs) with low drug resistance and greater antibacterial activities were developed by Wu et al. (2022). *In vitro* and *in vivo* studies showed excellent antibacterial activity of LCDs (Wu et al., 2022). The antibacterial activity of recently reported CDs and their applications in delivery of antimicrobials are summarized in Table 1.

More research in the use of CDs as antimicrobials can be explored by preventing ROS from damaging the normal cells. To further improvise the antimicrobial efficacy, it is needed to investigate the use of high performing precursor as a source of carbon for the synthesis of CDs and that should be water soluble and dispersible for ease of penetration and delivery.

3.2 CDs in ocular drug delivery

Ocular infection such as bacterial keratitis or endophthalmitis are not uncommon and various nanomaterials such as silver, copper oxide, iron oxide, titanium oxide, and zinc oxide particles received attention for their anti-bacterial properties. However, the toxicity of these inorganic materials and metal oxide poses a major concern and can be circumvented with the use of CDs. Moreover, the small nanoparticle size of CDs (<10 nm) further makes them suitable drug delivery vehicle as it causes no or minimal irritation in the eyes following administration (Garner et al., 2020).

Though CDs have good potential in novel biomedical applications due to their physicochemical properties like biocompatibility, fluorescence, and conjugation ability with various therapeutic agents, there are limited studies available regarding their applications for ocular drug delivery (Garner et al., 2020). Jian et al. (2017), developed an antibacterial agent for topical treatment of bacterial keratitis (BK) using carbon quantum dots (CQDs). The possible antibacterial mechanism suggested that the super-cationic CQDs prepared by direct pyrolysis of spermidine (Spd) (CQD_{Spds}) had a small size and a large positive charge which ruptured the bacterial membrane. In addition, topical ocular application of CQD_{Spds} can cause the tight junction of corneal epithelial cells to open, resulting in a significant antibacterial effect in rabbits with *S. aureus* induced BK. These findings demonstrated CQD_{Spds} to be a viable antibacterial option for the treatment of eye-related bacterial infections and even chronic bacteria-induced illnesses (Jian et al., 2017). Shoval et al. (2019), developed ocular nanomedicine using hybrid aptamer modified-CDs for controlled release of inhibitors of vascular endothelial growth factor (VEGF), which plays a main role in the pathogenesis of angiogenic ocular diseases. The hybrid nanoparticles were made using CDs that had been functionalized with the VEGF aptamer. The hybrid CDs efficiently suppressed

VEGF-stimulated angiogenesis in choroidal blood vessels in both *in vitro* and *in vivo* models (Shoval et al., 2019). Wang et al. (2022b), developed ocular drug delivery system based upon CDs embedded in thermosensitive *in situ* gel for the topical administration of diclofenac sodium (DS). *In vitro* results showed sustained release of DS for 12 h and *ex vivo* fluorescence delivery indicated that this system could be used for cell imaging and ocular tissues tracing. A positive charge on the composite of DS-CD along with the gel prolonged the precorneal retention and thus improved the bioavailability (Wang et al., 2022b). In another study, Wang et al. (2021a), prepared a composite system for ocular delivery that combined self-targeted CDs and thermosensitive *in situ* hydrogels. Electrostatic interactions were used to load DS onto the surface of CDs, resulting in DS-CDs nanoparticles that have the characteristics of biphasic drug release. The *in vivo* fluorescence and corneal penetrability studies revealed that drug retention duration was extended, and corneal transmittance was increased. The DS-CD Gel demonstrated high cytocompatibility and CD44 targeting in cellular studies (Wang et al., 2021a). There are only limited number of scientific reports available on CDs application in the ocular field, therefore the potential application of CDs in this area needs to be explored further.

3.3 CDs for drug delivery in the brain

The human brain is the most complex interconnected network and the most important part of the body. Major causes for brain disorders are illness, genetic changes and traumatic injury. Main hurdle for drug delivery in brain is the BBB (Dong, 2018). Drug delivery across the BBB is very challenging, particularly in brain tumor and Alzheimer's disease (AD). Most remedies and drugs have limited application when it comes to brain delivery due to their inability to cross the BBB. To that end, some exciting research is being performed to enhance the delivery of therapeutic agents to the brain using nanomaterials, especially CDs. CDs were reported to cross the BBB through passive diffusion owing to their very small size, amphiphilicity, positive surface charge and receptor-mediated endocytosis (Zhang W. et al., 2021).

3.3.1 CDs-mediated BBB permeability

CDs also have limitations regarding BBB penetrability as other small molecules. Mintz et al. (2019), proposed that if CDs can be synthesized from a precursor molecule that can cross the BBB, there are chances that the attached original precursor molecule with the CDs can enter the brain. As a result, they produced tryptophan CDs utilizing the amino acid method for crossing the BBB via LAT1 transporter-mediated endocytosis. Urea and 1,2-ethylenediamine were used as nitrogen source to develop tryptophan CDs. These CDs were evaluated in zebrafish central nervous system to assess their BBB permeability. Results revealed that CDs prepared with tryptophan amino acid acted as a promising carrier system for drug delivery and imaging in the brain (Mintz et al., 2019). Zhou et al. (2019), synthesized yellow-emissive CDs (Y-CDs) as promising drug nanocarriers across BBB using *o*-phenylenediamine and citric acid as raw material. The ability of synthesized Y-CDs to cross BBB was evaluated in wild-type zebrafish using confocal image analysis. Results showed that Y-CDs crossed the BBB most possibly by means of passive diffusion owing to their amphiphilic nature. Furthermore, Y-CDs suppressed the overexpression of human amyloid precursor protein (APP) and amyloid (A), both of which are involved in AD pathogenesis. Hence, results suggested the drug delivery potential of Y-CDs in brain as well as their ability to inhibit Aβ-related pathology in AD (Zhou et al., 2019). Zhou et al. (2020), directly conjugated two different CD models, black CDs (B-CDs) and gel-like CDs (G-CDs) for potential application of CDs as nanocarrier for brain delivery. As a result of conjugation, black-gel CDs (B-G CDs) possessed properties from both CDs, such as greater thermostability, better aqueous stability and red-shifted photoluminescence emission. Also, nanostructure formed with the decreased mass ratio of B-CDs to G-CDs showed good potential of CDs as Lego-like building blocks. Moreover, zebrafish bioimaging exhibited the bone targeting and BBB crossing potential of B-G CDs (Zhou et al., 2020). Despite showing promising drug carrier potential, a better understanding of drug loading capacity and release kinetics needs to be investigated. Few *in vitro* studies have shown CDs to produce an immune response at high concentrations (Lategan et al., 2018). Therefore, it is also important to optimize the dose of CDs for future clinical studies.

3.3.2 CDs as nanocarriers for delivery of neuroprotective drugs

In order to treat a brain-related medical condition, delivery of therapeutic agent across BBB was a major bottleneck. Since CDs have the ability to cross BBB, various therapeutic agents can be delivered in desired concentration to achieve a desired pharmacological effect in the brain. Herein, we have discussed studies showing efficacy of CDs in delivering therapeutic agents either *in vitro* or *in vivo*. Hettiarachchi et al. (2019), developed CDs based triple conjugated system for delivering drug in glioblastoma brain tumors. Triple conjugated system of CDs was formed with targeted ligand transferrin and anticancer drugs, temozolomide and epirubicin. Glioblastoma brain tumor cell lines were used for *in vitro* evaluation. The efficacy of the synthesized triple conjugated CDs system was compared to free drug combinations, non-transferrin CDs–drugs, and dual conjugated systems (single drug conjugation along with transferrin). Triple conjugated CDs system at a very low concentration showed the lowest cell viability. Moreover, the triple conjugated CDs system caused more cytotoxicity to brain tumor cell lines as compared to other groups (Hettiarachchi et al., 2019). Chung et al. (2020), developed β-amyloid (Aβ) protein targeted photomodulating CDs for treatment of AD, as Aβ peptide aggregates worsen neuropathy and cognitive impairment in AD. Similarly, nanocarrier ability of carbon nitride dots (CNDs) were evaluated for targeted pediatric glioblastoma cells using gemcitabine as model drug by Liyanage et al. (2020). In another work, Li et al. (2021), created new boron-containing CDs (BCDs) for boron neutron capture therapy (BNCT) for glioma treatment with higher water solubility and excellent optical properties for tracing ^{10}B *in vitro* and *in vivo*. Fluorescent imaging showed internalization of BCD–Exosomes around the nuclei of U-87-MG glioma cells *in vitro*. Prominent BNCT effect of the BCD–Exosomes-treated brain glioma in the mice model was demonstrated with 100% survival ratio (Li et al., 2021). CDs derived from metformin (Met-CDs) were developed for mitochondrial and nucleus localizations along with BBB penetration. Bioimaging studies showed Met-CDs penetration in the cell membrane and their localization specifically inside the cancer cells mitochondria. *In vivo* study performed in zebrafish study confirmed BBB penetrability of Met-CDs without the prerequisite of any other ligands (Kirbas Cilingir et al., 2021). Zhang et al. (2021c), derived novel *Crinis Carbonisatus* CDs (CrCi-CDs) obtained from carbonization of human hair, and investigated their neuroprotective effect against cerebral infarction in stroke. Neuroprotective study results in *in vivo* middle cerebral artery occlusion (MCAO) model showed significant reduction in neurological deficits (Zhang et al., 2021c). Presently, most CDs based nanocarriers showed BBB penetration ability which depends upon specific ligands for ligand-mediated endocytosis. So, self-targeting CDs with potential of penetrating the BBB need to be explored further by considering various precursors, drug and nanocarrier compared to non-self-targeting CDs. Apart from this, CDs mechanism for BBB penetration need to be understood well for their CNS drug delivery applicability (Zhang W. et al., 2021).

3.4 CDs as nanocarrier for gene delivery

Progress of novel multifunctional gene delivery systems with greater efficacy is important. In recent years, CDs has emerged as an imaging-trackable nanocarrier for gene delivery applications which may yield nanoparticles with positive charge for interaction with the nucleic acids bearing negative charge (Mickaël et al., 2019; Mohammadinejad et al., 2019). Due to their high transfection efficiency (TE), CDs can be used efficiently for plasmid DNA and siRNA delivery to the targeted cells without any toxic effects (Mohammadinejad et al., 2019). He et al. (2019), synthesized CDs from Gd(III) salts/complexes (L-CD/C-CD), cationic polymers, and citric acid for application in gene delivery and multi-modal (MR/FL) imaging. *In vitro* gene transfection studies using L-CD exhibited 74 times higher efficiency of transfection and anti-serum abilities compared to PEI 25 kDa. Gene delivery process was evaluated by confocal laser scanning microscopy, which showed blue or green fluorescence in HeLa cell lines. Besides, the L-CD/C-CDs possess appropriate particle size that resulted in increased buildup at the tumor location via the enhanced permeability and retention effect (EPR) thereby proving it to be more effective than a widely used contrast agent, i.e., Gd-DTPA (diethylenetriamine penta-acetic acid) in *in vivo* tumor-specific MRI imaging (He et al., 2019a). Another study from the same lab also reported two cationic polymer-derived CDs with blue fluorescence for creating biocompatible, multipurpose gene vectors with high TE (He et al., 2019b). Mickaël et al. (2019), developed cationic CDs by citric acid/bPEI600 (1/4, w/w) pyrolysis to remove the unreacted low molecular weight reagents which causes nanoparticles separation problem from residual polymer that is harmful to cells. Eleven CDs exhibiting greater water solubility were developed after evaluating reaction conditions and activation modes. CDs showed noticeable variation in their gene delivery efficiency in epithelial cell line A549 using a pDNA encoding the *Gaussia princeps* luciferase gene after having similar physical properties. CDs synthesized in domestic oven under microwave irradiation revealed to be superior to all the other CDs. It was also compared with the bPEI25k, gold standard transfection reagent which is associated with cytotoxicity. Results showed that optimal CD/pDNA w/w ratio shifted down to 2 while it was ca. 4 with bPEI25k and thus limiting the toxicity associated with bPEI and related compounds (Mickaël et al., 2019). Chen et al. (2020), synthesized hydrophobically modified CDs from PEI via an epoxide ring-opening reaction. Study results presented the dual-channel imaging capability of CDs, due to which intracellularly delivered DNA can be tracked. Oleyl-modified-CDs showed 200 times more TE as compare to PEI 25 kDa in the presence of serum in A549 cells (Chen et al., 2020). In another study, CDs PAMAM nanohybrids were developed by self-assembling of CDs and G4-G6 (polyamidoamine) PAMAM-NH2 dendrimers for transfection and bioimaging purposes. The nanohybrids were found to be more photostable, compared to pristine CDs. These nanoscale hybrids were internalized in the cells with excellent TE thereby proving promising applications in the biomedical field (Martins et al., 2021). In summary, more studies are needed to fully understand the interaction of CDs with living cells and to further explore their potential in living cells or species that are resistant to transformation. More work needs to be pursued at the clinical level for efficient bench-to-bedside translation of CDs as a carrier for gene delivery.

3.5 CDs as nanocarrier in anticancer drug delivery

Cancer refers to a group of diseases which can affect any part of the body causing uncontrollable and abnormal cell growth which potentially invades or spreads to the adjoining parts of the body. Over 100 types of cancer forms are there which are affecting humans worldwide. As per World Health Organization, it is estimated that cancer-related deaths are expected to increase to around 13.1 million by the year 2030 (Stewart and Kleihues, 2003). Advancements of various nanotechnology tools is being used for the treatment of various deadly diseases including cancer (Montané et al., 2020). CDs belonging to the family of carbonaceous nanomaterials are identified as potential candidates in nanotheranostics for the treatment, bioimaging and early diagnosis of cancer due to their exclusive optical properties and intrinsic theranostic properties, which are summarized in Table 2 (Jia et al., 2020; Singh et al., 2021).

Recent studies showed greater potential of CDs as nanocarriers in the field of cancer drug delivery and biological imaging. Das et al. (2019), developed sulfur and nitrogen doped photoluminescent CDs from κ-carrageenan and folic acid for cancer cell targeting. The folate receptor present on cancer cells led to remarkable cancer cells targetability by CDs which makes them a potential tool for biomedical studies as shown in Figure 3 (Das et al., 2019). Arsalani et al. (2019), developed polyethylene glycol passivated fluorescent CDs (CDs-PEG) from gelatin and PEG as nanocarrier for tumor treatment using methotrexate (MTX) as anticancer drug. The prepared CDs-PEG emitted blue photoluminescence with a maximum quantum yield of 34%. The effect of PEG on PL intensity of CDs was investigated and results showed stronger PL behavior of CDs-PEG as compared to pure CDs from gelatin. *In vitro* anticancer

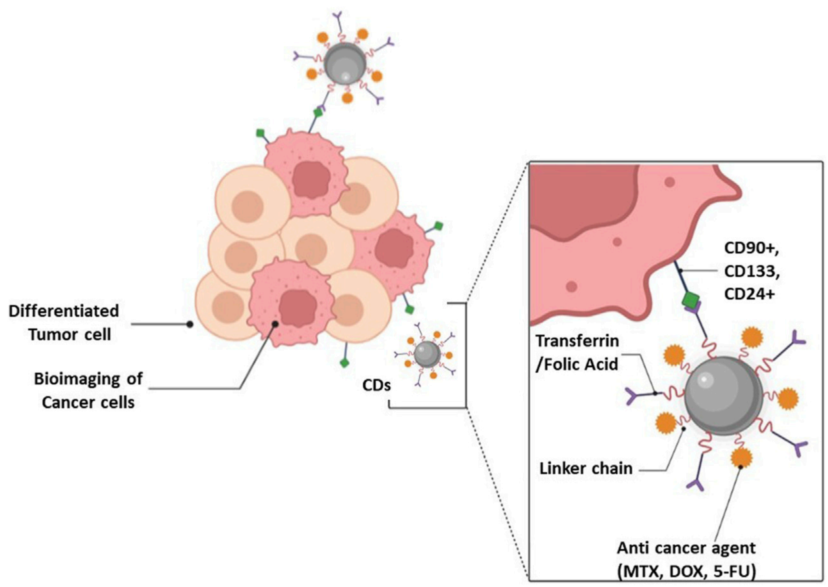

FIGURE 3
CDs theranostic application in cancer treatment.

activity of CDs-PEG showed good antitumor efficacy than free MTX because of its greater *in vitro* nuclear delivery and thus proving the potential of CDs for targeted cancer therapy (Arsalani et al., 2019). Li et al. (2020a), developed smart mesoporous silica nanoparticles (MSNs) grafted with CDs and poly (N-vinylcaprolactam) (PNVCL) as a mixed shell (CDs/PNVCL polymer grafted MSNs) that allowed real-time monitoring and pH-triggered anticancer drug release. Doxorubicin (DOX) was loaded with the prepared CDs as a model drug. The study results demonstrated the qualities of excellent nanocarriers, such as low toxicity, limiting early release in the bloodstream by "caps" of CDs, and collapse of PNVCL. The composite allowed burst release of anticancer drug at the tumor site due to the rupture of Schiff base bonds. Through MTT experiments it was also suggested that CDs/PNVCL polymer grafted MSNs killed cancer cells without affecting normal cells. The ability of CDs fluorescence to monitor medication release in real time was studied and the results revealed linear connection in cumulative release of DOX and the fluorescence change of CDs (Li et al., 2020a). On the other hand, Su et al. (2020), reported that red-emissive carbon quantum dots (CQD), can be targeted to nuclei of cancer cells and cancer stem cells. DOX loaded on the surface of CQD reduced the cell viability of HeLa cells to 21% in contrast to 50% when cells were exposed to free DOX. The study results showed remarkable killing impact of CDs on tumor cells and improved treatment effectiveness with no recurrence (Su W. et al., 2020).

Li et al. (2020b), developed fluorescent-based CQD with photosensitizer functionalized and chemo drug-loaded nanocarrier system in which CQD and 5-aminolevulinic acid (5-ALA) were coupled with a mono-(5-BOC-protected-glutamine-6-deoxy) b-cyclodextrin (CQD-Glub-CD) moiety, and then DOX was loaded into the 5-ALA-CQD-Glub-CD system. *In vitro* drug release pattern of DOX from the system was found to be pH-dependent with higher release at acidic pH 2.8. The photodynamic action of ROS production causes cell damage and morphological alterations in cells tested for breast cancer cell line (Li et al., 2020b). Hailing et al. (2020), developed fluorescent CDs loaded with DOX and passivated with PEI (CD-PEI-DOX) as a drug delivery system for treating cancer. Results showed prolonged drug release from the system with improved toxic effect on liver cancer cells (MHCC-97L and Hep3B cells) compared to free DOX (Hailing et al., 2020). Sun et al. (2020), developed DOX conjugated CDs (DOX-CDs) for improved intracellular drug delivery and cellular imaging. Uptake of DOX-CDs by cancer cells was seen in fluorescent cell labelling studies. Moreover, it was also observed that the DOX release from DOX-CDse was endo-lysosomal pH-dependent. MTT assay performed in ovarian cancer cell lines showed the enhanced cytotoxic potential of DOX-CDs. Additionally, in an animal imaging study, the CDs displayed bright fluorescent signal and low toxicity after administration for 7 and 21 days (Sun et al., 2020). Liu et al. (2021), developed endogenous NO-releasing carbon nanodots for gas therapy as cancer treatment. *In vitro* studies performed on human breast cancer cell line MCF-7, female gastric cancer cell line BGC-823, male lung cancer cell line A549 and female leukemic cell line K562 showed that carbon nanodots killed tumor cells without affecting normal cells. *In vivo* results also showed antitumor efficacy of carbon nanodots (Liu et al., 2021). Wang et al. (2020), developed a CDs-DOX delivery carrier and imaging probe for liver cancer targeted therapy with high fluorescence quantum yield (97%). Folic acid, as targeting component was used to modify CDs (FA-CDs) to which DOX was further loaded to form FA-CDs-DOX. Confocal microscope showed excellent capability of fluorescence imaging of developed system in liver cancer cells. *In vivo* imaging study showed stronger fluorescence intensity of FA-CDs-DOX which makes it easy to penetrate tumor tissue and skin. *In vivo* tumor inhibition studies indicated the higher targeting ability of FA-CDs-DOX as compare to free DOX, showing improved therapeutic effect. Cutrim et al. (2021), showed the nanofabrication of drug delivery system based on the self-assembly of the 5-Flurouracil (5-FU) onto the surface of CQD. The 5-FU-CQD nanoconjugate was less hazardous to normal cells than free 5-FU at equal concentrations, yet it had the same anticancer effect against a breast cancer cell line (MCF-7) as free 5-FU. The findings clearly suggested that the 5-FU-CQD nanoconjugate may improve cancer therapy effectiveness by lowering the toxicity of 5-FU to normal cells, reduce side effects as well that are intolerable for patients while retaining the therapeutic efficacy of 5-FU (Cutrim et al., 2021). In another study, Qin et al. (2021), reported fluorescent CQDs for *in vivo* bioimaging and targeted cancer therapy. Similarly, Ren et al. (2021), developed a red emissive polymer CDs-based nanocarrier system of coptisine, a poorly bioavailable drug, with integrated functionality for *in vivo* and *in vitro* simultaneous imaging and drug administration. Red emissive CDs serve many purposes in this nanocarrier system, including drug carrier, EPR effect, and simultaneous imaging. *In vitro* test demonstrated that polymer-based red emissive CDs might provide a prolonged drug release and improve coptisine effectiveness against cancer cells. The fluorescent CDs usefulness as a tumor-targeted drug delivery carrier of coptisine for cancer treatment was proven in an *in vivo* investigation (Ren et al., 2021). Lv et al. (2021), synthesized multi-functional CDs using folic acid as nitrogen source and for tumor targeting. Gallic acid was used as a carbon source as well as active antitumor moiety. *In vitro* cell imaging studies and *in vivo* antitumor studies performed on HeLa cell lines showed targeted imaging and antitumor abilities (Lv et al., 2021).

There are various phytochemicals which are reported for its anti-cancer activity, curcumin is one of them which has been reported effective against various cancers but due to its low aqueous solubility, stability, and poor bioavailability, its clinical results were not satisfactory. Sharma et al. (2021), developed curcumin CDs (CurCDs) using curcumin as carbon source and as an active molecule owing to its anti-cancer properties. CurCDs were compared with the plain curcumin and evaluated further for its anti-proliferative, apoptotic, and anti-migratory activities in glioblastoma (GBM) cells. Study revealed the superiority of CurCDs over free curcumin in terms of improved stability and enhanced bioavailability (Sharma et al., 2021). Mohammadi et al. (2021), developed CDs-chitosan nanocomposite hydrogels for multicolor imaging of MCF-7 cancer cells. These nanocomposite detects *microRNA-21* in MCF-7 cancer cells and thus demonstrate enhanced sensing properties for biomarker detection (Mohammadi et al., 2021). 6-mercaptopurine (6-MP) used for treatment of acute lymphoblastic leukemia, suffers from short half-life, poor bioavailability with severe side effects. To overcome all these shortcomings, 6-MP was conjugated with CDs through GSH-sensitive carbonyl vinyl sulfide linkage, and biotin was attached to the surface. Resulting compound revealed excellent stability in the phosphate buffer saline (PBS), lower cellular toxicity on normal cell lines (CHO) and good activity, comparable to free 6-MP against MCF-7 and HepG2 cancer cells (Talib and Mohammed, 2021). In another study, folic acid-based CDs (FACDs) were investigated for DOX delivery and diagnosis by Fahmi et al. (2021). Wen et al. (2020), synthesized novel nitrogen and sulfur co-doped CDs with bright orange fluorescence for mitoxantrone (MTO) delivery. In wide pH range, the prepared CDs displayed good fluorescence stability in a wide range of pH and its fluorescence quenched by folate, showing its sensitivity to FA with a detection limit as low as 0.85 nM. CDs also exhibited biocompatibility and greater photobleaching resistance due to which they could be applicable in cell imaging and drug tracking. *In vitro* studies were performed using MTO-CDs and their results showed cell inhibition confirmed by MTT assay and change in cell morphology. The combination of MTO-CDs provide a nanosystem allowing simultaneous imaging and anticancer effect and the presence of fluorescence did not affect the cell killing property of MTO (Wen et al., 2020).

CDs are also reported to have potential application for photodynamic and photothermal therapy in diagnosing and treating cancer (Nocito et al., 2021). Metal and heteroatom-doped CDs have potential applications in PDT for cancer diagnosis and treatment (Sekar et al., 2022). Nasrin et al. (2020), synthesized nucleus targeting CDs for PDT in oral cancer treatment. Li et al., (2020c), prepared sulphur doped CDs (S-CDs), as an PI3/Akt pathway inhibitor thereby significantly reducing cancer cell survival with high PDT performance. In another study, nuclei acid targeted CDs were developed by Xu et al. (2021), from quinolone derivatives (Cl-CDs, I-CDs). *In vitro*, these CDs produces RNA fluorescence and due to iodine doping possesses PDT led to the killing of cancer cells (Xu et al., 2021). Chen et al. (2021b), fabricated an injectable hydrogel by developing amido modified CDs (NCDs) for simultaneous phototherapy and PDT for cancer treatment. Phototherapy agents were incorporated into hydrogels with high loading efficiency. NCDs, acting as phototherapy agent, showed effective tumor inhibition and thus provided a new strategy for advanced tumor treatment (Chen et al., 2021b). In another study, Yue et al. (2021), synthesized green fluorescent riboflavin-based CDs having singlet oxygen generation ability for PDT in cancer treatment. *In vivo* results showed significant inhibition of tumor growth after PDT with CDs (Yue et al., 2021). Novel iodine doped CDs (I-CDs) exhibiting PDT performance and nucleic acid targeting properties were synthesized by Xu et al. (2021). *In vitro* results revealed that photodynamic I-CDs significantly killed cancer cells thereby confirming the targeting capabilities of CDs (Xu et al., 2021). Hu et al. (2021), synthesized and evaluated Sn nanocluster CDs for potential application in PDT in cancer treatment. *In vitro* and *in vivo* study results showed promising potential of CDs in PDT (Hu et al., 2021). Also, novel green fluorescent fluorine and nitrogen co-doped carbon dots (F, NCDs) for image guided PDT of cancers were synthesized and evaluated by Wu et al. (2022). *In vitro* study on HepG2 cell lines showed higher photodynamic efficiency and better cell imaging capability of the F, NCDs (Wu et al., 2022). Conclusively, recently reported studies showed significant potential of CDs as photosensitizer in photodynamic and photothermal therapy in cancer treatment. Although the applications of CDs in cancer theranostics showed promising potential, various challenges limit its use in humans due to lack of information on its genotoxic potential. This needs to be investigated thoroughly so that the CDs can be delivered to the cell nuclei targeting bad genetic material in order to augment antitumor efficacy. Furthermore, currently phototherapy entails an imaging agent that has an overlapping absorption coefficient and lies in the biological transparency window of 650–950 nm. Therefore, it is an urgent requirement to develop CDs with emission in the NIR region.

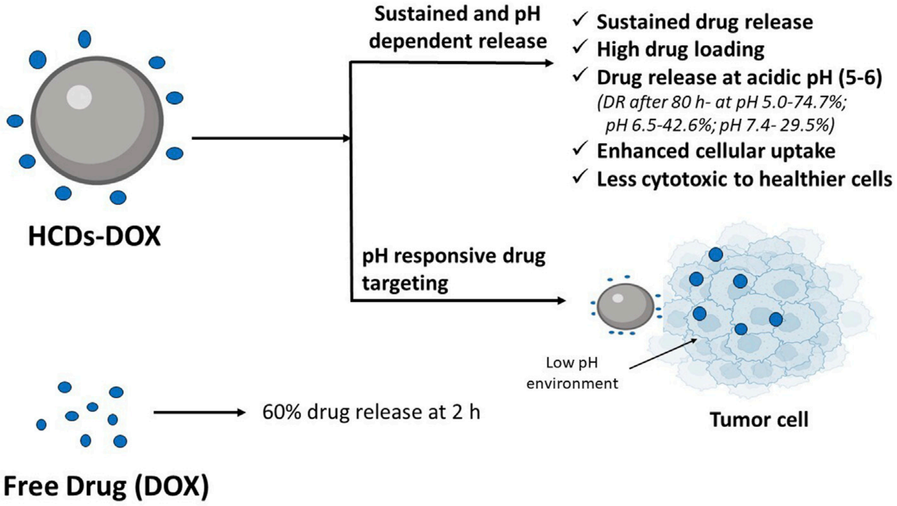

FIGURE 4
Hollow CDs (HCDs) for sustained and pH responsive drug delivery of doxorubicin (DOX). *In vitro* drug release study showed 74.7% of DOX release from HCDs at pH 5.0, 42.6% at pH 6.5% and 29.5% at pH 7.4 after 80 h. In case of free DOX release profile, 60% of the drug was released after 2 h (Zhang et al., 2019a).

3.6 CDs in controlled release and smart stimuli-responsive drug delivery system

A sustained drug delivery system tries to release the drug slowly for an extended period of time to maintain the constant concentration of the drug in blood or target tissue and thus leads to desired therapeutic effect in diseased conditions that requires drug concentration to be maintained for a long period of time. Smart stimuli-responsive drug delivery system uses natural or synthetic polymers that are designed to show therapeutic responses against the physicochemical and physiological processes, as well as external stimuli. This is particularly advantageous in reducing the side effects due to premature release of drug and assist in achieving the delivery of drug at the targeted site (Indermun et al., 2018). Zhang et al. (2019a), developed hollow CDs (HCDs) as a drug carrier for sustained delivery of DOX. After 80 h of *in vitro* drug release study, 74.7% DOX was released at pH 5.0, 42.6% at pH 6.5% and 29.5% at pH 7.4 (Figure 4). This was due to the dissociation of carboxylic acid hydrazine bond of HCDs-DOX by hydrolysis in acidic condition. In the case of free DOX release profile, no significant difference was observed at 5.0, 6.5, and 7.4 pH. 60% of the drug was released within 2 h. This indicated that free DOX could not reach the tumor cell effectively and HCD-DOX could be used as a potential sustained release drug delivery system for cancer treatment. The results of the study further demonstrated that HCDs-DOX effectively inhibited cancer cell proliferation and showed lower cytotoxicity to healthy cells as compared to DOX (Zhang et al., 2019a). Duan et al. (2020) introduced heparin (Hep), an anticoagulant, in conjunction with a drug delivery method based on CDs, i.e., DOX-CDs-Hyaluronic acid (HA) that can delivers DOX to cancer patients with the complication of thrombosis with reduced adverse effect. Drug release studies showed double trigger release of DOX from CDs-HA-Hep/DOX system due to acidic environment of the tumor and presence of HA, which was found to be dependent on the concentration of HA and pH value. *In vitro* MTT and scratch tests results further confirmed the inhibition of growth and migration of cancer cells, respectively. Visual tracking of the drug from the developed delivery system based upon CDs was also feasible (Duan et al., 2020). Chung et al. (2022), synthesized CDs/hydroxyapatite (CD-HAP) nanocomposite as a carrier system for acetaminophen using sugarcane bagasse char as a biowaste precursor via hydrothermal method. The pairing of CDs with hydroxyapatite improved the fluorescence property. The highest drug loading capacity of 48.5% was found in CD-HAP-40, which was synthesized using 40 mL of CDs. However, the best sustained acetaminophen release behavior was seen in CD-HAP-20 synthesized using 20 mL of CD, and the release kinetics followed Higuchi model showing diffusion mechanism of drug release. This study concluded the use of CD-HAP as a potential candidate for drug delivery application (Chung et al., 2020). Rahmani et al. (2021), developed pH-sensitive chitosan nanogel of rivastigmine by incorporating N-CDs. These nanogels exhibited pH-sensitive drug release. Swelling capacity and drug entrapment efficiency also improved by incorporating N-CDs in the nanogel. Many stimuli sensitive polymers exist that show immense potential, but their use is restricted due to their biocompatibility and toxicity related issues and therefore more research is warranted for safe and effective drug delivery using stimuli polymers.

3.7 CDs in vaccine delivery

CDs finds application in field of vaccine delivery and especially in cancer immunotherapy. The performance of therapeutic vaccine in cancer immunotherapy is not promising as it is not able to generate a robust immune response in body's incapacitated immune system. The tumor associated antigen (TAAs) used in therapeutic vaccine is not able to stimulate the immune response resulting in limited success in developing vaccine for cancer. Ideally, a vaccine drug delivery system should be able to deliver antigen effectively and it should also act as adjuvant. Photoluminescent CDs are reported to have potential application as a vaccine adjuvant. Luo et al. (2018), successfully designed a nanocomposite consisting of uniform-sized CDs and tumor model antigen protein, ovalbumin (OVA). OVA can stimulate the maturation of dendritic cells resulting in augmenting the expression of costimulatory molecules, CD80 and CD86. It further led to the activation of T cells and subsequently their proliferation, vital for killing the cancer cells (Luo et al., 2018). Li et al. (2018), evaluated the efficacy of PEI modified fluorescent CDs as vaccine delivery system via intranasal route. In this study, a model protein antigen, i.e., OVA was delivered through intranasal route using PEI modified CDs as a carrier. Their results showed elevated levels of IgG and IgA titres and increased cytokine IFN-γ secretion by splenocytes, and memory T cells following administration. This study further validated the role of CDs as a carrier of vaccine antigen as well as also helps on trafficking the movement from the administration site to immune organs (Li et al., 2018). In another study, Huang et al. (2020), studied the role of quarternized cationic CDs prepared using biquarternary ammonium salt (BQAS-CDs) as a potent vaccine adjuvant *in vivo* and a viable alternative to alum in producing both Th1 and Th2 response. It is well known that alum is incapable of producing cellular immune response required for cancer management and microbial infections. In this study, OVA was used as a model antigen that is negatively charged and was adsorbed on cationic BQAS-CDs to form nanocomplex. *In vivo* studies in mice showed that the nanocomplex triggered Th2 humoral response which was measured by the IgG1 antibodies and was found to be similar to alum. However, the Th1 cellular immune response determined by measuring the IgG2a and IgG2b antibodies was more dominant in group of mice administered with BQAS-CDs + OVA nanocomplex. Furthermore, it was also found that a BQAS-CDs + OVA nanocomplex induce proliferation of OVA-specific $CD4^+$ and $CD8^+$ T cells compared to alum-OVA and naked OVA groups without affecting the hematological and histological parameters. Notably, the results of this study confirmed that BQAS-CDs can serve as a potential adjuvant and a delivery vehicle of antigen (Huang et al., 2020). Cheng et al. (2019), investigated the potential of CQD's as a nanovehicle for protein antigen gp85. The protein antigen had been found to be effective in producing immune response against avian leukosis virus subgroup J (ALV-J) in chickens. Their study results revealed that the nanocomplex of gp85 with CQD produced high IgG levels and confer long-term protection. The study also confirmed the role of CQD's as an adjuvant in potentiating the immune response (Cheng et al., 2019). Conclusively, several reports highlight the potential application of CDs as a nanovehicle for vaccine delivery. Furthermore, CDs-mediated vaccine drug delivery system needs to be explored preclinically and clinically to investigate the ability of CDs to induce cellular or humoral immunity.

3.8 Antiviral properties of CDs and as nanocarrier in antiviral drug delivery

The current approach of dealing with the viral infection is to prevent its adherence to host cells or to interfere with its replication. Virus eradication is an enduring challenge now a days and CDs play a vital role due to their antiviral properties. One of the studies conducted by Fahmi et al. (2016), demonstrated the potential of boronic acid modified CQD's against HIV virus using MOLT-4 cells as a host cell system. The results of this study found that the boronic acid sites on CQD's could bind to the glycoprotein expressed on HIV virus which is responsible for its adherence to host cells (Fahmi et al., 2016). A similar study was performed on CDs derived from benzoxazine monomer and found to be effective against a variety of viruses such as adenovirus-associated virus, porcine parvovirus, zika virus, dengue virus, and Japanese encephalitis virus. CDs hinders virus attachment to the host cells through the mechanism of binding to proteins present on the virus surface (Kotta et al., 2020).

There are studies that further explore the potential of modified CDs and found that it does not only interfere with the entry of viruses into host cells, but also affects its replication. Garg et al. (2020), found that the antiviral properties of CDs inhibiting the replication of virus can be achieved by doping it with heteroatom. In their study, CDs were doped with triazole derivatives and formed a series of bioisosters. The study results found that the heteroatom co-doped with CQD's act by targeting the viral enzymes such as helicase and 3CLpro, required for viral replication. Triazaole derivatized CQD's can be used to combat the SARS-CoV-2 infection, owing to the ability of virus to encode for non-structural proteins including the 3CLpro. Their mode of action is contrary to surface functionalized CQD's that prevents the entry of virus to host cells (Garg et al., 2020). In another study, Łoczechin et al. (2019), studied the CQD's potential to inhibit human coronavirus HCoV-229E. CQDs were linked separately with different chemical moieties to form seven different CQD's and it was found that all of them inhibited the interaction of S protein receptor of HCoV-229E with the host cells. Chemical modification of CQD's was done by introducing the boronic acid sites on it which resulted in augmentation of its antiviral property by interfering with S protein receptor and thus suppressed the syncytium formation. Preventing the syncytium formation led to prevention of HCoV-229E entry into the host cells. The timing of addition of CQD's had been found to affect its mechanism of action as the addition of CQD's after 5.5 h after the virus entered in host cells resulted in inhibition of genomic replication of virus. This could be due to interaction of CQD's with the cell surface protein affecting the signal transduction and consequently replication or the interaction of CQD's with the cytosolic proteins of cells after internalization. The antiviral effect of cationic curcumin CDs (CCM-CQD's) was investigated, and it was found that they not only inhibit the viral entry but also its replication in a porcine epidemic diarrhea virus (PEDV) coronavirus model. The CCM-CQD's interferes with the surface protein of virus and thereby preventing its entry into host cells. The study results also showed that CCM-CQD's target viral RNA replication by producing interferon-stimulating genes (ISGs) and pro-inflammatory cytokines. Based on the study results, it was deduced that CCM-CQD's can be used as alternative treatment strategy for patients infected with coronavirus (Ting et al., 2020).

Aung et al. (2020), developed amino phenylboronic acid-modified CQD's (APBA-CQD's) and conjugated it with antiviral drug, Duviral to further enhance its antiviral efficacy against HIV-1 infection. The modification on CDs improved its toxicity profile, biocompatibility, and imparts higher stability. The APBA-CQD's acts by preventing the entry of virus to host cells by engaging with gp120 expressed on virus and thus prevents the formation of syncytia. Combination of APBA-CQD's with Duviral, which is a multicomponent drug consisting of Lamivudine and Zidovudine, act by inhibiting the enzyme nucleoside reverse transcriptase and inactivate HIV-1 by intracellular and extracellular blocking. This combination showed better results in targeting virus and thus warrants further investigation as it is expected to improve the survival rate and life expectancy of patients (Aung et al., 2020). Iannazzo et al. (2018), also explored the potential of polycarboxylated graphene quantum dots (GQD's) as a carrier of two antiviral drugs. The drug molecules chosen for the study were CHI499 and CDF119, which belong to the class of non-nucleoside reverse transcriptase inhibitors (NNRTI) and anchored to GQD's. Results showed that the conjugate of GQD's and antiviral drugs showed marked enhancement in antiviral efficacy compared to drug alone. The increased anti-HIV activity of the conjugate was due to dual nature of mechanism achieved by the conjugate. The NNRTI acts by inhibiting the reverse transcriptase and GQD's acts by inhibiting the binding of virus to host cells (Iannazzo et al., 2018). In another study, Ju et al. (2020), successfully demonstrated the CQD's-mediated delivery of locked nucleic acid (LNA) against Kaposi's sarcoma-associated herpesvirus (KSHV) and AIDS related non-Hodgkin B-cell lymphoma. *In vitro* results showed that the conjugate of CQD-LNA acts by inhibition of proliferation of KSHV-associated primary effusion lymphoma (PEL) cells by inducing apoptosis and knockdown of KSHV micro-RNA's, such as *miR-K12-1*, *miR-K12-4* and *miR-K12-11*. The conjugate had proven its efficacy in PEL nurtured xenograft mouse model by causing the regression of tumor growth and thus greatly increasing the survival rate (Ju et al., 2020). On similar lines, a study used antiviral compound glycyrrhizic acid (Gly), a traditional Chinese herbal medicine, as a precursor to synthesize antiviral CQD's. It was found that Gly-CQD's inhibited virus proliferation by approximately 5 orders of magnitude. This conjugate also provides the advantage of reduced side effects of glycyrrhizic acid that are more pronounced when given alone. Gly-CQD conjugate had been found to be act in many ways, namely: a) inhibiting virus proliferation; b) inhibiting virus invasion and replication; c) controlling the expression of antiviral genes; d) stimulating the production of interferons; e) regulating the production of virus-induced reactive oxygen species (ROS) (Tong et al., 2020; Xue et al., 2022). Undoubtedly, CDs confer alternative option in dealing with viral infection, however, most of the studies were performed *in-vitro* and there is a need to do more studies *in vivo* to validate the efficacy of CDs in the delivery of antiviral drugs. Additionally, CDs must be hydrophilic and exhibit colloidal stability in physiological conditions. A profound understanding of the structure activity relationship in terms of size, shape, surface charge, etc., to increase the efficacy of CDs as carrier of antiviral agents is required as well. Moreover, more research in developing CDs is required to combat virus mutation and the emergence of new strains.

4 Diagnostic applications of CDs

As a captivating part of fluorescent carbon nanomaterials, CDs demonstrates significant potential in bioimaging and biosensing field owing to their small size, better aqueous stability, excellent photostability and biocompatibility (Kong et al., 2020).

4.1 Bioimaging

Bioimaging enables visualization of cell and its orgnanelles that allows better understanding of their structure and physiological functions. In the past decade, the use of green fluorescent protein (GFP) in biomedical research allowed monitoring of interaction among proteins and gene expression. However, poor photostability and weak fluorescence of GFP restricted its further widespread utility. The discovery of fluorescent CDs possessed unique properties such as multicolor emission with high QY, tunable optical properties, excellent photostability and dispersion properties. CD-based optical imaging utilizes optical contrast between the image and surrounding region and enables early detection, screening, and diagnosis of life threatening disease conditions. The imaging capabilities of CDs is either due to its unique optical property, i.e., intrinsic fluorescence or due to the presence of functionality in its core or surface (Wang B. et al., 2022).

Herein, we have discussed the research outcomes of the various studies conducted using fluorescent CD probes. Hua et al. (2019) prepared red emissive, nucleolus targeted Ni–pPCDs using p-phenylenediame (pPDA) and nickel ions (Ni^{2+}) to achieve the maximum quantum yield (QY) with excellent photostability. *In vitro* and *in vivo* studies revealed the biocompatibility of Ni–pPCDs and their utilization for high-resolution imaging of cell nuclei and high-contrast imaging of tumor-bearing mice and zebrafish (Hua et al., 2019). Zhang et al. (2019b), prepared N-CDs, a kind of green and red emissive CDs, that were loaded with multifunctional Mn^{2+} complex-modified polydopamine (PDA) nanoparticles (NPs) for fluorescent imaging. PDA-N-CDs (Mn) NPs can provide contrast for magnetic resonance imaging (MR) due to the automated chelation of Mn^{2+} ions. It was possible to effectively show the use of PDA-N-CDs (Mn) NPs for fluorescence, photothermal, and MR *in vivo* imaging. Furthermore, the PDA-N-CDs (Mn) NPs exhibited outstanding biocompatibility and minimal biological toxicity, as evidenced by cytotoxicity testing, hemolytic testing, histological analysis of viscera sections, and blood biochemical analysis (Zhang et al., 2019b). Mintz et al. (2021) showed that CDs are capable of quantitatively detecting water in organic solvents. Also, transferrin conjugation enhanced the CDs biocompatibility. These were used for cellular imaging of neuroblastoma cell lines (Mintz et al., 2022). Ren et al. (2020) developed blue fluorescent N-CDs using microwave-assisted method for cell imaging and metronidazole detection. Kong et al. (2020) developed an effective nanosystem based on the DNA aptamer AS1411 modified CDs with PEI as connecting bridge for bioimaging. Confocal microscopy and flow cytometry displayed higher cellular uptake of the CDs-PEI-AS1411 in MCF-7 breast cancer cells as compared to non-cancerous L929 fibroblast cells, thereby showing very specific capacity to identify nucleolin-positive cells. Results showed the application of synthesized CDs-PEI-AS1411 nanosystem in cancer cell targeted imaging (Kong et al., 2020). Gudimella et al. (2021) reported a sand bath assisted method for the preparation of fluorescent CDs using peels of citrus fruit. Prepared CDs revealed biocompatibility, low toxicity and significant free radical scavenging activity. Folic acid was conjugated with the CDs to enhance its potential as biological labels for cellular imaging at multiple excitations (Gudimella et al., 2021). CDs with protein like structure were created with the combination of fluorescent blinking domains and RNA-binding motifs, allowing for better nucleolar ultrastructure imaging. The picture enables precise differentiation of distinct cells from the same cell type by extracting multidimensional information from the nucleolus. Furthermore, it was shown that this CD-depicted nucleolar ultrastructure can be used as a sensitive hallmark to recognize and distinguish subtle responses to several stressors, as well as to provide RNA-related information that has previously been unavailable using traditional immunofluorescence methods. This protein-mimicking CDs might be used to investigate nucleolar stress in cell diagnostics and therapies (He et al., 2021). Ermis et al. (2022) also reported red emissive biocompatible CDs (R-CDs) based fluorescent probe for live 3D bioimaging of U-87 microglia tumor spheroids.

CDs exhibiting fluorescence in NIR region (700–1700 nm) are also gaining interest because of there application as nanomaterials in bioimaging. They are reported to be highly efficient in photothermal therapy. CDs exhibiting fluorescence in NIR window has a distinct advantage over other photoluminescent agents in high-contrast *in vivo* fluorescence imaging owing to its deeper tissue penetration, high resolution, lower tissue self-absorption/scattering, and less autofluorescence (Wang T. et al., 2021; Zhao et al., 2023). Bao et al. (2018) developed sulfur and nitrogen codoped NIR CDs for *in vivo* fluorescence and photoacoustic imaging with high photothermal conversion efficiency of 59%. Ding et al. (2019) synthesised highly fluorescent CDs emitting near infrared from lemon juice for potential bioimaging application. QY was reported to be 31%. Liu et al. (2022) fabricated large conjugated perylene derivates for synthesising CDs which exhibited high contrast *in vivo* NIR fluorescence bioimaging in mice model. Zhao et al. (2023) demonstrated application of CDs with NIR-I (700–950 nm) emission and NIR-II (1000–1700 nm) absorption in multiple photon bioimaging and photothermal therapy. Multiphoton-induced NIR-I emission with quantum yield of 29% and NIR-II induced heat with photothermal conversion efficiency of 41.19% was reported (Zhao et al., 2023). Overall, CDs exhibiting photoluminescence in the NIR region are reported to be of potential application in the field of bioimaging. However, synthesis of CDs exhibiting fluorescence in NIR region with higher QY is a major challenge.

Imaging using CDs emitting blue/green light of shorter wavelength have limitation of background interference and poor penetration in the biological tissues. Therefore, it is desired to use CDs that can emit in the NIR region while enabling good penetration of light in the biological tissue with minimal photodamage. Various studies have been done on different cell lines, mice and zebra fish have reported excellent biocompatibility of CDs, but more studies needs to be done at clinical level to ensure the safety of CDs. To gain more confidence in the use of CDs at clinical level, studies related to mechanism of interaction of CDs with biological system warrants further exploration.

4.2 Biological sensing

Biological sensing refers to identification and measuring the analytes concentration based on properties such as photoluminescence and electrical conductivity. The CDs are endowed with both of them and upon interaction with analytes lead to change in the optical emission characteristics such as change in fluorescence intensity or colorimetric wavelength. Based on these properties, CDs are further classified into three categories, i.e., on-off, off-on, and fluorescence shift. The on-off category is also called fluorescence quenching and used for the detection of cations, anions, and small molecules. In this, upon interaction of CDs with metal ion, the electron are transferred from CDs to empty d-orbital of metal ions resulting in fluorescence quenching. In the case of off-on category, the CDs regain its fluorescence and reach back to emission state upon interaction with the analyte. And lastly fluorescence shift category detects analytes based on partial overlap of donor emission and acceptor absorption spectra (Wang B. et al., 2022).

Herein, we have discussed the snapshot of various studies conducted by researchers on biosensing analytes using CDs. Zhu et al. (2019), prepared titanium carbides (Ti_3C_2) nanosheets mixed with red-emitting CDs (RCDs), where Ti_3C_2 showed selective and effective fluorescent turn-on nano sensor for glucose detection. The nanosensor can also be used to monitor glucose by using H_2O_2 produced by the oxidation of glucose catalysed by glucose oxidase (Zhu et al., 2019). For calcium ions detection, novel fluorescent CDs were developed in which the surface of the CDs was modified by ethylene-bis (oxyethylenenitrilo) tetra acetic acid (EGTA). The CDs emit bright blue fluorescence, and the intensity of the fluorescence declines significantly as the calcium concentration increases. The findings proved that calcium ion detection by CDs is a static fluorescence quenching mechanism. Also, cytotoxicity and cellular imaging investigations have demonstrated nontoxic and biocompatibility profile of CDs (Yue et al., 2019). Yu et al. (2019), prepared N-CDs which were extremely dispersible in water and can be utilised as an optical probe for label-free detection of Fe^{3+} via a switched off change. Also, in the presence of pyrophosphate, such sensing nanoplatforms can be restored. This on-off-on technique is likely to open up new opportunities for producing efficient sensors in industrial settings (Yu et al., 2019). A selective and environmentally friendly fluorescence immunoassay approach based on N-CDs for the exposure of nuclear matrix protein 22 (NMP22, antigen), was developed by Othman et al. (2020). The immunocomplex on the carboxylated N-CDs caused fluorescence intensity quenching. NMP22 was effectively detected in human urine samples using this approach, with recoveries ranging from 96.50% to 103.61%. These findings give substantial evidence that N-CDs can be used as fluorescent labels in immunoassays. Geng et al. (2020), reported a lysosome-specific fluorescent CDs for ATP detection in acidic lysosomes with “off-on” changes of yellow fluorescence. These CDs were effectively used for real-time monitoring of lysosomal ATP shifting concentration caused due to drug stimulation (e.g., chloroquine, etoposide, and oligomycin) (Geng et al., 2020). Orange–red emissive CDs (OR-CDs) were developed by calcining carbon sources like 5-amino-1, 10-phenanthroline (Aphen), and salicylic acid (SA), which worked as a “turn on” type fluorescence probe for Cd^{2+} detection. OR-CDs showed potential to reduce cadmium poisoning in living organisms in addition to being employed for intracellular Cd^{2+} imaging (Xu et al., 2022). Chattopadhyay et al. (2021), prepared CDs from peptic digest of animal tissue, which is easily available, without using any other chemical reagent for surface functionalization. The utilisation of these CDs as a fluorescent nanoprobe for the detection of metal ions (Cu^{2+} and Hg^{2+}) via chelation, radical scavenging, and cellular imaging has been examined. They also displayed fast cell exocytosis,

TABLE 3 Diagnostic application of CDs.

No.	Diagnostic approach	CD type	Conjugate/drug/precursor	Method of preparation	Applications	Ref.
1	Bioimaging	Red emissive CDs	Nucleolus targeted Ni–pPCDs using p-phenylenediame (pPDA) and nickel ions (Ni^{2+})	Hydrothermal method; QY was 64.9%	High-resolution imaging of nucleus, high contrast imaging of tumor-bearing mice and zebrafish	Hua et al. (2019)
		Mn^{2+} complex-modified polydopamine and dual emissive CDs based nanoparticles	Polydopamine (PDA) and manganese ion (Mn^{2+})	Self-polymerization; QY was 4.5% and photothermal conversion efficiency was 28.2%	Used in fluorescence, photothermal, and magnetic resonance (MR) *in vivo* imaging.	Zhang et al. (2019b)
		Red-emissive CDs	Transferrin conjugation o-pheylenediamine (o-PDA) as precursor	Oligomerization reaction	Quantitatively detection of water in organic solvents; Cellular imaging of neuroblastoma cell lines	Mintz et al. (2022)
		Blue, fluorescent nitrogen-doped CDs (N-CDs)	L-tartaric acid and triethylenetetramine	Microwave-assisted method, QY was 31%	Cell imaging and metronidazole detection	Ren et al. (2020)
		DNA aptamer AS1411 modified CDs	polyethylenimine (PEI)	Hydrothermal method	Have great detection ability of nucleolin-positive cells	Kong et al. (2020)
		Fluorescent CDs using peel of citrus fruits	Citrus peel and folic acid	Sand bath assisted green synthesis; significant free radical scavenging activity (EC50: 4.7382 μg mL^{-1})	Cancer cell imaging	Gudimella et al. (2021)
		Red emissive CDs	Paraphenylenediamine and thiourea	One-pot water based hydrothermal method; QY was 13%	Used for live 3D bioimaging of tumor spheroids	Ermis et al. (2022)
2	Biological and chemical sensing	Fluorescent CDs	Ethylene-bis (oxyethylenenitrilo) tetra acetic acid (EGTA)	Hydrothermal method	Calcium ion detection with detection limit (LOD) of 0.38 μM	Yue et al. (2019)
		Nitrogen doped CDs (N-CDs)	Citric acid and urea	Hydrothermal method	Detection of nuclear matrix protein (NMP22) in immunoassays with detection limit of 0.047 ng/mL	Othman et al. (2020)
		Lysosome-specific fluorescent CDs	5-amino-1, 10-phenanthroline (Aphen), and salicylic acid (SA)	Calcination	Detection of Cd^{2+} with LOD 0.30 μM	Xu et al. (2022)
		Blue emissive CDs	Peptic digest of animal tissue	Hydrothermal method; QY was 61%	Detection of metal ions (Cu^{2+} and Hg^{2+}); Alternative to synthetic organic dyes for cellular imaging	Chattopadhyay et al. (2021)
		NIR ratiometric fluorescence CDs	Black pepper	Solvothermal method; QY was 10.25%	Ascorbic acid measurement	Tang et al. (2021)
		Green, fluorescent CDs	Triphenylphosphonium (TPP)	One-pot carbonization synthesis technique; QY was found to 61%	Detection of tetracycline and mitochondrial labelling in cancer cells	Rajendran et al. (2021)
		CDs	Coconut husk	Thermal calcination	Sensing amino acid and L-tyrosine with LOD of 0.96 nM	Chauhan et al. (2022)
		Nitrogen-doped fluorescent CDs (PT-NCDs)	Grape peel	Solid phase thermal method	Detection of baicalin used for cancer treatment	Tang et al. (2022)

indicating that they have a lot of potential for chelation treatment. For fluorescence-based cell imaging, they can also be utilised as an alternative to synthetic organic dyes (Chattopadhyay et al., 2021). Tang et al. (2021), developed CDs using black pepper as raw material and designed them as NIR ratiometric nanoprobe for ascorbic acid measurement based on off-on mode with good selectivity and sensitivity. The suggested technique has enormous potential to increase the applications of dual-emission CDs in biological disciplines (Tang et al., 2021). Rajendran et al. (2021), reported green fluorescent CDs with quantum yield of up to 61% for tetracycline detection and mitochondrial labelling in cancer cells. CDs derived from coconut husk with good quantum yield and biocompatibility were synthesized by Chauhan et al. (2022), for sensing amino acid, L-tyrosine. Mathad et al. (2022), developed β-Cyclodextrin (CD) anchored neem (Azadirachta indica) CDs for greater electrochemical sensing performance of lapatinib, an anticancer drug, via host-guest inclusion. The proposed sensor could be used for determining lapatinib in pharmaceutical formulations and urine samples (Mathad et al., 2022). Blue fluorescent CDs conjugated with thiomalic acid (TMA)-capped $AgInS_2$ quantum dots were developed and evaluated for determination of ibandronic acid, a bisphosphonate pharmaceutical, by Castro et al. (2022). Sohail et al. (2022), investigated Zn-doped CDs-based bioanalytical probe for the determination of antioxidant activity index (AAI) as traditional techniques lack truncated strength, high interference effect in complex samples, photo-bleaching and stability. Tang et al. (2022), synthesised nitrogen-doped fluorescent carbon dots from grape peel biowaste for detection of baicalin, a flavonoid compound used for liver cancer treatment. Further advancement in technology led to rapid detection of analytes via smartphones due to their ease of portability and accessibility. Su et al. (2020) developed light sensing CDs and integrate with smartphones that allows rapid detection of 2,4-dichlorophenoxyacetic acid in real time. Currently, there is limited application of this technology and more work is needed in the area to expand this technology for the detection of analytes in other disease conditions. Recently reported diagnostic applications of CDs are summarized in Table 3.

5 Miscellaneous applications of CDs

Some other miscellaneous applications of CDs are reported in the literature, such as Kandra and Bajpai (2020), reported that impregnation of CDs into chitosan film caused seven-fold reduction in its water absorption capacity. Moisture permeation abilities of the plain chitosan and CDs loaded chitosan film matrix was found to be 1758 and 956 g/m^2/day, respectively. Additionally, for chitosan film, bovine serum albumin (BSA) adsorption was found to be 24.2 mg/m^2 which got reduced to 14.1 mg/m^2 for CDs loaded chitosan film matrix. (Kandra and Bajpai, 2020). Lee et al. (2020), developed a CDs nanoparticle to investigate their potential as a new antiplatelet agent for arterial thrombotic diseases treatment without causing any cytotoxicity. Antiplatelet action was exerted due to the inhibition of collagen-stimulated human platelet aggregation. *In vivo* study showed reduced survival in mice with ADP-induced acute pulmonary thromboembolism without altering the bleeding time, which is the foremost adverse effect of antiplatelet agents (Lee et al., 2020). Zhao et al. (2022), evaluated Armeniacae Semen Amarum (ASA)-Carbonisata-derived CDs (ASAC-CDs) for its anti-inflammatory effects in rat model of acute lung injury (ALI). ASAC-CDs reduced inflammation by reducing the level of inflammatory mediators. CDs also showed antioxidant activity by reducing malondialdehyde (MDA), myeloperoxidase (MPO) content and increasing superoxide dismutase (SOD) activity and glutathione (GSH) content. Results demonstrated the potential application of developed system in clinical anti-pneumonia (Zhao et al., 2022). Gudimella et al. (2022), prepared fluorescent CDs from Carica papaya leaves which were examined for free radical scavenging activity, antioxidant activity and *in vitro* anti-inflammatory activity.

6 Conclusion and future perspectives

CDs are emerging nanoparticles due to various advantages, such as high photostability, less cytotoxicity, biocompatibility, high chemical inertness, eco-friendliness, nontoxicity, easy functionalization, non-blinking photoluminescence, and good water solubility. CDs demonstrates potential drug delivery applications as nanomaterial for treating cancer, brain, ocular and infectious diseases. They also have application in gene, vaccine and antiviral drug delivery. Due to their versatile physicochemical properties, CDs are capable of achieving sustained release action, pH responsive drug delivery, smart stimuli-responsive and targeted drug delivery. Although CDs based nanomaterials are found to be promising nanocarriers in diagnostics and therapeutics drug delivery, further advances are still desirable to enhance their performance, sustainability, durability and cost-effectiveness for efficient industrial scale-up. Although, numerous cell lines and *in vivo* cytotoxicity studies have reported that the CDs based nanomaterials did not induce any toxic effects, more detailed investigations are still required to explain their toxicity profiles and biodegradation mechanism for efficient drug delivery application. CDs needs to be explored for preclinical long-term toxicity before proceeding to their clinical applicability.

Author contributions

Conceptualization, HK and DV; methodology, HK and DV; resources, HK, DV, and DK; data curation, HK and DV; writing—original draft preparation, HK and DV; writing—review and editing, HK, AB, and SS; supervision, HK, AB, and SS; project administration, HK. All authors contributed to the article and approved the submitted version.

Acknowledgments

The authors would like to thank Shoolini University of Biotechnology and Management Sciences for constant support and guidance. The authors would also like to thank Larkin University for the funds granted for the publication of this manuscript.

Conflict of interest

Author AB was employed by Perrigo Company Plc.

The remaining authors declare that the research was conducted in the absence of any commercial or financial relationships that could be construed as a potential conflict of interest.

Publisher's note

References

Adrita, S. H., Tasnim, K. N., Ryu, J. H., and Sharker, S. M. (2020). Nanotheranostic carbon dots as an emerging platform for cancer therapy. *J. Nanotheranostics* 1 (1), 58–77. doi:10.3390/jnt1010006

Ahuja, V., Banerjee, S., Roy, P., and Bhatt, A. K. J. B. (2021). Fluorescent xylitol carbon dots: A potent antimicrobial agent and drug carrier. *Biotechnol. Appl. Biochem.* 69, 1679–1689. doi:10.1002/bab.2237

An, Y., Lin, X., Zhou, Y., Li, Y., Zheng, Y., Wu, C., et al. (2021). Red, green, and blue light-emitting carbon dots prepared from o-phenylenediamine. *RSC Adv.* 11 (43), 26915–26919. doi:10.1039/d1ra02298a

Arsalani, N., Nezhad-Mokhtari, P., and Jabbari, E. J. A. (2019). Microwave-assisted and one-step synthesis of PEG passivated fluorescent carbon dots from gelatin as an efficient nanocarrier for methotrexate delivery. *Artif. cells, nanomedicine, Biotechnol.* 47 (1), 540–547. doi:10.1080/21691401.2018.1562460

Aung, Y. Y., Kristanti, A. N., Khairunisa, S. Q., Nasronudin, N., and Fahmi, M. Z. (2020). Inactivation of HIV-1 infection through integrative blocking with amino phenylboronic acid attributed carbon dots. *ACS Biomater. Sci. Eng.* 6 (8), 4490–4501. doi:10.1021/acsbiomaterials.0c00508

Bao, X., Yuan, Y., Chen, J., Zhang, B., Li, D., Zhou, D., et al. (2018). *In vivo* theranostics with near-infrared-emitting carbon dots-highly efficient photothermal therapy based on passive targeting after intravenous administration. *Light Sci. Appl.* 7, 91. doi:10.1038/s41377-018-0090-1

Biswal, M. R., and Bhatia, S. (2021). Carbon dot nanoparticles: Exploring the potential use for gene delivery in ophthalmic diseases. *Nanomater. (Basel).* 11 (4), 935. doi:10.3390/nano11040935

Boobalan, T., Sethupathi, M., Sengottuvelan, N., Kumar, P., Balaji, P., Gulyás, B., et al. (2020). Mushroom-derived carbon dots for toxic metal ion detection and as antibacterial and anticancer agents. *ACS Appl. Nano Mater.* 3 (6), 5910–5919. doi:10.1021/acsanm.0c01058

Carbonaro, C. M., Corpino, R., Salis, M., Mocci, F., Thakkar, S. V., Olla, C., et al. (2019). On the emission properties of carbon dots: Reviewing data and discussing models. *C* 5 (4), 60. doi:10.3390/c5040060

Castro, R. C., Páscoa, R. N., Saraiva, M. L. M., Santos, J. L., and Ribeiro, D. S. J. S. A. P. A. M. (2022). Photoluminescent and visual determination of ibandronic acid using a carbon dots/AgInS2 quantum dots ratiometric sensing platform. *Spectrochim. Acta A Mol. Biomol. Spectrosc.* 267, 120592. doi:10.1016/j.saa.2021.120592

Chattopadhyay, S., Mehrotra, N., Jain, S., and Singh, H. J. M. J. (2021). Development of novel blue emissive carbon dots for sensitive detection of dual metal ions and their potential applications in bioimaging and chelation therapy. *Microchem. J.* 170, 106706. doi:10.1016/j.microc.2021.106706

Chauhan, P., Mundekkad, D., Mukherjee, A., Chaudhary, S., Umar, A., and Baskoutas, S. J. N. (2022). Coconut carbon dots: Progressive large-scale synthesis, detailed biological activities and smart sensing aptitudes towards tyrosine. *Nanomaterials* 12 (1), 162. doi:10.3390/nano12010162

Chen, P., Zhang, J., He, X., Liu, Y. H., and Yu, X. Q. (2020). Hydrophobically modified carbon dots as a multifunctional platform for serum-resistant gene delivery and cell imaging. *Biomater. Sci.* 8 (13), 3730–3740. doi:10.1039/d0bm00651c

Chen, T., Yao, T., Peng, H., Whittaker, A. K., Li, Y., Zhu, S., et al. (2021b). An injectable hydrogel for simultaneous photothermal therapy and photodynamic therapy with ultrahigh efficiency based on carbon dots and modified cellulose nanocrystals. *Adv. Funct. Mater* 31 (45), 2106079. doi:10.1002/adfm.202106079

Chen, W., Shen, J., Wang, Z., Liu, X., Xu, Y., Zhao, H., et al. (2021a). Turning waste into wealth: Facile and green synthesis of carbon nanodots from pollutants and applications to bioimaging. *Chem. Sci.* 12 (35), 11722–11729. doi:10.1039/d1sc02837e

Cheng, J., Xu, Y., Zhou, D., Liu, K., Geng, N., Lu, J., et al. (2019). Novel carbon quantum dots can serve as an excellent adjuvant for the gp85 protein vaccine against avian leukosis virus subgroup J in chickens. *Poult. Sci.* 98 (11), 5315–5320. doi:10.3382/ps/pez313

Chu, X., Wu, F., Sun, B., Zhang, M., Song, S., Zhang, P., et al. (2020). Genipin cross-linked carbon dots for antimicrobial, bioimaging and bacterial discrimination. *Colloids Surfaces B Biointerfaces.* 190, 110930. doi:10.1016/j.colsurfb.2020.110930

Chung, H. K., Wongso, V., Sambudi, G. S., and Isnaeni, N. S. (2020). Biowaste-derived carbon dots/hydroxyapatite nanocomposite as drug delivery vehicle for acetaminophen. *J. Sol-Gel Sci. Technol.* 93 (1), 214–223. doi:10.1007/s10971-019-05141-w

Cui, F., Ye, Y., Ping, J., and Sun, X. J. B. (2020). Carbon dots: Current advances in pathogenic bacteria monitoring and prospect applications. *Biosens. Bioelectron.* 156, 112085. doi:10.1016/j.bios.2020.112085

Cutrim, E. S., Vale, A. A., Manzani, D., Barud, H. S., Rodriguez-Castellon, E., Santos, A. P., et al. (2021). Preparation, characterization and *in vitro* anticancer performance of nanoconjugate based on carbon quantum dots and 5-Fluorouracil. *Mater Sci. Eng. C Mater Biol. Appl.* 120, 111781. doi:10.1016/j.msec.2020.111781

Das, P., Ganguly, S., Agarwal, T., Maity, P., Ghosh, S., Choudhary, S., et al. (2019). Heteroatom doped blue luminescent carbon dots as a nano-probe for targeted cell labeling and anticancer drug delivery vehicle. *Mater. Chem. Phys.* 237, 121860. doi:10.1016/j.matchemphys.2019.121860

Das, P., Maruthapandi, M., Saravanan, A., Natan, M., Jacobi, G., Banin, E., et al. (2020). Carbon dots for heavy-metal sensing, pH-sensitive cargo delivery, and antibacterial applications. *ACS Appl. Nano Mater.* 3 (12), 11777–11790. doi:10.1021/acsanm.0c02305

Demirci, S., McNally, A. B., Ayyala, R. S., Lawson, L. B., and Sahiner, N. (2020). Synthesis and characterization of nitrogen-doped carbon dots as fluorescent nanoprobes with antimicrobial properties and skin permeability. *J. Drug Deliv. Sci. Technol.* 59, 101889. doi:10.1016/j.jddst.2020.101889

Ding, H., Zhou, X., Qin, B., Zhou, Z., and Zhao, Y. (2019). Highly fluorescent near-infrared emitting carbon dots derived from lemon juice and its bioimaging application. *J. Luminescence* 211, 298–304. doi:10.1016/j.jlumin.2019.03.064

Dong, X. (2018). Current strategies for brain drug delivery. *Theranostics* 8 (6), 1481–1493. doi:10.7150/thno.21254

Dong, X., Liang, W., Meziani, M. J., Sun, Y-P., and Yang, L. J. T. (2020). Carbon dots as potent antimicrobial agents. *Theranostics* 10 (2), 671–686. doi:10.7150/thno.39863

Duan, Q., Ma, L., Zhang, B., Zhang, Y., Li, X., Wang, T., et al. (2020). Construction and application of targeted drug delivery system based on hyaluronic acid and heparin functionalised carbon dots. *Colloids Surf. B Biointerfaces* 188, 110768. doi:10.1016/j.colsurfb.2019.110768

El-Shafey, A. M. (2021). Carbon dots: Discovery, structure, fluorescent properties, and applications. *Green Process. Synthesis* 10 (1), 134–156. doi:10.1515/gps-2021-0006

Ermis, E., Bagheri, Z., Behroodi, E., Latifi, H., Rahimifard, M., and Ajorlou, E. (2022). Red emissive N–S co-doped carbon dots for live imaging of tumor spheroid in the microfluidic device. *J. Sci. Adv. Mater. Devices* 7 (2), 100404. doi:10.1016/j.jsamd.2021.11.006

Fahmi, M. Z., Sholihah, N. F., Wibrianto, A., Sakti, S. C. W., Firdaus, F., and Chang, J. Y. (2021). Simple and fast design of folic acid-based carbon dots as theranostic agent and its drug release aspect. *Mater. Chem. Phys.* 267, 124596. doi:10.1016/j.matchemphys.2021.124596

Fahmi, M. Z., Sukmayani, W., Khairunisa, S. Q., Witaningrum, A. M., Indriati, D. W., Matondang, M. Q. Y., et al. (2016). Design of boronic acid-attributed carbon dots on inhibits HIV-1 entry. *RSC Adv.* 6 (95), 92996–93002. doi:10.1039/c6ra21062g

Garg, P., Sangam, S., Kochhar, D., Pahari, S., Kar, C., and Mukherjee, M. (2020). Exploring the role of triazole functionalized heteroatom co-doped carbon quantum dots against human coronaviruses. *Nano Today* 35, 101001. doi:10.1016/j.nantod.2020.101001

Garner, I., Vichare, R., Paulson, R., Appavu, R., Panguluri, S. K., Tzekov, R., et al. (2020). Carbon dots fabrication: Ocular imaging and therapeutic potential. *Front. Bioeng. Biotechnol.* 8, 573407. doi:10.3389/fbioe.2020.573407

Geng, X., Sun, Y., Guo, Y., Zhao, Y., Zhang, K., Xiao, L., et al. (2020). Fluorescent carbon dots for *in situ* monitoring of lysosomal ATP levels. *Anal. Chem.* 92 (11), 7940–7946. doi:10.1021/acs.analchem.0c01335

Ghirardello, M., Ramos-Soriano, J., and Galan, M. C. J. N. (2021). Carbon dots as an emergent class of antimicrobial agents. *Nanomaterials* 11 (8), 1877. doi:10.3390/nano11081877

Gudimella, K. K., Appidi, T., Wu, H-F., Battula, V., Jogdand, A., Rengan, A. K., et al. (2021). Sand bath assisted green synthesis of carbon dots from citrus fruit peels for free radical scavenging and cell imaging. *Colloids Surf. B Biointerfaces* 197, 111362. doi:10.1016/j.colsurfb.2020.111362

Gudimella, K. K., Gedda, G., Kumar, P. S., Babu, B. K., Yamajala, B., Rao, B. V., et al. (2022). Novel synthesis of fluorescent carbon dots from bio-based Carica Papaya Leaves: Optical and structural properties with antioxidant and anti-inflammatory activities. *Environ. Res.* 204, 111854. doi:10.1016/j.envres.2021.111854

Hailing, Y., Xiufang, L., Lili, W., Baoqiang, L., Kaichen, H., Yongquan, H., et al. (2020). Doxorubicin-loaded fluorescent carbon dots with PEI passivation as a drug delivery system for cancer therapy. *Nanoscale* 12 (33), 17222–17237. doi:10.1039/d0nr01236j

He, H., Chen, X., Feng, Z., Liu, L., Wang, Q., and Bi, S. (2021). Nanoscopic imaging of nucleolar stress enabled by protein-mimicking carbon dots. *Nano Lett.* 21 (13), 5689–5696. doi:10.1021/acs.nanolett.1c01420

He, X., Chen, P., Zhang, J., Luo, T. Y., Wang, H. J., Liu, Y. H., et al. (2019b). Cationic polymer-derived carbon dots for enhanced gene delivery and cell imaging. *Biomater. Sci.* 7 (5), 1940–1948. doi:10.1039/c8bm01578c

He, X., Luo, Q., Zhang, J., Chen, P., Wang, H-J., Luo, K., et al. (2019a). Gadolinium-doped carbon dots as nano-theranostic agents for MR/FL diagnosis and gene delivery. *Nanoscale* 11 (27), 12973–12982. doi:10.1039/c9nr03988k

Hettiarachchi, S. D., Graham, R. M., Mintz, K. J., Zhou, Y., Vanni, S., Peng, Z., et al. (2019). Triple conjugated carbon dots as a nano-drug delivery model for glioblastoma brain tumors. *Nanoscale* 11 (13), 6192–6205. doi:10.1039/c8nr08970a

Hsu, P-C., Chen, P-C., Ou, C-M., Chang, H-Y., and Chang, H-T. (2013). Extremely high inhibition activity of photoluminescent carbon nanodots toward cancer cells. *J. Mater. Chem. B* 1 (13), 1774–1781. doi:10.1039/c3tb00545c

Hu, X., Wang, S., Luo, Q., Ge, B., Cheng, Q., Dong, C., et al. (2021). Synthesis of Sn nanocluster@ carbon dots for photodynamic therapy application. *J. Chin. Chem. Lett.* 32 (7), 2287–2291. doi:10.1016/j.cclet.2021.01.039

Hua, X-W., Bao, Y-W., Zeng, J., and Wu, F-G. (2019). Nucleolus-targeted red emissive carbon dots with polarity-sensitive and excitation-independent fluorescence emission: High-resolution cell imaging and *in vivo* tracking. *ACS Appl. Mater Interfaces* 11 (36), 32647–32658. doi:10.1021/acsami.9b09590

Huang, S., Li, B., Ashraf, U., Li, Q., Lu, X., Gao, X., et al. (2020). Quaternized cationic carbon dots as antigen delivery systems for improving humoral and cellular immune responses. *ACS Appl. Nano Mater* 3 (9), 9449–9461. doi:10.1021/acsanm.0c02062

Iannazzo, D., Pistone, A., Ferro, S., De Luca, L., Monforte, A. M., Romeo, R., et al. (2018). Graphene quantum dots based systems as HIV inhibitors. *J. Bioconjugate Chem.* 29 (9), 3084–3093. doi:10.1021/acs.bioconjchem.8b00448

Indermun, S., Govender, M., Kumar, P., Choonara, Y. E., and Pillay, V. (2018). Stimuli-responsive polymers as smart drug delivery systems: Classifications based on carrier type and triggered-release mechanism. *Stimuli Responsive Polym. Nanocarriers Drug Deliv. Appl.* 1, 43–58. doi:10.1016/B978-0-08-101997-9.00002-3

Jia, Q., Zhao, Z., Liang, K., Nan, F., Li, Y., Wang, J., et al. (2020). Recent advances and prospects of carbon dots in cancer nanotheranostics. *Mater. Chem. Front.* 4 (2), 449–471. doi:10.1039/c9qm00667b

Jian, H-J., Wu, R-S., Lin, T-Y., Li, Y-J., Lin, H-J., Harroun, S. G., et al. (2017). Super-cationic carbon quantum dots synthesized from spermidine as an eye drop formulation for topical treatment of bacterial keratitis. *ACS Nano* 11 (7), 6703–6716. doi:10.1021/acsnano.7b01023

John, T. S., Yadav, P. K., Kumar, D., Singh, S. K., and Hasan, S. H. (2020). Highly fluorescent carbon dots from wheat bran as a novel drug delivery system for bacterial inhibition. *Luminescence* 35 (6), 913–923. doi:10.1002/bio.3801

Ju, E., Li, T., Liu, Z., da Silva, S. R., Wei, S., Zhang, X., et al. (2020). Specific inhibition of viral MicroRNAs by carbon dots-mediated delivery of locked nucleic acids for therapy of virus-induced cancer. *J. ACS Nano* 14 (1), 476–487. doi:10.1021/acsnano.9b06333

Kandra, R., and Bajpai, S. (2020). Synthesis, mechanical properties of fluorescent carbon dots loaded nanocomposites chitosan film for wound healing and drug delivery. *Arabian J. Chem.* 13 (4), 4882–4894. doi:10.1016/j.arabjc.2019.12.010

Kirbas Cilingir, E., Seven, E. S., Zhou, Y., Walters, B. M., Mintz, K. J., Pandey, R. R., et al. (2021). Metformin derived carbon dots: Highly biocompatible fluorescent nanomaterials as mitochondrial targeting and blood-brain barrier penetrating biomarkers. *J. Colloid Interface Sci.* 592, 485–497. doi:10.1016/j.jcis.2021.02.058

Kong, T., Zhou, R., Zhang, Y., Hao, L., Cai, X., and Zhu, B. (2020). AS1411 aptamer modified carbon dots via polyethylenimine-assisted strategy for efficient targeted cancer cell imaging. *Cell Prolif.* 53 (1), e12713. doi:10.1111/cpr.12713

Kotta, S., Aldawsari, H. M., Badr-Eldin, S. M., Alhakamy, N. A., Shadab, M., Nair, A. B., et al. (2020). Exploring the potential of carbon dots to combat COVID-19. *Front. Mol. Biosci.* 7, 616575. doi:10.3389/fmolb.2020.616575

Koulivand, H., Shahbazi, A., Vatanpour, V., and Rahmandoost, M. (2020). Novel antifouling and antibacterial polyethersulfone membrane prepared by embedding nitrogen-doped carbon dots for efficient salt and dye rejection. *Mater Sci. Eng. C Mater Biol. Appl.* 111, 110787. doi:10.1016/j.msec.2020.110787

Kung, J-C., Tseng, I-T., Chien, C-S., Lin, S-H., Wang, C-C., and Shih, C-J. (2020). Microwave assisted synthesis of negative-charge carbon dots with potential antibacterial activity against multi-drug resistant bacteria. *RSC Adv.* 10 (67), 41202–41208. doi:10.1039/d0ra07106d

Lategan, K., Fowler, J., Bayati, M., Fidalgo de Cortalezzi, M., and Pool, E. (2018). The effects of carbon dots on immune system biomarkers, using the murine macrophage cell line RAW 264.7 and human whole blood cell cultures. *Nanomater. (Basel)* 8 (6), 388. doi:10.3390/nano8060388

Lee, T-Y., Jayakumar, T., Thanasekaran, P., Lin, K-C., Chen, H-M., Veerakumar, P., et al. (2020). Carbon dot nanoparticles exert inhibitory effects on human platelets and reduce mortality in mice with acute pulmonary thromboembolism. *Nanomaterials* 10 (7), 1254. doi:10.3390/nano10071254

Li, C-L., Ou, C-M., Huang, C-C., Wu, W-C., Chen, Y-P., Lin, T-E., et al. (2014). Carbon dots prepared from ginger exhibiting efficient inhibition of human hepatocellular carcinoma cells. *J. Mater. Chem.* 2 (28), 4564–4571. doi:10.1039/c4tb00216d

Li, J., Kong, J., Ma, S., Li, J., Mao, M., Chen, K., et al. (2021). Exosome-Coated 10B carbon dots for precise boron neutron capture therapy in a mouse model of glioma *in situ*. *Adv. Funct. Mater.* 31 (24), 2100969. doi:10.1002/adfm.202100969

Li, R. S., Gao, P. F., Zhang, H. Z., Zheng, L. L., Li, C. M., Wang, J., et al. (2017). Chiral nanoprobes for targeting and long-term imaging of the Golgi apparatus. *Chem. Sci.* 8 (10), 6829–6835. doi:10.1039/c7sc01316g

Li, S., Guo, Z., Zeng, G., Zhang, Y., Xue, W., and Liu, Z. (2018). Polyethylenimine-modified fluorescent carbon dots as vaccine delivery system for intranasal immunization. *ACS Biomater. Sci. Eng.* 4 (1), 142–150. doi:10.1021/acsbiomaterials.7b00370

Li, X., Hu, S., Lin, Z., Yi, J., Liu, X., Tang, X., et al. (2020a). Dual-responsive mesoporous silica nanoparticles coated with carbon dots and polymers for drug encapsulation and delivery. *Nanomedicine* 15 (25), 2447–2458. doi:10.2217/nnm-2019-0440

Li, X., Vinothini, K., Ramesh, T., Rajan, M., and Ramu, A. (2020b). Combined photodynamic-chemotherapy investigation of cancer cells using carbon quantum dot-based drug carrier system. *Drug Deliv.* 27 (1), 791–804. doi:10.1080/10717544.2020.1765431

Li, Y., Wu, S., Zhang, J., Zhou, R., and Cai, X. (2020c). Sulphur doped carbon dots enhance photodynamic therapy via PI3K/Akt signalling pathway. *Cell Prolif.* 53 (5), e12821. doi:10.1111/cpr.12821

Liang, J., Li, W., Chen, J., Huang, X., Liu, Y., Zhang, X., et al. (2021). Antibacterial activity and synergetic mechanism of carbon dots against gram-positive and-negative bacteria. *ACS Appl. Bio Mater.* 4 (9), 6937–6945. doi:10.1021/acsabm.1c00618

Lim, S. Y., Shen, W., and Gao, Z. (2015). Carbon quantum dots and their applications. *Chem. Soc. Rev.* 44 (1), 362–381. doi:10.1039/c4cs00269e

Liu, J., Li, R., and Yang, B. (2020). Carbon dots: A new type of carbon-based nanomaterial with wide applications. *ACS Cent. Sci.* 6 (12), 2179–2195. doi:10.1021/acscentsci.0c01306

Liu, X., Liu, Y., Thakor, A. S., Kevadiya, B. D., Cheng, J., Chen, M., et al. (2021). Endogenous NO-releasing carbon nanodots for tumor-specific gas therapy. *Acta Biomater.* 136, 485–494. doi:10.1016/j.actbio.2021.09.051

Liu, Y., Lei, J. H., Wang, G., Zhang, Z., Wu, J., Zhang, B., et al. (2022). Toward strong near-infrared absorption/emission from carbon dots in aqueous media through solvothermal fusion of large conjugated perylene derivatives with post-surface engineering. *Adv. Sci. (Weinh).* 9 (23), e2202283. doi:10.1002/advs.202202283

Liyanage, P. Y., Zhou, Y., Al-Youbi, A. O., Bashammakh, A. S., El-Shahawi, M. S., Vanni, S., et al. (2020). Pediatric glioblastoma target-specific efficient delivery of gemcitabine across the blood–brain barrier via carbon nitride dots. *Nanoscale* 12 (14), 7927–7938. doi:10.1039/d0nr01647k

Łoczechin, A., Séron, K., Barras, A., Giovanelli, E., Belouzard, S., Chen, Y-T., et al. (2019). Functional carbon quantum dots as medical countermeasures to human coronavirus. *ACS Appl. Mater Interfaces* 11 (46), 42964–42974. doi:10.1021/acsami.9b15032

Luo, L., Liu, C., He, T., Zeng, L., Xing, J., Xia, Y., et al. (2018). Engineered fluorescent carbon dots as promising immune adjuvants to efficiently enhance cancer immunotherapy. *Nanoscale* 10 (46), 22035–22043. doi:10.1039/c8nr07252c

Lv, R., Li, G., Lu, S., and Wang, T. (2021). Synthesis of multi-functional carbon quantum dots for targeted antitumor therapy. *J. Fluoresc.* 31 (2), 339–348. doi:10.1007/s10895-020-02661-5

Martins, I., Tomás, H., Lahoz, F., and Rodrigues, J. (2021). Engineered fluorescent carbon dots and G4-G6 PAMAM dendrimer nanohybrids for bioimaging and gene delivery. *Biomacromolecules* 22 (6), 2436–2450. doi:10.1021/acs.biomac.1c00232

Mathad, A. S., Seetharamappa, J., and Kalanur, S. S. (2022). β-Cyclodextrin anchored neem carbon dots for enhanced electrochemical sensing performance of an anticancer drug, lapatinib via host-guest inclusion. *J. Mol. Liq.* 350, 118582. doi:10.1016/j.molliq.2022.118582

Mickaël, C., Jiahui, F., Mickaël, R., Françoise, P., and Luc, L. (2019). Influence of carbonization conditions on luminescence and gene delivery properties of nitrogen-doped carbon dots. *RSC Adv.* 9 (6), 3493–3502. doi:10.1039/c8ra09651a

Ming, H., Ma, Z., Liu, Y., Pan, K., Yu, H., Wang, F., et al. (2012). Large scale electrochemical synthesis of high quality carbon nanodots and their photocatalytic property. *Dalton Trans.* 41 (31), 9526–9531. doi:10.1039/c2dt30985h

Mintz, K. J., Bartoli, M., Rovere, M., Zhou, Y., Hettiarachchi, S. D., Paudyal, S., et al. (2021). A deep investigation into the structure of carbon dots. *Carbon* 173, 433–447. doi:10.1016/j.carbon.2020.11.017

Mintz, K. J., Cilingir, E. K., Nagaro, G., Paudyal, S., Zhou, Y., Khadka, D., et al. (2022). Development of red-emissive carbon dots for bioimaging through a building block approach: Fundamental and applied studies. *Bioconjug Chem.* 33 (1), 226–237. doi:10.1021/acs.bioconjchem.1c00544

Mintz, K. J., Mercado, G., Zhou, Y., Ji, Y., Hettiarachchi, S. D., Liyanage, P. Y., et al. (2019). Tryptophan carbon dots and their ability to cross the blood-brain barrier. *Colloids Surfaces B Biointerfaces.* 176, 488–493. doi:10.1016/j.colsurfb.2019.01.031

Mohammadi, S., Mohammadi, S., and Salimi, A. (2021). A 3D hydrogel based on chitosan and carbon dots for sensitive fluorescence detection of microRNA-21 in breast cancer cells. *Talanta* 224, 121895. doi:10.1016/j.talanta.2020.121895

Mohammadinejad, R., Dadashzadeh, A., Moghassemi, S., Ashrafizadeh, M., Dehshahri, A., Pardakhty, A., et al. (2019). Shedding light on gene therapy: Carbon dots for the minimally invasive image-guided delivery of plasmids and noncoding RNAs-A review. *J. Adv. Res.* 18, 81–93. doi:10.1016/j.jare.2019.01.004

Montané, X., Bajek, A., Roszkowski, K., Montornés, J. M., Giamberini, M., Roszkowski, S., et al. (2020). Encapsulation for cancer therapy. *Molecules* 25 (7), 1605. doi:10.3390/molecules25071605

Naik, K., Chaudhary, S., Ye, L., and Parmar, A. S. (2022). A strategic review on carbon quantum dots for cancer-diagnostics and treatment. *Front. Bioeng. Biotechnol.* 10, 882100. doi:10.3389/fbioe.2022.882100

Nasrin, A., Hassan, M., and Gomes, V. G. (2020). Two-photon active nucleus-targeting carbon dots: Enhanced ROS generation and photodynamic therapy for oral cancer. *Nanoscale* 12 (40), 20598–20603. doi:10.1039/d0nr05210h

Nocito, G., Calabrese, G., Forte, S., Petralia, S., Puglisi, C., Campolo, M., et al. (2021). Carbon dots as promising tools for cancer diagnosis and therapy. *Cancers* 13 (9), 1991. doi:10.3390/cancers13091991

Othman, H. O., Salehnia, F., Hosseini, M., Hassan, R., Faizullah, A., and Ganjali, M. R. (2020). Fluorescence immunoassay based on nitrogen doped carbon dots for the detection of human nuclear matrix protein NMP22 as biomarker for early stage diagnosis of bladder cancer. *Microchem. J.* 157, 104966. doi:10.1016/j.microc.2020.104966

Pandey, A., Devkota, A., Yadegari, Z., Dumenyo, K., and Taheri, A. (2021). Antibacterial properties of citric acid/β-alanine carbon dots against gram-negative bacteria. *Nanomaterials* 11 (8), 2012. doi:10.3390/nano11082012

Qin, X., Liu, J., Zhang, Q., Chen, W., Zhong, X., and He, J. (2021). Synthesis of yellow-fluorescent carbon nano-dots by microplasma for imaging and photocatalytic inactivation of cancer cells. *Nanoscale Res. Lett.* 16 (1), 14–19. doi:10.1186/s11671-021-03478-2

Rahmani, Z., Ghaemy, M., and Olad, A. (2021). Preparation of nanogels based on kappa-carrageenan/chitosan and N-doped carbon dots: Study of drug delivery behavior. *Polym. Bull.* 78 (5), 2709–2726. doi:10.1007/s00289-020-03236-x

Rajendran, S., Zichri, S. B., Usha Vipinachandran, V., Jelinek, R., and Bhunia, S. K. (2021). Triphenylphosphonium-derived bright green fluorescent carbon dots for mitochondrial targeting and rapid selective detection of tetracycline. *ChemNanoMat* 7 (5), 545–552. doi:10.1002/cnma.202100125

Ren, G., Hou, X., Kang, Y., Zhang, R., Zhang, M., Liu, W., et al. (2020). Efficient preparation of nitrogen-doped fluorescent carbon dots for highly sensitive detection of metronidazole and live cell imaging. *Spectrochim. Acta A Mol. Biomol. Spectrosc.* 234, 118251. doi:10.1016/j.saa.2020.118251

Ren, W., Chen, S., Liao, Y., Li, S., Ge, J., Tao, F., et al. (2019). Near-infrared fluorescent carbon dots encapsulated liposomes as multifunctional nano-carrier and tracer of the anticancer agent cinobufagin *in vivo* and *in vitro*. *Colloids Surfaces B Biointerfaces.* 174, 384–392. doi:10.1016/j.colsurfb.2018.11.041

Ren, W., Nan, F., Li, S., Yang, S., Ge, J., and Zhao, Z. (2021). Red emissive carbon dots prepared from polymers as an efficient nanocarrier for coptisine delivery *in vivo* and *in vitro*. *ChemMedChem* 16 (4), 646–653. doi:10.1002/cmdc.202000420

Romero, M. P., Alves, F., Stringasci, M. D., Buzzá, H. H., Ciol, H., Inada, N. M., et al. (2021). One-pot microwave-assisted synthesis of carbon dots and *in vivo* and *in vitro* antimicrobial photodynamic applications. *Front. Microbiol.* 12, 662149. doi:10.3389/fmicb.2021.662149

Sahu, S., Behera, B., Maiti, T. K., and Mohapatra, S. (2012). Simple one-step synthesis of highly luminescent carbon dots from orange juice: Application as excellent bio-imaging agents. *Chem. Commun. (Camb).* 48 (70), 8835–8837. doi:10.1039/c2cc33796g

Saravanan, A., Maruthapandi, M., Das, P., Ganguly, S., Margel, S., Luong, J. H., et al. (2020). Applications of N-doped carbon dots as antimicrobial agents, antibiotic carriers, and selective fluorescent probes for nitro explosives. *ACS Appl. Bio Mater.* 3 (11), 8023–8031. doi:10.1021/acsabm.0c01104

Saravanan, A., Maruthapandi, M., Das, P., Luong, J. H., and Gedanken, A. (2021). Green synthesis of multifunctional carbon dots with antibacterial activities. *Nanomaterials* 11 (2), 369. doi:10.3390/nano11020369

Sekar, R., Basavegowda, N., Jena, S., Jayakodi, S., Elumalai, P., Chaitanyakumar, A., et al. (2022). Recent developments in heteroatom/metal-doped carbon dot-based image-guided photodynamic therapy for cancer. *Pharmaceutics* 14 (9), 1869. doi:10.3390/pharmaceutics14091869

Sen, P., and Nyokong, T. (2021). Promising photodynamic antimicrobial activity of polyimine substituted zinc phthalocyanine and its polycationic derivative when conjugated to nitrogen, sulfur, co-doped graphene quantum dots against *Staphylococcus aureus*. *Photodiagnosis Photodyn. Ther.* 34, 102300. doi:10.1016/j.pdpdt.2021.102300

Sharma, A., Panwar, V., Thomas, J., Chopra, V., Roy, H. S., and Ghosh, D. (2021). Actin-binding carbon dots selectively target glioblastoma cells while sparing normal cells. *Colloids Surf. B Biointerfaces* 200, 111572. doi:10.1016/j.colsurfb.2021.111572

Shoval, A., Markus, A., Zhou, Z., Liu, X., Cazelles, R., Willner, I., et al. (2019). Anti-VEGF-aptamer modified C-dots—a hybrid nanocomposite for topical treatment of ocular vascular disorders. *Small* 15 (40), 1902776. doi:10.1002/smll.201902776

Singh, G., Kaur, H., Sharma, A., Singh, J., Alajangi, H. K., Kumar, S., et al. (2021). Carbon based nanodots in early diagnosis of cancer. *Front. Chem.* 9, 669169. doi:10.3389/fchem.2021.669169

Singh, S., Mishra, A., Kumari, R., Sinha, K. K., Singh, M. K., and Das, P. (2017). Carbon dots assisted formation of DNA hydrogel for sustained release of drug. *Carbon* 114, 169–176. doi:10.1016/j.carbon.2016.12.020

Singh, V., Rawat, K. S., Mishra, S., Baghel, T., Fatima, S., John, A. A., et al. (2018). Biocompatible fluorescent carbon quantum dots prepared from beetroot extract for *in vivo* live imaging in *C. elegans* and BALB/c mice. *J. Mater Chem. B* 6 (20), 3366–3371. doi:10.1039/c8tb00503f

Sk, M. P., Jaiswal, A., Paul, A., Ghosh, S. S., and Chattopadhyay, A. (2012). Presence of amorphous carbon nanoparticles in food caramels. *Sci. Rep.* 2, 383. doi:10.1038/srep00383

Sohail, M., Xie, B., Li, B., and Huang, H. (2022). Zn-Doped carbon dots-based versatile bioanalytical probe for precise estimation of antioxidant activity index of multiple samples via fenton Chemistry. *J. Sensors Actuators B Chem.* 363, 131558. doi:10.1016/j.snb.2022.131558

Stewart, B. W., and Kleihues, P. (2003). *World cancer report*. France: IARC press Lyon.

Su, D., Han, X., Yan, X., Jin, R., Li, H., Kong, D., et al. (2020b). Smartphone-assisted robust sensing platform for on-site quantitation of 2,4-dichlorophenoxyacetic acid using red emissive carbon dots. *Anal. Chem.* 92 (18), 12716–12724. doi:10.1021/acs.analchem.0c03275

Su, W., Guo, R., Yuan, F., Li, Y., Li, X., Zhang, Y., et al. (2020a). Red-emissive carbon quantum dots for nuclear drug delivery in cancer stem cells. *J. Phys. Chem. Lett.* 11 (4), 1357–1363. doi:10.1021/acs.jpclett.9b03891

Sun, B., Wu, F., Zhang, Q., Chu, X., Wang, Z., Huang, X., et al. (2021). Insight into the effect of particle size distribution differences on the antibacterial activity of carbon dots. *J. Colloid Interface Sci.* 584, 505–519. doi:10.1016/j.jcis.2020.10.015

Sun, Y., Zheng, S., Liu, L., Kong, Y., Zhang, A., Xu, K., et al. (2020). The cost-effective preparation of green fluorescent carbon dots for bioimaging and enhanced intracellular drug delivery. *Nanoscale Res. Lett.* 15 (1), 55–59. doi:10.1186/s11671-020-3288-0

Talib, A. B., and Mohammed, M. H. (2021). Preparation, characterization and preliminary cytotoxic evaluation of 6-mercaptopurine-coated biotinylated carbon dots nanoparticles as a drug delivery system. *Mater. Today Proc.* 80, 2327–2333. doi:10.1016/j.matpr.2021.06.341

Tang, C., Long, R., Tong, X., Guo, Y., Tong, C., and Shi, S. (2021). Dual-emission biomass carbon dots for near-infrared ratiometric fluorescence determination and imaging of ascorbic acid. *Microchem. J.* 164, 106000. doi:10.1016/j.microc.2021.106000

Tang, X., Wang, H., Yu, H., Bui, B., Zhang, W., Wang, S., et al. (2022). Exploration of nitrogen-doped grape peels carbon dots for baicalin detection. *Mater. Today Phys.* 22, 100576. doi:10.1016/j.mtphys.2021.100576

Tao, H., Yang, K., Ma, Z., Wan, J., Zhang, Y., Kang, Z., et al. (2012). *In vivo* NIR fluorescence imaging, biodistribution, and toxicology of photoluminescent carbon dots produced from carbon nanotubes and graphite. *Small* 8 (2), 281–290. doi:10.1002/smll.201101706

Ting, D., Dong, N., Fang, L., Lu, J., Bi, J., Xiao, S., et al. (2020). Correction to multisite inhibitors for enteric coronavirus: Antiviral cationic carbon dots based on curcumin. *ACS Appl. Nano Mater* 3 (5), 4913. doi:10.1021/acsanm.0c00970

Tong, T., Hu, H., Zhou, J., Deng, S., Zhang, X., Tang, W., et al. (2020). Glycyrrhizic-acid-based carbon dots with high antiviral activity by multisite inhibition mechanisms. *Small* 16 (13), 1906206. doi:10.1002/smll.201906206

Wang, B., Cai, H., Waterhouse, G. I. N., Qu, X., Yang, B., and Lu, S. (2022a). Carbon dots in bioimaging, biosensing and therapeutics: A comprehensive review. *Small Sci.* 2 (6), 2200012. doi:10.1002/smsc.202200012

Wang, L., Pan, H., Gu, D., Li, P., Su, Y., and Pan, W. (2022b). A composite system combining self-targeted carbon dots and thermosensitive hydrogels for challenging ocular drug delivery. *J. Pharm. Sci.* 111 (5), 1391–1400. doi:10.1016/j.xphs.2021.09.026

Wang, L., Pan, H., Gu, D., Sun, H., Chen, K., Tan, G., et al. (2021a). A novel carbon dots/thermo-sensitive *in situ* gel for a composite ocular drug delivery system: Characterization, eEx-vVivo imaging, and *in vivo* evaluation. *Int. J. Mol. Sci.* 22 (18), 9934. doi:10.3390/ijms22189934

Wang, Q., Zhang, S., Wang, B., Yang, X., Zou, B., Yang, B., et al. (2019). Pressure-triggered aggregation-induced emission enhancement in red emissive amorphous carbon dots. *Nanoscale Horizons* 4 (5), 1227–1231. doi:10.1039/c9nh00287a

Wang, S., Chen, L., Wang, J., Du, J., Li, Q., Gao, Y., et al. (2020). Enhanced-fluorescent imaging and targeted therapy of liver cancer using highly luminescent carbon dots-conjugated foliate. *Mater Sci. Eng. C Mater Biol. Appl.* 116, 111233. doi:10.1016/j.msec.2020.111233

Wang, T., Wang, S., Liu, Z., He, Z., Yu, P., Zhao, M., et al. (2021b). A hybrid erbium(III)-bacteriochlorin near-infrared probe for multiplexed biomedical imaging. *Nat. Mater* 20 (11), 1571–1578. doi:10.1038/s41563-021-01063-7

Weiss, M., Fan, J., Claudel, M., Sonntag, T., Didier, P., Ronzani, C., et al. (2021). Density of surface charge is a more predictive factor of the toxicity of cationic carbon nanoparticles than zeta potential. *J. Nanobiotechnology* 19 (1), 5. doi:10.1186/s12951-020-00747-7

Wen, X., Zhao, Z., Zhai, S., Wang, X., and Li, Y. (2020). Stable nitrogen and sulfur co-doped carbon dots for selective folate sensing, *in vivo* imaging and drug delivery. *Diam. Relat. Mater.* 105, 107791. doi:10.1016/j.diamond.2020.107791

Wu, L-N., Yang, Y-J., Huang, L-X., Zhong, Y., Chen, Y., Gao, Y-R., et al. (2022). Levofloxacin-based carbon dots to enhance antibacterial activities and combat antibiotic resistance. *Carbon* 186, 452–464. doi:10.1016/j.carbon.2021.10.020

Xu, N., Du, J., Yao, Q., Ge, H., Shi, C., Xu, F., et al. (2021). Carbon dots inspired by structure-inherent targeting for nucleic acid imaging and localized photodynamic therapy. *Sensors Actuators B Chem.* 344, 130322. doi:10.1016/j.snb.2021.130322

Xu, X., Ray, R., Gu, Y., Ploehn, H. J., Gearheart, L., Raker, K., et al. (2004). Electrophoretic analysis and purification of fluorescent single-walled carbon nanotube fragments. *J. Am. Chem. Soc.* 126 (40), 12736–12737. doi:10.1021/ja040082h

Xu, X., Zhang, K., Zhao, L., Li, C., Bu, W., Shen, Y., et al. (2016). Aspirin-based carbon dots, a good biocompatibility of material applied for bioimaging and anti-inflammation. *ACS Appl. Mater Interfaces* 8 (48), 32706–32716. doi:10.1021/acsami.6b12252

Xu, Y., Wang, C., Jiang, T., Ran, G., and Song, Q. (2022). Cadmium induced aggregation of orange–red emissive carbon dots with enhanced fluorescence for intracellular imaging. *J. Hazard. Mater.* 427, 128092. doi:10.1016/j.jhazmat.2021.128092

Xue, Y., Liu, C., Andrews, G., Wang, J., and Ge, Y. (2022). Recent advances in carbon quantum dots for virus detection, as well as inhibition and treatment of viral infection. *J. Nano Converg.* 9 (1), 15–31. doi:10.1186/s40580-022-00307-9

Yadav, P. K., Chandra, S., Kumar, V., Kumar, D., and Hasan, S. H. (2023). Carbon quantum dots: Synthesis, structure, properties, and catalytic applications for organic synthesis. *Catalysts* 13 (2), 422. doi:10.3390/catal13020422

Ye, Z., Li, G., Lei, J., Liu, M., Jin, Y., and Li, B. (2020). One-Step and one-precursor hydrothermal synthesis of carbon dots with superior antibacterial activity. *ACS Appl. Bio Mater.* 3 (10), 7095–7102. doi:10.1021/acsabm.0c00923

Yu, A., Tang, Y., Li, K., Gao, J., Zheng, Y., and Zeng, Z. (2019). Tunable photoluminescence studies based on blue-emissive carbon dots and sequential determination of Fe (III) and pyrophosphate ions. *Spectrochim. Acta A Mol. Biomol. Spectrosc.* 222, 117231. doi:10.1016/j.saa.2019.117231

Yue, J., Li, L., Cao, L., Zan, M., Yang, D., Wang, Z., et al. (2019). Two-step hydrothermal preparation of carbon dots for calcium ion detection. *ACS Appl. Mater. Interfaces* 11 (47), 44566–44572. doi:10.1021/acsami.9b13737

Yue, J., Li, L., Jiang, C., Mei, Q., Dong, W-F., and Yan, R. (2021). Riboflavin-based carbon dots with high singlet oxygen generation for photodynamic therapy. *J. Mater Chem. B* 9 (38), 7972–7978. doi:10.1039/d1tb01291f

Zeng, Q., Shao, D., He, X., Ren, Z., Ji, W., Shan, C., et al. (2016). Carbon dots as a trackable drug delivery carrier for localized cancer therapy *in vivo*. *J. Mater. Chem. B* 4 (30), 5119–5126. doi:10.1039/c6tb01259k

Zhang, M., Zhai, X., Ma, T., Huang, Y., Yan, C. H., and Du, Y. (2021b). Multifunctional cerium doped carbon dots nanoplatform and its applications for wound healing. *Chem. Eng. J.* 423, 130301. doi:10.1016/j.cej.2021.130301

Zhang, M., Zheng, T., Sheng, B., Wu, F., Zhang, Q., Wang, W., et al. (2019b). Mn2+ complex-modified polydopamine-and dual emissive carbon dots based nanoparticles for *in vitro* and *in vivo* trimodality fluorescent, photothermal, and magnetic resonance imaging. *Chem. Eng. J.* 373, 1054–1063. doi:10.1016/j.cej.2019.05.107

Zhang, W., Sigdel, G., Mintz, K. J., Seven, E. S., Zhou, Y., Wang, C., et al. (2021a). Carbon dots: A future blood–brain barrier penetrating nanomedicine and drug nanocarrier. *Int. J. nanomedicine* 16, 5003–5016. doi:10.2147/ijn.s318732

Zhang, Y., Wang, S., Lu, F., Zhang, M., Kong, H., Cheng, J., et al. (2021c). The neuroprotective effect of pretreatment with carbon dots from Crinis Carbonisatus (carbonized human hair) against cerebral ischemia reperfusion injury. *J. Nanobiotechnology* 19 (1), 257. doi:10.1186/s12951-021-00908-2

Zhang, Z., Lei, Y., Yang, X., Shi, N., Geng, L., Wang, S., et al. (2019a). High drug-loading system of hollow carbon dots–doxorubicin: Preparation, *in vitro* release and pH-targeted research. *J. Mater Chem. B* 7 (13), 2130–2137. doi:10.1039/c9tb00032a

Zhao, C., Wang, X., Wu, L., Wu, W., Zheng, Y., Lin, L., et al. (2019). Nitrogen-doped carbon quantum dots as an antimicrobial agent against Staphylococcus for the treatment of infected wounds. *Colloids Surfaces B Biointerfaces* 179, 17–27. doi:10.1016/j.colsurfb.2019.03.042

Zhao, D., Zhang, Z., Liu, X., Zhang, R., and Xiao, X. (2021). Rapid and low-temperature synthesis of N, P co-doped yellow emitting carbon dots and their applications as antibacterial agent and detection probe to Sudan Red I. *Mater. Sci. Eng. C* 119, 111468. doi:10.1016/j.msec.2020.111468

Zhao, W-B., Chen, D-D., Liu, K-K., Wang, Y., Zhou, R., Song, S-Y., et al. (2023). Near-infrared I/II emission and absorption carbon dots via constructing localized excited/charge transfer state for multiphoton imaging and photothermal therapy. *Chem. Eng. J.* 452, 139231. doi:10.1016/j.cej.2022.139231

Zhao, Y., Zhang, Y., Kong, H., Cheng, G., Qu, H., and Zhao, Y. (2022). Protective effects of carbon dots derived from Armeniacae semen Amarum carbonisata against acute lung injury induced by lipopolysaccharides in rats. *Int. J. Nanomedicine* 17, 1–14. doi:10.2147/ijn.s338886

Zhou, Y., Liyanage, P. Y., Devadoss, D., Guevara, L. R. R., Cheng, L., Graham, R. M., et al. (2019). Nontoxic amphiphilic carbon dots as promising drug nanocarriers across the blood–brain barrier and inhibitors of β-amyloid. *Nanoscale* 11 (46), 22387–22397. doi:10.1039/c9nr08194a

Zhou, Y., Mintz, K. J., Cheng, L., Chen, J., Ferreira, B., Hettiarachchi, S. D., et al. (2020). Direct conjugation of distinct carbon dots as Lego-like building blocks for the assembly of versatile drug nanocarriers. *J. Colloid Interface Sci.* 576, 412–425. doi:10.1016/j.jcis.2020.05.005

Zhu, X., Pang, X., Zhang, Y., and Yao, S. (2019). Titanium carbide MXenes combined with red-emitting carbon dots as a unique turn-on fluorescent nanosensor for label-free determination of glucose. *J. Mater Chem. B* 7 (48), 7729–7735. doi:10.1039/c9tb02060h

Zu, F., Yan, F., Bai, Z., Xu, J., Wang, Y., Huang, Y., et al. (2017). The quenching of the fluorescence of carbon dots: A review on mechanisms and applications. *Microchim. Acta* 184 (7), 1899–1914. doi:10.1007/s00604-017-2318-9

Zuo, P., Lu, X., Sun, Z., Guo, Y., and He, H. (2016). A review on syntheses, properties, characterization and bioanalytical applications of fluorescent carbon dots. *Microchim. Acta* 183 (2), 519–542. doi:10.1007/s00604-015-1705-3

Frontiers in Chemistry

TYPE Original Research
PUBLISHED 20 July 2023
DOI 10.3389/fchem.2023.1214072

OPEN ACCESS

EDITED BY
Naoufal Bahlawane,
Luxembourg Institute of Science and Technology (LIST), Luxembourg

REVIEWED BY
Angela Longo,
National Research Council (CNR), Italy
Andjelika Bjelajac,
Luxembourg Institute of Science and Technology (LIST), Luxembourg

*CORRESPONDENCE
Cristian Vacacela Gomez,
✉ vacacela@lnf.infn.it
Stefano Bellucci,
✉ bellucci@lnf.infn.it

RECEIVED 28 April 2023
ACCEPTED 29 June 2023
PUBLISHED 20 July 2023

CITATION
Tene T, Guevara M, Benalcázar Palacios F, Morocho Barrionuevo TP, Vacacela Gomez C and Bellucci S (2023), Optical properties of graphene oxide. *Front. Chem.* 11:1214072.
doi: 10.3389/fchem.2023.1214072

Optical properties of graphene oxide

Talia Tene[1], Marco Guevara[2], Freddy Benalcázar Palacios[3], Tania Paulina Morocho Barrionuevo[4], Cristian Vacacela Gomez[5]* and Stefano Bellucci[5]*

[1]Department of Chemistry, Universidad Técnica Particular de Loja, Loja, Ecuador, [2]Facultad de Ingeniería Mecánica, Escuela Superior Politécnica de Chimborazo (ESPOCH), Riobamba, Ecuador, [3]Facultad de Ingeniería en Sistemas Electrónica e Industrial, Universidad Técnica de Ambato, Ambato, Ecuador, [4]Facultad de Ciencias, Carrera de Estadística, Escuela Superior Politécnica de Chimborazo (ESPOCH), Riobamba, Ecuador, [5]INFN-Laboratori Nazionali di Frascati, Frascati, Italy

The study of the optical properties of graphene oxide (GO) is crucial in designing functionalized GO materials with specific optical properties for various applications such as (bio) sensors, optoelectronics, and energy storage. The present work aims to investigate the electronic transitions, optical bandgap, and absorption coefficient of GO under different conditions. Specifically, the study examines the effects of drying times ranging from 0 to 120 h while maintaining a fixed temperature of 80°C and low temperatures ranging from 40°C to 100°C, with a constant drying time of 24 h. Our findings indicate that exposing the GO sample to a drying time of up to 120 h at 80°C can lead to a reduction in the optical bandgap, decreasing it from 4.09 to 2.76 eV. The $\pi - \pi^*$ transition was found to be the most affected, shifting from approximately 230 nm at 0 h to 244 nm after 120 h of drying time. Absorption coefficients of 3140–5507 ml mg^{-1} m^{-1} were measured, which are similar to those reported for exfoliated graphene dispersions but up to two times higher, confirming the improved optical properties of GO. Our findings can provide insights into determining the optimal temperature and duration required for transforming GO into its reduced form for a specific application through extrapolation. The study is complemented by analyzing the elemental composition, surface morphology change, and electrical properties.

KEYWORDS

graphene oxide, optical bandgap, electronic transitions, absorption coefficient, Tauc analysis

1 Introduction

Over the past decade, oxidized graphenes have gained significant attention due to their unique physical and chemical properties (Chaudhuri and Yun, 2023). For instance, graphene oxide (GO) is produced by oxidizing graphene, a two-dimensional honeycomb material, with strong acids and oxidizing agents (Haydari et al., 2023). This process introduces oxygen-containing functional groups, such as hydroxyl, epoxy, and carboxyl groups (Ferrari et al., 2023), onto the graphene lattice and modifies its electronic structure, creating an intrinsic bandgap. GO offers several advantages over pure graphene, including improved processability, versatility, and cost-effectiveness (Grewal et al., 2018). Specifically, GO possesses interesting properties such as high hydrophilicity, solubility in water, large surface area, excellent dispersibility, and biocompatibility, making it an attractive material for various applications in fields such as energy storage (Safari and Mazloom, 2023), biosensors (Kadhim et al., 2023), water purification (Tene et al., 2022a), electronic devices (Wu et al., 2023), and drug delivery (Sontakke et al., 2023).

However, the presence of oxygen-containing functional groups in GO diminishes its electrical conductivity and mechanical strength (Liu et al., 2022). To address these limitations, GO is often reduced to obtain reduced GO (rGO), which restores the sp^2 carbon network and partially recovers the electronic properties of graphene (Yu et al., 2023). This reduction process can be achieved chemically, electrochemically, or thermally. Among these, the thermal reduction at high temperatures (> 900℃) is the most attractive since it does not imply the use of strong chemical agents or subsequent processes. As a result, rGO has a lower oxygen content and higher electronic conductivity compared to GO while retaining some of the unique properties of graphene such as large surface area and excellent electrical conductivity.

The electronic and optical properties of GO and rGO are critical for next-generation devices, making it essential to comprehend their behavior in various environments. Explicitly, understanding the electronic transitions and bandgap of these materials is important for optimizing their performance in electronic and photonic devices, designing functional materials, and identifying potential applications. The bandgap of GO and rGO can be estimated using various techniques, including X-ray photoelectron spectroscopy (XPS) and UV-visible spectroscopy (Baragau et al., 2023; Nagaiah et al., 2023). In particular, the Tauc method, which is widely used for estimating the bandgap of semiconducting materials from the absorption spectrum, has also been applied to GO and rGO in several studies (Aragaw, 2020). This method assumes that the absorption coefficient follows a power law as a function of photon energy, and the bandgap can then be estimated as the intercept of the linear portion with the x-axis. Therefore, the Tauc approach can be a useful approximation for estimating the bandgap of oxidized graphenes.

To put the reason for this research field in a broader context, Kumar et al. (2014) introduced a scalable thermal annealing process to enhance the properties of graphene oxide (GO). The annealing induces a phase transformation, resulting in improved optical and electronic properties of GO without compromising its oxygen content. The findings offer a pathway for the bulk processing of GO with enhanced properties for various applications. Very recently, Valentini et al., (2023) investigated the use of low-temperature thermal annealing to tune the electrical properties of GO and rGO. The authors optimized the annealing conditions and show that it is possible to achieve low resistivities and enhanced electrochemical performance in rGO films. This approach is scalable, environmentally friendly, and holds promise for applications in flexible and wearable electronics. These papers propose intriguing methods for producing GO in large quantities with specified features, however, they do not provide further information about the optical bandgap, electrical transitions, or absorption coefficients. To fully understand the possibilities of this strategy in changing the properties of GO, more research is therefore required.

Additionally, in our previous study (Arias Arias et al., 2020), we investigated the effects of drying time on GO with a specific focus on a maximum drying time of 24 h at a temperature of 80°C. Through the use of Raman spectroscopy, UV-visible spectroscopy, and TEM, we discussed changes in defects, absorption spectra, as well as the stacking of GO sheets. The findings contribute to enhancing the production of GO powder, within the limitations of the drying time and temperature parameters explored. With this in mind, in the present work, we extended our study to widely understand the change in electronic transitions, optical bandgap, and spectral weight of several GO samples under the effects of drying time (up to 120 h) and low temperatures (80°C and 50°C). Our analysis includes UV-visible spectroscopy to estimate the bandgap using the Tauc method, as well as energy-dispersive X-ray spectroscopy (EDS) and scanning electron microscopy (SEM) to gain additional insights into the elemental composition and morphology of the obtained materials. Additionally, we discuss in detail the values of the optical absorption coefficient under different environments as well as the related electrical characteristics. These findings provide never-discussed valuable insights into the electronic transitions and optical properties of GO.

2 Materials and methods

It is important to note that details of the oxidation-reduction process and the successful transformation of GO into chemically treated rGO can be found in our previous works (Arias Arias et al., 2020; Tene et al., 2021), along with its applications in pollutant removal, such as methylene blue (Arias Arias et al., 2020) and Hg(II) (Tene et al., 2022b). Here, we provide a brief overview of the synthesis process (Figure 1) and concentrate on discussing the chemical and physical properties of thermally treated GO.

2.1 Materials

Graphite powder (150 m, 99.99%), sulfuric acid (H_2SO_4, ACS reagent, 95.0%–98.0%), potassium permanganate ($KMnO_4$, ACS reagent, 99.0%), and hydrochloric acid (HCl, ACS reagent, 37%) were purchased from Sigma Aldrich. Hydrogen peroxide (H_2O_2, 30%) was obtained from Merk. All chemicals were used as received without further purification.

2.2 Synthesis of GO

A homogeneous mixture was obtained by adding 3.0 g of graphite powder to 70 mL of H_2SO_4 and stirring. The mixture was then placed in an ice bath, and 9 g of $KMnO_4$ was added, keeping the temperature under 20°C. After 30 min, the mixture was transferred to a water bath and heated to 50°C for 30 min while constantly stirring. Subsequently, 150 ml of distilled water was gradually added to the solution over 20 min, ensuring that the temperature did not exceed 90°C. Then, 500 ml of distilled water was added, and 15 ml of H_2O_2 was introduced. After 1 h, the precipitated material was divided into centrifuge tubes and washed with a 1:10 solution of HCl and distilled water via several centrifugations at 10000 rpm for 10 min. The precipitate was then placed in a Teflon

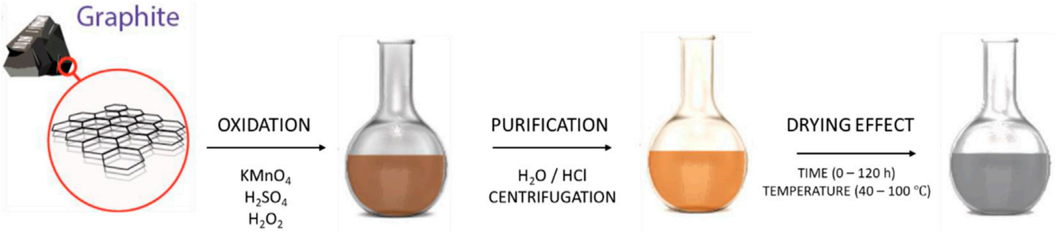

FIGURE 1
Schematic representation of the synthesis process.

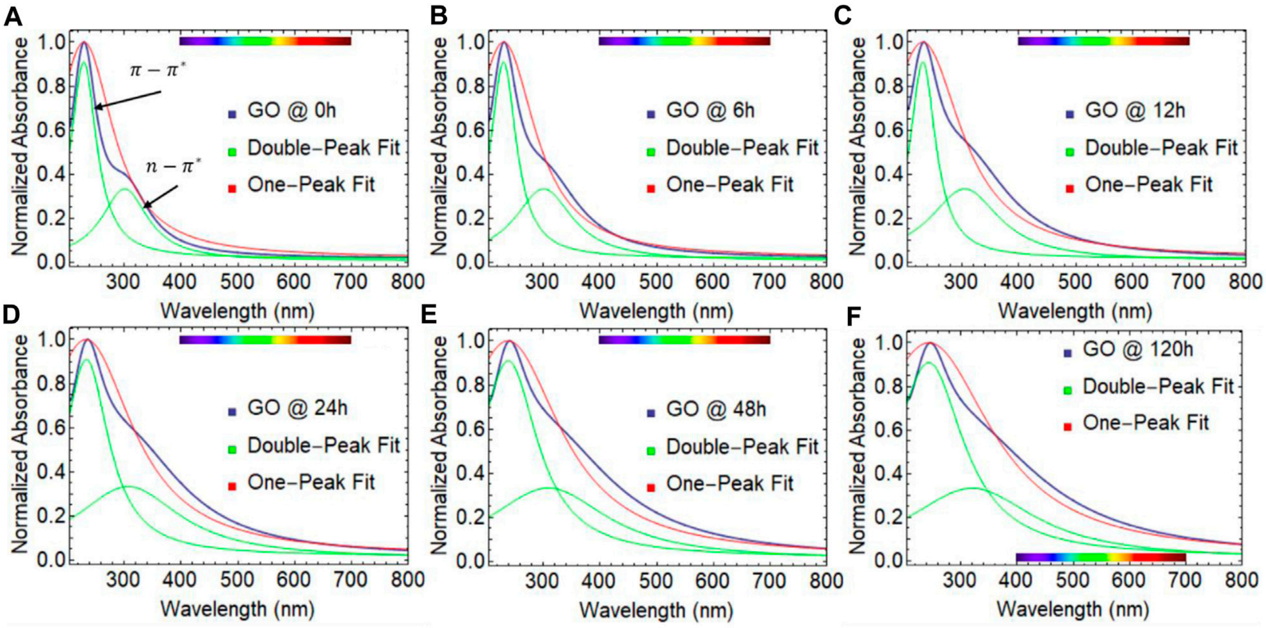

FIGURE 2
UV-visible spectra of graphene oxide (GO) dried at 80°C considering different drying times: **(A)** 0 h, **(B)** 6 h, **(C)** 12 h, **(D)** 24 h, **(E)** 48 h, and **(F)** 120 h. The red and green curves represent the one- and double-peak Lorentz fit, respectively.

container and dried in an oven at a temperature of 45°C for 48 h to obtain graphite oxide powder.

For low-temperature treatment, 100 mg of graphite oxide powder was sonicated for 30 min in 500 ml of distilled water and centrifuged at 500 rpm for 10 min to obtain a homogeneous GO suspension. This suspension was divided into two equal parts. The first part was dried at 80°C considering different drying times ranging from 0 h to 120 h. The second part was dried considering different temperatures from 40°C to 100°C and fixing the drying time at 24 h. The temperature treatment was carried out in a POL-EKO drying stove.

After treatment (drying time or temperature), the samples were sonicated for several minutes to re-disperse them before measuring their optical properties. However, it should be noted that the samples kept at 120°C for 24 h and 80°C for 120 h required an extra sonication time compared to the other samples.

2.3 Characterization

The absorption spectra of GO and rGO were recorded using a Thermo Scientific Evolution 220 spectrophotometer with a resolution of 0.1 nm in a wavelength window from 190 to 1000 nm. The optical absorption coefficient was obtained by setting $\lambda = 660$ nm. Quartz cuvettes (3.5 ml) with a 10 mm optical path were used. Spectra were normalized to the maximum of the prominent peak and conventional Lorentz functions were used to fit the curve. The surface morphology of the obtained samples was taken out on a scanning electron microscope (SEM, JSM-IT100 InTouchScope) with an accelerating voltage of 20 kV and equipped with a JEOL-made energy-dispersive X-ray spectrometer (EDS). The electrical characterization was carried out by using a KEI2450 instrument. Raman measurements were carried with a LabRAM HR Evolution

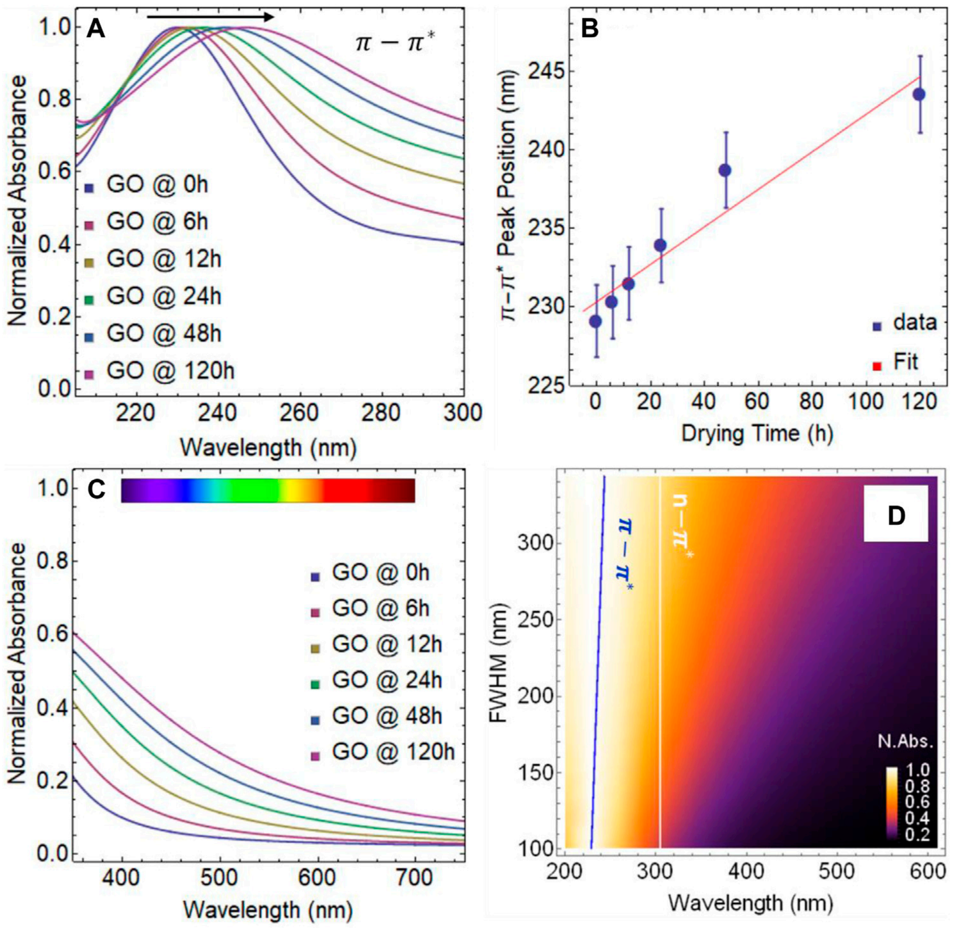

FIGURE 3
(A) UV-visible spectra of graphene oxide (GO) from 200 to 300 nm. **(B)** Position of the $\pi - \pi^*$ transition as a function of drying time. **(C)** UV-visible spectra of GO from 350 to 750 nm. **(D)** Normalized absorbance as a function of full-width half maximum (FWHM) *vs*. wavelength.

micro-Raman spectrometer (Horiba Jobin-Yvon, operating at 532 nm).

3 Results and discussions

To provide context for the significance of our work, it is important to understand the various methods available for treating GO. These methods include chemical, electrochemical, and thermal reduction approaches.

- Chemical reduction involves using agents such as hydrazine, sodium borohydride, hydroiodic acid, or citric acid to remove oxygen functional groups, restoring the sp^2 carbon network. While simple, this method may introduce defects and impurities (Tene et al., 2022b).
- Electrochemical reduction applies a voltage or current to a GO electrode immersed in a reducing electrolyte solution (Tian et al., 2023). It offers better control and higher-quality results but requires specialized equipment and time.
- Thermal reduction involves heating GO at high temperatures in the presence of a reducing agent, resulting in the breakdown of functional groups and the restoration of the graphene lattice. Different heating methods and reducing agents can be used (Sengupta et al., 2018). This approach is simple and cost-effective but requires high temperatures and long processing times.

Some works have explored low-temperature reduction or thermolysis, where GO is heated below 100°C in a vacuum or inert atmosphere (Wang et al., 2012). Despite numerous studies on GO reduction, there is a lack of reports on a simple, low-temperature treatment without a reducing agent or controlled atmosphere.

3.1 Absorption spectra *vs.* drying time

The temperature of 80°C was selected as a representative value within the studied temperature range. By keeping the temperature constant at 80°C, we aimed to isolate the influence of drying time alone. Additionally, starting with this fixed temperature allows for a direct comparison with some results reported by Kumar et al., (2014).

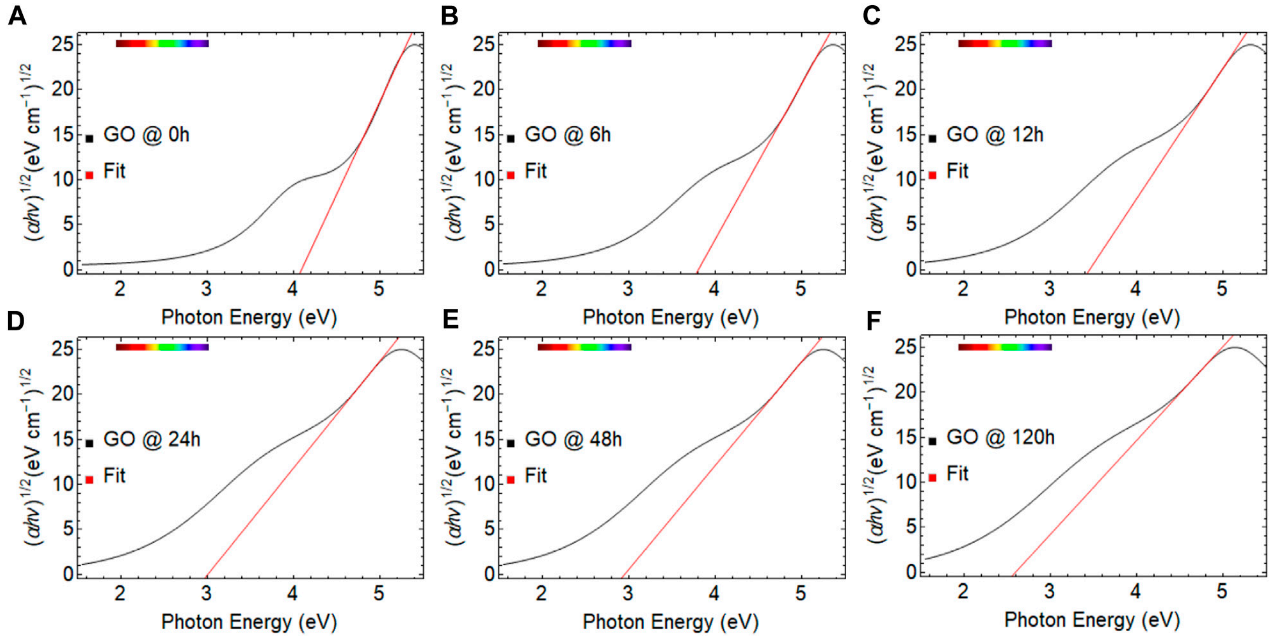

FIGURE 4
Tauc plots of graphene oxide (GO) dried at 80°C considering different drying times: **(A)** 0 h, **(B)** 6 h, **(C)** 12 h, **(D)** 24 h, **(E)** 48 h, and **(F)** 120 h. The linear part of the plot is extrapolated to the x-axis (red line).

TABLE 1 Estimated optical bandgap values of graphene oxide (GO) as a function of drying time from 0 to 120 h. R^2 is the coefficient of determination (R-squared).

Drying time (h)	Optical bandgap (eV)	R^2
0	4.09	0.996
6	3.82	0.996
12	3.48	0.998
24	3.08	0.998
48	2.94	0.998
120	2.76	0.999

TABLE 2 Optical absorption coefficient estimated by a linear fit of the optical absorbance over cell length as a function of concentration under different drying times. R^2 is the coefficient of determination (R-squared).

Material	Absorption coefficient (ml mg^{-1} m^{-1})	R^2
GO @ 0 h	3932.22	0.992
GO @ 48 h	4586.71	0.992
GO @ 120 h	5507.15	0.985

Figure 2 depicts the absorption spectra of GO at 80°C with varying sample drying times, ranging from 0 to 120 h. The red and green lines represent the Lorentzian fit using one or two peaks. Two distinct electronic transitions are observed: the $\pi - \pi^*$ transition and the $n - \pi^*$ transition (see Supplementary Figure S1 for energy levels). All the spectra are featureless in the visible region (400–700 nm) (Supplementary Figure S2). The wavelength position values of these electronic transitions can be found in Supplementary Table S1.

To contextualize, the $\pi - \pi^*$ transition is a type of electronic transition that occurs in molecules or materials containing conjugated π systems. A π system is a network of atoms with adjacent p orbitals that overlap to form delocalized π molecular orbitals. During the $\pi - \pi^*$ electronic transition, an electron in the π bonding molecular orbital is excited to the corresponding π^* anti-bonding molecular orbital. This transition typically results in the absorption of light in the ultraviolet or visible range. In the case of GO, the $\pi - \pi^*$ transition is related to the delocalized π bonding network present in the graphene plane.

On the other hand, the $n - \pi^*$ electronic transition involves the excitation of an electron from a non-bonding, or lone pair, orbital (n) to the anti-bonding π^* orbital. The $n - \pi^*$ transition typically also results in the absorption of light in the ultraviolet or visible range. In the case of GO, the $n - \pi^*$ transition is related to the oxygen-containing functional groups that are present on the graphene surface. The presence of functional groups in GO can induce changes in the electronic structure of the graphene lattice, including the opening of a bandgap, which can significantly alter the electronic and optical properties of the material.

Then, one interesting observation is the shift in the position of the $\pi - \pi^*$ transition (Figure 3A), which changes from 229.63 nm after 0 h to 243.81 nm after 120 h. This shift corresponds to a change in energy from 5.40 to 5.09 eV. This observation shows that the electronic properties of the GO are changing over drying time, possibly due to the partial removal of oxygen-containing functional groups. Furthermore, we have analyzed the absorbance spectrum of GO at 144 h of drying (result not shown here), however, there is no

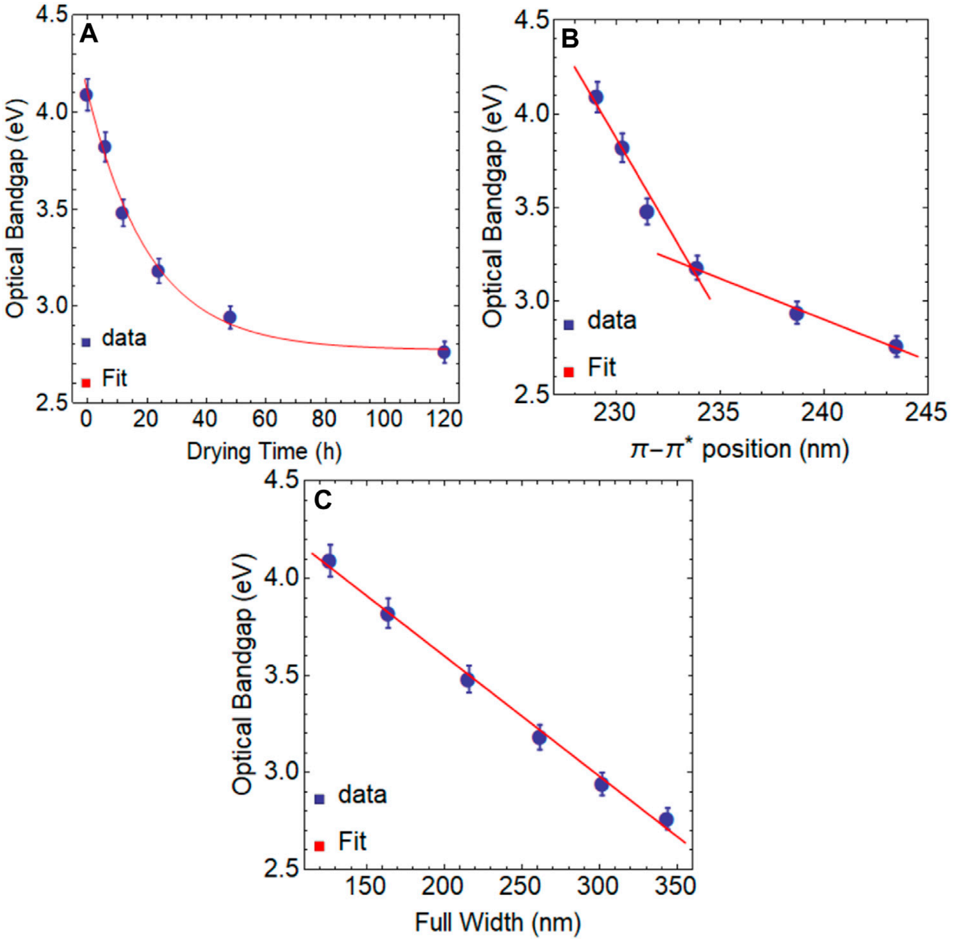

FIGURE 5
Optical bandgap of graphene oxide (GO) as a function of **(A)** drying time, **(B)** position of the $\pi - \pi^*$ transition, and **(C)** full width at half maximum (FWHM).

significant disparity between the obtained result at 144 h ($\lambda_{\pi-\pi^*}$ = 244.13 nm, $\lambda_{n-\pi^*}$ = 311.9 nm, FWHM = 342.11 nm, and $R^2 = 0.985$) and the observed results at 120 h (Figure 2F). Given these observations, we focus our study on the drying window of 0–120 h and the one-peak fit approach through the text.

When performing a linear regression analysis on the data points of the $\pi - \pi^*$ transition shift over drying time (Figure 3B), the resulting equation is $y = 0.119\,t + 230.33$ ($R^2 = 0.929$). The slope of the line, 0.119, represents the rate of change of the $\pi - \pi^*$ transition shift concerning drying time. Specifically, a slope of 0.119 means that for every one-unit increase in time (e.g., 1 hour), the $\pi - \pi^*$ transition shift is expected to increase by 0.119 nm/h. This rate of change is constant and can be used to make predictions about the $\pi - \pi^*$ transition shift at future drying time points. However, it is important to note that there is a maximum shift detected for graphene dispersions, which is around 280 nm (Vacacela Gómez et al., 2021). This means that the value of y cannot continue to shift indefinitely over drying time, and will eventually reach a plateau, as starts to be observed at 120 (see Figure 3B). Additionally, the y-intercept of the line, 230.33 nm, represents the estimated initial position of the $\pi - \pi^*$ transition at time 0 h.

A marginal effect is observed in the position of the $n - \pi^*$ transition (~ 305 nm), which suggests the presence of oxygenated functional groups, however, we point out that the structure of the absorbance spectrum is different at 120 h of drying time (Figure 2F). Interestingly enough, GO samples subject to continuous drying time at 80°C became strongly absorbent in the visible region (Figure 3C), showing an increase in the collection of photons in the wavelength range 350–700 nm.

As our study progresses, a previously unreported finding has come to light, a linear correlation between the full width at half maximum (FWHM) and absorbance spectra of dried GO samples. As the drying time increases, so does the width of the absorbance curve, which is constructed by both the $\pi - \pi^*$ and $n - \pi^*$ transitions. To illustrate this finding, Figure 3D displays the normalized absorbance as a function of FWHM vs. wavelength. A clear trend emerges as drying time increases, i.e., the spectral weight of FWHM increases from approximately 327 nm to almost 588 nm. As stated, the $\pi - \pi^*$ transition shifts towards longer wavelengths (blue line), while the $n - \pi^*$ transition remains relatively constant (white line).

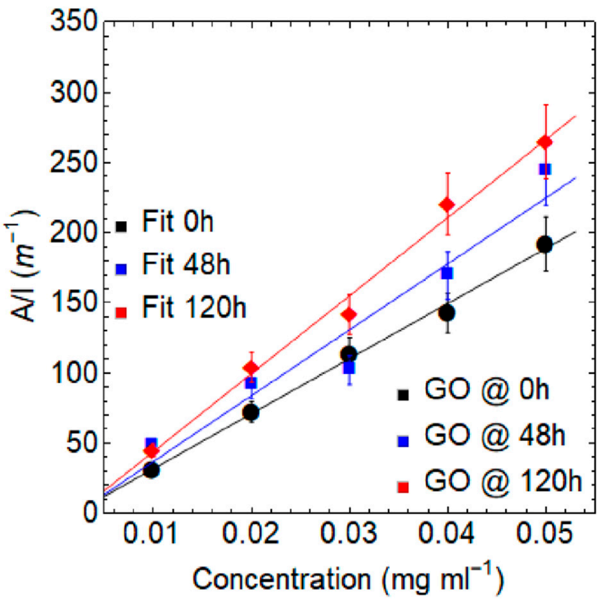

FIGURE 6
Optical absorbance at 660 nm divided by cell length as a function of concentration for graphene oxide (GO) subject to different drying times (0, 48, and 120 h).

3.2 Optical bandgap *vs*. drying time

In the Tauc approach, the absorption coefficient (α) is proportional to the energy of the incident photon energy (E) raised to the power of the Tauc exponent (γ), as given by the equation:

$$(\alpha h\nu)^{1/\gamma} = B(h\nu - Eg) \quad (1)$$

where $h\nu$ is the energy of the incident photons, Eg is the optical bandgap energy, and B is an energy-independent constant. Depending on nature transmission, γ can take the values of 1/2 for direct allowed transitions and 2 for indirect allowed transitions. In this sense, we assume an indirect bandgap nature as widely adopted (Romero et al., 2017).

To determine the optical bandgap of GO using the Tauc approach, we first analyzed the absorbance spectrum of each sample. Next, we plotted the absorption coefficient (α) as a function of the photon energy ($h\nu$). Using this data, we generated a Tauc plot by plotting $(\alpha h\nu)^{1/2}$ on the y-axis and $h\nu$ on the x-axis. By identifying the intercept of the linear section of the plot with the x-axis ($h\nu = 0$), we estimated the optical bandgap of GO samples (Figure 4).

Figure 4 depicts the Tauc plot of GO at 80°C, where the drying time was varied from 0 to 120 h. The red line corresponds to the fitted region showing a steep linear increase of light absorption with increasing energy, which is a characteristic of semiconductor materials (Makuła et al., 2018). Table 1 provides the optical bandgap values estimated for each GO sample.

In Figure 4, all spectra exhibit a marked change in absorbance in the energy region of 4.1–5.5 eV, which is also characteristic of wide bandgap semiconductors. This pronounced change corresponds to the $\pi - \pi^*$ transition in GO in the wavelength region of 200–300 nm (Figure 2). Previous studies have estimated the bandgap by fitting the second linear region, which in our case is located between 3.0 and 4.0 eV and corresponds to the $n - \pi^*$ transition (300 and 400 nm, Figure 2). However, this approach is flawed and leads to an underestimation of the optical bandgap value. It is worth noting that the current study almost allows for the fitting of the second linear region after 120 h of drying time due to the displacement of the first linear region towards lower energy values (Figure 3F). An important aspect to consider is that with increasing drying time, the optical bandgap decreases from 4.09 eV (0 h) to 2.76 eV (120 h) (Table 2).

In Figure 5A, we present the relationship between the optical bandgap and the drying time, which exhibits a clear exponential decreasing trend. By performing a fit analysis, we obtained the expression: $y = 1.33\,e^{-0.048\,t} + 2.77$. While we observe a negative decreasing rate in the relationship between the optical bandgap and the drying time, the rate of change is relatively small (-4.78×10^{-2}/h). Specifically, for drying times up to 120 h, we observe a decrease of approximately 1.33 eV in the optical bandgap. Moreover, this equation demonstrates that it is not feasible to extend its application to a hypothetical optical bandgap of $y = 0$ eV, which corresponds to zero-gap graphene. This is because the maximum attainable optical bandgap is 2.77 eV by using the drying time effect. In a real situation, achieving full recovery of the graphene structure may not be feasible due to the presence of embedded oxygen functional groups in its basal plane that are challenging to remove.

It is important to mention that materials possessing a bandgap of ~ 3 eV are highly versatile and can be utilized in numerous fields. Wide bandgap materials are ideal for use in the top layer of multi-junction solar cells, high-speed electronics, UV photodetectors, and optoelectronic devices. Wide bandgap materials are also used in the creation of blue or violet LEDs and lasers, which have numerous applications in lighting, displays, and optical communications.

Moreover, we have uncovered an inverse correlation between the position of the $\pi - \pi^*$ transition and the optical bandgap, which exhibits two regions of linearity (Figure 5B). The first is observed between 230 nm and 234 nm, while the second lies between 235 nm and 245 nm. Our findings demonstrate that as the $\pi - \pi^*$ transition shifts toward the red end of the spectrum, the bandgap decreases, leading to the restoration of the graphene properties. As well, we have observed a stronger linear relationship between the optical bandgap and FWHM (Figure 5C), indicating that as the bandgap decreases, the width of the absorption curve should increase proportionally.

3.3 Absorption coefficient *vs*. drying time

The adsorption coefficient (α) was calculated according to the well-known expression of the Beer-Lamber law:

$$A = \alpha_{660}\, c\, l \quad (2)$$

where A is the absorbance data, c is the concentration, and l is the cuvette path length. The value of α was calculated by preparing a series of dispersions at given concentrations. As shown in Table 2; Figure 6, the value of α at 660 nm increases by increasing the drying time. For each given sample, the absorbance increases linearly with

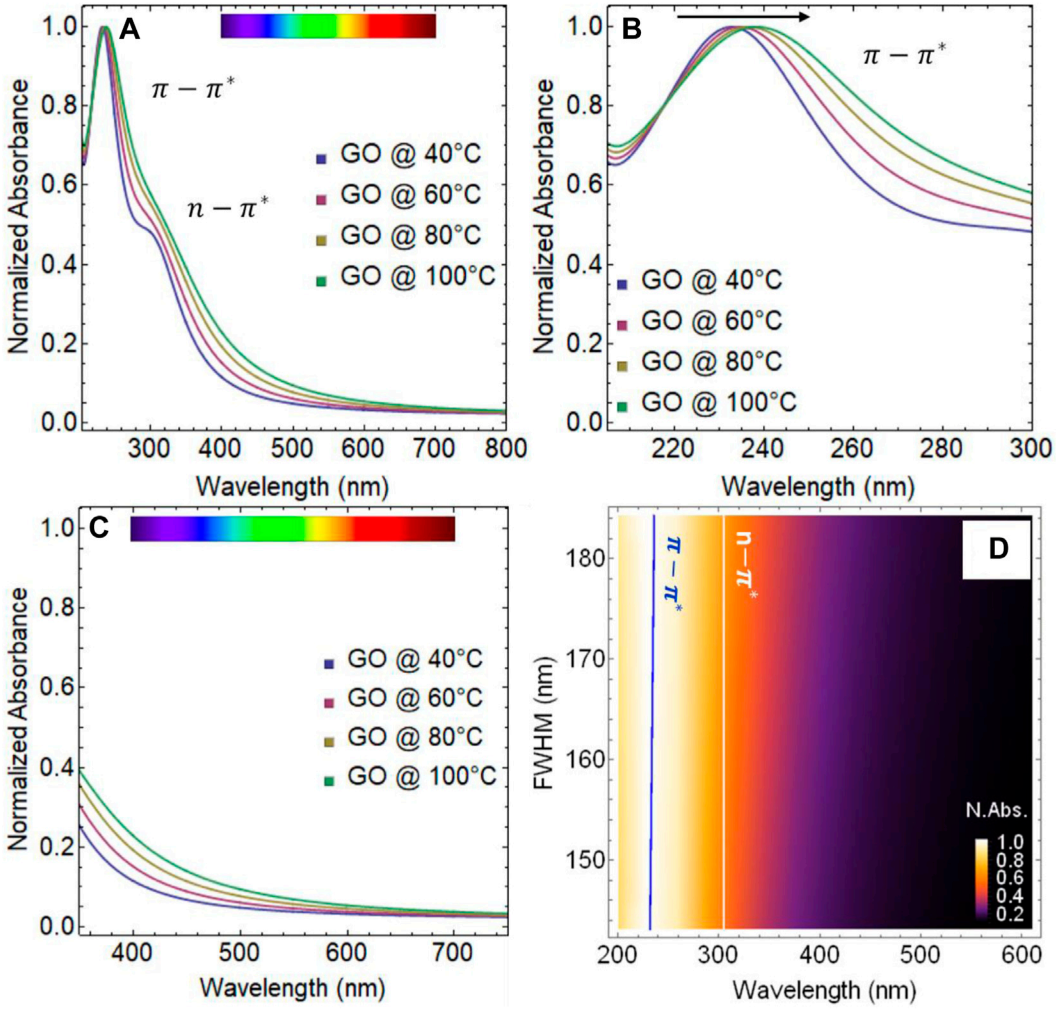

FIGURE 7
UV-visible spectra of graphene oxide (GO) **(A)** from 200 to 800 nm, **(B)** from 200 to 300 nm, **(C)** from 350 to 750 nm. **(D)** Normalized absorbance as a function of full-width half maximum (FWHM) *vs.* wavelength.

increasing concentration, indicating that GO dispersions follow the behavior of Eq. 2.

The values of α were determined by calculating the slope of the linear fit. The results show that α is approximately 3932 ml mg^{-1} m^{-1} at 0 h, 4587 ml mg^{-1} m^{-1} at 48 h, and 5507 ml mg^{-1} m^{-1} at 120 h. It is worth noting that these absorption coefficients are similar in orders of magnitude to the reported value for exfoliated graphene dispersions in water or alcohols, which is around 2460 ml mg^{-1} m^{-1}, with a $\pi - \pi^*$ transition observed at approximately 265 nm (Hernandez et al., 2008).

The absorption coefficient of GO is higher than that of exfoliated graphene, likely due to the presence of oxygen-containing functional groups on its surface. These functional groups introduce defects in the hexagonal carbon lattice of graphene, creating localized states that can interact with photons at a wider range of energies than the delocalized $\pi-$ electrons in pure graphene. This interaction results in a higher absorption coefficient for GO. In addition, the oxygen functional groups on the surface of GO can induce dipole moments and charge transfer, further enhancing the absorption of electromagnetic radiation. Therefore, the higher absorption coefficient of GO compared to graphene makes it useful for applications such as photovoltaics, photocatalysis, and optoelectronics.

3.4 Effect of temperature

The impact of temperature on the optical properties of GO is examined in this section. Four different temperatures, namely 40°C, 60°C, 80°C, and 100°C, have been selected for the experiment. The duration of the experiment has been set at 24 h to ensure homogeneity, as the water in the GO dispersion evaporates rapidly at 100°C. Therefore, a fixed duration of 24 h has been chosen to keep the experimental conditions as consistent as possible.

The absorbance spectra of GO subjected to different temperatures are shown in Figure 7A and the corresponding position of the $\pi - \pi^*$ and $n - \pi^*$ transitions can be found in

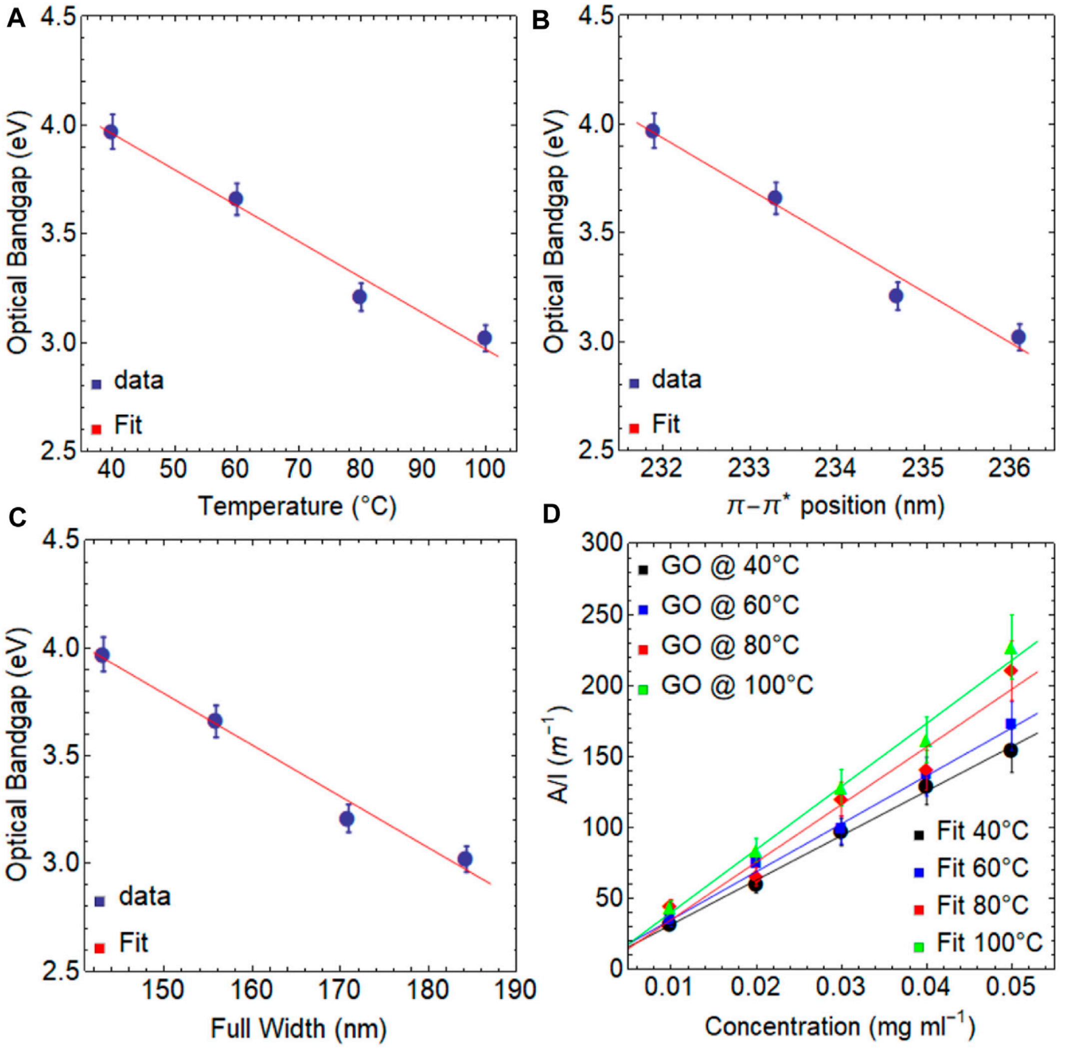

FIGURE 8
Optical bandgap of graphene oxide (GO) as a function of **(A)** drying time, **(B)** position of the $\pi - \pi^*$ transition, **(C)** full width at half maximum (FWHM), and **(D)** Optical absorbance as a function of concentration for graphene oxide (GO) subject to different temperatures.

TABLE 3 Estimated optical bandgap values of graphene oxide (GO) as a function of temperature from 40 to 100 ℃. R^2 is the coefficient of determination (R-squared).

Temperature (℃)	Optical bandgap (eV)	R^2
40	3.97	0.998
60	3.70	0.996
80	3.19	0.997
100	3.06	0.998

TABLE 4 Optical absorption coefficient estimated by a linear fit of the optical absorbance over cell length as a function of concentration under different temperatures. R^2 is the coefficient of determination (R-squared).

Material	Absorption coefficient (ml mg^{-1} m^{-1})	R^2
GO @ 40 ℃	3139.97	0.997
GO @ 60 ℃	3382.52	0.996
GO @ 80 ℃	4061.18	0.962
GO @ 100 ℃	4443.84	0.988

Supplementary Table S2. It appears that the effect of temperature for 24 h is minimal. The absorbance spectrum shows visible $\pi - \pi^*$ and $n - \pi^*$ transitions and no significant change in their structure are observed with varying temperatures (Supplementary Figure S3). Even at 40°C and 100°C, the $\pi - \pi^*$ transition is located at about 231 and 236 nm, respectively (Figure 7B), indicating a shift of less than 6 nm. Moreover, the effect of temperature on the $n - \pi^*$ transition is also found to be marginal, and it remains relatively constant at ~ 301 nm. As well, GO samples subject to different temperatures became also good absorbent in the visible region (Figure 7C), in the wavelength range 350–700 nm, but this effect is less than that observed under drying time (Figure 3C).

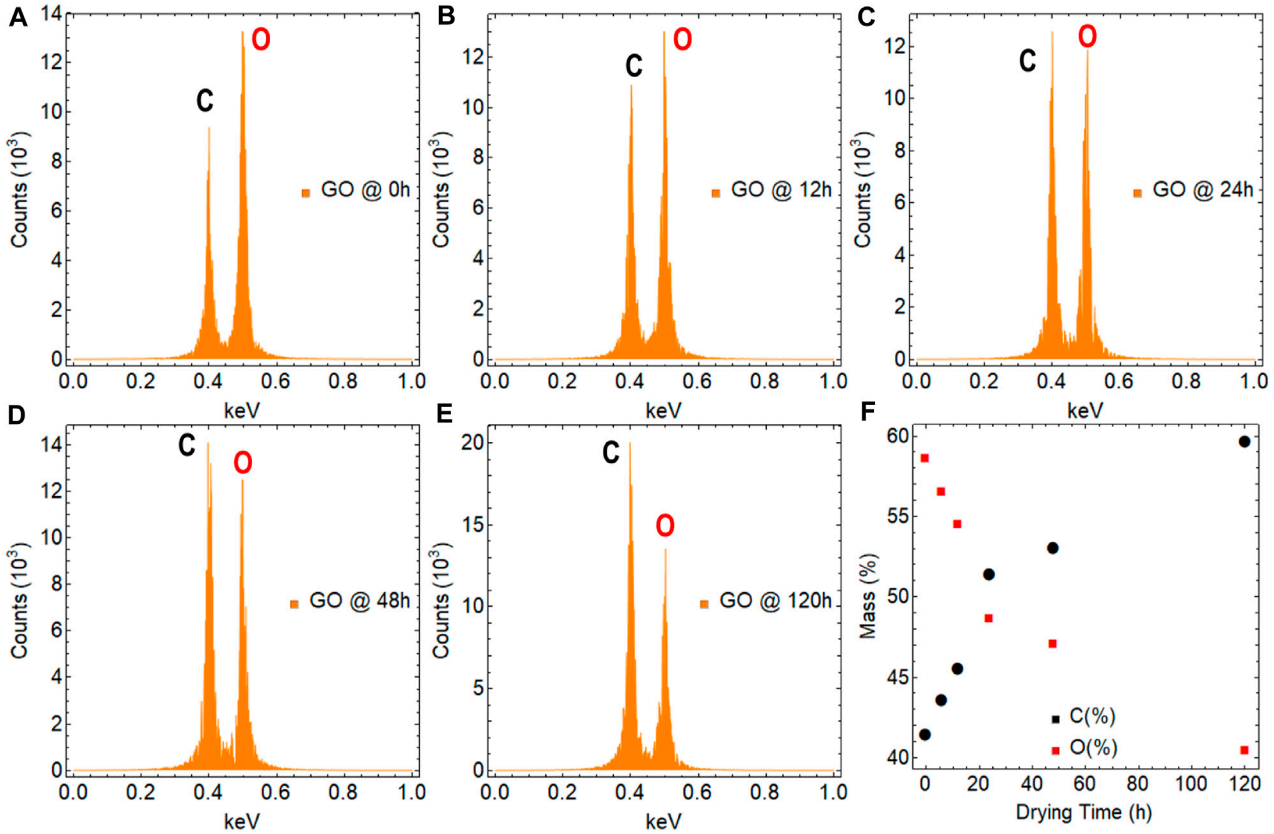

FIGURE 9
EDS measurements on graphene oxide (GO) subjects at different temperatures: **(A–E)** 0–120 h while maintaining a fixed temperature of 80°C, respectively. **(F)** Percentual mass as a function of drying time.

Figure 7D displays the normalized absorbance as a function of FWHM vs. wavelength. The blue line indicates that the shift of the $\pi - \pi^*$ transition is minimal, while the white line shows that the $n - \pi^*$ transition remains constant. Building on our previous analysis, we can infer that temperature has a less significant impact on steepening the GO absorption spectrum curve compared to drying time, as evidenced by the less pronounced FWHM spectral weight from 371 to 420 nm.

Figure 8A displays a linear correlation between the optical bandgap and temperature. The optical bandgap decreases from 3.97 eV at 40°C to 3.06 eV at 100°C (Table 3, Supplementary Figure S4), with a variation of less than 1.0 eV. A linear fit of these data yields the following expression: $y = -1.65 \times 10^{-2}\, t + 4.62$, indicating that a temperature of 280°C is required to reach a bandgap of zero (freestanding graphene). However, the reduction process of GO is complex and often necessitates higher temperatures or strong chemical reductant agents, as mentioned at the beginning of Section 3. Then, as seen in Figure 5A, the bandgap tends to follow a decreasing exponential trend due to achieving full recovery of the graphene properties is a challenge.

As well, a linear correlation is also observed between the optical bandgap and the position of the $\pi - \pi^*$ transition (Figure 8B) or FWHM (Figure 8C).

Figure 8C; Table 4 demonstrate a trend similar to what was discussed previously. As the temperature increases, the absorption coefficient increases from 3140 ml mg^{-1}m^{-1} at 40°C to 4061 ml mg^{-1} m^{-1} at 100°C. However, these values are slightly lower than those obtained due to the effect of drying time (see Table 2). All these results demonstrate the remarkable versatility of graphene oxide in modulating its electronic transitions, optical bandgap, and absorption coefficient through simple control of temperature and drying time.

3.5 Elemental composition and surface morphology

EDS analysis is a powerful technique that can be used to investigate the elemental composition of GO. Specifically, it can identify the presence of elements such as carbon, oxygen, and impurities. In this study, a sufficiently large area of GO samples was investigated using EDS to ensure the reliability of the results. However, it is important to note that to obtain a complete characterization of the material, other analytical techniques may also need to be employed in conjunction with EDS.

The results obtained are presented in Figure 9; Supplementary Figure S6, and Supplementary Table S3. To provide a basis for comparison, we first analyzed graphite (Supplementary Figure S5), which is composed primarily of carbon. As expected, the analysis showed a high carbon content of approximately 99%, which is

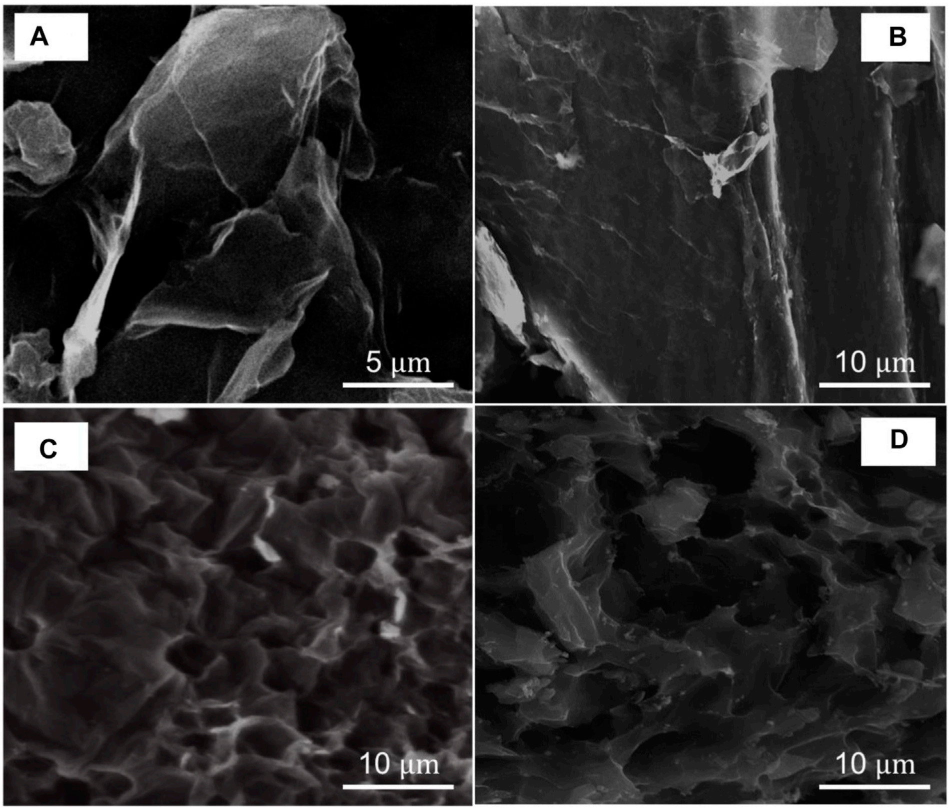

FIGURE 10
SEM images of graphene oxide (GO) under different drying times while maintaining a fixed temperature of 80°C: **(A)** 0 h and **(B)** 120 h as well as under different temperatures for 24 h of drying: **(C)** 40°C and **(D)** 100°C.

consistent with the elemental composition of natural graphite. While this result is not surprising, it serves as a useful reference point for comparing the results obtained from other samples that may have more complex elemental compositions such as GO under the effect of drying time and temperature.

The impact of drying time on the oxygen content of GO can be understood by analyzing samples at two extreme points, at 0 h (Figure 9A) and 120 h (Figure 9E). The results indicate that as drying time increases, the oxygen content decreases from approximately 59%–40% (Figure 9F), indicating the removal of oxygen in various functional groups. This reduction in oxygen content, mainly, is attributed to the evaporation of water and other oxygen-containing functional groups (Saxena et al., 2011). These findings have implications for understanding the stability and properties of GO and can inform strategies for optimizing its synthesis and postprocessing conditions.

As well, the influence of temperature on GO can be examined by investigating extreme values, specifically at 40°C and 100°C. Intriguingly, exposing GO to 40°C for 24 h led to a rise of around 64% in oxygen content. This effect can be attributed to the fact that the resulting GO sample remained in the form of an aqueous dispersion after 24 h, and the evaporated water molecules could become intercalated within the internal structure of GO. Conversely, after 24 h at 100°C, the oxygen content decreased to 43%. This can be attributed to the fact that even though the sample was dry, the water molecules that were trapped and intercalated within GO required more time to escape from the internal structure.

The morphology of the samples is illustrated in Figure 10. The starting graphite powder used in this study exhibited medium to large, corrugated flakes on the surface (Supplementary Figure S7). Conversely, the GO sample with 0 h of drying time exhibited a relatively smaller size, surface wrinkles, and several folds on the edges, confirming the chemical exfoliation of the materials by oxidation (Figure 10A). Furthermore, GO subjected to 120 h of drying time displayed a similar behavior with folded edges, but its surface morphology is more uniform, implying the partial recovery of sp^2 hybridization, at least at the base of the GO plane (Figure 10B).

Conversely, when GO was exposed to temperatures of 40°C (Figure 10C) and 100°C (Figure 10D) for 24 h, no discernible changes were observed, and the surface remained corrugated with several folded edges. This outcome suggests that GO continued to exhibit a predominant sp^3 hybridization, which is attributed to the presence of oxygen functional groups that still existed in the GO structure.

The Raman analysis of GO under different conditions (i.e., drying time and temperature) (Supplementary Figure S8; Supplementary Table S4) reveals four prominent peaks: D, D**, G, and D′. Each peak represents specific molecular vibrations and provides insights into its structure (Arias Arias et al., 2020). The D peak (~ 1341 cm^{-1}) indicates lattice defects caused by the introduction of oxygen functional groups during oxidation. The

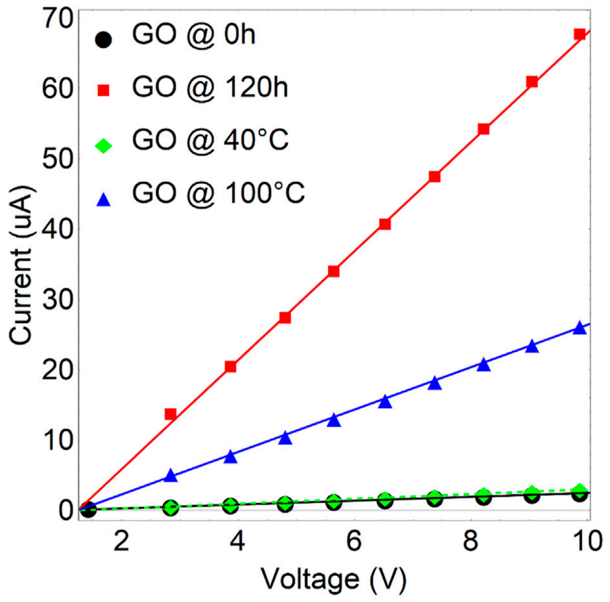

FIGURE 11
I-V characteristics of graphene oxide (GO) under varying drying times and temperatures are presented. The green and blue curves depict GO dried for 24 h at 40°C and 100°C, respectively. Meanwhile, the black and red curves represent GO dried at 80°C for 0 and 120 h, respectively.

D** peak (~ 1480 cm^{-1}) arises from double resonance Raman scattering, reflecting the density of electronic states and structural disorder. The G peak (~ 1570 cm^{-1}) corresponds to graphitic sp^2 carbon domains, indicating the presence of graphene-like regions. The D′ peak (~ 1690 cm^{-1}) originates from sp^3 carbon atoms due to epoxy or hydroxyl functional groups, reflecting their abundance. An important finding obtained from the Raman measurements is that the I_D/I_G intensity ratio increases when the samples are subjected to drying, regardless of the drying time or temperature. For instance, the I_D/I_G intensity ratio in GO goes from 1.07 at 0 h and 80°C to 1.33 after drying for 24 h at 100°C. These findings have been extensively discussed in our previous work (Arias Arias et al., 2020).

The EDS, Raman, and SEM results provided further confirmation that when operating at low temperatures ($\leq$ 100°C), the drying time was the most crucial factor, which corroborates the earlier findings obtained from UV-visible spectroscopy and Tauc analysis.

To further characterize the treated samples, Figure 11; Supplementary Table S5 show the current vs. voltage plots (*I-V* curves) for GO treated at 0 h (black line), 120 h (red line), 40°C (green line), and 100°C (blue line). GO at 0 h (3.65×10^6 Ω) and GO at 40°C (2.90×10^6 Ω) exhibit insulating properties irrespective of the magnitude of the applied voltage. The current of GO at 120 h (1.29×10^5 Ω) and GO at 100°C (3.32×10^5 Ω) increase gradually with biasing the voltage, and the insulating characteristic starts to be modified. At 10 eV, the conductivity is around 2.5 (0 h), 67.5 (120 h), 3.0 (40°C), and 26.3 (100°C) μA. It has been observed that the resistance of GO is lowest after 120 h of drying time. This can be attributed to the removal of some oxygen functional groups. However, GO still contains numerous oxygen functional groups, which makes it an insulating material. This is evidenced and confirmed by the wide bandgap estimated through the Tauc approach (2.8 eV).

4 Conclusion

In summary, we explored the physical and chemical properties of GO treated at low temperatures. Our focus is on investigating the electronic and optical characteristics of GO and the changes in these features upon drying time (from 0 h to 120 h while maintaining a fixed temperature of 80°C) and low temperatures (from 40 ℃ to 100 ℃ with a constant drying time of 24 h).

We found that the $\pi - \pi^*$ transition is the most affected, shifting from approximately 230 nm–244 nm after 120 h of drying time, while the $n - \pi^*$ transition remains unchanged in wavelength but decreases in intensity. The absorption coefficient was measured to be 5507 ml mg^{-1} m^{-1} at 120 h, similar to the absorption coefficients in order of magnitude reported for dispersions of liquid-phase exfoliated graphene (2344 ml mg^{-1} m^{-1}). The optical bandgap was found to be 2.8 eV for dried samples at 120 h. Furthermore, we found a linear relationship never noted between the optical bandgap and the position of the main absorbance peak or FWHM curve. The study is complemented by using EDS analysis, SEM measurements, and *I-V* curves. In particular, the EDS analysis revealed a notable trend as the drying time increased: the oxygen content decreased from approximately 59%–40%. This finding strongly suggests the removal of oxygen functional groups. Furthermore, SEM observations indicated distinct characteristics between GO samples with 0 h and 120 h of drying time. GO samples with 0 h of drying time exhibited smaller sizes, surface wrinkles, and multiple folds along the edges. Conversely, GO subjected to 120 h of drying time displayed a similar folded edge behavior, but its surface morphology appeared more uniform, indicating a partial recovery of sp^2 hybridization. I-V measurements provided additional insights, showing that the resistance of GO was at its lowest (1.29×10^5 Ω) after 120 h of drying time. The latter can be attributed to the effective removal of oxygen functional groups.

Our findings can be used to tailor the use of GO in various contexts by determining the optimal temperature and duration for a specific application. Additionally, this study provides valuable insights into the electronic transitions and optical properties of GO and fills a gap in the literature on low-temperature treatment processes for GO without strong reductant agents or controlled environments.

Finally, we would like to underscore the significance of our findings concerning the optical properties of GO, however, it is crucial to point out that a more comprehensive understanding of the results presented in this study could be attained through the inclusion of complementary XPS measurements. By integrating XPS analysis, one can be able to delve deeper into the intricate aspects of our findings and acquire a more thorough understanding of the observed phenomena.

Data availability statement

The authors declare that the data supporting the findings of this study are available within the paper (and its Supplementary Information files). Further raw data are also available from the corresponding author upon reasonable request.

Author contributions

CVG and SB supervised the work. TT prepared GO samples. FB, TP, and MG performed EDS analysis and SEM observation. TP and TT performed the statistical analysis. TT conducted UV-visible measurements. All authors contributed to the scientific discussion and manuscript preparation. TT and CVG wrote the manuscript. All authors contributed to the article and approved the submitted version.

Funding

This work was funded by the Universidad Técnica Particular de Loja (UTPL-Ecuador) under the project: "Análisis de las propiedades térmicas del grafeno y zeolita" Grand No: PROY_INV_QU_2022_362. This work was partially supported by LNF-INFN: Progetto HPSWFOOD Regione Lazio—CUP I35F20000400005.

Acknowledgments

CVG, MG, and TT wish to thank Escuela Superior Politécnica de Chimborazo for their hospitality during the completion of this work.

Conflict of interest

The authors declare that the research was conducted in the absence of any commercial or financial relationships that could be construed as a potential conflict of interest.

Publisher's note

Supplementary material

The Supplementary Material for this article can be found online at: https://www.frontiersin.org/articles/10.3389/fchem.2023.1214072/full#supplementary-material

References

Aragaw, B. A. (2020). Reduced graphene oxide-intercalated graphene oxide nano-hybrid for enhanced photoelectrochemical water reduction. *J. Nanostructure Chem.* 10, 9–18. doi:10.1007/s40097-019-00324-x

Arias Arias, F., Guevara, M., Tene, T., Angamarca, P., Molina, R., Valarezo, A., et al. (2020). The adsorption of methylene blue on eco-friendly reduced graphene oxide. *Nanomaterials* 10, 681. doi:10.3390/nano10040681

Baragau, I-A., Buckeridge, J., Nguyen, K. G., Heil, T., Sajjad, M. T., Thomson, S. A. J., et al. (2023). Outstanding visible light photocatalysis using nano-TiO_2 hybrids with nitrogen-doped carbon quantum dots and/or reduced graphene oxide. *J. Mater. Chem. A* 11, 9791–9806. doi:10.1039/D2TA09586F

Chaudhuri, H., and Yun, Y-S. (2023). A critical review on the properties and energy storage applications of graphene oxide/layered double hydroxides and graphene oxide/MXenes. *J. Power Sources* 564, 232870. doi:10.1016/j.jpowsour.2023.232870

Ferrari, I., Motta, A., Zanoni, R., Scaramuzzo, F. A., Amato, F., Dalchiele, E. A., et al. (2023). Understanding the nature of graphene oxide functional groups by modulation of the electrochemical reduction: A combined experimental and theoretical approach. *Carbon* 203, 29–38. doi:10.1016/j.carbon.2022.11.052

Grewal, S., Macedo Andrade, A., Nelson, A. J., Thai, K., Karimaghaloo, A., Lee, E., et al. (2018). Critical impact of graphene functionalization for transition metal oxide/graphene hybrids on oxygen reduction reaction. *J. Phys. Chem. C* 122, 10017–10026. doi:10.1021/acs.jpcc.8b01893

Haydari, I., Aziz, K., Kaya, S., Daştan, T., Ouazzani, N., Mandi, L., et al. (2023). Green synthesis of reduced graphene oxide and their use on column adsorption of phenol from olive mill wastewater. *Process Saf. Environ. Prot.* 170, 1079–1091. doi:10.1016/j.psep.2022.12.086

Hernandez, Y., Nicolosi, V., Lotya, M., Blighe, F. M., Sun, Z., De, S., et al. (2008). High-yield production of graphene by liquid-phase exfoliation of graphite. *Nat. Nanotechnol.* 3, 563–568. doi:10.1038/nnano.2008.215

Kadhim, M. M., Rheima, A. M., Abbas, Z. S., Jlood, H. H., Hachim, S. K., Kadhum, W. R., et al. (2023). Evaluation of a biosensor-based graphene oxide-DNA nanohybrid for lung cancer. *RSC Adv.* 13, 2487–2500. doi:10.1039/d2ra05808a

Kumar, P. V., Bardhan, N. M., Tongay, S., Wu, J., Belcher, A. M., and Grossman, J. C. (2014). Scalable enhancement of graphene oxide properties by thermally driven phase transformation. *Nat. Chem.* 6, 151–158. doi:10.1038/nchem.1820

Liu, C., Hunag, X., Wu, Y. Y., Deng, X., Zheng, Z., and Yang, B. (2022). Studies on mechanical properties and durability of steel fiber reinforced concrete incorporating graphene oxide. *Cem. Concr. Compos.* 130, 104508. doi:10.1016/j.cemconcomp.2022.104508

Makuła, P., Pacia, M., and Macyk, W. (2018). How to correctly determine the band gap energy of modified semiconductor photocatalysts based on UV–Vis spectra. *J. Phys. Chem. Lett.* 9, 6814–6817. doi:10.1021/acs.jpclett.8b02892

Nagaiah, K., A.b., K., R., S. R., and Akkera, H. S. (2023). Effects of the phase, morphology, band gap and hydrogen evolution of vanadium oxide with reduced graphene oxide. *Mater. Today Commun.* 34, 105478. doi:10.1016/j.mtcomm.2023.105478

Romero, U. A. M., Soto, M. Á. V., Jiménez, L. L., Quintana, J. Á., and García, S. A. P. (2017). *Graphene derivatives: Controlled properties, nanocomposites, and energy harvesting applications*. London, UK: IntechOpen, 77–96.

Safari, M., and Mazloom, J. (2023). Outstanding energy storage performance in CoFe bimetallic metal-organic framework spindles via decorating with reduced graphene oxide nanosheets. *J. Energy Storage* 58, 106390. doi:10.1016/j.est.2022.106390

Saxena, S., Tyson, T. A., Shukla, S., Negusse, E., Chen, H., and Bai, J. (2011). Investigation of structural and electronic properties of graphene oxide. *Appl. Phys. Lett.* 99, 013104. doi:10.1063/1.3607305

Sengupta, I., Chakraborty, S., Talukdar, M., Pal, S-K., and Chakraborty, S. (2018). Thermal reduction of graphene oxide: How temperature influences purity. *J. Mater. Res.* 33, 4113–4122. doi:10.1557/jmr.2018.338

Sontakke, A. D., Tiwari, S., and Purkait, M. K. (2023). A comprehensive review on graphene oxide-based nanocarriers: Synthesis, functionalization and biomedical applications. *FlatChem* 38, 100484. doi:10.1016/j.flatc.2023.100484

Tene, T., Arias Arias, F., Guevara, M., Nuñez, A., Villamagua, L., Tapia, C., et al. (2022b). Removal of mercury (II) from aqueous solution by partially reduced graphene oxide. *Sci. Rep.* 12, 6326. doi:10.1038/s41598-022-10259-z

Tene, T., Bellucci, S., Guevara, M., Arias Arias, F., Sáez Paguay, M. Á., Quispillo Moyota, J. M., et al. (2022a). Adsorption of mercury on oxidized graphenes. *Nanomaterials* 17, 3025. doi:10.3390/nano12173025

Tene, T., Guevara, M., Valarezo, A., Salguero, O., Arias Arias, F., Arias, M., et al. (2021). Drying-time study in graphene oxide. *Nanomaterials* 11, 1035. doi:10.3390/nano11041035

Tian, Y., Han, S., Chen, P., Cao, L., Hu, A., Li, M., et al. (2023). Electrochemically reduced graphene oxide (ERGO)-Cu bilayer structure fabricated at room temperature for future interconnects. *RSC Adv.* 13 (4), 2372–2378. doi:10.1039/D2RA07223H

Vacacela Gómez, C., Guevara, M., Tene, T., Villamagua, L., Usca, G. T., Maldonado, F., et al. (2021). The liquid exfoliation of graphene in polar solvents. *Appl. Surf. Sci.* 546, 149046. doi:10.1016/j.apsusc.2021.149046

Valentini, C., Montes-García, V., Livio, P. A., Chudziak, T., Raya, J., Ciesielski, A., et al. (2023). Tuning the electrical properties of graphene oxide through low-temperature thermal annealing. *Nanoscale* 15, 5743–5755. doi:10.1039/d2nr06091d

Wang, Z., Xu, D., Huang, Y., Wu, Z., Wang, L. m., and Zhang, X. b. (2012). Facile mild and fast thermal-decomposition reduction of graphene oxide in air and its application in high-performance lithium batteries. *Chem. Commun.* 48 (7), 976–978. doi:10.1039/c2cc16239c

Wu, J., Lin, H., Moss, D. J., Loh, K. P., and Jia, B. (2023). Graphene oxide for photonics, electronics and optoelectronics. *Nat. Rev. Chem.* 7, 162–183. doi:10.1038/s41570-022-00458-7

Yu, Y., Chen, K., Wu, Q., Zhang, Y., Shi, D., and Li, H. (2023). Recent progress on reduced graphene oxide supported Pt-based catalysts and electrocatalytic oxidation performance of methanol. *Int. J. Hydrogen Energy* 48 (5), 1785–1812. doi:10.1016/j.ijhydene.2022.10.021

Frontiers in Chemistry

TYPE Original Research
PUBLISHED 20 October 2023
DOI 10.3389/fchem.2023.1281168

OPEN ACCESS

EDITED BY
Lucheng Peng,
The Institute of Photonic Sciences (ICFO),
Spain

REVIEWED BY
Preeti Gupta,
Leibniz Institute for Solid State and Materials Research Dresden (IFW Dresden), Germany
Lakshmi Narayanan Mosur Saravana Murthy,
Intel, United States

*CORRESPONDENCE
Yoshitane Imai,
✉ y-imai@apch.kindai.ac.jp

RECEIVED 22 August 2023
ACCEPTED 02 October 2023
PUBLISHED 20 October 2023

CITATION
Kuroda T, Kitahara M, Yagi S and Imai Y (2023), External magnetic field-induced circularly polarized luminescence and electroluminescence from optically inactive thermally activated delayed fluorescence material 4CzIPN.
Front. Chem. 11:1281168.
doi: 10.3389/fchem.2023.1281168

External magnetic field-induced circularly polarized luminescence and electroluminescence from optically inactive thermally activated delayed fluorescence material 4CzIPN

Takumi Kuroda[1], Maho Kitahara[1], Shigeyuki Yagi[2] and Yoshitane Imai[1]*

[1]Department of Applied Chemistry, Faculty of Science and Engineering, Kindai University, Higashi-osaka, Japan, [2]Department of Applied Chemistry, Graduate School of Engineering, Osaka Metropolitan University, Osaka, Japan

An achiral optically inactive organic luminophore, 4CzIPN, exhibits circularly polarized thermally activated delayed fluorescence when photoexcited under an external magnetic field. By embedding this luminophore in an active emission layer, an external-magnetic-field-induced circularly polarized electroluminescent device is developed in this study. The Faraday geometry of the applied magnetic field completely controls the direction of rotation of 4CzIPN-derived circularly polarized luminescence and electroluminescence.

KEYWORDS

chiral, circularly polarized organic light-emitting diode, 4CzIPN, electroluminescence, magnetic circular dichroism, magnetic circularly polarized luminescence, MCP-OLED device, thermally activated delayed fluorescence

1 Introduction

Many chiral light-emitting materials that exhibit circularly polarized luminescence (CPL) upon unpolarized photoexcitation have, in recent years, been discovered. These luminescent materials have optical properties of anisotropy factor (g_{CPL}) and high quantum yield (Φ_{PL}). Therefore, they have been used in circularly polarized light-emitting diodes (CP-LEDs) (Peeters et al., 1997; Zinna et al., 2015; Brandt et al., 2016; Zinna et al., 2017; Li et al., 2018; Frédéric et al., 2020; Jiang et al., 2020; Frédéric et al., 2021; Xie et al., 2021; Yan et al., 2021; Hara et al., 2022). Chiral organic luminophores with sharp CPL bandshapes and high anisotropy factors over a wide range of wavelengths are efficient for use in high-performance CPEL devices. However, obtaining enantiomerically pure luminescent isomers through green and economical methods is difficult. Therefore, it is very important to develop new approaches to the achievement of CPL and circularly polarized electroluminescence (CPEL). CPL and CPEL have various applications, including energy-efficient three-dimensional displays, advanced security tags, and LED-based plant growth control, and new industries using this special polarized light are expected to emerge.

Recently, thermally activated delayed fluorescence (TADF) materials have attracted attention as a third-generation luminescent material with excellent energy-conversion efficiency. This is because the small energy gap between singlet and triplet excited states facilitates endothermic conversion of the triplet to singlet exciton via an inverse intersystem crossing (Endo et al., 2009; Endo et al., 2011; Hirata et al., 2015; Hatakeyama et al., 2016; Guo et al., 2017; Spuling et al., 2018; Congrave et al., 2019). In more detail, the electric current excitation of a luminescent material, as in OLED, gives rise to the spin-statistic generation of singlet and triplet excited states in a ratio of 1:3. According to this spin statics theory, OLEDs comprising conventional fluorescent materials achieve a maximum internal quantum efficiency (IQE) of 25%. Conversely, OLEDs employing TADF emitters can utilize prompt fluorescent emission (i.e., emission from the first generated singlet excited state) as well as delayed fluorescent emission from the singlet excited state generated afterward through thermal triplet-to-singlet up-conversion. Consequently, TADF-based electroluminescent devices utilize whole excitons to achieve extremely high electricity-to-light conversion efficiency (i.e., internal quantum efficiency), theoretically as high as 100% (Uoyama et al., 2012; Zhang et al., 2012; Tao et al., 2014; Kaji et al., 2015; Liu et al., 2018; Kondo et al., 2019). TADF luminophores that exhibit CPL (Zhang et al., 2018; Sharma et al., 2019; Yang et al., 2020; Frédéric et al., 2021) and circularly polarized organic light-emitting diodes (CP-OLEDs) using chiral TADF luminophores that exhibit CPEL (Feuillastre et al., 2016; Wang et al., 2019; Frédéric et al., 2020; Frédéric et al., 2021; Xie et al., 2021) have also attracted considerable attention.

However, CPL materials and CP-OLEDs using TADF also require optical isomers with a high enantiomeric purity. Therefore, new and innovative approaches are required to more conveniently realize CPL and CPEL from TADF materials. One solution to this challenge is to utilize the magnetic circular dichroism (MCD) theory proposed by Riehl and Richardson (Riehl and Richardson, 1977; Ghidinelli et al., 2021) to induce CPL because MCPL can be viewed as the reverse process of MCD. According to this theory, as a versatile physical bias, external static magnetic fields can induce chiral spectral signals from both ground and photoexcited states in many achiral and racemic optically inactive organic, organometallic, and inorganic luminescent materials (Rikken and Raupach, 1997; Valiev et al., 2014; Knowles et al., 2015; Wu et al., 2017; Ivchenko, 2018; Ghidinelli et al., 2020; Imai, 2020; Imai, 2021; Kitahara et al., 2021; Zhang et al., 2021; Hara et al., 2022).

Pyrene-based chiral organic luminescent materials exhibit CPL. We recently found that an achiral optically inactive pyrene luminescent molecule exhibits external-magnetic-field-driven CPL (MCPL) when photoexcited under a 1.6 T external magnetic field (Kaji et al., 2020). Notably, the signs of these MCPL spectra could be completely controlled by modulating the Faraday configuration of the applied external magnetic field direction [N→S (N-up) and S→N (S-up)]. In the Faraday configuration here, the direction of the light is parallel to that of the magnetic field, and N-up and S-up represent the parallel and antiparallel configurations of the longitudinal magnetic field, respectively, concerning the unpolarized incoming light.

In this work, we successfully generated MCPL by photoexciting TADF-active 1,2,3,5-tetrakis(carbazol-9-yl)-4,6-dicyanobenzene (or 2,4,5,6-tetrakis(9*H*-carbazol-9-yl)isophthalonitrile (4CzIPN) in solution and poly(methyl methacrylate) (PMMA)-film states under a 1.7 T external magnetic field (Figure 1). Furthermore, a new magnetic circularly polarized organic light-emitting diode (MCP-OLED) incorporating 4CzIPN as an emitting dopant has been successfully developed. By applying a 1.7 T external magnetic field and an appropriate voltage to the developed MCP-OLED, magnetic circularly polarized electroluminescence (MCPEL) could be emitted. Furthermore, by changing the Faraday configuration of the applied external magnetic field from N-up to S-up, the transition sign between the MCPL and MCPEL processes was completely controlled.

2 Methods

2.1 Production of the MCP-OLED device

4CzIPN was purchased from Sigma-Aldrich Japan (Tokyo, Japan). Indium tin oxide (ITO) substrates were ultrasonically cleaned in solution using ultrapure water and an alkaline detergent. The cleaned substrate surface was wetted with isopropyl alcohol vapor and treated with ultraviolet ozone. All organic thin films and Al were then deposited on the substrate

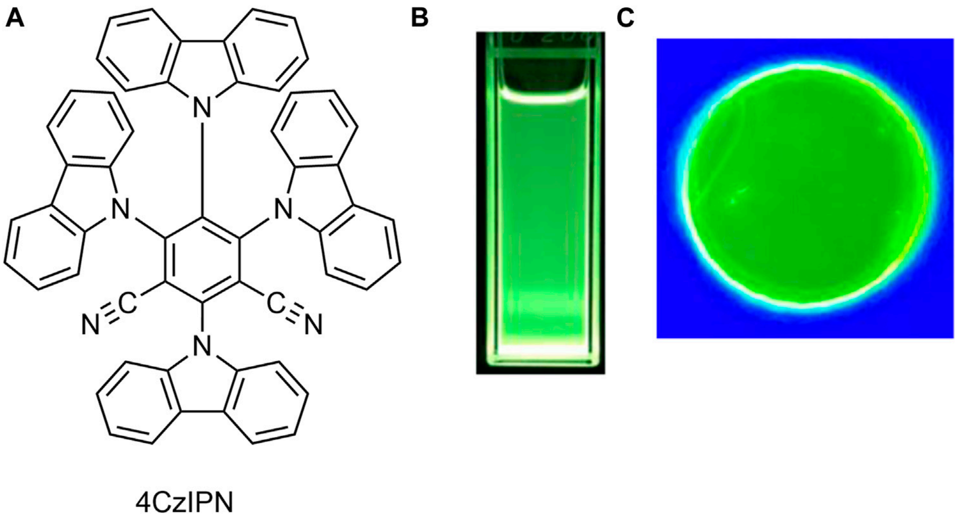

FIGURE 1
Molecular structure of **(A)** the achiral TADF luminophore, 4CzIPN, and photographs of emitting samples of 4CzIPN in **(B)** deoxygenated $CHCl_3$ and **(C)** PMMA film under 365 nm light.

using the vacuum evaporation method. During deposition, the temperature and deposition rate of the deposition source were precisely controlled to adjust the doping concentration of the luminescent active layer. Specifically, organic layers, such as HATCN, NPD, TCTA, DBT-TRZ, and Liq, were thermally evaporated under 10^{-5} Pa at a deposition rate of 0.1–2.0 Å/s. For the co-evaporated layers of the luminescent active layer (EML and nBphen:Liq), the constituent ratio was adjusted by tuning the vacuum-deposition rates of each material. The deposition system was connected to a glove box via a load lock chamber, and oxygen and moisture concentrations were controlled to <10 ppm. Thus, during device fabrication, the substrate with layer-by-layer thin films of the constituent materials was almost shielded from oxygen and moisture. After deposition, the devices were completely sealed in a glass container to protect them from the external atmosphere.

2.2 MCD and ultraviolet (UV)–visible absorption spectroscopy

The MCD and ultraviolet (UV)–visible absorption spectra of 4CzIPN in a deoxygenated $CHCl_3$ solution and a PMMA doped film were recorded using a JASCO J-1700 spectropolarimeter (Hachioji, Tokyo, Japan) at 25°C. An external magnetic field of 1.7 T was applied using a JASCO PM-491 permanent magnet. The bandwidth was set to 2 nm, the scan rate was 100 nm/min, and the spectrum was measured for single acquisition. The optical path length for the solution-state measurement was 5 mm. The PMMA films incorporated with 4CzIPN for MCD and UV–visible absorption spectroscopy were prepared using the same method described for preparing samples for MCPL and magnetic photoluminescence (MPL) evaluations.

2.3 MCPL and MPL spectroscopy

The MCPL and MPL spectra of 4CzIPN were recorded at 25°C using a JASCO CPL-300 spectrofluoropolarimeter (Hachioji, Tokyo, Japan). A 1.7 T external magnetic field was applied using a JASCO PM-491 permanent magnet. Spectra were recorded under unpolarized monochromatic UV light (380 nm) excitation with a bandwidth of 10 nm and a scattering angle of 0°. The optical path length for spectroscopic measurements in solution was 5 mm. The 4CzIPN-doped PMMA films were prepared by the spin-coating method using a Mikasa spin-coater (MS-A100) (Tokyo, Japan) rotating at 3,000 rpm. A mixture of 7.9 mg of 4CzIPN and 10 mg of PMMA was dissolved in $CHCl_3$ (1.0 mL), and a portion of the solution (0.8 mL) was used for spin-coating to prepare a 4CzIPN-doped PMMA film.

2.4 Evaluation of electroluminescence (EL), magnetic electroluminescence (MEL), and MCPEL

MCPEL and unpolarized MEL spectra of the MCP-OLEDs were acquired at 25°C using a JASCO CPL-300 spectrofluoropolarimeter (Hachioji, Tokyo, Japan). A 1.7 T external magnetic field was applied using a JASCO PM-491 permanent magnet. The emission bandwidth was 10 nm. The brightness of emission was recorded using a BM-9 luminance meter (TOPCON TECHNOHOUSE CORPORATION, Japan). The external quantum efficiency (EQE) of the fabricated device was evaluated at 25 °C using a Hamamatsu Photonics C-9920-11 organic EL device evaluating system (Hamamatsu, Japan).

3 Results and discussion

3.1 MCD and MCPL properties of 4CzIPN

4CzIPN is an achiral optically inactive compound; neither circular dichroism (CD) nor CPL was observed under ambient conditions. Therefore, we investigated the magnetic-field-induced CD and CPL (MCD and MCPL) properties of 4CzIPN dissolved in deoxygenated $CHCl_3$ by applying a 1.7 T external magnetic field. The experimental MCD, MCPL, and MPL spectra obtained under the applied magnetic field are shown in Figures 2A, B, respectively. Although 4CzIPN is an optically inactive luminophore, the MCD cotton effects were observed at 324, 350, 429, and 454 nm. As expected, a set of mirror-symmetric MCPL signals corresponding to the MPL signal was observed at 525 nm. Notably, when the direction of the applied external magnetic field was reversed (N-up or S-up), the signs of the MCD (blue line for S-up and red line for N-up) and MCPL (blue line for S-up and red line for N-up) spectra were also reversed.

The magnitude of circular polarization in the ground state is expressed by the MCD anisotropy factor given by the equation:

$$g_{\mathrm{MCD}} = \frac{(\mathrm{Abs_L} - \mathrm{Abs_R})}{[(\mathrm{Abs_L} + \mathrm{Abs_R})/2]}$$

In this equation, $\mathrm{Abs_L}$ and $\mathrm{Abs_R}$ represent the absorbances of left- and right-rotating circularly polarized light, respectively, under an external magnetic field. In contrast, to quantitatively evaluate the magnitude of MCPL, the MCPL anisotropy coefficient, given by

$$g_{\mathrm{MCPL}} = \frac{(I_{\mathrm{L}} - I_{\mathrm{R}})}{[(I_{\mathrm{L}} + I_{\mathrm{R}})/2]}$$

was investigated. In this equation, I_L and I_R are the intensities of the left- and right-rotating MCPL, respectively, observed upon unpolarized UV light excitation under a magnetic field. In other words, a positive sign in the MCPL spectrum indicates left-handed circularly polarized emission, whereas a negative sign indicates right-handed circularly polarized emission. The absolute values of the anisotropy factors of 4CzIPN, $|g_{\mathrm{MCD}}|$ and $|g_{\mathrm{MCPL}}|$, in the $CHCl_3$ solution were 2.1×10^{-4} (T^{-1}) at the longest magnetic circular dichroic absorption wavelength (λ_{MCD}) of 454 nm and 4.6×10^{-4} (T^{-1}) at the MCPL wavelength (λ_{MCPL}) of 525 nm, respectively.

When considering the use of 4CzIPN as an emitting dopant in an MCPEL device, it is important to study its chiroptical properties in a solid film state rather than in a solution state. This is because luminescence phenomena in a solution and solid matrix often differ significantly, and studying the luminescence behavior in solid organic media, such as PMMA polymers, is important for predicting the field emission behavior of OLEDs.

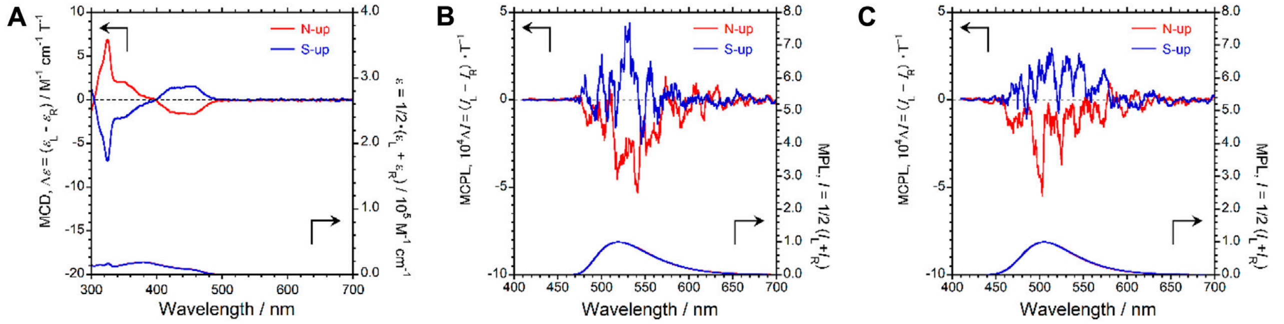

FIGURE 2
MCD (top panel) and UV–visible absorption spectra (bottom panel) of 4CzIPN in **(A)** deoxygenated $CHCl_3$ (conc = 1.0×10^{-4} M). MCPL (top) and MPL spectra (bottom) of 4CzIPN in **(B)** deoxygenated $CHCl_3$ (conc = 1.0×10^{-3} M) and **(C)** PMMA-film state under magnetic fields (1.7 T). Red and blue lines show N-up and S-up Faraday geometries, respectively.

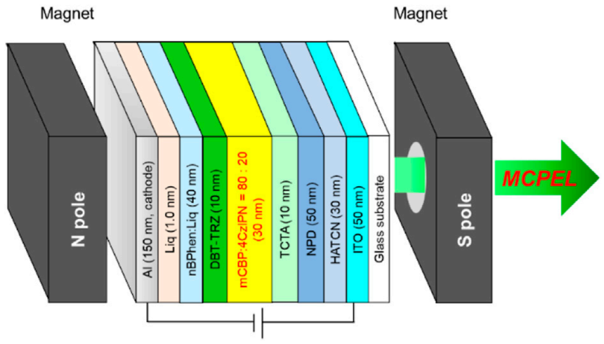

FIGURE 3
Configuration diagram of the MCP-OLED system composed of OLED structure and small interchangeable N- and S-pole magnets.

Therefore, we doped 4CzIPN in a PMMA film and investigated the MCPL properties of the resultant film. When the 4CzIPN-incorporated PMMA film was photoexcited under a 1.7 T external magnetic field, a set of mirror-image MCPL spectra was observed at 508 nm, the spectral shapes of which correspond to that of the MPL spectrum, as shown in Figure 2C. Notably, as observed in the solution state, the sign of the MCPL spectrum (blue and red lines for S-up and N-up, respectively) could be completely reversed by changing the direction of the applied magnetic field from N-up to S-up. The absolute value of the anisotropy factor $|g_{MCPL}|$ of MCPL exhibited by the 4CzIPN-doped PMMA film was 4.3×10^{-4} (T^{-1}).

As described, although 4CzIPN is an optically inactive luminescent material, MCPL was successfully observed in both the $CHCl_3$ solution state and the PMMA-film state upon photoexcitation under an external magnetic field. A slight increase in the anisotropy factor was observed in the excited state in relation to that in the ground state. Conversely, no significant difference was observed in the anisotropy factors of the excited states of the luminophore in the $CHCl_3$ solution and PMMA-film states. This result indicates that the effect observed under the external magnetic field does not depend on the external environment of the luminophore, i.e., fluidic $CHCl_3$ or solid PMMA.

3.2 Evaluation of device properties

The OLED using 4CzIPN as an emitting dopant in the active emission layer was fabricated and investigated for its MCPEL properties. The direction of the applied external magnetic field was changed to N-up and S-up, and the MCPEL profiles were obtained at room temperature.

The multi-stack structure of the fabricated 4CzIPN-based device is shown in Figure 3. It was structured as follows: ITO (anode, 50 nm)/HATCN (30 nm)/NPD (50 nm)/TCTA (10 nm)/emission layer (EML, 30 nm)/DBT-TRZ (10 nm)/nBPhen:Liq (40 nm)/Liq (1.0 nm)/Al (cathode, 150 nm). In this, HATCN, NPD, TCTA, DBT-TRZ, nBPhen:Liq and Liq are abbreviations for 1,4,5,8,9,11-hexaazatriphenylenehexacarbonitrile, *N*,*N*′-di-1-naphthyl-*N*,*N*′-diphenylbenzidine, 4,4′,4″-tri(9-carbazolyl)triphenylamine, 2-(3’-(dibenzo[*b*,*d*]thiophen-4-yl)-[1,1′-biphenyl]-3-yl)-4,6-diphenyl-1,3,5-triazine, 2,9-bis(naphthalen-2-yl)-4,7-diphenyl-1,10-phenanthroline: lithium quinolin-8-olate, and lithium quinolin-8-olate, respectively. The EML consists of 3,3′-di(9*H*-carbazol-9-yl)-1,1′-biphenyl (mCBP) and 4CzIPN at 80/20 w/w. HATCN is a charge-generation and hole-injection layer, facilitating the generation-injection of positively charged carriers (holes) to the organic layers from the ITO anode. NPD and TCTA are hole-transporting layers with p-type semiconducting characteristics, which receive holes from the neighboring hole-injection layer and inject them into the EML. DBT-TRZ is a hole-blocking layer with a deep highest occupied molecular orbital (HOMO) of 6.2 eV below the vacuum level (Saito et al., 2021). As the host matrix of the EML is mCBP with p-type semiconducting characters, the holes are blocked and pooled at the EML/DBT-TRZ interface. nBPhen:Liq is an electron-transporting layer with n-type semiconducting characteristics, facilitating the injection of electrons to the EML via the DBT-TRZ layer. Liq is an electron-injection layer to assist the smooth insertion of electrons from the Al cathode to the electron-transporting layer. This type of multi-stacked device structure allows us to achieve efficient hole–electron recombination at the EML through the well-ordered, unidirectional injection of holes and electrons from the anode and cathode, respectively, achieving a high luminous efficiency. The current density–voltage–luminance (*J*–*V*–*L*) curves, the EL spectrum, and the related parameters were recorded; the corresponding results are shown in Figure 4 and summarized in Table 1.

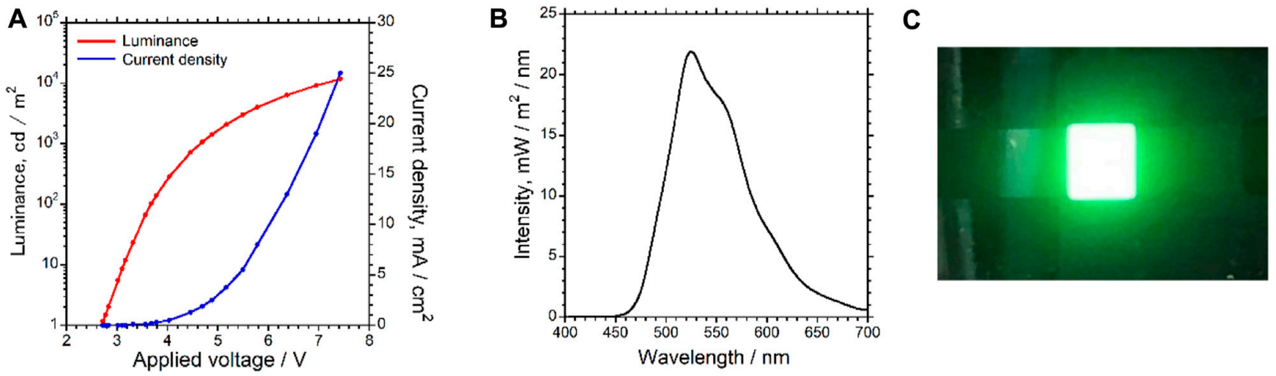

FIGURE 4
(A) Current density vs. voltage vs. luminance (*J*–*V*–*L*) profiles and **(B)** electroluminescence (EL) spectrum for the 4CzIPN-based device. **(C)** Photograph of the 4CzIPN-based device upon application of an electric voltage of 8 V.

TABLE 1 Performance of the 4CzIPN-based device.

λ_{EL} (nm)	V_{on}[a] (V)	L_{max}[b] (cd·m^{-2}) [@V]	$\eta_{j,\ max}$[b] (cd·A^{-1}) [@V]	CIE (*x, y*)[c]	EQE$_{max}$[d] (%) [@V]
524	2.7	11770 [7.4]	57.44 [4.5]	(0.34, 0.59)	15.5 [6.5]

[a]Turn-on voltage at which a luminance of 1 cd m^{-2} or higher was obtained. [b] Maximum values of luminance (*L*) and current efficiency (η_j). Corresponding operating voltages are provided in parentheses. [c] Commission Internationale de L'Eclairage (CIE) chromaticity coordinates. [d] Maximum value of the EQE.

As seen in the *J*–*V*–*L* curves (Figure 4A), the fabricated device exhibited a semiconductive behavior and started to emit green EL upon applying a voltage of 2.7 V, as seen in Figures 4B, C. When a voltage of 7.4 V was applied to this device, the maximum luminance (L_{max}) was 11770 cd m^{-2} at 7.4 V, indicating that the device performance was suitable for MEL and MCPEL data acquisition under an externally applied magnetic field. Figure 4B shows that the EL spectrum was almost comparable to the PL spectrum of 4CzIPN, in which no emission from the host material mCBP was observed. Thus, charge carrier and/or exciton transfer from mCBP to 4CzIPN occurred efficiently. The Commission Internationale de L'Eclairage chromaticity coordinates at the L_{max} were to be (x, y) (0.34, 0.59). Furthermore, the device parameters shown in Table 1 suggest that the present device exhibits highly efficient device performance. Notably, the EQE of the device (maximum value: 15.5% at 6.5 V) was considerably higher than the theoretical limit of EQE for conventional fluorescent OLEDs (~5%) (Uoyama et al., 2012), which is a characteristic of TADF-based OLEDs. This result strongly suggests that the observed EL consisted of prompt and delayed fluorescence emissions from 4CzIPN. Therefore, the fabricated 4CzIPN-containing OLED device should be a suitable candidate for TADF-based MCPEL devices.

Next, under a 1.7 T magnetic field, the MCPEL properties of the 4CzIPN-based device were studied at 25°C. In the measurement of the MCPEL and MEL characteristics of this device, the applied voltage was fixed at 8 V. Figure 5 shows the obtained MCPEL and MEL spectra. As expected, we succeeded in obtaining green MCPEL from the 4CzIPN-based device although it is composed entirely of achiral and optically inactive components. Furthermore, mirror-image MCPEL spectra were recorded upon alternating the Faraday configuration of the N-up/S-up external magnetic fields. These results prove that the direction of rotation of MCPEL exhibited by the device can be easily controlled by changing the direction of the applied external magnetic field.

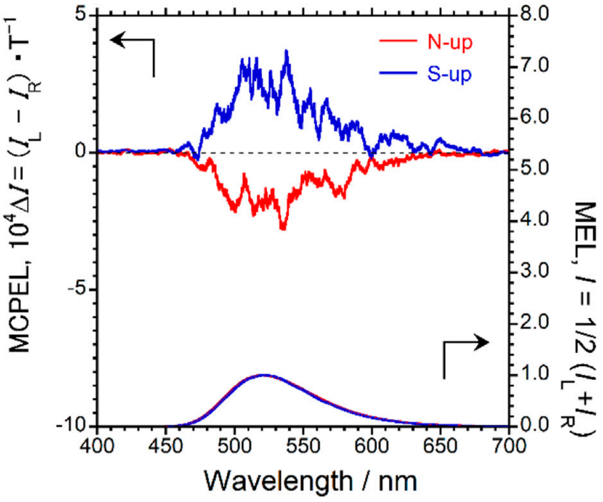

FIGURE 5
MCPEL (top panel) and MEL (bottom panel) spectra of the 4CzIPN-based device under magnetic fields (1.7 T). Red and blue lines show N-up and S-up Faraday geometry, respectively.

The MCPEL and MEL spectra of the 4CzIPN-based device were similar to the MCPL and MPL spectra of 4CzIPN in the PMMA-film state, respectively. It is very common that the EL spectra of OLEDs and the PL spectra of emitting materials used are similar. When comparing the MCPEL spectra of the device to the MCPL spectra of the emitting material, the signs of the MCPEL and MCPL spectra were observed to be negative (−) in the N-up geometry, whereas they were positive (+) in the S-up geometry. In other words, the direction of rotation of MCPEL exhibited by this device was the same as that of MCPL exhibited by the same 4CzIPN luminescent material in $CHCl_3$ solution and under PMMA-film conditions. This comparison shows that this generalization also applies to the present 4CzIPN-based device.

The performance of the devices that exhibit MCPEL upon the application of an external magnetic field is quantitatively evaluated using the anisotropy factor,

$$g_{\mathrm{MCPEL}} = \frac{(I_{\mathrm{L}} - I_{\mathrm{R}})}{[(I_{\mathrm{L}} + I_{\mathrm{R}})/2]}$$

similar to the performance evaluation of CPEL. I_L and I_R are the amplitude intensities of the left- and right-handed MCPEL, respectively. As with the MCPL spectrum, positive sign in the MCPEL spectrum indicate leftward circularly polarized electroluminescence, whereas negative sign indicate rightward circularly polarized electroluminescence. For this 4CzIPN-based device, the anisotropy factor $|g_{\mathrm{MCPEL}}|$ was 3.7×10^{-4} (T^{-1}) at 537 nm. In general, the anisotropy factor of the CP-OLED devices decreases when multiple interfaces of the multilayer device interfere unfavorably with circular polarization. However, the $|g_{\mathrm{MCPEL}}|$ value of this 4CzIPN-based was almost identical to the corresponding values obtained from a $CHCl_3$ solution (4.6×10^{-4} (T^{-1}) at 525 nm) or a PMMA film (4.3×10^{-4} (T^{-1}) at 508 nm). This indicates that, in this 4CzIPN-based system, the circular polarization of the photoexcited luminescence and the electroluminescence are the same.

These results indicate that efficient MCPEL can be observed under a 1.7 T magnetic field and at an appropriate voltage for OLEDs containing optically inert 4CzIPN emitters. This study, using TADF-active 4CzIPN, is the first example of MCPEL generated from TADF-OLED and shows that it is possible to promote the development of highly functional MCPEL devices using optically inactive TADF luminescent materials with various functionalities.

4 Conclusion

Optically inactive 4CzIPN with TADF properties does not exhibit CPL under conventional photoexcitation conditions. However, upon applying a 1.7 T external magnetic field, it exhibited MCPL. Furthermore, an MCP-OLED using 4CzIPN as an emitting dopant exhibited green MCPEL under a 1.7 T magnetic field. The chiroptical sign of MCPEL exhibited by this device could be accurately controlled by modulating the Faraday geometry of the magnetic field (N-up or S-up), which was observed with the chiroptical sign of the MCPL of 4CzIPN. This external-magnetic-field-driven MCP-OLED device is expected to have promising application potential in CPEL and spin-LED devices.

Data availability statement

The original contributions presented in the study are included in the article/Supplementary Material, further inquiries can be directed to the corresponding author.

Author contributions

TK: Data curation, Formal Analysis, Investigation, Writing–original draft. MK: Data curation, Formal Analysis, Investigation, Writing–review and editing. SY: Formal Analysis, Writing–review and editing. YI: Conceptualization, Writing–original draft.

Funding

The authors declare financial support was received for the research, authorship, and/or publication of this article. This research was supported by the JST-CREST (JPMJCR2001), JST-A-STEP (JPMJTM22D9), Grants-in-Aid for Scientific Research (KAKENHI JP21K18940 and JP23H02040) from the MEXT/Japan Society for the Promotion of Science, and grants from the Takahashi Industrial and Economic Research Foundation (2020), Research Foundation for Opto-Science and Technology (2020-5), Ichimura Foundation for New Technology (2020-04), and SCAT Foundation (2021).

Conflict of interest

The authors declare that the research was conducted in the absence of any commercial or financial relationships that could be construed as a potential conflict of interest.

Publisher's note

References

Brandt, J. R., Wang, X., Yang, Y., Campbell, A. J., and Fuchter, M. J. (2016). Circularly polarized phosphorescent electroluminescence with a high dissymmetry factor from PHOLEDs based on a platinahelicene. *J. Am. Chem. Soc.* 138, 9743–9746. doi:10.1021/jacs.6b02463

Congrave, D. G., Drummond, B. H., Conaghan, P. J., Francis, H., Jones, S. T. E., Grey, C. P., et al. (2019). A simple molecular design strategy for delayed fluorescence toward 1000 nm. *J. Am. Chem. Soc.* 141, 18390–18394. doi:10.1021/jacs.9b09323

Endo, A., Ogasawara, M., Takahashi, A., Yokoyama, D., Kato, Y., and Adachi, C. (2009). Thermally activated delayed fluorescence from Sn^{4+}-porphyrin complexes and their application to organic light-emitting diodes – a novel mechanism for electroluminescence. *Adv. Mater.* 21, 4802–4806. doi:10.1002/adma.200900983

Endo, A., Sato, K., Yoshimura, K., Kai, T., Kawada, A., Miyazaki, H., et al. (2011). Efficient up-conversion of triplet excitons into a singlet state and its application for organic light emitting diodes. *Appl. Phys. Lett.* 98, 083302. doi:10.1063/1.3558906

Feuillastre, S., Pauton, M., Gao, L., Desmarchelier, A., Riives, A. J., Prim, D., et al. (2016). Design and synthesis of new circularly polarized thermally activated delayed fluorescence emitters. *J. Am. Chem. Soc.* 138, 3990–3993. doi:10.1021/jacs.6b00850

Frédéric, L., Desmarchelier, A., Favereau, L., and Pieters, G. (2021). Designs and applications of circularly polarized thermally activated delayed fluorescence molecules. *Adv. Funct. Mater.* 31, 2010281. doi:10.1002/adfm.202010281

Frédéric, L., Desmarchelier, A., Plais, R., Lavnevich, L., Muller, G., Villafuerte, C., et al. (2020). Maximizing chiral perturbation on thermally activated delayed fluorescence emitters and elaboration of the first top-emission circularly polarized OLED. *Adv. Funct. Mater.* 30, 2004838. doi:10.1002/adfm.202004838

Ghidinelli, S., Abbate, S., Mazzeo, G., Paolesse, R., Pomarico, G., and Longhi, G. (2021). MCD and MCPL characterization of luminescent Si(IV) and P(V) tritolylcorroles: the role of coordination number. *ACS Omega* 6, 26659–26671. doi:10.1021/acsomega.1c04028

Ghidinelli, S., Abbate, S., Mazzeo, G., Paoloni, L., Viola, E., Ercolani, C., et al. (2020). Characterization of tetrakis(thiadiazole)porphyrazine metal complexes by magnetic circular dichroism and magnetic circularly polarized luminescence. *Chirality* 32, 808–816. doi:10.1002/chir.23221

Guo, J., Li, X., Nie, H., Luo, W., Gan, S., Hu, S., et al. (2017) Achieving high-performance nondoped OLEDs with extremely small efficiency Roll-Off by combining aggregation-induced emission and thermally activated delayed fluorescence. *Adv. Funct. Mater.* 27, 1606458 (9 pages). doi:10.1002/adfm.201606458

Hara, K., Morimoto, A., Matsudaira, K., Suzuki, S., Yagi, S., Fujiki, M., et al. (2022). External magnetic field driven, ambidextrous circularly polarized electroluminescence from organic light emitting diodes containing racemic cyclometalated iridium(III) complexes. *ChemPhotoChem* 6, e202100253. doi:10.1002/cptc.202100253

Hatakeyama, T., Shiren, K., Nakajima, K., Nomura, S., Nakatsuka, S., Kinoshita, K., et al. (2016). Ultra pure blue thermally activated delayed fluorescence molecules: efficient HOMO–LUMO separation by the multiple resonance effect. *Adv. Mater.* 28, 2777–2781. doi:10.1002/adma.201505491

Hirata, S., Sakai, Y., Masui, K., Tanaka, H., Lee, S. Y., Nomura, H., et al. (2015). Highly efficient blue electroluminescence based on thermally activated delayed fluorescence. *Nat. Mater.* 14, 330–336. doi:10.1038/nmat4154

Imai, Y. (2021). Circularly polarized luminescence (CPL) induced by an external magnetic field: magnetic CPL (MCPL). *ChemPhotoChem* 5, 969–973. doi:10.1002/cptc.202100142

Imai, Y. (2020). Generation of circularly polarized luminescence by symmetry breaking. *Symmetry* 12, 1786 (13). doi:10.3390/sym12111786

Ivchenko, E. L. (2018). Magnetic circular polarization of exciton photoluminescence. *Phys. Solid State.* 60, 1514–1526. doi:10.1134/S1063783418080127

Jiang, Z., Wang, J., Gao, T., Ma, J., Liu, Z., and Chen, R. (2020). Rational design of axially chiral Platinabinaphthalenes with aggregation-induced emission for red circularly polarized phosphorescent organic light-emitting diodes. *ACS Appl. Mater. Interfaces.* 12, 9520–9527. doi:10.1021/acsami.9b20568

Kaji, D., Okada, H., Hara, N., Kondo, Y., Suzuki, S., Miyasaka, M., et al. (2020). Non-classically controlled sign in a 1.6 Tesla magnetic circularly polarized luminescence of three pyrenes in a chloroform and a PMMA film. *Chem. Lett.* 49, 674–676. doi:10.1246/cl.200136

Kaji, H., Suzuki, H., Fukushima, T., Shizu, K., Suzuki, K., Kubo, S., et al. (2015). Purely organic electroluminescent material realizing 100% conversion from electricity to light. *Nat. Commun.* 6, 8476 (8). doi:10.1038/ncomms9476

Kitahara, M., Suzuki, S., Matsudaira, K., Yagi, S., Fujiki, M., and Imai, Y. (2021). Red–green-blue-yellow (RGBY) magnetic circularly polarised luminescence (MCPL) from optically inactive phosphorescent Ir(III) complexes. *ChemistrySelect* 6, 11182–11187. doi:10.1002/slct.202103117

Knowles, K. E., Nelson, H. D., Kilburn, T. B., and Gamelin, D. R. (2015). Singlet–triplet splittings in the luminescent excited states of colloidal Cu^+:CdSe, Cu^+:InP, and $CuInS_2$ nanocrystals: charge-transfer configurations and self-trapped excitons. *J. Am. Chem. Soc.* 137, 13138–13147. doi:10.1021/jacs.5b08547

Kondo, Y., Yoshiura, K., Kitera, S., Nishi, H., Oda, S., Gotoh, H., et al. (2019). Narrowband deep-blue organic light-emitting diode featuring an organoboron-based emitter. *Nat. Photonics.* 13, 678–682. doi:10.1038/s41566-019-0476-5

Li, M., Li, S. H., Zhang, D., Cai, M., Duan, L., Fung, M. K., et al. (2018). Stable enantiomers displaying thermally activated delayed fluorescence: efficient OLEDs with circularly polarized electroluminescence. *Angew. Chem. Int. Ed.* 57, 2889–2893. doi:10.1002/anie.201800198

Liu, H., Zeng, J., Guo, J., Nie, H., Zhao, Z., and Tang, B. Z. (2018). High-performance non-doped OLEDs with nearly 100% exciton use and negligible efficiency roll-off. *Angew. Chem. Int. Ed. Engl.* 57, 9290–9294. doi:10.1002/anie.201802060

Peeters, E., Christiaans, M. P. T., Janssen, R. A. J., Schoo, H. F. M., Dekkers, H. P. J. M., and Meijer, E. W. (1997). Circularly polarized electroluminescence from a polymer light-emitting diode. *J. Am. Chem. Soc.* 119, 9909–9910. doi:10.1021/ja971912c

Riehl, J. P., and Richardson, F. S. (1977). Theory of magnetic circularly polarized emission. *J. Chem. Phys.* 66, 1988–1998. doi:10.1063/1.434156

Rikken, G. L. J. A., and Raupach, E. (1997). Observation of magneto-chiral dichroism. *Nature* 390, 493–494. doi:10.1038/37323

Saito, D., Sasabe, H., Kikuchi, T., Ito, T., Tsuneyama, H., and Kido, J. (2021). Improved operational lifetime of deep-red phosphorescent organic light-emitting diodes using a benzothienobenzothiophene (BTBT)-based p-type host material. *J. Mater. Chem. C* 9, 1215–1220. doi:10.1039/D0TC05234E

Sharma, N., Spuling, E., Mattern, C. M., Li, W., Fuhr, O., Tsuchiya, Y., et al. (2019). Turn on of sky-blue thermally activated delayed fluorescence and circularly polarized luminescence (CPL) via increased torsion by a bulky carbazolophane donor. *Chem. Sci.* 10, 6689–6696. doi:10.1039/c9sc01821b

Spuling, E., Sharma, N., Samuel, I. D. W., Zysman-Colman, E., and Bräse, S. (2018). Deep blue through-space conjugated TADF emitters based on [2.2]paracyclophanes. *Chem. Commun. (Camb).* 54, 9278–9281. doi:10.1039/c8cc04594a

Tao, Y., Yuan, K., Chen, T., Xu, P., Li, H., Chen, R., et al. (2014). Thermally activated delayed fluorescence materials towards the breakthrough of organoelectronics. *Adv. Mater.* 26, 7931–7958. doi:10.1002/adma.201402532

Uoyama, H., Goushi, K., Shizu, K., Nomura, H., and Adachi, C. (2012). Highly efficient organic light-emitting diodes from delayed fluorescence. *Nature* 492, 234–238. doi:10.1038/nature11687

Valiev, U. V., Gruber, J. B., Burdick, G. W., Mukhammadiev, A. K., Fu, D., and Pelenovich, V. O. (2014). Analysis of the optical and magnetooptical spectra of non-Kramers $Pr^{3+}(4f^2)$ in $Y_3Al_5O_{12}$ complemented by crystal-field modelling. *J. Lumin.* 145, 393–401. doi:10.1016/j.jlumin.2013.07.070

Wang, Y., Zhang, Y., Hu, W., Quan, Y., Li, Y., and Cheng, Y. (2019). Circularly polarized electroluminescence of thermally activated delayed fluorescence-active chiral binaphthyl-based luminogens. *ACS Appl. Mater. Interfaces.* 11, 26165–26173. doi:10.1021/acsami.9b07005

Wu, T., Kapitán, J., Andrushchenko, V., and Bouř, P. (2017). Identification of lanthanide(III) luminophores in magnetic circularly polarized luminescence using Raman optical activity instrumentation. *Anal. Chem.* 89, 5043–5049. doi:10.1021/acs.analchem.7b00435

Xie, F. M., Zhou, J. X., Zeng, X. Y., An, Z. D., Li, Y. Q., Han, D. X., et al. (2021). Efficient circularly polarized electroluminescence from chiral thermally activated delayed fluorescence emitters featuring symmetrical and rigid coplanar acceptors. *Adv. Opt. Mater.* 9, 2100017. doi:10.1002/adom.202100017

Yan, Z. P., Liu, T. T., Wu, R., Liang, X., Li, Z. Q., Zhou, L., et al. (2021). Chiral thermally activated delayed fluorescence materials based on *R*/*S*-*N*2,*N*2'-Diphenyl-[1,1'-binaphthalene]-2,2'-diamine donor with narrow emission spectra for highly efficient circularly polarized electroluminescence. *Adv. Funct. Mater.* 31, 2103875 (10). doi:10.1002/adfm.202103875

Yang, S. Y., Wang, Y. K., Peng, C. C., Wu, Z. G., Yuan, S., Yu, Y. J., et al. (2020). Circularly polarized thermally activated delayed fluorescence emitters in through-space charge transfer on asymmetric spiro skeletons. *J. Am. Chem. Soc.* 142, 17756–17765. doi:10.1021/jacs.0c08980

Zhang, J., Dai, L., Webster, A. M., Chan, W. T. K., Mackenzie, L. E., Pal, R., et al. (2021). Unusual magnetic field responsive circularly polarized luminescence probes with highly emissive chiral europium(III) complexes. *Angew. Chem. Int. Ed.* 60, 1004–1010. doi:10.1002/anie.202012133

Zhang, M. Y., Li, Z. Y., Lu, B., Wang, Y., Ma, Y. D., and Zhao, C. H. (2018). Solid-state emissive triarylborane-based [2.2]paracyclophanes displaying circularly polarized luminescence and thermally activated delayed fluorescence. *Org. Lett.* 20, 6868–6871. doi:10.1021/acs.orglett.8b02995

Zhang, Q., Li, J., Shizu, K., Huang, S., Hirata, S., Miyazaki, H., et al. (2012). Design of efficient thermally activated delayed fluorescence materials for pure blue organic light emitting diodes. *J. Am. Chem. Soc.* 134, 14706–14709. doi:10.1021/ja306538w

Zinna, F., Giovanella, U., and Bari Di, L. (2015). Highly circularly polarized electroluminescence from a chiral europium complex. *Adv. Mater.* 27, 1791–1795. doi:10.1002/adma.201404891

Zinna, F., Pasini, M., Galeotti, F., Botta, C., Di Bari, L. D., and Giovanella, U. (2017). Design of lanthanide-based OLEDs with remarkable circularly polarized electroluminescence. *Adv. Funct. Mater.* 27, 1603719. doi:10.1002/adfm.201603719

Nomenclature

4CzIPN	1,2,3,5-tetrakis (carbazol-9-yl)-4,6-dicyanobenzene (or 2,4,5,6-tetrakis (9*H*-carbazol-9-yl)isophthalonitrile)
MCPEL	Magnetic-field-driven circularly polarized electroluminescence
MCPL	Magnetic-field-driven circularly polarized luminescence
MPL	Magnetic photoluminescence
OLED	Organic light-emitting diode
PMMA film	Poly (methyl methacrylate) film
TADF	Thermally activated delayed fluorescence
CD	Circular dichroism

Frontiers in Chemistry

Explores all fields of chemical science across the periodic table

Advances our understanding of how atoms, ions, and molecules come together and come apart. It explores the role of chemistry in our everyday lives - from electronic devices to health and wellbeing.

Discover the latest Research Topics

See more →

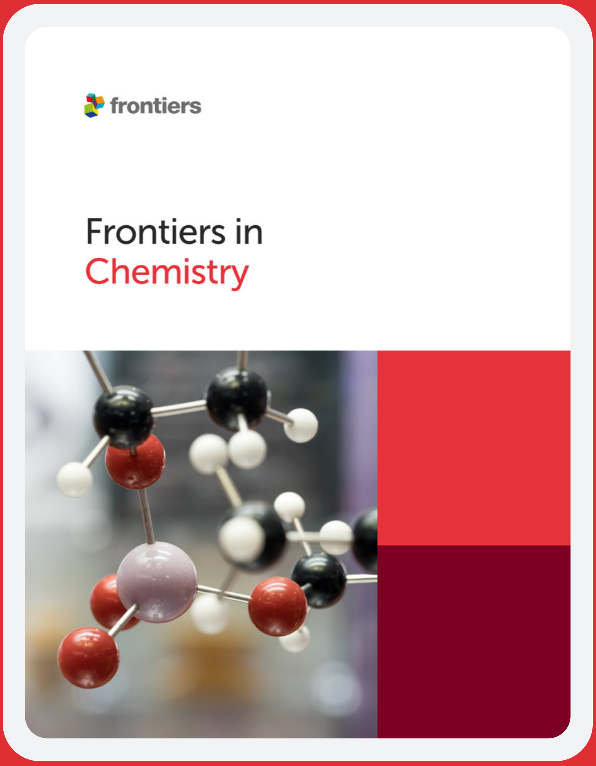

Frontiers

Avenue du Tribunal-Fédéral 34
1005 Lausanne, Switzerland
frontiersin.org

Contact us

+41 (0)21 510 17 00
frontiersin.org/about/contact